Modelling Shallow Landslides: The Importance of Hydrological Controls and Lateral Reinforcement

David Graham Milledge

A thesis submitted in fulfilment of the requirements for the degree of Doctor of Philosophy

Department of Geography

Durham University

September 2008

Declaration of Copyright

I confirm that no part of the material presented in this thesis has previously been submitted by me or any other persons for a degree in this or any other University. In all cases, where it is relevant, material from the work of others has been acknowledged. The copyright of this thesis rests with the author, information derived from it should be acknowledged.

Signed

Date

i. Abstract

Shallow landslides are important as geomorphic agents of erosion, sources of catchment sediment and potential hazards to life and infrastructure. The importance of these mass movements is difficult to define using solely field-based approaches because these are often too limited in both duration and resolution to fully determine the magnitude and frequency of these processes. Modelling is a powerful alternative tool for providing insight into underlying processes governing shallow landslides and for testing new hypotheses regarding environmental and land-use change impacts. The explanatory power of models is a function of their process representation and predictive ability. Current models suitable for catchment-scale application provide valuable probabilistic information on failure, but not detailed deterministic predictions. Using the English Lake District as a study area, this thesis addresses three issues necessary to provide the process-basis of these probabilistic analyses.

First, poorly constrained or spatially variable input parameters such as soil depth, root reinforcement or material properties are often used to explain the locations of failure within a larger area that has a high, sometimes equal, probability of failure. The thesis develops rigorous new methods to quantify and minimise error in these parameters, representing them as distributions to capture both their natural variability and the error in their measurement. Results suggest that lateral root reinforcement even for grasses and shrubs may provide important additional strength (as much as 6 kPa) in the top 0.5 m of the soil.

Second, infinite slope stability analysis neglects important additional lateral friction and root reinforcement effects at the margins of an unstable block. More sophisticated three-dimensional stability analyses can represent this process but are limited in their applicability by computational and data resolution requirements. This thesis derives from first principles a set of analytical governing equations for three-dimensional analysis; tests these against benchmark geotechnical methods; and applies them to establish key landslide scaling relationships.

Third, shallow landslides in the UK are almost exclusively hydrologically-triggered, resulting from local high pore water pressures. In line with the current paradigm existing stability models assume that the topography plays a dominant role in defining the spatial pattern of soil moisture and therefore pore water pressures in the landscape. This hypothesis is tested: first at the hillslope scale (10^{-1} km^2) with a network of ~100 wells; then the catchment scale (10^2 km^2) using high resolution orthorectified aerial photographs to identify vegetation indicative of wet habitats and applying these as a proxy for soil moisture. These studies indicate that, for the case-study, wet areas are controlled at the landscape scale by a set of broad topographic limits in terms of slope and contributing area. Within these there is considerable scatter, resulting from the interplay of local factors such as: bedrock topography, preferential flow and soil stratification.

Lateral root cohesion represents an important source of additional strength which can be included within analytical stability equations to create a threshold dependence on landslide size. Patterns of instability will then depend on the spatial pattern of other influencing factors (e.g. soil strength and pore pressure). At present the limits to available data and our understanding of hillslope hydrology constrain our ability to predict slope instability in environments like the Lake District. Future research might usefully identify landscape scale controls on this predictability.

ii. Acknowledgements

Refreshingly, I'm told this is probably the only part of the thesis where the grammar can be somewhat postmodern, I'm also told this should fit onto one page... I will try my best. So thanks:

To Jeff for being a great supervisor and a great friend, door always open, enthusiasm unending, fieldwork super human, scepticism refreshing. To Stuart for being a spiffing top hole chap and coming up trumps when it mattered most. For being astonishingly brilliant but nice with it and for having the attitude that if I didn't understand you hadn't explained it right – something I aspire to.

To all in the Geography laboratories, in particular Eddie and Merv for putting up with my 'pragmatic' approach to field equipment; To the finance team, especially Derek H for monetary miracles and sailing chats. To Dave, Mark, Shaun and Terry for great support behind the scenes. To NERC for providing the money and then letting me get on with it; the 3.5 year idea was a great one guys! And to ERDAS inc for 24hr coffee and office space in the final throes.

To Hamish R who is largely responsible for setting me on the course I now follow. To officemates past and present: Mouldo, Emma, Dapeng, Sim, Ian, Jonah, Carly, Chris, Dave H. To Mouldo my procrastination partner for sardonic wit and healthy scepticism; to Emma for proof reading and organisational brilliance, Sim for never ending stream of random ideas and modelling related knowledge; Ian P for revisiting long dormant A-level maths with me; Fritz and Stefano for being fantastic Iti accomplices, Fritz for being extremely amusing anytime anywhere, Stefano for sacrificing time and energy and a handkerchief when it was most needed and for giving without asking anything in return; Mark S for trips to Spain discussions on water slide technique and putting up with way too much work chat. In fact on that note the Durham postgraduates for bearing the brunt of my (over)enthusiasm especially the Katies, Emma W, Tash and Nima as well as to Gareth P and James B for being cool human geographers. Alona A, Sarah C and Rich J and Andy M variously for road trip company amazing fieldwork assistance, floors to sleep on and supervisor tips. To Rob D for challenging everything, for late night tea and chat, quintessential English charm, good humour and patience. Peter and Maja S for being great role models and teaching me about petrol pumps, BBQs, baking trays... The Emmanuel Church faithful, especially John P and Jon C you guys are great; the residents of 14 the Hallgarth and Sarah L for putting up with an absentee housemate; the Dambusters as they now all are for effective distraction across the country; the Leeds church for their part in setting me on course in a different sense; Lydia, Karolyn, Tim, Sam, Ralph and Katie for unconditional and unfathomable love; the E block massive especially Dan and James, for being patient with my anti-social ways and for always being there. To the Durham contingent, Danny D, Alex D, Nicks R and O, Rich H, Wish M, Nick C, Rob F and Pat C for help on every topic from Delaunay to Devensian and back again. Further afield, to Dave M, Bill D, Jeff McD, Mike C, Jim McK, Mike K, Joe H, Dick I and Mark R for being generous with their time despite being both busy and eminent. To the American contingent: Ciaran H, Adrian H, Holly B, Doug J and Sarah G for being inspiring. To Mark W, Isa B, Claire G and Lucy C for conference related antics.

To Mum, Dad and Si, for support and understanding not just during but before and in fact consistently since 1982.

To Tori, for everything and a bit more, maybe I'll get a chance to return the favour someday.

iii. Table of Contents

4. RE-FORMULATING THE FACTOR OF SAFETY: MODEL DEVELOPMENT

5. RE-FORMULATING THE FACTOR OF SAFETY: MODEL TESTING AND SENSITIVITY ANALYSIS

iv. List of Figures

v. List of Tables

1.Thesis Aim, Background and Objectives

1.1. Thesis Aim

This thesis aims to improve our understanding of why the predictions from shallow landslide models differ from observations. In this Chapter, I justify this aim in relation to current understanding, identify a series of objectives that will allow this aim to be achieved (Objectives; Section 1.3) and describe the thesis structure (Section 1.4).

1.2. Background

Shallow landslides are important. They carve out landscapes (Rapp, 1960; Dietrich and Dunne, 1978; Hovius *et al.*, 1998); provide sediment to rivers (Benda and Dunne, 1997; Sutherland *et al.*, 2002) and can be extremely destructive (Brabb, 1993; Winchester and Chaujar, 2002; Ballantyne, 2002). However, their importance is difficult to define using solely field-based approaches; field datasets are often too limited in both duration and resolution to fully determine the magnitude and frequency of these processes (Reid, 1998; Guthrie and Evans, 2004). Modelling is a powerful alternative tool for providing insight into underlying processes governing shallow landslides (Montgomery and Dietrich, 1994; Iverson, 2000) and for testing new hypotheses regarding environmental and land-use change impacts (Collison *et al.*, 2000; Glade, 2003). The explanatory power of such models is a function of their process representation and predictive ability (Mulligan and Wainwright, 2004; Murray, 2007).

Early GIS based slope stability models combined an infinite slope geotechnical model with a distributed physically based hydrological model (Okimura and Ichikawa, 1985), to provide valuable probabilistic information on failure, but not detailed deterministic predictions (Montgomery and Dietrich, 1994; Pack *et al.*, 1998). More recent models have applied a similar approach (combining infinite slope and process based hydrological models) in a deterministic framework to predict the volumes and timings of slope failures given a real or synthetic rainfall time series (Bathurst *et al.*, 2005; Claessens *et al.*, 2007). These approaches

have a problem: they commonly predict much larger unstable areas than are observed. This mismatch between predictions and observations has often been related to spatial variability or error in the model's input parameters (Montgomery and Dietrich, 1994; Zaitchick *et al.*, 2003).

However, careful analysis of these models suggests that they contain two critical assumptions. First, the infinite slope geotechnical model assumes that any unstable block is infinitely long and wide so that effects at its margins can be neglected (Taylor, 1948). Second, the hydrological models that provide spatial pore water pressure predictions all rely to some extent on gravity driven flow across hydraulic gradients that are strongly defined by surface topography. These two assumptions are central to the conceptual model of slope stability coded within these catchment scale stability models yet their applicability and impact are poorly constrained. In this thesis I design and implement a set of detailed experiments to test and improve these assumptions.

1.3. Thesis Objectives

Each experiment is addressed as one of my objectives, covering first the hypothesis that the models' predictive power is related to their measured parameters then the two critical assumptions within the models: infinite slope stability and topographically driven wetness. In the sections below I will deal with each in turn.

1.3.1. Collect High Quality Input Parameter Data for Slope Stability Analysis; Quantify Natural Variability and Error

Poorly constrained or spatially variable input parameters such as soil depth, root reinforcement or material properties are often used to explain the locations of failure within a larger area that has a high, sometimes equal, probability of failure (Dunne, 1998; Montgomery *et al.*, 1998). Many of these variables are extremely difficult to characterise at the catchment scale since they vary over fine spatial scales and are difficult to measure.

In some cases there is a mismatch between the modelled, measured and observed effect of a parameter. For example, the dense lateral root mats observed at many landslide scars (Preston and Crozier, 1999; Warburton *et al.*, 2008) can add significant strength to the soil (Zhou *et al.*, 1998; Schmidt *et al.*, 2001), but their reinforcing effect is underrepresented in the literature. In other cases such as the soil material properties (strength, density and depth) the parameters are simply highly variable (Zaitchick *et al.*, 2003). Elevation data can be measured with more certainty, and are a powerful tool, defining both the geotechnical and hydrological energy gradients important for slope stability. Advances in remote sensing continually improve the precision and resolution of this data (Paylor *et al.*, 2005). However there remains considerable uncertainty around its quality and that of the variables derived from it (Milledge *et al.*, 2008).

For all these parameters, it is not only their magnitude that is important and but also their associated uncertainty, either due to measurement error or true spatial variability. This information, in the context of the model's sensitivity to its parameters can be used to quantify predictive confidence or identify 'limiting' parameters on which future measurement efforts might be concentrated. In doing so, I hope to identify their influence on stability models and the potential for improving their representation. Finally, by adopting a rigorous measurement campaign I hope to address a key question: do better parameter measurements help to improve stability models?

1.3.2. Establish the Importance of Lateral Reinforcement for Slope Stability in a Catchment Scale Modelling Context

The infinite slope stability analysis (Taylor, 1948) that is widely applied in catchment scale stability modelling (from Okimura and Ichikawa, 1985; to Simoni *et al.*, 2008) neglects lateral reinforcement effects, yet field observations (Schmidt *et al.*, 2001) suggest that these may be important. If reinforcing effects are important then this has exciting implications for future catchment scale stability models and may identify one of the causes of over-prediction in existing models. This information might be most easily accessed through sensitivity analysis of a multi-dimensional stability model to identify and quantify the control that a block's geometry (length, width and depth) exerts on its stability. Such an analysis requires a model that can represent both lateral root cohesion

and friction effects on the margins of an unstable block. Existing geotechnical models do one or the other and are often computationally intensive (Duncan, 1996; Chugh, 2003) rendering them unsuitable for catchment scale application. Multi-dimensional stability modelling at the catchment scale requires analytically tractable governing equations that account for both roots and friction to make its application feasible. Such a model has the potential to be used as a powerful tool for catchment scale slope stability modelling; but it needs to be tested to allow confident assertions on the implications of its predictions for relationships between geometry and stability. This is problematic since slope stability is difficult to measure (it is either stable or unstable) and the effects of model and parameter uncertainty on predictive ability are difficult to separate. An alternative approach could be to compare the model's results with 'benchmark' predictions from standard limit equilibrium models. I aim to develop and test a set of analytical governing equations for three-dimensional analysis then use these to establish key landslide scaling relationships.

1.3.3. Assess the Topographic Control on Temperate Upland Hydrology and the Influence of Scale and Material properties

Existing stability models require pore water pressure predictions as a key input into their geotechnical model, these are provided by process based hydrological models spanning the full range of dimensions and degrees of process representation (Montgomery and Dietrich, 1994; Godt *et al.*, 2008; Simoni *et al.*, 2008). All these models treat soils and rocks as broadly continuous porous media that obey Darcy's law and, in the absence of good data on subsurface properties, predict wetness patterns that are driven almost exclusively by the landscape's topographic form. Observations from natural slopes suggest that their hydrology is strongly influenced by preferential flow through discontinuities such as fractures (Wilson and Dietrich, 1987; Montgomery *et al.*, 2002) and macropores (Sidle and Swanston, 1982; Weiler and Naef, 2003).

Existing hillslope scale studies (Freeze, 1972; Freer *et al.*, 2002; Montgomery *et al.*, 2002) that have applied traditional hydro-geological techniques (trenched slopes, wells, piezometers, rainfall and stage data) have yielded results that both improve our understanding of the specific conditions at the site and the

mechanisms of hillslope hydrology in general. By building up a bank of these studies then analysing each with reference to understanding accrued at the others we can begin to use these hillslope scale studies as a powerful tool in distilling the key drivers of hillslope hydrology (Freer *et al.,* 1997; Uchida *et al.*, 2006). I hope to take advantage of this mode of operation to gain an understanding of the character of hillslope hydrology within the context of a steep temperate landscape with a strong glacial legacy.

Data acquisition at the catchment scale is difficult since applying traditional hydro-geological techniques at a suitable resolution would be prohibitively expensive (Lane *et al.*, 2006). An integrated measure of spatial wetness is required at high resolution over a wide spatial extent; such data might be most effectively collected using remote sensing. Researchers have begun to use vegetation stress measured from hyper-spectral imagery as a wetness indicator (Harris *et al.*, 2005); others use traditional ground based vegetation species maps as surrogates for wetness given knowledge of the species' ecological amplitude (Rodhe and Seibert, 1999; Wang *et al.*, 2000). I hope to connect these advances to take advantage of widely available aerial imagery and the links between vegetation and wetness to develop a new tool for widening the area of hydrological investigation by remotely mapping patterns of indicator species then using these as a surrogate for wetness. This is important since expanding the study to the catchment scale allows assessment of the broader controls on where is wet in the landscape and identification of emergent trends above the noise often inherent at the hillslope scale. I aim to test the hypothesis that wetness is topographically driven at both the hillslope and catchment scale, identifying the perturbing processes that disrupt this relationship and assessing the extent that this is influenced by landscape scale characteristics and material properties (soil, geology).

1.4. Thesis Structure

The thesis is split into seven core chapters. The substantive research is contained in Chapters 3 to 6, with Chapter 3 addressing the first objective, Chapters 4 and 5 the second and Chapter 6 the third. Chapter 2 provides relevant background from literature and field study and Chapter 7 synthesises

observations from the substantive research chapters. In the following section I will guide you through the thesis chapter by chapter indicating their scope and focus.

1.4.1. Chapter 2

In Chapter 2 I introduce my study question, justify my approach and provide the necessary background on which I will build the rest of the thesis. The chapter combines review of existing literature with examples from my Lake District study area to highlight key observations that have particularly influenced my research focus. I look first at why and how we study landslides, define shallow translational landslides, then introduce my study area. I identify key aspects of shallow landslide process and form focusing in particular on debris mantled hillslopes in temperate environments. I introduce some key soil mechanics concepts (on which later chapters will rely), before reviewing the geotechnical and hydrological aspects of physically-based catchment scale stability models. Finally, I apply a simple GIS based stability model to illustrate the reasons for exploring some of its key limitations.

1.4.2. Chapter 3

In Chapter 3 I deal with: soil strength, root reinforcement, soil density, soil depth and topographic data. For each parameter: I review existing theoretical and empirical research to address its nature and to identify measurement options; I report the measurement methods that I adopted; I compare my findings with data from other empirical or mechanical studies; and discuss the issues related to their application in slope stability modelling. In Section 3.2 I characterise soil strength and its variability for different locations and contexts within my study area reporting results in terms of both peak and critical strength. In Section 3.3 I quantify lateral root reinforcement and its variability for the three main vegetation types in the study area (*Eriophorum*, *Pteridium* and *Juncus*) and put these estimates into the context of results from relevant studies. In Section 3.4 I tackle soil bulk density, focusing on the soil density for the full sample, then its variation with moisture or material properties. In each case the implications for stability modelling are addressed as they are encountered. In Section 3.5 I test

a range of soil depth measures to find a reliable method of estimating soil depth and variability. I present the effective soil depths measured at scars across the study area, discuss their statistical properties and the implications for parameterising slope stability models. In Section 3.6 I review the literature on elevation data: sources, resolution and filtering before focusing on my study area to assess the quality of the available topographic data.

1.4.3. Chapter 4

In Chapter 4 I derive the Finite Slope stability model, a new set of analytical governing equations for three-dimensional stability. First, I identify the importance of landslide size and the need for a new three-dimensional stability method that can be applied at the catchment scale. Second, I review the existing methods available for multi-dimensional slope stability analysis, assessing their applicability in a catchment scale modelling context. Third, I derive the new model from first principles using earth pressure theory and lateral root cohesion to calculate the driving and resisting forces on each plane of a soil block.

1.4.4. Chapter 5

In Chapter 5: I establish the effectiveness of the Finite Slope model; and quantify the control that a block's geometry exerts on its stability. I address the first by comparing the Finite Slope model's results with those from two standard two-dimensional limit equilibrium models in a set of benchmark tests. I address the second using sensitivity analysis in a set of numerical experiments designed to be representative of my study area. I treat length and width effects individually first, then relative to one another and finally in combination using the full three-dimensional formulation of the Finite Slope model. I quantify the effects using back calculation as well as the Factor of Safety, in order to compare their magnitude with that of parameter uncertainty (from Chapter 3).

1.4.5. Chapter 6

In Chapter 6 I apply field measurement, monitoring and remote sensing to establish the extent to which wetness patterns in the Lake District are topographically driven. I discuss the relevant background for this investigation focusing on the topographic wetness hypothesis (its origins, agreement with observations and the factors that can disrupt it). I detail the experimental design for the study, which will operate at two different scales, the hillslope (10^{-1} km^2) and catchment (10^0-10^2 km^2) scale. I deal individually with the methods that I applied at each of these scales then apply the same structure to the results dealing first with the results at the hillslope scale then at the catchment scale. I finish the chapter by bringing the results at these two scales together and identifying their implications for slope stability modelling.

1.4.6. Chapter 7

In Chapter 7 I highlight the key results from the preceding chapters, then deal with each in turn, comparing theoretical controls on landslide distributions (spatial and non-spatial) derived from analytical models or hydrological observations, with empirical data from the Lake District 2005 landslide inventory. First, I examine the geotechnical and geometric controls on hillslope stability, then the hydrological controls on stability, before considering the implications for catchment scale stability modelling. I finish the chapter by applying my findings using Lake District data to provide a physical explanation for the commonly debated form of landslide magnitude / frequency relationships.

2. Conceptualisation of Research Focus

2.1. Scope of the Chapter

My aims for this chapter are twofold: 1) to justify my area of study and my approach to studying it; and 2) to provide the necessary background information to allow the reader safe passage through the rest of the thesis. Whilst some parts of the chapter are strongly focussed on reviewing the existing literature, others use examples and observations from my own study area to illustrate these points. This mix is both necessary and advantageous; it allows me to illustrate the findings that others have made in the context of my study area and to highlight key observations that have particularly influenced my own research focus.

Figure 2-1 outlines of my approach to this task. I look first at landslides in general why we study them, how we study them, and what type of landslide in particular I will focus on in this thesis (Section 2.2). In Section 2.3 I provide the relevant background information on my study area; then identify key aspects of shallow landslide process and form in a UK context (Section 2.4). Section 2.4.2 sets out a simple conceptual model for slope stability and relevant aspects of hillslope hydrology. This is useful as a framework within which to interpret the characteristics of shallow landslides in general and those in the Lake District in particular (Section 2.4.3). A more detailed model of the mechanics of failure can then be illustrated after some fundamental soil mechanics concepts have been explained in Section 2.5. This leads to a review of the geotechnical then the hydrological aspects of physically-based catchment stability models (Section 2.5). Finally I apply the SHALSTAB model to the study area to illustrate the utility of this type of model and its limitations. I conclude the chapter with a series of research objectives (Section 2.7) linking it to the main body of the thesis.

Figure 2-1: A schematic illustrating the structure of the Chapter.

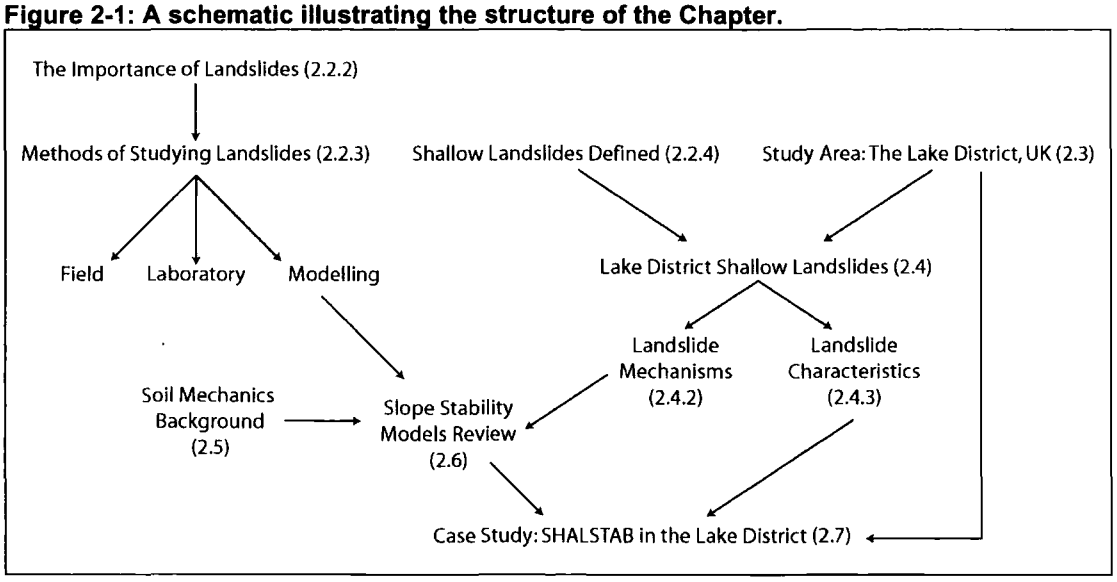

2.2. Landslides – why, how and what are we studying?

2.2.1. Scope of the Section

In this section I discuss the importance of landslides (Section 2.2.2) and outline the range of methods used to study them (Section 2.2.3) before finally defining the particular focus of my study: shallow landsliding (Section 2.2.4).

2.2.2. The Importance of Landslides

Landslides and debris flows are important as potential hazards, as agents of landscape change and in terms of the sediment that they deliver to the fluvial system. Landslides are one of the most destructive geological processes and are a major cause of loss of life and economic damage (Brabb, 1993). In 2004, there were more than 7000 fatalities from landslides worldwide (Oven, 2005). This included significant extreme events such as in Haiti, where high intensity rainfall from Hurricanes Jeanne and Ivan triggered extensive landslides causing more than 3000 fatalities (UNEP/OCHA, 2004) and in the Philippines, where over 1000 people were killed by typhoon triggered mudslides (IFRC, 2004). There are clearly strong societal drivers associated with landslide risk. Global databases record lowest deaths for high income countries (Petley *et al.*, 2005; Alexander, 2005). However, even in high-income countries the impacts are non-trivial; landslides are widespread in the U.S. and cause $1 to 2 billion in

damages and more than 25 fatalities each year (USGS, 2008). In the UK, landslides represent a potential hazard to structures and communications in upland areas: damming bridges (Common, 1954), blocking culverts (Ballantyne 2004), burying roads (Common, 1954; Winchester and Chaujar, 2002; Ballantyne, 2002) and railways (Ballantyne, 2002); damaging houses (Jenkins *et al.*, 1988) and trapping cars (Winchester and Chaujar, 2002). Whilst an improved understanding of process doesn't directly translate into reduced risk, an understanding of physical process can provide significant steps towards effective risk reduction (Alexander, 2007).

Studies in a variety of environments have identified shallow landslides, or the debris flows that they mobilise, as the dominant agents of mass movement in steep upland catchments (e.g. Rapp, 1960; Dietrich and Dunne, 1978; Benda and Dunne, 1987; Ballantyne, 1991). They modify the landscape by cutting scars or gullies in the regolith and depositing debris at the foot of the slope (Ballantyne, 2002). These processes make shallow landslides and debris flows important as sources of sediment for downstream transfer. High rates of sediment delivery can cause downstream problems resulting in: 1) accelerated rates of sediment accumulation; 2) enhanced flood risk; 3) bank erosion; and 4) reduced biodiversity (Montgomery *et al.*, 1999; Lane *et al.*, 2008). Careful management is required in order to prepare for and attempt to minimise these impacts. Traditional engineering methods are logistically difficult and expensive; source control (identifying sediment sources and managing them to control their impact) is an increasingly popular management approach (Lane *et al.*, 2008) but requires a broad scientific knowledge base. The impacts of future changes in climate or land use are unknown and offer the potential to worsen the situation; the effect of these external factors on sediment generation should be a vital part of management plans (Reid, 2005).

2.2.3. Methods of Studying Landslides

This study builds on a significant body of research that investigates the physical processes controlling landslides. This work can be broadly grouped into field, laboratory and model-based approaches and has been undertaken at a range of scales and using a range of techniques; the following section briefly reviews these approaches.

Detailed **field studies**, often within a sediment budget framework, place landslides in the context of other geomorphic events (Rapp, 1960; Dietrich and Dunne, 1978) and provide estimates of their relative importance. Sediment budgets can be applied at the individual slide (10^{-1} km^2; Johnson *et al.*, 2008), catchment (10^2 km^2; Campbell and Church, 2003) and basin scale (10^3 km^2; Hovius *et al.*, 1997). At the largest scale these landslide inventories provide estimates of the magnitude and frequency of landslides usually by substituting time for space in an ergodic framework (Brardinoni and Church, 2004; Malamud *et al.*, 2004; Stark and Hovius, 2001). Other studies use dating techniques (Kotarba, 1992; Luckman, 1992; Winchester and Chaujar, 2002) or sequential aerial photography (Chandler and Brunsden, 1995; Zanutta *et al.*, 2006) to generate a temporal landslide record so as to investigate landslide magnitude and frequency. Accounts of individual events (Beven *et al.*, 1978; Jenkins *et al.*, 1984; Johnson *et al.*, 2008) apply detailed observation, provide qualitative process description and indicate possible mechanisms within a case study framework.

Alternatively, **laboratory based research** is generally conducted at a reduced scale or with reduced complexity. Approaches include physical models where failure mechanisms can be studied in simplified materials such as sand piles (Densmore *et al.*, 1997; Roering *et al.*, 2001) or miniature hillslopes (Reid *et al.*, 1997). Reid *et al.* (1997) created artificial slope failures under carefully controlled experimental conditions with intensive monitoring of hydrologic and deformation responses. Comparable control in the field would be difficult to achieve and this remains one of the key advantages of laboratory approaches.

Landslide **models** range in architecture and scope from data-driven (Glade *et al.*, 2000; Pitman *et al.*, 2003) to process-based (Montgomery and Dietrich, 1994; Simoni *et al.*, 2008) models and from those designed to inform decision making to those designed as an exploratory framework with which to formulate hypotheses. Data-driven statistical models are widely used in landslide research, chiefly for hazard delineation; for which they are often highly effective. However, their inherent assumptions and their empirical focus mean that they provide only one perspective on landslide processes. Process-based models

offer an alternative perspective. The particular attraction these models is their ability to improve our understanding of the processes that drive landslides by allowing us to move beyond the 'here and now' to study processes at scales that we could not otherwise tackle. This is particularly useful for studying landslides, where their spatially and temporally episodic nature of occurrence requires wide areas or long timescales of study to effectively characterise them. Process based modelling allows us to: 1) study the behaviour of the entire system in an integrated way 2) elucidate key controls using sensitivity analysis; 3) extend the spatial and temporal reference of the study; and 4) simulate future scenarios. These models, which are necessarily process-based, are the focus of this study.

2.2.4. Shallow Translational Landslides

A landslide involves "movement of rock, debris or earth down a slope" (Crudden, 1991); and encompasses a full range of very rapid to extremely slow movements of ground or earth. In order to systematically describe this phenomenon numerous landslide classifications have been developed one of the simplest and most widely accepted is that of Varnes (1978), modified by Crudden and Varnes (1996). Within this framework my study focuses on sliding: the downslope movement of a soil or rock mass as a coherent body on surfaces of rupture or zones of intense shear strain. Slides are characterised by the presence of a clearly defined shear surface at the contact between the moving mass and the underlying soil or rock. My particular focus is on shallow translational slides, where: *"mass displaces along a planar or undulating surface of rupture, sliding out over the original ground surface"* (Crudden and Varnes, 1996). The slides can involve various combinations of bedrock, broken bedrock, and unconsolidated surficial material; the displaced material may be either greatly deformed or nearly intact. Shallow translational landslides are by far the most common form of landslide occurring in soils (Selby, 2005). They are always shallow features and have essentially linear slide planes, which usually develop along a boundary between soil materials of different density or permeability. Depth to the failure plane is usually in the range 1 to 4 m and the length of the slide is commonly large compared with its depth.

2.2.5. Section Summary

Landslides are important, impacting significantly on both people and the environment. They are worth studying, not only because they are interesting, but because by understanding them better, we can create a more complete picture of the world in which we live and can use this to inform our actions. Modelling is one tool that we can use to do this, offering the opportunity to study landslides in a way that other methods cannot. Although both models and landslides come in many forms I will focus on process-based modelling of shallow translational landslides

2.3. Study Area – The Northern Lake District, UK

2.3.1. Scope of the Section

Any study is necessarily rooted in place, the source of our measurements, observations or perceptions, mine is the Lake District, situated in North West England (between latitude 54° and 55° N). It covers an area of 2279 km^2 (Tarn and Wilson, 1994), most of which lies above 250 m O.D. with the highest point Scafell Pike at 978 m O.D. The present landscape of the Lake District is a product of many millions of years of evolution. Below I describe this as a chronological sequence, beginning with the bedrock geology (Section 2.3.2), the glacial history and regolith development (Section 2.3.3); and the related vegetation history (Section 2.3.4). I then go on to detail the current climate (Section 2.3.5), soil (2.3.6), vegetation and landuse (Section 2.3.7). Although this is a time sequence it is particularly useful when thinking in terms of landslides since the climatic legacy leaves a landscape signature manifest as a sequence that moves up from the bedrock to the surface. Much of the study site information in this Section is designed to provide sufficient key information to put my landslide research into the context of the study area. It relies heavily on the synthesis provided by Johnson (2001). More complete treatments of these topics can be found in: Johnson (2001) for a general overview; Moseley (1990) for details on the region's Geology; Boardman (1992, 1996) and Evans (1997) for its geomorphology; Pennington (1997) for a vegetation chronology; Manley (1973) and Tufnell (1997) for contemporary climate; and Bendelow (1984) for its soils.

2.3.2. Geology

The solid geology of the study area is dominated by rocks from the lower Palaeozoic era, specifically of the Ordovician period (500-440 Ma), which consist mainly of deposits from the Skiddaw and Borrowdale groups (Figure 2-2). The Skiddaw group (the oldest exposed rocks) are composed primarily of turbidity current derived siltstone and mudstone (KST and BUF in Figure 2-2) with subsidiary greywacke sandstone (RNM in Figure 2-2; Moseley, 1990). These give rise to smooth conical shaped slopes, generally unbroken by rock outcrops. The Skiddaw group is succeeded by volcanic rocks, typical of subduction at active plate margins (Millward *et al.*, 1978; Moseley, 1990). The Borrowdale Volcanic group to the south of the Skiddaw Slates (Figure 2-2) include basalt, basaltic andesite, normal andesite, dacite, rhyolite and ignimbrite, of lava flow and pyroclastic origin (Millward *et al.*, 1978; Moseley, 1990). These result in more rugged stepped topography, where resistant beds stand out as steep cliffs.

2.3.3. Geomorphological History

The current Lake District landscape is heavily dominated by the legacy of surface processes operating during the Quaternary (Boardman, 1992, 1996), particularly glacial activity during the Dimlington and Loch Lomond Stadials of the Devensian late glacial (King, 1976; Moseley, 1978). Steep hillslopes merge with the zone of glacial deposition where drift features can still be clearly observed (Figure 2-3). However, the rates of glacial process activity during these periods are insufficient to explain the full form of the Lake District landscape: periglacial and restricted glacial processes are also important (Boardman, 1992). Restricted glaciation (small cirque and valley glaciers) was probably the norm for long periods of the Quaternary, particularly the sustained cold non-ice sheet phases of climate between 75 and 30 ka BP (Boardman, 1992). Regional glaciation was rare and ineffective, with cirques developing over a series of local glaciations (Evans, 1997). Periglacial processes have operated in the area for prolonged periods, particularly during restricted glaciation, with considerable geomorphic impact (Boardman, 1992). Many

slopes have thick covers of frost shattered debris, formed in the cold and wet conditions of the Loch Lomond Stadial (Johnson, 2001). Much of the material produced travelled short distances covering hillslopes, (Talus in Figure 2-3) whilst material reaching river channels was transported to other storage sites such as alluvial fans, floodplains and lake basins (Figure 2-3). The valley floors contain deep glacio-fluvial and more recent fluvial and colluvial deposits supplied by the upper hillslopes as well as the drift features described above.

Figure 2-2: Solid Geology map for the Northern and Central Lake District with the key units labelled on the map.

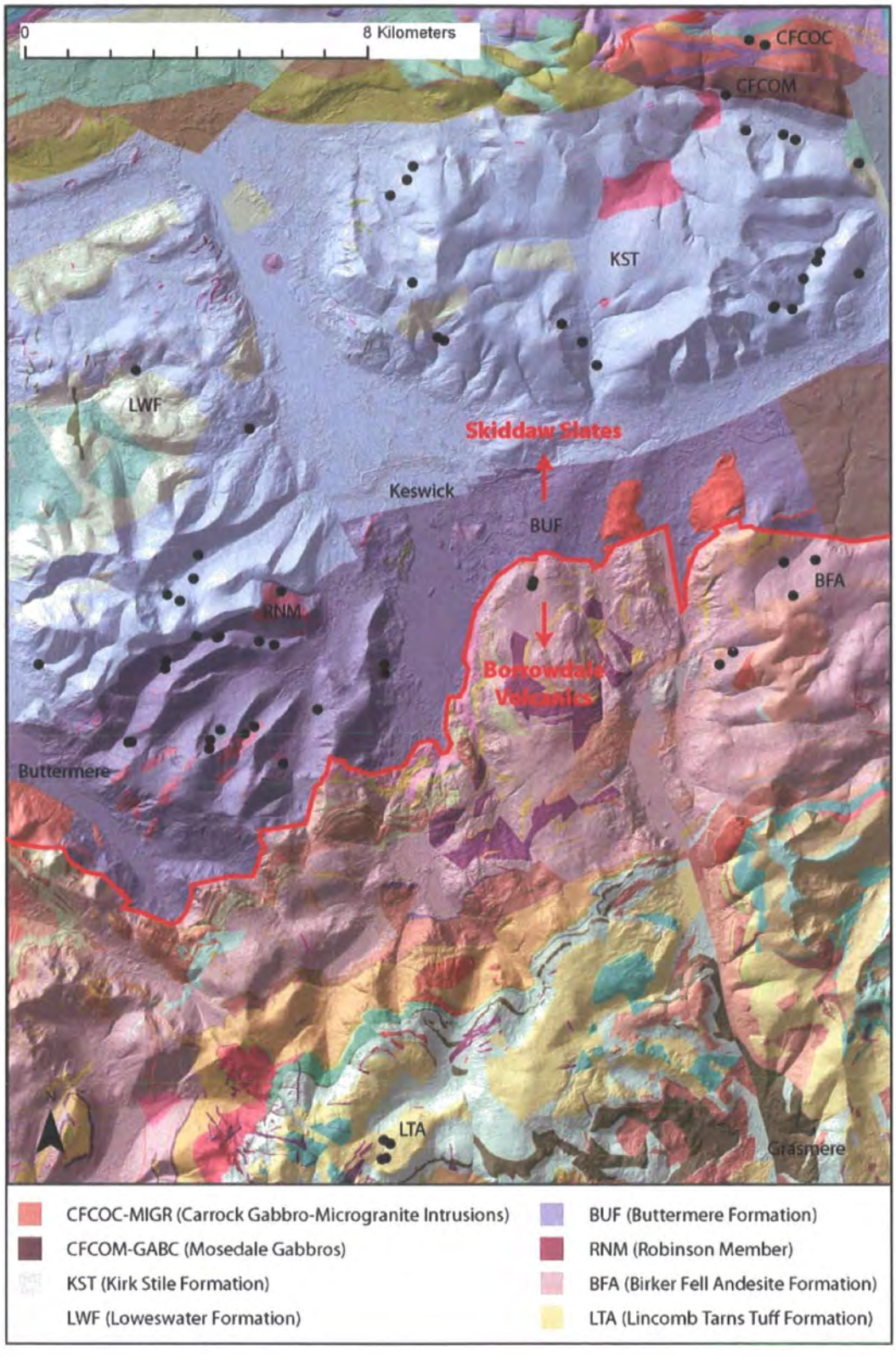

Figure 2-3: Surficial Geology map for the Northern and Central Lake District.

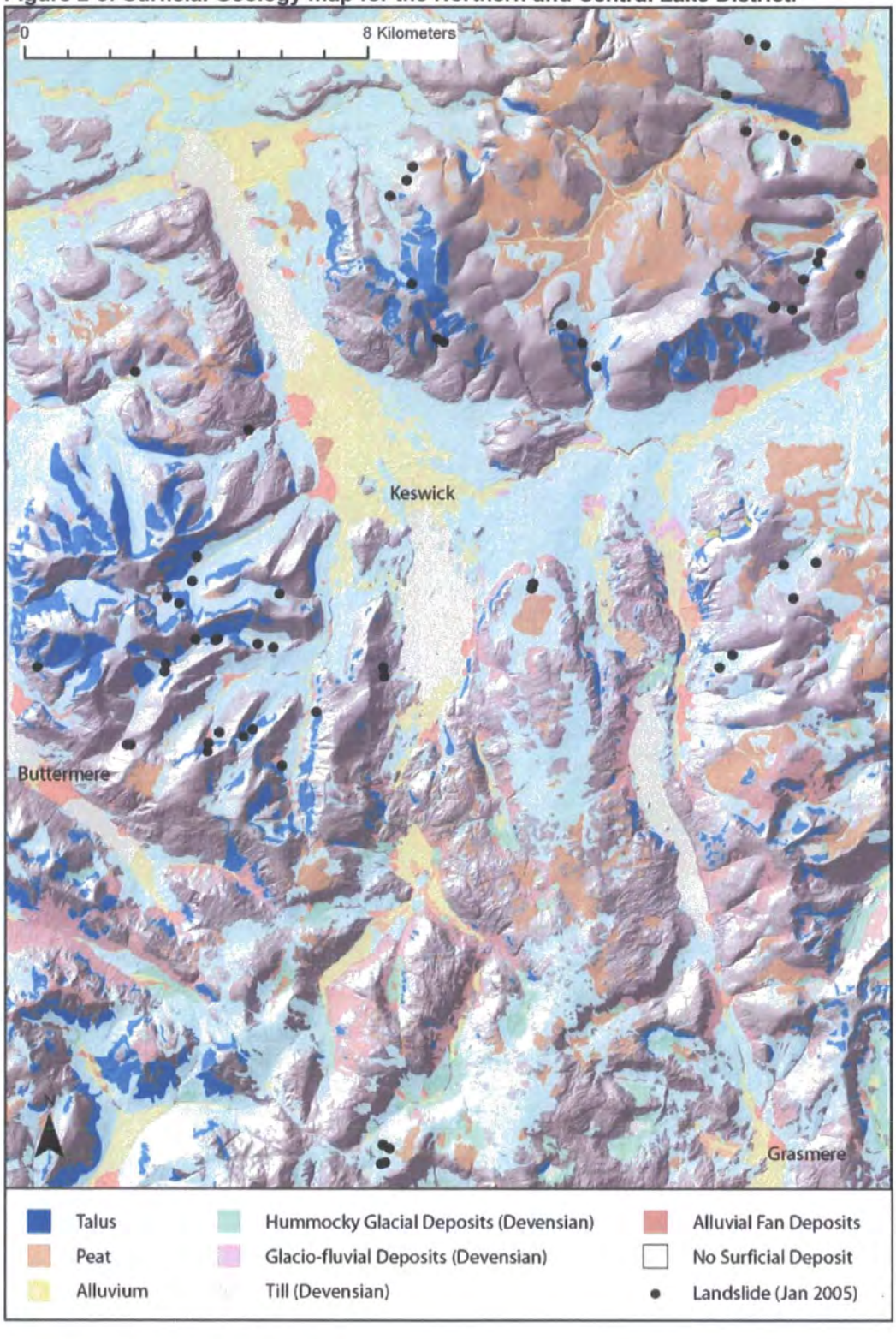

2.3.4. Vegetation History

The vegetation history of the Lake District has been strongly influenced by both climate and early human settlement. Pennington (1997) provides a review of the Cumbrian vegetation chronology from the Lateglacial period to the present. Few

plants existed in the Lateglacial period or in the polar terrain that followed during initial deglaciation. Later in deglaciation, plants migrated from southern England, forming pioneer cold tolerant communities. After 14,000 BP the pioneer vegetation became more 'luxuriant' and was succeeded by grasslands. By 13,000 BP a milder climate enabled the spread of woody vegetation forming open woodlands composed of *Juniperus* and *Betula* supplemented with grasses. This ended ~11,000 BP with the onset of the cooler Loch Lomond Stadial causing the formation of small glaciers. Soil surfaces were disturbed leading to a breakdown in the previous vegetation communities. Plants existing in this colder environment were those tolerant to disturbance, and trees disappeared for approximately 1000 years. The onset of the Holocene (10,000 BP) allowed *Juniperus* to become dominant again, leading to a closed canopy of *Betula* woodland (though probably more open at elevations >500 m). *Corlyus* spread started about 9700 BP to eventually surpass *Betula*, whilst *Quercus* and *Ulmus* spread from the south later. Between 7500 and 5000 BP vegetation was dominantly arboreal, composed of: *Quercus, Ulmus, Corlyus, Alnus* and *Betula*. Hunter-gatherer's began carrying out burning of upland vegetation in Britain ~14,000 BP but impact in the Lake District was extremely limited before 4,500 BP. The main regional forest clearance was completed by 1,000 BP in association with Norse settlements, and later Monastic land use. The woodland was replaced first with *Calluna*-dominated heath then grasslands associated with upland sheep farming (Pennington, 1997; 1997; Johnson, 2001).

2.3.5. Current Climate

The Lake District climate is characteristic of the interaction between orographic forcing, a small group of mountains and valleys, and large-scale weather systems, with a particular influence from westerly air masses (Manley, 1973). There is significant rainfall variability spatially (Miller, 1849; Macan, 1970; Bendelow, 1984; Tarn and Wilson, 1994; Ratcliffe, 1997b), which can be more than 500%, (e.g. between Low Furness and Sprinkling Tarn, where rainfall is 4699 mm a^{-1}). The general pattern of rainfall increases from a low at the coast to a maximum in the central fells and declines in a north and east direction, a secondary peak occurs on the Skiddaw Massif (Manley, 1973). The valley heads of the central Lake District (e.g. Borrowdale) intercept over 3810 mm a^{-1},

as a result of orographic forcing and the convergence of surface air streams along the radial Lake District valleys (Manley, 1973).

Lake District winters are particularly mild, and its summers are relatively cool as a function of the warming influence of the North Atlantic drift and the passage of low pressure systems (Tufnell, 1997). Locally, temperatures at Grizedale (south Lake District) are not too dissimilar to those recorded elsewhere in North West England, although consistently slightly colder, as a result of cold air drainage from the surrounding hills (Tufnell, 1997). The lakes have an ameliorating effect cooling the surrounding areas in summer and warming them in winter (Manley, 1973). Upland and mountain areas show marked contrasts with lower elevations. An important feature of high level climate is the greater frequency of temperature oscillations about freezing point so that a freeze thaw climate prevails for long periods of every winter resulting in a high frequency of oscillations between cold rain, sleet or driving snow (Manley, 1973). The valley floors around Keswick experience around 25 days in which snow falls, primarily between December and March. On Lake District summits in excess of 700 m snow cover may persist for ~100 days (Manley, 1973). Although much of this climatic data is somewhat dated, having been collected largely by Manley (1973), it remains a useful indicator of the general climatic conditions experienced within the study area.

2.3.6. Soils

The Lake District is dominated by soil units 311 (humic rankers), 611 (typical brown podzolic soils), and 1011 (raw oligo fiberous peat soils) (Bendelow, 1984; Figure 2-4). Other soils include units 713 (Cambic stagnogley soils) 541 (typical brown earths), 721 (Cambic stagnohumic gley soils), and more localised areas of iron pan stagnopodzols (651). These soils represent a development series (Pearsall and Pennington, 1973). Ranker soils (311) occur where lichens and mountain top plants build up humus amongst and over bedrock or skeletal minerogenic soils. On steeper slopes there are more developed brown earth soils (611) where surface layers are leached and have a mull humus, or soils with a mor humus and a podzolic transition in the underlying mineral soil (often found under Calluna vegetation). Gleyed soils develop in waterlogged areas, often under *Juncus* vegetation, where the mineral soil has a characteristic blue-

grey colour due to ferrous iron salts. Peat (1011) occurs where free drainage is impeded and mor humus transforms to peat. Blanket peat occurs on wide areas of flat or gently sloping ground above 450 m, and contains ancient wood fragments from pre-clearance vegetation.

Figure 2-4: A map of Lake District Soil Units (from Soils of Northern England, 1:250, 000, Soil Survey of England and Wales, 1982).

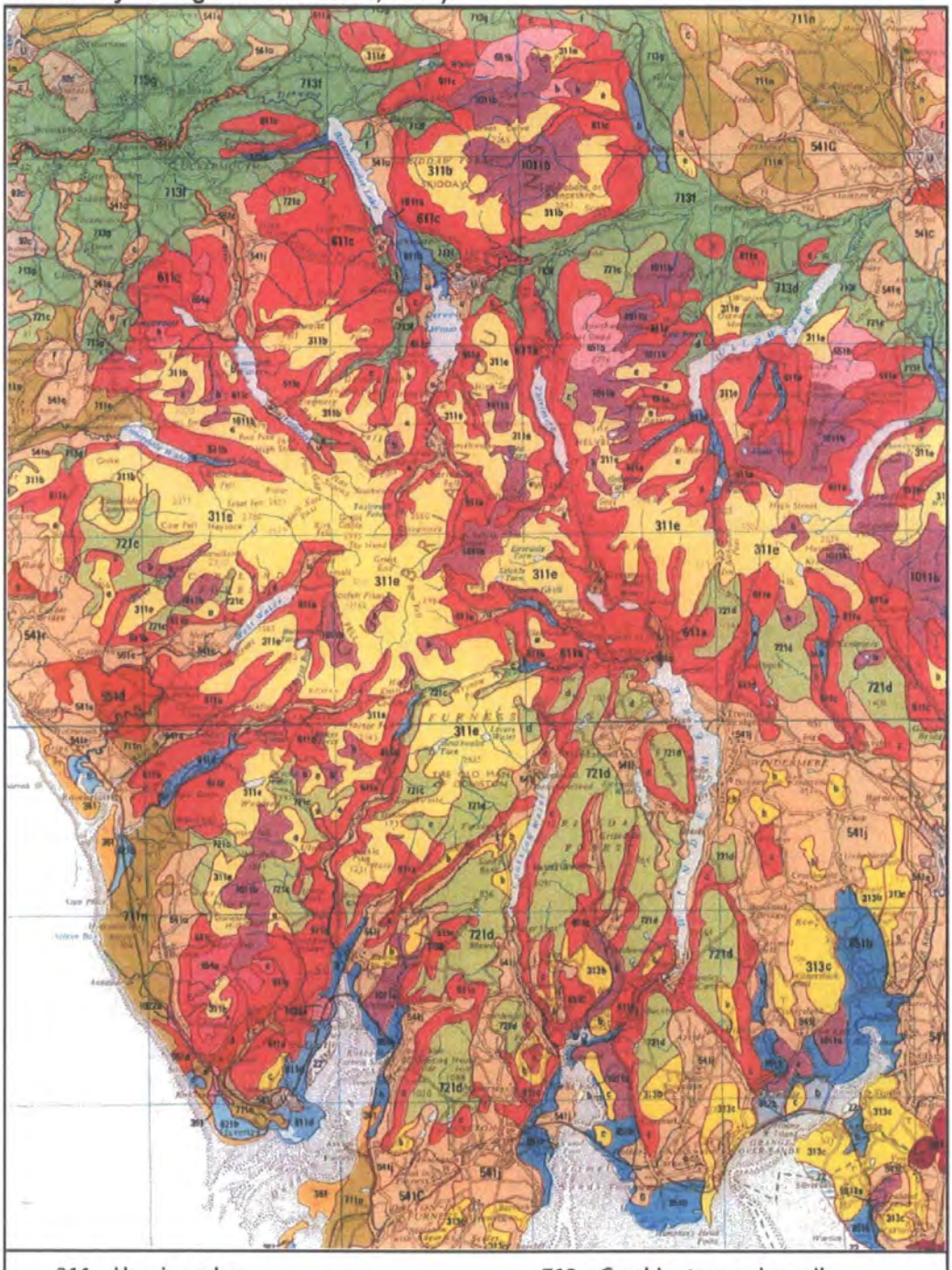

2.3.7. Current Vegetation and Landuse

The Lake District is dominated by sub-montane habitat (heaths, grasslands, mires) with small areas of montane habitat at higher elevations (Fielding and Haworth, 1999). Contemporary vegetation can be divided into three areas: lakes and valley bottoms; woods and lower ravines; and fells. On the fells, deforestation was followed by the expansion of dwarf shrub heath (*Calluna vulgaris*, *Erica cinerea*, *Vaccinium myrtiluus*). Since then, sheep grazing and moor burning have reduced the heath replacing it with acidic grassland (e.g. *Festuca*, *Agrostis*, *Nardus*, and *Juncus*) and bracken (*Pteridium*) up to 450 m O.D (Ratcliffe, 1997c). Landuse is broadly managed by the Lake District National Park Authority, aiming to conserve and enhance the park, secure the future of local communities and allow the continued appreciation of the area. The bases and implementation of these aims, which are pursued in association with local stakeholders, are outlined in the current 'Lake District National Park Management Plan' (LDNPA, 1999). Much of the land area is dominated by moorland extensively grazed by sheep. The area remaining for agricultural use is small and productive agricultural land is confined to the valley sides and floors (Tarn and Wilson, 1994). Grazing maintains the diversity of grassland and moorland but where stocking is too high physical erosion can occur.

2.3.8. Section Summary

In the sections above I have provided a general picture of the character of the landscape in which this study has been performed; each section also has particular relevance to slope stability. Bedrock geology and geomorphic history influence the landscape's form and (through their influence on soil) its material properties. Soil influences the strength of the potentially unstable material and the ease with which water can pass through it. Vegetation history in combination with the geomorphic history provides background from which we can understand how the current landscape may still be adjusting to historic drivers. Vegetation and landuse influence both the soil's hydrological conditions and its strength, due to the reinforcing effect of roots. Climatic conditions, in particular spatial and temporal rainfall patterns, influence soil moisture

conditions and as a result pore water pressures. The links between these properties and their physical importance will be dealt with in detail later Section 2.4. I finished Section 2.2 by defining the process of interest: shallow landslides. In this section I have introduced the boundary conditions within which these processes will operate. Next I will add flesh to these bones by illustrating the characteristics of shallow landslides in the Lake District and conceptualising their mechanics.

2.4. Key Characteristics of UK Shallow Landslides

2.4.1. Scope of the Section

In this section I aim to identify the phenomena that this thesis will tackle starting with general concepts then moving on to draw key characteristics from a local case study. In Section 2.4.2 I outline a conceptual model for the process of shallow landsliding in a UK context. There is a particular focus here on landslide hydrology, outlining a conceptual model of UK upland hillslope hydrology as relevant to the stability of a slope (a more detailed analysis of the geotechnical conditions will follow in Section 2.5). In Section 2.4.3 I provide a detailed description of the characteristics of the Lake District landslides, and tie these into observations from other studies. I introduce the storm that triggered the landslides; describe their distribution (spatially and in terms of magnitude frequency); and report the geometric, hydrological and vegetation characteristics of the landslide scars. In each case I highlight the implications of these observations for the broader question as I address them, before drawing these together at the end of the section.

2.4.2. Landslide Mechanisms

The downslope component of the weight of soil above a potential slip plane increases with slope angle whereas the normal component and therefore the frictional strength decreases, until a maximum angle of repose at which shear stress exceeds strength and the soil moves downslope. Since the soil's material properties are invariant over short timescales (< years) for a fixed slope geometry a more rapid change in local conditions is required to initiate failure. Saturation reduces shear strength through the development of positive pore

water pressure. If the slope is close to its angle of repose in dry conditions heavy rain will destabilise it sufficiently for failure to occur (Jenkins *et al.*, 1984). Other natural trigger mechanisms suggested for shallow landslides include: undrained loading resulting from rockfall activity (Ballantyne, 1981); and vibrations created by earthquakes (Harp and Jibson, 1996) or moving flows (Okuda *et al.*, 1980). These alternative triggers are rare in the UK and most shallow landslides are therefore triggered by shallow saturated flow in response to rainfall, surface runoff and snowmelt (Innes, 1983; Iverson, 1997).

Rainfall triggering of shallow landslides has been the subject of intensive study, including: assessments of empirical relationships between landslide occurrence and rainfall intensities and durations (Caine, 1980; Cannon and Ellen, 1985); deterministic assessments of the hydrologic processes involved (Campbell, 1975; Leach and Herbert, 1982; Reid *et al.*, 1988; Buchanon *et al.*, 1990; Johnson and Sitar, 1990; Wilson and Wieczorek, 1995); and analyses that account explicitly for uncertainty in soil hydraulic parameters such as hydraulic conductivity (Reddi and Wu, 1991).

Shallow landslides can be triggered under wholly unsaturated conditions by infiltration that increases the soil weight or reduces the soil moisture suction (Brand, 1981). However, most studies suggest that landslides result from development of positive pore water pressures resulting from saturation (Iverson, 1997). Positive pore water pressures in hillslope soil can develop by vertical infiltration of water from the ground surface, throughflow from adjacent soil and / or groundwater rise (Figure 2-5). Saturation and positive pore water pressures often develop when infiltrating water encounters soil with lower hydraulic conductivity, and transient water table perching occurs (Campbell, 1975; Reid *et al.*, 1988). Alternatively, infiltrating water may elevate the regional water table until it intersects the soil. Significant lateral inflow to these soils may occur by saturated throughflow from adjacent materials (Figure 2-5). A sloping water table, three-dimensional topographic convergence and other factors may help direct the saturated flow laterally (Anderson and Burt, 1978). Traditional hydrological models treat soils and rocks as continuous porous media that obey Darcy's law. Observations from natural slopes suggest that their hydrology is strongly influenced by preferential flow (both vertically and laterally) through

discontinuities such as fractures and macropores (Figure 2-5). Sidle and Swanston (1982), Pierson (1983) and McDonnell (1990) reported the potentially dominating influence of macropores due to root channels and animal burrows on hillslope hydrology and slope stability. Vertical preferential flow can also be manifest as rapid infiltration through shrinkage cracks (Rogers and Selby, 1980) and other macropores (Weiler and Naef, 2003). At other field sites (Wilson and Dietrich, 1987; Mathewson *et al.*, 1990; Anderson *et al.*, 1997; Montgomery *et al.*, 1997, 2002) bedrock fractures or blockages can cause groundwater exfiltration into overlying soils. Concentrated water discharge into the soil due to either preferential subsurface flow or blockages results in locally elevated pore pressures and outward directed hydraulic gradients that enhance the potential for slope failure (Rogers and Selby, 1980; Reid and Iverson, 1992).

Figure 2-5: A schematic illustrating some of the key hydrological processes at work over a two-dimensional slice of hillslope

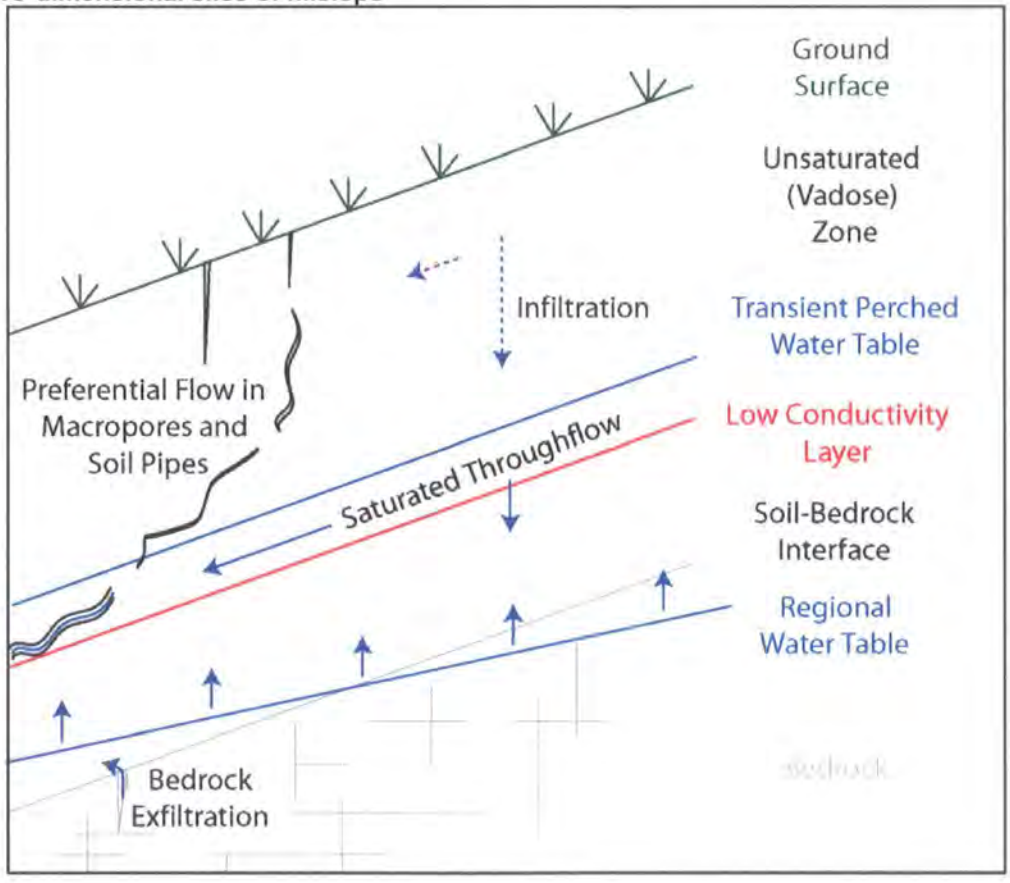

2.4.3. Landslide Characteristics

To illustrate the key characteristics of UK shallow landslides I will draw on: 1) the limited literature on these landslides in the UK; 2) wider studies from other

areas where similarity in form and process of instability can be inferred; and 3) field observations, drawn largely from an inventory of landslides resulting from a high magnitude rainfall event in the Lake District in January 2005.

Shallow landslides have been most extensively investigated in the Scottish Highlands (Innes, 1982, 1983, Jenkins *et al.*, 1988; Luckman, 1992) but also in parts of Wales (Statham, 1976; Addison, 1987; Winchester and Chaujar, 2002); the Lake District (Johnson and Warburton, 2003; Johnson *et al.*, 2008); and the Howgill Fells of Northwest England (Harvey, 1986; Wells and Harvey, 1987; Harvey, 2001). There is also a considerable body of literature on peat mass movements (Kirk, 2001; Mills, 2002; Warburton *et al.*, 2004; Dykes and Kirk, 2006) with some similarities in form and process to slides in shallow colluvial soils. These studies include inventories indicating magnitude and frequency (Mills, 2002), detailed morphological descriptions (Warburton *et al.*, 2003) and studies on the hydrological (Warburton *et al.*, 2004; Dykes and Warburton, 2007) and geotechnical (Dykes, 2008) controls on stability in peat. The Lake District 2005 Landslide Inventory is a complete inventory of ~70 shallow translational landslides that occurred in the 457km^2 study area (Figure 2-6) as a result of a high magnitude rainfall event in January 2005 (Figure 2-7). The majority of the following information on the characteristics of UK landslides in general and Lake District landslides in particular is drawn from observations and measurements collected in this inventory. However, the assertions are supported by measurements and observations from older Lake District landslides (Johnson, 2001; Johnson *et al.*, 2008), and from other UK upland areas (Gifford, 1953; Beven *et al.*, 1977; Innes, 1982; Jenkins, *et al.*, 1988; Ballantyne, 2002). In particular, Gifford's (1953) study of the landslides that occurred during the Boscastle floods (Exmoor, UK) highlights key features in common with our observations of Lake District landslides from the 2005 inventory, despite differences in their location, setting and trigger events.

In this section I will first introduce the high magnitude rainfall event of January 2005 that triggered many landslides throughout my study area. I will then look at the distribution of these landslides both spatially and a-spatially, using a magnitude frequency relationship. I will follow this with an analysis of the more local characteristics of the landslide scars: their geometric, hydrological and

vegetation characteristics. These general trends and similarities in site specific observations at landslide scars have important implications for the driving processes. Observations of these characteristics have played a large part in defining my conceptualisation of Lake District landslides and as a result the direction of my model development. I will highlight the particularly relevant observations as I address them; then draw these together at the end of the section.

Figure 2-6: A map of the study area for the Lake District 2005 Landslide Inventory showing the spatial distribution of landslides.

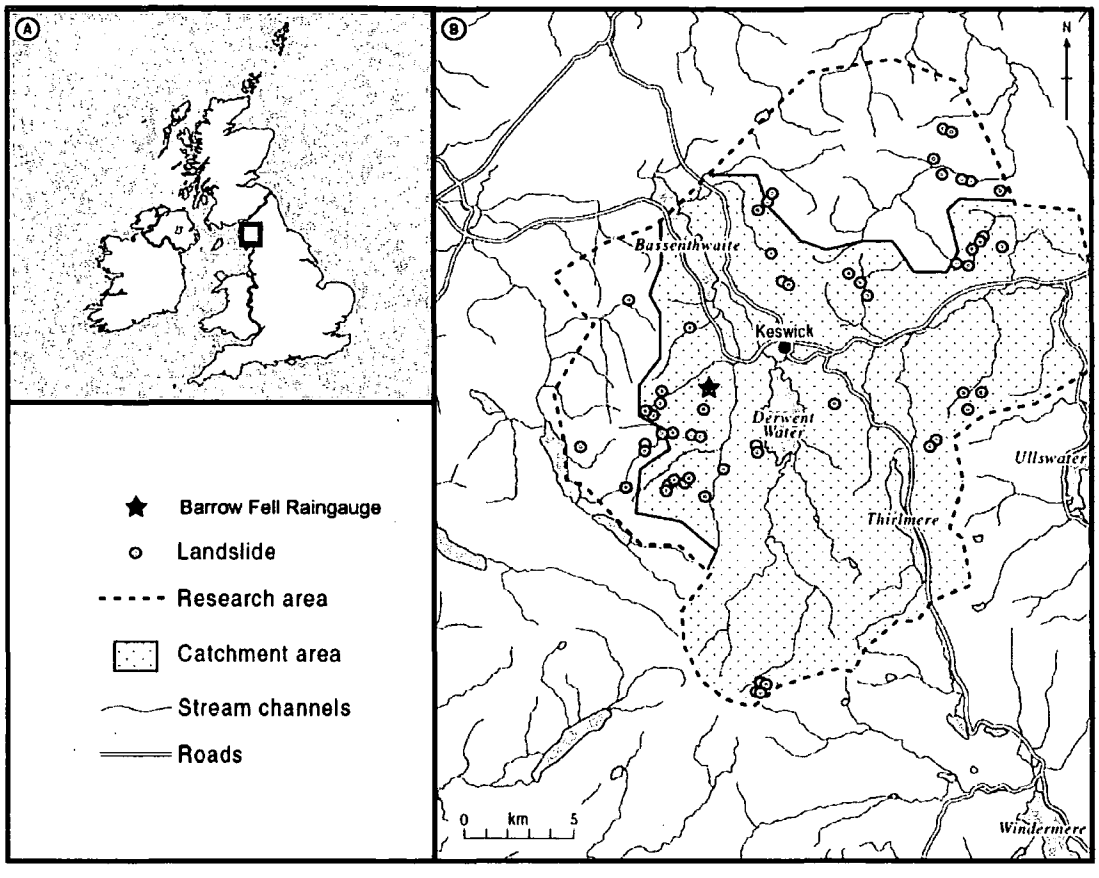

Trigger Rainfall Event

The landslides that occurred in the Lake District in January 2005 were predominantly triggered by elevated pore water pressures as a result of intense rainfall. Figure 2-7 shows a NIMROD RADAR image (British Atmospheric Data Centre, 2003) showing rainfall (mm) at 0200h and 2130h on 7 January 2005. Intense rain is clearly visible over Cumbria in both pictures. Heavy rain fell for most of the day, with a small respite between 0300 and 0900h, resulting in many of the Environment Agency rain gauges in the central Lake District recording some of the highest 24h values on record.

Table 2-1 shows all the gauges which recorded in excess of 100mm on 7 January 2005. All records are from automatic tipping bucket rain gauges (recording every 15 minutes) except those (*) which are from storage gauges (measured daily totals). Values are as high as 180 mm and span a broad area across the northwest and central sections of the study area out to the eastern Lake District, which corresponds to the area of active landsliding (Figure 2-6). At some of the recording rain gauge sites hourly rainfall intensities exceeded 100 mm hr-1 for brief bursts. Rainfall of this type is a well documented trigger for shallow landsliding in UK upland environments (Dykes and Warburton, 2007, 2008).

Figure 2-7: NIMROD RADAR image showing rainfall (mm) at 0200h (left) and 2130h (right) on 7 January 2005. Intense rain is clearly visible over Cumbria (from Warburton *et al.*, 2008).

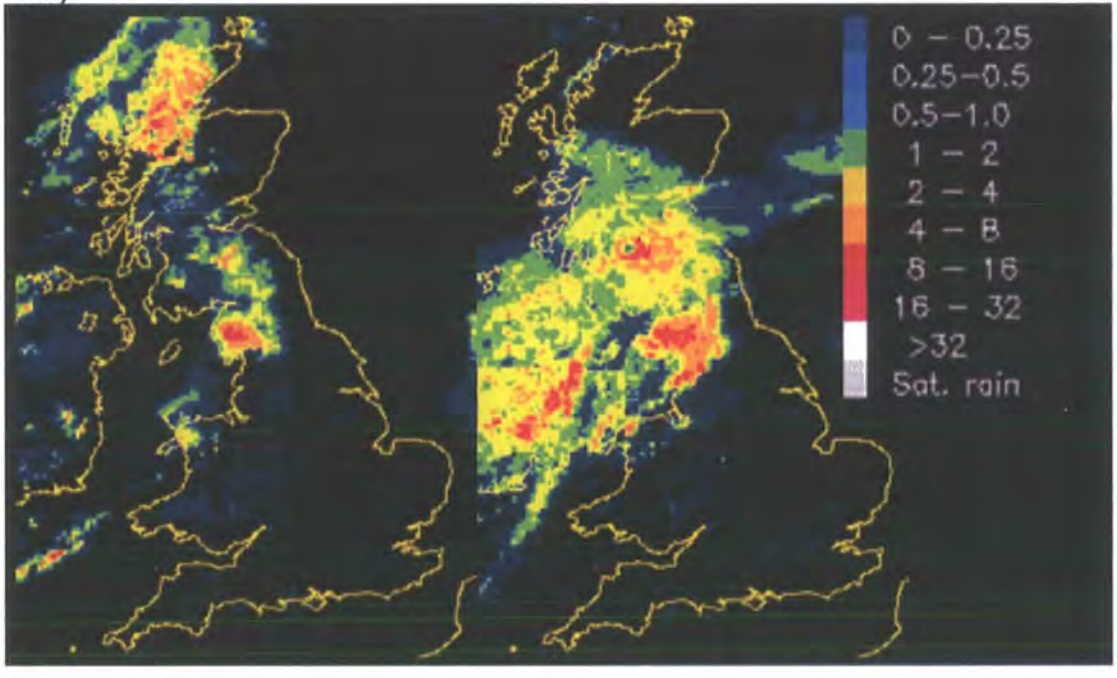

Table 2-1: Environment Agency rain gauge totals (> 100 mm) for 7th January 2005. All records are from automatic tipping bucket rain gauges (recording every 15 minutes) except those (*) which are from storage gauges (measured daily totals).

Rain Gauge	Daily Total (mm)
Rydal Hall	180 *
Honister Pass	164
Seathwaite Farm	159
Black Sail, Ennerdale	153
High Snab Farm, Newlands	148
Dale Head Hall, Thirlmere	144 *
Wet Sleddale Reservoir	137
St John's Beck	131
Grasmere, Tanner Croft	129 *
Burnbanks, Haweswater	126
Elterwater, Carr How	121 *
Moorahill Farm, Bampton	113
Brothers Water	112

Landslide Spatial Distribution

The landslides are not evenly distributed across the 457 km^2 study area, but show a considerable degree of clustering (Figure 2-6). The majority of landslides occurred to the North of the area on the Kirk Stile and Buttermere formations (Figure 2-2), with smaller clusters to the south and east. Based on this evidence it is tempting to conclude that geology is exerting some control over the distribution. This must be treated cautiously because we are dealing with shallow landslides which occur in the overlying regolith and it is the characteristics of this material (soil properties, geotechnical strength, hydrological properties and vegetation) that are important in determining stability. Hence geology often exerts a secondary influence on failures through its influence on the general topographic form of the landscape and material properties. For example, the distribution of failures in Figure 2-6 also reflects the particular storm rainfall distribution (and intensity) across the study area (Figure 2-7) and the influence of the local topography. It is clear from the shaded relief shown in Figure 2-2 that most of the landslide sites occur on the steeper slopes.

Landslide Magnitude Frequency Distributions

Landslide distributions can be analysed not only in terms of their spatial distribution but also a-spatially in magnitude frequency distributions. The

magnitude and frequency of landslides defines their impact on people (Alexander, 2005) and the landscape (Benda and Dunne, 1997). In particular, these distributions are useful in the stochastic modelling of geomorphic systems, where the realistic simulation of mass-wasting processes remains a challenge (Stark and Hovius, 2001). However, there are particular challenges in defining such magnitude frequency distributions (Brardinoni and Church, 2004). There is considerable debate over the best method of generating them, their statistical properties and their implications for 'scale invariance' (Evans *et al.*, 2003; Malamud *et al.*, 2004). For many landslide inventories, the magnitude frequency distribution of medium and large landslides has been found to closely approximate an inverse power law (Fujii, 1969; Whitehouse and Griffiths, 1983; Ohmori and Hirano, 1988; Sasaki *et al.*, 1991; Noever, 1993; Sugai *et al.*, 1994; Yokoi *et al.*, 1995; Pelletier *et al.*, 1997; Hovius *et al.*, 1997, 2000; Dai and Lee, 2001; Guzzetti *et al.*, 2002; Dussauge-Peisser *et al.*, 2002; Dussauge *et al.*, 2003) despite large differences in landslide types, sizes, distributions, patterns, and triggering mechanisms. This power law magnitude frequency relationship has been linked by some to self organised criticality (after Bak *et al.*, 1988) in the system (Noever, 1993; Hergarten and Neugebauer, 1998). Other explanations for the power-law dependence have been given by Hergarten and Neugebauer (2000) who proposed two alternative models that both give power law distributions; and Pelletier *et al.* (1997) who combined a slope stability and soil-moisture analysis to obtain a power-law distribution. Following these studies, Malamud *et al.* (2004) found that three landslide inventories (Northridge, Umbria and Guatemala in Figure 2-8) were well represented by an inverse gamma distribution combining a power law tail and exponential roll-over. They suggested this as a generally applicable landslide magnitude frequency relationship. If this is the case it has exciting implications: 1) the average area of landslides that occur in an event will be the same for every 'complete' inventory; 2) landslides can be defined in terms of a 'magnitude' for each event similar to that for earthquakes by specifying the total number, area, and/or volume of landslides in an event; and 3) incomplete inventories, for example where smaller landslides are not included due to censoring, can be compared with the general landslide probability distributions to infer the corresponding landslide-event magnitude (Malamud *et al.*, 2004).

However, others have found exponential (Montgomery *et al.*, 1998) or log-normal (Evans, 2003) landslide magnitude frequency relationships. Evans (2003) suggested that the general conclusion that landslides follow power-law scaling for all size ranges, and that "scale invariance is a general property of the landslide mechanism" (Hovius, 2000) may be premature. The debate over a landslide's scale specificity is important because: if "in earth sciences, scaling never applies over unlimited ranges" (Evans, 2003), then scaling relationships cannot be used to make up for limited measurement resolution or to extrapolate but are confined to interpolation and estimation within the range of the data.

Figure 2-8: Magnitude frequency relationships for the January 2005 Lake District landslides in the context of other relationships derived from the landslide inventories detailed in Table 2-2 (modified from Stark and Hovius, 2001; Malamud *et al.*, 2004; and Brardinoni and Church, 2004).

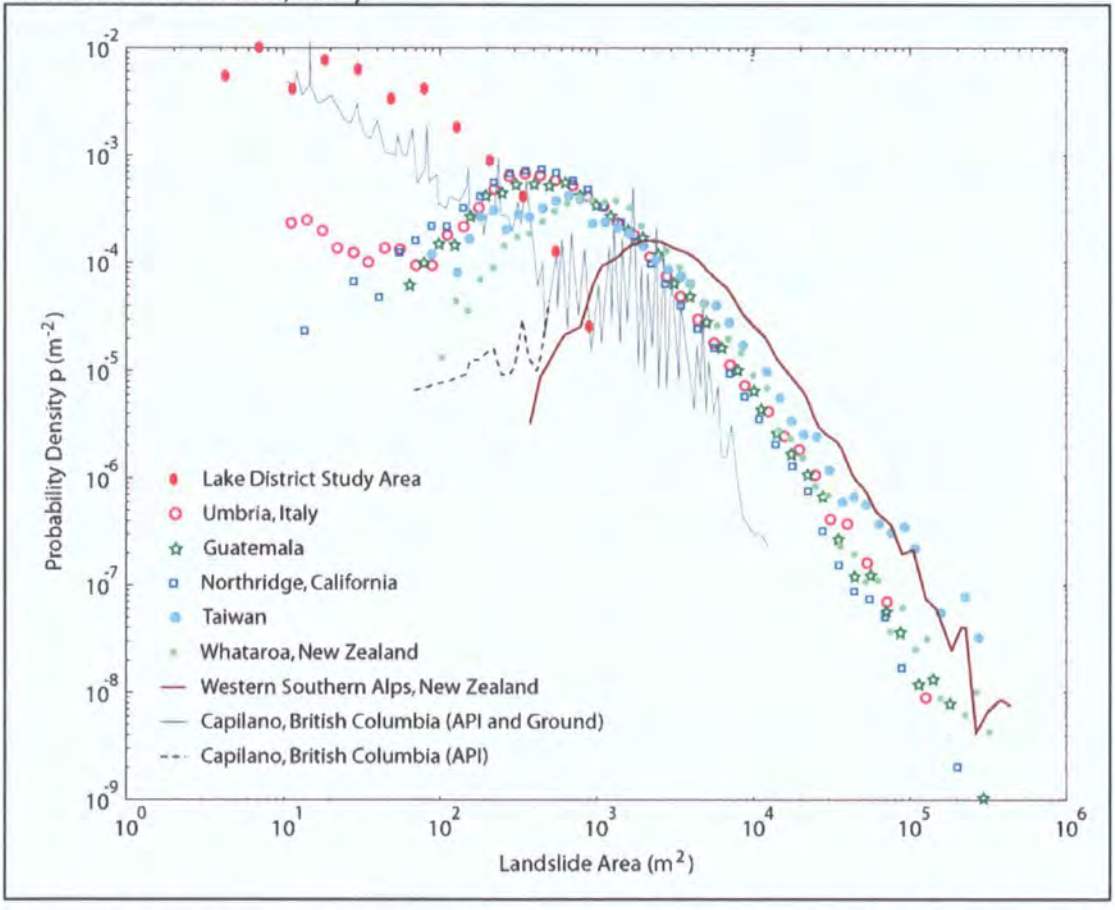

Figure 2-8 shows characteristic landslide magnitude frequency distributions for six large landslide inventories (Table 2-2) in differing settings and with differing triggers (Malamud, 2004). The Lake District landslides do not fit the same distribution. However, they do follow a similar trend to the data of Brardinoni and Church (2004) acquired using both aerial photograph interpretation and

ground survey. The inventory from Brardinoni and Church (2004) based only on aerial photograph interpretation follows a similar pattern to that of the other inventories. They suggest that, when ground surveyed landslides are included, the rollover disappears and the power law continues down to very small (~10^1 m^2) landslides. This is similar to the magnitude frequency distribution for Lake District landslides. However, in the Lake District case the distribution deviates from a power law and does appear to display some rollover for very small landslides (Figure 2-8). These observations are important and I will return to them in Chapter 7 where I revisit my observations from the study area in the context of the results from the preceding chapters. The lively debate among earth scientists over the form of landslide magnitude frequency relationships and its implications suggests that our understanding of landslide processes is not limited to spatial analysis. Even assessed non-spatially landslide distributions are important indicators of both landslide's geomorphic power and the processes that drive them.

Table 2-2: Details on the landslide inventories from which the magnitude frequency relationships in Figure 2-8 are derived (API denotes Aerial Photo Interpretation).

Location	Sample Size	Method	References
Northridge, California, USA	11111	API	(Harp and Jibson, 1995; 1996)
Umbria, Italy	4233	API	(Cardinali *et al.*, 2000)
Guatemala	9594	API	(Bucknam *et al.*, 2001)
Taiwan	1040	API	(Hovius *et al.*, 2000)
Whataroa, New Zealand	3986	API	(Hovius *et al.*, 1997)
Western Southern Alps, New Zealand	5086	API	(Hovius *et al.*, 1997)
Capilano, British Columbia, Canada	865	API	(Brardinoni and Church, 2004)
Capilano, British Columbia, Canada		API & Ground	(Brardinoni and Church, 2004)
Northern Lake District, UK	68	API & Ground	This thesis

Scar Geometry

Lake District landslide scars vary in size from small streamside scars, to major hillslope failures as large as 1700 m^3, on slopes from 6° to 44° (Figure 2-10); however they do display certain common characteristics. Typically they have flat slide planes (Figure 2-11), which usually develop along a boundary between soil materials of different density or permeability (Figure 2-9). Depth to the landslide failure plane is usually <3 m (Figure 2-10) and the length of the slide is commonly large compared with its depth. Following failure a distinctive scar

remains on the hillside below which debris is deposited in a linear runout track (Figure 2-9).

Figure 2-9: Schematic illustrating the key characteristics of a typical shallow translational landslide in the study area

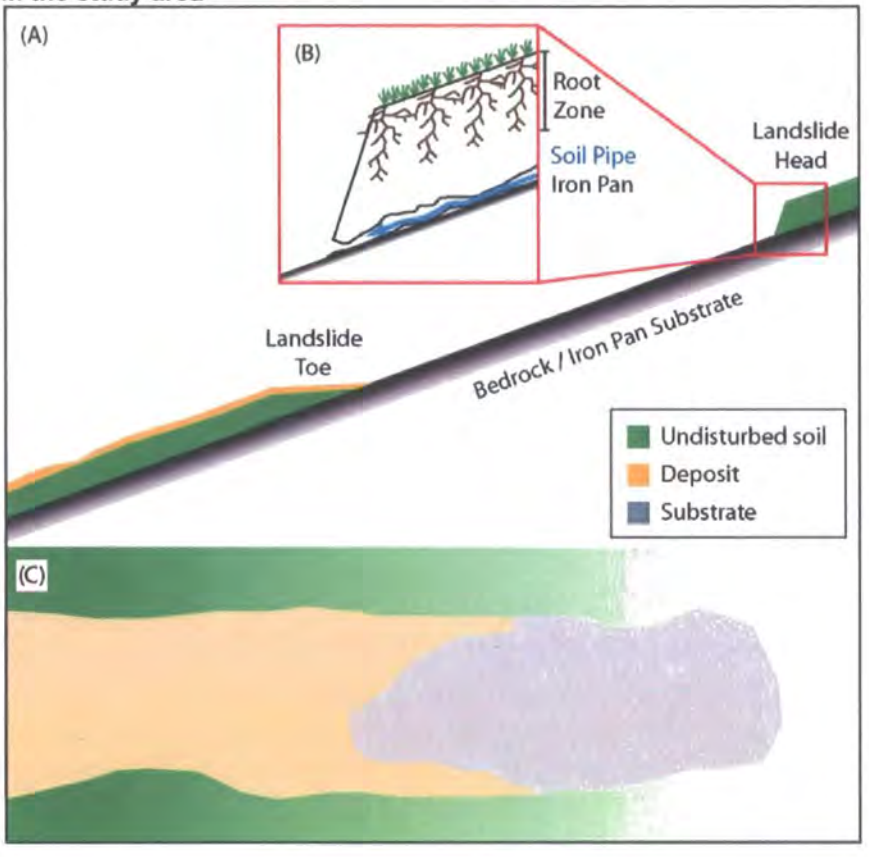

Figure 2-10: Frequency distributions from the Lake District Landslide Inventory for: A) mean scar depth and B) slope of the failure plane.

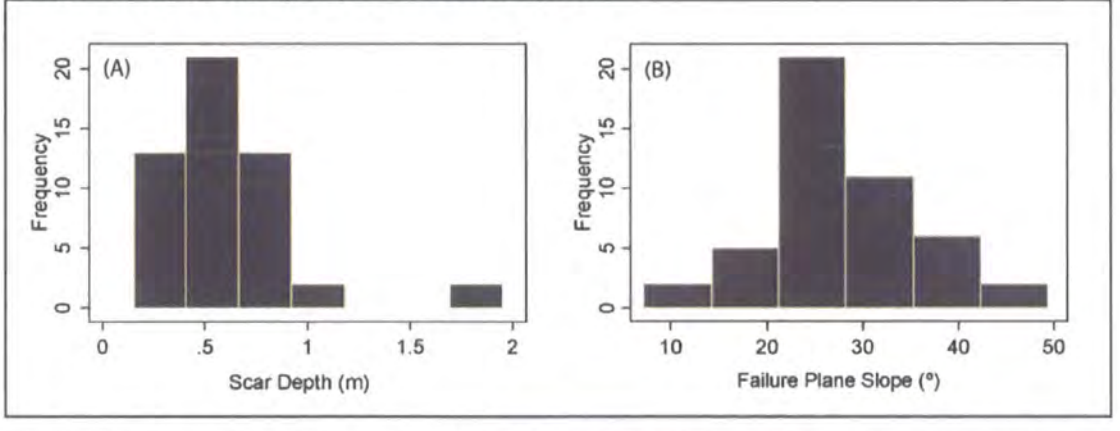

The landslide failure plane is parallel to the ground surface over much of the scar but must deviate from this at some point to intersect the surface at its lower boundary; I term this zone the landslide toe (Figure 2-9A). The profile form of the scars varies from wedge failures with no appreciable change in failure plane

slope towards the downslope margin, to trapezoidal failures with a distinct toe (Figure 2-11). Observed toe angles (angle of inflexion between the failure plane and the toe) range from 0-60°. Interestingly landslide toes rarely result in a reversal of the failure plane slope; i.e. if the failure plane inclination from horizontal is considered as a negative sign the angle of the toe from horizontal almost always has the same sign. These results have important implications for the mechanics of the soil's resistance at the toe which will differ from those in the main body of the landslide. I return to these properties in Chapter 4 where I parameterise the additional strength supplied by this toe region.

Figure 2-11: Landslide profiles from the Lake District Landslides Inventory measured using DGPS. Profiles are normalised to represent horizontal and vertical distances from the landslide head, their downslope end represents the first contact with undisturbed soil.

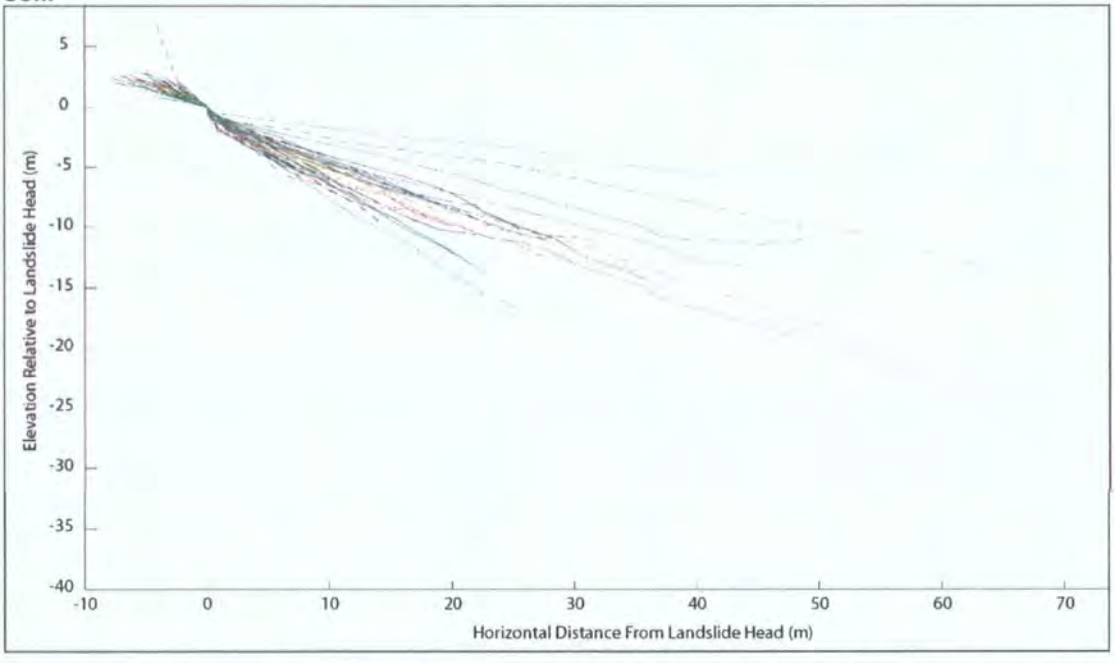

Comparing the length scales (length, width and depth) of observed landslide scars, width rarely exceeds length (i.e. aspect ratio is greater than or equal to one). Landslides shallower than 0.5 m appear to follow a linear length width trend, with a slope between 1 and 2 and an intercept of ~0 (Figure 2-12). The slope of the line connecting any point to the origin reflects the aspect ratio (length / width) of that scar. For landslides shallower than 0.5 m, scar aspect ratios are small and independent of size. The size of these slides is well constrained with minimum lengths and widths of 2.6 m and 2.9 m respectively and maximum lengths and widths 21 m and 17 m respectively (Table 7-1). It is worth noting here that these landslide lengths and widths in particular and those

in the study area in general are skewed towards low values (small landslides) and that these conditions violate a key assumption of the infinite slope stability model (discussed in detail in Section 2.6.3) on which most catchment stability models are based. Assessing the importance of this violation is a key rationale behind the research in Chapters 4 and 5 and will be dealt with in more detail in Section 2.6 below.

Table 2-3: Width and length statistics for landslides grouped by scar depth

Depth (m)	n	Length (m)			Width (m)		
		Mean	min	max	mean	min	max
< 0.5	19	11.42	2.58	20.74	8.36	2.91	16.81
0.5 – 1	32	26.10	7.58	74.13	9.94	5.06	24.52
> 1	5	42.99	16.62	61.21	12.96	7.87	21.37

Landslides between 0.5 and 1 m depth follow a steeper trend between width and depth, with more scatter (Figure 2-12). Their minima are higher than the shallower scars, 7.6 m and 5.1 m for length and width respectively (Table 7-1). Landslides deeper than 1 m: plot within the same space as the 0.5 to 1 m deep landslides, have no clear width length relationship and have minimum widths and lengths larger than the smaller depth classes. However, the small number (n=5) of landslides deeper than 1 m and their considerable scatter in width depth space makes it difficult to draw too many confident conclusions from these points. These observed landslide scar geometries may reflect geometric controls on stability or the spatial distribution of soil properties (for example soil strength or pore water pressure). Later in this thesis (Chapter 7) I will address this question by comparing observed geometries with stability predictions from a new stability model that takes into account the additional strength supplied by the margins of an unstable block.

Figure 2-12: The distributions of and relations between landslide lengths and widths from the Lake District 2005 inventory (symbol type and size indicates landslide depth).

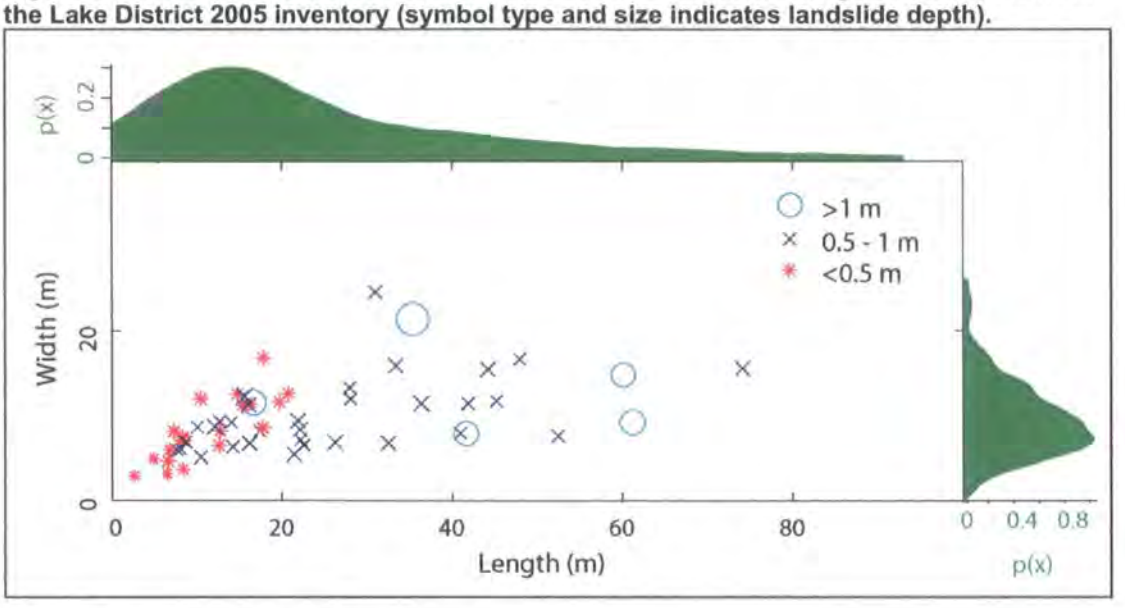

Other Site Characteristics

Observations of the failure scars after the event revealed several site characteristics that may have been important in defining the location or geometry of the failures. In particular, the presence of soil pipes at the head of the scars and the location of the failure plane at a hydrological discontinuity (Figure 2-9) corresponding with a hard layer which both impedes hydraulic conductivity and increases soil strength. For Lake District landslides, at over half the sites, this interface occurred at the soil-bedrock boundary (Figure 2-9). This is consistent with a range of other reports from landslide inventories both in the UK and elsewhere. For example, Gifford (1953) found on Exmoor that "Bare rock is now exposed at the head of most scars". However, this generalization should not be applied ubiquitously because soil depth does not always equate directly with the total thickness of unconsolidated material. In some locations, a translational failure plane may develop at any hydraulic conductivity discontinuity where positive pore water pressures can develop (Brooks and Richards, 1993; Brooks and Collison, 1996). These layers will affect the behaviour of both the water table (Campbell, 1975; Reid *et al.*, 1988) and the magnitude of local seepage forces, which can be re-orientated by conductivity contrasts of less than an order of magnitude (Reid and Iverson, 1992). Therefore the depth to the failure plane may be much less than the depth to competent bedrock. In the Lake District study area:

1) At nearly two thirds of the sites the failure plane was in the overlying substrate and not at the bedrock interface as is assumed in many slope stability models;

2) Failure in the substrate occurred on more resistant layers often in association with an iron pan (Figure 2-13);

3) Soil pipes were found in the head scars of nearly three quarters of the landslides and these were located at or just above the failure plane (Figure 2-14).

Figure 2-13: Examples of iron pans exposed on the surface of landslide scars (from 2005): A) Angle Tarn, B), Lonscale Fell, C) Cinderdale and D) Southerndale. Iron pans were covered with a layer of deposit in some cases and at others were both black and rusty red in colour.

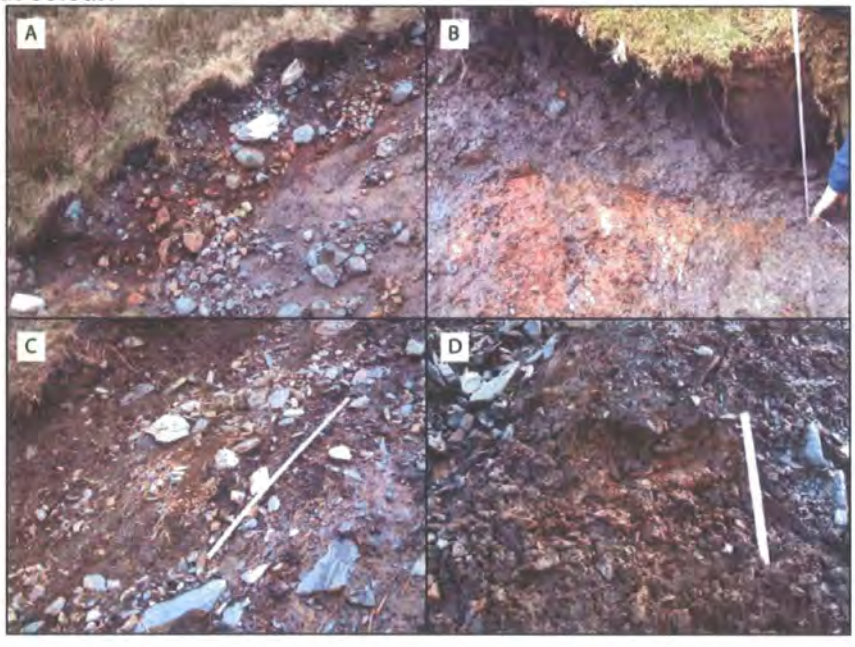

Figure 2-14: Examples of soil pipes exposed within the scars of shallow landslides in the Northern Lake District in January 2005: Slades Beck (A), Angle Tarn (B), Mosedale Beck (C), Catbells (D). Pipes tend to be located at the failure plane.

The effect of soil pipes on the hydrological behaviour of the soil is complex and it is difficult to draw direct links between failure and the presence of soil pipes. If soil pipes drain freely, they contribute to slope stability by increasing the rate of soil drainage and limiting the development of perched groundwater conditions (Uchida *et al.*, 2001; Kosugi, 2004). However, if the rate of water concentration to the pipe network is higher than the pipe flow transmission capacity, the pipe will fill with water increasing the pore water pressure in the surrounding matrix and inducing slope instability (Uchida *et al.*, 2001). These conditions could arise as a result of: 1) a soil pipe having a closed end (Sidle, 1984; Brand *et al.*, 1986; Kosugi, 2004); 2) a pipe becoming blocked for example as a result of pipe erosion and roof collapse (Onda, 1994; Zhu, 1997); 3) the rate of water supply to the soil pipe network in excess of its capacity (McDonnell, 1990; Montgomery and Dietrich, 1995). Such conditions are not unreasonable: in a study of peat catchments across the UK, Holden (2005) found that soil pipe size and density did not increase simply with distance downslope, suggesting that pipe networks are discontinuous and susceptible to blockage. While the process relationship between soil pipes, pore water pressures and slope instability is still poorly understood there are a large number of observations suggesting that soil pipes are found in the heads of many landslide scars in a variety of environments both

in Britain (Gifford, 1953; Jenkins *et al.*, 1988; Warburton *et al.*, 2004; Dykes and Warburton, 2007) and elsewhere (Brand *et al.*, 1986; Selby, 1993). Gifford (1953) reports that at some sites there was *"slight seepage of water along well defined slip planes* [at others] *water drained into the scar through a series of channels the size of rabbit-holes"*. Jenkins *et al.* (1988) reports water flowing from similar *"pipes and fissures"* at the interface between till and bedrock. Both observations are very similar to those from Lake District landslide scars (Figure 2-14).

Scars also appear closely associated with certain vegetation types, in particular *Juncus effusus* rushes were found at head of 85% of the Lake District landslide scars. This relationship between vegetation and landslide location has been observed in other areas of the UK. Gifford (1953) states that: *"It is the vegetation cover, which is itself an indicator of groundwater conditions, rather than with angle of slope that the distribution of landslides can be most clearly correlated"*. She found that: *"Most of the landslide scars lie within patches of wet vegetation (rushes, tussock grass and bog moss)"* and that slides rarely began in dry vegetation with no scars found on heather covered slopes. It is unclear whether *Juncus* vegetation is simply an indicator of wet conditions or whether these plants provide less root reinforcement, reducing the soil's shear strength and increasing its susceptibility to failure. Gifford (1953) suggests that it is both, since there is a clear link between these vegetation types and wetness and anecdotal evidence that they provide reduced cohesive strength to the soil. In Section 3.3 I will tackle this question by measuring the lateral root cohesion of *Juncus* and other typical Lake District vegetation types. In Section 6.7 I will return to this link between wetness and vegetation to broaden my hydrological study area using remote sensing.

Finally, many landslide scars exposed dense lateral root mats (Figure 2-15) but few roots were left extending through the basal failure plane. This observation appears common to many environments susceptible to shallow landsliding (Gifford, 1953; Preston and Crozier, 1999; Schmidt *et al.*, 2001). Existing studies suggest that root density varies with depth (O'Loughlin and Ziemer, 1982; Reubens *et al.*, 2007). Evidence from landslide scars (Figure 2-15) suggests that the density of roots declines with depth and that this is often a

step change, which coincides closely with the change from organic to mineral horizon. These observations are important because they suggest that it is the reinforcing effect of lateral rather than basal roots that is important for slope stability. Properly representing these effects requires different measurement techniques (discussed in Chapter 3) and modelling approaches (discussed in Chapter 4) it has significant implications for the controls on landslide scaling and failure geometry (discussed in Chapter 5).

Figure 2-15: Soil profiles at the margins of Lake District landslide scars: A) Poddy Gill, B) Hindscarth, C) Rigg Beck, D) Angle Tarn 4, E) Bowscale Village, F) Keskadale, G) Cinderdale.

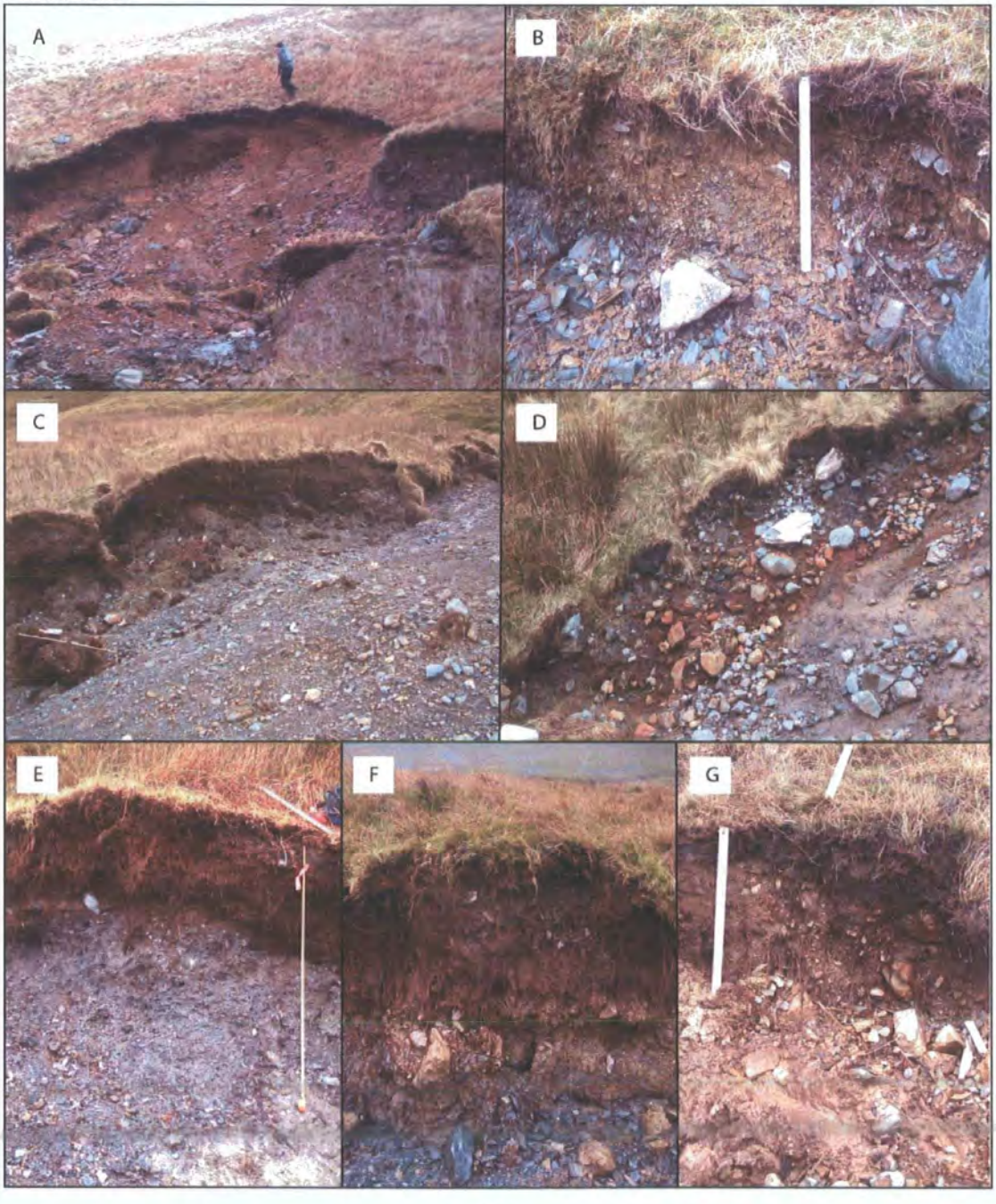

2.4.4. Section Summary

Most shallow landslides are triggered by elevated pore water pressure in response to rainfall or snowmelt. Infiltration, throughflow and groundwater rise are key components linking these processes; and in any combination they can elevate pore pressures sufficiently for failure to occur. These hydrological processes have traditionally been represented within models that treat soils and rocks as continuous porous media. However, observations from natural slopes suggest that their hydrology is strongly influenced by preferential flow through discontinuities such as fractures and macropores.

In the case of the Lake District landslides in January 2005 the trigger was intense rainfall (Table 2-1). Their spatial distribution over the study area appears closely related to both the track of the January 2005 storm cell (Figure 2-7) and the area's solid geology (Figure 2-2). A physical explanation for the latter invokes the geological control on the landscapes topographic form and material properties, which in turn control its stability. Their magnitude frequency distribution (Figure 2-8) does not closely match the power law relation found in some studies although it does have a rollover at very small slides. The Lake District's landslides are shallow (Figure 2-10) and translational (Figure 2-11), they have common geometric characteristics similar to those observed in other parts of Britain (Figure 2-12). They also display a series of common features indicative of the key processes driving instability (Figure 2-9). In particular: the failure plane is almost always at an interface in the soil (bedrock or iron pan; Figure 2-13); soil pipes are present in >70% of scars (Figure 2-14); *Juncus* grows at the margins of >85% of scars; and lateral roots are ubiquitous at the lateral scar edges but are extremely rare in the basal failure surface (Figure 2-15).

These observations have been instrumental in directing my research agenda, highlighting the key processes driving instability in my Lake District study area. However, many of the observed features are not unique to the Lake District but have been reported in field accounts of landslide sites across the world. Based on these observations I identified that: 1) failure plane depth did not necessarily

equate to depth to bedrock; 2) lateral root cohesion was likely to be an important control on stability; 3) the hydrological conditions at landslide sites may not be well represented by the conventional topographically driven hydrological models; but 4) they may be effectively indicated by the presence of certain surface vegetation (*Juncus*).

As a result of finding 1 I was prompted to carefully examine each of the input parameters to any slope stability model and try to ensure that the parameter in the model and that measured in the field matched as closely as possible this is the agenda for chapter 3.

Finding 2 highlighted a mismatch between an observed process in lateral root cohesion and its representation in the models, which was solely basal. This opened a broader question for me about the extent to which additional strength supplied by the margins of a slide and routinely neglected in catchment stability models might represent an important control on stability. I start to address these questions in Chapters 4 and 5.

Findings 3 and 4 presented both a problem, since, as I will explain in Section 2.6.5, landslide models are often founded on an assumption that wetness is topographically driven, this was something I felt needed to be assessed for my study area (the subject of Chapter 6). In this respect 4 offered a potential solution, or at least a potential research approach since combined with remotely sensed imagery a vegetation proxy for wetness might allow a much broader assessment of its relationship with topography.

2.5. Soil Mechanics for Slope Stability: an introduction

2.5.1. Scope of the Section

In this section I briefly summarise the key geotechnical terms and concepts applied in this thesis. Further background can be found in: Craig (2004) and Powrie (2002). Soil is a three phase material composed of both solid grains and voids filled with water or air. This granular multiphase characteristic has important implications for its behaviour and failure mechanics, which differ from

those of other materials. Here I define three key concepts common to all materials: stress, stain and strength (Section 2.5.2). Characteristics more particular to soil are then dealt with including: total and effective stress; the effect of pore water pressure; and drained and undrained strength; which are all important in modelling slope stability (Section 2.5.3). Finally, I explain the basis for representing soil shear strength using a friction angle; detail the distinction between peak and critical strength and explain the commonly applied soil cohesion parameter (Section 2.5.4). These concepts are the building blocks on which stability models are based, I introduce them first here then refer back to them throughout the following section that deals with limit equilibrium stability modelling and forms a bridge between soil mechanics theory of this section and its application in catchment stability models as illustrated in Section 2.7. The application of particular concepts in stability models is flagged briefly where it first occurs simply to highlight to the reader that this is something on which I will be relying later in the chapter.

2.5.2. Stress, Strain and Strength

Stress (σ) is the average force (F) acting on a unit area (A) in any chosen direction (tensile, shearing or compressive):

Equation 2-1

$$\sigma = \frac{F}{A}$$

For slope stability: $F = M\,g$, $M = V\rho$, where g is gravitational acceleration, M is the mass of the body, V is its volume and ρ its density. These relationships are central to slope stability and are the basic information required for limit equilibrium stability models (discussed in detail later). Stresses acting on a plane are decomposed into three mutually orthogonal components, with one component acting normal to the surface (normal stress) and the other two acting tangential to the surface (shear stresses). Normal stresses tend to change the volume of the material and are resisted by the body's bulk modulus. Shear stresses tend to deform the material without changing its volume, and are resisted by the body's shear modulus. Defining a set of planes aligned with Cartesian co-ordinates allows the stress state at a point to be described relative to x, y and z coordinate directions. Under static equilibrium (no net force) the

stress state at a point can be described by nine stress components from three planes. These nine components represent the stress matrix:

Equation 2-2

$$\begin{bmatrix} \sigma_{xx} & \sigma_{xy} & \sigma_{xz} \\ \sigma_{yx} & \sigma_{yy} & \sigma_{yz} \\ \sigma_{zx} & \sigma_{zy} & \sigma_{zz} \end{bmatrix}$$

Where the first subscript denotes the direction of the surface normal to which the stress acts and the second denotes the direction of the stress component. Applying conservation of momentum, equilibrium can be described by three differential equations:

Equation 2-3

$$\begin{cases} \frac{\partial \sigma_{xx}}{\partial_x} + \frac{\partial \sigma_{yx}}{\partial_y} + \frac{\partial \sigma_{zx}}{\partial_z} = 0 \\ \frac{\partial \sigma_{xy}}{\partial_x} + \frac{\partial \sigma_{yy}}{\partial_y} + \frac{\partial \sigma_{zy}}{\partial_z} = 0 \\ \frac{\partial \sigma_{xz}}{\partial_x} + \frac{\partial \sigma_{yz}}{\partial_y} + \frac{\partial \sigma_{zz}}{\partial_z} = 0 \end{cases}$$

In the case of two-dimensional plane stress these equations reduce to:

Equation 2-4

$$\begin{cases} \frac{\partial \sigma_x}{\partial_x} + \frac{\partial \tau_{yx}}{\partial_y} = 0 \\ \frac{\partial \tau_{xy}}{\partial_x} + \frac{\partial \sigma_y}{\partial_y} = 0 \end{cases}$$

These equilibrium equations in two and three dimensions are the basis for slope stability models, applied at the element scale in continuum mechanics approaches and to the entire mass, slices or columns in limit equilibrium analysis.

Strain is a dimensionless ratio, defined as the ratio of elongation (du) with respect to the original length (dx).

Equation 2-5

$$\varepsilon = \frac{dx' - dx}{dx} = \frac{du}{dx}$$

Where: dx is the original length, dx' is the new length and displacement u=x'–x. Where the strain in one direction is much less than the strain in the other orthogonal directions the smallest strain can be ignored and the body is said to experience plane strain analogous to plane stress. This is important for slope

stability models since plane strain is a key assumption for limit equilibrium methods in one and two dimensions.

Strength is the ability of a material to resist deformation (strain) by compressive, tensile or shear stresses. Deformation problems encountered in soil mechanics can be divided into two categories related to their stress strain behaviour. When stress levels are relatively low crystalline solids respond to imposed loads elastically (i.e. strain is proportional to load and original dimensions are recoverable). When the stress levels exceed the capacity of the solid to deform elastically it undergoes ductile, irrecoverable deformation and finally fracture (failure). These problems are considered to be in the plastic range and are analysed using plasticity theories. These two categories can be visualised on an idealised representation of a stress strain curve (Figure 2-16). Stress, strain and strength are related in that failure is defined by the stress strain relationship and strength is defined by the stress at failure.

Figure 2-16: Idealised stress strain relationship showing elastic plastic behaviour (from Fredlund and Rahardjo, 1993).

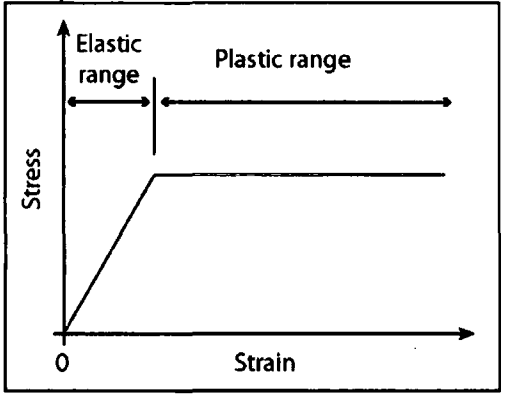

2.5.3. Total and Effective stress

Existing catchment scale slope stability models apply effective stresses assuming that the soil is under drained conditions. I will make the same assumptions throughout this thesis. The important distinction here is between total or effective stresses under undrained or drained conditions. **Total** vertical stress acting at a point below the ground surface is due to the weight of everything lying above: both soil and water. Total stress (σ_{zt}) increases with depth (z) and density (ρ, which varies with the water content of the soil):

Equation 2-6

$$\sigma_{zt} = \rho g z$$

Existing catchment scale slope stability models assume hydrostatic conditions (i.e. they do not account for hydrodynamic water flow). Under these conditions the pore pressure at a point (u) is given by the hydrostatic pressure:

Equation 2-7

$$u = \rho_w g z_w$$

where z_w is the depth below the water table. The combined effect of total stress (σ_{zt}) and pore pressure (u) controls soil behaviour such as shear strength.

Equation 2-8

$$\sigma'_{zt} = \sigma_{zt} - u$$

This **effective** normal stress (σ'_{zt}) represents the stresses transmitted through the soil skeleton only. As normal stress is increased, the soil particles immediately try to take up new positions closer together. However, water is incompressible and if the soil is laterally confined no particle rearrangement and therefore no increase in the interparticle forces is possible unless some pore water can escape. Under these (**undrained**) conditions, pore water pressure increases with increased normal stress while the interparticle stress, the effective normal stress and therefore the shear strength remain constant. If the excess pore water pressures are allowed to dissipate the soil returns to the **drained** condition. Note that drained conditions do not describe dry conditions (although the concept can be applied in such conditions) but those where there is no stress-induced pressure in the pore water. Because shear stress in the soil can be resisted only by the soil skeleton, shear strength should be expressed as a function of effective normal stress at failure; the shear strength parameters being conventionally denoted with prime notation (c' and φ'). However, for ease of expression, and in line with the literature, I will assume effective soil conditions throughout this thesis, dropping the prime notation (so that c = c' and φ = φ').

These concepts are relevant to my research because of their effect on measured strength parameters (which differ depending on the stress conditions in which they are measured). They are also important as the foundations for our conceptual model of pore water pressure driven slope instability. If shear strength (s) is proportional to effective normal stress (σ) so that changes in effective stress cause changes in strength, then as the pore water pressure (u) in the soil increases, effective stresses are reduced by Δσ and soil strength is

reduced by Δs. If this reduced strength is less than the downslope shear stress then the result will be failure.

2.5.4. Soil Shear Strength Representation

Soil is able to withstand shear stresses due interparticle friction similar to those of a solid block sliding on a plane (Figure 2-17). This shear strength (s) is directly related to the effective normal stress (σ_n) by the coefficient of friction (μ):

Equation 2-9

$$s = \sigma'_n \mu$$

Alternatively, the coefficient of friction (μ) can be expressed as a friction angle (φ). This is the angle of inclination of the resultant stress (S_r) on the sliding interface, measured from the normal (Figure 2-17A).

Figure 2-17: A schematic of (A) the inclination of resultant forces on an interface; (B) the relationship between τ and σ_n when a block starts to slide (From Powrie, 2002).

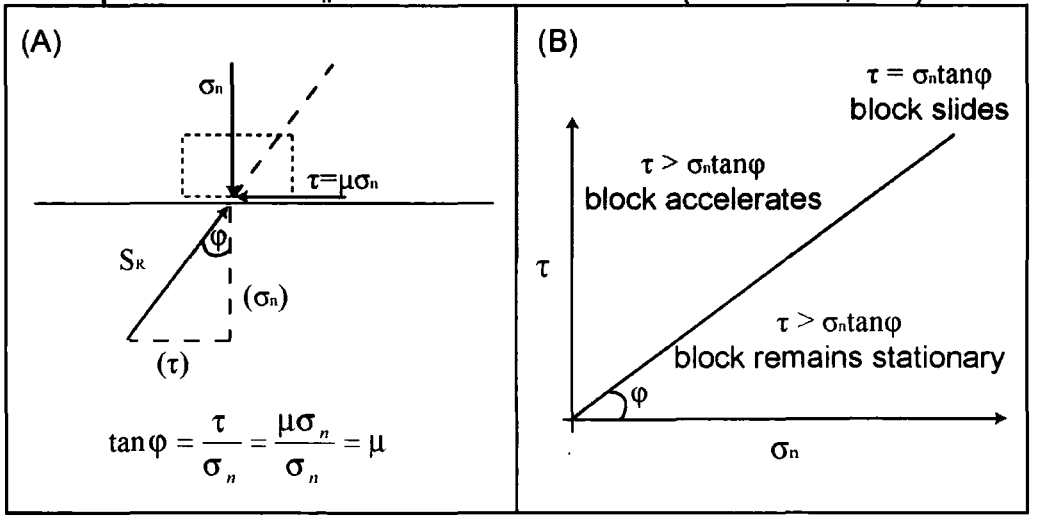

It follows then, that this is also the slope of the line defining shear and normal stress at sliding (Figure 2-17B), often referred to as the Mohr-Coulomb failure envelope. Substituting μ=tanφ into Equation 2-9 results in:

Equation 2-10

$$\tau = \sigma \tan \varphi$$

The inter-particle friction angle, for frictional resistance alone (φ_μ), ranges from 26° to 28° for quartz and feldspar and from 7° to 23° for mica (Horn and Deere, 1962; Lee and Seed, 1967). However, in soil (which is an aggregate of interlocking particles) the friction angle is less a function of friction than of the micro-mechanical interaction of particles. Frictional resistance may have little influence on the effective friction angle because: particles may move relative to each other mainly by rolling rather than sliding (Ni, 2003); and additional energy

is required to dilate, rearrange, or crush particles in order to shear the soil (Rowe, 1962; 1963; Lee and Seed, 1967).

Conceptually, soil has three distinct strengths: peak, critical (or ultimate) and residual defined by the relationship between strain, specific volume and normal stress. **Peak** strength is the maximum value of shear stress attained during failure (Figure 2-18). At its **critical** state, unlimited shear strain can be applied without further changes in specific volume, normal effective stress or shear stress. The soil continues to distort at constant effective stress and volume. The shear stress required to displace it in this state defines its critical strength (Figure 2-18). **Residual** strength is the lowest strength which occurs after very large displacements. For sand, the residual and critical strengths are the same. For clays, residual strength is about half critical strength and occurs when the flat clay particles become aligned parallel to the direction of shear.

Figure 2-18: Idealised stress strain relationship showing peak and critical strengths for an initially dense and an initially loose soil (modified from Powrie, 2002).

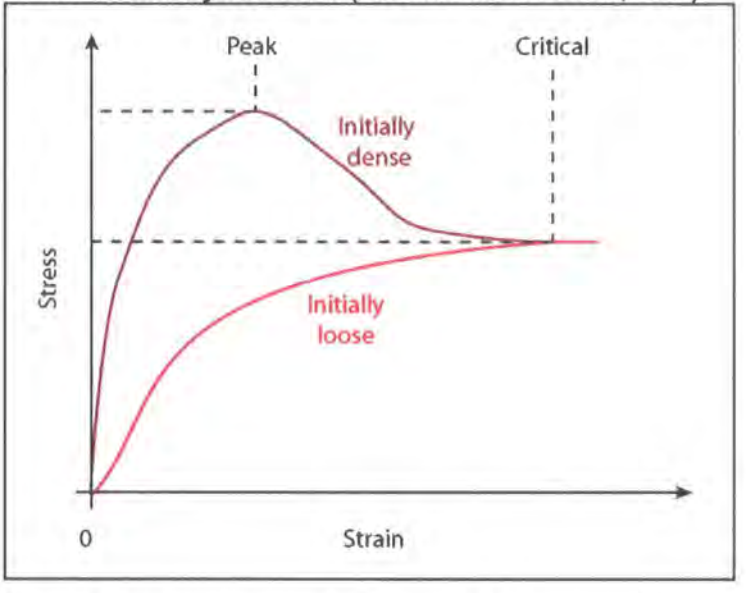

The ability of a soil to develop peak strength before reaching a critical state depends on its ability to increase in volume, or dilate (e.g. the initially dense soil in Figure 2-18). The peak stress ratio (peak / critical strength) decreases as the normal effective stress increases, reducing void ratio and diminishing the potential for dilation. As a result, the Mohr-Coulomb envelope formed by peak strength is curved (Figure 2-19A). Fitting a straight best fit line (Figure 2-19B) to this data results in misrepresentation at either high or low effective stresses, a power function might provide a better fit (Miller and Borgman, 1984; Hammond

et al., 1992; Preston and Crozier, 1999, Powrie, 2002). However, linear failure envelopes are the simplest and most commonly applied method of characterising soil strength, these take the form:

Equation 2-11

$$s = c_s + \sigma_n \tan\varphi$$

where: c_s, the effective soil cohesion, is the shear strength at zero normal force (Figure 2-19B). This positive intercept is commonly attributed to temporary negative pore water pressures (suction); or diagenetic effects such as chemical bonding, cementation of grains and creep effects (Hammond *et al.*, 1992). However, although some soil particles may be lightly cemented, the bonds are brittle and once broken, their strength is lost. Surface forces in clays can be significant at low effective stresses but at depths greater than a few centimetres they are generally small relative to the weight of the soil. As a result, interparticle 'friction' is the main source of strength for nearly all soils, whether they are predominantly sand, silt or clay (Powrie, 2002).

Figure 2-19: Mohr-Coulomb failure envelopes plotted with peak strength data, showing: A) the curved failure envelope and its relationship with critical state strength; B) the overestimation at low normal stress resulting from a linear failure envelope.

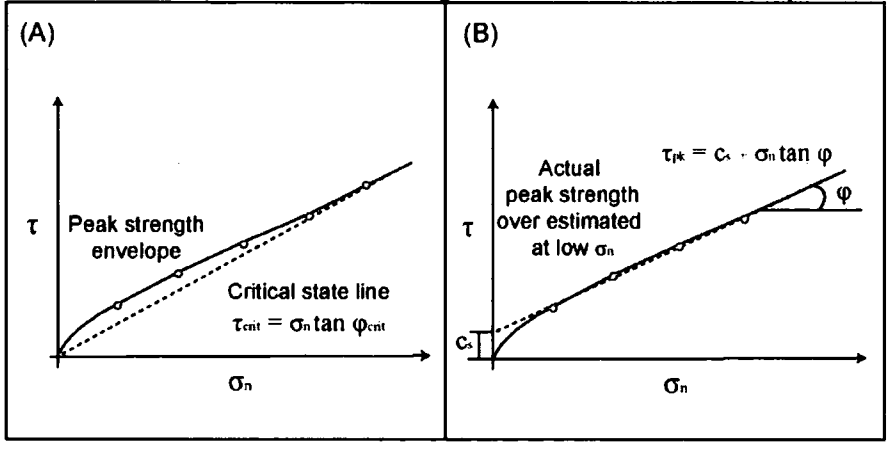

Large values of soil cohesion in apparently cohesionless sands and gravels (Holtz and Gibbs, 1956; Schroeder and Alto, 1983; Schroeder and Swanston, 1987) can result from: fitting a straight failure envelope to curved test data (Figure 2-19); or from scattered test data due to specimen variability or testing errors. These c_s and φ values may be inappropriate for two reasons. First, they will overestimate shear strength at small effective stresses (shallow soil depths or steep slopes). Second, there is no guarantee that peak strength will be uniformly mobilised everywhere it is needed at the same time. It is more likely that some soil elements will reach their peak strength first, fail and shed load to

their neighbours, which will also become overstressed and fail, leading to a progressive slope collapse analogous to fibre bundle failure models (Powrie, 2002). However, ignoring the cohesion intercept and using only the reported φ value for shear strength could underestimate real shear strengths at all confining stresses.

These problems can be minimised by: 1) modelling the failure envelope as a curve with a power function (Figure 2-19B); 2) performing shear tests at normal stresses consistent with the *in situ* conditions; or 3) using critical rather than peak strength to characterise the soil (Figure 2-19A). Critical state strength should be free of both cohesion and dilation effects, and as a result should have a linear failure envelope without soil cohesion. Critical strength is only reached after some strain, which may only be achieved as the entire mass begins to fail. In practice, the soil strength integrated over the spatial extent of the failing mass and over the time period in which the failure occurs should lie somewhere between these two. By measuring both peak and critical strength it is possible to put an upper and lower bound on the soil strength. This is the approach that I will apply to soil strength characterisation for slope stability in Section 3.2.

2.5.5. Section Summary

Stress, strain and strength are related in that failure is defined by the stress strain relationship and strength is defined by the stress at failure. The equilibrium equations, which describe the state of stress at a point in static equilibrium, are the basis for the existing slope stability models that I will go on to review in Section 2.6.

These models apply effective stresses assuming drained conditions and I do the same throughout this thesis, this is important because it defines the measurement conditions required to collect the soil strength parameters in Section 4.2. Effective stress theory is also the basis for the conceptual model of pore water pressure driven slope instability that I described in Section 2.4.2 and express functionally in Section 2.6.3.

Interparticle friction is the main source of strength for nearly all soils; it is proportional to normal stress and can be parameterised using the friction angle (φ) to define a Mohr-Coulomb failure envelope. This friction angle is a central parameter in all catchment stability models, understanding its provenance is important because it is a parameter that I rely on throughout the thesis. Strength can be defined as peak or critical depending on its strain conditions. Peak strengths are related to dilation; their failure envelope is non-linear and is often parameterised using an effective soil cohesion (only reasonable under particular circumstances). Critical strength is unaffected by dilation, is only reached after some strain as the entire mass begins to fail. The spatially and temporally integrated soil strength that is relevant for slope stability in a landslide context should lie somewhere between these two. In Section 3.2 I will measure both to put an upper and lower bound on the soil strength.

2.6. Review of Slope stability models

2.6.1. Scope of the Section

Process-based mathematical modelling, one of the tools identified in Section 2.2.3, combines the conceptual models developed in Section 2.4.2, and the soil mechanics theory developed in Section 2.5. It draws on the building blocks from soil mechanics, placing them within a framework that functionally expresses the conceptual models of Section 2.4.2. Over the last century geotechnical engineers have developed a range of mathematical models to predict a slope's stability based on material properties and slope geometry. These models either represent the processes using continuum mechanics, solving the equations using numerical techniques, or they use a limit equilibrium approach assuming that the soil is a single block or a series of rigid blocks. Continuum mechanics approaches allow closer representation of the physical process, but their data and computational requirements make them unfeasible at the catchment scale. Limit equilibrium approaches are computationally less demanding; have data requirements closer to those available at the catchment scale; and can be solved in one, two or three dimensions. These advantages make it a powerful and widely used tool for catchment scale slope stability; I will follow the limit equilibrium approach in this thesis.

In Section 2.6.2 I introduce the factor of safety, and describe the limit equilibrium approach to stability calculation, its conceptual basis and assumptions. In Section 2.6.3 I focus on the infinite slope procedure, the most widely used limit equilibrium method within catchment slope stability modelling. I show how it is derived from the soil mechanics principles (Section 2.5) and relate it back to the conceptual model for slope stability (Section 2.4.2). In Section 2.6.4 I identify the data requirements for slope stability models highlighting the parameters to which the model is most sensitive. Finally, in Section 2.6.5 I review the hydrological models that provide the pore water pressure estimates for the geotechnical model within catchment scale slope stability models.

2.6.2. Limiting Equilibrium and the Factor of Safety

The factor of safety (*FoS*) is the factor by which shear strength must be decreased to maintain equilibrium with shear stress or the ratio of shear strength of the soil (s) to the shear stress (τ) required for equilibrium.

Equation 2-12

$$FoS = \frac{s}{\tau}$$

When FoS is unity, shear stress and strength are equal and the slope is just stable or in a state of 'limiting equilibrium' (the name given to procedures that use this method to estimate slope stability). Equilibrium can be calculated either 1) for the entire mass of the soil with its bottom at the failure plane and its top at the surface (e.g. Infinite slope procedure); or 2) by dividing the soil mass into slices and solving the equilibrium equations for each slice, a procedure termed the method of slices (e.g. Bishop's, 1955; or Spencer's, 1967). There are three static equilibrium conditions to be satisfied, equilibrium of: 1) vertical forces 2) horizontal forces; and 3) moments about any point. When applying limiting equilibrium methods there are more unknowns than the number of equilibrium equations so that the problem of calculating the factor of safety is statically indeterminate (i.e. cannot be calculated from statics alone) and assumptions are required to balance the equations and the unknowns.

The majority of slope stability analyses are currently performed using one or two-dimensional limit equilibrium methods, assuming plane strain (Section 2.5.2). The failure surface is assumed to be infinitely wide in the two-dimensional model negating the edge effects on the sides of the slide mass (Figure 2-20). The two-dimensional method of slices can be conceptualised as a train of vertical blocks resting on a curved slip surface. The blocks are attached to each other and to the slip surface with rigid-plastic glue, conforming to the Mohr-Coulomb shear strength envelope. The blocks are considered rigid and their properties are not related to those of soil. No deflection occurs prior to failure and at failure all blocks begin to slide slowly downwards together – without accelerating (Chugh, 2003). Most three-dimensional methods use a column based approach (Xie *et al.*, 2004). In this case, the two-dimensional conceptual model extends in the x direction to the natural boundaries such as end walls of the slide mass (Figure 2-20), and the two-dimensional vertical blocks become three-dimensional columns (Chugh, 2003).

Figure 2-20: Schematics illustrating the assumptions associated with stability models in 1, 2 and 3 dimensions, blue lines indicate phreatic surface, red lines indicate failure plane.

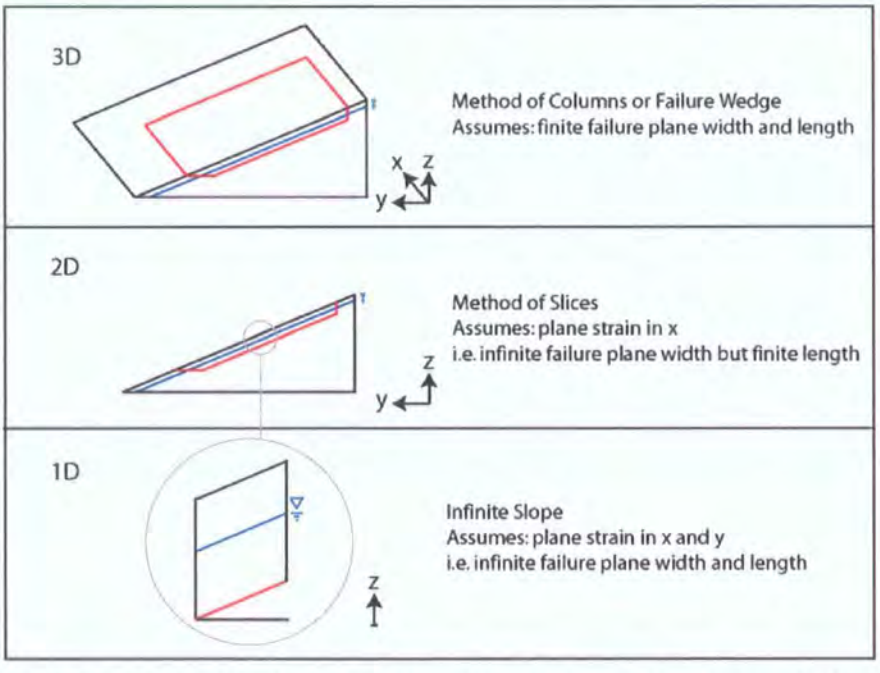

Two and three-dimensional methods allow improved representation of the failure geometry. However, they require fine scale discretisation of the slope, phreatic surface and failure plane geometries and are statically indeterminate (so that they need to be solved iteratively). These data and computational requirements limit their applicability at the catchment scale where analysis

almost invariably involves the simpler one-dimensional infinite slope procedure. This is considered a reasonable approximation for shallow landslides where the failure plane depth is much smaller than landslide width or length (an assumption that is revisited in Chapters 4 and 5).

2.6.3. Infinite Slope Procedure

The Infinite Slope procedure (Taylor, 1948) makes two key assumptions: 1) that sliding occurs along a plane parallel to the face of the slope; and 2) that the slope extends infinitely in all directions so that stresses are the same on the two planes perpendicular to the slope (e.g. stresses A-A' = stresses B-B' in Figure 2-21). These forces are collinear, equal in magnitude and opposite in direction. Therefore they exactly balance each other and can be ignored. The equilibrium equations are derived using a rectangular block (e.g. A-B-B'-A'). All the forces perpendicular and parallel to the failure plane are summed to give:

Equation 2-13

$$F_s = F_w \sin\beta$$

Equation 2-14

$$F_n = F_w \cos\beta$$

where: β is the block's slope; F_w is the weight of block; F_s is the shear force on slip plane; and F_n is normal force on slip plane.

Figure 2-21: Schematic profile view through an infinite slope showing forces and lengths.

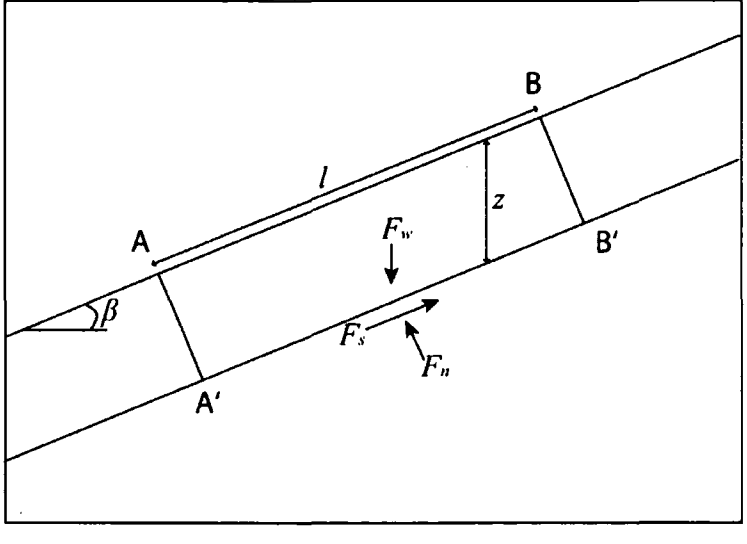

For a block of unit width:

Equation 2-15

$$F_w = \rho_s glz\cos\beta$$

where: ρ_s is the soil density; g is gravitational acceleration; l is the distance between the two ends of the block; and z is the vertical depth to the shear plane. Substituting Equation 2-15 into Equation 2-13 and Equation 2-14 gives:

Equation 2-16

$$F_s = \rho_s glz\cos\beta\sin\beta$$

Equation 2-17

$$F_n = \rho_s glz\cos^2\beta$$

Shear and normal stresses on the shear plane are constant for an infinite slope; they are obtained by dividing Equation 2-16 and Equation 2-17 by the area of the plane ($1l$) to give:

Equation 2-18

$$\tau = \frac{\rho_s glz\cos\beta\sin\beta}{1l} = \rho_s gz\cos\beta\sin\beta$$

Equation 2-19

$$\sigma = \frac{\rho_s glz\cos^2\beta}{1l} = \rho_s gz\cos^2\beta$$

Shear strength (s) for effective stresses is expressed by the Mohr–Coulomb equation (Section 2.5.4) as:

Equation 2-20

$$s = c(\sigma - u)\tan\varphi$$

where: c is effective soil cohesion; u is pore water pressure; and σ is normal pressure. Substituting Equation 2-18, Equation 2-19 and Equation 2-20 into Equation 2-12 to calculate the factor of safety (*FoS*):

Equation 2-21

$$FoS = \frac{c + (\sigma - u)\tan\varphi}{\tau} = \frac{c + (\rho gz\cos^2\beta - u)\tan\varphi}{\rho gz\cos\beta\sin\beta}$$

Assuming hydrostatic conditions:

Equation 2-22

$$\sigma = \cos^2\beta(\rho_s g(z - z_w) + (\rho_s g - \rho_w g)z_w)$$

where: ρ_s is soil density; ρ_w is water density; and z_w is the height of water table above failure plane. Substituting Equation 2-20 into Equation 2-21 to calculate the infinite slope factor of safety for hydrostatic conditions (Section 2.5.3):

Equation 2-23

$$FoS = \frac{c + (\cos^2\beta(\rho_s g(z - z_w) + (\rho_s g - \rho_w g)z_w))\tan\varphi}{\rho_s gz\cos\beta\sin\beta}$$

For cohesionless slopes:

Equation 2-24

$$FoS = \frac{(\cos^2 \beta - u)\tan\varphi}{\cos\beta \sin\beta}$$

In this case, the factor of safety is independent of the depth of the failure plane (z). Factors of safety for small and large depths are the same and it is equally probable that the failure surface will be deep or infinitely shallow. Therefore, in cohesionless soils, regardless of lateral dimensions an infinite slope treatment is appropriate. The procedure is also appropriate in cohesive soils if depth to the failure plane is limited (for example by soil depth) and is much smaller than the lateral extent. Infinite slope procedures satisfy all force equilibrium requirements (Section 2.5.2), moment equilibrium is not explicitly considered but it is assumed the forces on the ends are collinear and the normal force acts on the centre of the block.

The infinite slope procedure is widely applied in catchment slope stability models for two reasons 1) its assumptions (planar failure surfaces at shallow depths with high length / depth ratios) appear to mesh closely with the properties of observed shallow translational landslides; and 2) because it neglects the influence of the block's margins it is analytically tractable, extremely simple and computationally efficient. It effectively expresses the key processes described in the conceptual model of Section 2.4.2 in functional form:

"The downslope component of soil weight increases with slope angle [Equation 2-16] *whereas the normal component* [Equation 2-17] *and therefore the frictional strength* [Equation 2-20] *decreases, until a maximum angle of repose at which shear stress exceeds strength and the soil moves downslope* [Equation 2-21]. *Saturation reduces shear strength through the development of positive pore water pressure* [Equation 2-22] *and will cause failure if the slope is close to its angle of repose in dry conditions." (Section 2.4.2)*

However, the model's assumption that any unstable block is infinitely long and wide so that effects at the margins of the slide can be neglected is only reasonable where the soil is cohesionless and where the slides are very long and wide relative to their depth. My observations at landslide scars in the Lake

District (Section 2.4.3) suggest that lateral roots may provide important additional strength at the slide margins and that many slides are small, potentially violating this key assumption within the infinite slope model. I address this in detail in Chapters 4 and 5 where I assess the importance of lateral edge effects using a new finite slope model.

2.6.4. Data Requirements

All Limit Equilibrium models require: 1) the density of the material; 2) its strength (usually in terms of a Mohr-Coulomb failure envelope defined by a friction angle and in some cases soil cohesion); 3) the geometry of the ground and failure surfaces (to calculate volumes and partition stresses); and 4) the pore water pressure magnitude and distribution. For the infinite slope method: the geometry can be represented as a slope angle and depth to the failure plane; and the pore pressures are calculated from the height of the phreatic surface assuming hydrostatic conditions.

Figure 2-22 shows results from a sensitivity analysis of the infinite slope model, to identify the most important variables driving stability. In this case, sensitivity is analysed across a range of parameters representative of those expected in my study area: 1) variables are varied over a reasonable range (defined in Figure 2-22); 2) FoS is calculated using the central value for each variable; 3) FoS is calculated repeatedly as variables are altered individually across their reasonable range; and 4) percentage change in FoS relative to the base value is plotted against percentage change in each input variable. Increased soil and root strength will increase the FoS. Increased slope and saturation ratio (or water table height) will decrease the FoS. Generally the FoS is most sensitive to slope and insensitive to soil density. The relative sensitivity of FoS to other variables changes depending on the central values selected. As soil depth is decreased, the FoS becomes more sensitive to soil and root cohesion values and less sensitive to saturation ratio and friction angle. Soil and root cohesion values affect the FoS more for thin soils on steep saturated slopes, while friction angle affects FoS more on thick gently sloping soils because frictional strength is more important where normal stress is high and cohesive strength more important where it is low.

The results from this sensitivity analysis are useful because they help to identify the most influential parameters for slope stability (e.g. slope and friction angle; Figure 2-22). Error in these parameters will have a significant effect on the models predictive power whereas the effect of error in less influential parameters (e.g. soil density) will be small. In Chapter 3 I address each of the input parameters for slope stability models in turn, reporting measured values for my study area and the uncertainty associated with them. This information, combined with an understanding of the model's sensitivity to its parameters allows us to associate a confidence with our predictions; and to identify the 'limiting' parameters (those that are both influential and uncertain) on which future measurement efforts might be concentrated.

Figure 2-22: Sensitivity plot for the infinite slope equation (modified from Borga *et al.*, 2002).

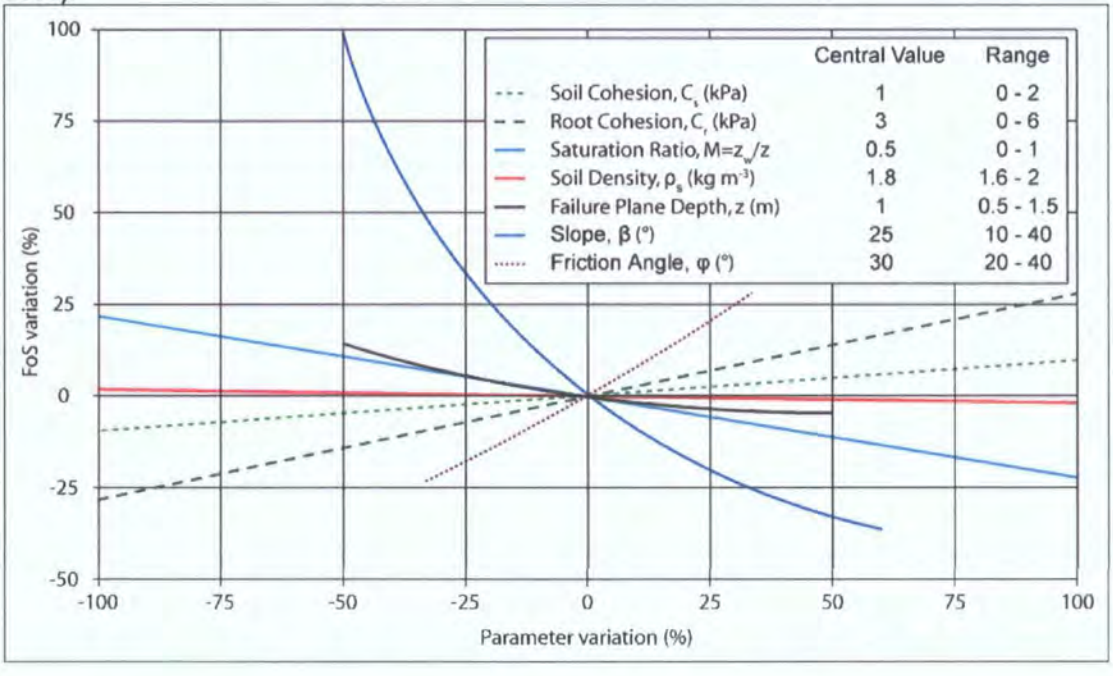

2.6.5. Hydrological Models

Sensitivity analysis for the infinite slope stability model indicates that slope stability (represented as a FoS) is sensitive to saturation ratio, a measure of the soil's pore water pressure. Soil moisture is highly variable across space and time so that pore water pressure represents both an important and variable parameter, making it a key priority in terms of input data for stability models.

Over the last 50 years, a large and growing body of research has developed within the hydrological literature concerned with modelling spatial patterns of soil moisture. Given the importance of soil moisture for slope stability, it is not surprising that hydrological models have been combined with geotechnical models to predict locations and timings of landslides. In fact the most distinctive factor differentiating catchment scale slope stability models is their method of predicting spatial soil moisture and pore water pressure.

Modelling landslide hydrology is not a new phenomenon and distributed physically-based hydrological models have been widely applied to slope stability modelling. However, even the most complete models represent a major simplification of our understanding of hillslope or catchment hydrology (Section 2.4.2). In particular, processes such as preferential flow in pipes or macropores are often ignored. Hence, it means that these models "*are based on flow physics in name, but the physics is very approximate*" (Beven, 2001); a situation that is likely to persist until field measurements improve to allow better description, particularly of subsurface flow. It is important that these hydrological models are physically-based since this maintains the connection between physical process and model predictions present in the geotechnical model. It is also important that their predictions can be spatially-distributed to provide the spatial pore water pressure field required to parameterise the geotechnical model. The broad spectrum of models that fulfil these criteria can be distinguished by the way they discretize the catchment and solve the process equations (Beven, 2001). I group them into four categories: fully process-based distributed models, kinematic wave models; steady state models; and one-dimensional infiltration models. In the sections below I deal with each in turn describing their salient features, identifying their advantages and disadvantages with reference to illustrative examples.

Fully process-based distributed models (solved in three dimensions) allow the prediction of local hydrological responses within a catchment but have many parameter values that must be specified for every grid element. This makes parameter calibration difficult but direct measurement or estimation of effective parameter values at the grid scale is also difficult due to heterogeneity of catchment characteristics and the limitations of available field measurements

(Beven, 2001). The large amounts of input data required and longer computation times involved have meant that few studies have attempted to simulate landslide hydrology in three dimensions (Griffiths *et al.*, 1999).

The SHETRAN model (Burton and Bathurst, 1998) was one of the first examples of slope stability prediction using a fully distributed physically based model. In this case it is a modified version of the Système Hydrologique Européen (SHE), a grid based, finite difference hydrological model (Beven *et al.*, 1980). Soil saturation conditions are modelled at a coarse resolution (200 m) with each grid element characterised by a single value of saturated zone thickness at each time step. Burton and Bathurst (1998) use a wetness index to link coarse scale saturated zone thickness with subgrid variability at the fine grid resolution (20 m). Griffiths *et al.* (1999) applied a three-dimensional extension of Collison *et al.*'s (2000) one-dimensional model. They represent infiltration, unsaturated and saturated flow, and throughflow, using a simple 'non-linear tank model' approach (Sugawara, 1995) with the soil profile split into by three layers.

GEOtop-FS (Simoni *et al.*, 2008) includes a treatment for the effects of matric suction on stability and accounts for transient responses of pore water pressure to rainfall infiltration; it accommodates horizontal variability in soil type, soil properties and vegetation cover. Soil moisture and matric suction within soil layers are computed for every time step by numerically integrating Richards' equation (Richards, 1931; Freeze and Harlan, 1969) in a three-dimensional scheme. The relationship between the suction potential and the volumetric water content is given by the van Genutchen (1980) model. The use of Richards' equation removes the need for the assumption of stationary conditions in subsurface flows allowing a full description of transient flows and infiltration, unlike the simplified steady state, saturated water flow model used in SHALSTAB (Montgomery and Dietrich, 1994) and dSLAM (Wu and Sidle, 1995).

Kinematic wave models can closely approximate those based on the extended Dupuit-Forchheimer assumptions in terms of predicting water table profiles (Beven, 1981). Kinematic wave models are usually limited to lateral flow in one

dimension (parallel to the impermeable layer and in a downslope direction) due to the problem of kinematic shocks when two waves converge on one another (Singh, 1996; Beven, 2001). Slope stability models applying a kinematic wave treatment of subsurface hydrology (Wu and Sidle, 1995) take a similar approach to that of the THALES and TOPOG models (Moore and Grayson, 1991; Grayson *et al.*, 1992, 1995; Vertessy *et al.*, 1993; Vertessy and Elsenbeer, 1999) and are based on the TAPES-C digital terrain analysis package (Moore, 1988). For each element in these models, the streamlines define no-flow boundaries; the upper contour is an inflow boundary and the lower contour an outflow boundary (Figure 2-25). These models (Wu and Sidle, 1995; Dhakal and Sidle, 2004) rarely account for vadose zone hydrology, implementing the kinematic wave in one dimension for the saturated zone only.

Steady state models, such as TOPMODEL, can be considered a further approximation to the kinematic wave description of subsurface flow (Kirkby, 1997), based on two assumptions: 1) the dynamics of the saturated zone can be approximated by successive steady state representations of the saturated zone on an area (*a)* draining to a point on a hillslope; and 2) the hydraulic gradient of the saturated zone can be approximated by the local surface topographic slope measured with respect to plan distance (tanβ). These assumptions lead to simple relationships between catchment storage deficit (the amount of additional water required for saturation) in which the main factor is the Kirkby topographic index: *a*/tanβ (Kirkby, 1975). Points with the same value of the index will be predicted as having the same hydrological responses. These assumptions are similar to those of the 'wetness' index developed independently by O'Loughlin (1981) and used in the TOPOG model (O'Loughlin, 1986; Moore *et al.*, 1988).

TOPMODEL in its original form (Beven and Kirkby, 1979) takes advantage of the mathematical simplification allowed by a third assumption: that the distribution of downslope transmissivity with depth is an exponential function of storage deficit or depth to the water table. Given this exponential transmissivity assumption, the appropriate topographic index of similarity is ln(*a*/tanβ). Other forms of transmissivity profile assumption lead to different forms of the topographic index; these have been examined by Ambroise *et al.* (1996). One

of the major attractions of this hydrological representation, which is based on a topographic index of hydrological similarity, is its simplicity and the small number of required parameters. Only upslope contributing area and local slope are required variables. These are relatively well constrained since they are derived from topographic data that are now of a high resolution and precision. However, even these parameters are sensitive to their source data, resolution and processing (examined in Section 3.6).

SHALSTAB (Montgomery and Dietrich, 1994) takes advantage of the simplicity of the steady state hydrological description to test the hypothesis that topography exerts a controlling influence on landslide locations. The advantage of the model is that its hydrological component is simple and computationally efficient, allowing quick analytical solution and making it suitable for application with high resolution topographic data - identified as an important control on a model's predictive capabilities (Lane *et al.*, 2004; Reid *et al.*, 2007). However, by assuming steady state rainfall, the model takes no account of transient conditions and is unable to predict temporal response of landslides to varying rainfall patterns (which was not its original aim).

Montgomery and Dietrich (1994) apply the TOPOG hydrological model (O'Loughlin, 1986) using a steady state net rainfall (precipitation less evapotranspiration and deep drainage into bedrock) and mapping the spatial pattern of equilibrium soil saturation based on analysis of upslope contributing areas, soil transmissivity, and local slope. They assume that all net rainfall becomes shallow subsurface flow, and is routed down slope. This allows calculation of the local flux through each cell, reducing the hydrological model to a calculation of wetness (m), which is the ratio of local flux at a given steady state rainfall to that at soil profile saturation:

Equation 2-25

$$m = \frac{qa}{T \sin \beta}$$

where: q is the steady state rainfall rate, a is the upslope contributing area per unit contour length, T is the saturated soil transmissivity (the depth integrated hydraulic conductivity) and β is the local slope. Their wetness index differs from that of Beven and Kirkby (1979) because they assume that saturated conductivity does not vary with depth and because they consider that

calculating local slope in terms of true rather than planimetric length is more physically correct hence sinβ rather than the conventional tanβ (Dietrich and Montgomery, 1998).

Many other landslide models have been developed following SHALSTAB which take a similar approach but with subtle differences (Borga *et al.*, 2002; Vanacker *et al.*, 2003). In particular, the SINMAP approach (Pack *et al.*, 1998) adds the capability of casting results into a probabilistic framework but handles the hydrology in the same way; and SEDMAP (Reid *et al.*, 2007) applies the network index version of TOPMODEL (Lane *et al.*, 2004) hypothesising that hydrological connectivity is the key property defining sediment delivery to the channel (Warburton *et al.*, 2008).

One-dimensional Infiltration Models represent an alternative hypothesis on the hydrological control on slope stability to that of the steady state models, which is most eloquently outlined by Iverson (2000). They hypothesise that that lateral redistribution is negligible relative to vertical infiltration over the time period of an individual storm (Iverson, 2000). As a result they simplify the representation of hydrological fluxes (represented in the Richard's equation) by reducing the problem from three-dimensions to one and considering only vertical infiltration. Originating from one-dimensional soil water-slope stability finite difference models (Anderson and Howes, 1985), these models have been developed to consider slope stability relative to climate, vegetation and paedogenesis (Brooks and Richards, 1993; Brooks *et al.*, 1995; Collison and Anderson, 1996).

Short-term pore water pressure variation has also been successfully simulated using pressure diffusion models (Haneberg, 1991; Reid, 1994; Iverson, 2000). This approach is applied in the USGS TRIGRS model which combines an infinite slope stability model with a vertical infiltration model based on Iverson's (2000) linearization of Richard's equation for transient unsaturated flow (Baum *et al.*, 2008). Results for a study area on the Puget sound, Washington suggest that the spatial pattern of instability is primarily controlled by topography (slope), while the intensity and duration of rainfall and the subsequent pore pressure responses control the temporal pattern of instability (Savage *et al.*, 2003). The

infiltration model applies mainly to soil depths that are shallow compared to the upslope contributing area and is unsuitable for simulating hydrologic response in dry soils. The results of these models are very sensitive to initial water table conditions: Baum *et al.* (2008) state that accurate initial conditions are probably the most significant input for the model. Obtaining such initial conditions requires a significant number of field observations and / or steady state modelling to generate these.

Summary

Most catchment stability models apply either one-dimensional or steady state hydrological models. Spatial pore water pressure predictions from steady state models are driven by topographic indices. The more complex three-dimensional or kinematic wave models represent flow dynamics more completely but their spatial predictions remain largely topographically-driven. Even one-dimensional model predictions, are sensitive to their initial conditions; when these are provided by a steady state model (as suggested by Baum *et al.*, 2008) they will also produce topographically driven spatial soil moisture patterns.

This is important because it suggests that all hydrological models include an assumption that wetness is topographically driven. The models do not account for some soil water processes, such as preferential flow in soil macropores, identified as potentially important to Lake District landslide hydrology (Section 2.4.3). This is unsurprising, since there is no adequate descriptive equation to represent them (Beven, 2001) and our current understanding of their behaviour is limited. The simplified conceptual model represented in even the most complete physically based models is unlikely to hold at all scales, but is likely to hold at some, particularly the broadest (catchment) scale. The key question is: how adequate is this for slope stability modelling? Or phrased slightly differently: does the emergent topographic signal drown the noise resulting from other factors described in our conceptual model of hillslope hydrology (Section 2.4.2)?

I tackle these questions in Chapter 6, where I test the hypothesis of topographically driven wetness, comparing observations to predictions primarily based on steady state wetness indices. These are the most widely applied

within the slope stability literature and they simply summarise the topographic wetness hypothesis for general conditions.

2.6.6. Section Summary

Two and three-dimensional methods allow improved representation of the failure geometry. However, their data and computational requirements limit their applicability at the catchment scale where analysis almost invariably involves the simpler one-dimensional infinite slope procedure. This approach is analytically tractable and effectively expresses the key processes described in the conceptual model of Section 2.4.2 in functional form. However, the infinite slope assumption which allows the effects at the slide margins to be neglected is only reasonable where the soil is cohesionless and where the slides are very long and wide relative to their depth. My observations from Section 2.4.3 suggest that lateral roots may provide important additional strength at the slide margins and that many slides are small, potentially violating this assumption.

Sensitivity analysis can identify the most influential parameters for slope stability. Error in these parameters will have a significant effect on the models predictive power. Information on parameter uncertainty, combined with an understanding of the model's sensitivity to its parameters allows us to associate a confidence with our predictions; and to identify the 'limiting' parameters on which future measurement efforts might be concentrated. Slope stability is extremely sensitive to the soil's pore water pressure, which is highly variable across space and time so that it represents a key priority in terms of input data for stability models. This information is conventionally provided by process based hydrological models. These models are based on an assumption that wetness is topographically driven and do not account for some soil water processes, such as preferential flow in soil macropores. The representativeness of these models is likely to depend on both the setting and the scale of enquiry, considerations that I return to in Chapter 6.

2.7. Case Study: SHALSTAB in the Lake District

The previous sections have reviewed catchment scale slope stability models in terms of their component geotechnical and hydrological models, indicating their inherent assumptions and the range of models available. To provide a practical illustration of the properties of these models I will finish the chapter by applying SHALSTAB to my Lake District study area as a case study of a simple catchment scale slope stability model. I use SHALSTAB in this context because it was one of the first examples of such models; it is also one of the simplest and most widely applied.

Substituting the saturation ratio (m) into Equation 2-23 from the discussion of infinite slope stability equations in Section 2.6.3:

Equation 2-26

$$FoS = \frac{c + \cos^2\beta\, g\, z(\rho_s - \rho_w m)\tan\varphi}{\rho_s\, g\, z \cos\beta \sin\beta}$$

where:

Equation 2-27

$$m = \frac{z_w}{z}$$

Then rearranging to solve for the critical saturation ratio required for failure (m_{crit}), i.e. solving for m where FoS=1:

Equation 2-28

$$m_{crit} = \frac{c}{\rho_w g z \cos\beta \tan\varphi} + \frac{\rho_s}{\rho_w}\left(1 - \frac{\tan\beta}{\tan\varphi}\right)$$

and using the hydrological treatment identified in my discussion of steady state models from Section 2.6.5 above, specifically Equation 2-25, which describes the soils saturation ratio m in terms of upslope contributing area per unit contour length (a), slope (β) rainfall rate (q) and soil transmissivity (T).

Equation 2-29

$$m = \frac{q}{T}\frac{a}{\sin\beta}$$

Substituting Equation 2-29 into Equation 2-28 and rearranging, we can describe the limiting stability for a soil element in terms of the ratio of rainfall rate (q) to transmissivity (T) using:

Equation 2-30

$$q/T_{crit} = \frac{\sin\beta}{a}\left[\frac{c}{\rho_w g z \cos\beta \tan\varphi} + \frac{\rho_s}{\rho_w}\left(1 - \frac{\tan\beta}{\tan\varphi}\right)\right]$$

Applying this model first to Coledale, a small catchment in the Lake District study area, in which there were several landslides in 2005 illustrates several interesting and widely reported properties of this type of model. Firstly, the model is not in perfect agreement with the observations. This is to be expected since the model is designed to predict zones where failure is most probable based on topography. Simple GIS based slope stability models such as SHALSTAB provide useful information on areas likely to be more susceptible to slope instability. However, when treated as fully deterministic using realistic parameters these models consistently predict larger, more numerous potential landslides than are observed (Carrara *et al.*, 1991; Montgomery and Dietrich, 1994; Montgomery *et al.*, 1998; Bathurst *et al.*, 2005; Figure 2-23). Failures do not occur at all sites predicted by the model and they do occur at some sites not predicted to fail. In some of the locations where landslides were observed in zones predicted as having a low probability of failure, this is a result of poor topographic representation. Although the elevation data used in Figure 2-23 has a 5 m resolution, slopes are often calculated using a square nine cell kernel, the landslide labelled A in Figure 2-23 was a small gully slide failure <10 m long, and the slope of the gully side is incompletely represented by the local slope value calculated from the elevation model.

Figure 2-23: SHALSTAB stability predictions represented as the ratio of rainfall to transmissivity log(q/T) for Coledale, Lake District, UK.

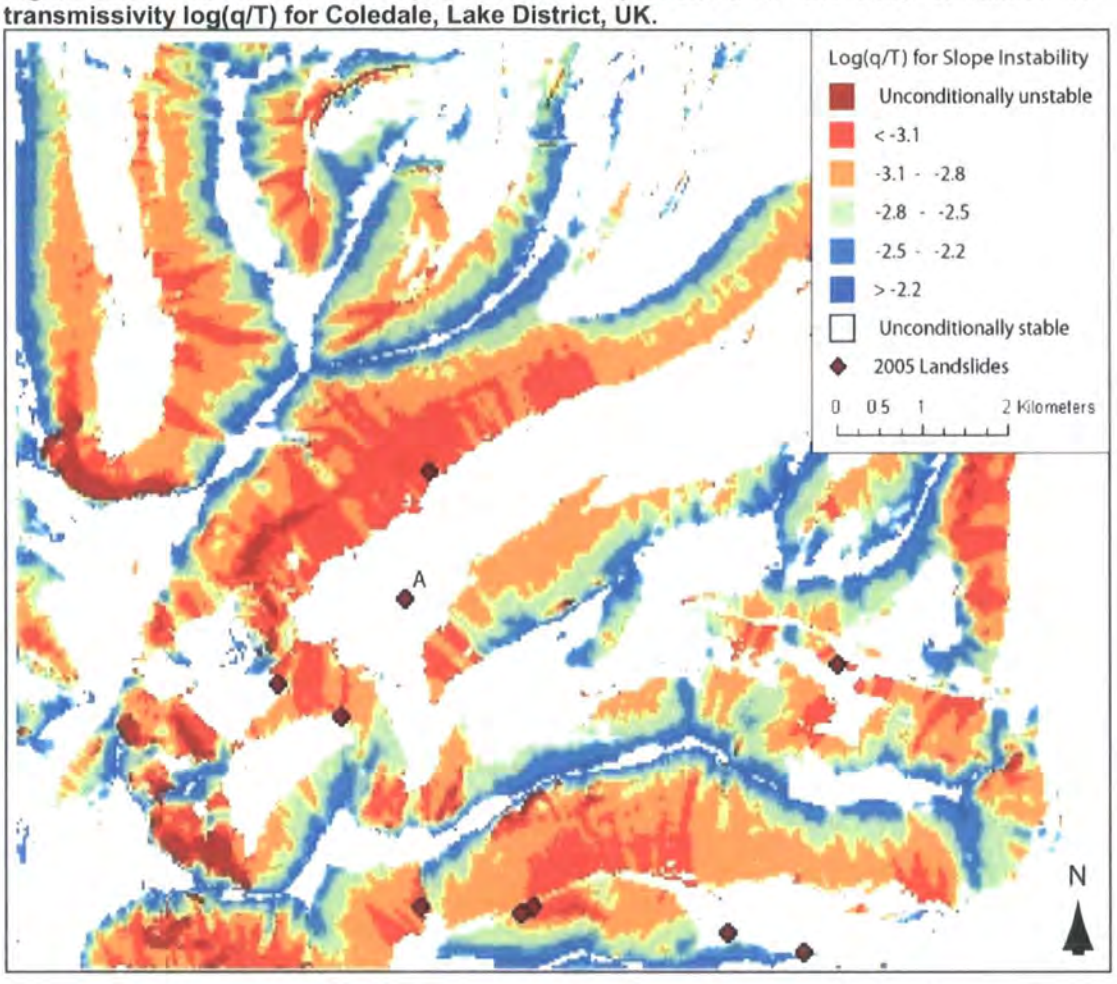

Spatial outputs from SHALSTAB for the entire study area of 457 km^2 are difficult to interpret. Therefore an alternative method of visualising the data is useful. Landscape elements (DEM cells) plotted in logarithmic space in terms of their local slope (x axis) and contributing area (y axis) can be partitioned into SHALSTAB relative stability predictions. These plots show three zones dependent on the relationship between the local slope and the assigned friction angle (Figure 2-24). Areas where the slope is so low that no failure can occur even when the cell is fully saturated are considered Unconditionally Stable. This zone is defined by:

Equation 2-31

$$\tan\beta < \left(1 - \frac{\rho_s}{\rho_w}\right)\tan\varphi + \frac{c}{\rho_s g\, z \cos\beta}$$

Areas where the local slope exceeds the friction angle so that even in unsaturated conditions the cell should fail are considered Unconditionally Unstable. This zone is defined by:

Equation 2-32

$$\tan\beta \geq \tan\varphi + \frac{c}{\rho_s g z \cos\beta}$$

Areas where the cell's stability is dependent on its degree of saturation and its local slope are considered Conditionally Stable. Saturation thresholds for the simple steady state hydrological model can be defined in slope area space for a given rainfall (q) and transmissivity (T) by solving Equation 2-29 for m=1. The conditional stability thresholds can also be defined for a given q and T using Equation 2-30. They begin at the point where the wetness threshold intersects the conditionally stable zone. At this point complete saturation is required for failure. The exponential decline in contributing area required for failure reflects the decreasing degree of saturation required to trigger failure as local slope increases towards the threshold of unconditional instability.

Figure 2-24: A schematic illustrating the SHALSTAB relative stability thresholds in slope area space. Each dashed line represents a doubling in steady state rainfall or 'storm magnitude' with decreasing T/q.

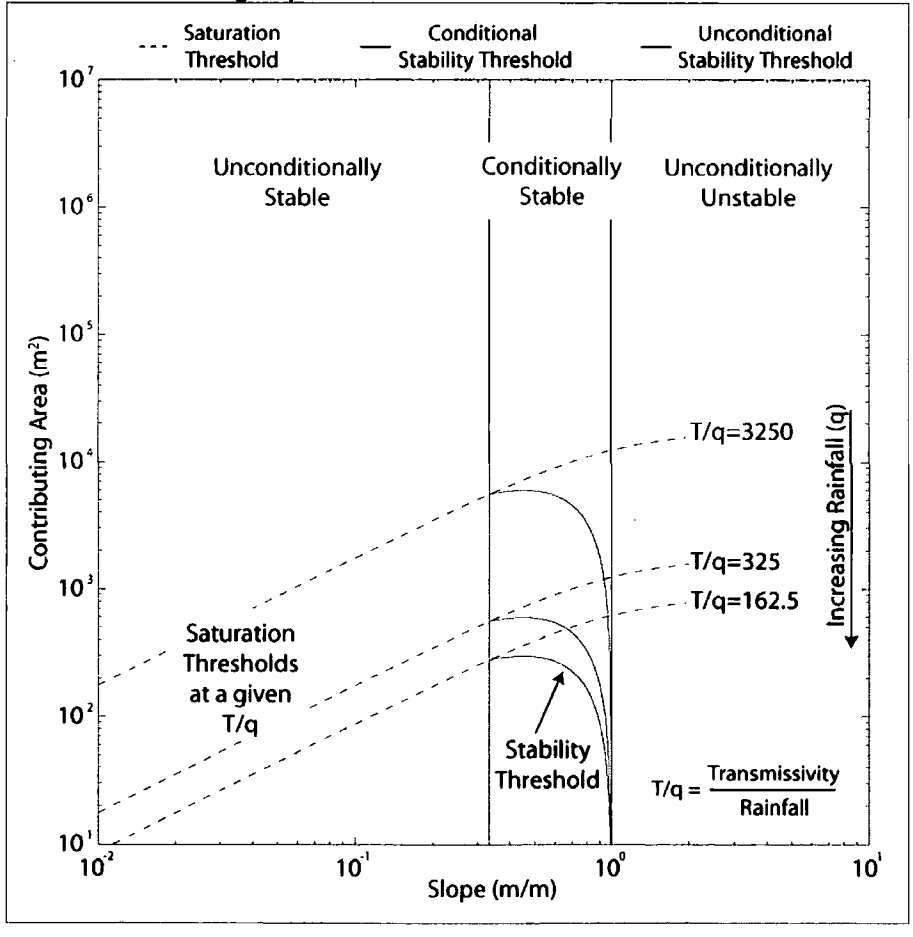

Viewing the data in this form illustrates similar trends to the spatial assessment for a smaller subset of the data (Figure 2-25). In particular cells containing

landslides appear to cluster in the mid range contributing areas (between 10^2 and 10^4 m^2) and largely in the conditional stability zone, with no landslide cells falling into the area predicted unconditionally unstable. The limiting slope angles for the conditional stability zone are defined by the soil strength parameters. In this case I have applied a friction angle of 45° without any cohesion (reasonable values for the coarse granular soils in the study area, Section 3.2). The fact that not all failing cells are captured within the conditional stability zone suggests that some or all aspects of soil strength (friction, cohesion or root reinforcement) vary spatially across the catchment. This is expected, and the choice of a single set of soil strength parameters is merely a simplifying assumption because: 1) our knowledge of soil strength and its spatial pattern is limited; and 2) it allows the model to represent only the effect of topography on stability. Some indication of the variability in soil strength parameters can be gained from tests *in situ* or in the laboratory; these are examined in Section 3.2.

Researchers often attribute the seemingly stochastic occurrence of landslides within the large predicted failure zones that these models produce to sub-grid variability in topography or spatial variations in soil depth, reinforcing effects from roots, precipitation, groundwater response and angle of internal friction (Dietrich *et al.*, 1995; Wu and Sidle, 1995; Montgomery *et al.*, 1997). Previous study in these areas has yielded some disappointing results for deterministic slope stability modelling (Montgomery *et al.*, 1997, 1998, 2002). In fact Montgomery *et al.* (2002) have suggested that because the characteristics of some of these parameters are so difficult to ascertain: models that attempt to represent them deterministically "may be no more insightful than interpretation of simple topographically driven models used to predict zones of high landslide potential" (Montgomery *et al.*, 2002). This suggests that deterministic stability predictions are unfeasible at present and that this is unlikely to be altered by small improvements in the quality of the input data (Chapter 3) or representation of failure mechanics (Chapter 4). However, it does not preclude the possibility that improvements in representation of the processes controlling failure will improve the ability of stability models to predict the locations of these broad zones; nor the potential of such additional constraints to provide information on the magnitude of landslides that might be expected in these zones. Finally, even the broad zones of predicted instability are controlled by the assumption

that wetness is topographically-driven, my research seeks to test this assumption.

Figure 2-25: All landscape elements in the study area (green) and the elements identified as landslides from the Lake District January 2005 inventory (red) plotted in slope area space with the SHALSTAB relative stability thresholds (explained in Figure 2-24).

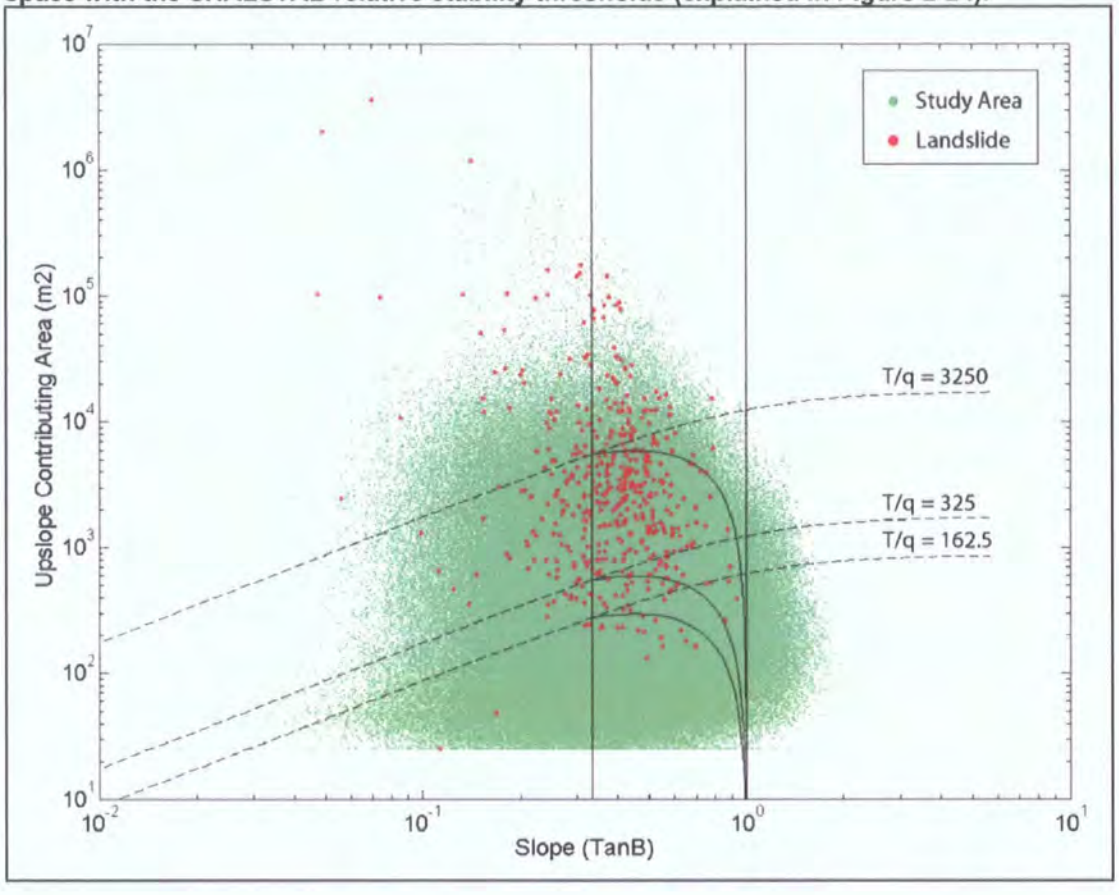

2.8. Chapter Summary and Research Objectives

Shallow landslides are an important geomorphological phenomenon that can be studied using a range of methods including process-based modelling. This thesis deals with shallow translational slides initiated by a reduction in effective normal stress as a result of increased pore water pressure. It focuses in particular on the English Lake District, a steep upland area with limited forestry and a temperate climate that has experienced considerable recent shallow landsliding. The location, timing and size of this type of landslide are often modelled at the catchment scale by combining an infinite slope geotechnical model with a distributed physically based hydrological model. Two of the areas where the assumptions of such models depart from observed conditions are: 1) that any unstable block is infinitely long and wide so that effects at the margins

of the slide can be neglected; and 2) that the spatial soil moisture pattern is topographically driven. To address these problems I will firstly develop a new way of accounting for the additional strength supplied by the margins of the block in Chapter 4. This will be tested and assessed for sensitivity (Chapter 5) allowing some important conclusions to be drawn regarding limiting landslide geometry. Secondly, I will test the topographic wetness hypothesis for the Lake District, both at the small and large scale, since it is the emergent pattern that I am interested in. However before making alterations to existing models it is essential that the input parameters are as well constrained as possible to avoid altering a good model structure to account for misrepresentation in model parameters. This is tackled next in Chapter 3, where I will deal with the data requirements for each parameter in turn.

3. Data Collection and Data Quality

3.1. Scope of the Chapter

In analysing model performance, characterising the quality and uncertainty of input parameters is an essential step. Chapter 2 gave a detailed review of distributed slope stability models. Section 2.6.4 identified five key input parameters, which are common to almost all slope stability models. This chapter deals with: soil strength (3.2); root reinforcement (3.3); soil density (3.4); soil depth (3.5); and topographic data, both for local slope and as a wetness indicator (3.6). For each parameter, this chapter addresses its nature; the measurement options; measurements adopted; and findings in relation to other empirical or mechanical studies.

3.2. Soil Strength

3.2.1. Scope of the Section

In Section 2.5 I identified soil strength as an important control on slope stability and reviewed the foundational soil mechanics associated with it. In Section 2.6.4 I have shown that the factor of safety, on which almost all slope stability models are based, is highly sensitive to the soil's strength which can be characterised using cohesion (c_s) and friction angle (φ). In Section 2.5.4 I suggested that, by measuring both peak and critical or residual strength it is possible to put an upper and lower bound on soil strength. This is useful because soil strength integrated over the spatial extent of a landslide and over the time period of failure should lie between these two values. In this Section I apply this approach to soil strength characterisation. There is strong evidence in the literature that soil strength is highly variable in three-dimensional space; observations of landslide failure planes at scars within the study area suggest that this is the case in the Lake District. I aim to characterise the soil strength and its variability for different locations and contexts within my study area.

In Section 3.2.2 I review existing theoretical and empirical research into soil strength to identify the key factors controlling it. In Section 3.2.3 I detail the methods that can be used to characterise this strength, discuss their pros and cons and finish by identifying the most suitable method for my study area. In

Sections 3.2.4 and 3.2.5 I describe my methods for collecting and processing the soil strength data. I measured both peak and critical strength and discuss these results separately in Sections 3.2.6 and 3.2.7 before comparing them in Section 3.2.8. Finally in Section 3.2.9, I put these measured soil strengths into the context of current mechanical understanding and relevant empirical relationships within the literature and discuss the issues related to their application in slope stability modelling.

3.2.2. Controls on Soil Shear Strength

Soil strength is almost exclusively frictional. It can be represented using a Mohr Coulomb envelope to define shear strength at a given normal stress. This comprises a friction angle related to the slope of the envelope and an apparent cohesion to adjust for non-linearity in the envelope where soils dilate during failure. The friction angle is less a function of friction than of the micro-mechanical interaction of soil particles. The inter-particle friction angle for a soil is generally larger than frictional resistance alone since additional energy is required to dilate, rearrange or crush particles in order to shear the soil (Rowe, 1962; Lee and Seed, 1967).

As the void ratio of sand decreases (i.e. density increases) so does particle interlocking and friction angle (Table 3-1). This is the most important factor controlling friction angle (Hammond *et al.*, 1992), especially for sands. In a dense state, the soil particles are interlocked to a higher degree and hence the effective friction angle is greater than in a loose state. However, once in the critical state (Section 2.5.4), the shear strength and density of loose and dense sand tend to approach each other (Rowe, 2001). Soil gradation, grain shape and roughness, grain size and mineralogy also have some effect, with grain shape being most significant. The friction angles of angular soils tend to be greater than those of rounded soils. Angular soil particles tend to have rougher surfaces and better interlocking ability (Hammond *et al.*, 1992; Rowe, 2001). A well-graded cohesionless soil will usually have a higher friction angle than a uniform soil (Hammond *et al.*, 1992). With more soil particles to fill in the small spaces between soil particles, there is more interlocking and friction resistance developed for a well-graded than a uniform cohesionless soil (Rowe, 2001).

Mineralogy is generally considered to have little effect on the shear strength of sands and gravels (Hammond and Hardcastle, 1987). However, soil particles composed of quartz tend to have a higher friction angle than those of weak carbonate (Rowe, 2001).

Table 3-1: Effective friction angles for different types of cohesionless soils at medium and dense packing densities (from Hough 1957).

Soil types	Effective friction angles φ at peak strength		Effective friction angle φ at critical strength
	Medium	Dense	
Silt (nonplastic)	28 - 32°	30 - 34°	26 - 30°
Uniform fine to medium sand	30 - 34°	32 - 36°	26 - 30°
Well-graded sand	34 - 40°	38 - 46°	30 - 34°
Sand and gravel mixtures	36 - 42°	40 - 48°	32 - 46°

It is generally assumed that because of greater interlocking, coarse grained soils have higher friction angles than fine grained soils at a given relative density. In particular, sand and gravel mixtures have a higher effective friction angle than non-plastic silts (Rowe, 2001). This relationship can be seen in Table 3-1 and Table 3-2. However, gradation and particle angularity generally play a more important role. Poorly graded silty gravels with rounded clasts (e.g. alluvial or glacial deposits) usually have lower friction angles than well graded silty sands with angular fragments (e.g. colluvial or residual soils) at the same relative density. Gravelly sands are assumed to have higher friction angles than those without gravel. However, the effect of gravel on soil shear strength is not fully understood and is difficult to assess because it is difficult to sample and test specimens containing large clasts. Conflicting test results are produced because the changes in gradation, void ratio and limiting unit weights that occur when coarse fragments are added or removed make comparison of shear strengths of fine and coarse soils uncertain (Leslie, 1963; Marachi *et al.*, 1969; Baladi and Wu, 1986; Hammond *et al.*, 1992). Several studies have shown an increase in friction angle, as coarse sand and gravel are added to a soil when compared at the same relative density (D_r in Table 3-2) (Holtz and Gibbs, 1956; Baladi and Wu, 1986). However, this effect is limited until the soils contain >50% gravel, since until this point the gravels float in the matrix of finer soil and shear strength is controlled by this matrix (Holtz and Ellis, 1961; Siddiqi, 1984). Also, Lambe and Whitman (1969) suggest that large particles may lead to lower

friction angles because their centres of gravity are further from the shear plane so they are able to roll more easily.

Summary

Soil strength is conventionally represented using a friction angle (φ) and an apparent cohesion (c_s). Steeper friction angles represent stronger soils. A soil's friction angle is defined largely by the grain on grain interactions rather than the friction of the material itself. As a result friction angle is strongly influenced by soil density and gradation, grain size, shape and roughness as well as mineralogy. These relationships mean that given knowledge of a soil's material properties (density, grain size distribution mineralogy) its strength can be characterised by a range of potential friction angles and effective cohesions (e.g. Table 3-1 and Table 3-2). However due to the spatial variability of these soil properties and the complexity of their interactions a more precise characterisation is presently unattainable.

Table 3-2: Values of soil density (ρ_s), cohesion (c_s) and friction angle (φ) for Coarse Gravel (GP), Medium Gravel (GM) and Coarse Sand (SM) classes from the Universal Soil Classification System (From Hammond *et al.* 1992; Gardiner and Dackombe, 1983)

Soil (USC)	% Dr	ρ_s (kg m^{-3}) or *void ratio*	C_s (kPa)	Φ (°)	Source	Notes
GP loose	0 - 35		0	33 - 36	7	
		1729–1890	0	27.5 - 32.5	15	
		0.44–0.73		30–38	4	Colluvium
GP medium - dense	35–65		0	36–39	7	
		1890–1986	0	32.5–37	15	
	50	1874–1954	13–20	38.7–40.4	3	65-82% gravel
		0.18–0.44		36–45	4	Colluvium
GP dense - very dense	65–100		0	39–43	7	
		1986–2146	0	37 – 42.5	15	
		1842–2002	0	>37	16	
		1778–1986	0	38–42	6	52–100% gravel (alluvium)
	70-90	2026–2067	20–20	40.4–44.4	3	65–82% gravel
GM loose	0–35		0	33–36	7	
		824–1457	4–9	33.6–43	9	Colluvium (graywacke)
GM medium - dense	35–65		0	36–39	7	
		1906–0	20–0	39.5	13	
GM dense - very dense	65–100		0	39–43	7	
		1922–2162	0	>37	16	
SM loose	0–35		0	27–34	7	Full grain size range
		1409–1762	0	27 – 32.5	15	
		1409–1489	0	32 – 35.5	2	Medium to fine grained
		1267–1593	0	24 – 31.6	1	Angular full grainsize range
		1515–1646	0	27 – 27.9	1	SR coarse to medium grained
		0.68–1.05		28–32	4	residual soil (general range)
SM medium - dense	35–65		0	30–37	7	Full grain size range
		1521–1858	0	31–36	15	
		1497–1657	-7–32	29.9–38.1	13	
		1505–1762	-17–5	27–50	14	most φ's=35-45
		1521–1569	0	36.7–39	2	Medium to fine grained
		1121–1713	0–40	30.6–41.4	8	Sandstone colluvium and till
	51–65	1600–1869	0	33.4–35.4	1	Angular full grainsize range
		0.49–0.68		32–38	4	residual soil (general range)
SM dense - very dense	65–100		0	33–41	7	Full grain size range
		1601–1938	0	34–41	15	
		1569–1890	0	32–46	5	
		1585–1649	0	40.2–43.5	2	
		1441–1922	-5–6	30–48	14	55% of φ's 38–42
		1729–2050	0	35.1–50.7	1	Angular full grainsize range
		0.15		45	4	Colluvium
glacial till				37	4	
			1.5–2.5	32–35	4	
slate soils		*0.6*	0	42	4	residual soil
		0.45–0.7		43	4	Colluvium, 85% gravel
		0.5		44	4	Colluvium, 57% gravel

3.2.3. Measuring Soil Shear Strength?

Three broad approaches are available to measure the strength of the soil: 1) laboratory methods including direct shear, triaxial compression, or ring shear testing (Bishop and Bjerrum, 1960; Negussey *et al.*, 1988); 2) back-analyses of observed slope failures; and 3) *in situ* measurement using direct shear, shear vane or cone penetrometer tests. Each of these techniques is suited to different conditions or questions such that data collection has to be tailored to environment and data requirements.

Laboratory methods allow parameters to be determined with more confidence and reduced measurement error, under controlled conditions. However, field conditions are difficult to replicate in the laboratory (Chandler, 1973, Carson, 1977). The apparatus is usually designed to test small samples of relatively homogeneous undisturbed or remoulded soil materials and overestimates friction angles where the ratio of specimen width / maximum particle size is <10 (Carson, 1977). Pedological soil and organic materials are often specifically excluded from testing because of the influence any structural discontinuities or compositional inhomogeneities may have on shear strength (Skempton and Hutchinson, 1969). The location of potential failure planes is often uncertain and soil samples are often difficult to excavate without disturbance so that samples are often taken from higher up the profile. However, the soil at the failure plane may not have the same properties as the overlying material. For example, there may be thin clay seams at the failure plane, or a frictional resistance between soil and bedrock that is less than within the soil mass itself (Alexander, 1989). Therefore, sampling or testing the upper soil material may give inappropriate values. These issues limit the ability of laboratory shear tests to represent the strength of coarse soils with significant structure or discontinuities.

Back calculation provides an integrated measure of soil strength over the area of the failure (Micheli and Kirchner, 2002). However it is sensitive to the method used to calculate stability (Gilbert *et al.*, 1998) and so this method should be carefully chosen to both properly represent the failure geometry and to provide estimates that are compatible with the method for which the stability parameters are being obtained. In particular three-dimensional effects, which increase the stability of a sliding block are rarely accounted for in stability analyses because

the resultant predictions are conservative (Stark and Eid, 1998). However, this is problematic since it will lead to overestimation of the soil's strength. Finally back calculation requires the other parameters within the stability model to be well constrained (Deschamps and Yankey, 2006). This is reasonable for failure geometry and density, which can be measured, but is rarely the case for pore water pressure at the time of failure. As a result back calculation can often only provide a range of potential soil strengths for a given range of pore water pressures.

In situ measurement of soil properties minimises the risk of disturbing the sample. Shear vane tests (Cadling and Odenstad, 1950) have been widely used to determine the *in situ* undrained shear strength of fine grained soils (Veneman and Edil, 1988). In soft clays these have approximated calculated *in situ* shear strength for real failures more closely than laboratory tests. However, they overestimate strength in mineral soils (Bjerrum, 1972) and are unreliable for organic rich deposit due to distortions caused by the fibrous character of the soil. Penetrometer tests involve driving a rod into the ground and recording the resistance to penetration. Results can be used to estimate *in situ* undrained shear strength from empirical correlations (Karakouzian *et al.*, 2003). The tests are simple, low cost and minimise disturbance. However, determination of the shear strength of some soils can be very unreliable and they should be used only as an approximation or in conjunction with other methods (Lambe and Whitman, 1969). Further, measuring soil friction angle requires the measurement of shear stress and normal stress at failure. This precludes the use of simple vane shear and penetrometer tests, which can determine *in situ* undrained shear strength but not normal stress.

Large scale direct shear tests conducted *in situ* under natural conditions are effective in incorporating macroscopic structural or compositional properties in large samples and minimising disturbance to the sample during preparation for testing. The sample is failed by direct shear along a predetermined plane under a range of normal stresses. A Mohr-Coulomb failure envelope for the sample is established by plotting normal stress against the shear stress required for failure. Such tests incorporate the pedogenic and biogenic structural discontinuities and compositional inhomogeneities, which are not adequately

represented in standard laboratory and field tests (Chandler *et al.* 1981). The disadvantage of such tests, compared with laboratory methods, is that they allow less control over the test procedure so their results include increased measurement uncertainty. Whilst the test apparatus is portable, these tests are longer and more labour intensive than alternative *in situ* measurements (e.g. penetrometer tests).

Summary

A range of methods are available to measure soil strength, all have advantages and limitations. It is important to match the method to the environment under consideration and the data requirements (i.e. the planned application for the measured values. The soils on hillslopes in my study area are largely coarse gravelly glacial tills and colluvial deposits containing large clasts (Section 2.3) rendering shear vane, laboratory direct shear or triaxial tests unsuitable. At many of the observed landslides in the study area failure occurs at a hard layer in the profile either at an iron pan layer or the soil / bedrock interface (Section 2.4.3). These samples would be difficult to excavate without disrupting their spatial structure and the conditions at the failure plane difficult to reproduce. I am interested in estimating an integrated measure of a landslide's soil strength at failure. However, back calculating the soil strength at landslide scars is not feasible since insufficient information is available to constrain other important parameters, in particular pore water pressure and root cohesion. Further, Chapters 4 and 5 will illustrate the importance of three-dimensional effects on stability, these are rarely incorporated in back calculation. Given the coarse and heterogeneous soils in the study area and the inherent uncertainty in the spatial pattern of soil strength (Section 3.2.2) my aim was to establish reasonable soil strength values, characterise the variability in strength and to put these properties into the context of existing soil strength data (reviewed in Section 3.2). I required a large number of tests to account for soil variability, incorporating undisturbed macroscopic soil structures and simulating *in situ* geostatic stresses, depths and inclinations. These requirements are met most effectively by a field shear box, which avoids many of the limitations associated with sample removal and, if a large box is used, allows better representation of failure in coarse soils. An integrated measure of soil strength can be obtained

by defining an envelope of soil strengths from peak (upper bound) and critical (lower bound) state strength tests.

3.2.4. Data Collection

Tests were located at the heads of landslide scars to ensure correct identification of the failure plane and to minimise disturbance. Two different landslides were chosen in order to establish soil strength variability within and between sites (Figure 3-1). Sites were chosen for accessibility and to represent the different failure plane locations observed at landslide scars in the study area. The 'Catbells' landslide (Grid Reference: 3273,5237 209 m O.D.) has a failure plane at bedrock, while the 'Coledale' (Grid Reference: 3205,5221 333 m O.D.) landslide failure plane is at an iron pan layer. To establish the extent to which failure plane soil strength differed from that of intact soil a third set of tests were performed on intact soil samples near the Coledale landslide at or close to the surface. Samples were tested under three of the common vegetation types in the study area (*Eriophorum*, *Pteridium* and *Juncus*) to account for the effect of vegetation on soil strength (Figure 3-1).

Figure 3-1: A flowchart illustrating the experimental design for the soil shear strength tests.

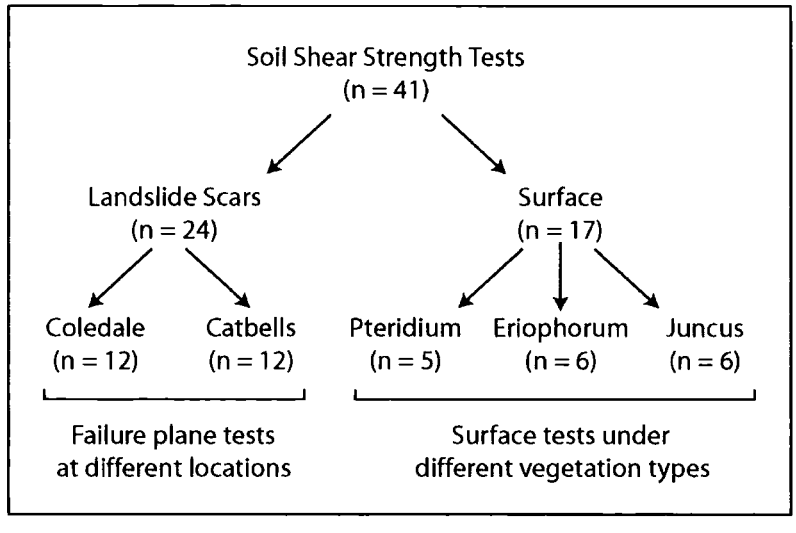

Given the review of soil strength measurements in Section 3.2.3 *in situ* direct shear tests are the most suitable for assessing soil strength in my study area. I performed these using a modified version of the open sided field shear box designed by Chandler *et al.* (1981) and sketched in Figure 3-2. In order to

measure sample's shear strength under a range of normal stresses 12 tests were performed at each landslide site at different locations across the scar head.

Figure 3-2: The experimental setup for direct *in situ* soil shear strength measurement using the open sided field shear box. A schematic of the open sided field shear box (A) and a photograph of the shear box in action (B), shows the winch and anchored base plate for applying shear stress measured using the load cell and recorded by the logger. Normal stress is applied through lead weights on top of the box and displacement measured by the LDVT. C provides a more detailed view of the box itself including its dimensions (A and C are modified from Chandler *et al.*, 1981).

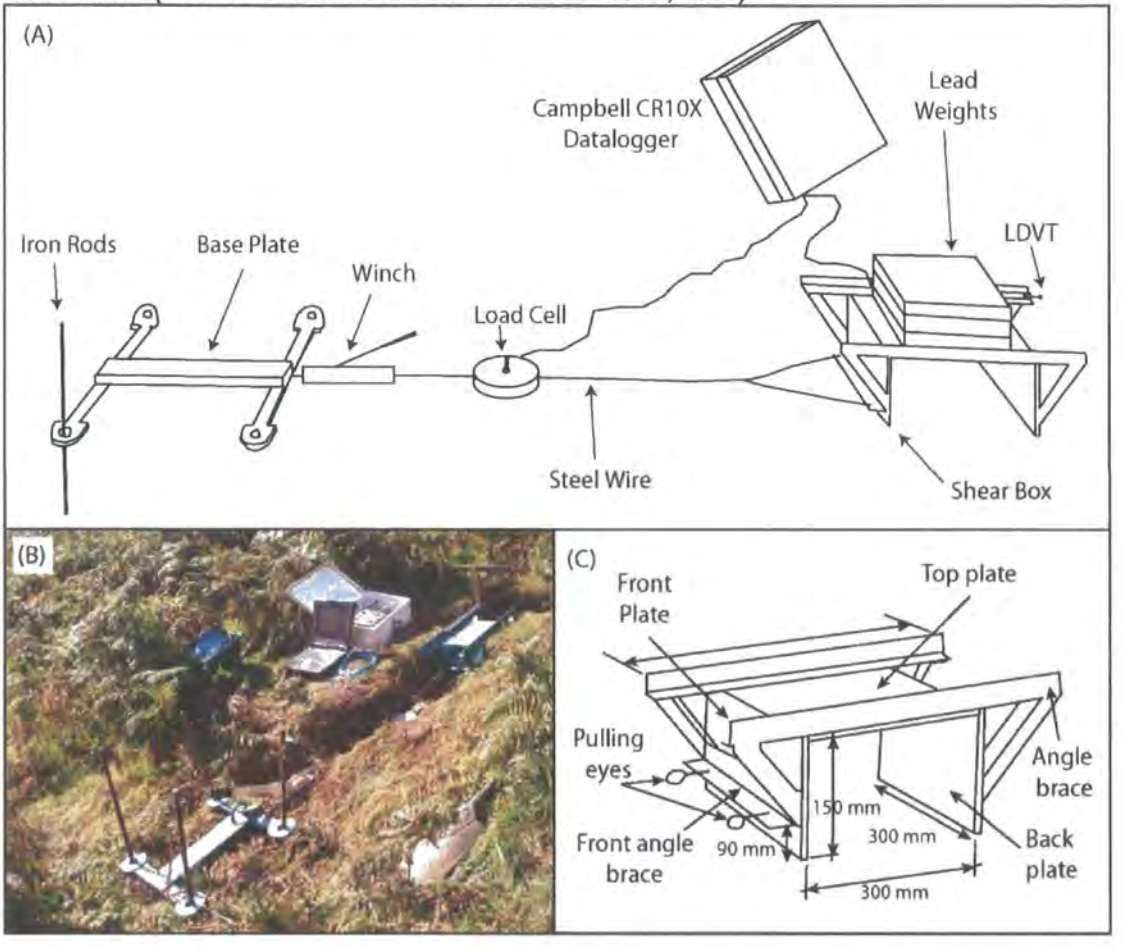

For each test, I dug back ~1 m into the scar head to expose a block of soil 0.3 m by 0.3 m, and 0.15 m deep with its base at the failure plane. Samples were sheared at the same inclination as the failure plane, which ranged from 7° to 38° across the full set of tests. The sides of the sample were trimmed so that they were flush with the box, leaving only the base intact. Normal stress is applied using lead weights secured on top of the box with their centre of gravity acting on the centre of the basal shear plane (Figure 3-2). Shear force was applied incrementally over a period of ~5 minutes using an anchored winch and

measured by a 10 kN load cell. Displacement is measured using a Linear Differential Variable Transformer (LDVT). Both the load cell and LDVT are connected to a Campbell Scientific data logger (logging at a frequency of 4 Hz) and are downloaded after each test (Figure 3-2). Effective stress measurements require the sample to be displaced at a rate that allows excess pore water pressure to dissipate (Section 2.5.3). In the coarse soils with low volumetric moisture content (mean values of 31% for Coledale and 19% for Catbells) tested here these displacement rates are suitable to obtain drained effective stress parameters (Chandler *et al.*, 1981).

Shear stress is derived by summing the down slope component of the weight force (S_g) with the force applied to the box by the winch (S_a), then converting to a stress using the equation:

Equation 3.1

$$s = \frac{S_a + S_g}{A_b} = \frac{S_a + (W + \rho_s g V)\sin\theta}{A_b}$$

where: W is the mass of the box and lead blocks (kN); ρ_s is the soil density (Kg m^{-3}); g is acceleration due to gravity (m s^{-2}); V is the volume of the soil sample (m^3); A_b is the basal shearing area (m^2); and θ is the sample slope (°). The normal stress acting on the shear plane σ_z is a function of the mass of the shear box and lead blocks, the mass of the enclosed soil specimen and the sample inclination acting over the area of the basal shear plane.

Equation 3.2

$$\sigma_z = \frac{Pz}{A_b} = \frac{(W + \rho_s g V)\cos\theta}{A_b}$$

Using this method peak and critical soil shear strength envelopes can be measured. These have been defined with reference to the stress displacement curve in Section 2.5.4, the following are my operational definitions to interpret the *in situ* shear box measurements. Peak strength was defined as the maximum strength recorded over the test period. Critical strength was identified based on a series of rules. For tests with a peak and a falling limb where the falling limb reached a constant or almost constant strength (Figure 3-3, A) I took the median of the values from the inflexion to the end of the test. For tests that underwent constant decline after the peak but where the strength did not reach a constant value (Figure 3-3, B), I took the minimum strength at full displacement (120 mm). For tests where there was no decline after the peak

strength was reached (Figure 3-3, C) I took the median of either the peak values or for displacements greater than 50 mm (where the peak was reached after displacements >50 mm). I chose 50 mm because in tests with an observable peak, critical strength was attained once displacements exceeded 50 mm. Calculating soil shear strength at both peak and critical conditions is useful because it allows me to establish an integrated measure of soil strength over the course of failure. In the following treatment and analysis these (peak and critical state) measurements are treated individually performing the same tests and analysis on each. The relationship between the two is analysed in Section 3.2.8.

Figure 3-3: Idealised Stress Displacement Curves for the Field Shear Box

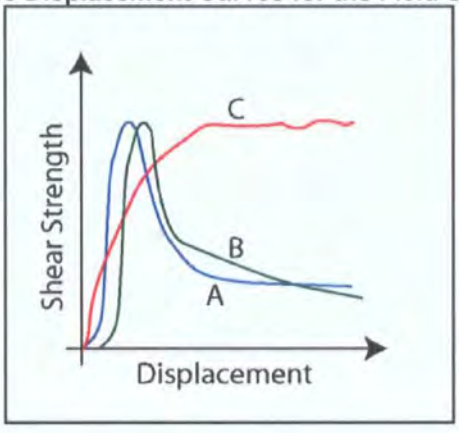

3.2.5. Data Treatment

After collecting peak and critical strength data for each measurement set the shear strength and normal stress data were processed to remove outliers and tested to establish their suitability for parametric statistical tests (Figure 3-4). The soil's friction angle and apparent cohesion can be calculated from the slope and intercept of the shear strength data plotted against normal stress (Figure 3-5).

Figure 3-4: A flowchart of the data treatment steps for shear box measurements, each task is carried out for peak and critical state measurements for each measurement set and subset indicated in Figure 3-1. Dashed lines link tasks with their relevant statistical tests.

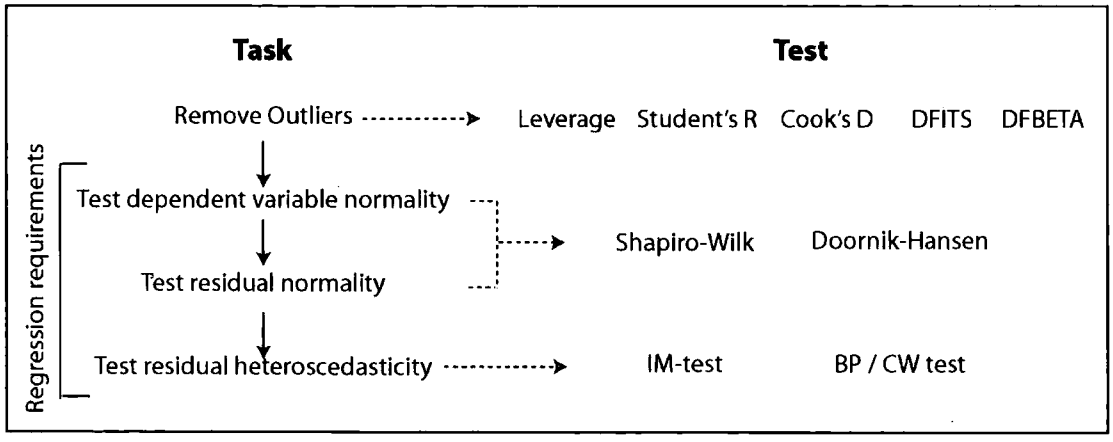

Strength measurements *in situ* experience occasional experiment failure due to the nature of the tests and the material that is being tested. Such results need to be removed to prevent them from introducing gross error into the strength parameters. Unusual or influential observations were identified statistically based on: 1) the degree to which the predictor deviates from the mean (Leverage); 2) their residuals from the regression line (student's R); 3) tests combining these measurements (Cook's D and DFITS); and 4) their influence on the regression coefficients (DFBETA). Once identified the metadata for these measurements were checked to establish their reliability. The results of these tests are shown in Table 3-3 for peak strength and Table 3-4 for critical strength, giving the results from each method for any observation failing one of the tests.

Figure 3-5: Plots of peak (A) and critical (B) shear strength against normal stress for samples at landslide failure planes and those under three different vegetation types (*Pteridium*, *Eriophorum* and *Juncus*). Labelled points highlight the outliers removed from each sample.

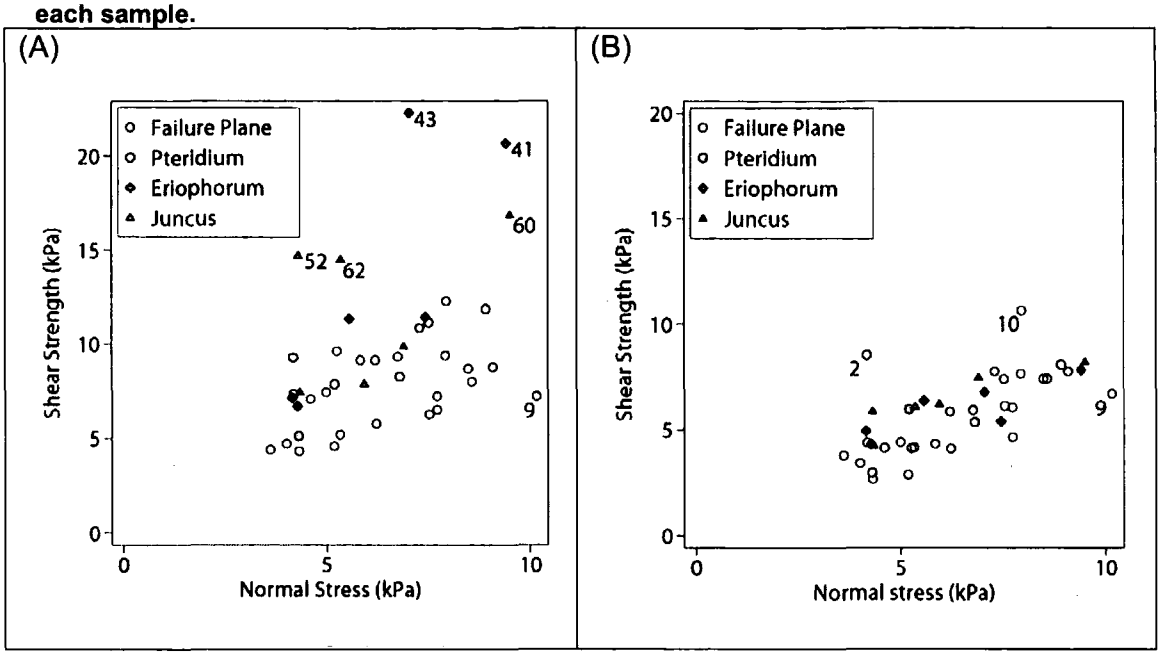

Table 3-3: Results from statistical tests to identify outliers in the peak strength measurements. The sites listed are those that failed at least one of the tests. For each test the threshold beyond which a point should be considered an outlier is provided algebraically and with reference to the sample. Scores greater than the relevant threshold are highlighted in bold.

Test	Threshold		SITE					
			9	41	43	52	60	62
Leverage	>(4)/n	0.10	**0.13**	0.10	0.03	0.06	0.10	0.03
Student's R	>2	±2.00	1.77	**2.53**	**4.05**	**2.26**	1.26	1.82
Cook's D	>4/n	0.10	**0.20**	**0.32**	**0.17**	**0.13**	**0.10**	0.05
DFITS	>2*sqrt(1/n)	±0.32	**-0.65**	**0.86**	**0.69**	**0.53**	**0.45**	**0.32**
DFBETA	>2/sqrt(n)	±0.32	**-0.59**	**0.74**	0.25	**-0.39**	**0.39**	-0.15

Table 3-4: Results from statistical tests to identify outliers in the critical strength measurements. The sites listed are those that failed at least one of the tests. For each test the threshold beyond which a point should be considered an outlier is provided algebraically and with reference to the sample. Scores greater than the relevant threshold are highlighted in bold.

Test	Threshold		SITE					
			2	9	10	14	20	22
Leverage	>(4)/n	0.10	0.06	**0.13**	0.04	0.06	0.04	0.03
RSFU	>2	±2.00	**3.17**	-1.39	**3.75**	-1.39	-1.64	-1.68
Cook's D	>4/n	0.10	**0.33**	**0.15**	**0.19**	0.06	0.05	0.05
DFITS	>2*sqrt(1/n)	±0.31	**0.94**	**-0.55**	**0.68**	**-0.34**	**-0.33**	**-0.32**
DFBETA	>2/sqrt(n)	±0.31	**-0.73**	**-0.50**	**0.45**	0.25	-0.20	0.17

These tests identified six unusual observations, analysis of their metadata, confirmed that these might be explained by experimental irregularities. During one of the failure plane tests (9) the sample toppled as it failed rather than failing in shear. For both peak and critical strength, four of the five indicators identify this point as an outlier. Peak strength results for two of the surface tests under *Eriophorum* (41 and 43) and two of the surface tests under *Juncus* (52 and 60) plot as outliers according to four of the indicators. A third *Juncus* test (62) fails only one statistical test (probably a result of its low leverage) but plots in similar space (Figure 3-5), suggesting that it is part of the same trend. However these samples do not plot as outliers in the critical strength trends. It is likely that these samples experienced elevated peak strength either due to dilation during failure or reinforcement by vertical roots. These samples had many vertical roots extending beyond the shear zone (200 mm) depth (Figure 3-6), which may have elevated their apparent cohesion. These six observations are not included in the following analysis for peak strength. Three critical strength results (2, 9 and 10) are identified as outliers in four of the five statistical tests. These sites may have failed in an unusual manner due to the size or distribution of clasts in the sample. They are excluded from the following analysis.

Figure 3-6: Soil cross section under *Juncus* vegetation cover (site 52), note the abundance of vertical roots extending more than 200mm down profile.

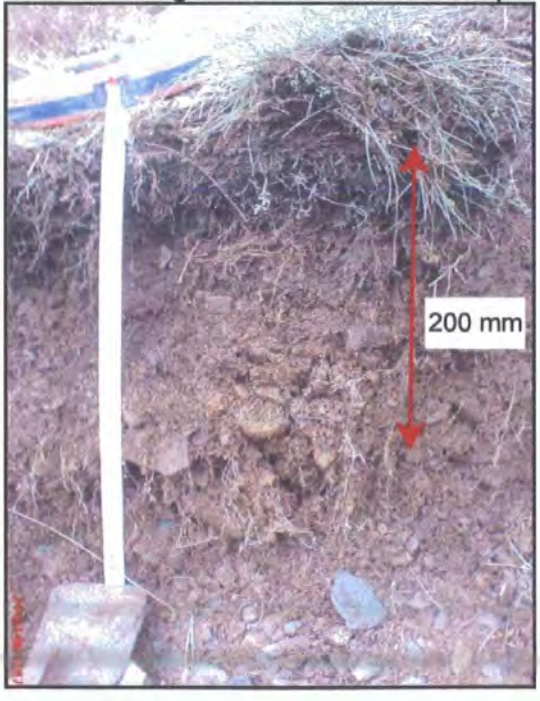

Statistical measures of agreement make assumptions about the characteristics of the data. Analysis of variance tests assume that the continuous variables approximate a Gaussian distribution. Normality of the shear strength values in each group was assessed using the Shapiro-Wilk (Shapiro and Wilk, 1965) and Doornik-Hansen (Doornik and Hansen, 1994) tests to establish how reasonable this assumption was for my data. For peak strength, all tests confirmed that the data were normally distributed (after outliers had been removed). Critical strengths for the landslides group failed the Shapiro-Wilk normality test at 95% confidence but passed the Doornik-Hansen test. Sample sizes for soils under the different vegetation types were very small (Table 3-5); their results should be treated with care.

Table 3-5: Results from tests to establish normality and homoscedsticity of peak shear strength and residuals. Tests represent null hypotheses (i.e. data is not normal or is heteroscedastic).

	n	Shear Strength Normality (Shapiro-Wilk)	Shear Strength Normality (Doornik-Hansen)	Normality of Residuals (Shapiro-Wilk)	Normality of Residuals (Doornik-Hansen)	IM-test Residual Hetero-scedasticity	BP / CW test for Residual Hetero-scedsticity
Full sample	35	0.390	0.730	0.128	0.343	0.582	0.634
Landslides	23	0.482	0.831	0.0326*	0.058	0.141	0.620
Coledale	11	0.826	0.341	0.278	0.647	0.156	0.374
Catbells	12	0.193	0.385	0.058	0.106	0.205	0.594
Intact Soil	12	0.588	0.944	0.584	0.517	0.569	0.467
Pteridium	5	0.923	N/A	0.952	N/A	0.167	0.279
Eriophorum	4	0.068	N/A	0.087	N/A	0.136	0.810
Juncus	3	0.347	N/A	0.271	N/A	0.223	0.721

Table 3-6: Results from tests to establish normality and homoscedasticity of critical shear strength and residuals. Tests represent null hypotheses (i.e. data is not normal or is heteroscedastic).

	n	Shear Strength Normality (Shapiro-Wilk)	Shear Strength Normality (Doornik-Hansen)	Normality of Residuals (Shapiro-Wilk)	Normality of Residuals (Doornik-Hansen)	IM-test Residual Hetero-scedasticity	BP / CW test for Residual Hetero-scedsticity
Full sample	38	0.059	0.353	0.767	0.648	0.121	0.419
Landslides	22	0.029*	0.414	0.857	0.760	0.584	0.759
Coledale	10	0.571	0.830	0.986	0.869	0.960	0.939
Catbells	12	0.056	0.507	0.535	0.741	0.829	0.918
Intact Soil	16	0.804	0.845	0.245	0.456	0.520	0.346
Pteridium	4	0.924	N/A	0.329	N/A	0.365	0.403
Eriophorum	6	0.921	N/A	0.654	N/A	0.263	0.804
Juncus	6	0.787	N/A	0.537	N/A	0.294	0.347

The assumptions associated with regression are satisfied for both peak and critical state datasets. Both the shear strength and normal stress variables are measured as intervals and are linearly related over the tested range (Figure 3-5 A and B) after outliers are removed. For critical state measurements (Table 3-6) Shapiro-Wilk (Shapiro and Wilk, 1965) and Doornik-Hansen tests (Doornik and Hansen, 1994) show that in every case there is insufficient evidence to reject the assumption that the residuals are normally distributed. For peak state measurements (Table 3-5) the residuals for the landslides group fail the Shapiro-Wilk normality test but pass the Doornik-Hansen test. All other groups pass both tests. All sample groups can be considered homoscedastic according to both the IM-test (Cameron and Trivedi, 1990) and the Breusch-Pagan / Cook-Weisberg tests (Breusch and Pagan, 1979; Cook and Weisberg, 1983). Finally, regression requires that the independent variable (normal stress) is measured without error. Normal stress was applied to the sample by loading it with weights, however, the partition of this weight stress into normal stress is dependent on the measured angle of the sample, precise to <1°. Cox (2006) suggests that where measurement error exists in both variables the reduced major axis is a more effective measure of their relationship and agreement. This can be estimated by calculating the standard deviation line (SD line) for the data. In the following analysis both regression and SD lines have been used to assess the fit between shear strength and normal stress.

Table 3-7: Summary of data treatment results, Columns show results for each group and subgroup of shear box measurements, (arrows link associated groups). The columns are split to give results for peak (left) and critical state (right) measurements. Rows contain processing steps, light blue indicates a pass and red a fail, for each statistical test.

	Full sample		Landslides		Coledale		Catbells		Intact Soil		Pteridium		Eriophorum		Juncus	
Sample size	41		24		12		12		17		5		6		6	
Outliers removed	6	3	1	2	1	2			5	1		1	2		3	
Post processed sample size	35	38	23	22	11	10	12	12	12	16	5	4	4	6	3	6
Normality of dependent variable (Shapiro-Wilk test)											Not tested sample size too small					
Normality of dependent variable (Doornik-Hansen test)																
Normality of Residuals (Shapiro-Wilk test)																
Normality of Residuals (Doornik-Hansen test)																
Residual Hetero-scedasticity (IM-test)																
Residual Hetero-scedsticity (BP / CW test)																

Summary

Outliers that corresponded with unusual conditions recorded in the metadata for each experiment were identified and removed. This constituted a loss of 6 peak and 3 critical strength measurements (Table 3-7). The following analysis is performed on both peak and critical datasets excluding these outliers. The new sample sizes are detailed in Table 3-7; they show that the datasets for landslides and for intact soil remain relatively large. However, care needs to be exercised when interpreting data from intact soil decomposed into individual vegetation types since these datasets are small (n <6). Visual and statistical analysis of normal stress, critical strength and peak strength data suggest that they are suitable for analysis using parametric tests. The data appear linearly correlated over the measurement range. Only the landslide dataset fails any of the statistical data checks and in the two cases where this occurs the data fail only one of the two available check methods (Table 3-7). There may be some measurement error in the independent variable so in the following analysis I will apply both standard regression and a more robust SD line analysis that accounts for this error.

3.2.6. Results - Peak Strength

In this section I display the results from peak strength measurements. I calculate the soil strength parameters friction angle and cohesion and quantify the error associated with them using two methods regression and SD line. Finally I analyse the variability between the measurement sets outlined in Figure 3-1 using ANOVA and ANCOVA.

For the full dataset, shear strength is related to normal stress by a positive correlation, albeit with considerable scatter (Figure 3-7). Tests at the failure plane of the Catbells landslide scar appear to plot with a lower gradient towards the lower end of the data's envelope. Tests at the Coledale landslide scar, and on intact samples, plot in the same space: towards the upper end of the envelope (Figure 3-7A). However, some Coledale tests fall into the envelope of the Catbells tests. The number of intact samples under each vegetation type is small so that it is reasonable to make only minor inferences for each vegetation type. However, we can see that results for all vegetation types plot in the same space; toward the upper end of the envelope for all data (Figure 3-7B).

Figure 3-7: Plots of peak shear strength against normal stress (with outliers removed) for: A) intact soil samples and those at the shear plane of two landslides; and B) focussing on intact soil and identifying three different vegetation types (landslide data for context). Note that intact soil observations plot in a similar space to the landslide observations.

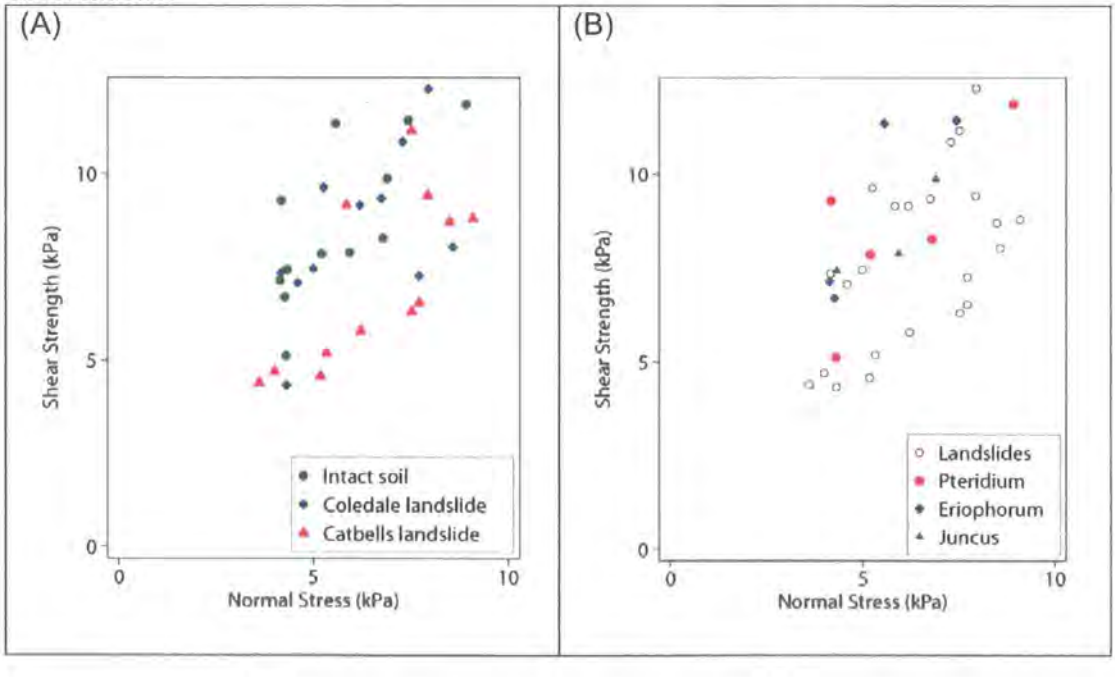

Regression results (Table 3-8) suggest significant relationships between shear strength and normal stress with greater than 99% confidence for: the full sample, the intact soil, the Catbells landslide and for the full set of landslide samples. Only in the Coledale landslide tests are shear strength and normal stress not significantly related ($p>0.05$, Table 3-8). The R^2 values are modest with 31–55% of variation explained by the trend line. The slopes of these relationships represent the friction angle of the soils, ranging from 37.5–45.0°. Results under individual vegetation types are extremely steep (41.6–55.8°). However, the small sample size and large standard error for these tests suggests that care needs to be exercised here. The cohesive strength (C_s) of the soil is given by the intercept on the shear strength normal stress plot (Figure 3-7). These results ranging from ~1.0–3.7 kPa represent small positive cohesions of a magnitude that we might expect in a granular soil. The standard errors (SE) for both slope and intercept appear closely related to the sample size, with the smallest SE for the full sample in both cases (Table 3-8).

Table 3-8: Results from ordinary least squares linear regression for peak shear strength against normal stress for each group of observations, used to determine the geotechnical properties (φ and C_s) of the soil. Significant differences at 95%*, 99% and 99.9%*** confidence are in red.**

	n	P > F	R^2	φ (°)	SE φ (°)	C_s (kPa)	SE C_s (kPa)
Full sample	35	0.0005***	0.31	**37.5**	±11.1	**3.37**	±1.25
Landslides	23	0.0036**	0.34	**38.7**	±13.7	**2.64**	±1.6
Coledale Landslide	11	0.0676	0.32	**37.6**	±20.4	**3.69**	±2.35
Catbells Landslide	12	0.0085**	0.52	**42.8**	±15.8	**1.02**	±1.91
Intact Soil	12	0.0057**	0.55	**45.0**	±15.9	**3.04**	±1.67
Pteridium	5	0.152	0.55	**42.2**	±25.4	**3.16**	±2.91
Eriophorum	4	0.1326	0.75	**55.8**	±30.8	**1.29**	±3.29
Juncus	3	0.308	0.78	**41.6**	±25.0	**3.34**	±2.71

Using the reduced major axis to assess the trend of the shear strength / normal stress plot, under the assumption that normal stresses include measurement error, the results differ from those using regression (Table 3-9). The slopes are steeper (52.2–54.0°) and the intercepts are smaller (-1.4–1.1 kPa). The different vegetation types show a wider range of slopes and intercepts but, as discussed above, should be treated with care because of their small sample size. Friction angles steeper than 50° and negative cohesion intercepts of the magnitudes

recorded using this method are extremely unlikely. Although the reduced major axis results better account for measurement error, they do not correspond well with theory or empirical data from other studies (Table 3-2). This overestimation of friction angle may be due to the reduced major axis' assumption of equivalent error in dependent and independent variables whereas any error in my normal stress measurement it is likely to be small relative to the error in shear strength.

Table 3-9: Results from bootstrapping with 1000 samples to calculate the reduced major axis for peak shear strength against normal stress for each group of observations used to determine the geotechnical properties (φ and C_s) of the soil. Significant differences at 95%*, 99% and 99.9%*** confidence are in red.**

	n	φ (°)	SE φ (°)	φ P > |z|	C_s (kPa)	SE C_s (kPa)	C_s P > |z|
Full sample	35	**53.8**	±8.9	0***	**-0.31**	±0.94	0.744
Landslides	23	**54.0**	±11.6	0***	**-1.01**	±1.24	0.415
Coledale Landslide	11	**53.5**	±24.7	0.003**	**0.10**	±2.88	0.972
Catbells Landslide	12	**52.2**	±17.1	0***	**-1.35**	±1.96	0.489
Intact Soil	12	**53.4**	±16.9	0***	**1.08**	±1.61	0.504
Pteridium	5	**50.8**	±73.5	0.717	**1.30**	±14.67	0.93
Eriophorum	4	**59.5**	±56.2	0.255	**0.09**	±6.63	0.989
Juncus	3	**45.0**	±31.8	0.106	**2.68**	±3.76	0.476

I applied t-tests, ANOVA, ANCOVA tests to address the extent to which sets of samples are statistically distinct from one another. Of particular interest here is the relationship between tests performed at the landslide scars (Coledale and Catbells) and the intact soil. t-tests (2 sets) and ANOVA (>2 sets) showed no significant difference in the shear strengths between these test types. Inclusion of normal stress as a continuous variable in ANCOVA improved the distinction between sample sets supporting observations from the scatter plots, which suggest that there is a significant difference in shear strength between the three sets of observations (Table 3-10). There are also significant differences between shear strengths at Coledale and Catbells, and Catbells and the intact soil. When all tests on landslide scars are grouped together their shear strength is significantly different to that of intact soil (Table 3-10). The intact soil samples are grouped by their vegetation type (*Pteridium*, *Eriophorum* and *Juncus*). t-tests, ANOVA and ANCOVA tests used to differentiate between shear strengths under different vegetation types found no significant difference between the sets.

Table 3-10: Significance results from ANOVA and ANCOVA tests indicating the extent to which peak shear strength differs between test types. Significant differences at 95%*, 99% and 99.9%*** confidence are in red.**

	n	ANOVA	ANCOVA
Coledale, Catbells	23	0.152	0.0294*
Coledale, Intact soil	23	0.778	0.325
Catbells, Intact soil	24	0.083	0.0011***
Coledale, Catbells, Intact soil	35	0.163	0.0038**
Landslide, Intact soil	35	0.229	0.0193*
Pteridium, Eriophorum	9	0.700	0.322
Pteridium, Juncus	8	0.960	0.957
Eriophorum, Juncus	7	0.667	0.280
Juncus, Eriophorum, Pteridium	12	0.882	0.470

Summary

Peak friction angles calculated using regression range from 37.5–45.0° and cohesions from 1.0–3.7 kPa. Reduced major axis calculations suggest higher friction angles (52.2–54.0°) and lower intercepts (-1.4–1.1 kPa), these measurements do not conform to results from other studies which tend to find an upper limit on soil friction angles ~45° (Table 3-2). This mismatch may arise from the assumption of equivalent error in both dependent and independent variables which over-compensates for the small error in normal stress measurement. These results suggest that regression is the most effective method of calculating strength envelopes for my peak strength data. There are significant differences in shear strength between measurement sets at landslide failure planes and between failure plane measurements and those on intact soil.

3.2.7. Results - Critical Strength

In this section I report the results for critical soil strength; calculate the soil strength parameters and quantify their error using regression and reduced major axis. Finally I analyse the variability in critical strength between the measurement sets outlined in Figure 3-1 using ANOVA and ANCOVA.

The relationship between critical strength and normal stress is positive but is less steep than that for peak strength and has less scatter (Figure 3-8). Catbells tests plot towards the lower end of the envelope (Figure 3-8A); the step change

around 7.5 kPa normal stress, is likely to be an artefact of scatter in the data. Tests on intact soil plot towards the upper end of the envelope. There appears to be little difference in soil strength between vegetation types. However, there is some evidence of a lower slope and higher intercept for soils under *Juncus* (Figure 3-8B).

Figure 3-8: Plots of critical shear strength against normal stress (with outliers removed) for: A) intact soil samples and those at the shear plane of two landslides; and B) focussing on intact soil and identifying three different vegetation types (landslide data for context). Note that intact soil observations plot in a similar space to the landslide observations.

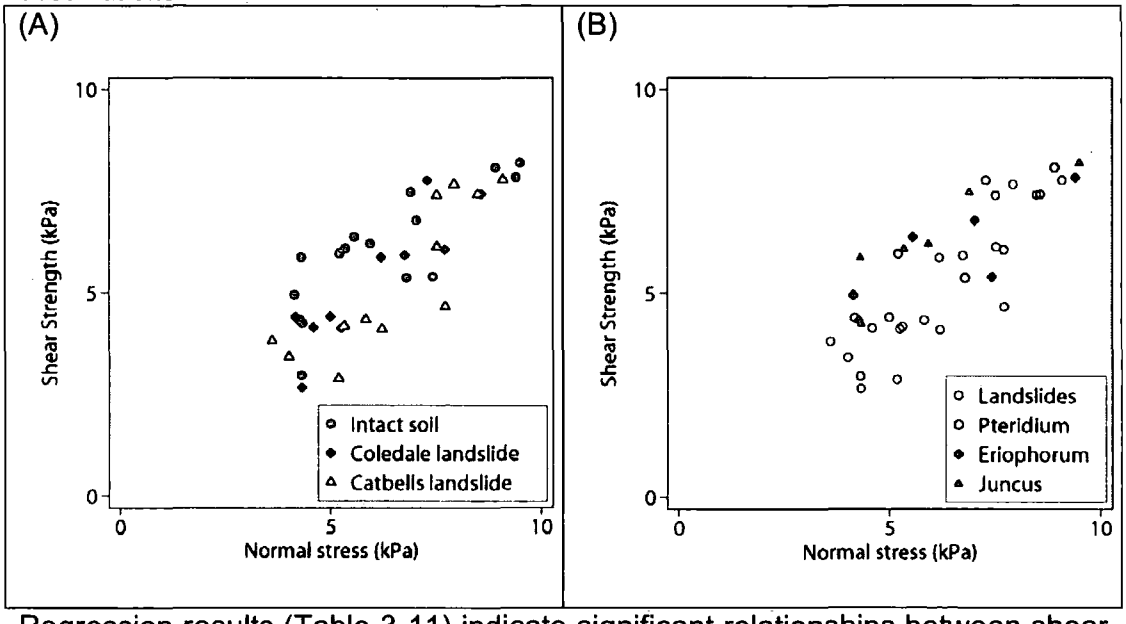

Regression results (Table 3-11) indicate significant relationships between shear strength and normal stress (99% confidence) for all test sets except the intact soils, split into individual vegetation subsets. The decreased confidence for these is probably the result of their small sample size (n = 4–6). Critical shear strength is more strongly correlated than peak shear strength to normal stress. R^2 values are considerably higher for critical than peak strength with 66–80% of variation in strength explained by normal stress. The soil friction angles (32.7–42.9°) and their standard errors (±5.2 to ±9.5°) are lower for critical than for peak strength. The friction angle of intact soil samples is less than those at landslides by almost 10°. Grouped by vegetation type samples under *Juncus* and *Eriophorum* have low observed friction angles (27.8 and 32.0° respectively); *Pteridium* is steeper (42.5°) but has a large standard error (±19.3°). The intercepts for critical strength cover a smaller range of lower values (-0.48 to 2.03 kPa) than those for peak strength. Only the intact soil has appreciable cohesion, the landslide envelopes both having small negative intercepts. For

critical strength standard error in the intercept (±0.59 to ±1.13 kPa) is considerably smaller than that for peak strength.

Table 3-11: Results from ordinary least squares linear regression for critical shear strength against normal stress for each group of observations, used to determine the geotechnical properties (φ and Cs) of the soil. Significant differences at 95%*, 99% and 99.9%*** confidence are in red.**

	n	P > F	R^2	φ (°)	SE φ (°)	C_s (kPa)	SE C_s (kPa)
Full sample	38	0***	0.66	**37.3**	±5.2	**0.85**	±0.59
Landslides	22	0***	0.74	**41.3**	±6.6	**-0.22**	±0.75
Coledale Landslide	10	0.0004***	0.80	**42.9**	±9.2	**-0.27**	±1.00
Catbells Landslide	12	0.0003***	0.74	**41.6**	±9.5	**-0.48**	±1.13
Intact Soil	16	0.0001***	0.67	**32.7**	±6.9	**2.03**	±0.79
Pteridium	4	0.12	0.77	**42.5**	±19.3	**-0.17**	±2.28
Eriophorum	6	0.0167*	0.80	**32.0**	±9.0	**2.57**	±1.00
Juncus	6	0.0402*	0.69	**27.8**	±10.0	**2.63**	±1.16

The reduced major axis (Table 3-12) for each dataset (43.2–46.0°) is steeper than the regression line for critical strength (Table 3-11) and shallower than the reduced major axis for peak strength (Table 3-9). The standard errors (±4 to ±12.5°) overlap with those from regression and are not consistently better or worse. The intercepts (-1.42 to 1.14 kPa) have a similar range but are smaller than those from regression (Table 3-12). Their standard errors (±0.51 to ±1.32 kPa) correspond closely with those from regression.

Table 3-12: Results from bootstrapping with 1000 samples to calculate the reduced major axis for critical shear strength against normal stress for each group of observations used to determine the geotechnical properties (φ and c_s) of the soil. Significant differences at 95%*, 99% and 99.9%*** confidence are in red.**

	n	φ (°)	SE φ (°)	φ P > |z|	C_s (kPa)	SE C_s (kPa)	C_s P > |z|
Full sample	38	**43.2**	±4.1	0***	**-0.26**	±0.51	0.613
Landslides	22	**45.5**	±6.0	0***	**-1.10**	±0.70	0.119
Coledale Landslide	10	**46.0**	±11.0	0***	**-0.91**	±1.12	0.418
Catbells Landslide	12	**45.9**	±10.1	0***	**-1.42**	±1.29	0.27
Intact Soil	16	**39.6**	±12.5	0***	**1.14**	±1.32	0.389
Pteridium	4	**46.1**	±33.4	0.114	**-0.96**	±3.52	0.786
Eriophorum	6	**32.3**	±17.0	0.039*	**1.96**	±1.84	0.285
Juncus	6	**35.0**	±65.6	0.75	**2.12**	±9.54	0.824

ANOVA and ANCOVA tests confirm observations from the scatter plots, which suggest no significant differences in critical shear strength between any of the groups of measurements when normal stress is unaccounted for (ANOVA). Accounting for normal stress using ANCOVA, the only significant difference in critical shear strength is between intact soil samples and those at landslide failure planes.

Table 3-13: Significance results from ANOVA and ANCOVA tests indicating the extent to which critical shear strength differs between test types. Significant differences at 95%*, 99% and 99.9%*** confidence are in red.**

	N	ANOVA	ANCOVA
Coledale, Catbells	22	0.961	0.234
Coledale, Intact soil	26	0.245	0.112
Catbells, Intact soil	28	0.276	0.015
Coledale, Catbells, Intact soil	38	0.421	0.028
Landslide, Intact soil	38	0.185	0.0126*
Pteridium, *Eriophorum*	10	0.749	0.599
Pteridium, *Juncus*	10	0.508	0.147
Eriophorum, *Juncus*	12	0.612	0.216
Juncus, *Eriophorum*, *Pteridium*	16	0.750	0.262

Summary

Fitting a linear envelope by regression, critical friction angles (32.7–42.9°) are lower than peak values. Landslide failure envelopes have small negative intercepts suggesting a cohesionless soil at critical state but intact soils maintain some apparent cohesion (~2 kPa). Reduced major axis calculations again predict considerably higher friction angles (43.2–46.0°) than regression. These values remain larger than the upper limit on soil friction angles in comparable studies (Table 3-2), supporting the hypothesis that the method over-compensates for error in normal stress measurement. The variability in critical strength is reduced both within (lower SEs in Table 3-11) and between measurement sets; the only significant difference (ANCOVA) is between landslide and intact soil measurement sets.

3.2.8. Relationships Between Peak and Critical Strength

The relationship between peak and critical strength for each test gives some indication of the material properties of the soil before and during failure. Larger

peak / critical strength ratios (PC ratios) indicate that the soil dilated during failure (Figure 3-9). PC ratios of 1 indicate strength displacement curves with no clear peak, ratios of 2 have a peak strength that is twice the critical strength. PC ratios cluster around 1.5, suggesting that in general critical strength is half peak strength. This does not vary significantly between landslides and intact soils (t-test: p = 0.3422). However, between the two landslide sites there is observable but not significant variability (p= 0.1118).

Figure 3-9: Box plots of the peak / critical ratio for shear strength by sample group

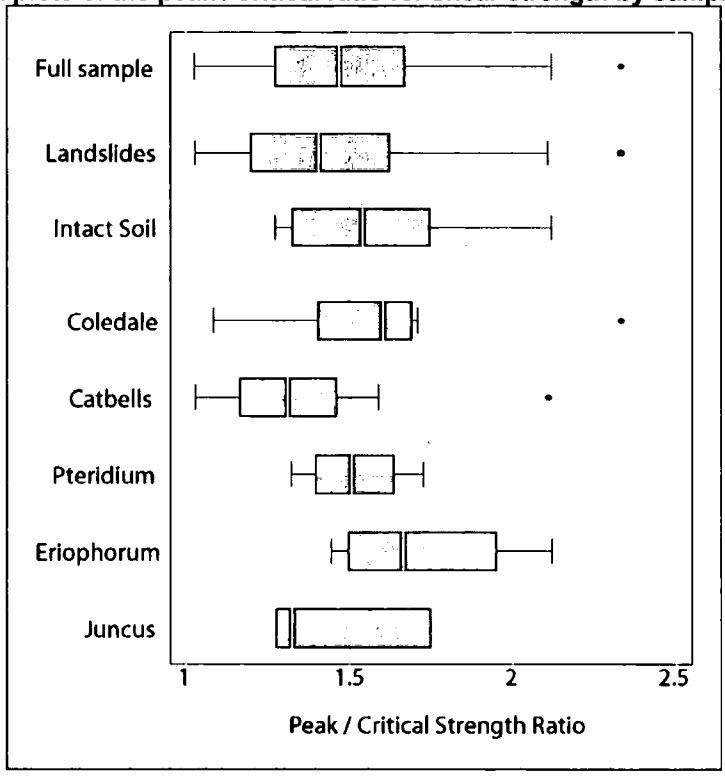

From theory, we would expect a negative correlation between PC ratio and normal stress. This is present at the Coledale landslide where variation in normal stress on each sample explains 48% of the variability in PC ratio (R^2 = 0.48 in Figure 3-10). However, the normal stress explains only 6% at the Catbells landslide and none of the variability in the intact samples (Figure 3-10). This is surprising given the large reduction in the slope of the failure envelope (17°) between peak (Table 3-8) and critical (Table 3-11) conditions for the intact samples.

Figure 3-10: Scatter plot showing the decline in peak / critical strength ratio with normal stress

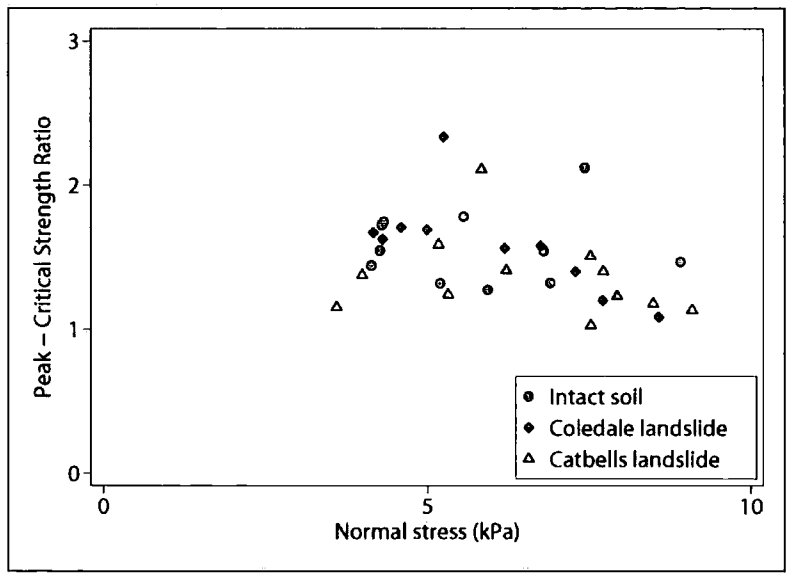

3.2.9. Discussion

Fitting a linear envelope by regression, the full sample peak friction angle is 37.5° ±11.1° (1 SE), and cohesion is 3.37 kPa ±1.25 kPa. Splitting the sample into subsets the range of friction angles is 37.5–45.0° and cohesions is 1.0–3.7 kPa. The full sample's critical friction angle (37.3° ±5.2°) is very similar to that for peak conditions; although the range within which it falls is considerably lower (32.7–42.9°). Critical soil cohesion is small (0.85 kPa ±0.59 kPa) for the full sample and negative at landslide sites; with values close to or less than their associated SE, suggesting a cohesionless soil at critical state.

Reduced major axis calculations suggest higher friction angles and lower cohesions, for both peak and critical conditions; these estimates are considerably larger than the upper limit on soil friction angles in comparable studies (Table 3-2). The mismatch may arise from the assumption of equivalent error in both dependent and independent variables, which over-compensates for the small error present in normal stress measurement. Given these results, regression is the most effective method of calculating strength envelopes for my peak strength data. For these reasons, and to maintain comparability with other studies (which almost exclusively use regression) further analysis is based on regression results.

For peak strength data there is considerable variability both within measurement sets (SEφ = ±11.1 to ±20.4° and SE C_s = ±1.02 to ±3.69 kPa) and between sets. There are significant differences in shear strength between measurement sets at different landslide failure planes and between failure plane measurements and those on intact soil. This is reduced in both cases for critical strength data. Standard error in friction angle is reduced to between ±5.2 and ±9.5° and in soil cohesion to between ±0.59 and ±1.13 kPa. The only significant shear strength difference between measurement sets is for landslides and intact soil.

Peak strength defines the maximum strength of the soil and critical strength is an approximation of its minimum (for non clay soils). I am interested in estimating an integrated measure of a landslide's soil strength at failure. Landslides are to some degree progressive, with failure propagating from a point rather than entire slopes failing simultaneously. In this situation, peak strength over-represents soil strength of the failed mass. Critical strength is only reached after some strain, which may only be achieved as the entire mass begins to fail. In practice, the soil strength integrated over the spatial extent of the failing mass and over the time period in which the failure occurs should lie somewhere between these two. By analysing material properties in both states I have created an envelope of potential strengths.

The relationship between peak strength and normal stress is represented as a linear relationship with gradient and intercept coefficients. This is likely to be a simplification of reality, where the true relationship is non-linear dependent on the degree of soil dilation and is better approximated by a power function (Section 2.5.4). However, the data are linearly related over the range of normal stresses tested, suggesting that this simplification is a reasonable representation of the data. If *in situ* conditions experience lower normal stresses, this representation may over-predict soil strength. However, normal stress calculations with reasonable worst case slope, failure plane depth and soil density parameters suggest that normal stresses lower than 4 kPa are rare at landslide failure planes. PC ratios at both Coledale and Catbells follow a negative trend with normal stress and are close to 1 at normal stresses of ~10

kPa, suggesting that for these soils, the effect of dilation (and therefore the non-linearity of the strength envelope) is limited beyond this point.

Peak and critical friction angles and soil cohesions calculated from the field shear tests are within the range expected for these soils. Grain size analyses indicate a large gravel fraction within all of the soils (Figure 3-11), which are classified as either gravel or muddy gravel. With the coarse fraction discounted, the soils are sandy silts for the landslide sites or silts for the intact samples (Figure 3-12). Friction angles for peak (37–45°) and critical (33–43°) strength correspond well with those estimated from Table 3-2, which range from 36–48° for sand and gravel mixtures depending on packing density. Soil cohesion is low for both peak (1.0–3.7 kPa) and critical (-0.5 to 2.0 kPa) strength as we would expect for soils with a large coarse fraction and only a negligible clay fraction.

Figure 3-11: Field shear test soil texture Red = Coledale, Blue = Catbells, Green = Surface

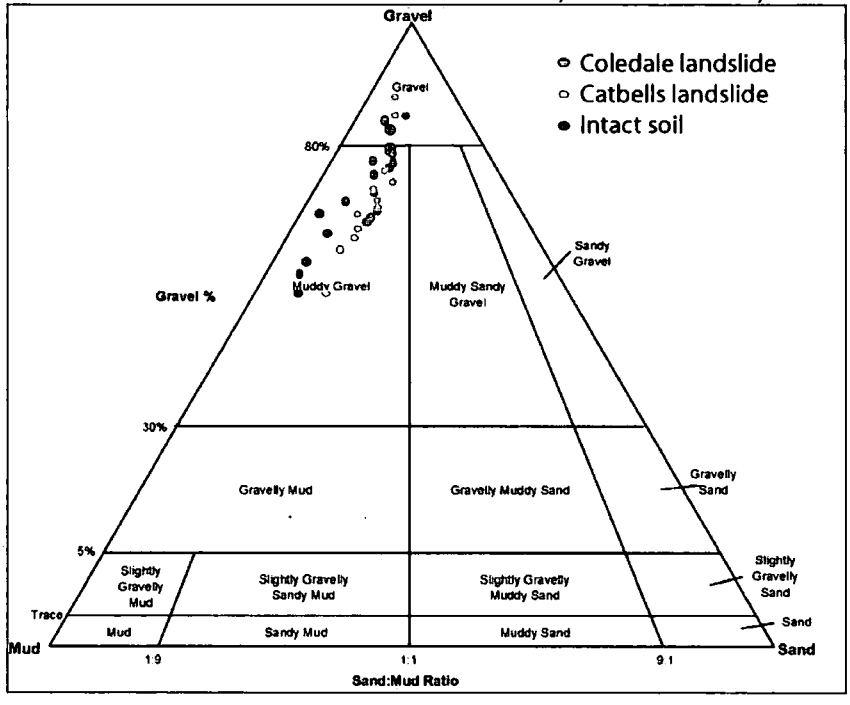

Figure 3-12: Field shear test soil texture Red = Coledale, Blue = Catbells, Green = Surface

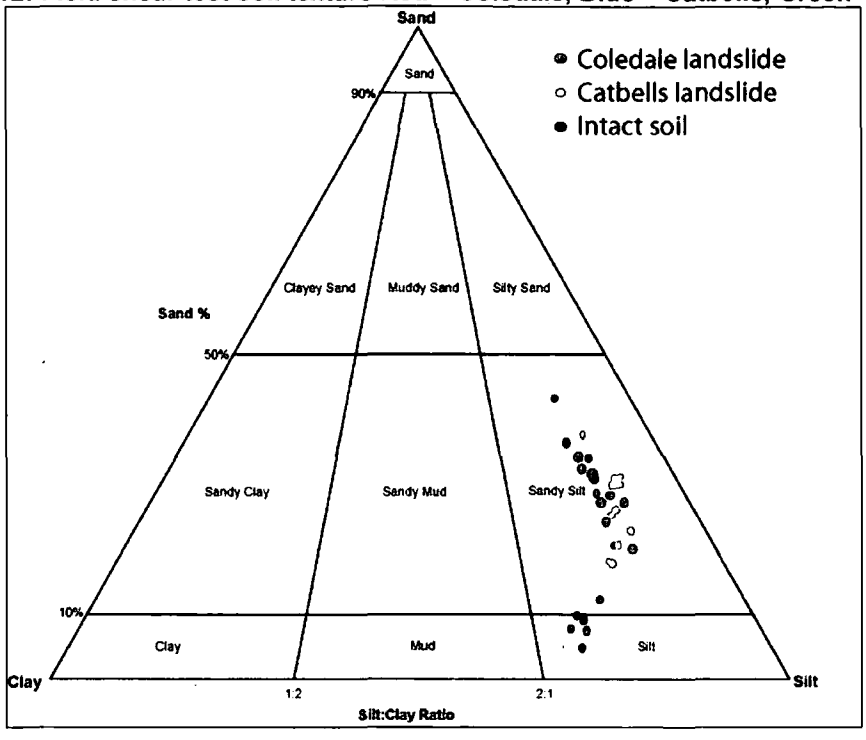

Landslide sites have friction angles that fall within the expected range (based on existing empirical data; Table 3-2) for both peak and critical states. The soils are predominantly silty gravels, (USCS GM = 16) but include silty sands (SM = 6) and poorly graded gravels (GP = 2). Table 3-2 suggests that friction angles from other studies in similar soils range from 36–48°. My measured friction angles range from 38–43° for peak and 41–43° for critical strength. There appears to be no correlation between soil type and soil strength within the landslide samples. However, the sample size for non GM soils is very limited. The variability between peak and critical strength is small. The full landslide sample and those at Coledale fit the expected trend, with peak strength apparent cohesions slightly higher than those of critical strength and friction angles that are slightly lower. The Catbells landslide has a similar drop in cohesion but a 1° increase in friction angle for critical state. For landslide sites, the difference between peak and critical friction angles may be associated with the samples' dilation during failure. There is reduced dilation and therefore a reduced PC ratio at higher normal stresses. Tests at landslide failure planes record small positive cohesions, which are probably an artefact of the linear representation of a non-linear relationship. Critical cohesions at both landslide sites are very small or negative, not significantly different from zero.

For peak strength, friction angles for intact samples are among the steepest. For critical strength they are the shallowest. These lower friction angles fit with theory and observations (Table 3-2), which suggest that less dense finer soils like those of the intact samples (Figure 3-12) have lower friction angles. Critical friction angles for intact soils, average 33° with a standard error of 6.9°, correspond well with the range in Table 3-2 (silty sands = 29–41°). The apparent cohesion in intact samples, present in both peak (1.67 kPa) and critical (2.03 kPa) states, may be the result of root reinforcement, which can continue to provide some additional soil strength even at large displacements (this is discussed in detail in Section 3.3.2). This additional root reinforcement may also be responsible for the increased strength of intact samples at peak strength relative to those at landslide scars. Alternatively, the differences may be related to the different material properties (soil density and grain size). Grain sizes for intact samples plot in different spaces on the ternary diagrams to those from landslide scars (Figure 3-11 and Figure 3-12). However, there is considerable variation in grain size within the intact sample subset.

The differences in peak shear strength / normal stress relationships between landslide sites suggests that 'between site' properties exert a control on soil strength that is identifiable despite large 'within site' variability. This variability may be the result of: 1) differences in material properties, (although these are not strongly differentiated in Figure 3-11 or Figure 3-12); or 2) differences in failure plane properties. The second is more plausible since the Catbells failure plane was at bedrock, while that at Coledale was an iron pan layer within the soil profile. However, considerable additional sampling would be required to perform a robust test of this hypothesis. While observations in Section 2.4.3 suggest that the majority of Lake District landslides occur either at the bedrock interface or an iron pan layer the bedrock strike and dip varied considerably between sites (Figure 3-13). As a result, characterisation of soil strength properties based on failure plane location would be unreasonable. Given these problems, the soil strength data collected here are used to give an estimate of reasonable soil strength and of the variability that might be expected around that strength.

Figure 3-13: Bedrock topography of landslide scars at Catbells (A), Force Crag (B and C) and Cinderdale (D). Note the variability in bedrock dip and consequently roughness, both between and within sites.

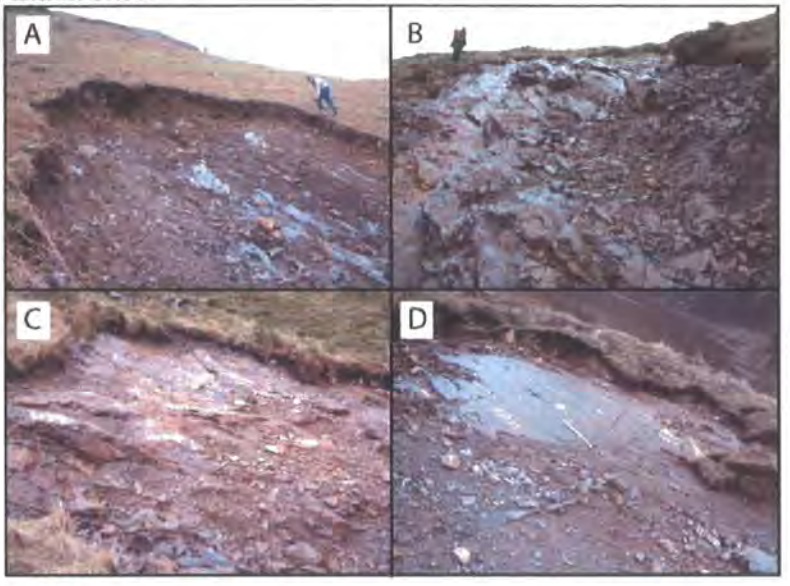

3.2.10. Section Summary - Soil Shear Strength

Peak and critical friction angles and soil cohesions calculated from direct *in situ* field shear tests in the Lake District are within the range expected for these soils (36–48°) based on existing data from other studies in similar settings (Table 3-2). Full sample peak friction angle is 37.5° ±11.1° (1 SE), and cohesion is 3.37 kPa ±1.25 kPa. The critical friction angle (37.3° ±5.2°) is very similar to that for peak conditions; although the range within which it falls is considerably lower (32.7–42.9°). Critical soil cohesion (0.85 kPa ±0.59 kPa) is small for the full sample and negative at landslide sites. Cohesion values are close to or less than their associated SEs and in many cases are not significantly different from 0, suggesting that the soil at the failure plane is cohesionless in its critical state. For peak strength data there is considerable variability both within and between sites. This is reduced in both cases for critical strength data. The similarity in peak and critical soil strength when compared with the within (SE) and between site (ANCOVA results) variability suggests that an integrated soil strength measure can be attained by applying the estimated friction angle from either peak or critical conditions in combination with their SE estimates. Variability between peak and critical conditions will fall within this envelope. These results are compatible with available data from similar soil types and with soil mechanics theory. They suggest that Lake District soils may be considered

cohesionless, that the failure envelope over the range of normal stresses under consideration is linear and that peak and critical strengths can be used as upper and lower bounds to a material strength estimate for the soil.

3.3. Root Cohesion

3.3.1. Scope of Section

Roots can significantly add to the strength of the soil by transferring stress across a failure plane, either at the base of the failure or its lateral edges. Vegetation has been used to control slope erosion and stabilise landslide scars for hundreds of years, Engineer Pan in Ming Dynasty China used willow plantings to stabilise slopes (Lee, 1985). However, before the 1960s, the effects of vegetation on slope stability were considered minor and usually neglected in stability analysis (Greenway, 1987). Evidence to the contrary came first from observations at an Alaskan slope that landslides significantly increased in size and frequency after logging (Bishop and Stevens, 1964). It is now widely accepted that vegetation provides strength to the soil through rooting. On steep lands with organic-rich, low-density soils, this root cohesion may dominate or provide a significant portion of the material's total shear strength (Dietrich *et al.*, 1995). However, these effects are poorly understood and rarely quantified. In this section I address two important issues: 1) dense lateral root mats have been observed in many landslide scars (Section 2.4.3) and considerable circumstantial evidence suggests that they are important but their reinforcing effect is under represented in the literature; and 2) UK upland vegetation types are unquantified in terms of root cohesion; analogous vegetation data provide a first estimate but the different locations, methods and objectives of other studies limit the transferability of their information.

To tackle these problems, this section aims to quantify the magnitude of this lateral reinforcement and its variability for the three main vegetation types in the study area (*Eriophorum*, *Pteridium* and *Juncus*). To achieve this aim, my objectives are to: 1) measure lateral root cohesion and its variability for the main vegetation types in the study area; 2) establish the effect of these vegetation types on root cohesion; and 3) establish the relationship between root cohesion and depth.

In this section I first review our current understanding of: the mechanisms of root reinforcement (Section 3.3.2), the factors controlling its effectiveness (Section 3.3.3); and the methods available to measure it (Section 3.3.4). After identifying direct *in situ* shear tests as a suitable method (Section 3.3.4) I describe my methods for collecting (Section 3.3.5) and processing (Section 3.3.6) the root cohesion data. I present and analyse these data in Section 3.3.7, focussing on: root cohesion values and variability for the full sample; and their variation with vegetation type and depth. Finally in Section 3.3.8, I put these root cohesion estimates into the context of results from other relevant studies and reflect on their implications for slope stability modelling.

3.3.2. Mechanisms of root reinforcement

Soil is strong in compression and weak in tension. Roots are strong in tension and weak in compression. When combined, the resultant soil-root matrix produces a mass which is much stronger than either the soil or the roots alone. Roots allow some of the soil shear stress to be transferred to the tensile stress on the roots and avoid local stress build-ups by distributing stresses throughout the soil. These mechanisms are described by earth reinforcement theory (Vidal, 1969). When vertical stress is applied to an unconfined soil element, it will strain laterally as it is compressed. If horizontal strips are placed within the soil as reinforcement, the soil's lateral movement generates friction between the soil and the reinforcing strips. Tensile force develops in the reinforcement generating a corresponding compressive lateral confining stress within the soil. The confining stress is proportional to the applied vertical stress to a limit defined as the 'critical confining stress'. Schlosser and Long (1972) found that, for fibre reinforced sand samples above the critical confining stress, reinforcement tended to fail in tension rather than slip or pull out of the soil. At this point, the increase in shear resistance from reinforcement becomes constant. As a result, the failure envelopes of both reinforced and unreinforced sand are parallel, both materials have the same friction angle and the additional strength resulting from reinforcement can be represented as apparent cohesion.

O'Loughlin and Ziemer (1982) suggested that roots reinforce soils by 1) anchoring unstable soil mantles to stable subsoils or substrata; 2) providing very localised 'buttresses', centres of great reinforcement in the close vicinity of individual trees; and 3) providing a laterally strong soil-root mantle. The taproot and sinker roots of many tree species anchor them into the slope and act as stabilising piles. Gray (1978) conceptualised the process as vertical root cylinders developed by sinker roots which penetrate into jointed bedrock and support or 'buttress' the soil upslope of the tree. The effectiveness of this anchoring strongly depends on the depth and spatial density of the roots. In many vegetation types, roots do not extend deep enough into the soil to anchor it but have high root densities close to the surface (O'Loughlin and Ziemer, 1982; Abe and Ziemer, 1991; Norris and Greenwood, 2006), providing a type of membrane strength or lateral cohesion that holds the underlying soil in place (O'Loughlin and Ziemer, 1982).

Shallow slope stability is typically approximated as the one or two-dimensional case where roots provide reinforcement only by basal anchoring and the significance of root reinforcement depends primarily on the depth of potential slip surfaces (Section 2.6). However, numerous researchers recognise that this infinite slope approximation ignores the contribution of roots along the perimeter of a potential landslide (Riestenberg and Sovonick-Dunford, 1983; Wu, 1984; Burroughs 1985; Reneau and Dietrich, 1987; Terwilliger and Waldron, 1991). Observations in my study area (Section 2.4.3) and elsewhere (Preston and Crozier, 1999), field studies (Zhou *et al.*, 1998; Schmidt *et al.*, 2001) and modelling (Casadei, *et al.*, 2003; Chok *et al.*, 2004) suggest that this lateral effect is important. Dunne (1991) suggested the separation of maximum apparent root cohesion into the sum of lateral root cohesion and basal anchoring by roots that penetrate bedrock fractures.

In my Lake District study area, roots rarely penetrate below landslide failure planes (Section 2.4.3). In such cases it is reasonable to assume that basal root cohesion is negligible. However, the vegetation does have dense lateral root mats in the top 0.2–0.5 m of the soil. Although lateral roots have been observed in many landslide scars where basal roots were absent and although both plant morphology and the geomorphic setting suggests that few roots will pass

through the basal failure plane, lateral root cohesion effects are under-represented in the literature. This may be a result of the additional complexity that the added dimensions associated with edge effects bring to slope stability problems. Partitioning the root cohesion as suggested by Dunne (1991) requires a move away from the simple one-dimensional infinite slope stability model towards three-dimensional slope stability modelling (this is discussed in detail in Chapter 4).

3.3.3. Controls on root strength in soils

The magnitude of root reinforcement will depend on the root tensile strength, density of the root network, the strength of the soil-root bond and the architecture of the root system at a range of scales.

Earth reinforcement theory, suggests that the **tensile strength** of individual root threads is a key control on the additional strength that they supply to the soil. This thread strength varies considerably between species and can be estimated based on vegetation type. However, such estimates need to be treated as a rough guide since thread strength varies with growing environment (Burroughs and Thomas, 1977), season (Hathaway and Penny, 1975), soil moisture (Collins, 2001), root orientation (Schiechtl, 1980) and diameter (Greenway *et al.*, 1984; Genet *et al.*, 2005) as well as species. Although tree roots are generally considered strongest, this is not always the case (Ziemer, 1981).

The **density** of the root network in the soil exerts a strong control on root reinforcement (Endo and Tsuruta, 1969; O'Loughlin, 1972; Ziemer, 1981). Studies have found a linear relationship between reinforcement and density (Ekanayake and Phillips, 1999), quantified using the root area ratio (*RAR*), the proportion of the shear plane that is roots).

Loss of root cohesion can occur by failure of the **soil-root bond**, so that the pull-out resistance of the root is less than its thread strength; maximum tensile strength is inappropriate for representing root reinforcement in this case (Abe and Iwamoto, 1986). The strength of the soil-root bond has been related to: the texture of the soil (Waldron and Dakessian, 1981; Tobias, 1994; Lawrance *et*

al., 1995), its strength (Pollen, 2007) and moisture content (Tobias, 1994; Pollen, 2007); and the diameter of the roots (Ennos, 1990; Pollen, 2007).

At the larger scale pull-out resistance is influenced by **root architecture**. Existing studies have shown the importance of: root asymmetry (Soethe *et al.*, 2006); number, length and geometry of lateral branches (Dupuy *et al.*, 2005); root bending, branching and root hairs (Abe and Ziemer, 1991); tapering; root orientation relative to the failure plane; root length to the previous branch and total root length after the intersection point (Wu *et al.* 1988; El-Khouhly, 1995; Wu, 1995). These factors are difficult to measure (Danjon *et al.*, 2006) and to predict (Dupuy *et al.* 2005b), since root morphology and distribution reflects both biological mechanisms and their disruption by environmental factors (Deans and Ford, 1983). Root architecture effects are most significant for coarse roots with heterogeneous three-dimensional distributions (Nicholl *et al.* 2006); the fine roots of grasses and herbs are characterised by a more even distribution and constant branching ratio (Fitter, 1987). In this case, root architecture is less important and the reinforcing effect of fine roots can be quantified from root density and strength (Reubens *et al.*, 2007).

3.3.4. Measuring Root Reinforcement

The reinforcing effect of roots on soil is generally measured using one of three methods: 1) Back calculation; 2) direct shear tests; and 3) tensile strength / root density measurements.

Back calculation

Root cohesion values are often back calculated (Sidle and Swanston, 1982; Buchanan and Savigny, 1990; Preston and Crozier, 1999) at existing landslide sites by re-arranging a limit equilibrium slope stability equation to solve for root cohesion assuming that the factor of safety at failure was unity. This method is the fastest and easiest way of obtaining data on root cohesion allowing regional coverage that is difficult using other methods. It also has the advantage of representing the parameter at the scale of interest to landslides (Micheli and Kirchner, 2002). However, back-analysis has key limitations: it presumes knowledge of material properties (angle of internal friction and cohesion) and

hydrologic conditions, which are difficult to measure and are rarely verifiable (Schmidt *et al.*, 2001). It uses slope stability models that represent the failure in one or two dimensions. These are suitable for cases where root reinforcement is by basal anchoring but may significantly under predict the magnitude of reinforcement if it is by lateral cohesion. As a result, root cohesion estimates from Back calculation are useful as a regional measure of the reasonable parameter space for root cohesion. However, they must be based upon a suitable stability model representative of the observed root reinforcement at the site.

Direct Shear Tests

The direct contribution of roots to soil shear strength can be measured *in situ* (Endo and Tsurata, 1969; O'Loughlin, 1974a, b; Ziemer, 1981; Wu *et al.*, 1988a; Wu and Watson, 1998; Lawrance *et al.*, 1995; Tobias, 1995; Ekanayake and Phillips, 1999; Docker, 2003; Norris, 2006b; Nicoll *et al.*, 2006) or in the laboratory (Waldron, 1977; Waldron and Dakessian, 1981; Waldron *et al.*, 1983; Terwilliger and Waldron, 1991; Pollen and Simon, 2005; Cazzuffi, 2006; Goldsmith, 2006). These tests apply a modified version of Coulomb's shear-box method (Lambe and Whitman, 1969). The method encloses a soil sample within a box and induces a failure plane at a pre-determined location by applying a shearing force to the sample. Through small-scale simulation of the failure process, these tests can provide a realistic assessment of the soil's shear resistance. They usually calculate root reinforcement as an apparent cohesion by comparing shear strength envelopes for soils with and without roots (for an exception see Ekanayake and Phillips, 1999).

Field tests have the obvious advantage of maintaining an undisturbed sample under close to natural conditions. However, such tests are difficult on steep rocky hillslopes. They are destructive and allow for less experimental control than those in the laboratory. They often fail to take into account the contribution of large roots and are generally only applicable to soil with small roots such as those found in grass, shrubs or young trees. Shear box design varies considerably between studies in terms of: the method of applying and measuring shearing force; the size and shape of box; and the number and orientation of planes in contact with the soil. Sizes of shear box vary from 0.15

m long, 0.15 m wide and 0.10 m high (Norris, 2006b) to 1 m long, 1 m wide and 0.3 – 1 m high (Abe and Iwamoto, 1986). Samples can have contact with the soil on one (Endo and Tsurata, 1969), two (Ziemer, 1981) or three sides (O'Loughlin, 1981). This variability makes direct comparison between studies extremely difficult, since the dimensions of the shear box can influence measured shear strength (Wu *et al.*, 1988).

In laboratory tests, the boundary conditions on the sample are easier to control allowing more robust experimental design and corresponding improvements in repeatability. Laboratory shear tests can be divided into those performed on samples extracted undisturbed from a field site (Pollen and Simon, 2005; Goldsmith, 2006) and those performed on samples grown in custom built shear boxes (Wu, 1976; Waldron, 1977; Waldron and Dakessian, 1981; Gray and Ohashi, 1983; Shewbridge 1985). Field tests of soil containing roots have been substantiated by laboratory studies to reveal the mechanism of the root reinforcing effect (e.g. Waldron, 1977) and by application of simplified soil-root models (Wu, 1976; Waldron, 1977; Wu *et al.*, 1979; Pollen and Simon, 2005) discussed in Appendix 2. These models can be used to calculate the increased soil strength by measuring the tensile strength of roots and the distribution of root density within the soil layer. The results from this approach for different tree species in a wide range of environments correspond well with field observations (Riestenberg and Sovonick-Dunford, 1983; Greenway, 1987; Shields and Gray, 1992).

Tensile Strength Tests

In tensile strength tests, a segment of root specimen is loaded in tension and the maximum value at failure is measured (O'Loughlin, 1974; Burroughs and Thomas, 1977; Ziemer and Swanston, 1977; Nakane *et al.*, 1983; Abe *et al.*, 1986; Schmidt *et al.* 2001). From these tests, the tensile strength of live roots have been measured for many tree species. Pull-out tests measure the maximum resistance when a root is pulled out of the soil providing a composite measure of the strength of the root and its bond with the soil. This information is used in models of root reinforcement to predict the integrated effect of roots given knowledge of their density, size distribution and tensile strength. These models are described and discussed in Appendix 2.

Summary

Each method is best suited to different conditions: (root size, density and morphology, soil type, landslide type) and provides data suitable for different applications. For my application, obtaining lateral cohesion estimates for vegetation with fine dense roots, direct *in situ* shear tests represent the most suitable method. Back calculation can significantly under predict the magnitude of lateral cohesion. Tensile strength tests rely on accurate root strength and density information that is difficult to collect in fine root mats; this information applied in classic root reinforcement models assumes instantaneous mobilisation of all root strength which is unlikely to reflect my site conditions. *In situ* (rather than laboratory) direct shear tests allow large samples to be sheared with minimum disturbance in close to natural conditions.

3.3.5. Data Collection

A total of 33 direct *in situ* shear tests were performed under the three predominant vegetation types in the study area to assess the effect of vegetation type on root reinforcement (Table 3-14). For each vegetation type, the majority of tests were performed on surface samples, with a small subset tested at different profile depths to assess the effectiveness of root reinforcement with depth.

Table 3-14: Sample sizes for direct shear measurements under different vegetation types with sides cut or intact.

	Pteridium	*Eriophorum*	*Juncus*	Total
Intact	8	7	6	21
Cut	5	4	3	12
Total	13	11	9	33

Direct *in situ* shear tests were performed using the shearbox and method detailed in Section 3.2.4. Samples were sheared parallel to the slope by winching them in a downslope direction. The tests were performed in silty gravel soils (intact soil samples in Figure 3-11 and Figure 3-12) at Coledale (Grid Reference: 320,522), sample inclinations ranged from 12° to 33°. To establish the effect of lateral root reinforcement tests were performed on samples with intact sides using a method similar to that of Ziemer (1981). To eliminate the effect of soil strength tests on freestanding soil pillars provided an estimate of

soil friction strength (φ and c_s) from the relationship between normal stress and shear strength.

The additional stress required to overcome friction strength on the lateral sides is also accounted for within the calculation of normal stress and shear strength so that the only difference between tests with intact or cut sides is the additional support provided by the lateral roots. To do this the calculations for normal and shear stress need to be extended from their basic form (Equation 3.1 and Equation 3.2) in Section 3.2.5. The new calculation for shear stress simply modifies Equation 3.1 to distribute the shear force over a larger shear surface (sides as well as base). Because each lateral side has an area half that of the base (Figure 3-2) Equation 3.1 becomes:

Equation 3.3

$$s = \frac{S_a + S_g}{2A_b} = \frac{S_a + (W + \rho_s g V)\sin\theta}{2A_b}$$

The representation of normal stress (Equation 3.2) also needs to be adjusted to account for both normal stress acting on the basal shear plane (σ_z) and the horizontal geostatic normal stresses acting on the side shear planes (σ_y); these are treated separately. Basal normal stress is unchanged from Equation 3.2. Normal stress on the sides can be approximated using 'at rest' earth pressure if we assume no active or passive yield between the sample and the intact soil (for a review of earth pressure theory see Appendix 1). The horizontal geostatic stress (σ_y) can then be estimated from vertical geostatic stress (σ_v) using a coefficient of lateral to vertical effective stresses (k):

Equation 3.4

$$\sigma_y = k\sigma_v$$

By further assuming that the samples are normally consolidated granular soils (which is reasonable given the results in Section 3.2), I can apply Jaky's (1944) empirical relation to estimate the coefficient of 'at rest' earth pressure (k_0):

Equation 3.5

$$k_0 = 1 - \sin\varphi'$$

This equation requires a prior estimate of the friction angle, for which I use the results from tests without sides. Vertical geostatic stress at the side shear surfaces is a composite of the stresses applied by the box and load on one side and those applied by the intact soil on the other. The mass of the box and weights can be represented as an equivalent soil thickness (h_e):

Equation 3.6

$$\rho_s g h_e = \frac{W}{A_b}\cos\theta$$

Both terms are then represented as heights and their arithmetic mean used in the earth pressure calculation. The vertical geostatic stress (σ_v) over the height of the side shear plane (d) is then:

Equation 3.7

$$\sigma_v = \tfrac{1}{2}\rho_s g(d + H + h_e)$$

and a horizontal geostatic normal stress can be determined:

Equation 3.8

$$\sigma_y = \tfrac{1}{2}k_0\rho_s g(d + H + h_e) = \tfrac{1}{2}k_0\left(\rho_s g(d + H) + \frac{W}{A}\cos\theta\right)$$

Total normal stress (σ_n) can then be approximated as the combined magnitudes of the normal forces (P_z and P_y), divided by the total area on which they act.

Equation 3.9

$$\sigma_n = \frac{P_z + 2P_y}{2A_b} = \frac{P_z}{2A_b} + \frac{P_y}{A} = \frac{\sigma_z + \sigma_y}{2}$$

Equation 3.1 (normal stress) and Equation 3.2 (shear stress) define the location of a sample with cut sides in the plot of shear strength against normal stress. Equation 3.3 (shear stress) and Equation 3.9 (normal stress, incorporating Equation 3.2 and Equation 3.8) define the location of a sample with intact sides in the same plot. Intact samples have a lower normal stress value than those with their sides cut due to the increased surface area and lower lateral stresses for these tests. However, the relationship between shear strength and normal stress remains the same. These different representations of shear and normal stress account for friction (and apparent cohesion) effects on the lateral sides of intact samples so that the only remaining difference between these and samples with their sides cut is the reinforcing effect of roots. Figure 3-14 uses a numerical experiment to test and illustrate this, bringing mathematical closure for a set of synthetic data.

Figure 3-14: A numerical experiment testing and illustrating my approach to root cohesion measurement.

A Numerical Experiment to Illustrate and Test the Method for Calculating Root Cohesion From Blocks With Intact and Cut Sides

The tables below provide values and symbols for the parameters required to simulate root cohesion calculation from *in-situ* direct shear measurements on samples with intact sides and others with their sides cut. Note that a friction angle and root cohesion are defined in the sample properties table to close the calculation loop and check the method. In this case alll mesurements are for granular cohesionless (c_s=0) surface samples inclined at 30° with a constant density of 1.8 kg m^{-2}, The box geometry is as outlined and illustrated in the soil shear strength section of this Chapter.

	Parameter	Units	Value
Sample	Inclination (θ)	°	30
	Depth to Box Top (H)	m	0
	Soil Density (ρ_s)	kg m^{-2}	1.8
	Friction Angle (φ)	°	35
	Root Cohesion (c_r)	kPa	4
	Earth Pressure Coefficient (k_o=1-sinφ)		0.43

	Parameter	Units	Value
Box	Length (l)	m	0.3
	Width (w)	m	0.3
	Thickness (d)	m	0.15
	Volume (V)	m^3	0.01
	Area - sides cut (A_b)	m^2	0.09
	Area - sides intact ($2A_b$)	m^2	0.18

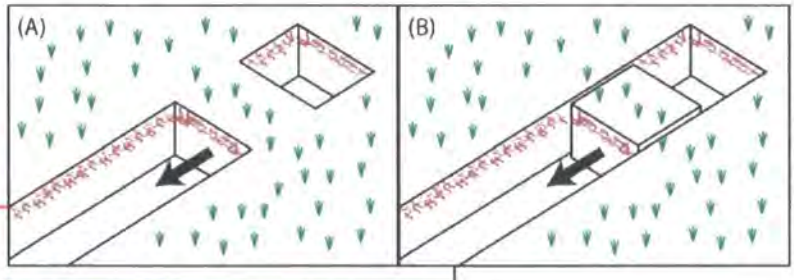

The schematics (left) illustrate the experimental setup for calculating lateral root cohesion by testing samples with their sides intact (A) and others with their sides cut (B). The equations below are used to calculate the shear and normal stress values in the table and graph from the parameter values in the tables above.

	Measurement Number	M1	M2	M3
	Load (W)	200	500	1000
Sides Cut	Applied Shearing Stress (S_a)	236	591	1182
	Basal Normal Stress (σ_z)	1927	4814	9625
	Shear Stress (s)	1348	3370	6739
Sides Intact	Applied Shearing Stress (S_a)	4262	4655	5309
	Basal Normal Stress (σ_z)	1927	4814	9625
	Lateral Normal Stress (σ_y)	411	1027	2053
	Total Normal Stress (σ_n)	1169	2920	5839
	Shear Stress (s)	4818	6045	8087

$$\sigma_z = \frac{(W + \rho_s g l')\cos\theta}{A_b}$$

$$s = \frac{S_a + (W + \rho_s g l')\sin\theta}{A_b}$$

$$\sigma_z = \frac{(W + \rho_s g l')\cos\theta}{A_b}$$

$$\sigma_y = \tfrac{1}{2} k_o \left(\rho_s g (d + H) + \frac{W}{A} \cos\theta \right)$$

$$\sigma_n = \frac{\sigma_z + \sigma_y}{2}$$

$$s = \frac{S_a + (W + \rho_s g l')\sin\theta}{2A_b}$$

The experiment simulates direct shear tests on samples with sides cut and sides intact under three different loads (200, 500 & 1000 kN).

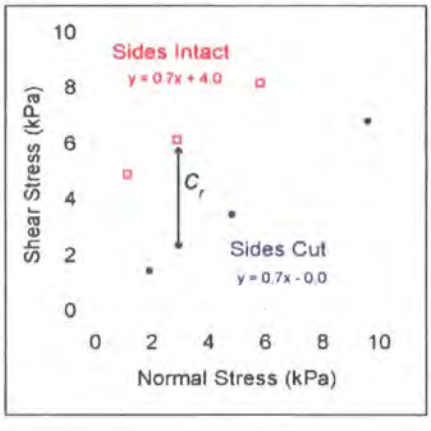

The applied shearing stress (S_a) required for failure is usually the value recorded on the load cell at the moment of failure. For the numerical experiment it is estimated from the sample's Mohr-Coulomb failure envelope (friction angle and root cohesion) and its normal stress at each load. The graph (left) shows the normal stress and shear stress at failue (shear strength) results for the intact and cut tests at the three different loads. Both intact and cut tests have the same gradient, which equates to the soils friction angle (tan35° = 0.7). Intact samples have lower normal stress values than those with their sides cut due to the increased surface area and lower lateral stress for these tests. The shear strength of intact samples is offset from those with their sides cut by 4 kPa. This offset represents the estimated root cohesion (c_r) from the tests. Therefore, the estimated root cohesion reproduces the value defined at the start of the experiment (highlighted in red in the sample parameter table).

3.3.6. Data Treatment

Peak root cohesion is calculated from the shear strength offset between the maximum strength of the rooted sample (red crosses in Figure 3-15) and the

strength of an unrooted sample estimated from the basal peak strength envelope (red line in Figure 3-15) for that experiment's normal stress conditions. Critical root cohesion is calculated in the same way but using the critical strength of the rooted sample (blue crosses in Figure 3-15) and calculating the offset from the basal critical strength envelope (blue line in Figure 3-15). Basal strength parameters were obtained by regression and are accompanied by estimations of the standard error in strength predictions at a given normal stress (Table 3-15).

Figure 3-15: Soil strength normal stress plots for peak (red) and critical (blue) strengths. Solid lines show basal soil strength, scatter points are the soil strength of rooted samples with sides intact. The offset between each point and the line is the reinforcing effect of roots for that test.

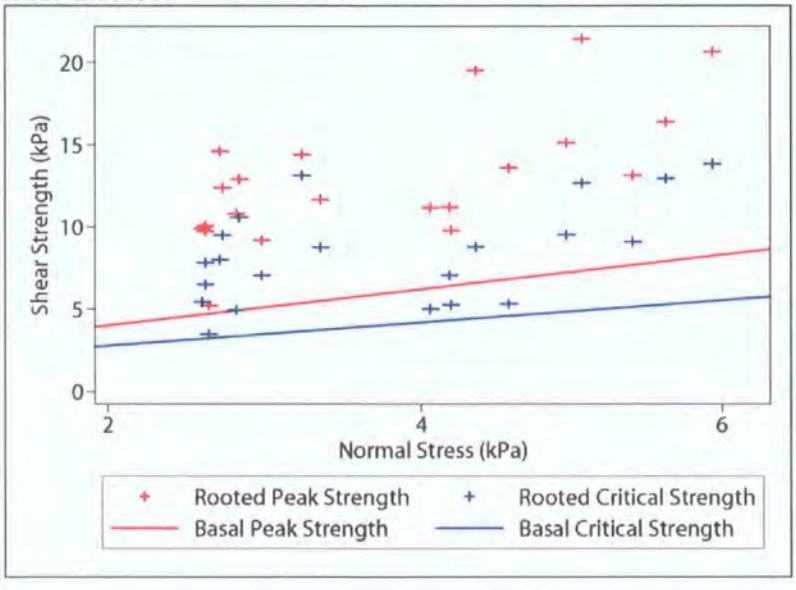

Basal strength estimates differ depending on the type of strength (critical or peak) and the sample that is used to define it (i.e. the full set or only intact soil samples). These impact root cohesion estimates by changing the baseline from which it is calculated (red or blue lines in Figure 3-15). Peak measurements compare the maximum strength of the soil with and without roots, while critical values compare the strength after some displacement (50 mm). There is a clear difference in root cohesion estimates between the two (red v blue distributions in Figure 3-16); they are considered in parallel in the following analysis. There is a smaller systematic reduction (~0.8 kPa) in root cohesion estimates using the full sample relative to the intact subset (dark v light tones in Figure 3-16); the difference is not significant and does not affect the trends in root cohesion with vegetation type or depth. Calculating basal soil strength from the larger full

sample might reduce uncertainty in the basal soil strength predictions. However, it is fairest to exclude samples from landslide scars and compare only intact soil samples with and without sides because: 1) they are likely to be most similar in terms of material properties; and 2) any effect of roots penetrating the base of the sample is discounted to measure only lateral root cohesion. The following analysis uses basal strength estimates from intact samples only.

Figure 3-16: Kernel density plots for root cohesion estimates using four different representations of basal strength.

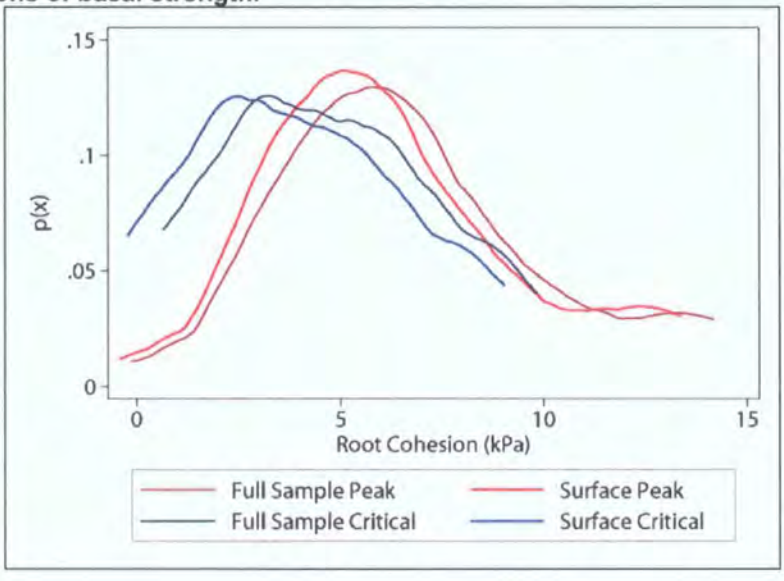

3.3.7. Results

I will look first at the force - displacement curves for cut and intact samples under different vegetation types, before calculating root cohesion for the full sample and its component vegetation subsamples. I will detail the variation in cohesion with vegetation type and with depth, highlighting the implications of these findings for modelling slope stability.

Force - Displacement Relationships

Figure 3-17 shows the shearing force applied to each block (S_a in Equation 3.1 and Equation 3.3) and its displacement in response to that force. Samples sheared without sides have force - displacement curves with low peaks and gentle falling limbs (Figure 3-17A). Only four curves have peaks greater than 1 kN. Samples under *Eriophorum* are strongest both in terms of their peak and critical strengths (Figure 3-17C). However, there is considerable variability in

force - displacement curves within the *Eriophorum* sample. Three curves plot with higher peaks and steeper falling limbs, they are separated by >1 kN from the peaks of the other *Eriophorum* samples. Of the four remaining samples three have very similar force displacement curves and one has a much steeper falling limb. Samples under *Juncus* are weakest, plotting close to but consistently above the basal strength data (Figure 3-17D). Most peak early and have gentle falling limbs. Two of the mid-range curves have steeper falling limbs, so that the critical values cluster into three higher and three lower critical strengths, separated by ~0.5 kN. Force displacement curves for samples under *Pteridium* (Figure 3-17B) plot between those for *Eriophorum* and *Juncus*, overlapping both. Most curves have an early peak and gentle falling limb. However, there are two exceptions: 1) the sample with the highest peak declines rapidly to the lowest force at displacements above 90 mm; and 2) a curve that does not peak but continues to rise even at displacements above 90 mm where the test ends. These may represent different root cohesion effects: the first suggests significant reinforcement at low displacements, which is quickly exhausted; the second, reinforcement mobilised gradually with displacement.

Figure 3-17: Force - displacement curves for: samples without sides (A); and those with sides under: *Pteridium* (B), *Eriophorum* (C) and *Juncus* (D).

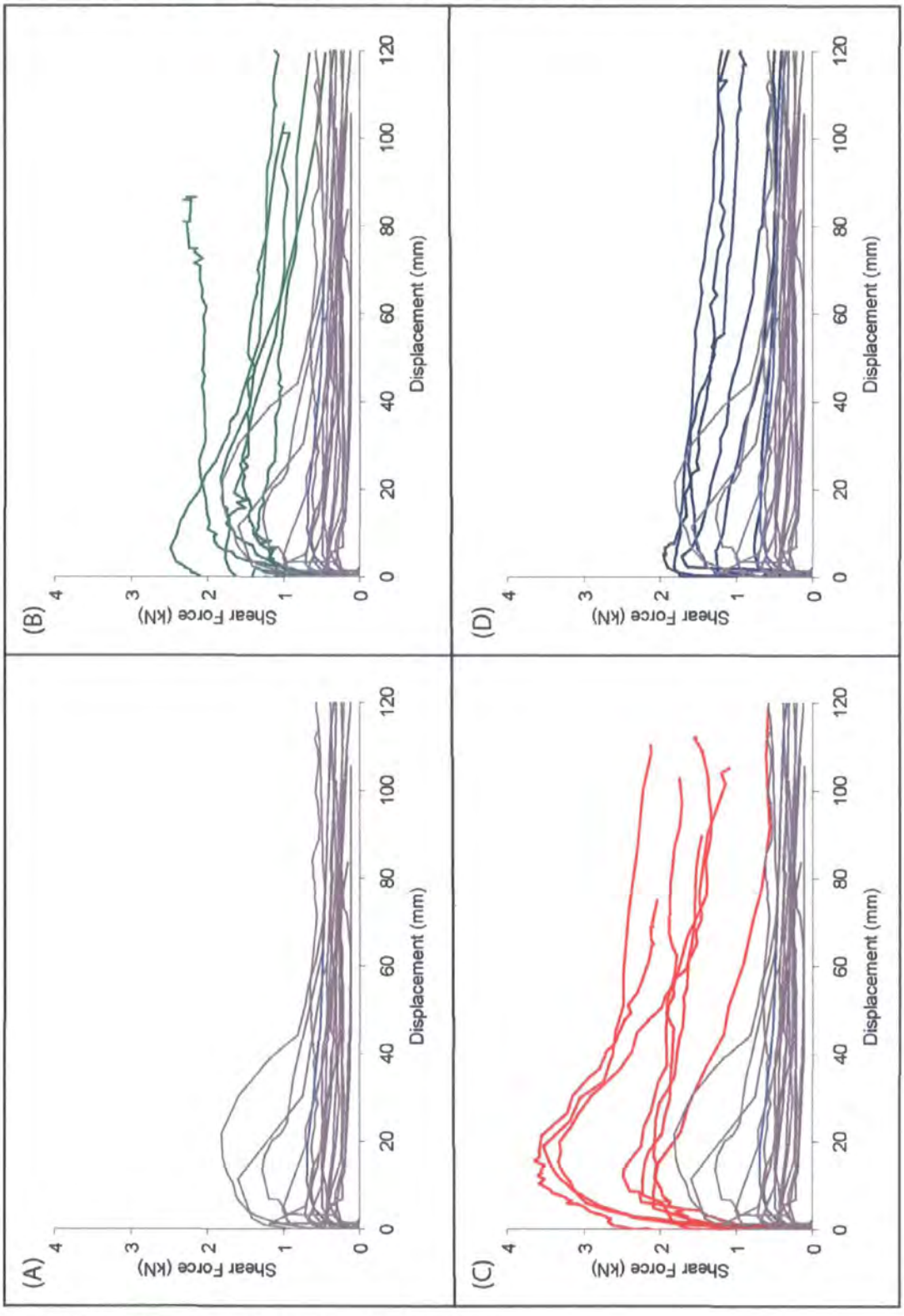

Root Cohesion Trends for the Full Sample

Root cohesion estimates range from -0.42 to 13.33 kPa for peak and -0.23 to 9.04 kPa for critical strength (Table 3-15). The smallest calculated cohesion values in both cases are negative; this is not a real effect but an artefact of

experimental error, which results from comparing point intact measurements with a fitted envelope for basal strength. The negative root cohesions are small and fall within the uncertainty in basal strength envelope (the standard error of the predictions from Table 3-15 is ±0.43 to ±0.73 kPa). This uncertainty is small relative to the variability in root cohesion estimates and tends to vary systematically with normal stress so that relative root cohesion relationships are insensitive to it. However, this offset resulting from error in basal strength estimates can alter absolute root cohesion estimates by >1.4 kPa and so needs to be accounted for within absolute root cohesion estimates.

Table 3-15: Peak and critical root cohesion statistics for the full sample and split into vegetation subsets (all values except sample size (n) are in kPa).

		Root Cohesion Estimates					Basal Strength Regression	
Vegetation	n	Min	Max	Median	Mean	Standard Deviation	Mean prediction SE	Range of prediction SEs
Peak Strength								
Full Sample	21	-0.42	13.33	5.30	6.19	±3.33	±0.73	±0.43–0.98
Pteridium	8	3.19	8.88	4.66	5.67	±2.22	±0.82	±0.43–0.98
Eriophorum	7	5.96	13.33	7.13	9.13	±3.09	±0.62	±0.43–0.95
Juncus	6	-0.42	5.30	4.27	3.44	±2.10	±0.73	±0.43–0.98
Critical Strength								
Full Sample	21	-0.23	9.04	3.95	3.87	±2.73	±0.38	±0.22–0.50
Pteridium	8	1.13	9.04	3.64	4.14	±2.75	±0.42	±0.23–0.50
Eriophorum	7	0.35	8.00	5.75	5.22	±2.62	±0.33	±0.22–0.48
Juncus	6	-0.23	4.58	1.67	1.94	±1.98	±0.38	±0.24–0.49

The relationship between the peak and critical root cohesion estimates (Figure 3-18) tells us something about the properties and type of root cohesion especially in combination with the stress displacement curves (Figure 3-17). In every case, the peak root cohesion is greater than the critical root cohesion, suggesting that most additional strength from roots is mobilised at small displacements (almost all peak strengths are at displacements <10 mm). At large displacements (>50 mm), root cohesion is considerably lower but is still present.

Figure 3-18: Box plot of peak and critical root cohesions for the three different vegetation types in the study area.

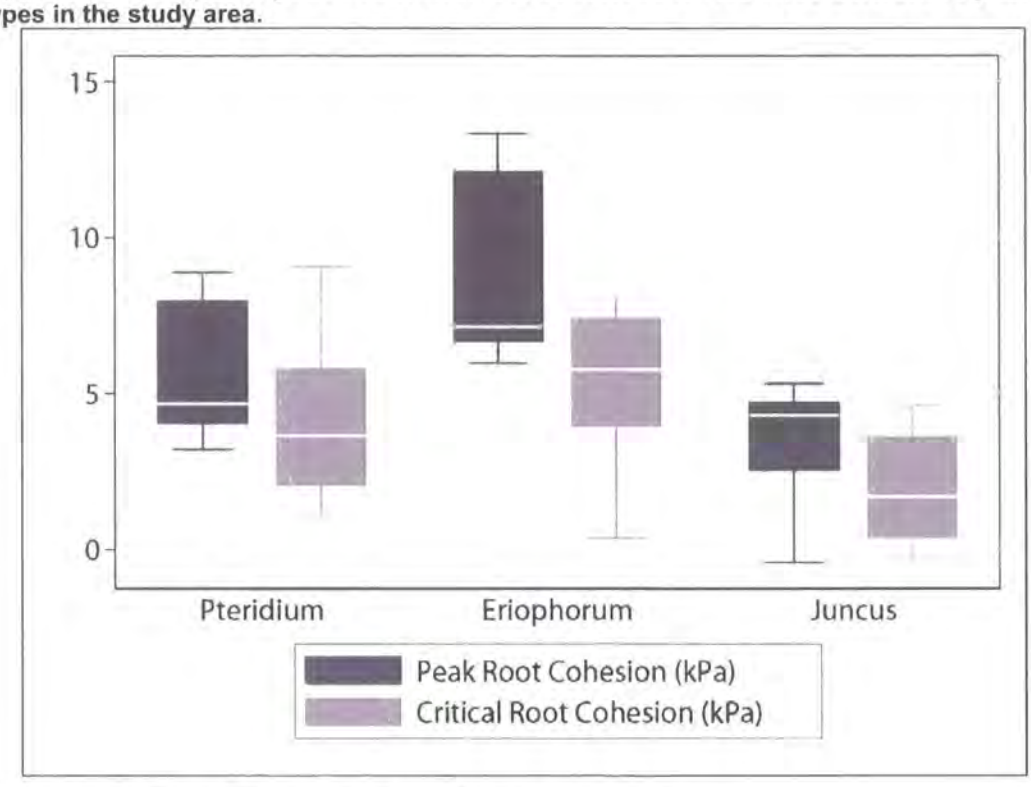

Variation in Root Cohesion with Vegetation Type

Table 3-16 and Figure 3-18 show that root cohesions differ significantly between the three vegetation types (ANOVA p = 0.0025); these differences are reduced for critical root cohesions (ANOVA p = 0.0866). *Eriophorum* provides the most root cohesion for critical and peak strength, with the highest median, mean and minimum root cohesions for both (Figure 3-18, Table 3-15). The high standard deviation for peak *Eriophorum* root cohesions reflects differences between tests at two different locations (visible in the stress displacement curves in Figure 3-17). *Juncus* provides the least root cohesion (peak and critical), with the lowest mean, median, minimum and maximum root cohesion in every case. Root cohesions under *Eriophorum* and *Juncus* are significantly different for peak (t-test p = 0.0029) and critical strength (p = 0.0294) and *Eriophorum*'s minimum peak root cohesion is greater than *Juncus*' maximum. *Pteridium* samples have root cohesions between these two end members. Their critical cohesions are not significantly different from either while their peak cohesions are significantly higher than *Juncus* those for samples (Table 3-16).

Table 3-16: Analysis of Variance and t-test p values for peak and critical root cohesion estimates grouped by vegetation type.

	n	Peak	Critical	Test
Pteridium, Eriophorum, Juncus	21	0.0025**	0.0866	(ANOVA)
Pteridium, Eriophorum	15	0.0258*	0.4551	(t-test)
Pteridium, Juncus	14	0.0819	0.1236	(t-test)
Eriophorum, Juncus	13	0.0029**	0.0294*	(t-test)

Variation in Root Cohesion with Depth

Existing studies suggest that lateral root cohesion should vary with depth and that this is likely to be largely a result of the reduced root density (O'Loughlin and Ziemer, 1982; Reubens *et al.*, 2007). Several studies report strong correlations between root cohesion and biomass (Zhou *et al.*, 1998) or root area ratio (Gray and Leiser, 1982; Ekanayake and Phillips, 1999). For the full sample from my study, there appears to be a slight negative correlation between root cohesion and depth (Figure 3-19). However, the sample size is small, is biased towards surface samples and does not account for differences in vegetation type. Root cohesion for the *Juncus* sample tested below the surface is the smallest for any test. There is a large difference between the surface and the subsurface samples for peak root cohesion (Figure 3-19A) and a smaller difference for critical cohesion (Figure 3-19B). Under *Pteridium*, peak root cohesion has no trend with depth; critical root cohesion decreases with depth but records the highest cohesion of the entire sample at 0.15 m depth. For *Eriophorum* only one sample was tested below the surface, both its peak and critical root cohesions plot within the range of surface values.

Figure 3-19: Scatter plots of peak (A) and critical (B) root cohesion with depth down the soil profile.

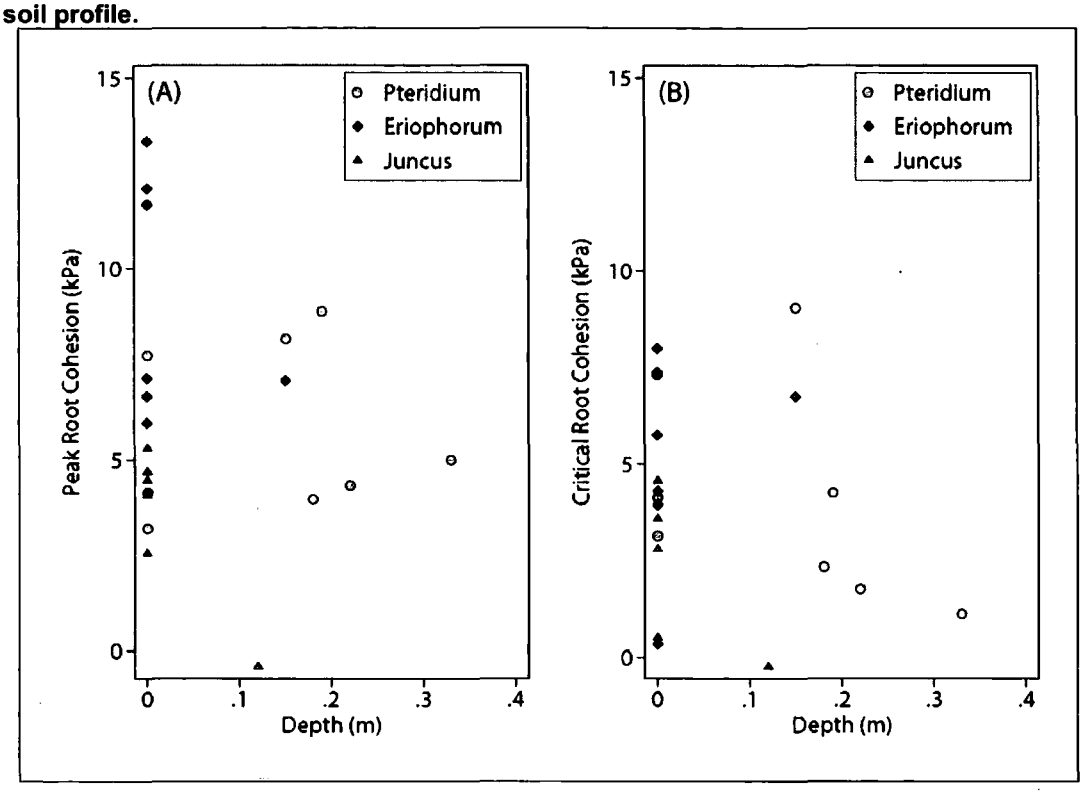

While the trend in root cohesion with depth is unclear, site photos (Figure 3-20) indicate that root density declines with depth and that this is often a step change, coinciding with the change from organic to mineral soil horizons. However, root density transects measured at a range of depths from landslide scars in the study area (Figure 3-21) suggest that roots are not limited to the organic horizon, and that root density is not strongly dependent on horizon type (t-test $p = 0.8111$), but declines as a power function of depth.

Figure 3-20: Soil profiles at the margins of landslide scars A) Poddy Gill, B) Hindscarth, C) Rigg Beck, D) Angle Tarn 4, E) Bowscale Village, F) Keskadale, G) Cinderdale.

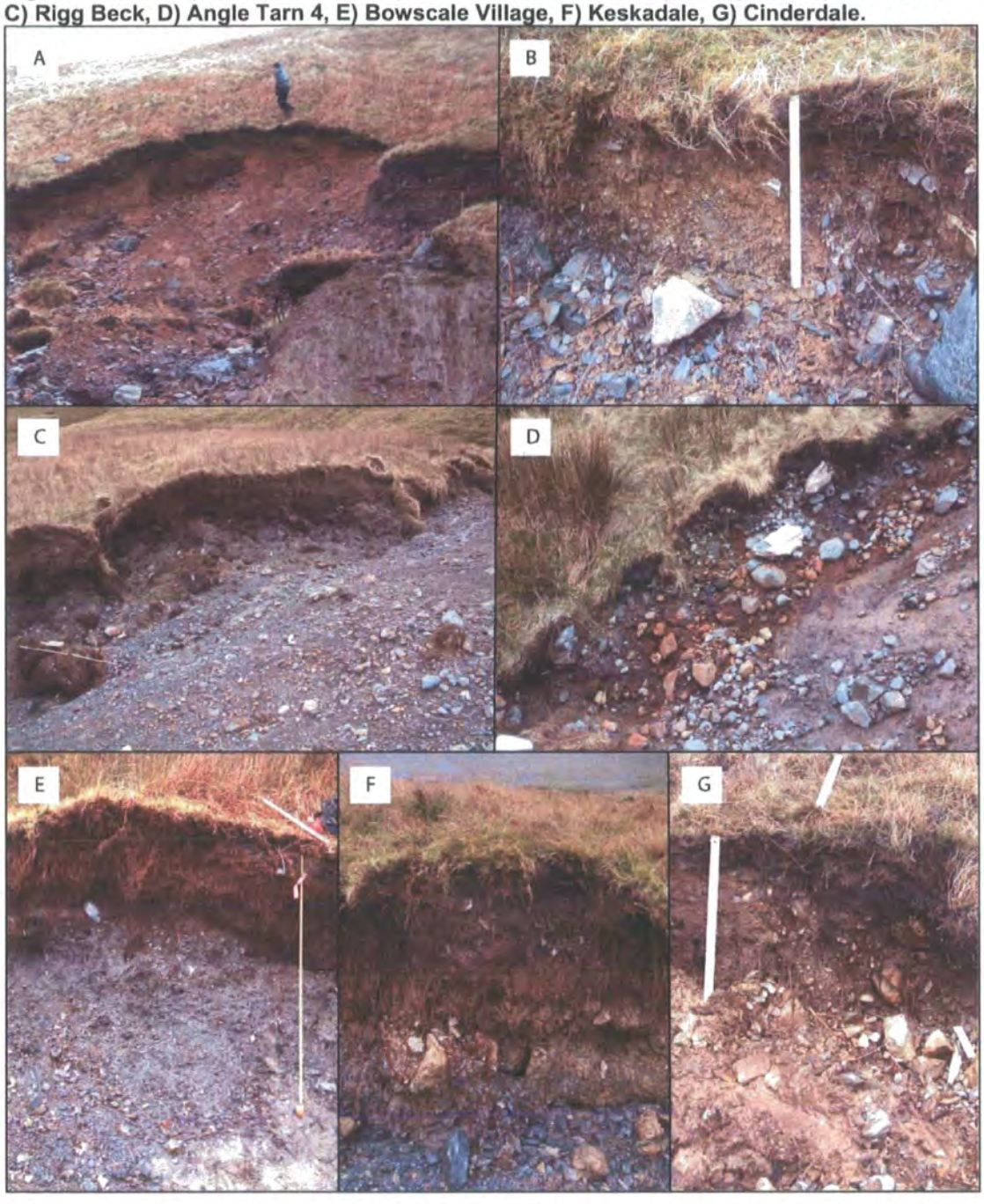

I have identified in Section 2.4.3 that additional strength at landslide margins may be important and I now have experimental data on the magnitude of lateral root cohesion at the surface. However, given the limited data on the variation in root cohesion with depth and conflicting observations on root density with depth how should we model these relationships? I will represent the change in lateral root cohesion with depth in three ways: 1) apply a constant root cohesion over the full profile depth, this is unlikely to be the true relationship but provides a useful maximum root reinforcement estimate; 2) scale root cohesion to

decrease with depth as a function of the root area ratio, in line with the theory that root density declines monotonically with depth according to some function; 3) assume root cohesion is effective only in the organic layer and apply uniform lateral root cohesion over this layer, driven by observations at sites suggesting that the majority of roots are concentrated in the organic layer. These three approaches cover the full range of potential scenarios: the first is likely to overestimate; and the last to underestimate; the effect of lateral root cohesion.

The first scenario is the most computationally simple and involves the least parameters, it simply involves multiplying the root cohesion (c_r) by the soil depth (z) to give root reinforcement per length of slide perimeter (R_r):

Equation 3-10

$$R_r = c_r \, z$$

The second scenario requires information on the relationship between root cohesion, root density (characterised by the root area ratio, RAR) and soil depth. There is considerable empirical evidence that root cohesion is proportional to root density. However, the form of the relationship varies between vegetation types. Gray and Leiser (1982) fit linear relationships with intercepts of zero that range from: Cr = 7 RAR to Cr = 213 RAR. Docker (2003) fits a linear relationship in three of the four cases in his study, he allows non-zero intercepts and has relationships between Cr = 38 RAR and Cr = 81 RAR. The 2005 landslide inventory includes two root transects ~500 mm in length at each site. These transects record the spatial pattern and diameter of roots (split into three classes: 0–1 mm, 1–5 mm and >5 mm). To estimate the root area ratio, mean diameters were estimated for each size class. For each transect, the number of roots in each class was multiplied by the mean diameter for that class. These were summed to give the length of each transect covered by roots, then divided by the total transect length to provide an estimate of root area ratio.

Figure 3-21: Root density (represented as root area ratios) with depth from transects measured at the heads of each landslide in the 2007 inventory.

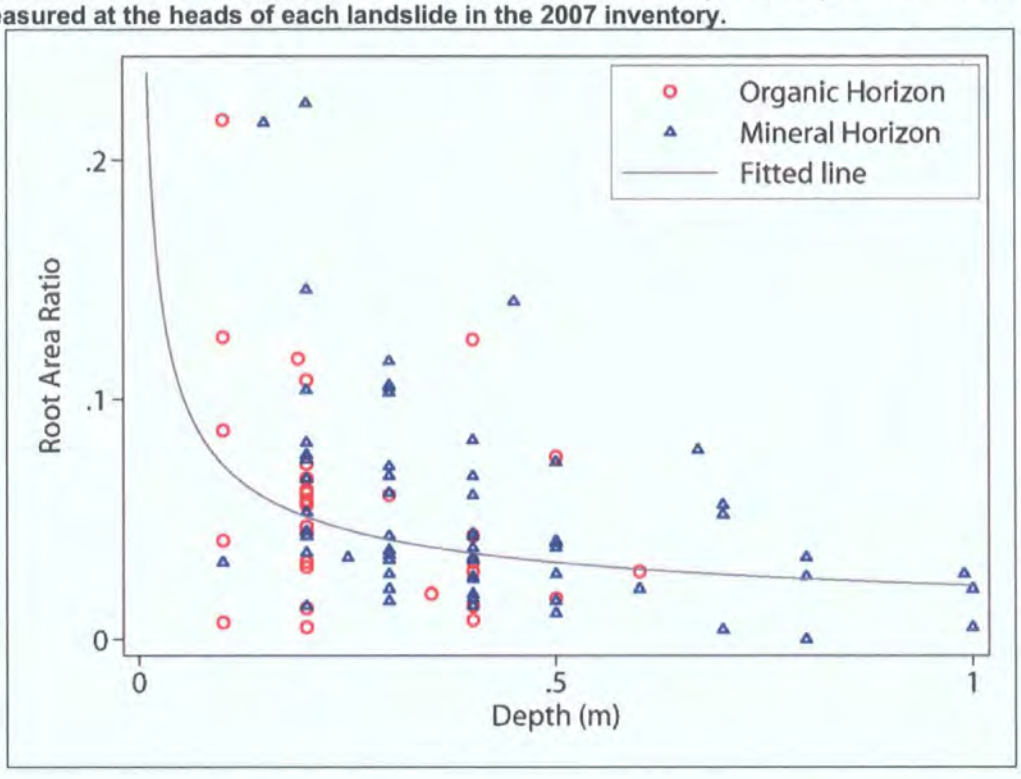

Figure 3-21 shows that root density declines with depth. This decline is most effectively modelled as a power function, which captures the rapid decrease at small depths and the gentler decline at greater depths. Least squares regression suggests that the power function with the closest fit to the data is:

Equation 3-11

$$y = 0.0223x^{-0.513}$$

Root cohesion measurements are predominantly from the top 150 mm of soil. To correlate these with root density, I calculate the expected root area ratio (RAR) for this zone by integrating the power function for depths from 0–150 mm:

Equation 3-12

$$\int_0^{0.15} 0.0223x^{-0.513}dx = \frac{0.0223}{0.487}x^{0.487} = 0.0182$$

then dividing this by the total depth (150 mm):

Equation 3-13

$$RAR_s \frac{0.0182}{0.15} = 0.121$$

Assuming that: 1) the root area ratio for surface tests is 0.121; 2) the root cohesion is zero when root area ratio is zero; and 3) that the relationship between root cohesion and root area ratio is linear; then root cohesion (Cr) for

the three vegetation types considered here can be related to root area ratio as follows:

Equation 3-14

Eriophorum Cr = 51 RAR

Equation 3-15

Pteridium Cr = 47 RAR

Equation 3-16

Juncus Cr = 28 RAR

Assuming that these relationships are reasonable we can use them and the relationship between root area ratio and depth to calculate root cohesion at different depths.

Equation 3-17

Eriophorum: $C_r = 51 \cdot 0.0223 z^{-0.513}$

Equation 3-18

Pteridium: $C_r = 47 \cdot 0.0223 z^{-0.513}$

Equation 3-19

Juncus: $C_r = 28 \cdot 0.0223 z^{-0.513}$

where: z = soil depth. Integrating the power function from the surface to depth z provides an estimate of root reinforcement per unit length (R_r) over the full depth:

Equation 3-20

Eriophorum: $R_r = \frac{51 \cdot 0.0223}{0.487} z^{0.487}$

Equation 3-21

Pteridium: $R_r = \frac{47 \cdot 0.0223}{0.487} z^{0.487}$

Equation 3-22

Juncus: $R_r = \frac{28 \cdot 0.0223}{0.487} z^{0.487}$

The final scenario assumes that root cohesion acts only in the organic layer and that we can apply uniform root cohesion over the depth of this layer. The Lake District landslide inventory (Section 2.4.3) provides data on the absolute and relative depth of organic horizons at the head of each slide. Relative depths of organic horizons appear more reasonable than absolute depths since both depth to the failure plane and organic horizon vary considerably over the study area but the two are correlated to some degree (Section 3.4). The relative depth of the organic layer could be represented as either a single value or a

distribution of values. In this case I have chosen to use the mean value (0.41) to keep things simple.

Equation 3-23

$$R_r = c_r\ 0.41\ z$$

Figure 3-22 shows the effect that each of these scenarios has upon an example soil column. As expected there is a linear increase in root reinforcement per unit length with depth when uniform root cohesion is applied over the full depth of the profile or only the organic layer. The power function has the most root reinforcement at very shallow depths but the least after ~0.9 m. There is only a small difference <0.5 kN m^{-1} between root reinforcement estimates from the power function and those assuming uniform reinforcement over the organic layer.

Figure 3-22: Root reinforcement per unit length for soils of different depths under *Pteridium*, represented using a uniform root cohesion depth relationship, a power law decay and applying uniform root cohesion over the organic horizon only.

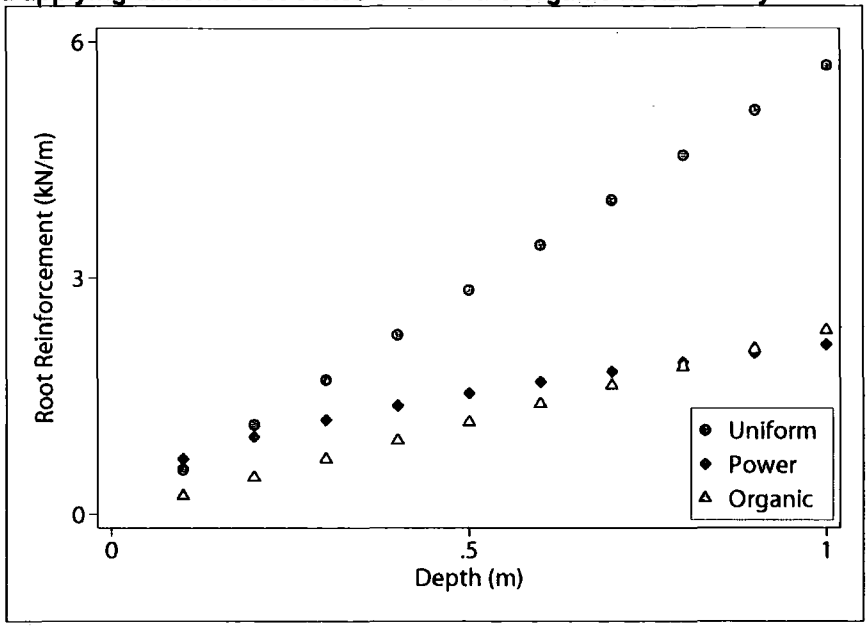

Summary

Most intact sample force - displacement curves have early peaks and gentle falling limbs suggesting that their strength is mobilised at small (<10 mm) displacements. Intact samples are displaced at consistently higher force than those with cut sides, which have low peaks and gentle falling limbs. Root cohesion estimates rage from 0-13 kPa for peak and 0–9 kPa for critical strength, their breakdown by vegetation type is in Table 3-17. *Eriophorum* samples are strongest at peak and critical strength, *Juncus* samples are weakest; there is no overlap between the distributions of their respective root

cohesion estimates. *Pteridium* root cohesions plot between these two end members.

Table 3-17: Summary table showing the range of peak and critical root cohesions and their mean values for different vegetation types and the full sample.

Vegetation	n	Peak Cohesion		Critical Cohesion	
		Range	Mean	Range	Mean
Full Sample	21	-0.42–13.33	6.19	-0.23–9.04	3.87
Pteridium	8	3.19–8.88	5.67	1.13–9.04	4.14
Eriophorum	7	5.96–13.33	9.13	0.35–8.00	5.22
Juncus	6	-0.42–5.30	3.44	-0.23–4.58	1.94

There is a weak negative correlation between root cohesion and depth, field evidence suggests that root density declines with depth and other studies suggest that root cohesion is strongly related to root density. The form of the relationship between root cohesion and depth can be represented using three different scenarios: uniform over the full soil depth, power law decay or uniform over part of the soils depth.

3.3.8. Discussion

Having reported my root cohesion results in Section 3.3.7, I will put these into the context of the relevant existing literature in the following section, highlighting and providing specific detail on studies of particular relevance to my results. I put the root cohesion estimates from my experiments into the context of controls on slope stability and compare this theory with vegetation patterns at recent landslide scars. I look briefly at the relationship between root cohesion and depth, comparing my measurements with observations on root network morphology from the ecological literature. Finally, I compare my observations on the form of the force - displacement curves with those from other studies.

Root cohesion for grasses and shrubs in the literature ranges from 0–60 kPa (Table 3-18); my root cohesion values, which range from 0–13 kPa (Table 3-17), fit within this range (Table 3-18). However, it is important to remember the difficulties associated with comparing data from other studies, which may be incommensurate in their settings and measurement techniques. *In situ* direct shear tests are normally performed on small samples near the surface; they will

be related to root density at that point, which may differ from that at depth. Applying root density and thread strength information in the Wu (1976) model accounts for variation in root density but represents an upper estimate of root strength by assuming that all roots fail simultaneously. Back calculation is a commonly used integrated measure of root reinforcement but contains inherent assumptions related to the stability method and other parameters used to perform the back calculation. For these root reinforcement estimates to be applied in slope stability models the measured and modelled processes need to be carefully matched to avoid misrepresentation. In this case I measured *lateral* root cohesion by *in situ* direct shear so my values represent cohesion in the top 0.15 m of the soil. Studies with vegetation similar to this study (*Pteridium*, *Eriophorum* and *Juncus*) are discussed in the following three paragraphs to put my measurements into context.

Ziemer (1981) reports from strength tests, that *Pteridium* roots (rhizomes) had ¼ of the tensile strength of conifer roots. Field measurements suggested that they have only 10% of the live root biomass found in coniferous forest for <17mm roots (which were considered the most important in this study). As a result, they were considered to contribute little to the strength of the soil. However, my results suggest that *Pteridium* provides 3–9 kPa of root cohesion with a mean peak cohesion of 5.7 kPa and critical cohesion of 4.1 kPa. These differences may reflect the different methods of measuring root cohesion although Ziemer's (1981) method (measuring root thread strength and density then applying a root reinforcement model) is usually considered to overestimate rather than underestimate root cohesion.

Micheli and Kirchner (2002) tested soil shear strength with a large shear vane (110 mm high and 76 mm diameter) in a riparian meadow in California (USA). They found shear strengths of 43 kPa under sedge (*Carex* sp) compared with 13 kPa on unvegetated meadow banks and of 38.1 kPa compared with 6.2 kPa on unvegetated bars (Table 3-18). Goldsmith (2006) performed laboratory direct shear tests on large samples (0.25 by 0.25 by 0.25 m) of Tussock sedge (*Carex stricta*) turf in Massachusetts (USA). Her results show 11–80 kPa of additional strength provided by sedge roots with a mean root cohesion of 51 kPa (Table 3-18). These results were calculated by comparing peak stresses for rooted and

fallow samples but are conservative since the stress values were still rising at the end of many tests. The root cohesion values of Micheli and Kirchner (2002) and Goldsmith (2006) are relevant to this study because *Eriophorum* is part of the same family (Cyperaceae) as Carex, so that its physical properties may be similar. The values reported in these studies are some of the highest in the literature for non tree species. This may be because they are generally surface samples rather than samples at depth or at the failure plane of a landslide. However, this makes them more readily comparable to the results of this study, which has been designed to measure root cohesion near the surface. Preston and Crozier (1999) back calculated root cohesion from 15 landslides on grass pasture in North Island New Zealand and found root cohesion values of 0.2–7.6 kPa (Table 3-18). However, these should be treated with caution because they are derived from Back calculation using an infinite slope procedure. This method estimates basal root cohesion where the authors indicate that the majority of the root cohesion in the study area is lateral. As a result, root cohesion is probably under-represented in this study. These studies show the potential for variability in root strength even among similar species in different environments or measured using different methods. The shear strength of *Eriophorum* measured in this study ranges from 0–13 kPa with mean peak cohesion of 9.1 kPa and critical cohesion of 5.2 kPa. These values are low compared with those measured for other sedge species but higher than most grass and shrub estimates in the rest of the literature.

Micheli and Kirchner (2002) report shear strengths of ~40 kPa in areas with rush (*Eleocharis* and *Juncus* sp) roots, compared with ~13 kPa in unvegetated areas (Table 3-18). Performing the same tests on sand and gravel bars they found average strength in *Juncus* vegetated areas was 46.3 kPa compared with 6.2 kPa in unvegetated areas and that soil strength was positively correlated with biomass. Root cohesion under *Juncus* in my study ranged from 0–5 kPa with mean peak cohesion of 3.4 kPa and critical cohesion of 1.9 kPa. These root cohesions are some of the lowest in the literature and are very different from those measured by Michelli and Kirchner (2002). However, these are not the lowest recorded root cohesions, many studies have reported zero or near zero root cohesion at the lower end of their measured range (e.g. Selby, 1993; Tobias, 1995; Lawrance, 1996; Table 3-18).

Comparing the results of this study with those from other studies is difficult and can provide little direct additional information aside from confirming that these values are within the reasonable range for root cohesion. The within sample variability is small compared to the variability between different studies, especially when the results are decomposed into vegetation type classes. The differences in root cohesion between vegetation types provide important additional information for our understanding of the factors controlling slope stability. Root cohesion under *Eriophorum* is significantly greater than that under *Juncus*. The implication of these results is that for slopes similar in all other respects, an *Eriophorum* slope will be most stable and a *Juncus* slope least stable. Observations of vegetation types around landslide scars (Section 2.4.3) would appear to support this suggestion; 85% of landslides that failed during the January 2005 event have some *Juncus* around their scar while the proportion of the catchment covered by *Juncus* is very much smaller (<5%, Section 6.7). However, this relationship may not be solely related to root cohesion, *Juncus* flourishes in wetland conditions where high pore water pressures are likely to promote instability (Section 2.4.3). *Juncus* patches are both small and sparse on slopes steep enough to be unstable. The majority of these slopes are covered by either *Pteridium* or *Eriophorum*, in this case, slopes covered with *Pteridium* should be less stable, although the vegetation dependence on other site conditions especially soil moisture may make this effect difficult to detect.

The literature suggests that root reinforcement is strongly related to the amount of root biomass in the soil. Observations at landslide scars suggest that biomass decreases rapidly with depth. Plant morphology theory and observations suggest that this relationship will vary between species and with a range of other environmental drivers. Given these assertions, root cohesion should decrease with depth down the soil profile. In *Juncus* the expected decline is observed, there is no root cohesion in the sample at 0.15–0.3 m depth but there is only one subsurface sample so the suggestion is tentative. However, this corresponds well with Richards and Clapham's (1941) description of *Juncus* roots: *"The rhizome* [roots] *runs more or less horizontally at 0.6–5 cm below the surface, forming a dense mat. It has two kinds of roots: Most are*

stout and straight, penetrating vertically downwards into substratum to depth of 15–25 cm below surface; finer roots extend sideways and upwards from the rhizome". In other vegetation types the relationship is less obvious. There is no relationship between root cohesion and depth down to 0.3 m in *Eriophorum*, or for peak cohesion of *Pteridium* down to 0.45 m. However, there is some decrease in *Pteridium*'s critical root cohesion with depth. Sample size is limited here and this limits the conclusions that can be made from the data. There appears to be some evidence to suggest that root cohesion in *Juncus* is the most and *Eriophorum* the least sensitive to depth down to 0.3 m but further research is required to cement this preliminary finding.

Given the uncertainty in the cohesion - depth relationship in my study area it is best represented by a range of scenarios rather than a set of vegetation specific relationships. The scenario set detailed in Section 3.3.7 (uniform full depth, uniform partial depth and power law decay) cover the range of potential cohesion - depth relationships. The form of this relationship has received little attention in the slope stability modelling literature, with those studies that do account for lateral root cohesion applying it as a constant value independent of depth (Casadie *et al.*, 2003; Gabet and Dunne, 2002). This is reasonable when root cohesion has been measured using a technique that integrates root strength over that depth. Thread strength and density methods using Wu's (1976) model or Pollen's (2004) more refined version are suitable for this but are inherently tuned to the conditions in which they were measured, and will become unrepresentative where these conditions differ significantly from those being modelled. This is particularly important if failure plane depth is not held constant within the stability model but is: spatially-varied, represented as a distribution, or calculated automatically (using a search algorithm). In Chapter 5 I will address this issue by applying the root cohesions values estimated here within the three scenarios detailed above to test the sensitivity of three-dimensional stability models to these scenarios.

Direct shear box tests show that in many cases the increased maximum shear strength of soil with roots is mobilised at a larger shear displacement than fallow soil (Waldron, 1977; Gray, 1978; Wu *et al.*, 1979; Abe and Iwamoto, 1986). Soils with roots produce broader and flatter peaked force - displacement curves.

These studies suggest that the reinforcing effect of roots is both to increase shear strength of the soil and the strain energy stored during extended shear displacement. My results suggest that there is some extension of the duration of peak strength in the force displacement curves (Figure 3-17) but this is small relative to the increase in peak strength. Also, the form of the force displacement curves and the increased root cohesion at peak compared with critical strength suggests that most of the root cohesion is mobilised at small displacements. However, the existence of a root cohesion offset even after >50 mm displacement suggests that some roots continue to reinforce the soil even after very large displacements. This is supported by observations from other landslide scars (Figure 3-23).

Figure 3-23: A photograph of roots under tension at a landslide scar, Dooncarton, Ireland.

Table 3-18: Root cohesion values for grasses shrubs and trees calculated from field and laboratory tests Back calculation and root tensile strength (adapted and amplified from: O'Loughlin and Ziemer, 1982; Schmidt *et al.*, 2001; Norris and Greenwood, 2006). Symbols indicate calculation methods: * = back calculation, ‡ = .thread strength model, † = *in situ* shear tests, § = laboratory shear tests.

Source	Vegetation, soil type and location	Cohesion (kPa)
Waldron (1977)	Alphalpha (*Medicago sativa*), grown in containers, California, USA	9.8
Waldron (1977)	Barley (*Hordeum vulgare*), grown in containers, California, USA	2
Sidle and Swanston * (1982)	Blueberry (*Vaccinium* sp.) and devil's club (Oplopanax horridus)	2.02
Wu ‡ (1984a)	Sphagnum moss (*Sphagnum cymbifolium*), Alaska, USA	3.5–7.0
Hewlett *et al.* † (1987)	Boulder clay embankment under grass, Jackhouse Reservoir, UK	3.0–5.0
Buchanan & Savigny * (1990)	Understorey vegetation (*Alnus, Tsuga, Carex, Polystichum*), glacial till soils, Washington, USA	1.6–2.1
Selby (1993)	Grass	0.1–9.8
Gray § (1995)	Reed fiber (*Phragmites communis*) in uniform sands, laboratory	40.7
Tobias † (1995)	*Alopecurus geniculatus*, forage meadow, Zurich, Switzerland	9
Tobias† (1995)	*Agrostis stolonifera*, forage meadow, Zurich, Switzerland	4.8–5.2
Tobias† (1995)	Mixed pioneer grasses (*Festuca pratensis, Festuca rubra, Poa pratensis*), alpine, Reschenpass, Switzerland	13.4
Tobias† (1995)	*Poa pratensis*(monoculture), Switzerland	7.5
Tobias† (1995)	Mixed grasses (*Lolium multiflorum, Agrostis stolonifera, Poa annua*), forage meadow, Zurich, Switzerland	-0.6–2.9
Lawrance *et al.*† (1995)	*Pennisetum purpureum*, in a silt clay loam, East Nepal	0–11.6
Lawrance *et al.*† (1995)	*Setaria anceps* in a locally stony sandy loam, East Nepal	0–2.7
Lawrance *et al.*† (1995)	*Cymbopogon microtheca, Thermeda* sp., *Neyraudia* sp. in a weathered phylitic shale, East Nepal	0–3.6
Lawrance *et al.*† (1995)	*Cymbopogon microtheca, Imperata* sp. In a friable loamy sand, East Nepal	0.6–10.7
Preston and Crozier * (1999)	Grass pasture, North Island, New Zealand	0.7–6.9
Micheli and Kirchner † (2002)	Rushes (*Juncus* sp., *Eleocharis* sp.), gravel/sand bar, California, USA	40.1
Micheli and Kirchner † (2002)	Rushes (*Juncus* sp., *Eleocharis* sp.) on floodplain, California, USA	27
Micheli and Kirchner † (2002)	Sedge (*Carex* sp.) on a gravel / sand bar, California, USA	31.9
Micheli and Kirchner † (2002)	Sedge (*Carex* sp.) on a floodplain terrace, California, USA	29.5
Pollen and Simon § (2005)	Switch grass (Ponicum virgatum), Mississippi, USA	1–18
Cazzuffi *et al.* § (2006)	Elygrass (*Elytrigia elongata*), clayey-sandy soil, Altomonto, Italy	10
Cazzuffi *et al.* § (2006)	Eragrass (*Eragrostis curvala*), clayey-sandy soil, Altomonto, Italy	2
Cazzuffi *et al.* § (2006)	Pangrass (*Panicum virgatum*), clayey-sandy soil, Altomonto, Italy	4
Cazzuffi *et al.* § (2006)	Vetiver (*Vetiveria zizanioides*), clayey-sandy soil, Altomonto, Italy	15
Goldsmith § (2006)	Switch grass (*Ponicum virgatum*), Massachusetts, USA	19.5–41.9
Goldsmith § (2006)	Black Willow (*Salix nigra*), Massachusetts, USA	4.8–64.8
Goldsmith § (2006)	Tussock sedge (*Carex stricta*), Massachusetts, USA	10.5–21.9
Goldsmith § (2006)	Common Cottonwood (*Populus deltoides*), Massachusetts, USA	4.8–24.8
Norris† (2006b)	Mixed grasses on London Clay embankment, London, England	~10.0
Van Beek *et al.* † (2005)	Natural understory vegetation (*Ulex parviflorus, Crataegus monogyna, Brachypodium* sp.) on hill slopes, Almudaina, Spain	0.5–6.3
Van Beek *et al.* † (2005)	*Vetiveria zizanoides*, terraced hill slope, Almudaina, Spain	7.5

3.3.9. Section Summary - Root Cohesion

There is limited root cohesion data available for the vegetation types in upland UK areas. Similar vegetation data can give general information on the range

within which root cohesions for grasses and shrubs should fall but the different locations, methods and objectives of other studies limit the transferability of their information. This study uses *in situ* direct shear tests on samples with and without intact sides to provide the first data on root cohesions for three of the UK's most common upland vegetation types: *Pteridium*, *Eriophorum* and *Juncus*. These cohesion estimates fit within the expected range from the published literature; they suggest that *Eriophorum* provides the most root cohesion (mean = 6.2 kPa); *Pteridium* provides less cohesion (mean = 5.7 kPa); and *Juncus* provides the least (mean = 3.4 kPa). These results support the observation of others in suggesting that grasses and shrubs have important strong lateral reinforcing effects on soils. Representing their effect on slope stability requires a move away from one-dimensional and infinite slope analyses towards three-dimensional analyses that represent edge effects. Chapter 4 lays the theoretical foundations for such an approach and derives a set of governing equations to represent it. Chapter 5 tests these equations and applies them in thought experiments and sensitivity analyses to establish the importance of a blocks margins in determining its stability. Root cohesion is generally strongest in the upper part of the soil profile where the root mat is densest. The behaviour of root cohesion with depth can be characterised through three distinct scenarios where the root cohesion declines as a power function of depth or where it is invariant with depth over all or part of the profile. These scenarios are applied in Section 5.6 to assess their effect on slope stability.

3.4. Soil Density

3.4.1. Scope of the Section

Bulk density is the apparent density of soil calculated from either the mass of the soil in field conditions (wet) or the oven dry (105°C) mass divided by the volume occupied in the field. For slope stability models soil bulk density is used in conjunction with the volume of the unstable material to calculate the mass of the body under consideration. In this case field bulk density is most appropriate. In Section 3.4.2 I describe the method that I used to calculate soil bulk density and in Section 3.4.3 I present the results, compare them with suitable values from the other studies and discuss their implications for slope stability

modelling. I use soil profile data (particularly organic horizon and profile depth) from the locations where samples were collected to give context to these results. I focus on the soil density for the full sample, then on how this varies: for field v dry conditions; organic v mineral horizons and with depth. In each case the implications for stability modelling are addressed as they are encountered.

3.4.2. Method

Soil profiles were recorded and bulk densities collected at the head of each of the landslides in the January 2005 inventory (Section 2.4.3). Sample collection involved pressing a stainless steel ring of 25 mm diameter and 50 mm length into the soil at the head of the scar. One sample was taken at each site, samples were located within the profile to characterise the dominant material type for that profile. At sites where no single soil type dominated further samples were collected from each of the dominant horizons, to ensure in particular that organic as well as mineral horizons were represented over the study site. Samples were kept cool and sealed with plastic caps and tape to prevent any moisture loss. Field bulk density was calculated from the mass of each sample divided by its volume. Dry bulk density was calculated using the same method after the sample had been oven dried at 105 °C for >48 hours.

3.4.3. Results and Discussion

The full sample of soil bulk densities from the January 2005 inventory closely approximates a normal distribution (Figure 3-24). Field bulk densities range from 543 to 2537 kg m^{-3} with a mean of 1473 kg m^{-3} (Table 3-19). This range is very broad, spanning almost the full range of reported soil densities (for examples of soil density measurements from other studies see Table 3-2). However, a considerable portion of this variability is explained by the horizon from which the sample was taken. Samples from organic horizons have a mean density of 1158 kg m^{-3} and do not exceed 1800 kg m^{-3} whereas all mineral horizons have densities greater than 800 kg m^{-3} with a mean density of 1603 kg m^{-3}. Figure 3-24 illustrates the relationship between organic and mineral bulk densities, which also closely approximate normal distributions. The full sample more closely resembles that of the mineral subset because the majority of the samples are from mineral horizons. There are 52 samples from mineral

horizons compared with only 23 from organic horizons (Table 3-19). This accounts for only 75 of the 84 samples in the full set. The remaining 9 samples are either from sites without accompanying soil profiles or where the soil profile indicates a mixed mineral organic sample.

Table 3-19: Descriptive statistics for field bulk density of samples collected from the heads of landslide scars (all values except sample size (n) are in kg m^{-3}).

	n	Minimum	Maximum	Median	Mean	Standard Deviation
Full Sample	84	543	2537	1462	1473	±376
Organic Horizons	23	543	1793	1127	1158	±246
Mineral Horizons	52	846	2537	1590	1603	±356

Figure 3-24: Kernel density plots of field bulk density for the organic, mineral and full sample illustrates the differences between horizons and their effect on the full sample.

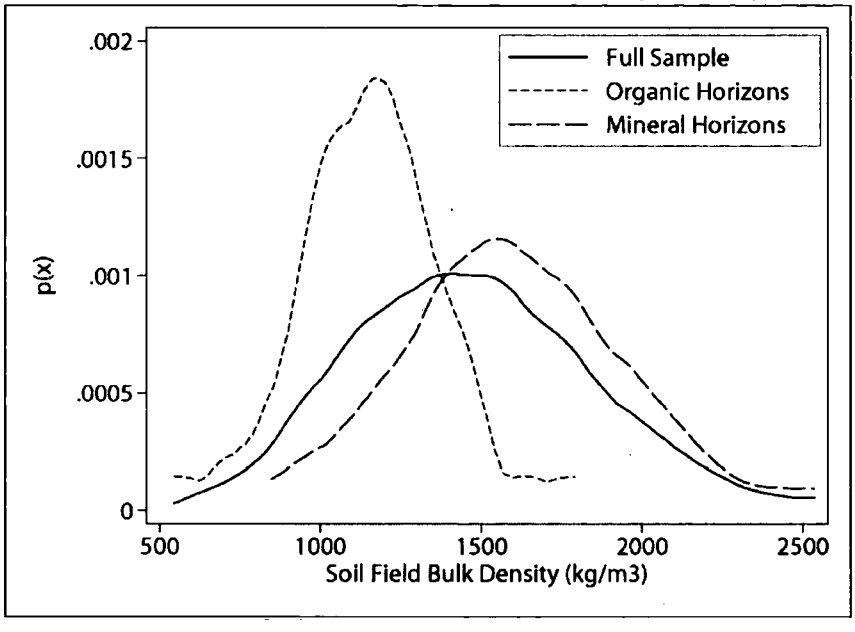

While field bulk density is the important parameter for slope stability modelling, dry bulk density is a more consistent and robust measure and is often reported in the literature instead of field bulk density. Field and dry bulk density are closely correlated and the difference between them is a measure of the soil's moisture content. Using field bulk density in the slope stability model assumes that the moisture content of the soil remains constant at roughly that measured here. Dry bulk density with an adjustment for moisture content would be a more precise representation of soil density. However: 1) slope stability models are relatively insensitive to variation in soil density; 2) the effect of fluctuations in moisture content on density are small relative to density variability between sites; and 3) spatially and temporally discrete estimates of unsaturated moisture

content would require a hydrological model of considerable complexity. For these reasons field bulk density is generally used to approximate soil density.

Figure 3-25: A scatter plot of dry and field bulk density illustrates their strong positive correlation and the offset resulting from soil moisture.

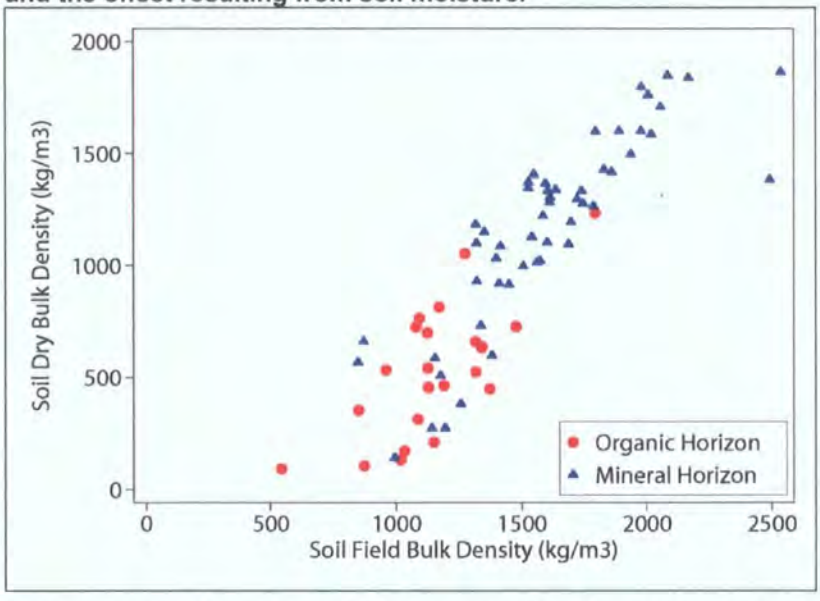

Figure 3-25 represents the relationship between field and dry bulk densities for my data. The relationship between the two variables can be estimated by calculating the semi-major axis of the data (Cox, 2007). The semi-major axis is used in place of standard regression because neither variable has been measured without error (an assumption within regression). The slope of the semi major axis is 1.3, suggesting, as we might expect, that moisture content decreases with soil density. The negative intercept (-885 kg m^{-3}) represents the offset in sample densities resulting from the moisture content of the samples.

Table 3-20: Descriptive statistics for dry bulk density of samples collected from the heads of landslide scars (all values except sample size (n) are in kg m^{-3}).

	n	Minimum	Maximum	Median	Mean	Standard Deviation
Full Sample	84	93	1864	1020	973	±474
Organic Horizons	23	93	1233	532	534	±294
Mineral Horizons	52	143	1864	1244	1167	±426

As expected, the dry bulk densities are lower than those for field conditions but their variability is larger in every case (standard deviations in Table 3-19 and Table 3-20) and they conform less well to a normal distribution. The difference between densities for organic and material horizons is also increased (Figure

3-26). A t-test indicates that the two distributions are significantly different with >99.9% confidence. The effect of these two distinct distributions on the full sample is visible in Figure 3-26 where the full sample appears almost bimodal.

Figure 3-26: Kernel density plots of dry bulk density for the organic, mineral and full sample illustrates the differences between horizons and their effect on the full sample.

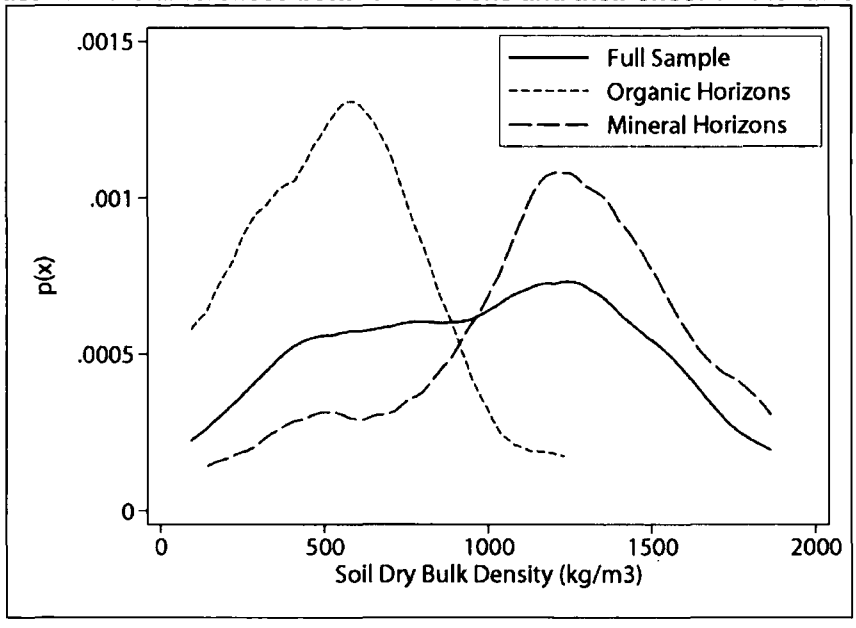

There appears to be very little correlation between density and depth for both dry and field state samples (Figure 3-27). As expected, the organic horizon tests plot with the lower depths and densities. However, there is variability across the full range of density from only 0.25 m depth. This variability is expected given the spatial variability in soil types and structure across the study area. The minimum density at any depth shows a more consistent decrease with depth. No mineral samples deeper than 1 m have densities less than 1100 kg m^{-3}. This trend reflects a depth control on minimum soil density that may be related to pedogenesis, material composition or increasing compressive force. These results suggest that while there may be some depth control on minimum density, there is no clear trend in density with depth and that modelling such a trend would be unprofitable.

Figure 3-27: Scatter plots of field (A) and dry (B) soil density against sample depth indicate a weak positive correlation with a great deal of scatter.

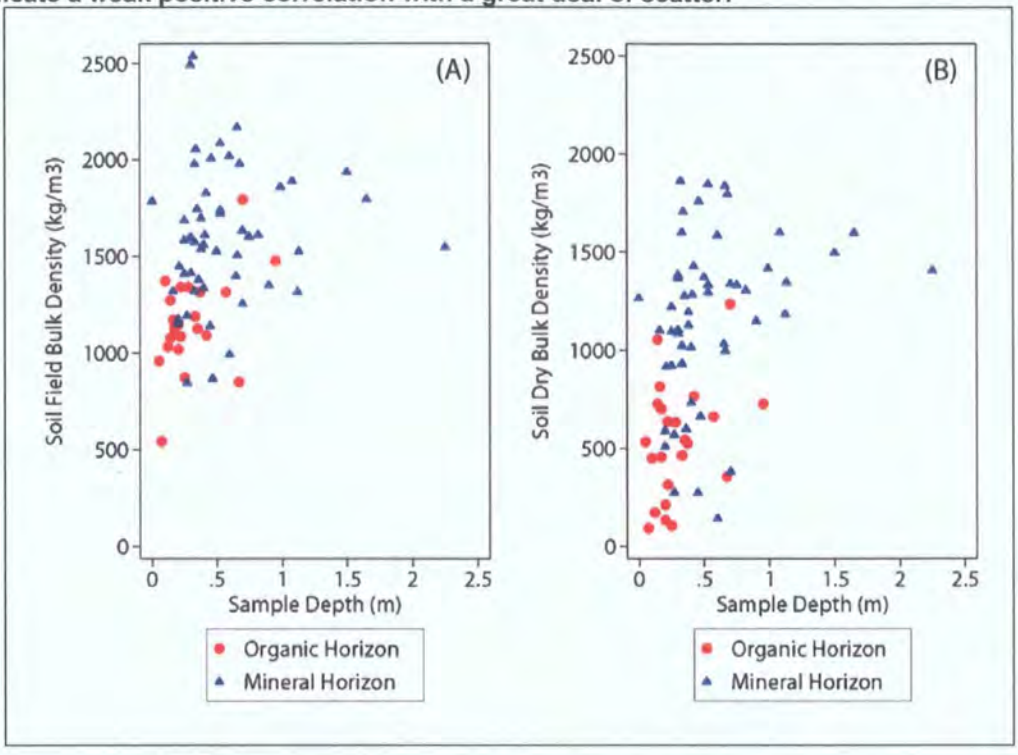

The significant differences between soil density in organic and mineral horizons will have important implications for the mass of the soil over the failure plane. Every soil profile records an organic horizon of some form. In some cases, this horizon can extend over the entire profile to the failure plane. This is particularly the case for peat soils and peat slides. The descriptive statistics in Table 3-21 illustrate the magnitude and variability of depth of the organic horizon which has a mean of 0.26 m and standard deviation of ±0.18 m. However, these statistics are difficult to interpret because of the variability in the depth of the full profile, which is almost twice that of the organic horizon (standard deviation ~±0.4 m).

Table 3-21: Descriptive statistics for the relative and absolute depths of organic horizons from soil profiles recorded in the January 2005 landslide inventory.

	n	Minimum	Maximum	Median	Mean	Standard Deviation
Profile Depth (m)	58	0.20	2.28	0.60	0.74	0.42
Organic Horizon Depth (m)	58	0.05	0.98	0.21	0.26	0.18
Organic Horizon Relative Depth	58	0.03	1.00	0.37	0.41	0.25

Alternatively, the organic horizon depth at each site can be normalised by the total profile depth to give a relative proportion of the profile occupied by organic soil. These organic horizon relative depths range from 0.03 (3%) to 1 (100%) illustrating the variability in soil type over the study area. They have a mean

value of 0.41 indicating that on average ~40% of the soil above the failure plane is in an organic horizon. Organic horizon relative depths are weakly bimodal (Figure 3-28) with the major mode at a relative depth between 0.2 and 0.3 and a second much smaller mode at ~0.9. This weak second mode is probably the result of the peat slide component to the January 2005 landslide inventory.

Figure 3-28: A kernel density plot of organic horizon relative depth, the depth of organic horizons normalised by full profile depth.

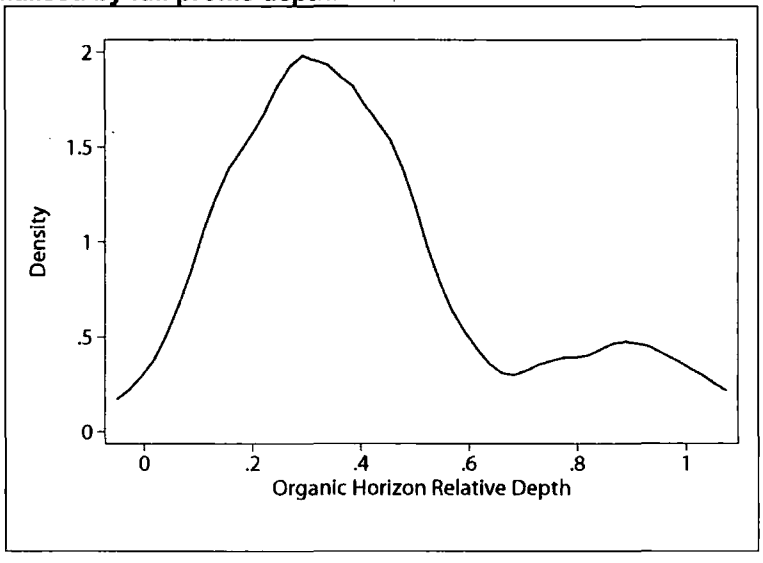

These organic horizon relative depths can be used in combination with the information on the magnitude and variability of soil density in organic and mineral horizons to improve representation of soil density in slope stability models. Exclusive use of mineral or organic soil density information would cause over or under prediction respectively of the composite density of the soil column above a failure plane. Using the mean values for the full sample would simply allow sampling density between the two horizons to define their relative importance. Alternatively we can use the relative depth of the organic horizon (D_r) as a weighting factor within a weighted average density (ρ_{stot}) that includes both organic (ρ_{so}) and mineral (ρ_{sm}) components:

Equation 3.24

$$\rho_{stot} = D_r \rho_{so} + (1 - D_r)\rho_{sm}$$

Applying this approach with mean values from the Lake District data gives:

Equation 3.25

$$\rho_{stot} = 0.41 \cdot 1158 + 0.59 \cdot 1603 = 1422 kg/m^3$$

This may be a good first approximation to the composite density of soil above a failure plane for our study area and could easily be adapted to a probabilistic representation of parameter variability.

3.4.4. Section Summary - Soil Density

Soil bulk density varies across the full reasonable range in my Lake District study area, reflecting the variability in soil types (chiefly humic rankers, podzolic and stagnogley soils; Section 2.3.6). A large amount of this variability can be explained by the type of horizon from which the sample originates (organic or mineral) and very little can be explained by variation in sample depth. Once split into horizon groups, the mineral horizon densities fall within the range of measurements of similar soil types (granular gravelly sands and silts) from other studies (Table 3-2). Dry bulk densities are strongly related to field bulk densities as expected, with soil moisture content decreasing with soil density. The variability in soil density resulting from variation in soil moisture content is small relative to the variability in density between sites. Given slope stability models' insensitivity to soil density (Section 2.6.4) and the additional complexity associated with spatially and temporally explicit predictions of unsaturated soil moisture approximating soil density at the time of failure using field bulk density represents a reasonable alternative. The difference between mineral and organic dry bulk densities was larger than that for field conditions almost causing bimodality in the full sample. The proportion of a profile occupied by each horizon can be characterised by normalising horizon depth by total profile depth. This allows the density of the column to be represented as a composite using relative depth of the organic horizon as a weighting factor in a weighted average of mineral and organic densities. This approach can be applied within slope stability models to better represent the depth integrated density of the soil column. It can be applied as either: a single spatially invariant mean value for the entire study area; or a probabilistic parameter representation using the distributions of relative horizon depth, mineral and organic soil density.

3.5. Soil Depth

3.5.1. Scope of the Section

Soil is the surficial material mantling the underlying weathered or fresh bedrock and lacking relict rock structure. Its depth influences slope stability by: 1) altering the mass of the soil body under consideration; 2) controlling soil

moisture and subsurface flow (Freer *et al.*, 2002; Tromp-van Meerveld and McDonnell, 2006); and 3) reducing the potential for roots to anchor the soil to the bedrock below (Dietrich *et al.*, 1995). In this section I aim to find a reliable measure of soil depth and its variability characterising some of the uncertainties related to its measurement as I do so. In Section 3.5.2 I provide the necessary background information on soil depth; its importance for stability, methods of modelling it and its representation within slope stability models. In Section 3.5.3 I report the three methods that I used to estimate soil depth in the study area but focus in particular on effective soil depth measurement at landslide scars. I present the effective soil depths measured at scars across the study area in Section 3.5.4 and use them to discuss first the variability in estimates resulting from different measurement techniques, then the statistical properties of these soil depths and their implications for parameterising slope stability models.

3.5.2. Background

At the broadest scale soils are typically thin or absent on sharp ridges and thickest in unchannelled valleys. More detailed estimates have been developed from: empirical correlation with digital terrain attributes (Moore *et al.*, 1993; Gessler *et al.*, 1995; 2000; Zhu *et al.*, 2001; Ziadat, 2005); or process based models (Heimsath *et al.*, 1997) coupling soil production (Heimsath *et al.*, 2000) and transport functions (Braun *et al.*, 2001). Spatial variation in soil depth has been estimated (Okimura, 1989; DeRose *et al.*, 1991; 1993); and incorporated into slope stability models both deterministically (Dietrich *et al.*, 1995) and by using probability density functions (PDFs) to characterise its variability (Hammond *et al.*, 1992; Koler, 1998; Haneberg, 2004). The soil depth parameter within slope stability models is somewhat of a misnomer since the appropriate length scale is in fact an 'effective soil depth': the vertical depth of the failure plane below the surface. However, the conventional soil depth (to bedrock) remains important as a boundary condition for subsurface hydrology. Where failure occurs at the soil – bedrock interface (Montgomery and Dietrich, 1994; Dietrich *et al.*, 1995) conventional and effective soil depth are commensurate; where failure is higher in the profile (Brooks *et al.*, 1993) they become disconnected. The Lake District Landslides in 2005 failed both at bedrock and at layers within the soil profile (Section 2.4.3).

3.5.3. Method

To gain an integrated picture of soil depth and effective soil depth at a range of scales over my study area I used three techniques in combination: soil depth probes, ground penetrating radar (GPR) and surveys of extant landslide scars.

Over 100 **soil depth probe** measurements were taken over an area ~0.05 km^2 at the Coledale study hillslope described in Section 6.4. Steel rods (25 mm diameter) were driven up to three meters vertically into the ground until they hit bedrock, this could be defined with confidence because once the probe made contact with the bedrock the pitch of each blow changed and the depth reading began to oscillate by ~10 mm. To ensure that this was a true contact the probe was driven for a further 50 blows after it began to oscillate. If no bedrock was found a value of >3 m was recorded. This was considered a reasonable cut-off depth since none of the landslides from 2005 had failure planes deeper than 3 m.

Ground penetrating radar (GPR) is a non invasive geophysical technique (Neal, 2004), which can identify the soil bedrock interface (Olson, 1985), or other layers within the profile (Davis and Annan, 1989). It offers the prospect of obtaining both the conventional and effective soil depths more rapidly and at a higher resolution than the conventional soil probe method. I assessed its effectiveness at the Coledale study hillslope (Section 6.4) by collecting GPR profiles using 800, 500 and 50 MHz antennae along transects between points of known bedrock depth. The results were poor; suggesting that in soils with many clasts GPR was ineffective at detecting bedrock or soil discontinuities.

Surveying **extant landslide scars** provides information on the depth of their failure plane. Although depth information is only available at existing scars, it is easily accessible at these locations and can be measured with greater confidence than with a probe or GPR, bypassing the problem of failure plane identification in measuring effective depth. As detailed in Section 2.4.3, the scars of landslides from the January 2005 storm event were surveyed using DGPS (accurate to ±0.05 m). Points were collected at breaks of slope and

changes in direction along the unaffected scar top and at a corresponding point inside the scar. At each site a profile (A-B) and at least one cross section (C-D in Figure 3-29) were surveyed, these extended out of the scar onto unaltered ground by ~5 m in each case.

Figure 3-29: Survey data collected using DGPS from one of the January 2005 landslide scars, illustrating the planform, profile and cross section data from which effective soil depth is estimated. The length H is the vertical height of the head of the scar.

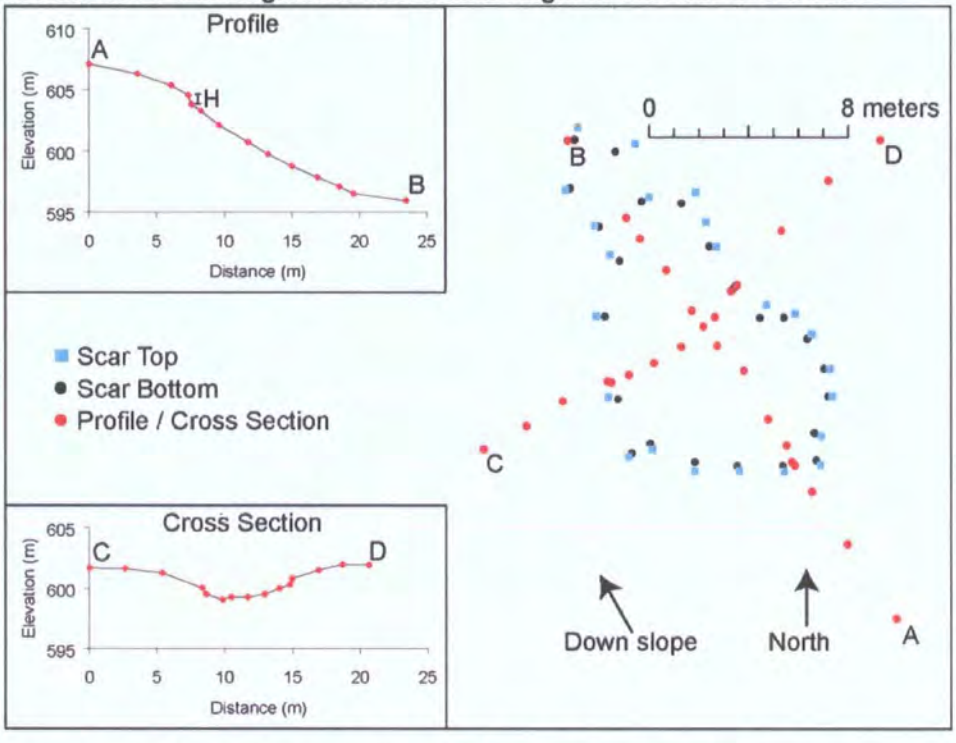

Landslide scars allow us to easily identify the failure plane; however there is incomplete information about the nature of the ground surface pre-failure. As a result depth can be estimated using a range of metrics illustrated in Figure 3-29 and Figure 3-30.

Figure 3-30: A schematic illustrating the framework of measurements used to generate 1D depth measurements from 3D landslide scar surveys. The methods used to generate the five coloured scar depth measurements (and 6th composite measure) are described below, their results discussed in Section 3.5.4. Each measure is coloured to match their linestyle in Figure 3-32. Cross section depth scenarios (I-IV) are discussed below and illustrated in Figure 3-31.

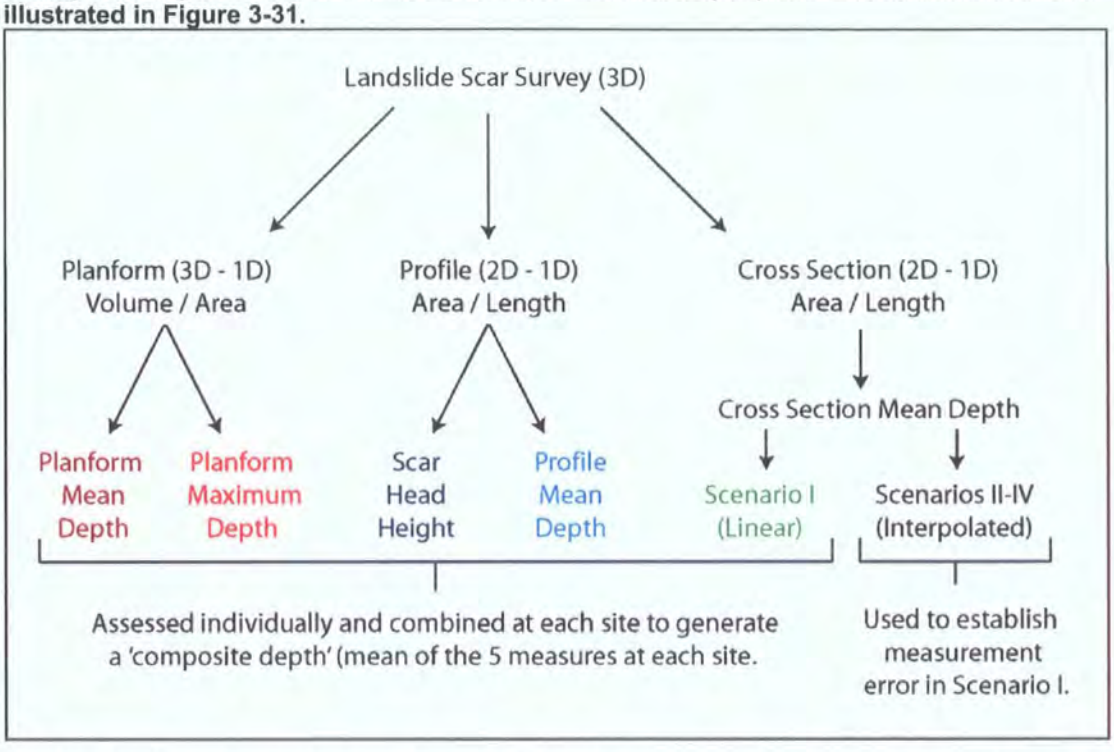

I calculated mean depth from three different representations of landslide form:

Equation 26

$$Planform\ Mean\ Depth = \frac{Total\ Scar\ Volume}{Total\ Scar\ Area}$$

Equation 27

$$Cross\ Section\ Mean\ Depth = \frac{Scar\ Cross\ sectional\ Area}{Scar\ Width}$$

Equation 28

$$Profile\ Mean\ Depth = \frac{Scar\ Profile\ Area}{Scar\ Length}$$

Scar volumes were calculated by linearly interpolating a surface across the scar using only points from intact soil then differencing this with a surface interpolated from both the intact points and those inside the scar. Both surfaces were interpolated by linear interpolation from a triangular irregular network at 0.01 m resolution. This method provides the most complete estimate of depth since it is integrated over the entire scar area. To calculate mean profile depth I projected a line from the scar head to the end of its toe, calculated the area under this line but above the scar outline and divided by the total horizontal

length of the slide. Cross sectional average depths were calculated in the same way but projecting the line from the intact soil on one side of the scar to the other (Figure 3-31A).

These calculations assume that: 1) the observed scar surface was the failure plane; 2) the failure plane extends to the edges of the scar; and 3) the ground above the scar was a straight plane from one intact side to the other. This final assumption is likely to be a simplification and may cause slight overestimation of failure plane depth where the scar is in a tight topographic hollow (e.g. Figure 3-29). To test this, and to obtain an estimate of the associated error, I have calculated mean depth from the cross sections under four scenarios. The simplest involves projecting a straight line from one scar edge to the other (Figure 3-31A). In the other scenarios I project two straight lines from each scar edge towards the centre of the scar (Figure 3-31 B-D) at an angle which is dependent on the scenario. In each case they are projected parallel to the slope from either: 1^{st} to 2^{nd} (Figure 3-31B), 1^{st} to 3^{rd} (Figure 3-31C), or 1^{st} to 4^{th} (Figure 3-31D) point out from the scar. The line continues into the scar until it either intersects the line from the other scar edge or it intersects the scar itself. Where the lines meet the area under them but above the scar is summed and divided by the width to give the mean depth. Where one of the lines intersects the scar the scenario is abandoned as unrealistic.

Figure 3-31: Schematic illustrating the four scenarios for the pre-failure ground surface and calculating failure plane depth from landslide scar cross sections.

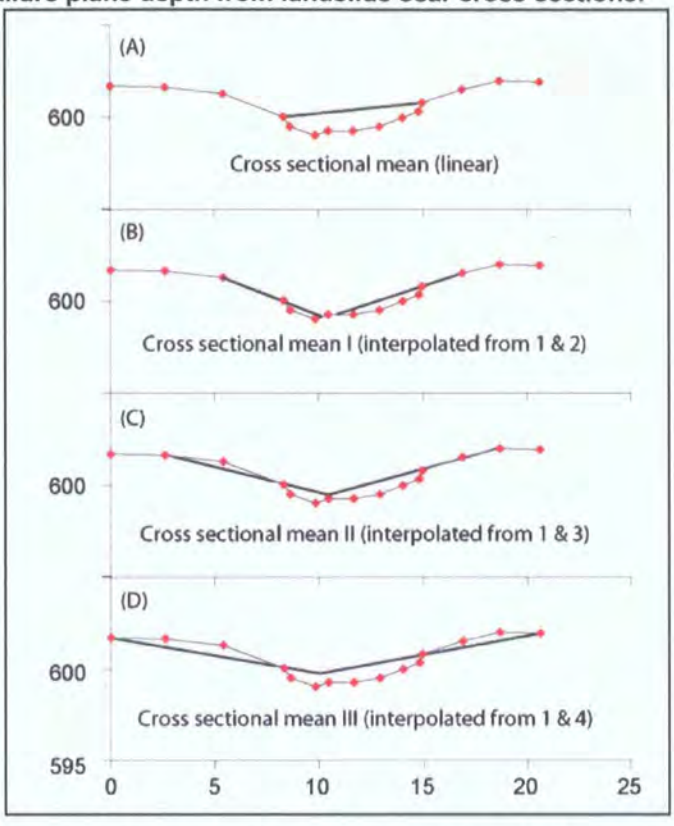

Two further measures of soil depth are: maximum planform depth, the largest difference between the interpolated pre and post failure surfaces; and scar head height, the vertical distance from the intact soil above the scar to the 1st point on the failure plane (length H in Figure 3-29).

3.5.4. Results and Discussion

In this section I focus on data from landslide scar surveys which are the most reliable source of effective soil depth data. First, I summarise the distribution of effective soil depth values from landslide scars before looking in detail at the influence of calculation methods on depth estimates. Maximum planform and cross section mean depth both require careful treatment. Finally I present the depth results treating maximum depth separately and applying an interpolated pre-failure surface for cross section mean depth.

Both effective soil depth and its variability (both within and between samples) are small (Figure 3-32; Table 3-22). However, although variability (standard deviations in Table 3-22) is small in absolute terms it is large relative to mean

depth. This variability between sites for a given depth measure is consistent with the expected spatial variability in soil depth across a catchment where soils will be shallower in divergent and deeper in convergent settings. The estimated depth of the failure plane ranges from 0.1–4.6 m but the mean failure plane depth for scars ranges from 0.1–3.4 m. The mean depth for each measurement method ranges from 0.64–0.99 m with the exception of planform maximum depth, which has a mean of 1.56 m.

Table 3-22: Summary statistics for the different methods of estimating the depth of the failure plane.

	n	Maximum	Minimum	Median	Mean	Standard Deviation
Planform mean	65	2.26	0.25	0.63	0.71	±0.33
Planform max	65	4.63	0.65	1.33	1.56	±0.82
Scar head height	61	1.73	0.10	0.55	0.64	±0.33
Profile mean	61	2.24	0.07	0.64	0.76	±0.49
Cross sectional mean	61	3.39	0.36	0.90	0.99	±0.53
Cross sectional mean I	44	2.97	0.03	0.50	0.59	±0.50
Cross sectional mean II	27	1.93	0.03	0.47	0.57	±0.41
Cross sectional mean III	33	3.13	0.03	0.61	0.75	±0.60

Probability Density Functions (PDFs) for depth estimates using scar head height, planform mean and profile mean stack on top of each other with the same modal depth but varying skew and dispersion (Figure 3-32). All datasets have some positive skew but in every case this is relatively small with almost all the mean scar depths falling into the 0–2 m range. Planform mean depth has a kink and scar head height a secondary mode at ~1 m, this may indicate some process distinction in the sample.

Figure 3-32: Kernel density plots of failure plane depths estimated using the different methods detailed above (Cross section mean uses scenario A from Figure 3-31) the dashed line represents a composite for each site (mean of 5 metrics for that site).

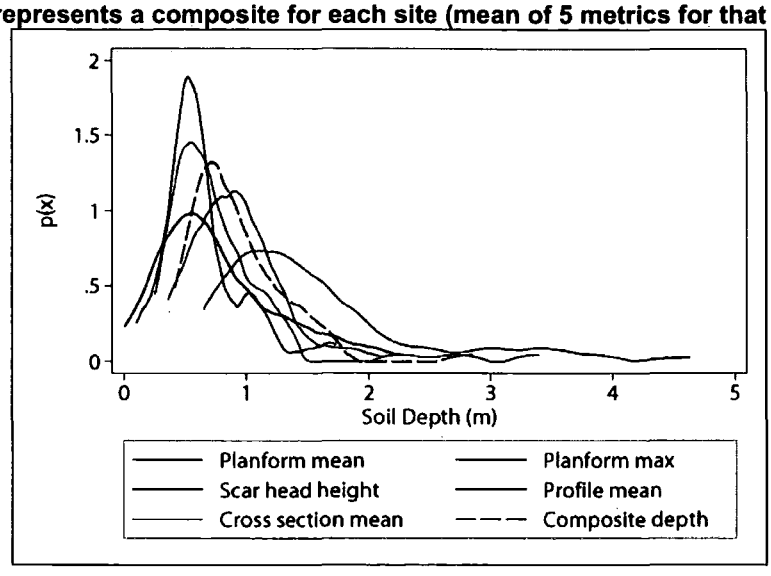

Maximum depth using the planform method is consistently deeper than the mean depths estimated by other measures (Table 3-22; Figure 3-32) and is strongly correlated with planform mean depth (Figure 3-33). This suggests that they are related (which is expected given the similarity in their methods) and importantly, that maximum failure plane depth may be an accurate predictor of mean depth, reducing the number of measurements required at a site. The relationships between other depth measurements are surprisingly weak (Figure 3-33), with many graphs displaying no clear trend and the only observable positive correlations being strongly heteroscedastic.

Figure 3-33: A matrix of scatter plots for soil depth estimates from the five selected methods.

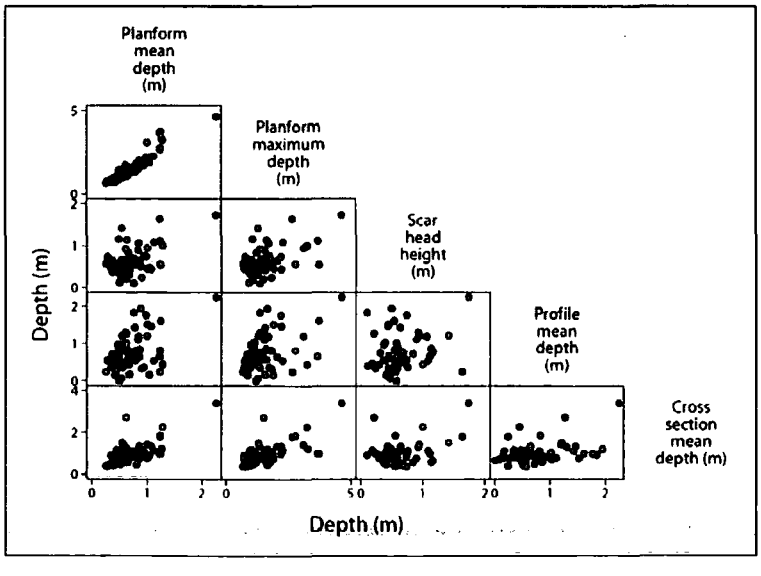

Representation of the pre-failure surface can have a significant effect on depth estimates. The cross section mean depth of the sample drops by >0.24 m (~25%) when any alternative representation of the pre-failure surface is applied (Scenarios II-IV in Figure 3-31). This, and the position of the PDF relative to the other estimates (Figure 3-32), suggests that the linear approach overestimates soil depths. Depth appears relatively insensitive to the choice of interpolation between: 1^{st}–2^{nd} or 1^{st}–3^{rd} points then begins to increase again for 1^{st}–4^{th} point interpolation (Figure 3-34). At each site these depth estimates are closely correlated, suggesting that the change in surface representation is either: 1) consistent in its effect across the sites; or 2) small relative to the between site variability in cross sectional depth.

Figure 3-34: Kernel density plots of soil depth estimated from cross sections under three different scenarios.

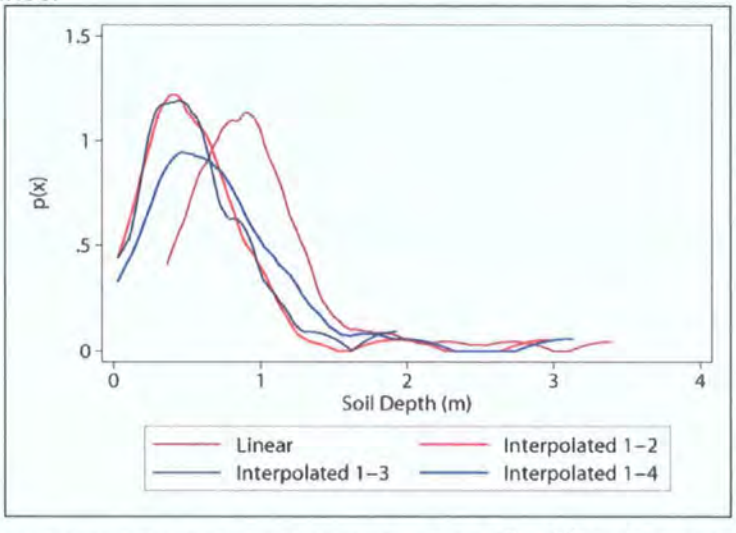

If cross section mean depth is calculated using 1^{st}–2^{nd} point interpolation (as a reasonable mid-range estimate of pre-failure surface geometry), its probability distribution is strongly similar to those for the other mean depth estimates (Figure 3-35). Only the planform maximum depth estimates plot outside this envelope, as we would expect. When a composite depth is calculated for each site as the mean of the four estimates excluding planform maximum depth, the resultant PDF closely resembles that of the planform mean depth estimates. This agreement with the estimates of other techniques increases our confidence in its reliability. The planform mean depth technique is also the most technically robust method and has the advantage of integrating depths from the largest area into its estimate. Planform mean depth estimates will be used to represent soil depth in following chapters.

Figure 3-35: Kernel density function for different soil depth measures. The dashed line is the composite for each site (mean of 4 metrics for that site, with planform max excluded in this case).

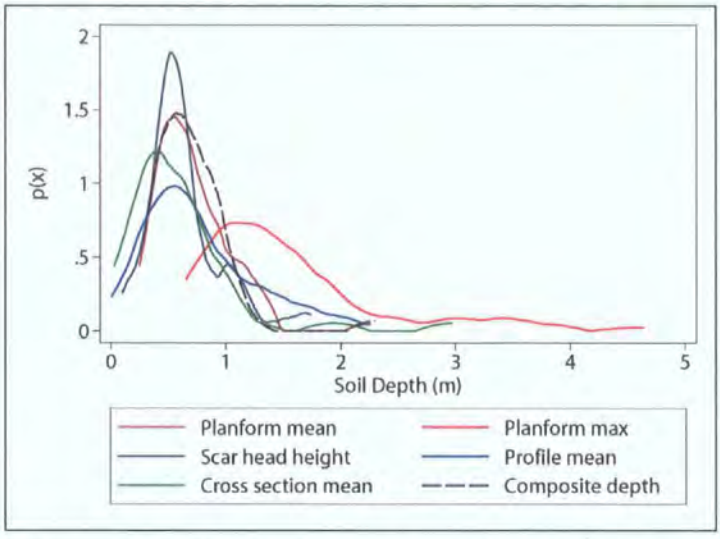

The similarity in estimated effective soil depth distributions from the four different methods (excluding maximum depth; Figure 3-35) is encouraging support for them individually. However, the scatter in relationships between depths estimated using these methods at each site (Figure 3-33) is concerning. This scatter indicates that at a site there can be considerable variability in depth estimates with different techniques. This has little impact on my study, which is interested in the distributions of potential landslide depths rather than their relationship at a site. However, it has important implications for landslide volumetric estimates, which are often calculated from the product of landslide depth and area. These results suggest that the magnitude of estimates may be highly dependent on the measurement technique and that this relationship is random rather than systematic.

3.5.5. Section Summary - Soil Depth

Past studies have modelled soil depth using empirical or physically based models. In the my study area this was not possible because: 1) techniques for rapidly acquiring soil depth data over large areas (e.g. GPR) were not effective in this environment; 2) the magnitude and variability in soil depth to bedrock was much larger than expected and contained a strong glacial fingerprint; and 3) the property of interest, effective depth (to the failure plane), differed in many cases from depth to bedrock so that this type of modelling would not be

profitable for this application. Soil depth probes on a hillslope that had experienced instability provided information on the potential depth of the soil mantle (often >3 m). Topographic surveys at landslide scars provided information on the depth of failure planes for recent landslides (rarely >2 m). As a result, a spatially lumped, average soil depth for the study area, and characterisation of the variability about this average was considered the best alternative. This information can then be applied in stochastic (Benda and Dunne, 1997) or probabilistic (Hammond *et al.*, 1992; Haneberg, 2000) frameworks for slope stability modelling. Failure plane depths were obtained from topographic surveys of extant landslide scars as part of the Lake District landslide inventory. Different methods of analysing DGPS survey data can lead to different depth estimates at a site. However, when considering spatially lumped depth distributions this variability is absorbed by the data. The *effective soil depth* is most reliably estimated by planform mean depth. From 65 landslides from the January 2005 inventory the mean depth was 0.7 m and the standard deviation 0.3 m in a range from 0.3–2.3 m. These or the distribution that they characterise are the present best available knowledge on effective soil depth for Lake District landslides. At present this information is best applied either as a single value with associated uncertainty or by sampling from the soil depth distribution.

3.6. Digital Elevation Data

3.6.1. Scope of the Section

Elevation data are important in defining the energy gradients for both the geotechnical and hydrological aspects of slope stability models. Recent advances in remote sensing have resulted in a range of available datasets at different precisions, resolutions and costs. Both precision and resolution are important in defining the effectiveness of topographic representation. These properties are defined by three key steps: acquisition, interpolation and post processing. Resolution and precision are affected at the acquisition stage by: the technique or sensor specification and by the survey type in particular the height of the sensor above the surface of interest. In Section 3.6.2 I review the three most common and most important acquisition techniques; the effect of

grid resolution on slope stability estimates has been dealt with in detail within the literature and is reviewed in Section 3.6.3. Elevation data is often post processed using a variety of filters to improve its topographic representation; I review these in Section 3.6.4. To put these reviews into the context of my study area I set out a research design in Section 3.6.5 to assess the quality of topographic data derived from two different sources (IfSAR and photogrammetry) and the performance of a range of filters, applied individually and in combination, to improve this quality. In Section 3.6.6 I present the results of this study and identify their implications for slope stability modelling.

3.6.2. Data sources

Improvement in the availability and quality of high resolution elevation data has resulted from advances in three remote sensing methods in particular: laser altimetry; radar remote sensing (e.g. Interferometric Synthetic Aperture Radar, IfSAR); and digital photogrammetry.

Laser altimetry (LiDAR), both airborne and terrestrial, is becoming increasingly popular in a variety of geomorphological applications (Lane *et al.*, 2003; Rosser *et al.*, 2005; Heritage and Hetherington, 2007). LiDAR involves active sensors, which use the travel time of a pulse of light to measure the distance between the sensor and the illuminated spot on the ground (Wehr and Lohr, 1999). Airborne LiDAR combines high point density (typically 1-10 points per square meter) and ranging accuracy (typically better than 0.05 m) with an ability to see through small openings in the vegetation cover (Wagner *et al.*, 2004). But, its cost means that its use is often limited to areas where the desired detail matches a particular need.

Radar altimetry has been used in the recent NASA SRTM to collect elevation data with global coverage at a resolution of 50 m and precision of ±16 m (Rabus *et al.*, 2003). Intermap have used the same technique on an airborne platform to collect national elevation datasets for Great Britain, Germany, Indonesia, Jamaica and the Philippines (Intermap, 2008). These datasets are now available, at a relatively low cost, in a large, rapidly growing database for general access. The elevation dataset, which will include complete coverage of

Western Europe and the USA by the end of 2008 has already been widely used in hydrological and geomorphic research in the UK (Bates *et al.*, 2005; Bradbrook *et al.*, 2005; Smith *et al.*, 2006). These data have a quoted vertical Root Mean Square Error (RMSE) of ±0.5 to ±3 m and sample spacing of 5 m (Mercer, 2004). They are generated from two Synthetic Aperture Radar (SAR) images, using differences in the phase of the waves returning to the sensor. Airborne IfSAR is usually collected in single pass mode, with the SAR images collected simultaneously by two antennae mounted on the same aircraft and separated by ~1 m (Li *et al.*, 2004). The data are generally post processed 'in house' to merge the DEMs into a single mosaic, interpolate over data gaps and correct potential blunders inherent in the dataset (Li *et al.*, 2004). Unlike LiDAR, IfSAR elevation observations integrate the signal over the extent of the cell. As a result, it is less effective in seeing through openings in vegetation cover.

Photogrammetry uses parallax to obtain three-dimensional object co-ordinates from two overlapping two-dimensional images. Despite the rapid progress in IfSAR and LiDAR technology, photogrammetry remains an important technique for obtaining elevation data. Archival air photos represent a unique opportunity to generate elevation models from historical imagery that can be used to identify change in topographic form over time (e.g. Chandler and Brunsden, 1995; Lane *et al.*, 2003). Digital photogrammetry is also developing. The availability of desktop photogrammetric software, automation of the photogrammetric workflow, improvements in image-matching techniques, and growth in processing power for desktop PCs, have allowed high density elevation data to be generated rapidly at a relatively low cost (Chandler, 1999; Lane, 2000).

3.6.3. Resolution

Topographic representation is necessarily controlled by the resolution or point density of the data. The most suitable resolution depends on the quality and density of the input data, size of the area to be mapped and accuracy required for the output data (Ward, 1981). In slope stability models local slope, upslope contributing area and topographic index are the important topographically derived variables (Section 2.6). With coarsening resolution, local slope tends to drop because local variation in terrain is smoothed, while the distribution of

upslope contributing area tends to shift towards larger values (Band and Moore, 1995; Claessens *et al.*, 2005). Researchers comparing topographic index distributions from DEMs of different resolutions (Quinn *et al.*, 1991, 1995; Zhang and Montgomery, 1994; Saulnier *et al.*, 1997; Lane *et al.*, 2004) have found that the number of low topographic index values increases with DEM resolution because more cells have low upslope contributing areas (Lane *et al.*, 2004). Relative stability predictions from models such as SHALSTAB are also sensitive to DEM resolution (from 30–6 m or 10–2 m in Dietrich and Montgomery, 1998; from 10–100 m in Claessens *et al.*; 2005; and from 2–50 m in Tarolli and Tarboton, 2006). Percentages of the landscape in the moderate landslide hazard classes are similar for coarse and fine resolutions, but with finer resolution topography, sites with highest instability increase and can be identified more precisely (Deitrich and Montgomery, 1998).

It appears intuitive to argue that the finest DEM resolution possible should be used since this will most closely approximate the true surface. However, there are limitations to the improvement which can be achieved by using very fine resolution topographic data due to: 1) error in the elevation model; or 2) the assumptions or scale of representation of the modelled processes. Firstly, slope uncertainty is inversely proportional to DEM resolution (Lane *et al.*, 2003), so that to prevent slope error from increasing vertical precision must increase with increasing horizontal resolution. Secondly, there are physical and modelling limits on the utility of fine resolution terrain data (Wolock and Price, 1994; Tarolli and Tarboton, 2006). For example, the assumption that the phreatic surface configuration mimics ground surface topography (which is common in hydrological models) often breaks down at finer digital terrain model resolutions (Wolock and Price, 1994). At very fine resolution slopes from the DEM also become disconnected from the slope of the failure surface in the infinite slope stability model (Tarolli and Tarboton, 2006).

Slope calculations become increasingly sensitive to elevation error at finer resolutions (discussed above) but also to true elevation differences. Commonly used algorithms for calculating slope from a DEM (e.g. Zevenbergen and Thorne, 1987) use a nine cell window. The length over which slope is calculated for 1, 5 and 10 m resolutions is then at least 2, 10 or 20 m. Topographic forms

with wavelengths smaller than this will be poorly represented and result in underestimation of slope. A key question here is the scale at which slope instability operates and the scale at which it is represented in the model. Observations in my study area suggest that instability can operate at a sub-grid scale for resolutions >5 m. Resolutions of 1, 5 and 10 m have corresponding areas of 1, 25 and 100 m^2 respectively while scars in the study area cover 6-1400 m^2 (Section 2.4.3). At 1 m resolution all recorded landslides cover an area greater than one cell; however, 6% of the landslides have scars smaller than 25 m^2 and 43% have scars smaller than 100 m^2. However, the mechanism of failure at these sites ought to be compatible with that assumed by an infinite slope stability treatment (i.e. translational failures with depth / length ratios <10%), these assumptions are satisfied for the Lake District inventory data in almost every case.

Figure 3-36: Slope prediction from a DEM interpolated at 1 m resolution from raw data points (blue) generated by photogrammetry. Note the disparity between pixel resolution (1 m) and the point spacing (>30 m in some cases).

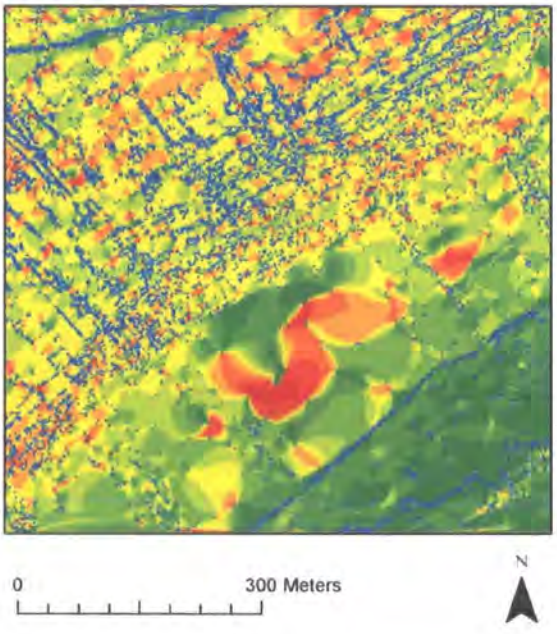

Finally the resolution of the interpolated grid and that of the data are not always the same. Fine resolution DEMs interpolated from sparse data give a misleading indication of the model's topographic representation (Figure 3-36). Gridded data that have been smoothed by convolution maintain an apparent cell size which differs from the true resolution of the information in each cell (Figure 3-37); this will be considered in more detail below.

Figure 3-37: Slope predictions from two DEMs interpolated at 1 m resolution from the same raw data. A is the raw data whereas B has been smoothed with a convolution filter

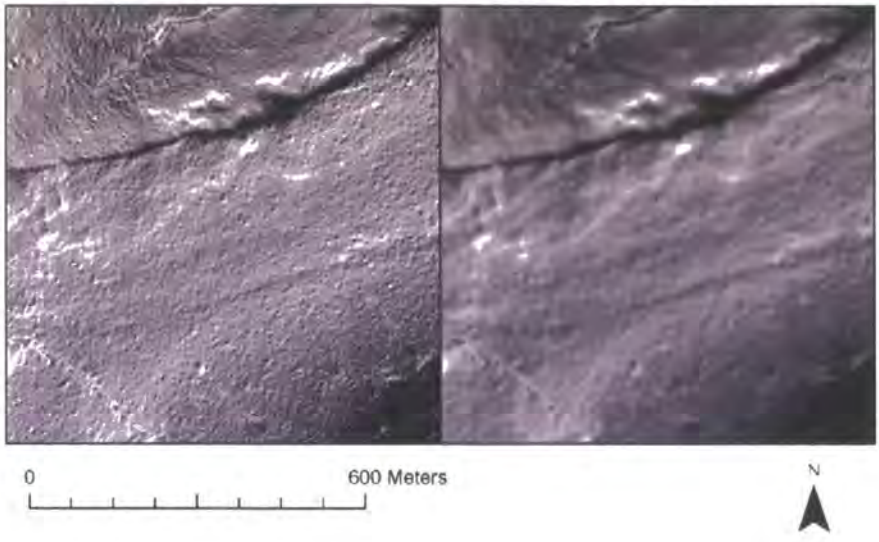

Summary

DEM resolution influences the properties of important input parameters for slope stability models (slope, upslope contributing area and topographic index). These effects have been widely studied but there is no accepted universal optimum resolution. This reflects the fact that the optimum DEM resolution is context dependent and will vary in both time and space. For slope stability finer DEMs are generally preferred; however, there are limitations to the improvement which can be achieved by using very fine resolution topographic data due to: 1) error in the elevation model; or 2) the assumptions or scale of representation of the modelled processes. Finally, DEM (grid) resolution and the resolution of the original topographic data can become disconnected, processing steps need to be carefully chosen and documented to minimise such problems.

3.6.4. Filtering

Independent of their source, remotely sensed topographic data contain erroneous points either as a result of error in the data collection or because they represent the 'first surface' (e.g. vegetation tops, buildings). Filters are required to remove or replace these erroneous points by: identifying erroneous points; then correcting or replacing them. The simplest filters (e.g. Gaussian filters) combine these two steps into one simultaneous action. However, smoothing does not always preserve correct elevation values (Lane *et al.*, 2004) and error

in one pixel may be transferred into adjacent pixels. More intelligent filtering approaches separate the identification and correction processes. Filters based on local variance (e.g. Chauvenet's criterion; Taylor, 1997) identify errors that are statistically different from the surrounding surface (Felicisimo, 1994; Lopez, 1997). However, errors rarely take the form of clearly identifiable spikes that are easily detected by these filters. Instead they cluster and, particularly when local topographic variance is high, identifying erroneous points is difficult. In photogrammetric DEMs, gross errors can be identified and minimised during stereo-matching using methods such as the Failure Warning Model (Gooch and Chandler, 2001) or Extant Optimisation (Milledge *et al.*, 2008a). However such methods are only effective for gross errors and rarely remove all of these.

Finally, error can be identified by evaluating the data with respect to *a priori* expectations. This approach is widely applied in laser altimetry, to produce bare earth models from datasets containing a combination of ground and non-ground points. Such filters can be grouped into four main types (Sithole and Vosselman, 2005): (1) slope based filters (Vosselman, 2000) work on the assumption that terrain slopes do not exceed a certain threshold; therefore, data that create slopes above this threshold do not belong to the natural terrain surface (Sithole, 2001); (2) block minimum approaches define a horizontal plane and accept all points within a buffer zone above it, with points outside the buffer rejected as non-ground points; (3) surface-based algorithms (Kraus and Pfeifer, 1998; Tóvári and Pfeifer, 2005), also work with a buffer zone but where its lower limit is defined by a parametric surface; and (4) segmentation-based filters (Sithole and Vosselman, 2005; Tóvári and Pfeifer, 2005) use the properties of each point to cluster them into similar groups. The degree to which the elevations of these clusters differ from their neighbours is then assessed as an indicator of whether they represent non-ground points.

3.6.5. Evaluating the Effect of Data Source and Filter Method on Topographic Data Quality

The quality of topographic data is important for stability modelling. In this and the following section I assess the quality of topographic data derived from two different sources (IfSAR and photogrammetry) and the performance of a range of filters, applied individually and in combination, to improve this quality (Figure

3-38). This study draws on research published in Milledge *et al.* (2008a), in which the issues discussed here are treated in more detail. The assessment was carried out over 1 km^2 of complex upland topography in Coledale (Grid Reference: 320,522, 200–700 MASL, Section 6.4). The area includes a range of topographic features including: valley side slopes, gullys, scree slopes, broad and tight topographic hollows, and two streams of different orders (1^{st} and 3^{rd}). Slopes range from 0° to 55° and an average slope of 30°. The area has a covering of: Bracken (*Pteridium Aquilinum*), Heather (*Calluna Vulgaris*) and Cotton Grass (*Eriophorum Vaginatum*) with patches of rushes (*Juncus Effusus*) and Sphagnum mosses in wetter areas and isolated small native deciduous trees.

I compare two **data sources**: IfSAR and photogrammetry (Figure 3-38) with and without filters. The IfSAR Digital Surface Models (DSMs) have a horizontal sampling interval of 5 m, they were collected during Intermap's NEXTmap Britain campaign and filtered to Digital Terrain Models (DTMs) using the TerrainFit algorithm (Intermap, 2004). These data were supplied with permission from the Natural and Environmental Research Council (NERC) Earth Observation Data Centre. The photogrammetry used true vertical colour images from a metric camera mounted on a light aircraft; photo-control points were collected using a differential global positioning system (DGPS, accurate to ±0.05 m); and the images were scanned from diapositives using photogrammetric scanners before being processed in Leica Photogrammetry Suite. Image interior orientations of the images were established with an error close to ±7 μm and exterior orientations calculated using a standard least squares block bundle adjustment with a standard deviation of unit weight of ±1 pixels. Extant optimisation was used to identify optimum matching parameter-sets (Milledge *et al.*, 2008b) and the elevation data generated as a point cloud (point density: ~0.6 points per m^2) to minimise the propagation of error across the surface before filtering. DEMs were generated with a horizontal sampling interval of 1 m.

Figure 3-38: Flowchart of the research design for assessing elevation data quality.

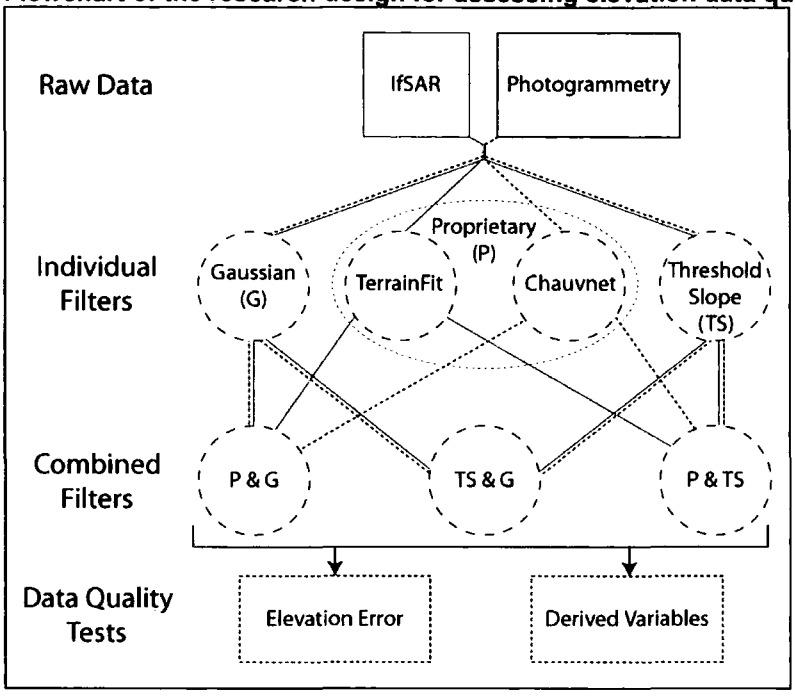

The **filters** represent three common situations in data acquisition (Figure 3-38). First, a Gaussian filter, which is a standard noise reduction technique for smoothing noisy elevation data (Walker and Willgoose, 1999, 2006). Second, the proprietary filter supplied with the data: a geostatistical filter, based on the Chauvenet criterion, for the photogrammetric data (e.g. Felicísimo, 1994); and TerrainFit, a hierarchical surface fitting technique for the IfSAR data (e.g. Wang *et al.*, 2001). Finally, a threshold slope based filter, similar to those that perform well for LiDAR data (Vosselman, 2000, Sithole, 2001). This filter recognizes the importance of *a priori* geomorphological knowledge for DEM analysis. It applies a maximum slope rule to a Triangular Irregular Network (TIN) generated from the elevation data. These filters are not mutually exclusive; they may treat different errors within the surface, so that best results are achieved by applying a suite of filters. To test this hypothesis, I assess the filters' impacts on surface quality, both individually and in combination (Figure 3-38).

I applied **data quality tests** based on: (1) Elevation error identified from independently-acquired DGPS check data (accurate to ±0.05 m); and (2) the impact of filtering upon derived geomorphological variables (Figure 3-38). The check data (n = 1000) were used to determine precision from the standard deviation of error (SDE) and bias from mean error (ME). To assess the effect of

the filters on slope stability predictions and to identify how those effects propagate through the models I calculated: slope; upslope contributing area; topographic index; and slope failure probability from each surface. Slope was calculated using the Zevenbergen and Thorne (1987) algorithm. Upslope contributing area was calculated using the deterministic infinity ($D\infty$) algorithm (Tarboton, 1997) after sinks had been filled using the Planchon and Darboux (2002) algorithm. The topographic index (I; Kirkby, 1975) is:

Equation 29

$$I = \ln\left(\frac{a}{\tan\beta}\right)$$

where: a is the upslope contributing area per unit contour length and β is the local slope. Slope failure probability was calculated using SHALSTAB (Montgomery and Dietrich, 1994; discussed and derived in Section 2.7).

3.6.6. Evaluation and Discussion

The elevation error results from independent check data show that certain datasets may benefit significantly from digital filtering. The standard deviation of error in unfiltered photogrammetric DEMs is very large but can be reduced by >50% by filtering (Table 3-23). Before filtering the IfSAR SDE is less than half that for photogrammetric DEMs; however, after filtering the photogrammetric DEMs achieve a smaller SDE than those from IfSAR (i.e. they are more precise).

Table 3-23: The mean and standard deviation of errors for the two elevation datasets, filtered using the Gaussian, proprietary and threshold slope filters individually and in combination.

	Mean Error (m)		Standard Deviation of Error (m)	
	Photogrammetric	IfSAR	Photogrammetric	IfSAR
Unfiltered Raw Data	1.71	-0.22	1.15	0.53
Gaussian (*G*)	1.17	-0.21	0.52	0.51
Proprietary (*P*)	1.55	-0.22	0.72	0.78
Threshold Slope (*TS*)	1.71	-0.22	0.51	0.52
P & *TS*	1.55	-0.22	0.61	0.78
P & *G*	1.53	-0.22	0.51	0.82
TS & *G*	1.71	-0.21	0.39	0.51

The integration of elevation values over each pixel (inherent in IfSAR data collection) meant that the surface was not noisy (Table 3-23) and contained few high magnitude errors (Figure 3-40). Gaussian and proprietary filters over-smoothed the surface and very few points had slopes steeper than the predefined threshold for the terrain sensitive filter. Digital photogrammetric DEMs contain random errors and gross errors even after matching parameter optimisation (Figure 3-39). As a result, filtering is essential to reduce the noise in the photogrammetric DEMs before meaningful variables can be derived from them. Gaussian filters, successfully smooth random errors but propagate remaining gross error (spikes) through the DEM. The terrain sensitive filter effectively removes many of these gross errors without such propagation (Figure 3-39).

Figure 3-39: A matrix of derived variables: slope (tan β), upslope contributing area (a), topographic index (ln(a/tan β)) and landslide probability (Q/T ratio) for the study area. These are derived from the photogrammetric DEM with each filter applied individually across the columns.

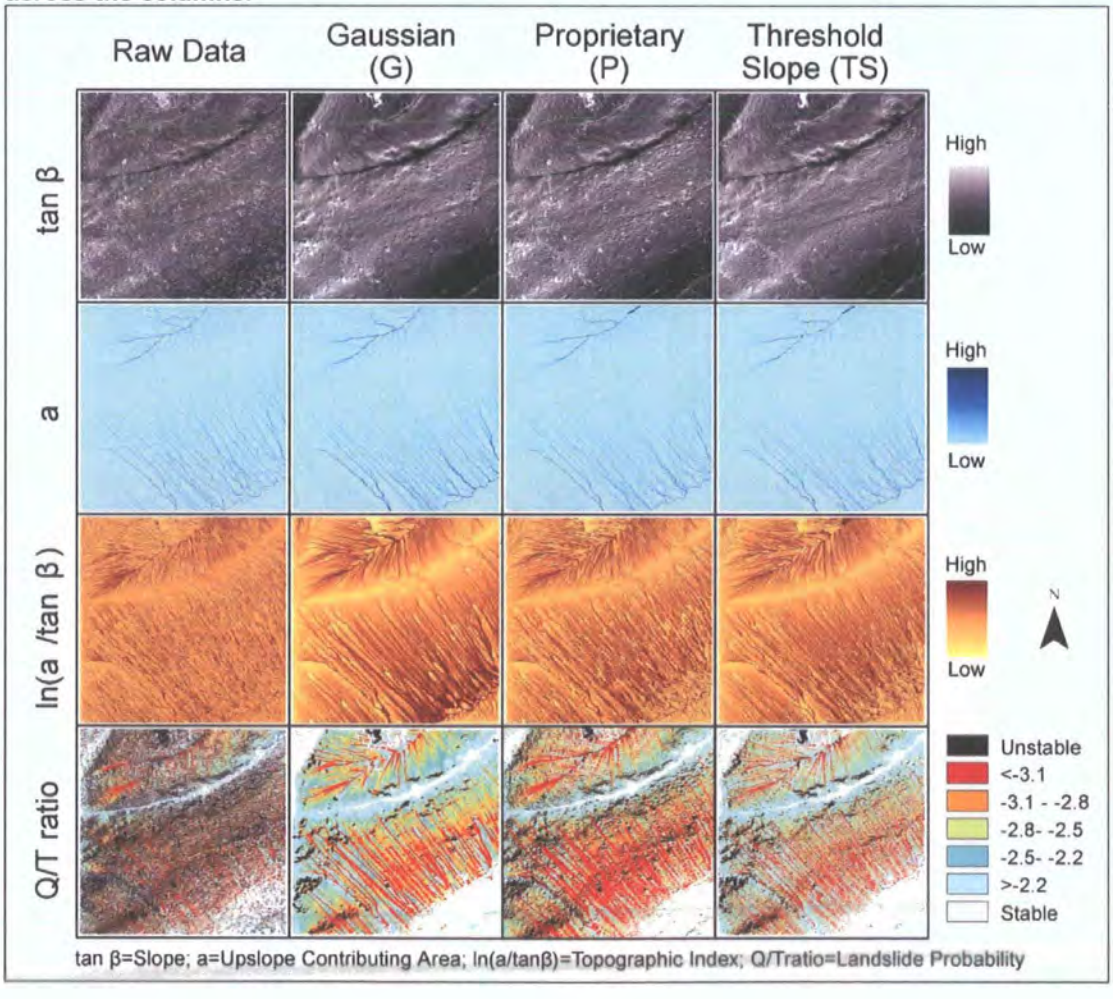

Improvements in elevation quality were accompanied by improvements in derived variables (Table 3-23 and Figure 3-39). This relationship was not linear, since derived variables were sensitive to low magnitude high frequency noise, particularly when assessed non-spatially (using cumulative frequencies), especially in relation to variables that cumulate across space. Here, localized error, even if small, can have major downstream impacts.

Figure 3-40: A matrix of derived variables: slope (tan β), upslope contributing area (a), topographic index (ln(a/tan β)) and landslide probability (Q/T ratio) for the study area. These are derived from the IfSAR DEM with each filter applied individually across the columns.

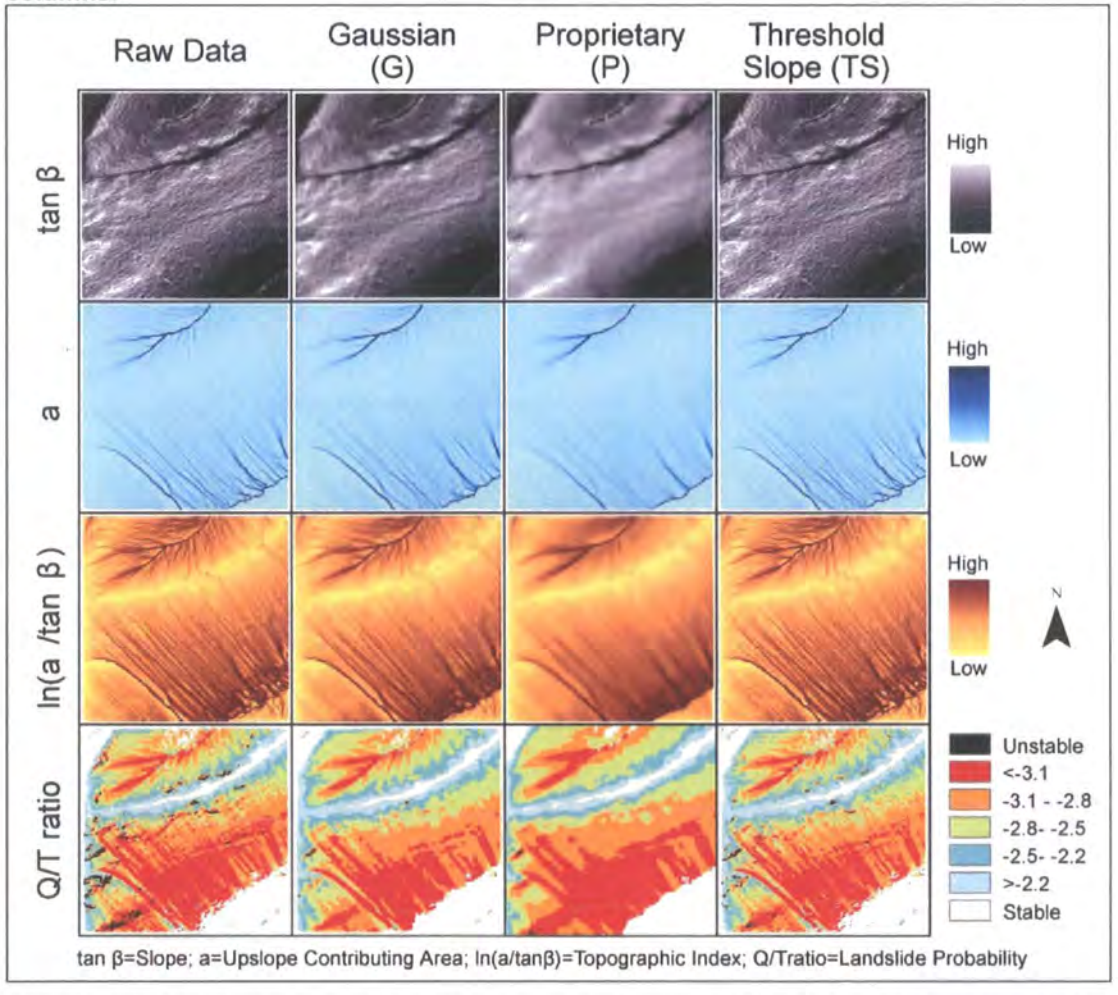

Proprietary filters performed poorly in every case (Table 3-23 and Figure 3-39). While the precision of the IfSAR DTM (±0.78 m) still exceeds its stated value (~±1 m), it is degraded relative to the unfiltered IfSAR DSM and the surface derivatives indicate over-smoothing (Figure 3-40). This study area represents a particularly strict test for the IfSAR's proprietary filter, since it has a complex topography and contains very few of the features that the filter was designed to remove. Its poor performance is surprising since it was reported to successfully

retain detail in steep complex topography in the USA (Wang *et al.*, 2001). These results suggest that the DSM rather than the DTM should be used for many geomorphological applications. The geostatistical filter within the photogrammetric software failed to remove clusters of high magnitude error, which originate from failure of the image-matching algorithms (Figure 3-39). In such a situation, surrounding error points are used to judge the reliability of a point and local variance based filters may fail to identify it as error.

Figure 3-41: A matrix of derived variables: slope (tan β), upslope contributing area (a), topographic index (ln(a/tan β)) and landslide probability (Q/T ratio) for the study area. These are derived from the photogrammetric DEM with filters applied in combination across the columns. The TS and G filter generates parameters with minimal noise and the smallest gross errors. Combination filters that include P do not improve on their individual components (Figure 3-39).

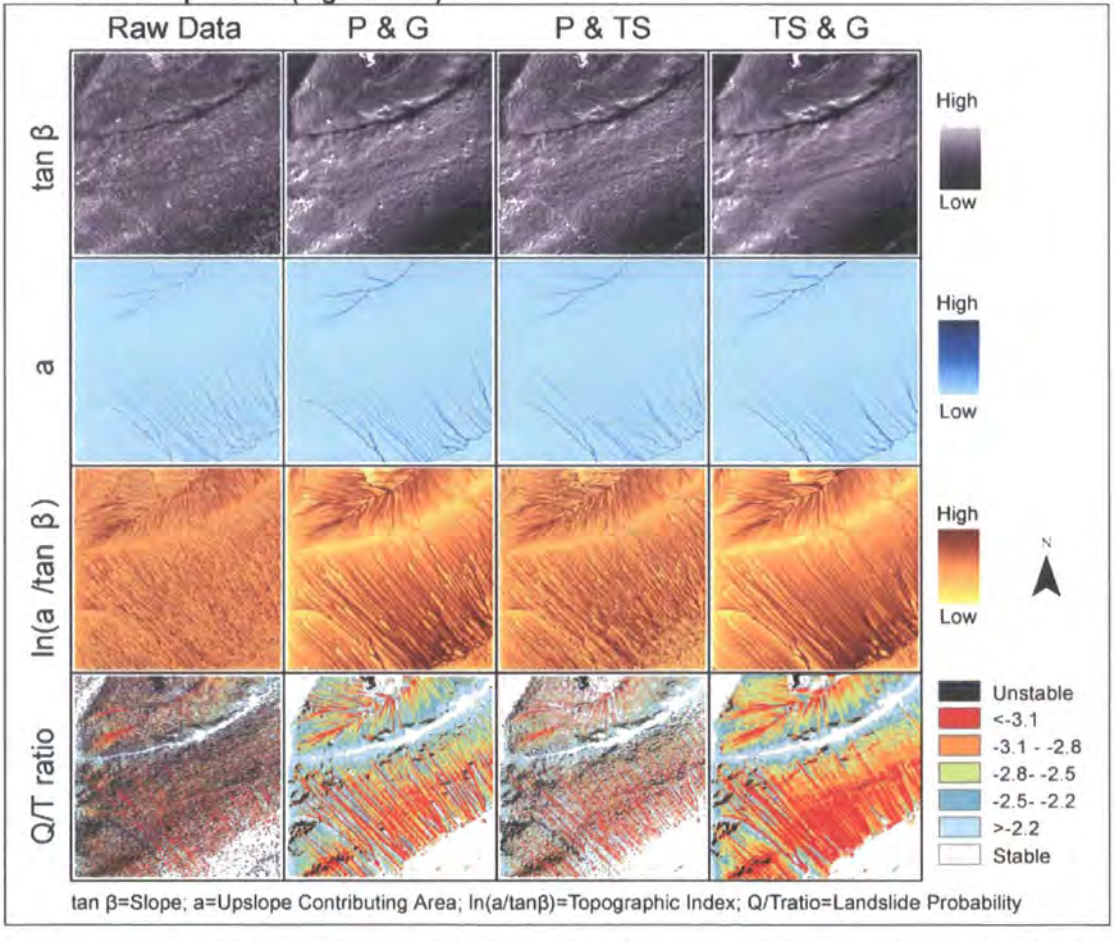

Comparing the best available surface from each dataset, the photogrammetric data provide the best elevation predictions, with standard deviations of error ±0.14 m more precise than the IfSAR DSM (Table 3-23). The raw IfSAR was surprisingly high quality (SDE: ±0.53 m; ME: –0.22 m; RMSE: ±0.58 m) in a study area with slopes from 0-55°, whilst the stated RMSE of the data is ~±1 m for flat surfaces, increasing by a factor of two or more on surfaces steeper than

20° (Intermap, 2004). The spatial pattern of variables calculated from the photogrammetric DEM (with Threshold Slope and Gaussian filters applied; Figure 3-41) and IfSAR DSM (Figure 3-40) display striking similarities, particularly in terms of the outputs from SHALSTAB. The IfSAR DTM data, filtered with the proprietary filter, were lower quality with an SDE of ±0.78 m suggesting that, in these environments, the IfSAR DSM should be used in preference to the DTM. The error in the IfSAR DTM is the result of over-smoothing; clearly illustrated by the blurred appearance of its derived variables (Figure 3-40). This highlights a difficult question for filtering: how much smoothing is too much? Clearly the raw photogrammetric data contains significant noise and benefits from some degree of smoothing. Equally, the IfSAR filtered with the proprietary filter (which includes a moving average filter) and a Gaussian filter is over-smoothed, the effects of fine scale topography are lost. What level of topographic representation or smoothing is acceptable must be defined by: (1) the scale at which the processes of interest operate or are represented and (2) the resolution and precision of the data.

Comparing data from these two sources is important in the context of their relative acquisition costs and their spatial coverage. The commissioned aerial photographs provide coverage for ~100 km^2 at a cost of £35 per km^2. The IfSAR data, which is part of a complete national dataset, was obtained free through academic license, but could be acquired commercially at a similar cost (£36 per km^2). However, this does not take into account the cost of processing, which is low for IfSAR data but considerably higher for photogrammetry. Given the surprising quality of IfSAR DEMs in this study, photogrammetrically derived elevation data only represent value for money where: 1) "off the shelf" IfSAR data is unavailable for the area or time period of interest; 2) the increased cost is warranted by a requirement for improved resolution and precision; or 3) the photographs represent an additional useful source of information to tackle the problem under consideration. In particular, for academic applications in the UK, the freely available national IfSAR dataset represents a valuable resource of comparable quality to photogrammetric data from high resolution aerial imagery.

3.6.7. Section Summary - Topographic Data

Elevation data define the energy gradients for the geotechnical and hydrological aspects of slope stability models. Remote sensing technology is rapidly advancing providing new elevation datasets with broader coverage, increased precision and resolution. DEM resolution (which is distinct from the resolution of the raw data) can strongly influence the outputs from slope stability models through its control on key parameters. No accepted optimum DEM resolution exists, instead it is context dependent. For slope stability finer DEMs are generally preferred; however, there are limitations to the improvement which can be achieved by using very fine resolution topographic data.

Digital photogrammetry data contain both random and gross errors, these can be effectively treated using a combination of threshold slope and Gaussian filters, improving precision by over 50%. These errors are less of a problem for IfSAR DEMs. Elevation error propagates through derived surface variables in a manner that is highly dependent on the magnitude, frequency and spatial pattern of elevation error. High frequency noise disrupts all geomorphological variables while high magnitude errors strongly influence their spatial patterns.

In this study digital photogrammetry offers the potential for improved precision (0.39 m) and resolution (1 m) relative to airborne IfSAR (0.51 m and 5 m respectively). However improvements in precision are small and the finer resolution is nominal to some extent since the surface has been smoothed with a Gaussian filter. In my case the incomplete coverage of the study area and the processing cost (time and computing resources) required to generate a photogrammetric DEM was prohibitive relative to the free full coverage available from IfSAR. Further topographic analysis in this thesis, particularly in Chapter 6 is performed using the IfSAR DSM. The DSM is chosen in preference to the DTM since the results in Section 3.6.6 indicate that the filtering algorithm used to convert IfSAR DSMs to DTMs degraded the quality of the elevation data for this area.

3.7. Chapter Summary

In an analysis of any model's over-prediction or under-performance, characterising the quality of / uncertainty in input parameters is an essential step. Chapter 2 gave a detailed review of the current state of science regarding distributed slope stability models. Five key input parameters were identified, which are common across almost all slope stability models: 1) soil strength; 2) root reinforcement; 3) soil density; 4) effective soil depth; 5) topography (both for local slope and as a wetness indicator). For each parameter I have reviewed the background to these parameters: the properties that they represent and how they can be measured. I have presented the methods that I have used to estimate them and the results from these studies, which in each case include both estimated values and the variability or uncertainty associated with them.

Results from *in situ* direct shear tests suggest that Lake District soils have friction angles in the range of 27–43° but that there is considerable variability both within and between sites. Full sample peak (37.5° ±11.1°) and critical friction angles (37.3° ±5.2°) are very similar; although the range of critical friction angles is considerably lower. For peak strength effective soil cohesions are small, between -1 and 4 kPa, for critical strength they are even lower, and in many cases are not significantly different from 0. These results are compatible with available data from similar soil types and with soil mechanics theory. They suggest that Lake District soils may be considered cohesionless, that the failure envelope over the range of normal stresses under consideration is linear and that peak and critical strengths can be used as upper and lower bounds to a material strength estimate for the soil. The similarity in peak and critical soil strength when compared with the within and between site variability suggests that an integrated soil strength measure can be attained by applying the estimated friction angle from either peak or critical conditions in combination with their SE estimates. Variability between peak and critical conditions will fall within this envelope.

A modified application of the same shear tests on samples with and without intact sides provides the first data on root cohesions for three of the UK's most common upland vegetation types: *Pteridium*, *Eriophorum* and *Juncus*. These cohesion estimates fit within the expected range from the published literature;

they suggest that *Eriophorum* provides the most root cohesion (~6.2 kPa); *Pteridium* provides less cohesion (~5.7 kPa); and *Juncus* provides the least (~3.4 kPa). These results support the observation of others in suggesting that grasses and shrubs have important strong reinforcing effects on soils. However, these effects are limited to the upper part of the soil profile. Representing their effect on slope stability requires a move away from one-dimensional and infinite slope analyses towards three-dimensional analyses that represent edge effects. I pursue these ideas in the following Chapters 4 and 5 where I derive a set of governing equations for three-dimensional stability; test these equations and apply them to establish the importance of a block's margins in determining its stability. Careful treatment of the behaviour of root cohesion with depth is required when characterising lateral root cohesion. I have characterised this using three distinct scenarios which will be applied in Section 5.6 to assess their effect on slope stability.

Soil bulk density varies across the full reasonable range in my Lake District study area, reflecting the variability in soil type. Much of this variability can be explained by the type of horizon that the sample represents (organic or mineral) and very little by variation in sample depth. Mineral horizon densities fall within the range of measurements of similar soil types from other studies. The variability in soil density resulting from variation in soil moisture content is small relative to the variability in density between sites. Given slope stability models' insensitivity to density and the additional complexity associated with spatially and temporally explicit predictions of unsaturated soil moisture field bulk density represents a reasonable alternative. The proportion of a profile occupied by each horizon can be characterised by normalising horizon depth by total profile depth. This allows the density of the column to be represented as a composite using relative depth of the organic horizon as a weighting factor in a weighted average of mineral and organic densities. This approach can be applied within slope stability models to better represent the depth integrated density of the soil column. It can be applied as either: a single spatially invariant mean value for the entire study area; or a probabilistic parameter representation using the distributions of relative horizon depth, mineral and organic soil density.

Spatial soil depth patterns could not be modelled in my study area because: 1) techniques for rapidly acquiring soil depth data over large areas were not effective in this environment; 2) the magnitude and variability in soil depth to bedrock contained a strong glacial fingerprint; and 3) the property of interest, effective depth (to the failure plane), differed in many cases from depth to bedrock so that this type of modelling would not be profitable for this application. Instead I calculated a spatially-lumped average soil depth for the study area, and characterised the variability about this average. Failure plane depths were obtained from topographic surveys of extant landslide scars. Different methods of analysing DGPS survey data can lead to different depth estimates at a site. However, when considering spatially-lumped depth distributions this variability is absorbed by the data. The effective soil depth is most reliably estimated by planform mean depth. From 65 landslides from the January 2005 inventory the mean depth was 0.7 m and the standard deviation 0.3 m in a range from 0.3–2.3 m. This data provides a useful indication of the variability in effective soil depth and could, in future, be applied in stochastic or probabilistic frameworks for slope stability modelling.

Elevation data for the study area are most effectively provided by IfSAR data at 5 m resolution. This is probably a representative resolution for calculating upslope contributing areas since subsurface flow is likely to be guided more by trends at this resolution than finer topographic detail. However, finer resolution data would be preferred for the slope calculations. Several observed failures are smaller than a single grid cell and there are examples of observed failures in locations that are predicted to be stable by SHALSTAB due to poor topographic representation. LiDAR is prohibitively expensive for catchment scale stability modelling and was unavailable for the study area. Digital photogrammetry offers improved precision and resolution relative to airborne IfSAR but the true improvements in resolution and precision are small. The increased cost of generating and processing photogrammetric DEMs relative to IfSAR data prevent them from being cost effective.

This chapter has detailed the provenance of the key parameters required within slope stability models. The parameter values that have been defined here, with their associated uncertainties are used in the chapters that follow, either directly

as inputs into stability models or as guides for reasonable values or ranges of values within sensitivity analysis. One of the most important findings from this chapter is that even grass and shrubs can provide considerable lateral root cohesion. This has important implications for slope stability modelling since it suggests that the geometry of an unstable area (its length width and depth) will play a role in defining its stability. These factors are presently unaccounted for in most catchment scale stability models. In Chapter 4 I will take the first step in addressing this lack by deriving a set of analytical governing equations for three-dimensional slope stability. In Chapter 5 I will benchmark this model against standard geotechnical methods for scenarios and parameter sets defined by the results from this chapter and use it to explore the geometric controls on stability. In Chapter 6 I will close the loop between elevation data, discussed here as a parameter for slope stability models, and the pore water pressure parameter required by the geotechnical component of stability models.

4. Re-formulating the Factor of Safety: Model Development

4.1. Scope of the Chapter

The size of the unstable area of a slope is important in defining both its stability and its impact in the event of failure. Traditionally catchment scale stability analyses have applied the one-dimensional infinite slope model which is simple to calculate but takes no account of the forces acting on the sides of the block (assuming instead that it is infinitely long and wide). Researchers from different disciplines (e.g. engineering, forest science and geomorphology) have recognised the importance of representing slope stability in three dimensions for three different reasons: geometry; friction; and root reinforcement (Figure 4-1). Of these, the engineering approaches are the most complete but are difficult to apply at a catchment scale and ignore important friction and root reinforcement effects. Geomorphologists rarely consider geometry or friction effects in their multi-dimensional stability analyses, concentrating instead on root reinforcement.

Figure 4-1: The different foci of 3D slope stability studies, the researchers that study them and settings in which they are applied.

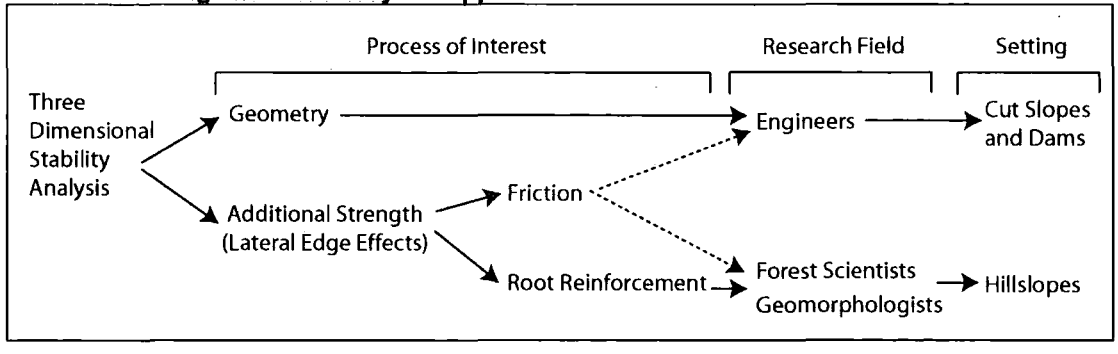

In this chapter I aim to merge the apparently disparate approaches outlined above. In Section 4.2 I identify the importance of landslide size and the need for a new three-dimensional stability method that can be applied at the catchment scale. In Section 4.3 I review the existing methods available for multidimensional slope stability analysis, assessing their applicability in a catchment scale modelling context. In Section 4.4 I derive a new set of analytical governing equations for the three-dimensional stability of a single

block using earth pressure theory and lateral root cohesion to calculate the driving and resisting forces on each plane of the block. The effectiveness of these governing equations is then tested in the following chapter and their implications for geometric controls on stability considered through sensitivity analysis.

4.2. The Importance of Three-dimensional Stability Analysis

A landslide's size and location defines its impact on: landscape evolution (Tucker and Bras, 1998); sediment discharge (Bathurst *et al.,* 2005); and downstream hazard (Lan *et al.*, 2004; Benda and Cundy, 1990; Fannin and Wise, 2001). Landslide size is important because it defines the volume of material transferred and therefore the amount of geomorphic work performed; the magnitude of the sediment flux; and the power of the destructive force. It also defines the potential and subsequent kinetic energy of the event. As a result, it is a key factor in deciding the mobility of a failed mass. This, in turn, is important for its mitigating effect on the control that landslide location exerts over a landslide's connectivity with infrastructure or other geomorphic transport agents.

Observations of landslide scars suggest that their dimensions tend to have characteristic values in a particular area (Lehre, 1982; Tochiki, 1985). These may reflect prevailing conditions of root strength, soil texture, hydrology and slope gradient (Casadei and Dietrich, 2003). Reneau and Dietrich (1987) suggested that: root strength along the margins of a potential landslide constrains its size and that typical scar size reflects the critical size required for instability. For a given set of marginally stable soil parameters there will be a critical area over which these conditions must exist for instability to occur. Stability is not solely dependant on the magnitude of parameter values at a point, but also on those of its neighbours. The size of the neighbourhood over which this is important is non-linear. Patch size should be smaller for high pore pressures, steeper slopes and lower root strengths (Casadei and Dietrich, 2003).

A considerable body of research based on landslide inventories for a range of spatial scales suggests that they follow a power law magnitude frequency relation (Harp and Jibson, 1995; Guzzetti *et al.*, 2000; Bucknam *et al.*, 2001; Stark and Hovius, 2001; Brardinoni and Church, 2004; Malamud *et al.*, 2004; Section 2.4.3). Many of these studies also report a 'rollover': a departure from the power law relationship at low magnitudes. This apparent lower limit on landslide size has been attributed to: the resolution of survey methods (Hovius *et al.*, 1997; 2000; Stark and Hovius, 2001; Brardinoni and Church, 2004); the method of aggregating and displaying the data (Brardinoni and Church, 2004); or real effects due to: material strength (Pelletier *et al.*, 1997; Guzzetti *et al.*, 2002) substrate properties or rootmass effects (Hovius *et al.*, 1997; 2000). Reneau and Dietrich (1987) found that, for a given parameter set, non-zero minimum lengths and widths of equal magnitude were imposed on potential landslides, although no maximum values were imposed. A more complete treatment using Burrough's (1985) method suggests that landslide size should be a function of failure depth: a thicker root zone forces failure planes to be deeper and should result in longer and wider landslides.

A conceptual explanation for a lower limit to landslide size can be derived from considerations of root reinforcement and failure geometry. To satisfy landslide geometry and equilibrium mechanics the depth of the failure must tend to zero as the length tends to zero. Even for a rotational failure, the depth of the failure cannot far exceed its length. For landslide size to tend to zero, depth must also be able to reach zero without requiring a change in the properties of failure. For vegetated slopes this is unlikely. For example, landslides with very shallow failure planes, exclusively within the root zone, will experience a significant increase in their shear strength independent of normal force as a result of root reinforcement. Since the weight force will also tend to zero with depth, the shear force will reduce accordingly but shear strength will remain high independent of weight.

Landslides have a three-dimensional geometry, so it is rational to consider the slope as three-dimensional when calculating its stability (Xie *et al.*, 2004). However, such calculations create considerable computational complexity and catchment scale slope stability models tend to apply the one-dimensional

infinite slope procedure (Figure 4-2) (Okimura, 1983; Montgomery and Dietrich, 1994). This approach ignores landslide dimensions and calculates stability for each individual grid cell. While these models have been modified to include the influence of spatially variable soil depth and vegetation (Dietrich *et al.*, 1995; Ried *et al.*, 2007), and temporally variable vegetation and precipitation (Wu and Sidle, 1995; Dhakal and Sidle, 2004), they continue to treat each grid cell independently.

Figure 4-2: Stability model dimensions and assumptions, blue lines indicate phreatic surface, red lines indicate failure plane.

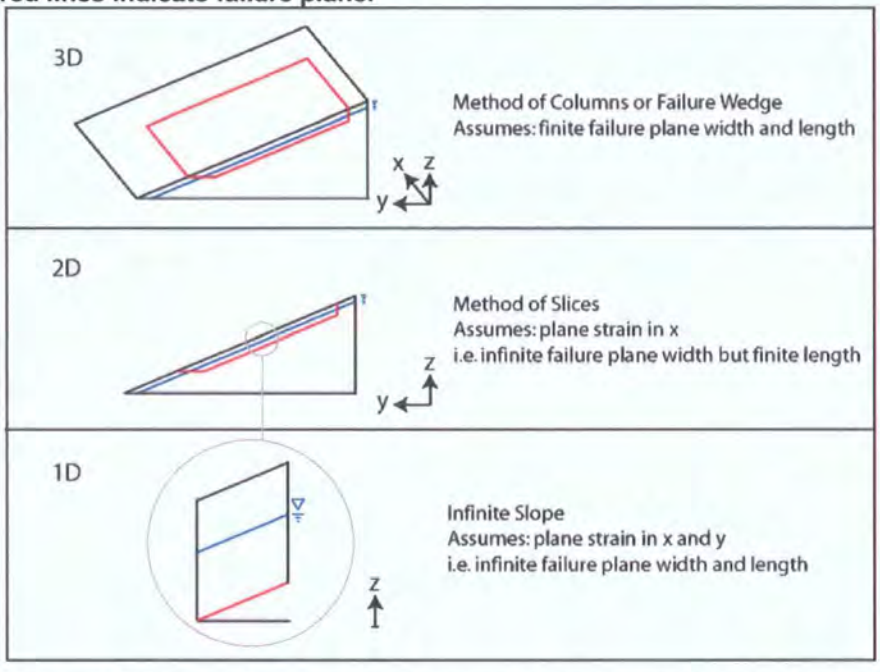

Infinite slope stability analysis can predict soil depths at failure (Dietrich *et al.*, 1995) but because it assumes that the failing mass is infinitely long and wide, it cannot be used to determine failure length and width. For the same reason, it only considers root cohesion in the vertical direction while in many environments roots do not extend below the critical failure plane and root reinforcement is dominantly in the lateral direction (Schmidt *et al.*, 2001). Accounting for the lateral reinforcement of roots in a stability analysis requires modification of the infinite slope model (Gabet and Dunne, 2002). A key improvement for catchment scale slope stability models would be to predict which cluster of cells might fail together, due to scale controls associated with strength effects on the boundaries and spatially-variable material and hydrologic properties.

4.3. Existing Multidimensional Slope Stability Analyses

Anagnosti (1969) developed the first three-dimensional stability analysis, extending the two-dimensional Morgenstern-Price method (1967) to determine the factor of safety for potential sliding masses. Comparison with two-dimensional analyses revealed factor of safety increases of over 50% in some cases. However, the method's assumptions limited it to surfaces of somewhat unusual shape (Hungr *et al.*, 1989). Baligh and Azzouz (1975) extended the two-dimensional circular arc method to evaluate the lateral edge effects of the three-dimensional slip surface. However, their analysis was limited to rotational failures and so is of limited application to shallow translational slides typical in my study area. Hovland's method (1977) is an extension of the assumptions associated with the two-dimensional ordinary method of slices for columns in three dimensions. In this method, all inter-column forces (ICFs) acting on the sides of the columns are ignored. The normal and shear forces acting on the base of each column are derived as components of the weight of the column. It is assumed that there is motion in only one direction and the equilibrium of the system is calculated in this direction. The factor of safety is defined as the ratio of total available resistance to the total mobilized stress along the failure surface (Hovland, 1977).

Figure 4-3: A schematic of the 3-D block type failure model designed by Chen (1981) (in Albatineh, 2006), note the classic engineered slope geometry with horizontal toe and crest.

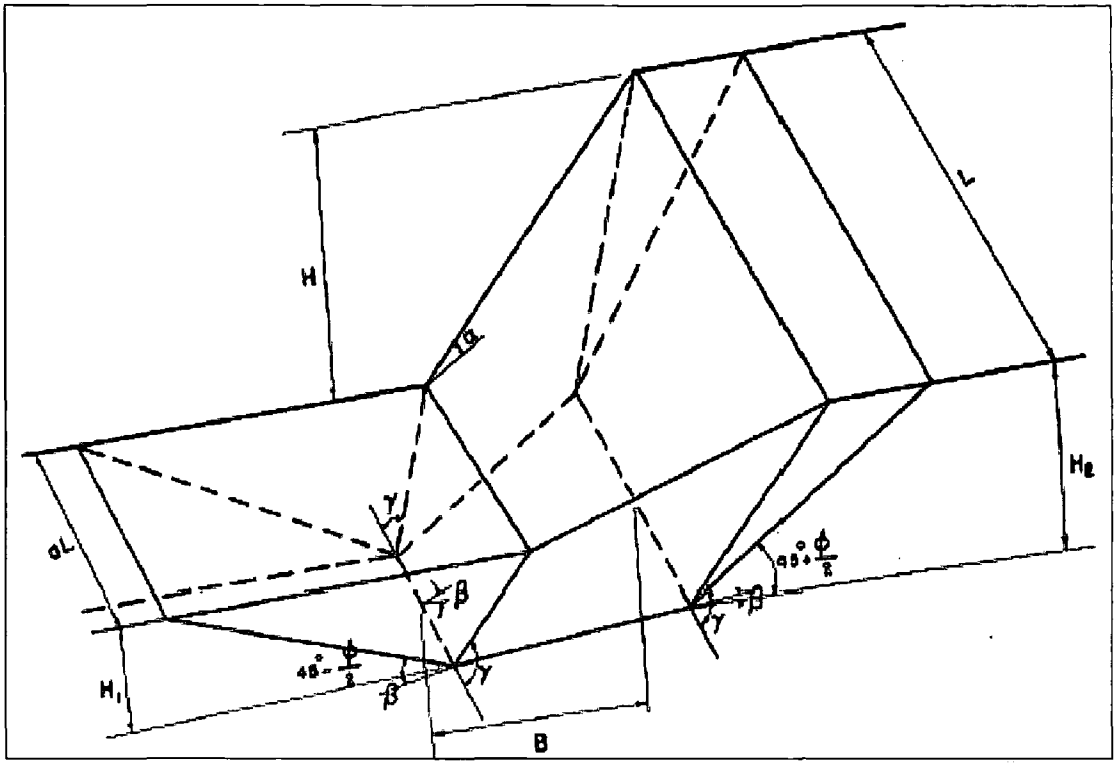

Chen, (1981) was the first to attempt three-dimensional slope stability for translational failures incorporating the effect of friction on the sides. He split the slope into 3 bodies (Figure 4-3) and quantified toe and head effects in terms of active and passive conditions. However, his model (in common with most engineering approaches) assumes classic cut slope morphology (Figure 4-4) enabling him to escape any complications in the calculation of active and passive pressures on sloping surfaces, but limiting the models applicability in other scenarios.

Figure 4-4: Schematic illustrating the differences in profile form between classic engineering cut slope scenario (modified from Chen, 1981) and that of a typical hillslope.

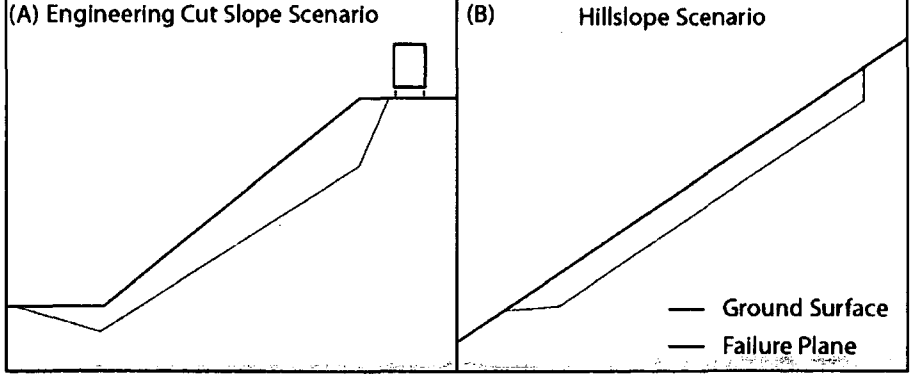

Chen and Chameau (1983) derived an extension to the two-dimensional Spencer Method (1967) and showed that Hovland's method was conservative (factor of safety predictions were low). However, Hutchinson and Sarma (1985), Cavounidius (1987) and Hungr (1987) have questioned some of the assumptions used by Chen and Chameau (1983); and Xing (1988) presented a simpler three-dimensional extension of Spencer's method. Leschinsky *et al.* (1985) proposed a three-dimensional mathematical approach to slope stability based on limit equilibrium and variational analysis introduced by Kopacsy (1957). This method and its subsequent developments are rigorous and can satisfy all global limiting equilibrium equations explicitly (Leshchinsky and Huang, 1992). However the complexity of the solution restricts its application to symmetrical slip surfaces where the complexity of the problem is significantly reduced. Hungr (1987) proposed a three-dimensional method that is a direct extension of the assumptions associated with Bishop's (1955) two-dimensional simplified method. Hungr *et al.* (1989) developed a three-dimensional extension of Janbu's (1956) simplified method, suitable for translational failure surfaces. It satisfies the horizontal and vertical force equilibrium but not moment equilibrium, deriving the factor of safety iteratively from horizontal force equilibrium. Janbu's method overestimates the factor of safety due to its assumption that resultant ISFs are horizontal. Empirical correction factors have been developed to account for the underestimation but these are unlikely to hold in three-dimensional and were not applied by Hungr *et al.* (1989).

Results from studies comparing two-dimensional and three-dimensional methods generally show higher factors of safety for two-dimensional than three-dimensional analyses (Baligh and Azzouz, 1975; Giger and Krizek, 1975; Leshchinsky *et al.*, 1985; Gens *et al.*, 1988; Leschinsky and Huang, 1992). Three-dimensional factor of safety exceeds that of the two-dimensional equivalent, provided that the two-dimensional factor of safety is calculated for the most critical two-dimensional section (Duncan, 1996).The ratio of the three-dimensional to two-dimensional factors of safety (F3 / F2) in a cohesionless soil is normally in the range of 1.00 to 1.08 but may rise to 1.30 as the cohesion increases (Azzoz *et al.*, 1981; Xie *et al.*, 2006). The F3 / F2 ratio is larger in cohesive than cohesionless soils and smaller in steep, weak soil layers than gently sloping layers.

These engineering methods were developed primarily to account for the effect of variable cross sectional geometry or parameter values on the stability of a block. Such methods do not generally account for friction on the vertical column boundaries, this extends to the slide margins where the end effects are rarely accounted for. Therefore, three-dimensional approaches account for the alterations in failure geometry and the effect that this has on the balance of forces for the slide mass. In some cases very similar factors of safety result from two-dimensional and three-dimensional methods. Because most three-dimensional methods are extensions from a particular two-dimensional method, the two-dimensional method is often a limiting case of the three-dimensional method under the assumption of plane strain (Hovland, 1977). This is supported by studies such as Stark and Eid (1998), which show very little difference between two-dimensional and three-dimensional stability of a slope that is uniform in the cross slope direction. Engineers limit the use of three-dimensional stability analysis to situations where: 1) the width to length ratio of the landslide is greater than two; 2) the depth of the failure plane changes significantly between the centre and sides of the slide; and 3) when there is significant variation in material properties or the groundwater conditions across the width of the slide (Cornforth, 2004). However, it is worth noting that all limit equilibrium approaches assume that failure occurs instantaneously throughout the entire unstable mass and that it fails as a single rigid body in a single direction. They do not account for progressive failure, spatially varying displacement vectors or the interaction between columns.

4.3.1. Applying Three-dimensional Slope Stability Analysis at the Catchment Scale

Engineering stability models, designed to deal with stability problems on man made slopes at small scales, are difficult to apply at the catchment scale. Limiting equilibrium approaches tend to be statically indeterminate (Section 2.6). Many of the two-dimensional and three-dimensional stability methods commonly applied by engineers employ computationally intensive iterative processing, to minimise the assumptions necessary to solve the equations. Hovland's (1977) method can be solved analytically by assuming

that there are no inter-column forces (ICFs), or that they cancel each other. The computational simplicity of this approach has made it attractive to researchers who aim to apply three-dimensional models at the catchment scale (Xie *et al.*, 2003; Qui *et al.*, 2007). However, its assumptions may render the method inaccurate (Duncan, 1996; Azzouz and Baligh, 1978).

An alternative approach was adopted by Okimura (1994) who developed a three-dimensional extension of an earlier two-dimensional multi-planar sliding surface method (Okimura, 1983). In this case, the multi-planar sliding surface method is applied to the cross section as well as to the longitudinal section. The model assumes a tension crack at one side and at the head of the potential slide mass then satisfies the equilibrium of forces in the cross sectional and longitudinal directions. The factor of safety is obtained iteratively from the equilibrium results in the X and Y directions. The model's stability predictions agree closely with those from the Hovland and simplified Janbu methods (Okimura, 1994). Like many three-dimensional stability models, the columns must be oriented parallel to the direction of downslope movement. For application at large spatial scales the model first identifies a least stable cell using an infinite slope stability model (Okimura and Ichikawa, 1985), then evaluates the critical slide mass for a rectangular failure oriented downslope. Applying the model to a small catchment, Okimura (1994) found good agreement between predicted location, size and shape of unstable sliding masses and those of observed failures. Okimura's model presents encouraging results using a novel three-dimensional slope stability approach, which is successfully applied at a spatial scale that is wider than that of other site specific engineering approaches. However, it was not pursued further after its first suggestion in 1994, where it was applied over a limited area and without any consideration of pore pressures or of friction or cohesion effects at the slide margins.

Qui *et al.* (2007) successfully apply a three-dimensional stability model at the catchment scale. This model uses a Monte Carlo based search algorithm to identify ellipsoidal potential slip surfaces then applies Hovland's method to solve their three-dimensional stability. The approach, first suggested by Xie *et al.* (2003), has been tested against other three-dimensional models and closed

form solutions for parametric test cases (Xie *et al.*, 2003; 2004; 2006). It has also been developed to incorporate a Green-Ampt based infiltration model (Qui *et al.*, 2007) and to apply other three-dimensional stability methods (modified Bishop's and Janbu's methods; Xie *et al.*, 2006). The authors have successfully solved two key problems for catchment scale slope stability modelling: 1) they have rearranged the three-dimensional methods to relax the restriction that the grid must be orientated parallel to the direction of sliding; and 2) they have developed an efficient method of searching the landscape for the least stable cells. However, their model, which is based on existing three-dimensional slope stability methods applied by engineers, does not account for edge effects on the sides of the potential failure mass. As a result the model tackles one aspect of the three-dimensional nature of landslides but is unable to handle the other.

4.3.2. Lateral edge effects in slope stability analysis

Lateral edge effects in two-dimensional limit equilibrium slope stability analyses are eliminated by assuming plane strain with an infinitely wide slip surface. In practice, two-dimensional analyses of slopes are considered reasonable because lower factors of safety result from ignoring the lateral edge effects (Stark and Eid, 1998). These lateral edge effects can be split into two types: friction strength related to the grain on grain interaction of the soil as the failing block moves past the static soil; and root reinforcement effects resulting from lateral roots that extend through the failing block. In practice these two effects have been dealt with individually, with those researchers who consider one important ignoring the other. I will deal first with friction strength effects at the lateral edges before considering lateral root reinforcement effects.

Friction Effects

Skempton (1985) developed a correction factor to relate back calculated shear strengths from two-dimensional and three-dimensional analysis methods:

Equation 4-1

$$S_u(3D) = S_u(2D)\frac{1}{1+\frac{KZ}{w}}$$

where: $S_u(3D)$ is back calculated shear strength using three-dimensional limit equilibrium analysis; $S_u(2D)$ is back calculated shear strength using two-

dimensional limit equilibrium analysis; K is earth pressure coefficient at failure; Z is the depth of the failure plane; and w is the width of the block. Skempton (1985) reported that this correction factor produced an average increase of 5% in the back calculated shear strength, but other studies have found considerably larger lateral edge effects. For width / height ratios less than five, a two-dimensional plane strain analysis is not considered appropriate due to the close proximity of the edges (Chugh, 2003). Lefebvre and Duncan (1973) showed that neglecting the edge effect can severely affect the factor of safety results especially for narrow slopes steeper than 20°. These lateral edge effects are most pronounced in translational failure modes (Stark and Eid, 1998). Baligh and Azzouz (1975) showed that ignoring the lateral edge effect can reduce the factor of safety by 40%. These studies emphasise the importance of lateral edge effects and demonstrate the need for powerful methods that can simulate such conditions accurately. However, almost all the three-dimensional limit equilibrium approaches ignore the shear resistance along the sides of the failing mass.

Stark and Eid (1998) identified the importance of shear resistance on the lateral edges for translational landslides and developed a method of parameterising this effect. They assumed that external horizontal and vertical forces act at the centre of the two parallel vertical sides of the sliding mass and that they are equivalent to the resultant of the 'at rest' earth pressures (for an introduction to earth pressure theory see Appendix 1). Given these assumptions, the shear resistance can be calculated using:

Equation 4-2

$$S'_y = \sigma'_x \tan\phi'$$

Stark and Eid (1998) tested this method on a translational slope using modified versions of both Bishop's (1955) and Janbu's (1956) simplified methods within the CLARA computer code (Hungr, 1989). They found that the factor of safety in three-dimensional limit equilibrium models is highly dependent on the analysis method but that side resistance had the same effect in both methods: increasing the factor of safety by 13%. Arellano and Stark (2000) conducted a parametric study to assess the effects of friction angle, slope length and angle on the F3 / F2 ratio when edge effects are included (Table 4-1). The results

suggested that slope configuration, geometry, boundary conditions and soil types all exert a strong influence on this ratio.

Table 4-1: Factor of safety results for Arellano and Stark's (2000) test slope illustrating: 1) the similarity in 2D and 3D results for a uniform slope when edge effects are ignored; and 2) the effect of adding a treatment for friction on the landslide sides (from a table in Chugh (2003) where FoS values are scaled from a graphical presentation in Arellano and Stark (2000)).

φ lower material	CLARA		Arellano and Stark (2000) modification of CLARA			
	2D	3D	3D			
			W/H = 1	W/H = 2	W/H = 5	W/H = 10
8°	0.90	0.90	2.85	1.45	1.05	1.00
10°	1.00	1.00	3.18	1.63	1.23	1.13
20°	1.70	1.70	4.80	2.58	2.00	1.82
30°	2.50	2.50	6.58	3.58	2.85	2.57

Chugh (2003) demonstrated the significance of boundary conditions using Stark and Eid's (1998) example slope and applying continuum mechanics based explicit finite difference computer programs FLAC and FLAC3D in two and three dimensions respectively. The results suggest that both real boundary conditions and the way that they are represented in limit equilibrium and continuum mechanics models have an important effect on stability predictions. FLAC3D results, with boundary conditions designed to represent true edge effects at the margins of a landslide (Table 4-1), are consistently more stable than those from the unmodified CLARA (Table 4-2) and less stable than those predicted by CLARA with Arellano and Stark's (2000) modification (compare Table 4-1 and Table 4-2).

Table 4-2: Factor of safety results for Arellano and Stark's (2000) test slope calculated using FLAC3D for a representative set of boundary conditions (from Chugh, 2003). When compared with Table 4-1 these factor of safety results always fall between those of CLARA3D with and without A & S's (2000) modification.

φ lower material	W/H = 1	W/H = 2	W/H = 5	W/H = 10
8	1.74	1.38	1.11	1.01
10	1.89	1.53	1.26	1.17
20	2.52	2.16	1.92	1.85
30	3.01	2.67	2.48	2.42

Albataineh (2006) also used a continuum mechanics based approach to calculate the factor of safety for the same scenario as Arellano and Stark

(2000). In this case, she used the strength reduction method in PLAXIS (Brinkgreve and Vermeer, 2001), a finite element model (FEM). The results suggest that accounting for edge effects increases the factor of safety by only 5%, a much smaller effect than that found by Stark and Eid (1998). This variation can be attributed to the assumption by Stark and Eid (1998) that normal stresses on the sides are equal to the soil 'at rest' stresses. Results from triaxial tests suggest that a horizontal strain of only 0.5% is required to develop active stresses and alter the conditions from 'at rest' to active (Lambe and Whitman, 1969). Albataineh (2006) suggests that vertical and horizontal movement of the soil mass along the sides of the sliding mass would generate active not 'at rest' stresses. Since 'at rest' stresses are always higher than active stresses, the confining force, soil strength and therefore factor of safety in these conditions is larger. Using the 'at rest' earth pressure coefficient as a way to account for three-dimensional slice forces (as recommended by Stark and Eid, 1998), can overestimate the factor of safety due to the state of the soil and the mobilisation of active stresses during the sliding of the soil mass. In reality, the slope will not fail instantaneously as one block but progressively; in these conditions there will be areas with active as well as those with 'at rest' stresses. These areas will result from the lateral edges of the sliding mass moving away from the surrounding soil. Over the entire mass of the slide, the stresses on the lateral edges of the slopes will be higher or equal to the active earth stresses but lower than the 'at rest' earth stresses. Therefore, the active earth pressure coefficient can be used to calculate the lower bound three-dimensional factor of safety and the 'at rest' earth pressure coefficient to calculate the upper bound.

Root Reinforcement Effects

Researchers in geomorphology and forestry have recognised for some time that a pure infinite slope model for failure is insufficient because the strength provided by roots along the margins of a soil block is ignored (Burroughs and Thomas, 1977; Wu, 1984). Recognition of the importance of lateral root cohesion has led to their inclusion in slope stability analyses by: Riestenberg and Sovonick-Dunford (1983), Burroughs (1985), Tsukamoto and Kusakabe (1984), Reneau and Dietrich, (1987), Gabet and Dunne (2002), Schmidt *et al.* (2001), Montgomery *et al.* (2000), and Casadei *et al.* (2003).

Riestenberg and Sovonick-Dunford (1983) modified the infinite slope stability equation to calculate the stability of individual blocks in a landslide complex. They calculated the volumes (V) lateral (A_s) and basal (A_b) areas of blocks and applied appropriate root reinforcement values to basal (S_b) and lateral (S_r) faces.

Equation 4-3

$$F = \frac{(cA + V(\rho_s - \rho_w)g\cos\beta + S_r A_s + S_b A_b)}{V\rho_s g \sin\beta}$$

where: c is soil strength, A is total block surface area, β is the inclination of the block, g is gravitational acceleration, and ρ_s and ρ_w are the densities of soil and water respectively. Their results suggest that 80-85% of the total force that resisted shear on the landslide could be attributed to root strength.

Reneau and Dietrich (1987) used an infinite slope analysis modified by adding root strength along the margins to solve for critical length and width. They made the following simplifying assumptions: 1) the colluvium is completely saturated, with hydrostatic pore pressures; 2) the basal shear surface is immediately below the rooting zone and strength here is entirely due to soil friction (no root strength or soil cohesion); and 3) roots along the entire perimeter of a deposit contribute strength equally. They ignore the effects of lateral pressure, passive pressure at the downslope end and buttressing (included by Burroughs, 1984) to allow a simple analytical solution suggesting that as long as failure depth is not significantly deeper than the rooting depth, Burroughs' (1985) equation provides similar results to their much simpler equation. They modify Equation 4-3 (Reistenberg and Sovonick-Dunford, 1983) to express the factor of safety as:

Equation 4-4

$$F = \frac{A_b(\rho_s - \rho_w)g\cos\beta\tan\varphi + C_r P}{A_b\rho_s g\sin\beta}$$

where: C_r is the strength of the roots at the margins, φ is the friction angle, and P is perimeter length. They found that, for a given parameter set, non-zero minimum lengths and widths of equal magnitude were imposed on potential landslides, although no maximum values were imposed.

Montgomery *et al.* (2000) and Schmidt *et al.* (2001) used a modified version of the infinite slope equation to account for lateral root strength and rearranged to

solve for the critical proportion of the soil that must be saturated to trigger slope failure:

Equation 4-5

$$m_c = \frac{C_l Pz + C_b A_b}{A_b \rho_w g z \cos^2 \beta \tan \varphi} + \frac{\rho_s}{\rho_w}\left(1 - \frac{\tan \beta}{\tan \varphi}\right)$$

where: C_l is lateral root cohesion and z is the depth of the failure plane. Applying this within a SHALSTAB framework (Montgomery and Dietrich, 1994), which assumes infiltration of rainfall and topographically driven flow through soil over impermeable bedrock, the relative potential for shallow landsliding can be given by the q/T required to generate instability:

Equation 4-6

$$\left(\frac{q}{T}\right)_c = \frac{\sin \beta}{a/b}\left[\frac{C_l Pz + C_b A_b}{A_b \rho_w g z \cos^2 \beta \tan \varphi} + \frac{\rho_s}{\rho_w}\left(1 - \frac{\tan \beta}{\tan \varphi}\right)\right]$$

where: a/b is the upslope contributing area per unit contour length. Schmidt *et al.* (2001) introduced the model as background theory and Montgomery *et al.* (2000) applied it to catchments in the Oregon Coast Range assuming landslide length is 10 m, width is 5 m and depth is 1 m. These models focussed on the effect of lateral roots in reinforcing the soil. The modified infinite slope equations ignored the edge effects resulting from granular friction or from the divergence from infinite slope conditions at the head and toe of the potential failure.

Gabet and Dunne (2002) built upon Reneau and Dietrich's (1987) model, but assumed that landslides are infinitely long in order to eliminate the length dependency and model only landslide width. They balance the forces on a slice of hillslope taken parallel to the contour lines, accounting for reinforcement along the side scarps of the failure. Gabet and Dunne (2002) calculated lateral earth forces but found that they accounted for only 10% of the total resistance and dismissed them as negligible given the uncertainty in the other terms. Using the model they illustrate the importance of vegetation type and root strength for slope stability and correctly predict relationships between landslide volume and hillslope angle.

Casadei *et al.* (2003) reapplied the methods of Reneau and Dietrich (1987) but relaxed the assumption that the soil column was completely saturated. They

applied several scenarios for landslide length / width ratio but made their final conclusions assuming that landslide length was infinite. In this respect, their method is similar to that of Gabet and Dunne (2002). Based on an in depth study of the parameter interaction using reasonable values from field study in the Oregon Coast Range, Casadei *et al.* (2003) suggested that landslide size was set by local combinations of root strength gaps, elevated soil thickness, high pore pressure and slope steepness. They predicted that landslide size would be smaller for high pore pressure, steeper slopes and lower root strength.

These studies deal almost exclusively with the effects of lateral roots on stability. Very little crossover exists between the two groups of multi-dimensional stability modellers. In the geomorphology community, only Tsukamoto and Kusakabe (1984), Burroughs (1985) and Dietrich *et al.* (2006) attempt a complete characterisation of both the additional lateral reinforcement of roots and the lateral and basal friction effects. Tsukamoto and Kusakabe (1984) assume that the failure mass consists of three blocks as illustrated in Figure 4-5 with their geometries satisfying $v_0 \cos\theta = v_1 = v_2 \cos\theta$. The safety factor is the ratio of total energy dissipation on the surface of velocity discontinuity to work done by the gravitational field. This method provides an alternative approach to those of Chen (1981) and Burroughs (1985), which rely on earth pressure theory. However, it is limiting in the geometries to which it can be applied.

Figure 4-5: A schematic in plan and profile of the failure plane geometry assumed by Tsukamoto and Kusakabe (1984).

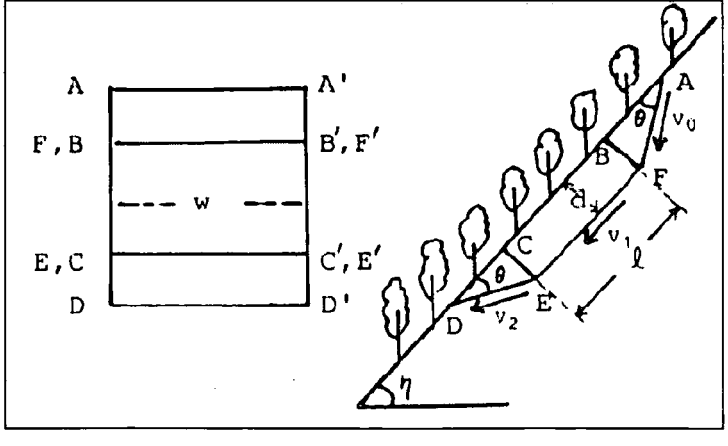

Burroughs (1985) developed force balance expressions that explicitly include root strength and lateral earth pressure terms in a three-dimensional formulation

of the shallow slope stability problem for the case of failure parallel to the ground surface. Burroughs (1985), who's research background was root reinforcement and its effect on slope stability, developed the model to evaluate the stability of drainage bottoms in proposed harvest areas. This model applied active pressure at the upslope margin of the block (using Rankine's active earth pressure coefficient for sloping surfaces) and 'at rest' earth pressure (using Jaky's (1944) empirical coefficient) on the lateral edges. At the downslope margin of the block, passive pressure was estimated from a Mohr diagram and a term to represent the buttressing effect of trees. This approach has been adapted by Dietrich *et al.* (2006) who neglect buttressing effects and include an analytical solution for passive earth pressure at the downslope margin of the block.

Figure 4-6: A diagram of the geometry of Burroughs' (1985) soil block and the forces acting on it (from Burroughs, 1985).

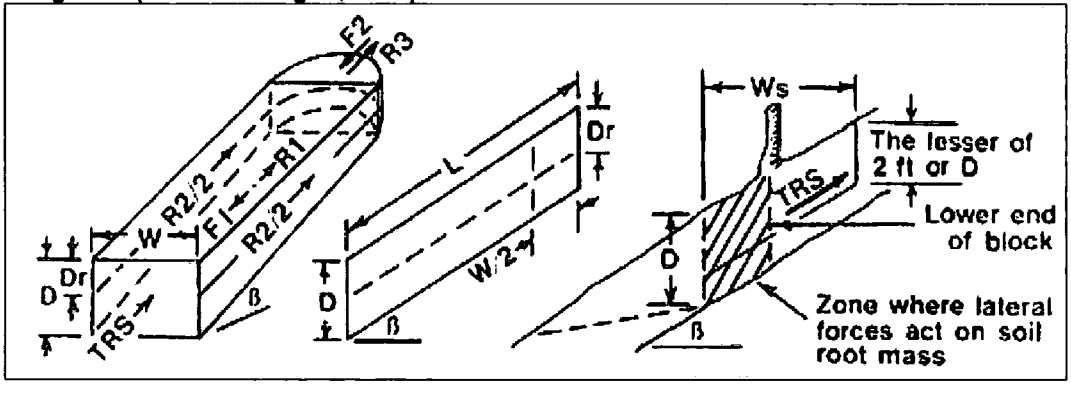

Summary

The lateral edge effect due to friction between the failing block and its static surroundings has been represented since Skempton (1985). Its magnitude is a function of the normal stress on the lateral edges, which can be represented using 'at rest' earth pressure (Stark and Eid, 1998). However, numerical experiments using continuum mechanics models suggest that this is likely to result in overestimation of its importance (Chugh, 2003; Albatineh, 2006), which is probably due to the zero strain assumption associated with 'at rest' stress conditions. The normal force could be represented using active earth pressure instead, but this is likely to underestimate normal stress. Since the stress conditions on the margins of a real landslide are likely to vary we can represent upper and lower bounds to stress conditions and therefore lateral friction

resistance using 'at rest' and active earth pressures respectively. This treatment is theoretically strong, well constrained by results from numerical experiments with continuum mechanics models and simple to implement requiring no additional parameters relative to traditional limit equilibrium approaches. I will pursue this further in Section 4.4.4, where I derive the equations for upper and lower bound friction resistance on the lateral edges. The earth pressure theory that is foundational to these approaches is covered in detail in Appendix 1.

Reinforcement from lateral roots has been recognised as an important stabilising effect for a long time. It was first represented to quantify the stability of individual slide blocks (Reistenberg and Sovonick-Dunford, 1983). These equations were adapted for dimensional and sensitivity analysis (Reneau and Dietrich, 1987; Gabet and Dunne, 2002; Casadie *et al.*, 2003), or catchment scale stability analysis assuming a particular failure geometry (Montgomery, 2000). These studies concentrate on the stabilising effects of lateral roots, discounting friction effects either for simplicity (Reneau and Dietrich, 1987; Casadei *et al.*, 2003) or because they are considered unimportant (Gabet and Dunne, 2002).

Very little crossover exists between the two groups of multi-dimensional stability modellers. From the engineering literature, few attempts are made to quantify or treat the additional reinforcement provided by roots. While within the geomorphology community, only Tsukamoto and Kusakabe (1984), Burroughs (1985) and Dietrich *et al.* (2006) attempt a complete characterisation of both the additional lateral reinforcement of roots *and* the lateral and basal friction effects.

4.4. Deriving the Finite Slope Model

In Section 4.3 I identified two groups of suitable models for catchment scale slope stability: column based models applying Hovland's (1977) method (Xie *et al.*, 2006) without any treatment of lateral edge effects; or single body approaches (Burroughs, 1985), which calculate limiting equilibrium conditions for a single block. I will concentrate specifically on the single body method, since this appears best suited to shallow translational failure mechanics and allows treatment of lateral edge effects.

Following Chen (1981), Burroughs (1985) and Dietrich *et al.* (2006), my method for three-dimensional slope stability represents the forces acting on each plane of a single cuboid block (Figure 4-7). For each plane, shear strength is present in two forms: granular friction and root reinforcement. The resistance forces are calculated by multiplying each plane's shear strength by the area over which it acts. These resisting forces are summed and divided by the driving forces to obtain a factor of safety.

For the base and lateral sides, the friction resistance is dependent on the normal stress on the plane and the angle of internal friction: $s = \sigma \tan \phi$. On the base of the slide (A'B'C'D' in Figure 4-7) this normal stress can be represented using the standard formulation of vertical geostatic stress. The normal stress on the lateral sides (ABB'A' and DCC'D' in Figure 4-7) can be represented using 'at rest' and active earth pressures to represent its upper and lower bounds respectively (Section 4.4.4). For the upslope and downslope boundaries of the block (BCC'B' and ADD'A respectively in Figure 4-7), any driving or resisting pressure is normal to the plane. The stresses on these planes can be calculated from earth pressure theory developed to assess the stability of earth retaining structures. In Section 4.4.5 I will review the available algorithms for calculating these stresses analytically.

In common with those studies reviewed in Section 4.3.2 root reinforcement on each plane is represented as an apparent cohesion. The depth to which this is applied and the magnitude of the reinforcement with depth are subject to debate. In Section 4.4.4 I will apply an apparent cohesion (based on empirical results from Section 3.3) and test a range of assumptions about the relationship between root reinforcement and depth. On the base and sides, root cohesion can simply be added to the resisting pressure. The effect of root cohesion on the upslope and downslope margins is less clear and the ability to represent cohesion within the theories requires careful thought and some minor auxillary assumptions, these are detailed and justified in Section 4.4.5.

Figure 4-7: Schematic showing forces and lengths for a three-dimensional slope stability problem in: (i) 3D, (ii) plan, (iii) cross section and (iv) profile.

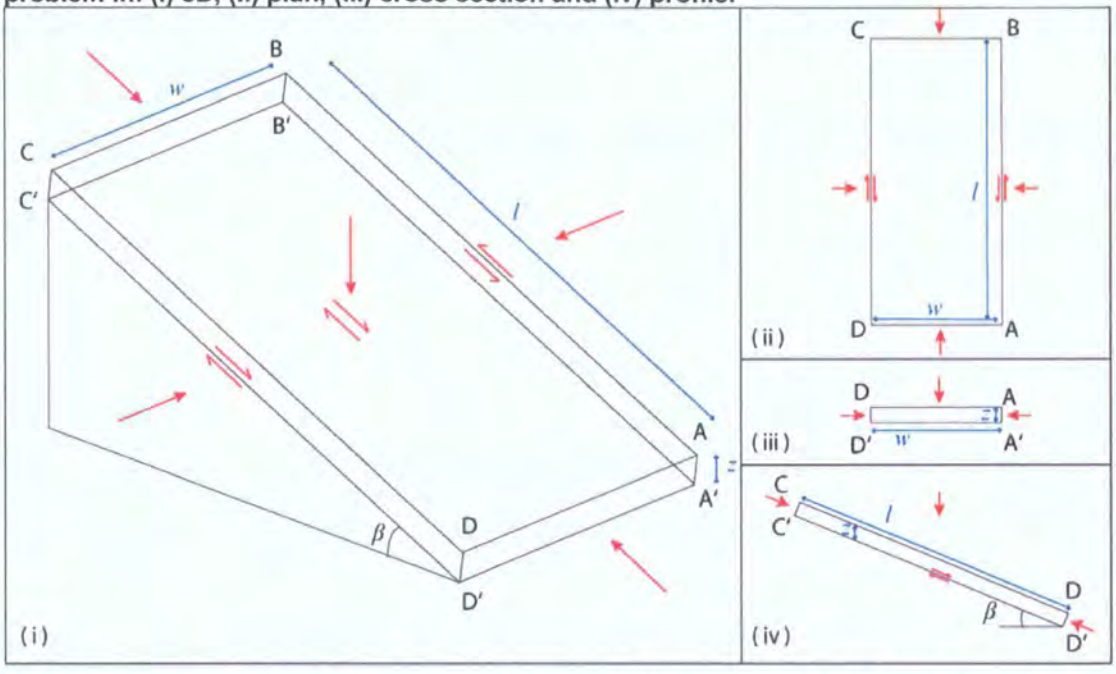

This method is conceptually similar to that of Burroughs (1985) and Dietrich *et al.* (2006) in that they deal with the forces on each plane of a single potentially unstable block of soil. In many cases, the methods represent the forces on these planes in a similar manner, including root cohesion and friction effects, applying active pressure at the upslope margin, passive pressure at the downslope margin and at rest pressure on the sides. However, there are considerable differences in their detail. Each model takes a different approach to calculating passive pressure and quantifying root cohesion on basal and lateral planes. I make several key adjustments, applying earth pressure coefficients suitable for sloping ground and including a flexible approach to the representation of: normal forces on the sides of the slide; and root reinforcement with depth.

4.4.1. Weight (FW) and Vertical stress (σz)

The weight of the soil mass or its corresponding vertical stress (σ_z) is a first order constraint on a block's frictional strength. For the base and lateral sides, this is because the soil's granular friction is dependant on the normal stress applied to these planes. For the upslope and downslope margins of the block, the normal stresses themselves define their strengths; each of these normal stresses can be calculated as a function of vertical stress and the inclination of

the plane. For a unit area of dry soil at a given inclination (β) the total (σ_{zt}) and effective (σ_z) vertical stresses are equal and can be calculated from the volume and density of the soil:

Equation 4-7

$$\sigma_{zt} = \sigma_z = \rho_s g\, z \cos\beta$$

where: the z cos β term converts the vertical soil depth to a soil thickness perpendicular to the slope. As discussed in Section 2.5, the total and effective stresses are equal for dry slopes. On partially saturated slopes, the effective vertical stress diverges from total vertical stress as a result of pore pressure (u). As previously indicated, I assume that slope instability occurs in drained conditions, and apply effective stresses throughout where:

Equation 4-8

$$\sigma_z = \sigma_{zt} - u$$

In line with existing catchment scale slope stability models (Sections 2.5 and 2.6) I assume: 1) that the phreatic surface is parallel to both the ground surface and base of the block; and 2) that groundwater conditions are hydrostatic (i.e. I do not account for water flow). Under these conditions the pore pressure at a point is given by the hydrostatic pressure:

Equation 4-9

$$u = \rho_w g z_w$$

where: z_w is the depth below the water table. With the aim of maintaining functional simplicity, I ignore any infiltration, suction or capillary rise effects in the unsaturated zone that might cause negative pore pressures in this region. Instead I partition the block into saturated and unsaturated zones, substituting Equation 4-7 and Equation 4-9 into Equation 4-8 to calculate the vertical pressure in the saturated zone and applying Equation 4-7 in the unsaturated zone. These can be combined as additive terms:

Equation 4-10

$$\sigma_z = \cos\beta(\rho_s g(z - z_w) + (\rho_s g - \rho_w g)z_w)$$

This can be simplified to:

Equation 4-11

$$\sigma_z = \cos\beta(\rho_s g\, z - \rho_w g\, z_w)$$

Using a ratio of water table height z_w, to the depth of the failure plane (z): $m=z_w/z$ to define a saturation ratio, I can further simplify Equation 4-11:

Equation 4-12

$$\sigma_z = \cos\beta\, z\, g(\rho_s - \rho_w m)$$

Effective vertical stress defined either from Equation 4-11 or Equation 4-12 provides the driving force for the granular effects on a particular plane of the block.

4.4.2. Basal Forces

The formulation for basal shear resistance force (F_{sb}) is similar to the infinite slope procedure; except that the assumption of plane strain is relaxed and the edges of the slide are no longer considered to cancel one another but are dealt with individually; and the force balance is calculated for a known slide area (A_b). Basal shear resistance force is:

Equation 4-13

$$F_{sb} = \sigma \tan \varphi A_b$$

where the slide area is measured parallel to the slope and can be calculated in this simplified case (for a cuboid block) as the width (w) and length (l) of the rectangular slide surface (Figure 4-7):

Equation 4-14

$$A_b = wl$$

Applying this for a hydrostatic phreatic surface that is parallel to both the ground surface and the base of the block, results in:

Equation 4-15

$$F_{sb} = \cos^2 \beta \, z \, g(\rho_s - \rho_w m) \tan \varphi A_b$$

Two additional factors add to the resisting force on the base of the block. For cohesive soils, or soils where a cohesion term is required, to parameterise for non-linearity in the failure envelope (as discussed in Section 2.5), basal soil cohesion (C_{sb}) can be applied over the basal area of the block. If roots extend through the base of the block their reinforcing effect can be quantified in a basal root cohesion term (C_{rb}) which is applied over the same area.

Equation 4-16

$$F_{sb} = \left(C_{rb} + C_s + \cos^2 \beta \, z \, g(\rho_s - \rho_w m) \tan \varphi\right) A_b$$

4.4.3. Lateral Forces

The driving and resisting forces acting on the lateral planes of the block are closely related to the forces acting normal to each plane. These can be approximated using earth pressure theory originally developed to solve stability

problems for engineering structures (Figure 4-8A). Further details on the background to and derivation of the relevant earth pressure theories is provided in Appendix 1. Lateral earth pressures can depend on the soil properties and the stress history of the soil and are highly strain dependent. They are treated in three categories depending on the degree and direction of strain that they have experienced. 'At rest' earth pressure represents the lateral pressure exerted by the soil on a plane where there is either no strain, or the strain is limited and is orientated parallel to the plane. 'Active' pressure results from the force that earth exerts on a retaining structure or soil block as it moves away from the soil. 'Passive' pressure results from the force that a structure or soil block exerts on the soil when the structure moves towards the soil. The normal stress on the landslide sides can be represented using either 'at rest' (Stark and Eid, 1998) or active (Albataineh, 2006) earth pressure conditions to calculate the frictional resistance on these planes. Active pressure conditions can be assumed at the upslope margin to estimate the force applied by the soil upslope of the block and the passive pressure required for failure of the material downslope of the block can be used to establish the additional strength supplied by the toe (Figure 4-8B). For each state, vertical stress is converted to lateral pressure using a different earth pressure coefficient.

Figure 4-8: A Schematic illustrating: A) a classic engineering application of active and passive earth pressure theory to calculate the stability of a retaining wall; and B) their application in a the soil block model, using active pressure to calculate additional driving forces on the block from upslope and passive pressure for the additional strength supplied at the downslope margin of the block.

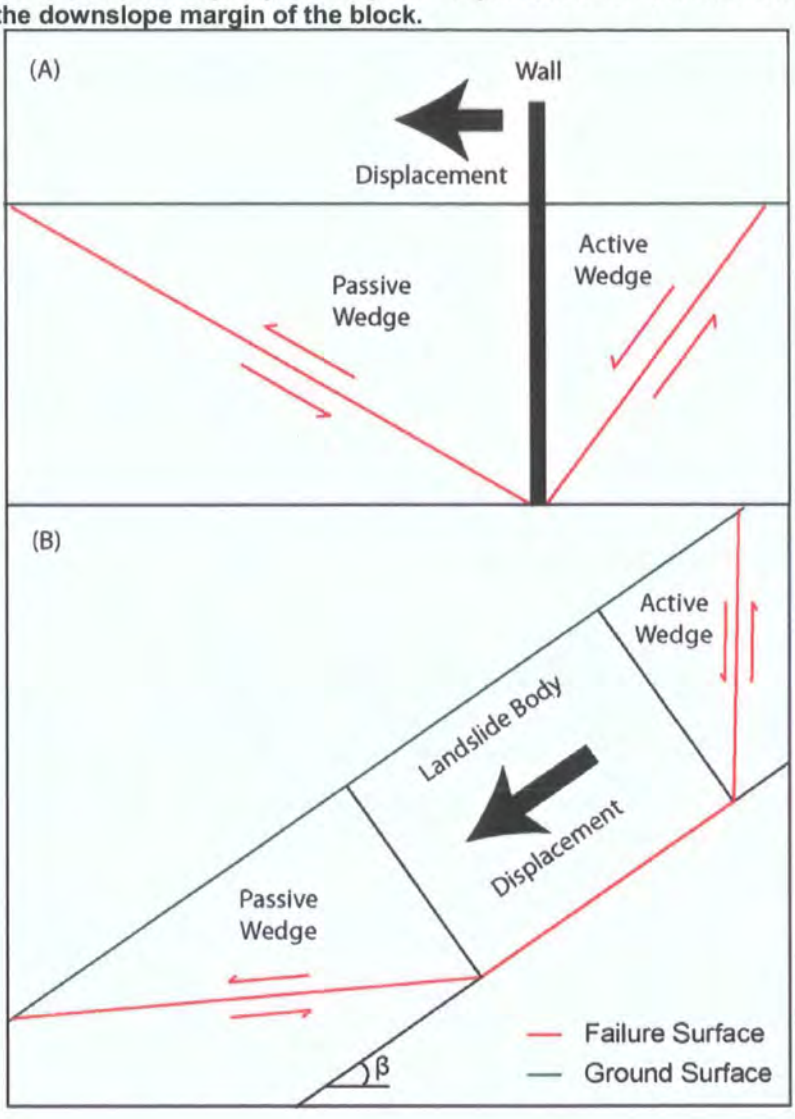

4.4.4. Block Lateral Sides

Friction

The assumption that the block is cuboid (Figure 4-7) with vertical lateral sides simplifies the calculations for side friction. It minimises the area of the side planes so that any estimate of their influence on stability is likely to be conservative in relation to that for real failures where the scar edges are often sloping (Stark and Eid, 1998). The sides of the block that extend parallel to the direction of sliding behave in a similar manner to the base. If we assume that the material has isotropic frictional properties, and if we calculate the magnitude

of the normal force on the lateral sides then we can calculate the lateral shear resistance due to earth pressure (s_l) at a point as:

Equation 4-17

$$s_l = \sigma_x \tan\varphi$$

where: σ_x is the horizontal stress at a point. If the normal force at the soil-soil interface is geostatic with no active or passive yield then 'at rest' lateral earth pressure conditions are reasonable (Chandler *et al.*, 1981). The coefficient of 'at rest' earth pressure K_o can be used to calculate lateral stress (σ_x) from vertical stress (σ_z) at a point:

Equation 4-18

$$\sigma_x = K_0 \sigma_z$$

If we assume that the soils are normally consolidated and cohesionless then we can estimate the 'at rest' earth pressure coefficient (K_0) from the soil's friction angle (φ) using Jaky's (1944) empirical relation for 'at rest' conditions:

Equation 4-19

$$K_0 = 1 - \sin\varphi$$

Further details on 'at rest' earth pressure and Jaky's empirical relation are provided in Appendix 1.

However if the interface experiences some positive strain (tension) in excess of 0.5%, then active earth pressure conditions may be more reasonable (Lambe and Whitman, 1969) and the active earth pressure coefficient K_a should be used to calculate lateral stress:

Equation 4-20

$$\sigma_x = K_a \sigma_z$$

Where the soil surface is horizontal, Coulomb's and Rankine's active earth pressure coefficients are equivalent and can be calculated as:

Equation 4-21

$$K_a = \tan^2\left(45° - \frac{\phi}{2}\right)$$

The background to these equations and their relation to one another is provided in Appendix 1. 'At rest' Equation 4-18 and active Equation 4-20 conditions can be applied in combination to calculate the upper and lower bounds for shear resistance on these planes. I calculate vertical stress at a point using Equation 4-12 then combine it with either the 'at rest' (Equation 4-18) or active (Equation 4-20) earth pressure coefficient in Equation 4-17 to calculate the resisting stress

at a given depth (z_i) on a vertical plane oriented parallel to the direction of sliding:

Equation 4-22

$$s_l = K \cos \beta \, z_i \, g(\rho_s - \rho_w m) \tan \varphi$$

where: K is the earth pressure coefficient, for the upper bound $K=K_0$ and for the lower bound $K=k_a$. The functional form of this relationship indicates that vertical stress, and therefore lateral stress and resisting stress, will increase linearly as a function of depth (z_i) and that these variables will all tend to zero at the surface. To calculate the lateral shear resistance force per unit length (S_l) I integrate Equation 4-22 from the surface (z_0) to the base of the block (z_b):

Equation 4-23

$$S_l = \int_{z_0}^{z_b} s_l dz$$

Equation 4-24

$$S_l = \int_{z_0}^{z_b} (K \cos \beta \, z \, g(\rho_s - \rho_w m) \tan \varphi) dz$$

Equation 4-25

$$S_l = \frac{1}{2} K \cos \beta \, z^2 \, g(\rho_s - \rho_w m) \tan \varphi$$

Applying the shear resistance force over the length of the block sides parallel to the direction of sliding we get a lateral shear resistance force for the landslide (F_{sl}):

Equation 4-26

$$F_{sl} = \frac{1}{2} K \cos \beta \, z^2 \, g(\rho_s - \rho_w m) \tan \varphi \, l_s$$

where: l_s is the length of the lateral sides of the landslide. For the simplified case discussed here, where the landslide has a rectangular planform shape $l_s=2l$. For soils where the failure envelope includes a cohesion value (C_{sl}) this is multiplied over the area of the lateral sides and added to the lateral shear resistance force:

Equation 4-27

$$F_{sl} = C_s \cos \beta \, z \, l_s + \frac{1}{2} K \cos \beta \, z^2 \, g(\rho_s - \rho_w m) \tan \varphi \, l_s$$

This can be simplified to:

Equation 4-28

$$F_{sl} = \left(C_s + \frac{1}{2} K \, z \, g(\rho_s - \rho_w m) \tan \varphi \right) \cos \beta \, z \, l_s$$

Root Cohesion

Representing lateral root cohesion is a more complex problem. As discussed in Chapter 3, the magnitude of the reinforcement provided by roots is primarily a function of the density of the roots and their strength. The relationship between root density and therefore root cohesion with depth might be considered to follow one of the following three scenarios:

1) roots extend to a maximum depth below the base of the soil block, and their density remains constant with depth;
2) roots extend to a shallower maximum depth than the base of the block but their density remains constant with depth up to this point; or
3) roots extend to a maximum depth below the base of the block but their density decreases with depth.

These three scenarios are discussed in Section 3.3, where I have developed three alternative representations to cover each scenario. Root reinforcement (R_{rl}) per unit length is the term dependent on these scenarios, it can be calculated in any of the three ways then multiplied by the length of the lateral sides and added to the lateral shear resistance force:

Equation 4-29

$$F_{sl} = \left(R_{rl} + C_s z + \frac{1}{2} K z^2 g(\rho_s - \rho_w m) \tan\varphi \right) \cos\beta l_s$$

Each representation results in a different function for lateral root reinforcement. The simplest representation assumes that root cohesion is uniform with depth and extends below the base of the block. In this case, root cohesion can be treated in the same way as soil cohesion, multiplied over the area of the lateral sides and added to the lateral shear resistance force:

Equation 4-30

$$R_{rl} = C_{rl} z$$

Under scenario 2, where root cohesion is assumed uniform to a maximum rooting depth (z_r), which is less than the depth of the soil block, the root cohesion is applied as a constant multiplied over the area of the lateral sides above the maximum rooting depth then added to the lateral shear resistance force:

Equation 4-31

$$R_{rl} = C_{rl} z_r$$

Finally, in scenario 3, root cohesion is predicted as a power function of depth. Its form is dictated by the density of the roots with depth (a power function of the form: $a\ z^b$) and the relationship between root density and root cohesion (R), which is assumed to be linear. These values are obtained either from field data or literature estimates of root strength and density.

Equation 4-32

$$C_r = R\,a\,z^b$$

Root cohesion is integrated over the depth of the block to give the total root reinforcement per unit perimeter length of the lateral edge (R_{rl}).

Equation 4-33

$$R_{rl} = \int_{z_0}^{z_b} C_r\,dz$$

Equation 4-34

$$R_{rl} = \frac{R\,a}{b+1} z^{b+1}$$

Each scenario results in a different lateral root reinforcement estimate for a given block thickness and root cohesion. These can be applied interchangeably to suit the conditions in the area under investigation.

4.4.5. Block Upslope and Downslope Margins

Friction

On the upslope and downslope margins of the block it is the normal stress itself that is important for stability. This is proportional to vertical stress and can be calculated using active (K_a) or passive (K_p) earth pressure coefficients using either Coulomb (Coulomb, 1776) or Rankine theory (Rankine, 1857). By applying both Coulomb (upper bound) and Rankine (lower bound) theory I establish an envelope for lateral stress at the upslope and downslope block margins. Although past studies (Chen, 1981; Burroughs, 1985) have used earth pressure theory to calculate the forces applied to a block by upslope and downslope soil wedges, these have either applied simple horizontal earth pressure coefficients (Chen, 1981) or have calculated the pressure graphically from Mohr stress diagrams (Burroughs, 1985). The background to and derivation of these coefficients is dealt with in detail in Appendix 1. This section deals with their application in a soil block based stability model.

For failure to occur the downslope margin of the block must fail under passive conditions. Passive pressure (p_p) at a point can be calculated from the vertical stress (σ_z) at that point using the coefficient of passive earth pressure (K_p):

Equation 4-35

$$p_p = K_p \sigma_z$$

where: Rankine's passive earth pressure coefficient (K_p) for sloping cohesionless soils can be calculated analytically as:

Equation 4-36

$$K_p = \frac{\cos\beta + \sqrt{(\cos^2\beta - \cos^2\phi}}{\cos\beta - \sqrt{(\cos^2\beta - \cos^2\phi}}$$

and Coulomb's passive earth pressure coefficient (K_p) is given by:

Equation 4-37

$$K_p = \left(\frac{\frac{\sin(\alpha+\phi)}{\sin\alpha}}{\sqrt{(\sin(\alpha-\delta))} + \sqrt{\left(\frac{\sin(\phi+\delta)\sin(\phi+\beta)}{\sin(\alpha-\beta)}\right)}} \right)^2$$

where: δ is the wall friction angle and α is the wall inclination from horizontal. I calculate vertical stress at a point using Equation 4-12 then combine it with Equation 4-35 to calculate the resisting stress at a given depth (z_i) on a plane perpendicular to the direction of sliding:

Equation 4-38

$$p_p = K_p z_i \, g(\rho_s - \rho_w m)$$

Vertical stress and therefore passive pressure increases linearly as a function of depth (z_i) and tends to zero at the surface. To calculate the passive force per unit length (P_p) I integrate Equation 4-22 from the surface (z_0) to the base of the block (z_b):

Equation 4-39

$$P_p = \int_{z_0}^{z_b} p_p dz$$

Equation 4-40

$$P_p = \int_{z_0}^{z_b} \left(K_p z \, g(\rho_s - \rho_w m)\right) dz$$

Equation 4-41

$$P_p = \frac{1}{2} K_p z^2 \, g(\rho_s - \rho_w m)$$

Total passive force (F_{pp}) on the downslope margin of the block can be calculated by applying the passive force over the width of the block (w) perpendicular to the direction of sliding:

Equation 4-42

$$F_{pp} = \frac{1}{2} K_p z^2 g(\rho_s - \rho_w m) w$$

The push force on the block applied by the active conditions at its upslope margin (F_{pa}) follows the same form and can be calculated from the same equation but using the active earth pressure coefficient (K_a) in place of the passive coefficient.

Equation 4-43

$$F_{pa} = \frac{1}{2} K_a z^2 g(\rho_s - \rho_w m) w$$

where: Rankine's active earth pressure coefficient (K_a) for sloping cohesionless soils can be calculated analytically as:

Equation 4-44

$$K_a = \frac{\cos\beta - \sqrt{(\cos^2\beta - \cos^2\phi)}}{\cos\beta + \sqrt{(\cos^2\beta - \cos^2\phi)}}$$

and Coulomb's active earth pressure coefficient (K_a) is given by:

Equation 4-45

$$K_a = \left(\frac{\frac{\sin(\alpha - \phi)}{\sin\alpha}}{\sqrt{(\sin(\alpha + \delta))} + \sqrt{\left(\frac{\sin(\phi + \delta)\sin(\phi - \beta)}{\sin(\alpha - \beta)} \right)}} \right)^2$$

Soil cohesion is not represented in these equations. The effect of soil cohesion on active or passive pressure can be calculated graphically for both Coulomb and Rankine Theory. An analytical solution for active pressure in cohesive sloping soils has been derived by Gananapragasam (2000). However, at present, no analytical solution exists for passive earth pressures in cohesive sloping soils.

Root Cohesion

A root cohesion force (F_{ch}) is present on both upslope and downslope margins of the block. At the upslope margin root strength is mobilised at very small strain as roots extending across the margin are stressed in tension. This effect can be

quantified by simply applying the root reinforcement per unit perimeter length over the width of the upslope margin of the block:

Equation 4-46

$$F_{ch} = R_{rl} w$$

The root reinforcement per unit perimeter length term varies depending on the choice of one of three scenarios: 1) constant root cohesion with depth to a maximum depth below the base of the block (Equation 4-30); 2) constant root cohesion with depth to a maximum depth (z_r) shallower than the base of the block (Equation 4-31); or 3) power law decline in root cohesion with depth (Equation 4-34).

Figure 4-9: Schematic A describes the lengths of different toe geometries: Lt_1 with a steep toe (large λ) and Lt_2 with a shallow toe (small λ). Toe angles never exceed horizontal so $\lambda_{max} = \lambda_2$ and $Lt_{min} = Lt_2$. Schematic B illustrates the toe length (Lt) calculations required as part of Equation 4-47.

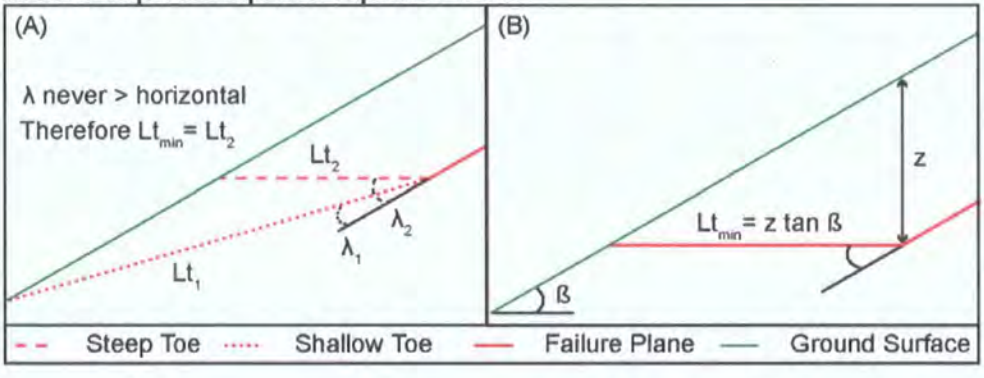

Roots are weak in compression. However, at the downslope margin of the failure, the plane for the passive wedge will be inclined at an angle to the slope (λ in Figure 4-9). Field data suggest that this toe angle rarely represents a negative slope (Section 2.4.3). In these conditions, the minimum toe length will be a horizontal plane connecting the base of the block to the surface. The area of the plane will be related to the width of the block, the depth of the block base and the inclination of the slope by:

Equation 4-47

$$A_t = wz \tan \beta$$

The cohesion acting on the toe will also vary according to the three scenarios defined above. However, when these are simplified to a root reinforcement per unit perimeter length (R_{rl}) the resisting force at the toe can be represented as:

Equation 4-48

$$F_{st} = \left(R_{rl} \tan \beta + \frac{1}{2} K_p z^2 g(\rho_s - \rho_w m) \right) w$$

4.4.6. Driving Forces Related to the Soil Mass

The driving stress (S_d) on the soil block is the downslope component of the total vertical stress (σ_{vt}):

Equation 4-49

$$s_d = \sigma_{zt} \sin\beta$$

In this case the vertical stress is total (σ_{zt}) not effective (σ_z) because pore pressures do not mitigate driving stress. Calculating driving stress from the density and volume of the block:

Equation 4-50

$$s_d = \cos\beta \, zg\rho_s \sin\beta$$

Multiplying the stress by the area of the block generates an estimate for its downslope driving force (F_d):

Equation 4-51

$$F_d = \cos\beta \, zg\rho_s \sin\beta \, A_b$$

4.5. Chapter Summary

Representing landslides three-dimensionally is important because their size influences their geomorphic and destructive power and their geometry may have important implications for stability. Modelling three-dimensional stability at the catchment scale is limited at present; models tend to tackle only limited aspects of three-dimensional stability. An important first step involves the formulation of a set of analytical governing equations for stability: this chapter achieves this. Next steps involve testing the model's effectiveness and examining its behaviour, these are undertaken in Chapter 5.

The governing equations derived in this chapter follow those of Chen (1981), Burroughs (1985) and Dietrich *et al.* (2006) in that they consider the forces on each plane of a block applying limit equilibrium analysis and earth pressure theory to calculate stability. Shear strength on each plane is represented in two forms: friction effects, relating to grain on grain interactions and root reinforcement effects. The model can be formulated for a cohesionless material (Figure 4-10); or for soils where effective cohesion is required to properly represent the failure envelope and / or where roots reinforce the block (Figure 4-11). In these conditions, the resisting forces (Equations: 16, 29, 46, 48) are summed and divided by the driving forces (Equations: 43 and 51) to obtain a

factor of safety. Resisting forces exist on the base, lateral sides, the downslope margin and, where root reinforcement is included, the upslope margin. Driving forces are due to the downslope component of the block's weight and the force exerted from the soil mass upslope. For the base and lateral sides, the friction resistance is dependent on the normal stress on the plane. On the base (A'B'C'D' in Figure 4-10) this is represented using vertical geostatic stress; and on the lateral sides (ABB'A' and DCC'D' in Figure 4-10) using 'at rest' and active earth pressures (providing a predictive uncertainty envelope). For the upslope and downslope boundaries (BCC'B' and ADD'A in Figure 4-10), any driving (upslope margin) or resisting (downslope margin) stress is normal to the plane. The stresses on these planes are calculated using active and passive earth pressure theory (using Coulomb and Rankine theory to provide upper and lower uncertainty bounds). Root reinforcement on each plane is represented as a depth varying apparent cohesion and has a flexible treatment of the relationship between root reinforcement and depth. On the base, sides and upslope margin, depth integrated root reinforcement is simply added to the resisting force. At the downslope margins root cohesion is applied over an assumed toe geometry.

The model makes several key adjustments to previous formulations:

1) It takes a new approach to calculating active and passive earth pressure, applying coefficients suitable for sloping ground and using Rankine and Coulomb theory in combination to quantify predictive uncertainty;

2) It includes a flexible approach to quantifying root cohesion on basal and lateral planes which explicitly accounts for variations in root cohesion with depth.

3) It treats recently identified uncertainties associated with quantifying normal stresses on the block's lateral sides by calculating both active and 'at rest' earth pressure to provide an envelope of potential normal stresses then propagates this through in order to generate upper and lower bounds for the friction resistance on these planes.

Figure 4-10: The stability equations for a soil block in cohesionless material, including the equation numbers for their derivation in the text.

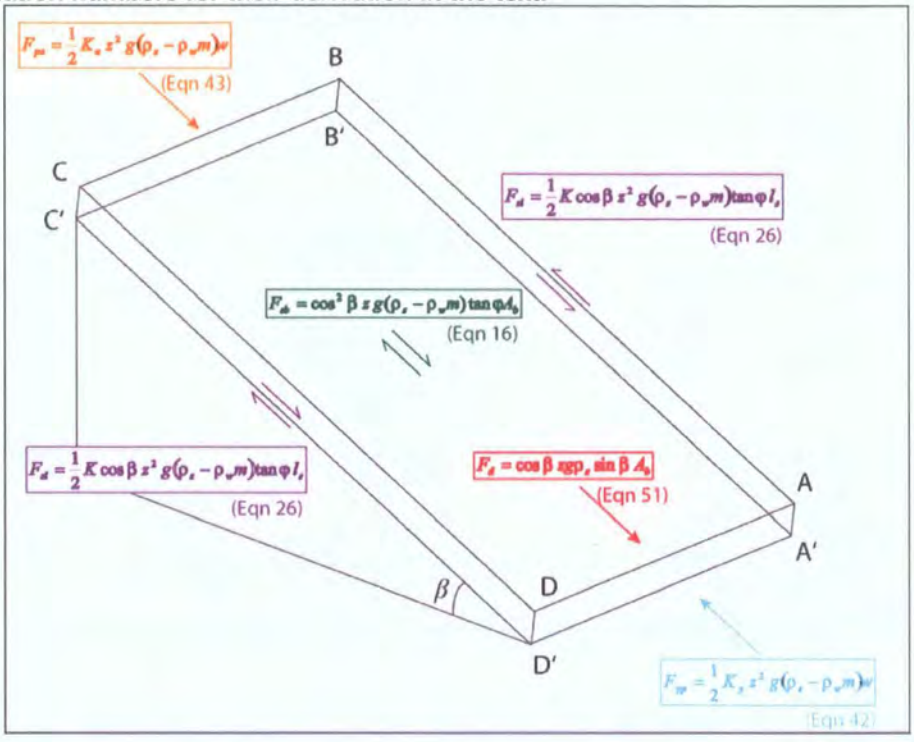

Figure 4-11: The stability equations for a soil block in cohesive material, including the equation numbers for their derivation in the text.

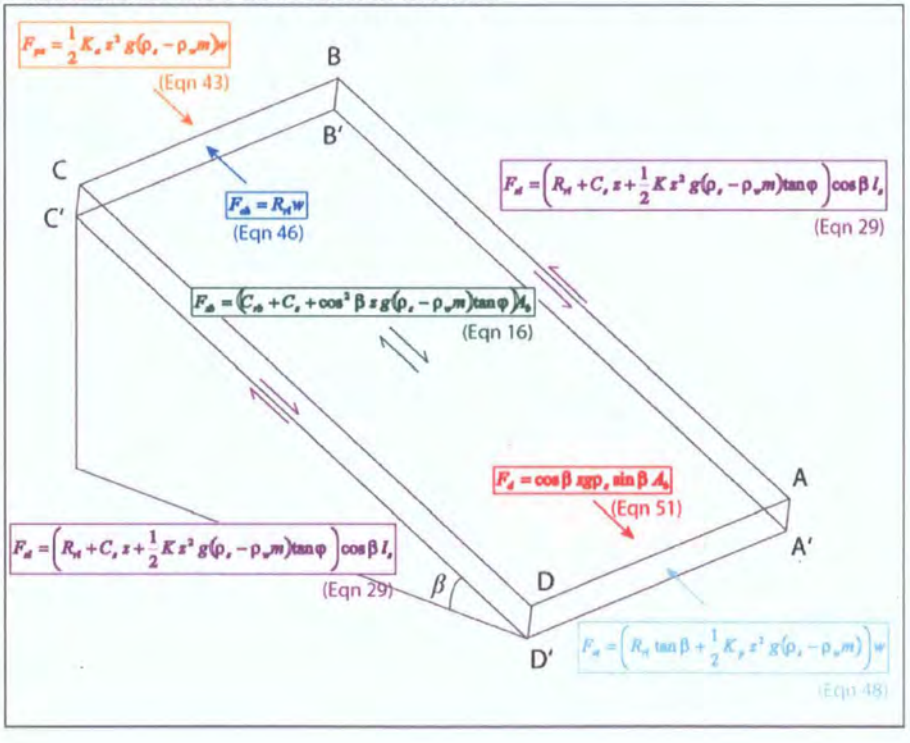

5. Re-formulating the Factor of Safety: Model Testing and Sensitivity Analysis

5.1. Scope of the Chapter

In Chapter 4 I derived a new set of analytical governing equations for three-dimensional stability. These constitute a new finite slope stability model that has the potential to be used as a powerful tool for catchment scale slope stability modelling. However, it is presently un-tested; to allow me to make confident assertions on the implications of its predictions for relationships between geometry and stability this needs to be addressed. Consequently, this Chapter has two key aims: 1) to establishing the effectiveness of the finite slope model; and 2) to quantify the control that a block's geometry exerts on its stability. I will address the first by comparing the finite slope model's results with those from two standard two-dimensional limit equilibrium models in a set of benchmark tests. I will address the second, using sensitivity analysis in a set of numerical experiments designed to be representative of my study area (based on the results from Chapter 3). I treat length and width effects individually first, then relative to one another and finally in combination using the full three-dimensional formulation of the finite slope model (Figure 5-1). I quantify the effects using two stability metrics: the FoS and Back calculation allowing me to compare their magnitude with that of parameter uncertainty.

Figure 5-1: A schematic illustrating the structure of the chapter.

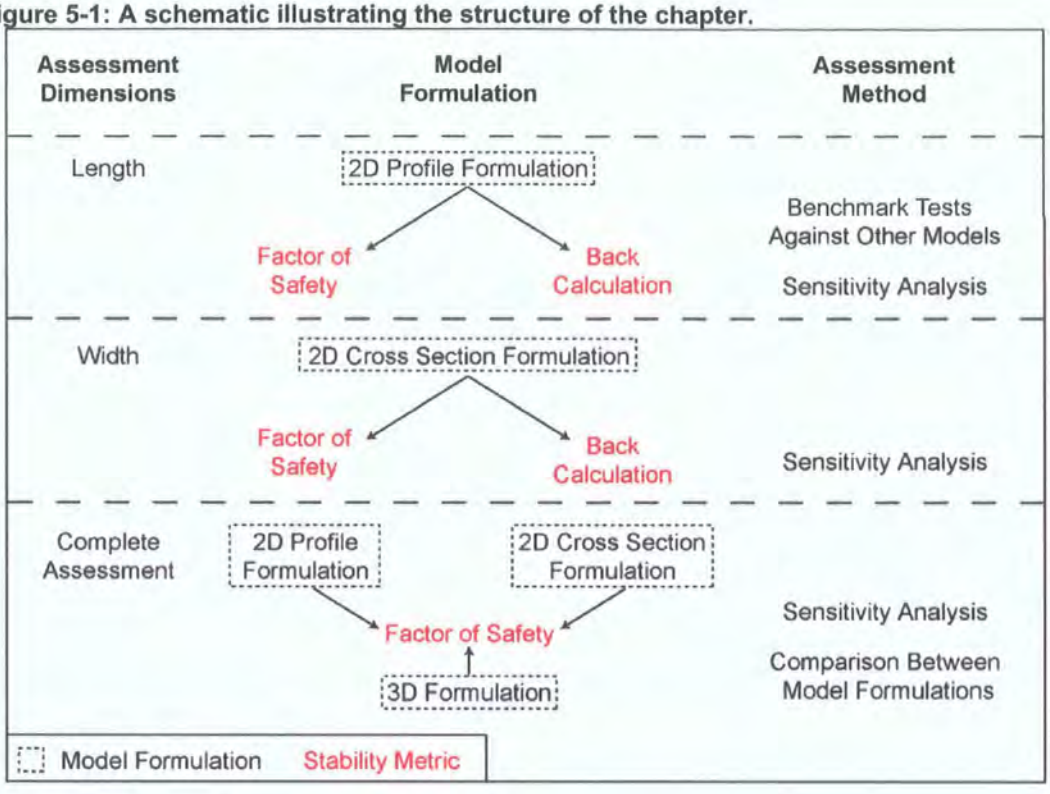

The Chapter sections follow the same structure. In Section 5.2 I introduce the key concepts: numerical experiments, sensitivity analyses and benchmarking. In Section 5.3 I detail the methodology for the numerical experiments on which this chapter is based, dealing first with the relevant details for benchmark testing before going on to describe the experimental design for the sensitivity analyses. The results Sections that follow are organised by the length scale on which their analysis is performed (Figure 5-1). In Sections 5.4 and 5.5 I report the results from analysis of a 2D profile formulation of the finite slope model. These include assessment of length effects on stability and of the ability of the finite slope model to reproduce benchmark predictions. In Section 5.6 I apply a two-dimensional cross section formulation of the finite slope model to assess the effect of block width on stability using both FoS and Back Calculation. In Section 5.7 I compare results from these two two-dimensional formulations for the same scenario in a complete assessment to establish the relative importance of each length scale. I then apply the full three-dimensional formulation of the finite slope model to establish the interaction between these controls. Finally, in Section 5.8 I draw together the key aspects of the results detailed above to address the aims of the chapter, in particular: establishing the effectiveness of the finite slope model and the control that a block's geometry exerts on its stability.

5.2. Background

Numerical experiments and sensitivity analyses fall between classic scenario based modelling and experimentation. Sensitivity analyses are the simplest form of analysis with a model, testing the model's response to variation in its components, boundary conditions or parameters. Numerical experiments use models as tools applying them within a well defined experimental design to test a set of hypotheses. In the context of this study I use the term numerical experiment to refer to the framework of my analysis (the scenarios or treatments that I compare) and sensitivity analysis to refer to the reaction of a model to variation in one of its parameters.

I am interested in the effect of a block's size and shape on its stability. This can be studied using sensitivity analysis with the newly developed model detailed in Chapter 4. However, before we can confidently apply such a sensitivity analysis we need to establish the level of confidence we can have in the model. This is difficult to achieve by comparing the model's stability predictions with observations because catchment slope stability observations are effectively binary (limited to stable or unstable). The situation is further complicated by the fact that the parameters involved are poorly constrained. Therefore any agreement or disagreement between predictions and observations cannot be solely related to the effectiveness of the model's process representation. An alternative approach is to 'benchmark' the new model against a single, or a group of, more accurate existing models. Although these are generally unsuitable for the task for which the new model has been developed, they overlap sufficiently to allow comparison with the new model within the same scenario. I will develop such an approach in Section 5.3.4.

No single existing model treats all of the effects tackled within the new model (Section 4.3). As a result, benchmarking requires a particular experimental design. The most distinctive aspect of the new model is its use of active and passive earth pressure theory to parameterise geometry effects at the upslope and downslope margins of a block of potentially unstable soil. This aspect is therefore in most urgent need of benchmarking. Two-dimensional limit equilibrium methods that calculate stability along a profile (given detailed information on the geometry of the surface and failure plane) have been applied

by geotechnical engineers for small scale site investigation. These are now considered accurate representations of the limit equilibrium mechanics of slopes in two dimensions (Bromhead, 1998). They are strong candidates for benchmarking the effectiveness of my parameterisation of the upslope and downslope margins. My parameterisation of the lateral edge effects is less distinctive, applying a similar method to those of other three-dimensional limit equilibrium approaches. Benchmarking this aspect of the model is both less vital and more difficult (since no more complete treatment is available). Therefore I do not undertake this.

5.3. Methodology

5.3.1. Scope of the Section

Both when benchmarking and when applying models in a sensitivity analysis, it is important to ensure that the comparison scenarios are consistent with those that the new model has been developed to represent. It is also important to explore the agreement between the models across the full range of scenarios in which we might aim to apply the new model. These considerations drive my experimental design for this study, the following sections detail and justify this design. The first three sections deal primarily with the methodology for the benchmark tests applied to the two-dimensional profile formulation of the Finite Slope model. In Section 5.3.2 I provide background information on the three groups of models compared in the benchmark tests: the candidate finite slope model, the benchmark methods of slices and the existing models for comparison. In Section 5.3.3 I introduce the stability metrics, explain their relevance and justify their application. In Section 5.3.4 I detail the experimental design for the benchmark tests, justifying it with reference to observations from Chapters 2 and 3. In Section 5.3.5 I describe the rationale for and structure of the numerical experiments and sensitivity analyses applied to understand the effects of block length and width on stability individually and in a complete assessment.

5.3.2. Model Choice and Formulation for Benchmark Testing

Benchmark testing involves two sets of models: the new model and the existing (benchmark) models against which they are to be compared. I describe these two sets below, describing the different treatments associated with the Finite Slope models that are being tested and justifying my chosen benchmark models. I finish with a brief note on two other models that are not used as benchmarks but to illustrate existing approaches against which my model is compared.

Candidate Model - Finite Slope Model

The Finite Slope model derived in Chapter 4 is formulated in three-dimensions, however to isolate the effect of length on stability and to allow the new model to be benchmarked against existing method of slices stability models it should be applied in two-dimensions to slope profiles. I reformulate the new model as a two-dimensional model of profile stability by assuming that the block of soil under consideration is infinitely wide (i.e. plane strain conditions). The profile model can then be split into two treatments, which differ in their representation of the driving force on the upslope margin of the block (Figure 5-2). First, the full Finite Slope (FSF) model resolves forces on all planes, including the upslope margin of the block, which is represented using active earth pressure. The second treatment represents the situation where there is a tension crack at the upslope margin of the block so that it is not influenced by the soil upslope of this margin. In this case stability is calculated from the resisting and driving forces neglecting those on the block's upslope margin; this is the Finite Slope model with a tension crack (FSTC). Each of these models incorporates a representation of model error by applying both Coulomb's and Rankine's earth pressure treatments to give upper and lower stability bounds (Figure 5-2).

Figure 5-2: A schematic showing the relationships between the four Finite Slope model treatments considered within the benchmark tests.

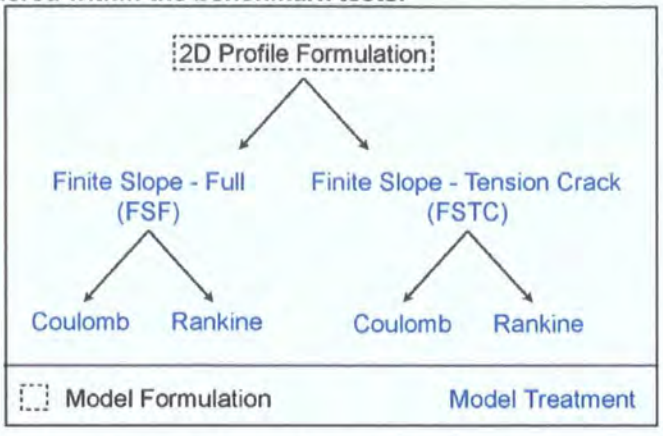

Benchmark Models - Spencer's and Sarma's Methods

Method of slices procedures are commonly applied by geotechnical engineers for site specific stability analysis (Brunsden, 1979). To establish the uncertainty in the method of slices predictions I perform each analysis using two procedures: the Spencer-Wright method (Spencer, 1967), and Sarma's (1973) method, which are considered two of the most rigorous limit equilibrium stability methods available (Abramson *et al.*, 1996). Presented together, these results act as both a check for gross errors in the model and as an estimate of the models' structural and functional uncertainty.

Models for Comparison – Infinite Slope and Ordinary Methods

Predictions from two other models are introduced in the analysis for comparison: the Infinite Slope method and the Ordinary method of slices (Fellenius, 1936). The Infinite Slope method is included as the current standard geotechnical representation for catchment stability modelling. The Ordinary method of slices is included because its three-dimensional extension (Hovland, 1977) has been applied in some catchment scale slope stability models (Section 4.3.1).

5.3.3. Stability Metrics

The stability of a slope can be quantified using: the factor of safety (FoS), or by back calculating the soil strength parameters required to maintain stability. In benchmark tests and sensitivity analyses that follow I use both metrics in combination.

The FoS represents the ratio of resisting to driving forces on a soil block (introduced in Section 2.6.3) changes in this metric are simple to interpret, allowing me to easily identify the most unstable failure plane form and assess the each model's effectiveness for a parameter set.

Back calculation involves holding the FoS constant (usually at the point of failure, FoS = 1) then rearranging the equations to solve for limiting input parameters, commonly the soil strength parameters: friction angle (φ) and soil cohesion (c_s). Plotting the limiting parameter combinations in terms of φ and c_s produces a curve. By comparing the form of φ c_s curves we can quantify the effects of other model parameters on stability in terms of soil strength. Distance towards the origin can be interpreted as an increase in stability with a magnitude that corresponds with the change in soil strength. Back calculation plots are less easily interpreted but provide more information on the behaviour of the slope at its point of instability across a range of soil strengths. These comparisons are particularly useful since they quantify slope length or model type effects in the units of an input parameter and therefore allow me to compare geometry effects with parameter uncertainty. Using this method I can begin to address questions like: How important is landslide size relative to variability in input parameters? Or, what is the importance of model error in the candidate (finite slope) stability models relative to the input parameter error?

5.3.4. Benchmark Tests - Design

I aim to represent observed landslides (discussed in Chapter 2) as closely as possible within the benchmark tests, whilst generalising them enough to ensure that they can be characterised by a small number of variables. The observed landslide scars are shallow (<2.3 m) and almost exclusively planar in profile, with very high radius of curvature (3–5 times scar length on average). Their form varies from wedge failures with no appreciable change in failure plane slope towards the toe, to trapezoidal failures with a distinct toe (Section 2.4.3).

To represent these characteristics I developed a synthetic landslide geometry with five parameters, varied over the course of the experiment: 1) slope length (l), from the head of the slide to the toe, where the failure plane returns to the

surface; 2) failure plane depth (z); 3) slope angle (β); 4) toe angle (λ); and 5) the saturation ratio (m, defined in Section 4.4.1). Each parameter can be altered whilst controlling for aspect ratio (l / z). A range of options are needed for landslide behaviour at the toe. We can simplify the landslide geometry by assuming that it is planar across the majority of its length and that this plane is parallel to the slope but we need to bring this failure plane to the surface at the toe. To simplify the scenario, ensure robust experimental design and minimise parameter covariance I applied the following rules:

1) slope length is measured along the surface from the head to the toe of the landslide (AD in Figure 5-3). It does not vary with toe angle;

2) failure plane depth is measured vertically from the surface to the failure plane;

3) the failure plane is parallel to the surface from the head to the start of the toe (BC);

4) the head is vertical (CD);

5) the phreatic surface is parallel to the ground surface at depth z-mz; and

6) the toe angle (λ) varies from 0-50°.

This toe angle is the angle of divergence of the failure plane at point B in Figure 5-3; λ = 0° indicates an un-divergent failure plane (where the toe is parallel to the failure plane upslope of B; λ = 50° indicates a very divergent trapezoidal toe (Figure 5-4). Because the length and depth must be independent of toe angle the angle is varied by changing the point on the failure plane at which the inflexion occurs (B in Figure 5-3). Scenarios with toe angles of 0° (no divergence) are wedge failures; as the toe angle increases to 50° the failure becomes more rectangular (Figure 5-4).

Figure 5-3: Schematic illustrating the rules applied to each failure surface scenario.

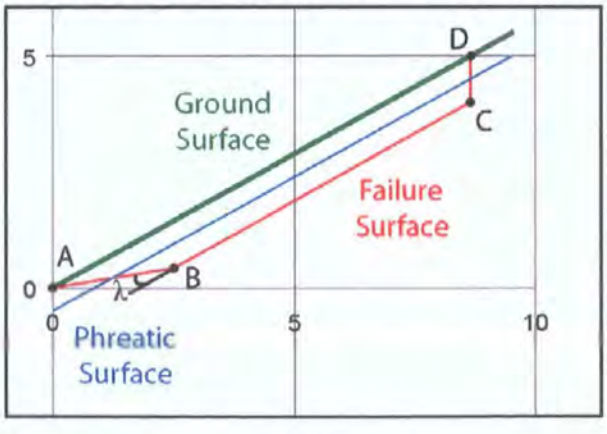

To effectively benchmark the models their agreement needs to be assessed across the full range of scenarios in which we might aim to apply them. These can be established from the characteristics of existing landslide scars (Table 5-1). Based on the central values and ranges from observed data I defined a set of parameter values designed to cover the range of potential scenarios and to focus on those that are most commonly encountered. While this approach cannot cover the full parameter space (this experimental setup requires >430 model runs, adding a single additional parameter costs a further 70-200 runs) it does represent the key characteristics encountered from field observation.

Table 5-1: The observed ranges of variables from the Lake District 2005 Landslide Inventory and the modelled values.

Variable	Observed Range	Observed Median	Modelled Values
Slope length (l)	2–90 m	18 m	10, 50, 100
Failure plane depth (z)	0.3–2.3 m	0.6 m	0.1, 0.2, 1, 2
Slope angle (β)	7–42°	25°	20, 30, 40
Toe angle (λ)	0–60°	18°	0, 10, 20, 30, 40, 50
Saturation (m)	0–1		0, 0.5
Aspect Ratio	7.7–5300	26	5, 10, 50, 100

We know from sensitivity analysis using the Infinite Slope method (Section 2.6.4) that the most important controls on stability are slope angle and pore water pressure. Therefore these variables need to be included in my analysis. The inclination of observed landslide scars ranges from 7–42°, with the majority falling between 20° and 40°. As a result, I modelled slopes with inclinations varying from 20–40° in 10° increments (Table 5-1). Slopes were tested in unsaturated and partially saturated conditions. Back calculation at existing landslide scars suggests that saturation ratios (m) greater than 0.5 are rarely required to initiate failure, and that larger values would require unrealistic material properties to maintain stability. As a result, a saturation ratio of 0 was used for unsaturated conditions and of 0.5 used to represent extremely wet slope conditions (Table 5-1).

Block size was varied on two length scales: length and depth across the full range of observed values. The effect of failure size on slope stability can be

represented either as an absolute or relative length (aspect ratio) allowing me to separate size and shape effects. Observed toe angles (angle of divergence between the failure plane and the toe, λ in Figure 5-3) range from 0–60° (Table 5-1). I apply toe angles from 0–50° to find the least stable toe geometry and compare this with observations from landslide scars (Figure 5-4).

Figure 5-4: Schematic representations of the method of slices input data for the numerical experiment showing variation in toe angles (A) 0, (B) 10, (C) 20, (D) 30, (E) 40, (F) 50 degrees.

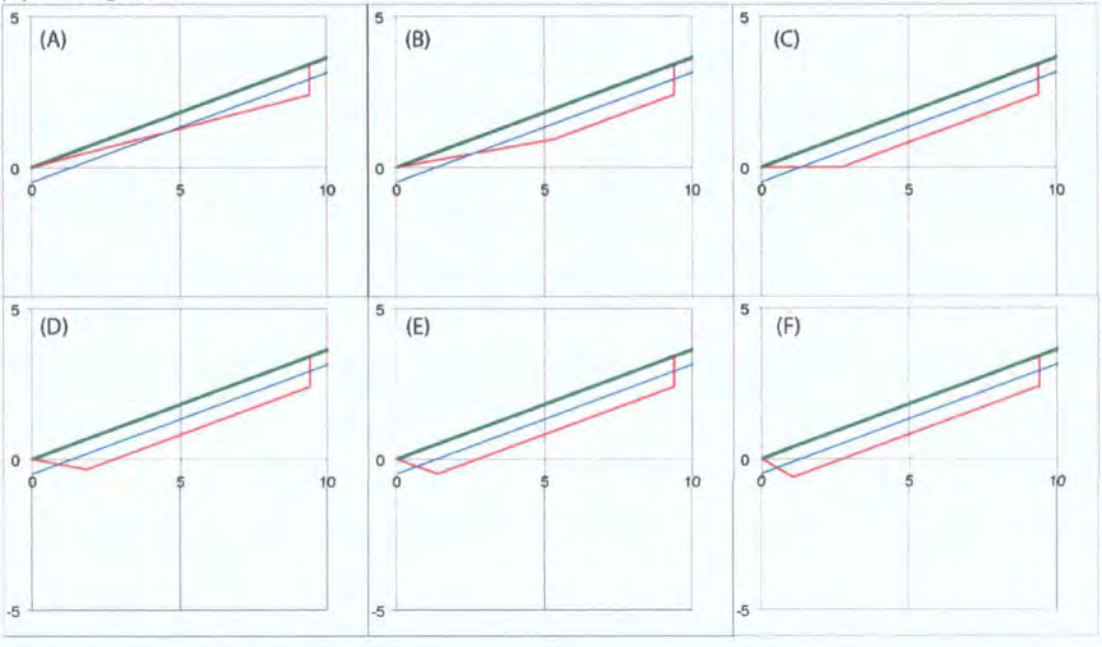

Soil strength properties are required to calculate the FoS but not for back calculation. I used two soil strength scenarios at the limits of those measured in my study area (Section 3.2). The soil strength properties were: $\varphi = 25.7°$, $c_s = 0.5$ kPa and $\varphi = 47.8°$, $c_s = 0.3$ kPa. For all experiments, the soil density was held constant at 1422 kg/m^3: the mean density from the Lake District landslides data, adjusted to account for a soil with both organic and mineral layers (Section 3.4). To maintain a simple experimental design and isolate differences in the model's representation of failure plane geometry effects root reinforcement was neglected. Given that these calculations are for landslide profiles and that observations suggest that very few roots penetrate the basal failure plane (Section 2.4.3) this is only a small simplification for my study area. The models were benchmarked in each scenario using a combination of FoS predictions and back calculated soil strength parameters as stability metrics (Figure 5-5).

Inevitably, in each case only part of the parameter space can be sampled. Considering the parameters in Table 5-1 alone, >430 model runs are required to carry out the analysis. The full experimental design including different soil strengths; and stability metrics involved >1000 runs for each model. The addition of only one further value to one of the parameters under consideration would require 200-500 further runs. Instead, I have chosen to focus on particular scenarios or parameter ranges that represent typical or end member situations for my study area. These scenarios are designed based on observations (Chapter 2) and measurements (Chapter 3) from my study area. Even this reduced parameter space cannot be fully illustrated and discussed here. Instead I will illustrate the trends and properties of the models' behaviour with key examples.

5.3.5. Sensitivity Analysis and Numerical Experiment - Design

To isolate the effects of length and width on stability I analyse these individually, then compare them before applying the full three-dimensional formulation (Figure 5-5).

Figure 5-5: A schematic illustrating the structure of the numerical experiments, which are grouped into length, width and complete assessments. Vegetation types 1-3 are *Eriophorum*, *Pteridium* and *Juncus* respectively, Cr scenarios 1-3 are full depth, partial depth and power law representations.

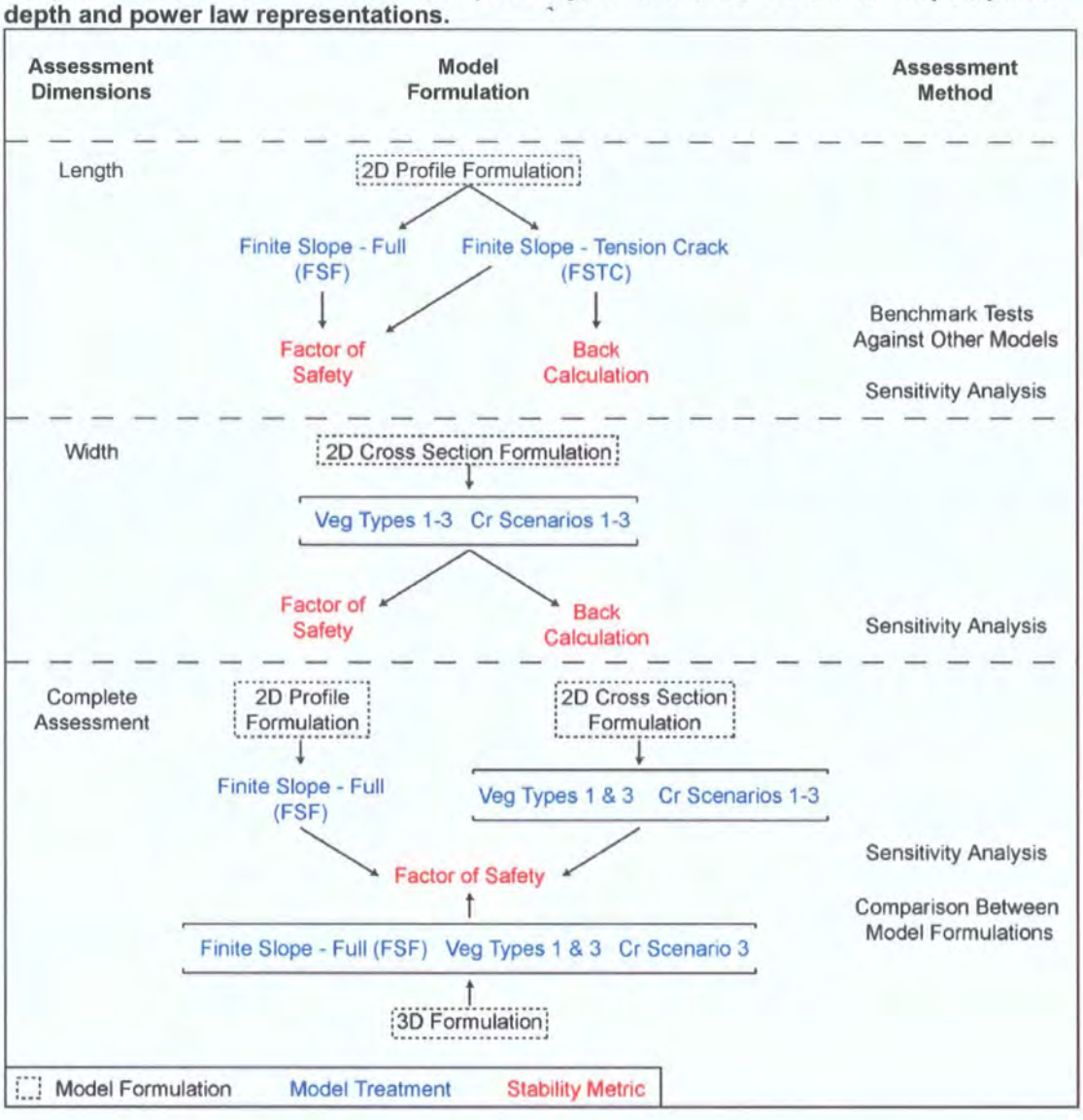

Length Effects

The experimental design that I have applied to establish the effect of block length on stability is closely related to the design of the benchmark tests (Section 5.3.4). I reformulate the Finite Slope model to predict the stability of a two-dimensional slope profile (as discussed in Section 0), then run the model for scenarios designed to both establish the effectiveness of the new model and to understand the relationships between block length and stability under a range of conditions. Because the benchmark tests need to cover the range of potential conditions that the model might need to represent these experimental designs

mesh closely. In the following results sections I will deal with length effects on stability and the effectiveness of the Finite Slope model in parallel.

Width Effects

My analysis of width effects focuses on the stabilising influence of lateral root cohesion and friction on the block's margins, both individually and in combination. The experimental design reflects this focus. I reformulate the Finite Slope model again, this time to predict the stability of a block that is infinitely long, but with a defined cross section. This approach is conceptually similar to that of Gabet and Dunne (2002). However, my approach differs because I conceptualise lateral resisting forces as a combination of friction effects and the additional strength provided by roots crossing the lateral failure planes (Section 4.4).

Root cohesion data collected for three of the most common vegetation types in the study area (*Juncus effesus*, a water loving reed; *Pteridium aquilinum,* a winter deciduous fern; and *Eriophorum vaginatum*, a perennial herbaceous sedge) can be applied to predict lateral root cohesion (Section 3.3). I apply average root cohesion estimates from each of these vegetation types as three different scenarios to represent the conditions in my study area (Figure 5-5). Root cohesion (calculated as a force per unit area) needs to be integrated over the depth of the block to convert it to a force per unit length. Two approaches are commonly adopted in the literature. Both assume uniform root cohesion with depth: one applies the cohesion over the block's full depth (Casadie *et al.*, 2003; Gabet and Dunne, 2002); the other assumes that the failure plane is below the rooting depth and applies the cohesion only over that depth (Burroughs, 1985). Here I have adopted a third approach based on the observation that root cohesion is often linearly correlated with root density, which tends to decrease as a power function of depth (see Section 1.3.3). The implications of the three representations for root reinforcement per unit perimeter length have been briefly examined in Section 1.3.7. In the following analysis I will apply each treatment to establish their impact on predicted stability across a range of scenarios (Figure 5-5).

In each case I compare the stability of the block using:

1) Infinite Slope predictions (always independent of block width);
2) the Finite Slope model accounting for only the stabilising effect of lateral roots;
3) the Finite Slope model accounting for only the friction effects; and
4) the Finite Slope model accounting for both root reinforcement and friction effects.

Scenarios 3 and 4 are split again into the friction effects assuming 'at rest' or active earth pressure on the block's lateral sides, which represent upper and lower bound reinforcement estimates respectively (Figure 5-6).

Figure 5-6: Treatment diagram illustrating the different scenarios for FoS prediction in terms of their model framework, treatment of lateral reinforcement and earth pressure.

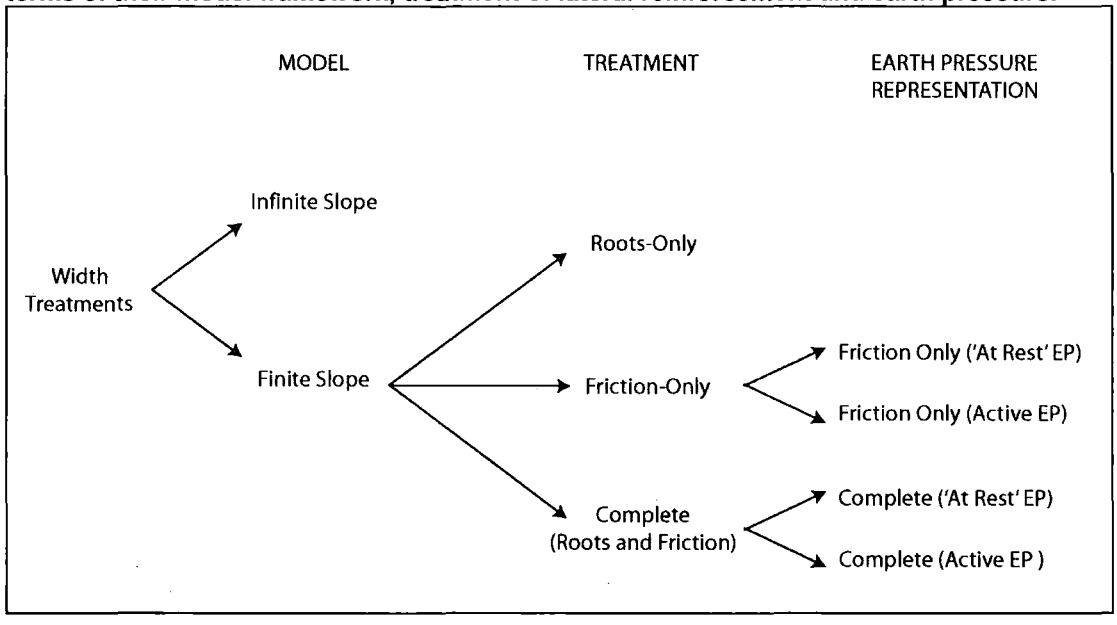

Complete Assessment

Two-dimensional profile or cross section formulations of the Finite Slope model can indicate the influence of length or width on stability and establish the variation in these controls as the block's other properties vary. The relative importance of length and width in defining stability is also interesting, since this might indicate some intrinsic mechanical control on landslide geometry. I compare stability predictions (in terms of factor of safety) from the Finite Slope model in its two two-dimensional forms for the same scenario to assess the relative importance of length and width effects (Figure 5-5). By altering the scenario (e.g. stronger roots or a shallower block) I can identify the factors that control the relationship between these two length scale controls on stability. Finally, by formulating the model in three-dimensions (Figure 5-5) I can consider both the relative importance of width and length and the interaction between them in defining a block's stability.

5.4. Length Effects - Factor of Safety Results

5.4.1. Scope of the Section

In this section I analyse results from a two-dimensional profile formulation of the Finite Slope model to characterise length effects on stability and establish the effectiveness of the Finite Slope model. I focus on factor of safety (FoS) results here, reporting benchmarking and sensitivity analysis in parallel since these results have implications for both applications. I begin by studying the length effects on stability that are identified by the method of slices stability analyses used to benchmark the Finite Slope model (Section 5.4.2). In Sections 5.4.3 and 5.4.4 I examine the effect of block length on stability in unsaturated and partially saturated conditions respectively for a range of slopes and soil strengths. In each case I compare the Finite Slope model predictions with those from existing analytical models and benchmark stability estimates. In Section 5.4.5 I apply the same framework to identify the effect of varying failure plane depth on stability predictions from the same group of models. Finally, in Section 5.4.6 I compare the predictive power of the Finite Slope model in its FSF and FSTC forms with the effectiveness of Infinite Slope and Ordinary methods (in terms of their ability to reproduce benchmark estimates).

5.4.2. Length Effects in Benchmark Models - Figure 5-7

For unsaturated soils there are consistent relationships between slope length, toe angle and FoS predicted using method of slices stability analyses. The pattern of FoS in response to changing toe angle follows a consistent trend for both Sarma and Spencer methods across different soil strengths, slope lengths and inclinations. FoS are highest at extreme toe angles (0° and 50°) and converge to a minimum at a toe angle of either 10° or 20° (Figure 5-7). In every case, the trends are attenuated (the variability in FoS with λ is reduced) as landslide length is increased. FoS for wedge failures (λ=0°) is always larger than for λ=10°. FoS at λ=50° is almost always greater than that at λ=0°. Since failure will occur at the least stable geometry (that with the lowest FoS) these least stable toe angles can be compared with toe angles at landslide scars. The toe angles predicted by the model are within the range of those recorded in the Lake District 2005 Landslide Inventory (Section 2.4.3). For n=62 landslides the mean measured toe angle was 10.8°, with a standard deviation of 9.4°. The least stable toe angles are also the most interesting and important for comparison with other predictions. Further analysis will use the least stable geometry in every case.

Comparing the results from the two methods of slices, Spencer's method almost always predicts a lower FoS than Sarma's. When it does not, this is generally the result of numerical errors in one or other of the models (e.g. toe angle of 50° in Figure 5-7E). The difference between the two models tends to increase with increasing FoS, suggesting that Sarma's method is more sensitive to variations in toe angle than Spencer's method. The extent to which Sarma's method is more sensitive than Spencer's varies with slope: Sarma's method becomes increasingly sensitive relative to Spencer's as slope increases.

The difference between minimum FoS for blocks 10 m long and those that are 50 m long is larger than the difference in FoS from the two different methods for a given block length (Figure 5-7). In this case, the variability between models can be used as a measure of model uncertainty so that we can reasonably suggest that for blocks shorter than or equal to 10 m there is a significant length influence on stability in comparison to model uncertainty. This is not the case for

longer blocks. There is more variability between the FoS due to different methods than variability between FoS using each method for blocks of 50 m compared to 100 m. It is reasonable to suggest that for blocks longer than 50 m the length effect is small in comparison to model error.

The Infinite Slope method almost always provides the lowest (least stable) FoS for each slope. This is a good check on the performance of the other models since for translational slides the Infinite Slope method should be accurate if edge effects are neglected. Exceptions are either the result of numerical errors in the method of slices (e.g. toe angle of 50° in Figure 5-7C) or slight differences in representation of the failure geometry (e.g. toe angles of 10° and 20° in Figure 5-7A). Long slopes are particularly susceptible to these effects since edge effects have already been minimised and very similar FoS predictions would be expected.

Figure 5-7: FoS predictions using method of slices and Infinite Slope approaches for different slope lengths, slope angles and material properties. Plots A, C and E are for slopes at 20, 30 and 40° respectively with unsaturated soil. B, D and F are the same but for partially saturated soil (m=0.5). Note different scales on y axes.

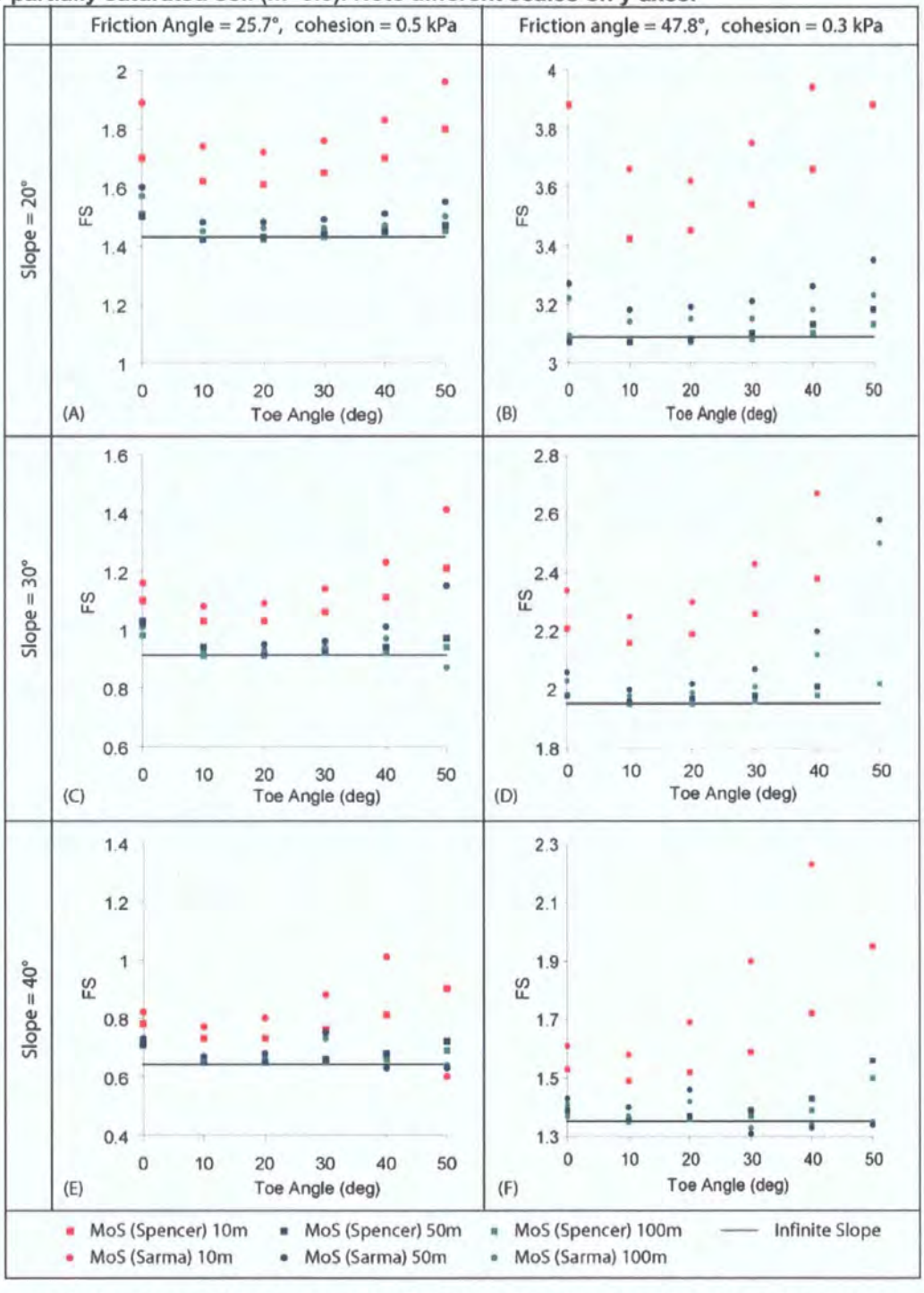

Although the form of the toe angle FoS relationship remains broadly similar with variation in other parameters, there are some key differences (Figure 5-7). The toe angles at which the FoS is lowest varies very little with slope angle or soil strength, remaining in the range 10-20° and very large toe angles are always stronger than very small angles. However, the relationship becomes increasingly asymmetrical as slope angle increases or for stronger soils (B D

and F in Figure 5-7). In these conditions (e.g. Figure 5-7F) the difference between steep and shallow toe angles becomes particularly accentuated.

5.4.3. Length Effects on Unsaturated Slopes - Figure 5-8

The influence of length on FoS at the least stable toe angle tends to increase slightly with increased soil strength or decreased slope angle. These relationships are difficult to untangle with the data presented in this form (Figure 5-7). Figure 5-8 presents the same data taking only the minimum FoS and plotting these against block length. This also allows easy comparison with other less complete stability models. These models can be solved analytically so that they return a far denser dataset for FoS against block length. Figure 5-8 shows the FoS for blocks of lengths from 1–100 m predicted using methods of slices, Infinite and Finite Slope methods. Points indicate the location in parameter space at which benchmark models were used and their FoS estimates. The red line represents predictions from the Ordinary method of slices. The blue lines on Figure 5-8 represent FoS predictions from the Finite Slope model.

The results from the numerical experiment using methods of slices suggest an exponential decline in FoS with block length (Figure 5-8). This effect is largest for short blocks and negligible for blocks longer than 50 m where the method of slices FoS converge on the Infinite Slope predictions. The Ordinary method is very similar to the Infinite Slope method in every case; edge effects in this model are negligible. Both the Ordinary and Infinite Slope methods perform well for slopes longer than 50 m; however, they perform poorly for short blocks under-predicting FoS by between 5 and 15% at 10 m block length.

The Infinite Slope FoS is invariant with length, plotting parallel to the x-axis and is lowest in almost every case (Figure 5-8). The Ordinary method predicts FoS that differ very little from the Infinite Slope method. The curves converge on the Infinite Slope predictions at lengths between 20 and 100 m. Four Finite Slope models are reported here, the light blue lines indicate results from the FSF model (resolving forces on all planes); the dark blue lines represent the FSTC model (assuming a tension crack at the upslope edge of the block). Each of these include an envelope of model uncertainty by applying Coulomb's and

Rankine's earth pressure treatments. Coulomb FoS estimates are always higher than Rankine estimates and the FSTC predictions are always higher than those from the FSF. Aside from these constraints there is considerable variation in relative and absolute FoS length relationships as the other parameters are varied. The difference between Coulomb and Rankine earth pressures; and therefore, the size of the uncertainty band, increases with slope.

Figure 5-8: Plots of FoS against block length for unsaturated soil, predicted using Spencer and Sarma methods as benchmarks and four analytical models: the Infinite Slope and Ordinary methods, and the new Finite Slope model in full (FSF) and with a tension crack at the upslope margin of the block (FSTC). Plots A, C and E are for slopes at 20°, 30° and 40° respectively with a friction angle of 25.7° and cohesion of 0.5 kPa. B, D and F have a friction angle of 47.8° and cohesion of 0.3 kPa. Note different scales on y axes.

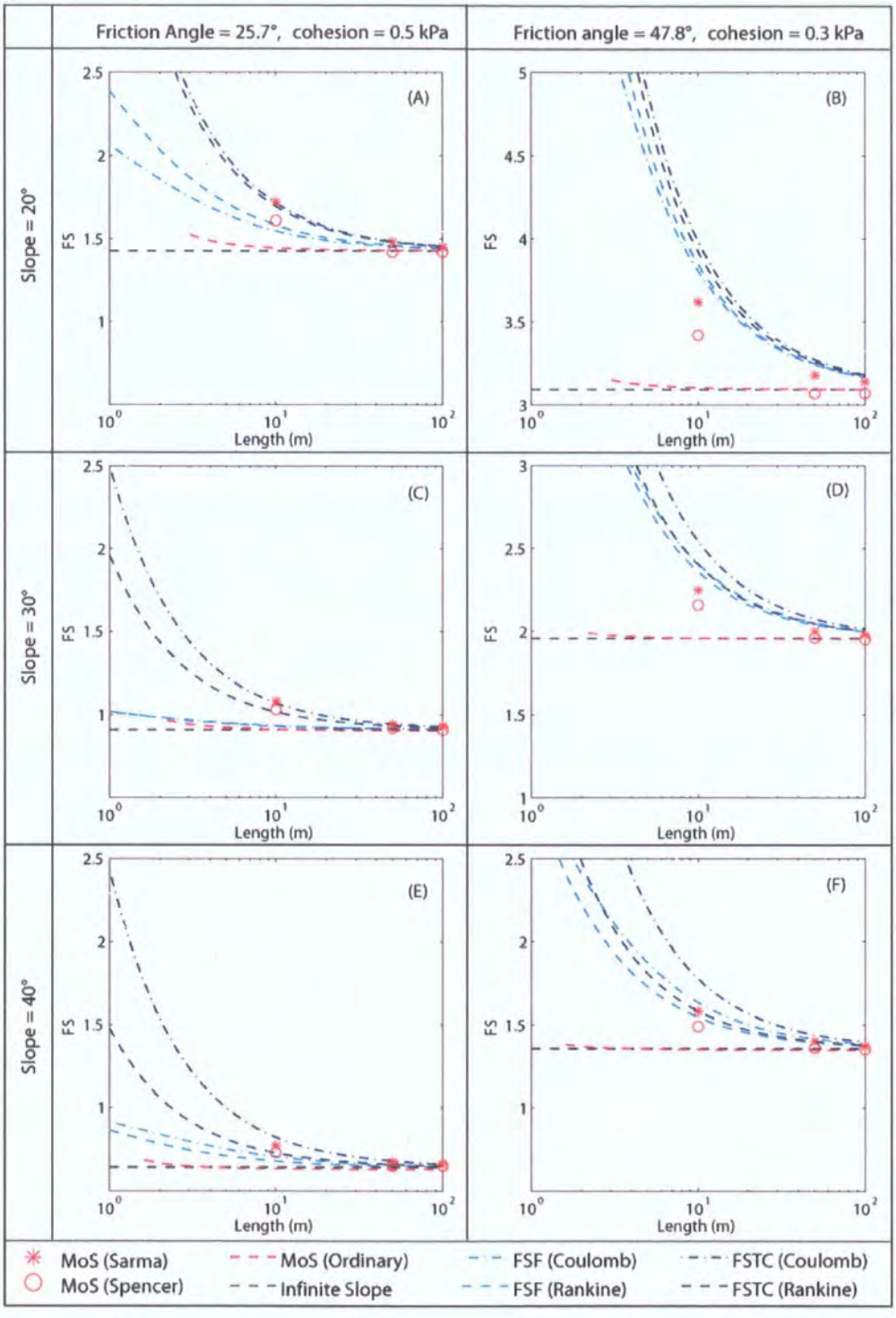

For **weaker soils** (friction angle = 25.7°) at low slopes (20°), predictions from the FSTC model correspond closely to the predictions from Sarma's method of

slices at all lengths (Figure 5-8A). As the slope is increased from 30° to 40°, the upper bound stays relatively constant but the lower bound drops by up to 25% (Figure 5-8 C and E). The method of slices stability predictions from both models fall within the envelope of FoS predicted by the FSTC model.

The FSF model predicts a moderate decline in FoS with length for low slopes (Figure 5-8A). It predicts FoS similar to those from Spencer's method of slices for all three lengths. When the slope becomes steeper than the friction angle both the magnitude of the FoS and its decrease with length are reduced considerably (Figure 5-8 C and E). For blocks longer than 10 m inclined at 30°, FoS predictions from the FSF model converge on those from the Ordinary method and the Infinite Slope method. Predicted FoS correspond well with those from the methods of slices for long (50 and 100 m) but not short (10 m) blocks. At very steep slopes (40°), the effects of the edges in the FSF model begin to increase once again although the relationship between length and FoS remains weak in comparison to the FSTC model (Figure 5-8 E). Both method of slices FoS agree well with FSF predictions at 50 and 100 m block lengths, at 10 m the FSF FoS is just below that of Spencer's method of slices.

For **stronger soils** (friction angle = 47.8°), Infinite Slope and Ordinary methods behave as for weaker soils (Figure 5-8 B, D and F). Both the method of slices and the Finite Slope FoS are more sensitive to changes in block length but the Finite Slope models are more sensitive than the methods of slices. The FSTC model tends to over-predict FoS at a given length. The FSF model slightly over-predicts FoS but performs best in almost every case, effectively capturing the FoS from Sarma's method of slices on steep slopes (40°; (Figure 5-8 F).

The benchmark models agree more closely with the Finite Slope models than with the Infinite Slope or Ordinary methods. In some cases, they agree most closely with the full representation (FSF) and in others with the version that assumes no influence from upslope material (FSTC). In general, these models tend to under-predict stability for weaker soils and over-predict for stronger soils. The FSTC model gives the best approximation to the benchmark FoS for weak soils while the FSF model appears most effective for strong slopes. These models provide a reasonable approximation of FoS predicted by the benchmark

approaches and allow us to form a more comprehensive picture of the relationship between FoS and length. The models predict exponential decrease in FoS as block length increases. This has important implications for minimum landslide length, since for blocks of 2 m length FoS can be >100% larger than that at 20 m length. These results fit observations from my study area where for soils ~1 m deep, landslides <8 m long are rare, suggesting that there remains a length control on block stability at this scale. However, these calculations suggest that for blocks longer than 12 m, the length effect is limited.

5.4.4. Length Effects on Partially Saturated Slopes - Figure 5-9

UK landslides are driven almost exclusively by changes in pore pressure; therefore it is important to examine the length effects for partially saturated slopes. However, these conditions are more difficult to model with method of slices approaches and can lead to numerical errors and uncertainty in the results. The same numerical experiment detailed above was conducted for partially saturated slopes. However, careful analysis of model results and of the accompanying meta-data suggested that many of the FoS were unreliable, as a result of numerical errors (Clover Technology pers. comm.).

For partially saturated slopes (Figure 5-9), the relationships between FoS and length for each model follow very similar patterns to the unsaturated case. All models except the Infinite Slope method (which is invariant with length) follow an exponential decrease in FoS with increasing block length. Key differences from the unsaturated scenarios are that the Ordinary and FSF models have become increasingly sensitive to block length. The decreased sensitivity of the FSF model to length once slope exceeds friction angle (Figure 5-9 C and E) is likely to be a result of the earth pressure parameterisation within the model. Calculating earth pressure on a sloping surface once slope becomes equal to friction angle, both active and passive earth pressures become constant values so that when both are applied to the block they cancel one another.

Figure 5-9: Plots of FoS against block length for partially saturated soil (m=0.5) from four analytical models: the Infinite Slope and Ordinary methods, and the new Finite Slope model in full (FSF) and with a tension crack at the upslope margin of the block (FSTC). Plots A, C and E are for slopes at 20°, 30° and 40° respectively with a friction angle of 25.7° and cohesion of 0.5 kPa. B, D and F have a friction angle of 47.8° and cohesion of 0.3 kPa. Note different scales on y axes.

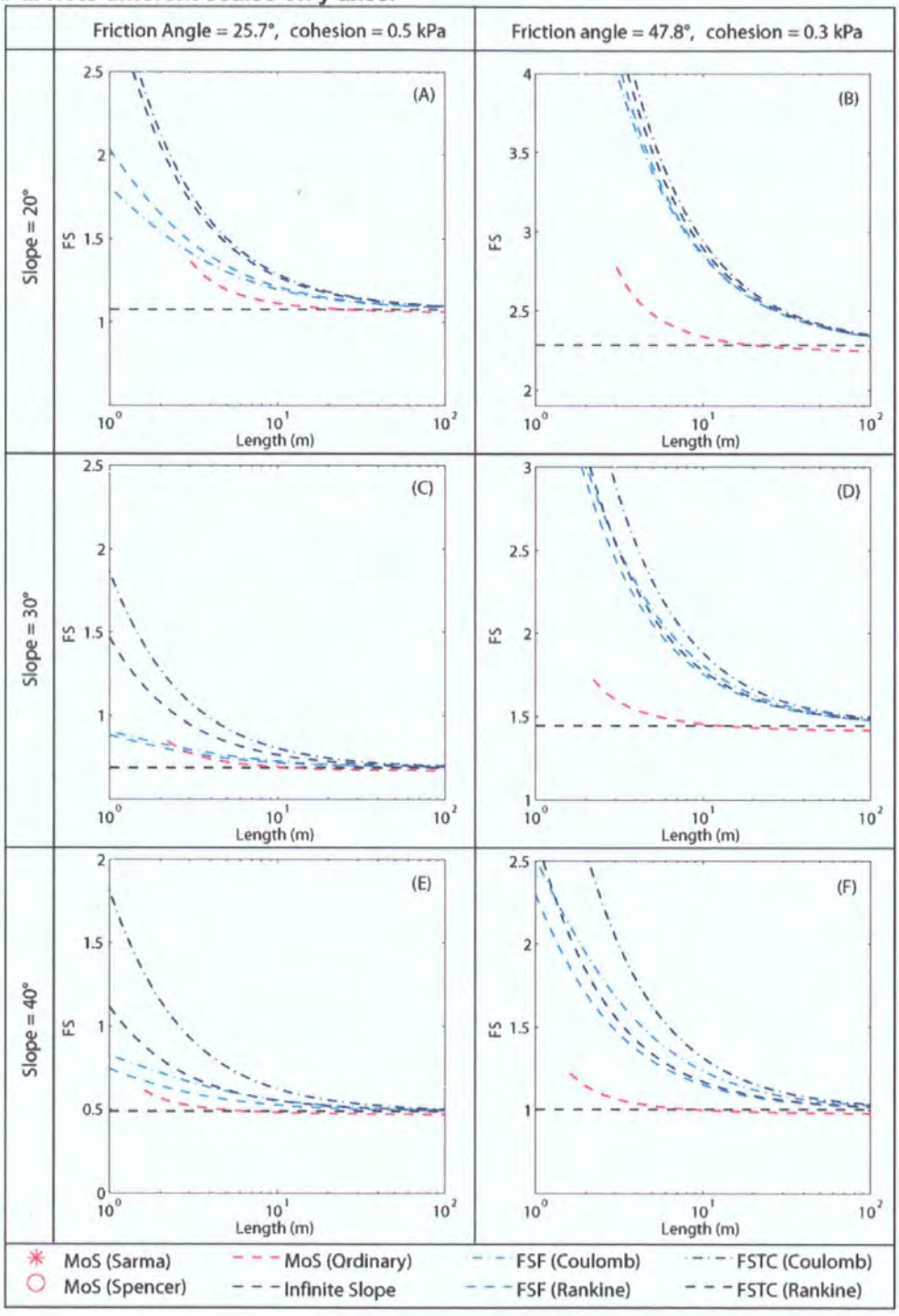

5.4.5. Length Effects for Varying Soil Depths - Figure 5-10

Increasing the depth of the block increases the sensitivity of FoS to length (Figure 5-10). The method of slices FoS are unchanged at 100 m. They

increase slightly at 50 m and significantly at 10 m. The form of the curves for the other models remains unchanged but their location on the x-axis is shifted to increased lengths. The FSTC model remains an extremely effective stability predictor with reference to the benchmark values (Figure 5-10 A and C).

Figure 5-10: Plots of FoS against block length for slopes where φ=25.7, c=0.5 kPa. Predicted using Spencer and Sarma methods as benchmarks and four analytical models: the Infinite Slope and Ordinary methods, and the new Finite Slope model in full (FSF) and with a tension crack at the upslope margin of the block (FSTC). Plots A and C are for depths of 1 and 2 m respectively with unsaturated soil, B and D are the same but for partially saturated soil (M=0.5).

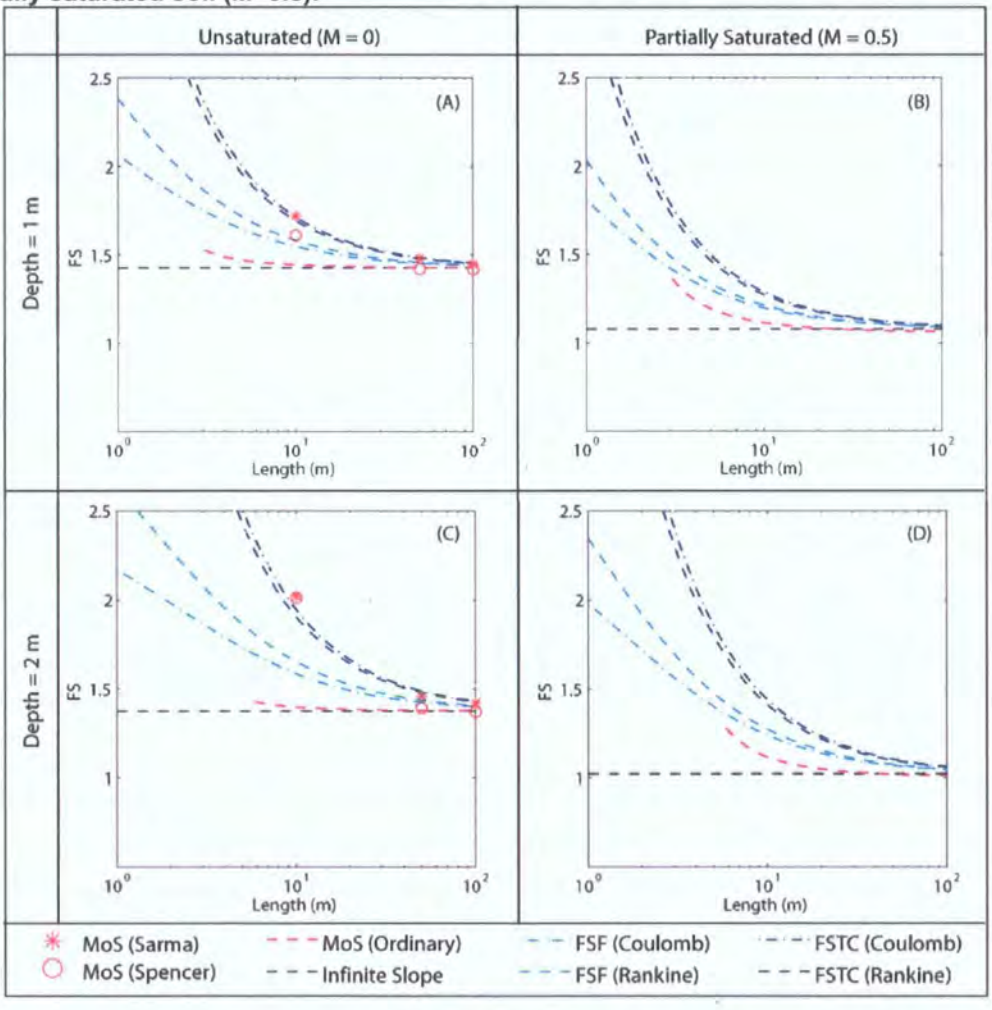

5.4.6. Comparing the Predictive Power of Analytical Methods

The Ordinary method consistently under-predicts stability, rarely differing from the Infinite Slope method. As a result, its predictions are often effective at 50 m and 100 m where the Infinite Slope method performs well but rarely so at 10 m (arguably where its representation matters most). This method does not capture the influence of length on stability. The envelope delimited by the new methods

effectively reproduces many of the benchmark stability estimates. However, stability estimates differ significantly between the FSF and FSTC versions. In some cases FSF predictions are very similar to those from the Ordinary method (Figure 5-9C), in others the FSTC model can predict extremely rapid increases in FoS with decreased length (Figure 5-9B).

Analysing all scenarios from the numerical experiment, we can compare stability predictions from the candidate (FSF and FSTC) and comparison (Infinite Slope and Ordinary) models with benchmark values (Figure 5-11). The results suggest that Infinite Slope and Ordinary methods under-predict stability in many cases (Figure 5-11 A and B). The magnitude of the under-prediction can be up to 1FoS. The Finite Slope models provide a good fit to the benchmark data and represent improvements on the previous options both when full force balance is used (Figure 5-11C) and when a tension crack is assumed at the upslope margin of the block (Figure 5-11D).

Figure 5-11: FoS from analytical models plotted against benchmark values for all dry slope scenarios in the numerical experiment. The black 1:1 line on each plot indicates perfect agreement. Plots show results for: A) the Ordinary method of slices; B) the Infinite Slope method; C) The new full Finite Slope model (FSF); and D) the new Finite Slope model assuming a tension crack at the upslope margin of the block (FSTC).

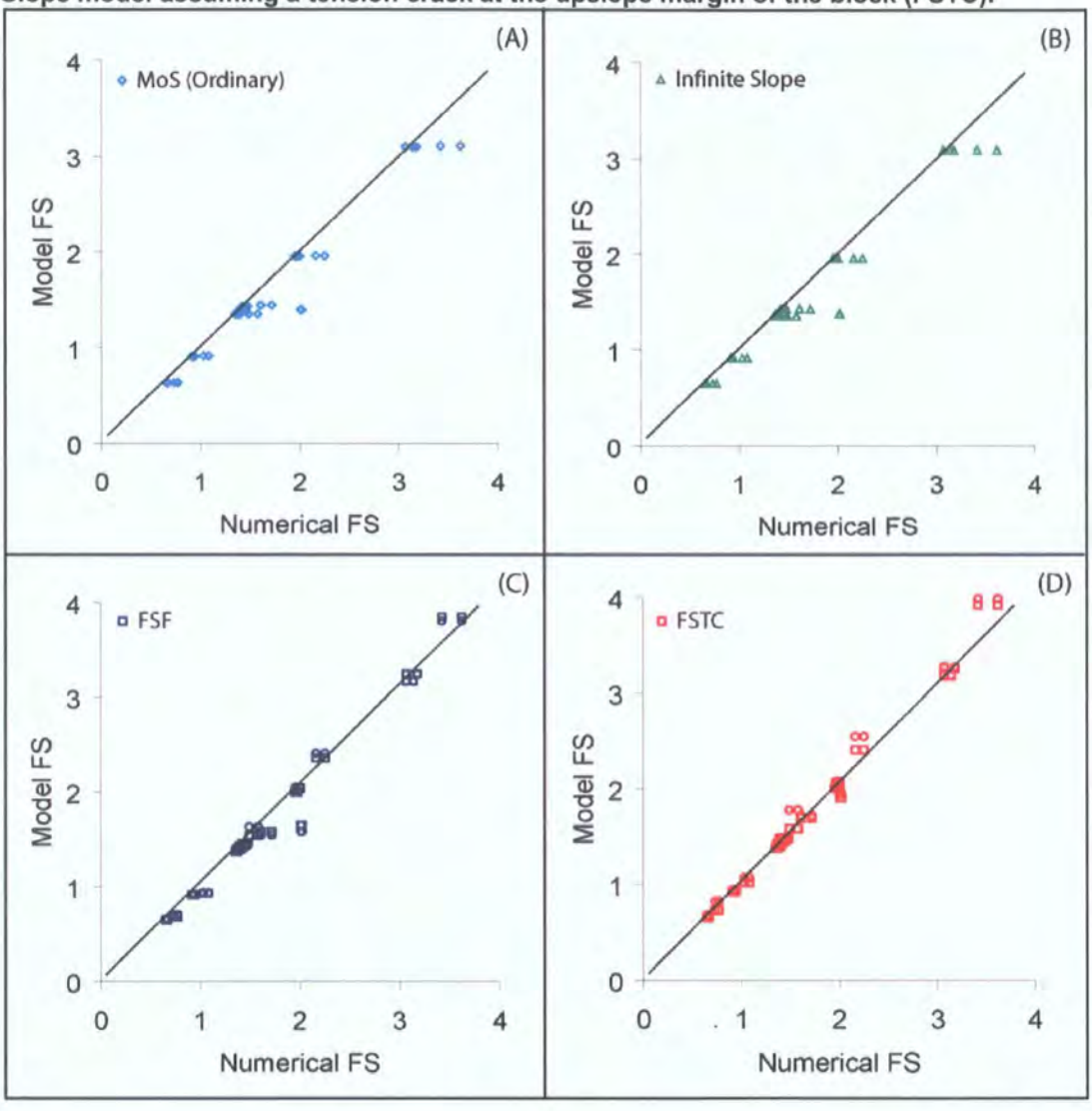

The FSTC model appears to provide a slightly better fit to the data and has a higher r^2 value (r^2=0.989). This may be the result of the assumed vertical scar head in the numerical experiment, preventing active pressures from developing in this zone. However, because the benchmark models also contain some error and because deviation from the 1:1 line is of interest in this case, a concordance correlation coefficient (Lin, 1989, 2000) is the most effective measure of agreement. Concordance correlation suggests that the full Finite Slope FoS agrees most closely with benchmark predictions.

Table 5-2: Agreement statistics for the relationship between predicted FoS from the analytical and benchmark methods. The Full Finite Slope model (FSF) performs best according to the concordance correlation coefficient and the Finite Slope model assuming a tension crack (FSTC) performs best according to linear regression.

	n	Concordance Correlation Coefficient	Reduced Major Axis		Linear Regression		
			Slope	Intercept	r^2	Slope	Intercept
Ordinary MoS	39	0.977	0.95	-0.013	0.971	0.94	0.009
Infinite Slope	39	0.975	0.94	-0.002	0.969	0.93	0.022
FSF	78	0.990	1.09	-0.118	0.987	1.08	-0.106
FSTC	78	0.987	1.10	-0.087	0.989	1.09	-0.078

5.5. Length Effects - Back Calculation Results

5.5.1. Scope of the Section

In this section I quantify the effect of a block's length on its stability using back calculation and compare predicted stability from Finite Slope models with those from the benchmark methods. I focus on the full finite slope model formulation (FSF), since this has performed well in FoS analysis and is a more complete treatment of the forces acting on the block than the FSTC model.

Back calculation quantifies instability in the units of an input parameter. This is useful because it allows me to compare the changes in stability resulting from alterations to the block geometry or model formulation with parameter uncertainty. Back calculation represents the limiting parameter combinations in terms of a plot of friction angle on the y-axis against soil cohesion on the x-axis (Figure 5-12); initially these can be difficult to interpret. However they are powerful since: by comparing the form of φ c_s curves we can quantify the changes in stability resulting from alterations to the block geometry or model formulation in terms of a measureable parameter. Distance towards the origin can be interpreted as an increase in stability with a magnitude that corresponds with the change in soil strength. If cohesion is held constant, an increase in φ corresponds to an increase in the friction angle required to maintain stability. If the friction angle is held constant, an increase in c_s corresponds to an increase in the soil cohesion required to maintain stability.

The structure of this section is similar to that of Section 5.4. I look first at the results from the benchmark models (Section 5.5.2), before comparing these with Finite Slope model's predictions for different slope lengths and inclinations (Section 5.5.3). Then, in Section 5.5.4, I introduce variation in the depth of the failure plane and assess the effect that this has on model representation and size effects. These size effects are complex since length and depth interact to control both the size and shape of the block; I isolate them in Section 5.5.5 and deal with each individually. Finally, in Section 5.5.6, I summarise the results from both back calculation and FoS analyses, using them to address two key questions: how important are length effects on stability? and how representative is the Finite Slope model?

5.5.2. Length Effects in Benchmark Models

Strength properties were back calculated using Spencer's and Sarma's methods for each of the scenarios examined in the numerical experiment introduced in Section 5.4. The effect of toe angle on stability followed a similar pattern to that identified by studying FoS: the least stable geometries were always for toe angles between 10° and 20°. Figure 5-12 shows an example plot for back calculated limiting strengths (φ and c_s) from a single scenario with a range of toe angles. As toe angle is increased from a wedge failure (0°), the friction angle or soil cohesion required to maintain stability increases, indicating that the geometry is less stable. This trend continues to a maximum required soil strength (least stable geometry) at a toe angle of 20°, after which the required soil strength begins to decrease again indicating that the geometry is becoming increasingly stable. A second visible trend as toe angle increases is the decreasing slope of the cohesion friction angle relationship, indicating that as toe angles become steeper stability becomes increasingly sensitive to friction angle and less sensitive to soil cohesion. Because failure can be assumed to occur at the least stable geometric configuration of the failure plane, the following analysis uses only the data from these least stable geometries (toe angles of either 10° or 20°).

Figure 5-12: Back calculated soil strength parameters (for FoS = 1) for a 10 m slope at an angle of 20° and with toe angles from 0–50° under unsaturated conditions.

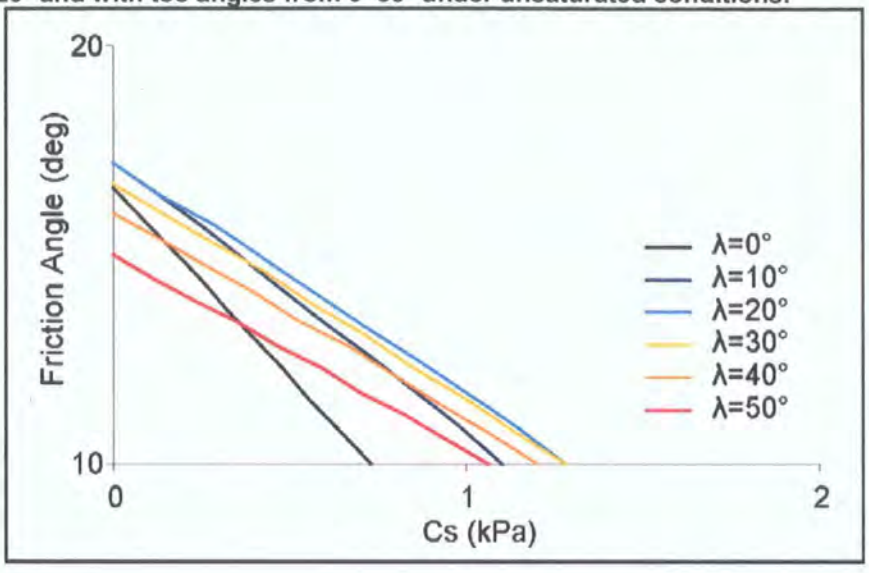

5.5.3. Length Effects on Unsaturated Slopes

Quantifying stability in φ c_s space allows us to examine the trends identified in the FoS analysis over the full range of soil strengths for unsaturated slopes. Back calculated values from Sarma's and Spencer's methods were unreliable for certain configurations of partially saturated slopes and are not discussed here. The relative relationships between slope length and stability are as expected from the FoS analysis, with 10 m slopes most stable and 100 m slopes least stable (Figure 5-13). The difference in stability between 10 and 50 m is very large relative to that between 50 and 100 m, indicating that the influence of slope length decreases with length and is small for lengths of more than 50 m. A reduction in slope length from 50 to 10 m increases stability by the equivalent friction angle of 1.7°–9° or cohesion of 0.4–1.6 kPa depending on the configuration of the other parameters. These differences due to slope length are large relative to the differences between algorithms applied for each method (Spencer versus Sarma for the method of slices; Coulomb versus Rankine for the Finite Slope model). The differences between Spencer's and Sarma's methods range from 0.2°–1.9° φ or 0.1–0.3 kPa c_s; those between Rankine and Coulomb methods range from 0.1°–4° or 0.01–0.70 kPa. These values represent differences across a range of slope lengths and angles. In particular, differences increase with increased slope. This increase is small for the method of slices but large for the Finite Slope model (Figure 5-13).

Figure 5-13: Back calculations of Soil cohesion (c_s) and friction angle (phi) at FoS = 1 using method of slices, infinite and Finite Slope stability procedures for an unsaturated slope of lengths 10, 50 and 100 m and angles of (A) 20, (B) 30 and (C) 40°.

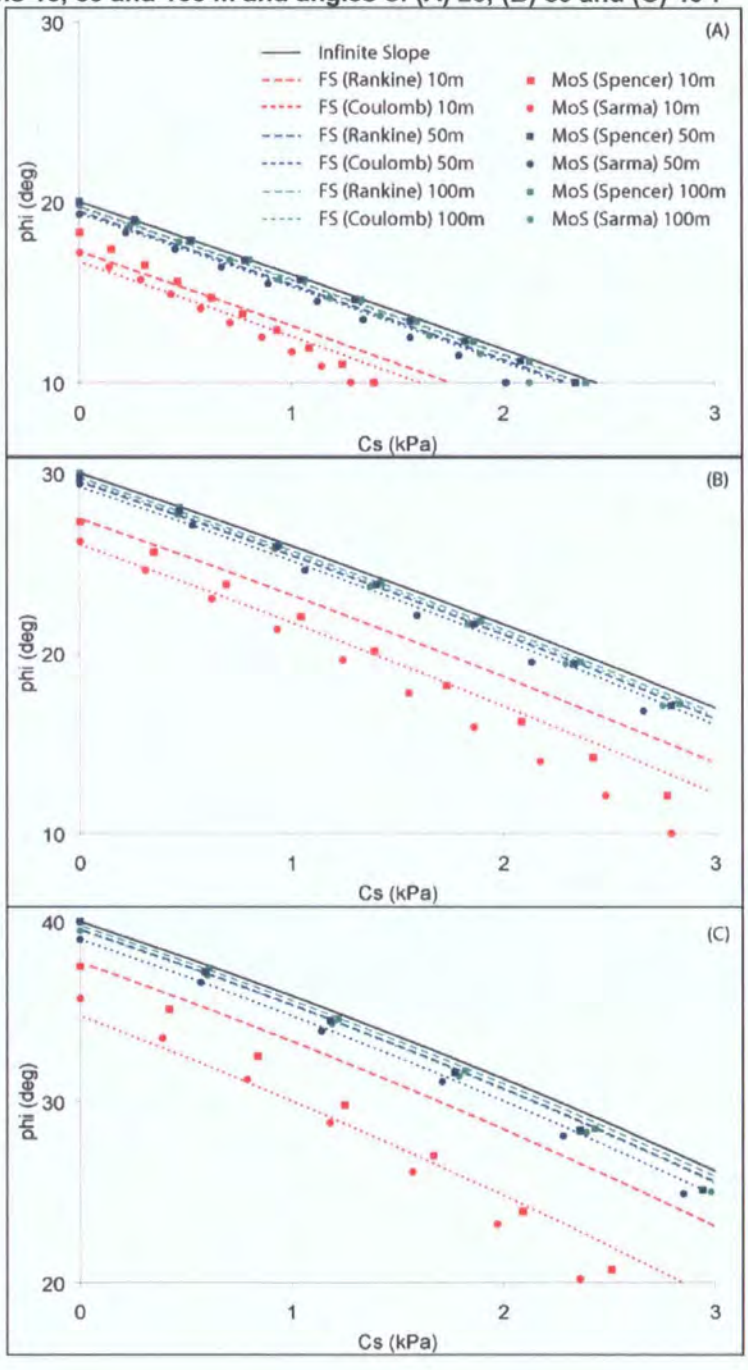

On average, Finite Slope models tend to predict less stable slopes than the methods of slices, although there is appreciable overlap. The difference is not constant in φ c_s space but is systematic. Finite Slope models have slightly shallower slopes in φ c_s space than those predicted from the method of slices (Figure 5-13). This is most noticeable for Sarma's method but is also visible in

Spencer's method at shorter slope lengths (1–10 m). The trend is present for all slopes, but is accentuated by increased slope angle or decreased slope length (Figure 5-13). As a result, Finite Slope predictions tend to be equally stable or slightly more stable compared with those from methods of slices at low cohesions (0–1 kPa) and less stable at high cohesions (1–3 kPa).

The variability between Spencer's and Sarma's methods of slices and between Coulomb and Rankine equations in the Finite Slope model provides an estimate of the within model variability resulting from the choice of solution or the functional form of the algorithm (function error). This is useful in establishing the uncertainty in these methods but complicates the task of quantifying the degree of agreement between methods. Rather than using a single set of observations to compare with each of the Finite Slope model's (Coulomb and Rankine) predictions the methods of slices provide two equally likely competing sets of benchmark values. Assuming that the space between benchmark values is more likely to contain the true value than the space outside them I use a simple mean of the differences (ME) between predicted values from each Finite Slope model (F) and those from Spencer's (M_{sp}) and Sarma's (M_{sa}) methods:

Equation 5-1

$$ME = \frac{1}{n}\left(\sum_{i=1}^{n}\left(\frac{2F_i - M_{sai} - M_{spi}}{2}\right)\right)$$

This allows positive residuals to cancel negatives when the predicted value falls between the results from Spencer and Sarma methods. Zero differences represent a prediction that falls exactly between the two benchmark estimates.

Table 5-3: Mean differences (ME) between back calculated parameter values predicted using Finite Slope models and benchmark values. Red values indicate the earth pressure representation that deviates least from the benchmark value.

		Friction Angle (°)		Soil Cohesion (kPa)	
		Coulomb	Rankine	Coulomb	Rankine
100	20	0.02	-0.04	-0.004	-0.018
	30	-0.06	-0.21	-0.045	-0.079
	40	-0.03	-0.35	-0.066	-0.135
50	20	0.07	-0.05	0.010	-0.018
	30	-0.03	-0.34	-0.047	-0.116
	40	0.05	-0.60	-0.075	-0.212
10	20	0.08	-0.50	-0.008	-0.150
	30	-0.63	-2.19	-0.158	-0.502
	40	-0.34	-3.82	-0.230	-0.906

If no assumption is made about the location of the true stability value, the mean of the absolute errors (MAE) provides a better representation of the performance of the Finite Slope models:

Equation 5-2

$$MAE = \frac{1}{n}\left(\sum_{i=1}^{n}\left(\frac{\left|F_i - M_{sai}\right| + \left|F_i - M_{spi}\right|}{2}\right)\right)$$

In this case, the absolute error for values that fall between the two benchmark estimates will be a constant with a value equal to half the distance between the two benchmark estimates.

Table 5-4: Mean absolute errors (MAE) between back calculated parameter values predicted using Finite Slope models and those observed from methods of slices. Red values indicate the earth pressure representation that deviates least from the benchmark value.

		Friction Angle (°)		Soil Cohesion (kPa)	
		Coulomb	Rankine	Coulomb	Rankine
100	20	0.25	0.24	0.067	0.067
	30	0.23	0.28	0.072	0.090
	40	0.24	0.39	0.089	0.139
50	20	0.44	0.44	0.112	0.112
	30	0.39	0.45	0.101	0.131
	40	0.39	0.66	0.125	0.220
10	20	0.61	0.75	0.157	0.204
	30	1.00	2.19	0.232	0.502
	40	1.43	3.82	0.360	0.906

The patterns in Table 5-3 and Table 5-4 are similar. Rankine's equation improves stability estimates for long shallow slopes. However, in the majority of cases Coulomb's equation is most effective. This is particularly the case for short steep slopes where the mean absolute error in friction angle for Finite Slope calculations using Coulomb's equation is half that using Rankine's. These results suggest that representing earth pressure within the Finite Slope model using Coulomb's equation produces stability predictions that agree more closely with those from methods of slices. The mean absolute errors between predictions from the method of slices and the optimum Finite Slope model (0.2–1.4° φ or 0.07–0.36 kPa c_s) are small relative to the error associated with the choice of algorithm for each model type.

Having tested the effect of landslide length on stability for a range of slopes and a constant depth I have established that length has important effects on stability and that these effects are largest for short slides. Several other geometric factors are likely to influence the length effect on stability, in particular: soil depth, landslide size and aspect ratio. These are discussed in detail below.

5.5.4. Length Effects for Varying Soil Depths

For cohesionless soils, the Infinite Slope stability estimates (or limiting soil strengths) are independent of soil depth, and friction angle is equal to the block

inclination (see Figure 5-14 A and B at c_s=0). For a given slope length, as the cohesion influence on soil strength increases, the soil strength required to maintain stability increases with depth, i.e. the stabililty of the slope is inversely proportional to depth. However, the stabilising influence of the toe also increases with depth so that, for a given slope length, the strength required to maintain stability is significantly less for a block 2 m deep (Figure 5-14B) than a 1 m block (Figure 5-14A).

Figure 5-14: Back calculated soil strength on a 20° slope of lengths 10, 50 and 100 m for unsaturated conditions and a failure plane depth of (A) 1 m and (B) 2 m depth.

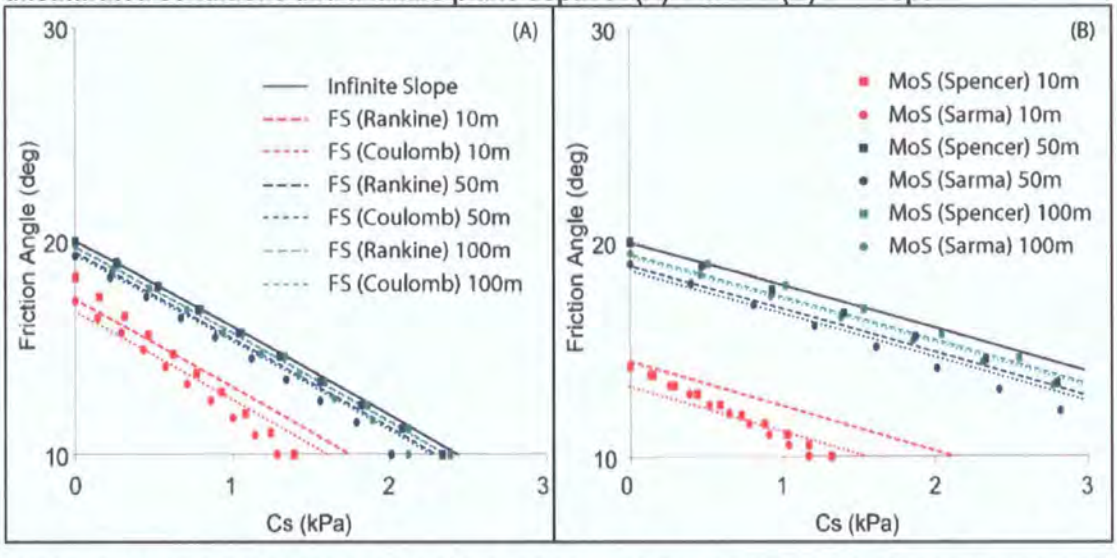

These plots indicate two competing effects with block depth: 1) as the block depth increases so does its weight and as a result its stability becomes increasingly sensitive to friction relative to cohesion, the slopes of the φ c_s curve becomes shallower and at a given cohesion the friction angle required to maintain stability increases; 2) as block depth increases but length is held constant, the aspect ratio of the block increases so that the stabilising influence of the toe is also increased. The second effect is clear from the very large offset (Figure 5-14) for a 2 m deep block between strength parameters required to maintain stability when the block is 10 m long and when its length is 50 m (equivalent to φ ~ 5.5°), compared to the smaller offset (equivalent to φ ~ 2.3°) for a block that is only 1 m deep. The same trends are visible in the back calculated strength parameters when depth is varied for a block of length 10 m at an inclination of 20° (Figure 5-15). Blocks with shallow failure planes have a steeply sloping φ c_s relationship suggesting that they are sensitive to cohesion. The Infinite Slope method performs particularly poorly for blocks with deeper

failure planes, overestimating limiting friction angle by >5° relative to the benchmark values. The Finite Slope model developed in Chapter 4 performs well at all depths.

Figure 5-15: Back calculated soil strength on an unsaturated 20° slope 10 m long with a failure plane at depths of 0.1, 0.2, 1, and 2 m. Thin blocks are highly sensitive to cohesion while for thick blocks there is a large offset between Infinite Slope parameter estimates and benchmark values. Finite Slope (FS) methods perform well.

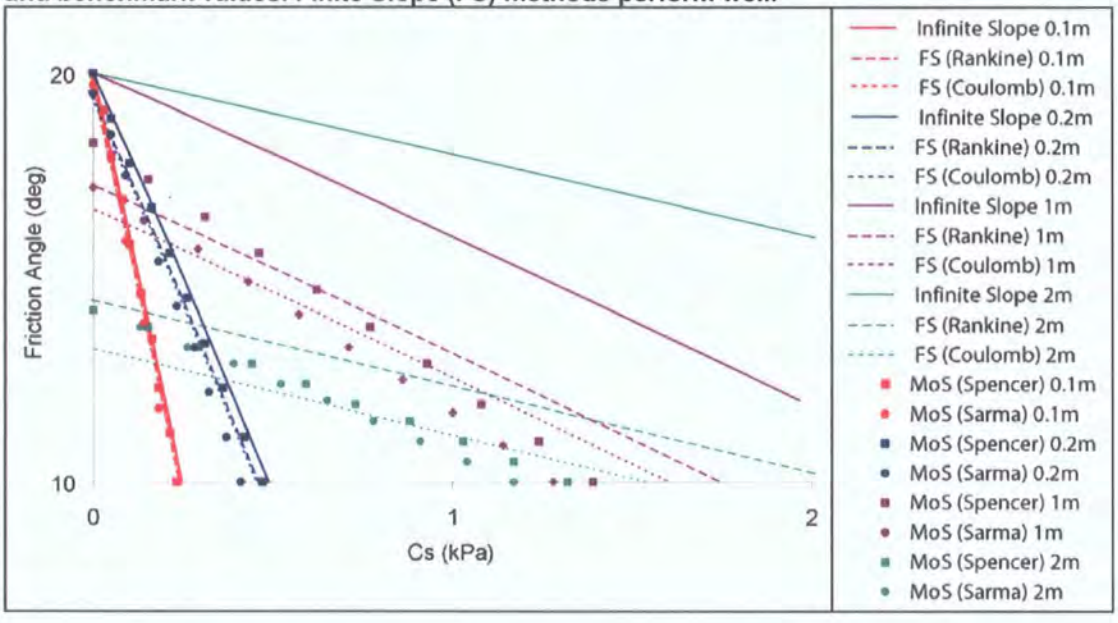

5.5.5. Length Effects for Varying Block Size and Aspect Ratio

These effects can be untangled by studying only the size of the block or only its aspect ratio. From Figure 5-16 it is clear that the block size influences the slope of the φ c_s relationship, while the aspect ratio influences the magnitude of the stabilising effect that the toe exerts on the block. When aspect ratio is held constant (Figure 5-16) the slope's stability becomes increasingly sensitive to friction angle with increased size (decreasing slope of the φ c_s relationship). When aspect ratio is varied for a constant landslide length, the reduction in friction angle required to maintain stability using the method of slices approach becomes larger relative to the Infinite Slope method. For an illustration of this, compare the offset in friction angle required to maintain stability between Sarma's method and the Infinite Slope method for a 100 m block at an aspect ratio of 50 (Figure 5-16A) and 100 (Figure 5-16B).

Figure 5-16: Back calculated soil strength on a 20° slope of lengths 10, 50 and 100 m with aspect ratio held constant at A) 50 and B) 100 for unsaturated conditions.

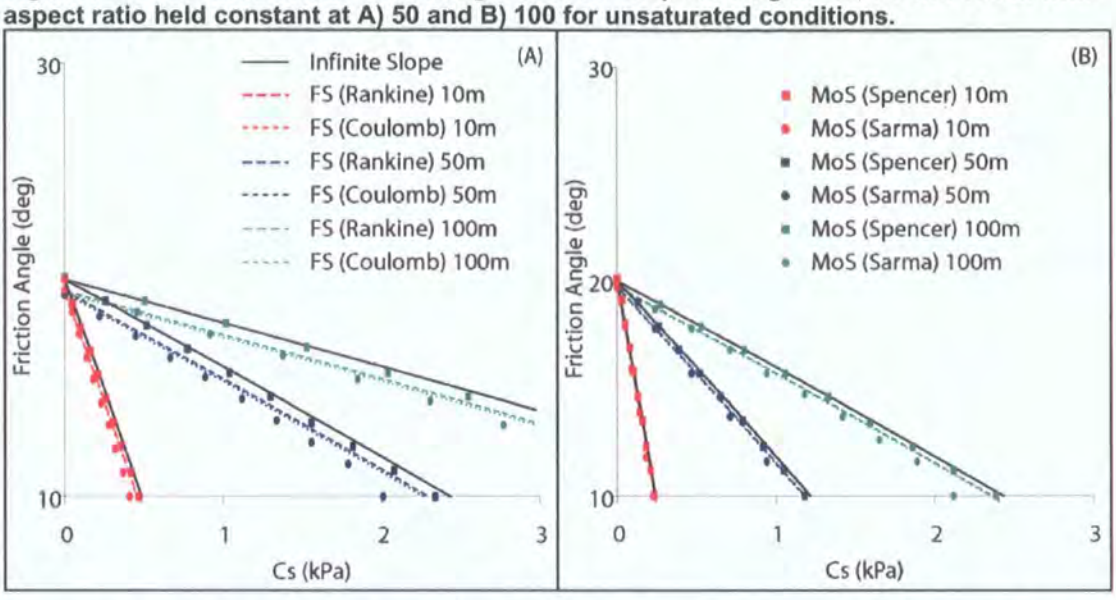

The effects of size and aspect ratio cannot be fully separated since the increased sensitivity to soil cohesion with decreasing size reduces the sensitivity of the block's stability to toe effects (largely a frictional resistance). The friction effect is constant throughout the parameter space, visible in the constant vertical offset between the friction angle required to maintain stability using the method of slices and that for the Infinite Slope. However, as size decreases and the slope of the φ c_s relationship increases, the cohesion offset between these methods reduces almost to zero.

5.5.6. Length Effects - Summary

Having tested the effect of a block's length on its stability for a range of block material properties, geometries (lengths and depths) and slopes, I have established that length has important effects on stability and that these effects are largest for short slides. Encouragingly, across the full range of block geometries (aspect ratios, lengths, depths and sizes) tested in these numerical experiments, the Finite Slope stability estimates effectively reproduce the results from the more complete and complex method of slices approaches that have been used as benchmarks. This suggests that the much simpler and computationally cheaper Finite Slope model can produce stability estimates that are precise relative to both the effect of block geometry on stability and to uncertainty in the soil strength parameters. The results from these models indicate that there is an exponential decrease in stability with increasing block

length, and that the form of this relationship varies with block geometry, inclination and material properties.

5.6. Width Effects

5.6.1. Scope of the Section

My analysis of width effects focuses on the stabilising influence of lateral root cohesion and friction on the block's margins, both individually and in combination. The friction effects are split into 'at rest' or active earth pressure representations to provide upper and lower bound reinforcement estimates. The root cohesion effects are represented in nine scenarios, which combine: different cohesion estimates from three vegetation types (*Juncus, Pteridium* and *Eriophorum*) with three different methods of integrating these values over the depth of the block (detailed in Section 5.3.5). These three methods assume either: 1) uniform root cohesion with depth over the block's full depth; 2) uniform cohesion over a partial (rooting) depth; or 3) root cohesion decreasing as a power function of depth. In Section 5.6.2 I apply each model treatment across the range of scenarios to establish their impact on predicted stability (in terms of FoS). In Section 5.6.3 I apply the same approach but using back calculated soil strength as the stability metric. Finally, in Section 5.6.4 I analyse the effect of variations in failure plane depth on the relationship between width and stability for key scenarios, chosen to represent typical and end member conditions for my study area.

5.6.2. Factor of Safety Results

Uniform partial depth (B, E and H in Figure 5-17) and power law decay representations (C, F and I in Figure 5-17) are very similar for all vegetation types. Uniform full depth representations (A, D and G in Figure 5-17) are consistently more stable with: 1) a steeper curve in the roots-only case; 2) an increased influence of roots relative to soil friction; and 3) a steeper curve when both friction and root cohesion are accounted for in a complete treatment. The FoS decreases exponentially with block width from very high values, more than twice those for an Infinite Slope at widths of 1 m. For the complete treatment, resisting forces consistently exceed driving forces by a factor of three compared

to less than half for the infinite slope case. As width increases, curves converge on each other, and on the Infinite Slope results. The inflexion in the curve is at a width of ~20 m but reduces at a rate which depends on the vegetation type and root reinforcement representation so that it has the range 10–30 m. For widths larger than 30 m the FoS is the same as that for an infinite slope in every case and is insensitive to further width increases. These results support those from Chapter 3 in suggesting that there is little difference between uniform partial depth and power law decay root reinforcement representations. They indicate that width controls on stability exist for block widths up to 30 m, and that these are strongest for uniform full depth root reinforcement representation.

Figure 5-17: A matrix of plots of FoS with width (plotted on a logarithmic scale) for a dry slope at an angle of 20°. The columns show results for different root reinforcement representations, the rows contain plots for the three different vegetation types.

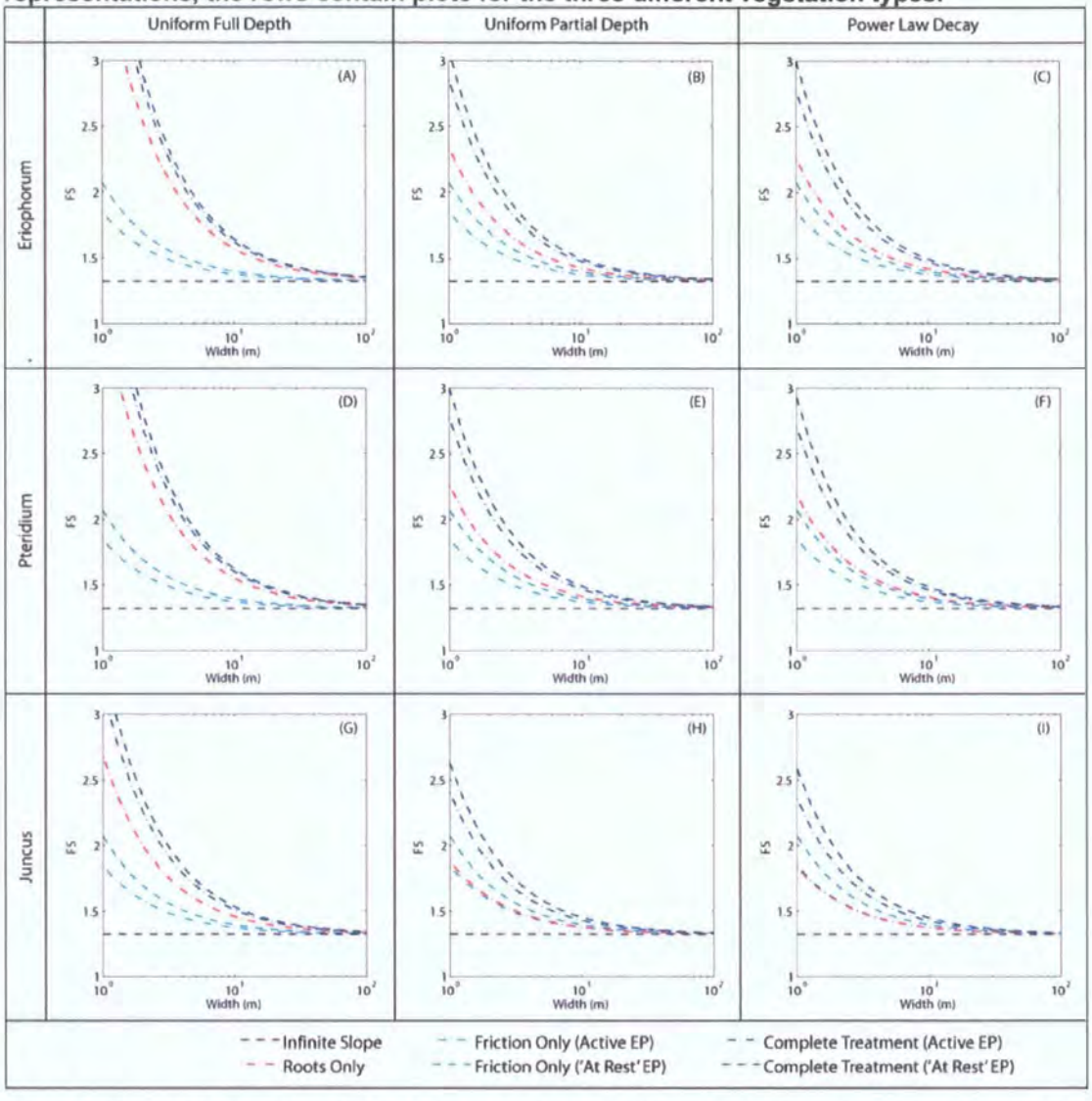

The friction-only treatment includes representations for 'at rest' and active earth pressure conditions to define its upper and lower bounds respectively. These curves (light blue in Figure 5-17) are unaffected by vegetation type and root reinforcement representation. They consistently plot as the lowest or equal lowest FoS at any given width. The difference in stability predictions between earth pressure representations is small relative to the differences between soil friction and root cohesion in most cases. Root cohesion effects are almost always stronger than friction effects. The FoS predictions neglecting friction effects and considering root reinforcement alone (red in Figure 5-17) only plots within the envelope of the results from friction only treatments for the weakest roots and the least conservative representations (Figure 5-17 H and I). For stronger root systems and using the more conservative (uniform full depth)

representation, root cohesion dominates the lateral effect. The difference between FoS neglecting friction and the complete representation is very small in such cases (Figure 5-17 A & D).

These results suggest that, in some cases, neglecting friction effects on the block sides may be reasonable because these effects are small relative to the root cohesion effect. However, this is critically dependent on the choice of root reinforcement representation. In fact, the relationship between roots-only and friction-only FoS, as well as the magnitude of the FoS for the complete treatment, are more sensitive to the assumptions regarding how root reinforcement is represented than they are to the vegetation type, strength and density of the roots. In this situation careful consideration needs to be given to the extent to which each representation effectively describes the conditions of interest. There is unlikely to be one universally applicable representation. In my case, the representation with the greatest impact (uniform root reinforcement across the full depth of the block) is also the least likely for my study area. In the following analysis, most attention is given to the power law decay representation since this seems to describe the conditions in my study area most reasonably. The uniform full depth representation is likely to overestimate the strength at the landslide edges but is included as an indicator of maximum potential lateral strength.

Comparing FoS for blocks of different widths (Figure 5-17) using roots-only, friction-only and the complete treatment clearly illustrates that: 1) landslide width influences stability (for blocks <30 m); 2) both friction and root cohesion effects combine to add strength at the edges; but 3) root cohesion is generally more important when the vegetation has root cohesion >3 kPa at the surface.

5.6.3. Back Calculation Results

The importance of these width effects is difficult to quantify by examining the FoS. By recoding the model to back calculate the critical friction angle required for limiting equilibrium (just stable) conditions I can quantify the differences between model treatments in terms of a measureable parameter to which the model is sensitive. By considering these differences in relation to measurement

uncertainty I can establish the importance of width in relation to something widely reported and quantifiable.

Comparing Figure 5-17 and Figure 5-18, the relationships for back calculated limiting friction angles versus width are similar but inverted versions of those for FoS. In every case, where edge effects are considered, the friction angle required to maintain stability increases logarithmically with width. The inflexion generally occurs at widths between 20 and 40 m, an increase relative to that for the FoS, which suggests that limiting friction angles are more sensitive than FoS to width effects.

Width does exert a strong control on stability. When both friction and root cohesion are considered for an *Eriophorum* covered block with uniform full depth root reinforcement representation, the increased stability of a block 5 m wide compared to one 10 m wide is equivalent to an increase in friction angle of 5° or 50%. The same scenario but using a power law decay for root reinforcement with depth indicates that the stability increase is equivalent to a 3.5° increase in friction angle. Under other vegetation types, in particular *Juncus*, the width effect is weaker. However, the logarithmic form of the relationship means that for even the weakest vegetation types, blocks with widths less than 1 m are very stable (Figure 5-18). The strength of the roots and the method of root representation alter the widths over which the effect is important. Calculating FoS or limiting friction angle for such narrow blocks (width <1 m) is useful, not because it represents the stability of a landslide (landslides narrower than 1 m are extremely rare), but because it offers an explanation for the infrequency of landslides narrower than a certain threshold.

Figure 5-18: Back calculated friction angle with width for a dry slope at an angle of 20°, the columns show results for different root reinforcement representations, the rows contain plots for the three different vegetation types.

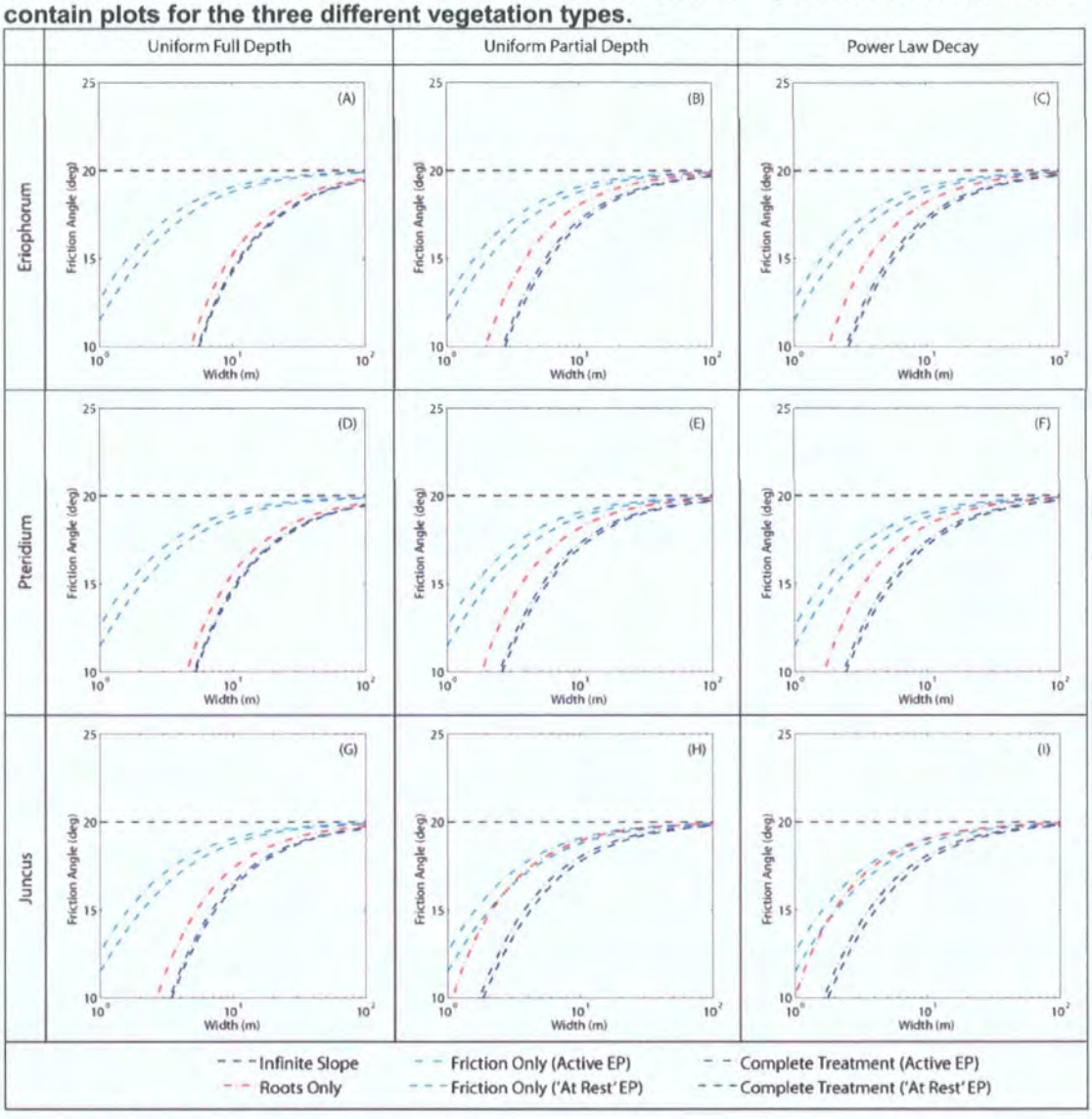

Limiting friction angles for each of the methods that apply only one form of strength (e.g. roots-only and friction-only in Figure 5-19) can be subtracted to estimate the limiting friction angle in a complete treatment (Figure 5-19). In general, the roots-only curve has its inflexion at larger widths than the friction-only curve. This reflects the increased influence of root cohesion relative to soil friction and is visible in the complete curves, which are often very similar to the roots-only version.

Figure 5-19: Back calculated friction angle with width for three vegetation types. For each vegetation type the lines form an envelope of potential limiting friction angles for that vegetation type by providing the upper and lower limits. The upper limits are estimates using the power law depth decay in root cohesion, the lower limits are set by results using a uniform root cohesion over the full depth of the block. Basal cohesion is ignored in all cases.

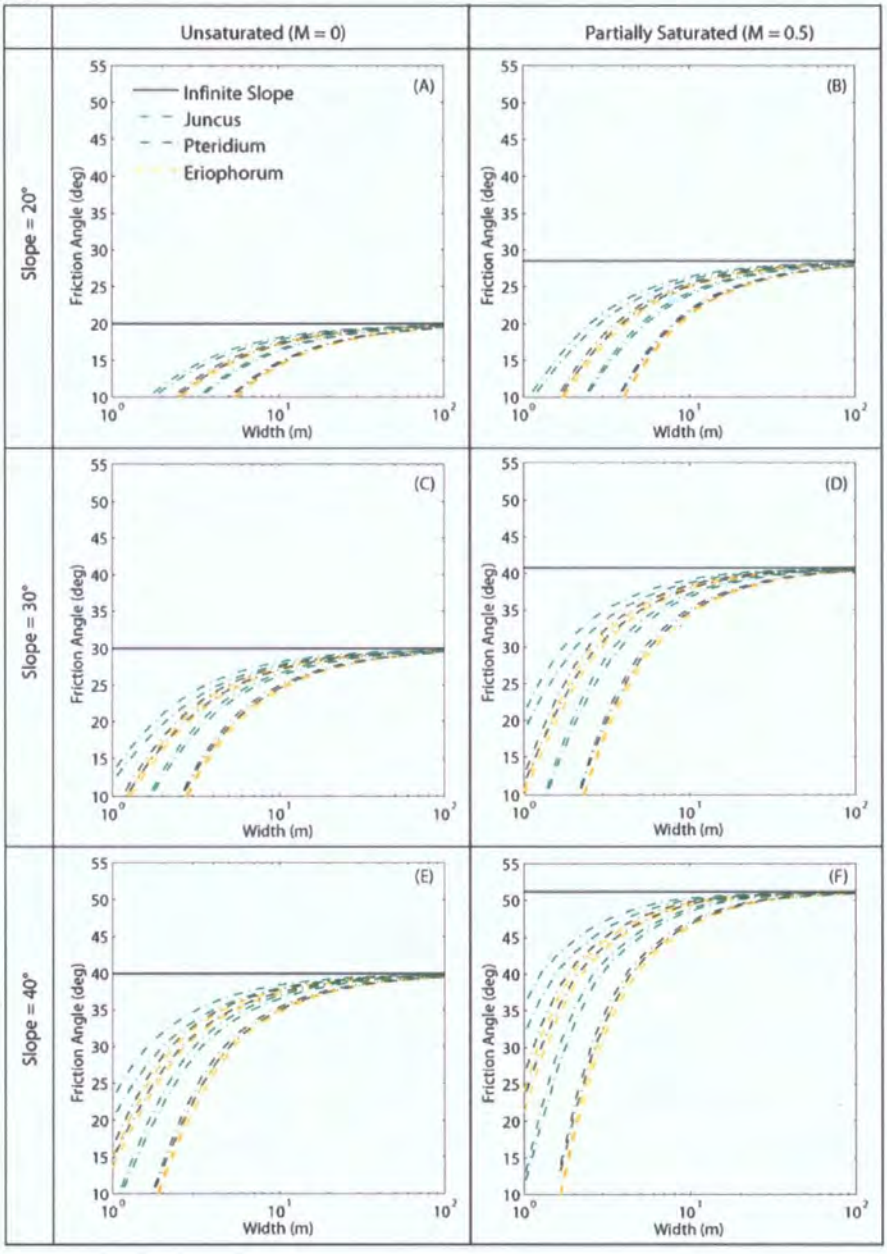

Infinite Slope methods and Finite Slope models with widths greater than 50 m show the expected width invariant trends for different slopes and saturation ratios (Figure 5-19). The absolute magnitude of the limiting friction angle at a given width varies with these parameters in all cases. The additional strength supplied by the lateral edge effects at a given width also varies with slope and saturation. For example, for a block 3 m wide under varying vegetation type the lateral edge effects provide additional strength equivalent to an increase in

friction angle of 5°-11°. For a given vegetation type the increases are usually larger for lower inclinations and partially saturated slopes. The variability in additional strength due to changes in slope and saturation is of a similar magnitude to the variability between blocks under different vegetation types (compare *Juncus* and *Eriophorum* in Figure 5-19 E and F). Although the form of the curves appears similar, their inflexion point is offset in the x direction, indicating that additional strength from the lateral sides is mobilised at different widths for different parameter combinations.

5.6.4. Width Effects for Varying Soil Depths

The relationship between width, depth and stability is particularly interesting. Plots of limiting friction angle with width for different block depths (Figure 5-20) show that strength due to root cohesion and friction react in opposite ways to changes in block depth. Both are sensitive to depth but in the complete treatment the changes with depth for each component offset each other so that friction angle is insensitive to width for this treatment. At shallow depths (Figure 5-20 A and E) the roots-only (red) and complete (dark blue) curves are very similar and the friction effect (light blue) is limited. This is a result of the small mass of the block, which defines the stress on the lateral edges and therefore its friction. As the soil depth increases both the normal stress at the lateral edges and friction also increase. The root effect is much stronger for the uniform full depth representation (Figure 5-20 A-D) than when using a power law decay (Figure 5-20 E-H) and remains constant independent of depth. In this case, the additional strength due to increased friction with depth increases the strength of the complete treatment (dark blue curves) and creates a small gap between it and the roots-only treatment (red curve).

The strength supplied by roots decreases rapidly with depth using the power law decay root representation (Figure 5-20 E-H). In this case, roots-only and friction-only treatments are equally stable at 1.5 m depth (Figure 5-20G) and the roots-only treatment becomes less stable than friction-only at 2 m (Figure 5-20H). The relative position of these curves can also be interpreted as their relative contributions to the complete treatment so that at shallow depths the roots dominate while friction becomes increasingly important until, for deep

blocks, friction becomes more important than the roots' effect. The response of the complete treatment is insensitive to depth but displays an interesting pattern which differs between root representations. For the uniform full depth root representation, stability increases with depth. However, for the power law decay root representation, stability initially decreases as the influence of roots is reduced then increases again as friction increases in magnitude. This relationship between depth and stability merits closer examination, it can be studied in more detail by plotting FoS against depth for each of the treatments but still assuming infinite landslide length (Figure 5-21).

Figure 5-20: Variation in limiting friction angle with width and depth (Z) for *Eriophorum* covered ground using two different representations of root cohesion with depth. For an unsaturated slope inclined at 20°. Results show that while root cohesion and friction are sensitive to depth individually they offset each other so that a complete treatment is relatively insensitive to depth. Note that these results assume no basal root cohesion.

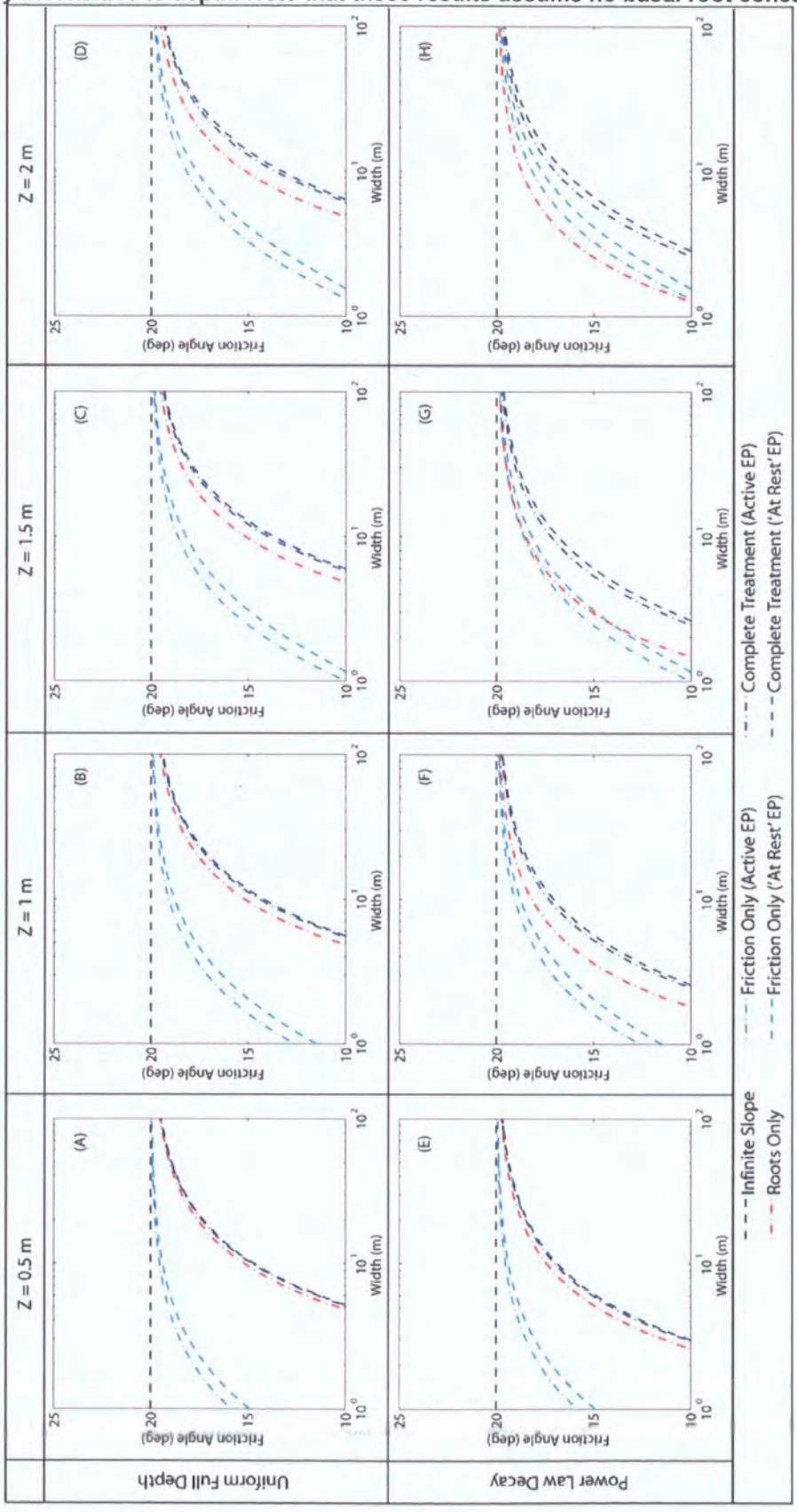

Figure 5-21: FoS with depth for a partially saturated (m = 0.5) soil element 10 m wide with a friction angle of 25.6°, lateral earth pressure is calculated using 'at rest' earth pressure and changes in lateral root cohesion with depth are represented by a power law decay root representation for: *Eriophorum* (A) and *Juncus* (B). The graphs show negative trends for FoS with depth when only lateral root cohesion is considered and positive trends when only lateral friction is considered. The complete treatment has a minimum value at ~1 m.

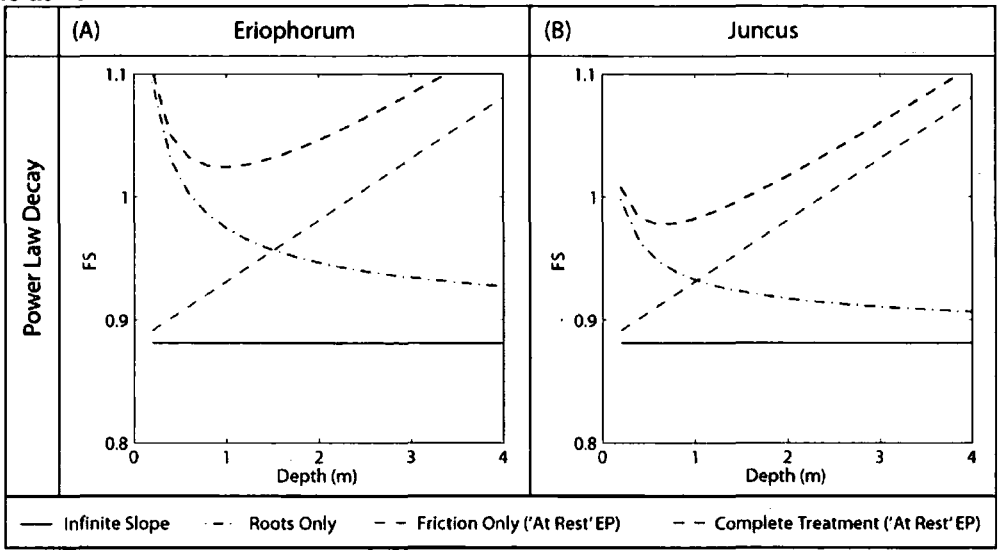

The FoS with depth for a partially saturated slope with *Eriophorum* (Figure 5-21A) and *Juncus* (Figure 5-21B) has consistent trends. The Infinite Slope method is insensitive to depth, as expected. The friction-only FoS (light blue) increases linearly with depth; the roots-only FoS (red) decreases non-linearly with depth. These two effects are combined in the complete treatment (dark blue) so that stability decreases with depth to a minimum ~1 m then begins to increase again. This minimum FoS at a given depth may represent an explanation of the depth distribution of observed translational landslides in my study area (mean depth = 0.7 m). The form of the relationship between stability and depth and the location of the point of minimum stability is a function of both the root reinforcement with depth relationship and that of friction with depth. In Figure 5-21, the form of this curve and the location of its apex are sensitive to vegetation type. It becomes less pronounced, with minimum stability points at shallower block depths, for the *Juncus* vegetation (Figure 5-21B) which has weaker roots. However, this scenario assumes that the roots act only laterally so that there is no basal root cohesion on the block. Figure 5-22 considers the same FoS depth relationship for *Eriophorum* but assumes isotropic root cohesion. In this case the three different root reinforcement representations return very different relationships between FoS and depth.

Figure 5-22: FoS with depth for the same partially saturated soil element as that in Figure 5-21 but with representations for basal and lateral root cohesion based on the: uniform full depth (A), uniform partial depth (B) and power law decay (C) representations. Note the change in axis scales between this figure and Figure 5-21.

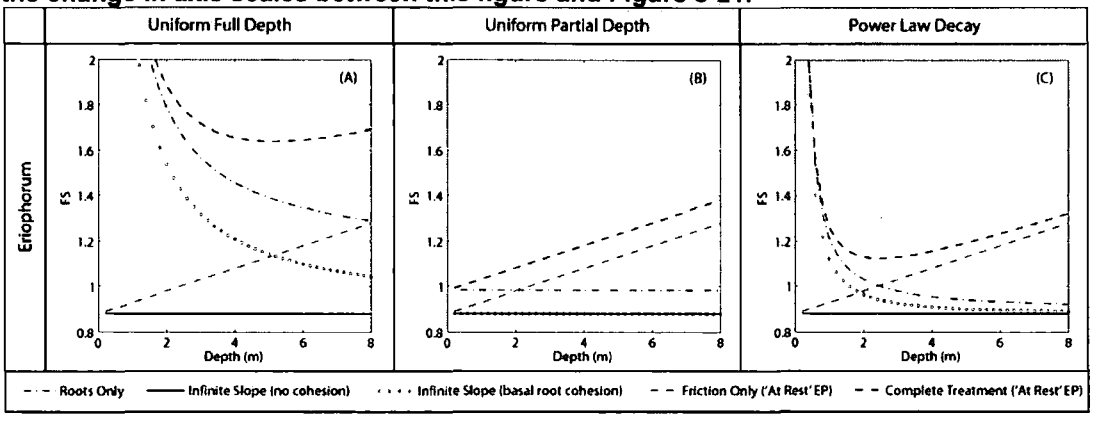

In every case, the Infinite Slope FoS ignoring cohesion is invariant with depth and the friction-only FoS increases linearly from a value equal to that of Infinite Slope method without cohesion at the surface. For the uniform full depth representation (Figure 5-22A) basal and lateral root cohesion is the same on every plane. The root effect on the base and sides decreases non-linearly with depth but the FoS of both is very high, even at depths of up to 2 m. The complete treatment has a minimum FoS of ~1.6 at 5 m depth. For the uniform partial depth representation (Figure 5-22B) root depth is scaled as a proportion of block depth so that no root cohesion is ever present on the base. As a result, the Infinite Slope FoS with and without basal root cohesion are equal, and the roots-only FoS is depth invariant. Under the complete treatment, FoS increases linearly with depth at a rate dictated by the relationship between friction and depth from an offset at the surface set by the lateral root cohesion. For the power law decay root representation (Figure 5-22C), FoS for the roots-only treatment and Infinite Slope method including basal root cohesion decline exponentially with depth (with an inflexion at ~1.5 m). The complete treatment closely reflects the roots-only treatment to depths of 1.5 m and then the friction-only treatment from depths >4 m. The minimum FoS is ~1.1 at a depth of 2.5 m. Both the minimum FoS and the depth at which it occurs are considerably reduced in the power law decay root representation compared to that assuming uniform root cohesion over the full depth.

5.6.5. Width Effects - Summary

Both friction and root cohesion effects combine to add strength at the block's lateral margins. These edge effects are important, especially for small blocks: on a 3 m block, they can provide additional strength equivalent to an increase in friction angle of 5°-11°. As a result, the FoS decreases exponentially with block width from very high values (more than twice those for an Infinite Slope at widths of 1 m). The inflexion in the exponential relationship is at ~20 m width but depends on site conditions and representation (varying from 10–30 m). Width controls are strongest for partially saturated blocks at lower inclinations with uniform root reinforcement over the full block depth. There is little difference between uniform partial depth and power law decay root reinforcement representations. Root cohesion effects are almost always stronger than friction effects and the difference in stability predictions between earth pressure representations is small relative to the differences between soil friction and root cohesion in most cases. These results suggest that friction effects might reasonably be ignored in some cases, but that this is critically dependent on the choice of root reinforcement representation. The behaviour of friction and root cohesion controls on stability with depth offset each other at large and small depths so that the point of minimum stability is at intermediate depths (~1–3 m). This has important implications in defining the most likely failure plane for shallow landslides, discussed further in Section 5.8.7.

5.7. Complete Assessment

The relative importance of length and width in determining the stability of a soil block are potentially key controls on landslide geometry. By comparing the FoS for finite length infinite width and finite width infinite length stability models we can start to understand the relationship between the two limiting length scales for landslide size and stability.

Figure 5-23: Comparison of the sensitivity of FoS to changing length scale for landslide models assuming: Infinite Slope width but finite length, Infinite Slope length but finite width or Infinite Slope width and length. The matrix shows the relative importance of landslide width and length and the effect of different root strengths and root reinforcement representations on these relationships.

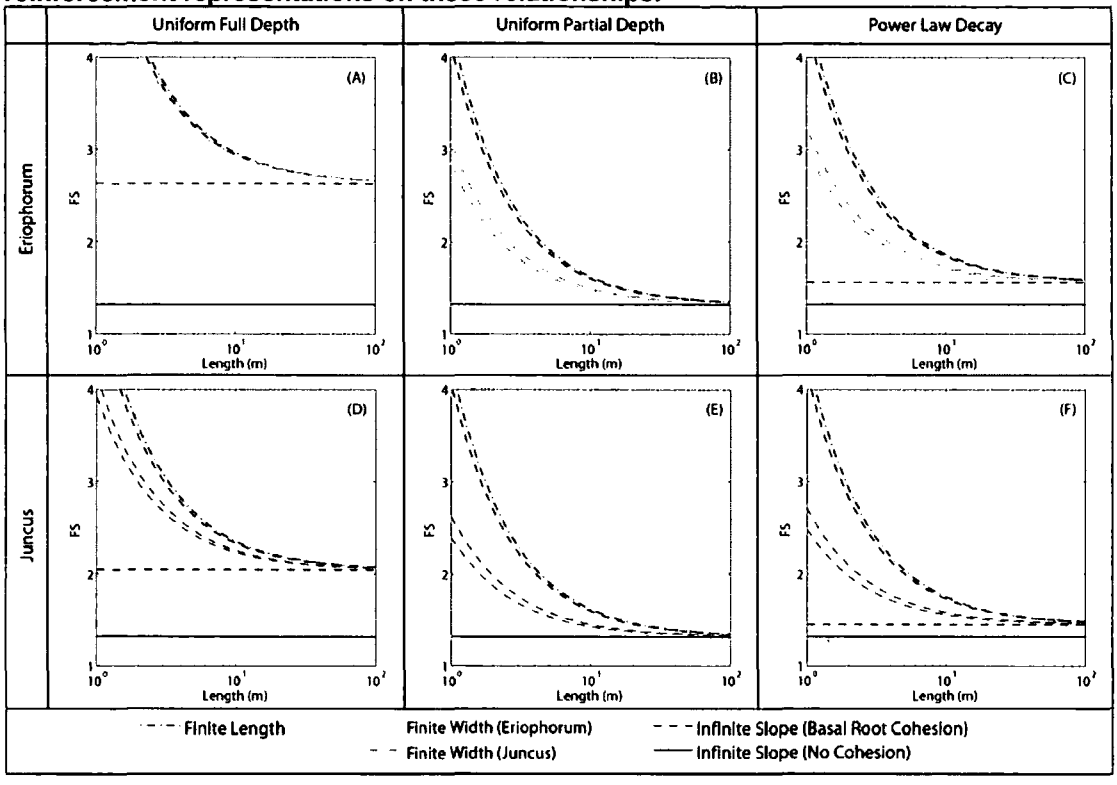

The FoS decreases more rapidly with increasing length than width (Figure 5-23). This difference suggests that landslide geometry should be controlled to some extent by the interplay of edge effects, and in particular their relative importance. Uniform full depth root representations have an elevated Infinite Slope FoS with basal root cohesion (Figure 5-23 A and D); these result from the assumptions that: roots extend below the failure plane; that they are uniform with depth; and that their reinforcement effect is isotropic. Uniform partial depth root representations (Figure 5-23 B and E) show no difference between Infinite Slope FoS with and without cohesion because the rooting depth is less than the total depth and no roots are considered to cross the basal failure plane. The power law decay root representation (Figure 5-23 C and F) has a small offset between Infinite Slope predictions with and without basal cohesion, representing the small number of roots present at this depth. The form of the depth relationship for both finite width and length models varies little between the uniform partial depth and power law decay root representations. Uniform full depth root representation results in a steeper curve for the finite width model and an increased importance of width relative to length. The reduction in root

strength from *Eriophorum* to *Juncus* results in: reduced offsets between Infinite Slope methods with and without cohesion; and reductions in FoS for finite width models, but no change for finite length models so that the difference between width and length effects increases. This effect is particularly accentuated in uniform partial depth and power law decay root representations.

Applying a power law decay root representation to unsaturated and partially saturated slopes at different inclinations under *Eriophorum* (Figure 5-24) and *Juncus* (Figure 5-25) we see consistent relationships in the relative influence of length and width on block stability. Block width never exerts a stronger influence on stability than block length at a given length scale (i.e. aspect ratio >1). Width and length influences are more similar for partially saturated than unsaturated slopes when everything else is held constant. The slope relationship is more complex. At shallow and steep slopes (20° and 40° respectively) the length effect is larger than the width effect at a given length scale. The difference between width and length effects is minimised at intermediate slopes (30°). The variability in FoS predictions increases with increased slope so that the envelope of FoS at 40° completely contains that for 20°. Parameter interaction does not appear to change the overall form of the relationships: each trend is consistent independent of changes in the other parameters.

The relationship between width and length effects with changing depth can be illustrated in the same way as for other parameters: by studying relationship between length, width and FoS. Including basal root cohesion effects allows a more complete assessment of the block's stability (Figure 5-26). However, it makes comparison between different block depths more difficult because it offsets both the width and length curves by the magnitude of the basal cohesion at that depth. In these analyses, where a power law decay root representation is applied, the offset varies with depth. This variability does not change the relationship between width and length effects, only the absolute magnitude of the FoS. By ignoring basal root cohesion we can compare the influence of depth on width and length effects more easily. These curves (Figure 5-27) show that the width effect is extremely insensitive to depth, as indicated in Figure 5-21 and Figure 5-22. However, the length effect is sensitive to depth. As depth increases so does rate at which FoS increases with length. Considering length

and width together, stability becomes increasingly sensitive to landslide length relative to width as depth increases.

Figure 5-24:comparison of the sensitivity of FoS to changing length scale for landslide models applying a power law depth decay for root cohesion and assuming: Infinite Slope width but finite length (blue), Infinite Slope length but finite width (brown) or Infinite Slope width and length (black). The matrix shows the relative importance of landslide width and length for unsaturated and partially saturated *Eriophorum* covered slopes at angles of: 20° 30° and 40°.

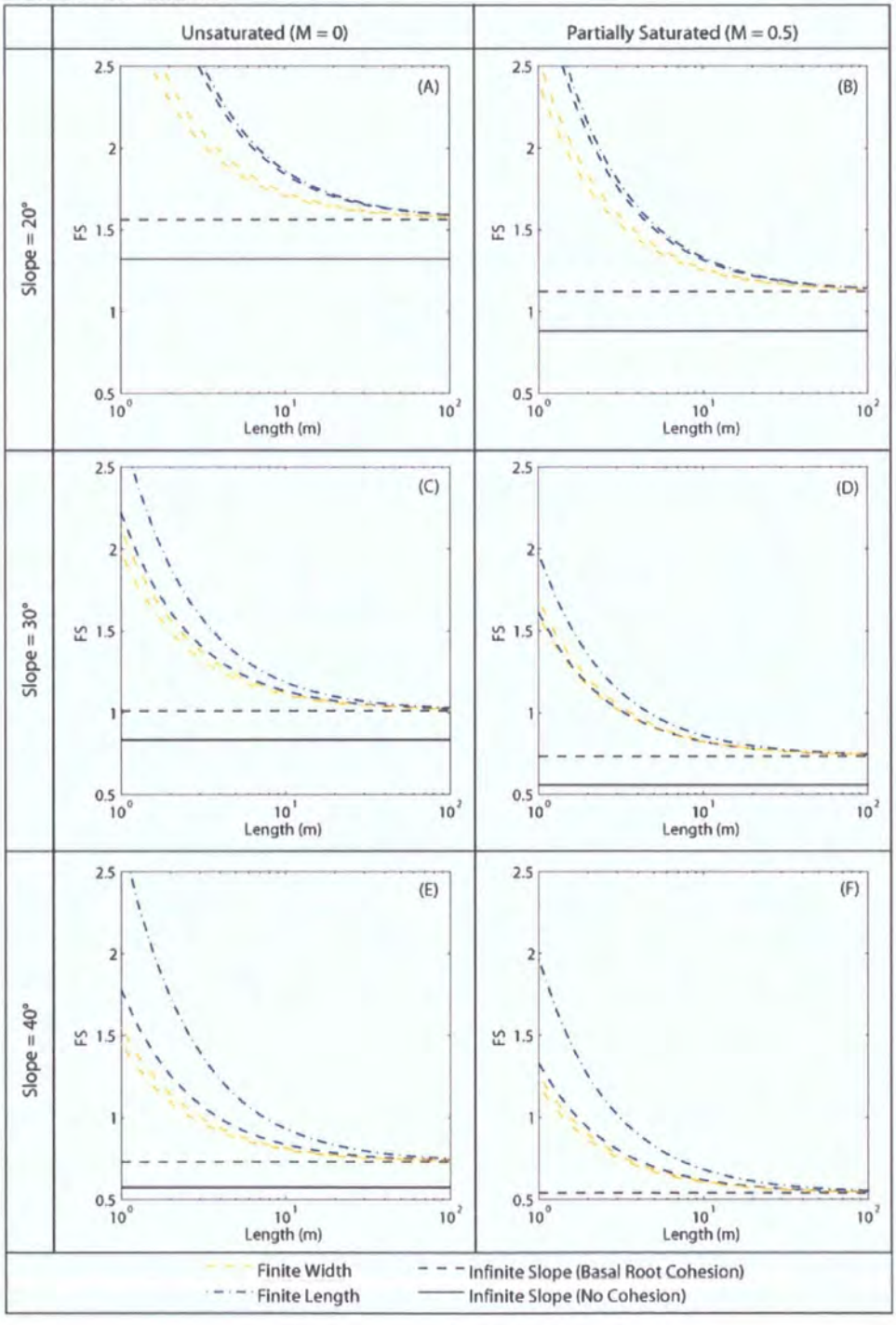

Figure 5-25: Comparison of the sensitivity of FoS to changing length scale for landslide models applying a power law depth decay for root cohesion and assuming: Infinite Slope width but finite length (blue), Infinite Slope length but finite width (green) or Infinite Slope width and length (black). The matrix shows the relative importance of landslide width and length for unsaturated and partially saturated *Juncus* covered slopes at angles of: 20° 30° and 40°.

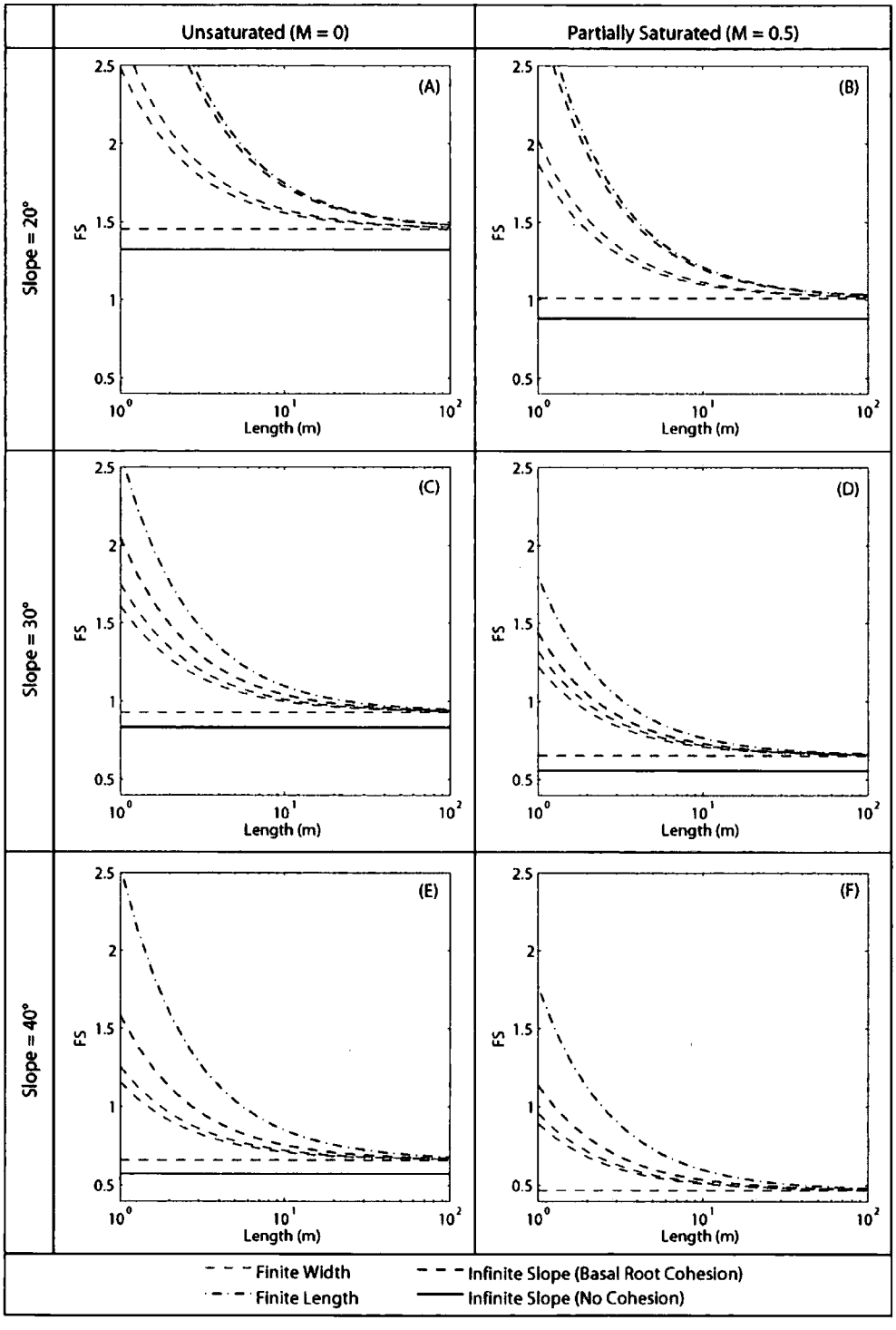

Figure 5-26: FoS for varying depth for two vegetation types *Eriophorum* and *Juncus* for an unsaturated slope at 20° with a friction angle of 25.6°, no soil cohesion and a power law depth decay treatment for root cohesion, which acts isotropically.

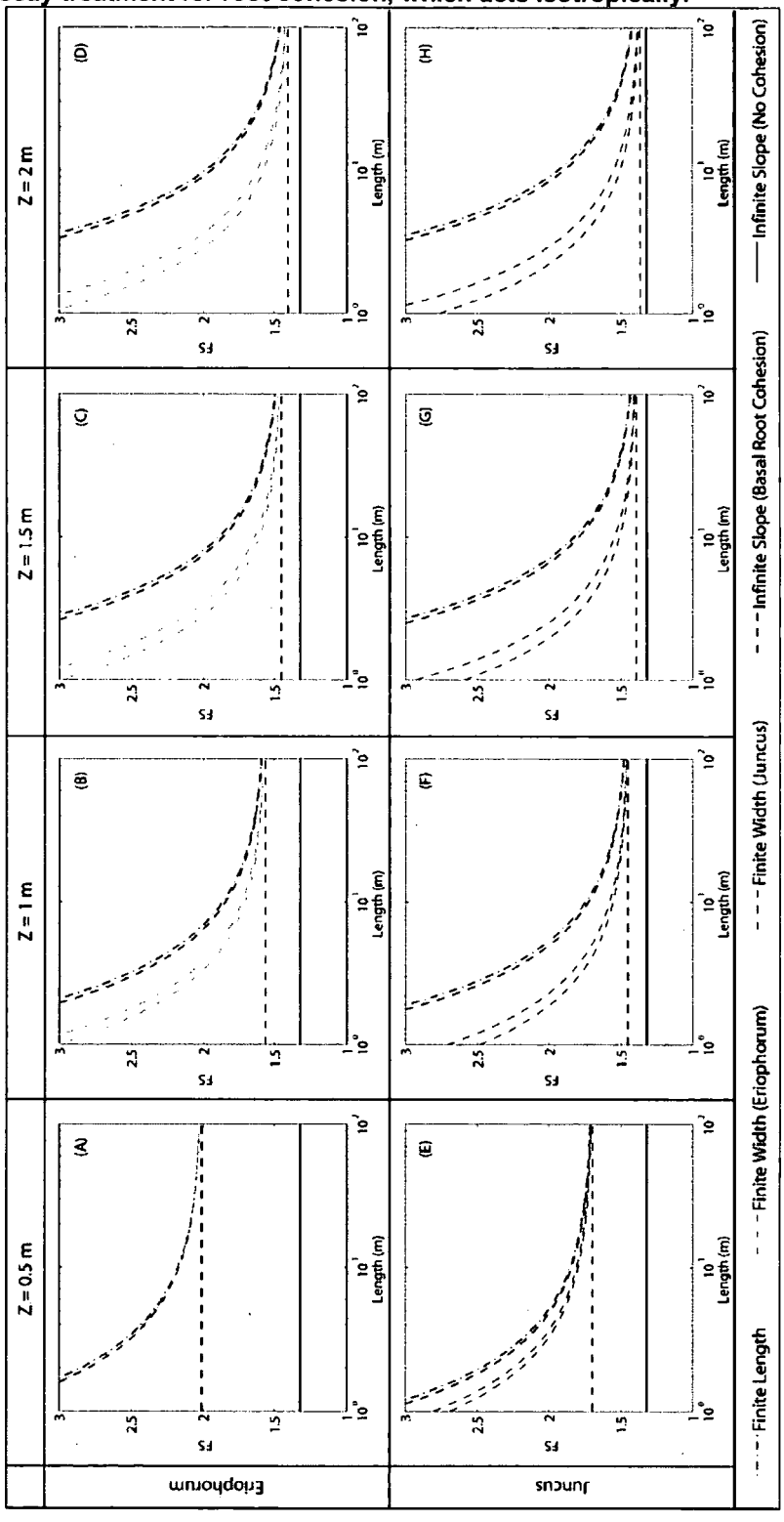

Figure 5-27: FoS for varying depth for two vegetation types *Eriophorum* and *Juncus* for an unsaturated slope at 20° with a friction angle of 25.6°, no soil cohesion and a power law depth decay treatment for root cohesion, which acts only laterally (these plots are the same as Figure 5-26 but neglecting basal root cohesion).

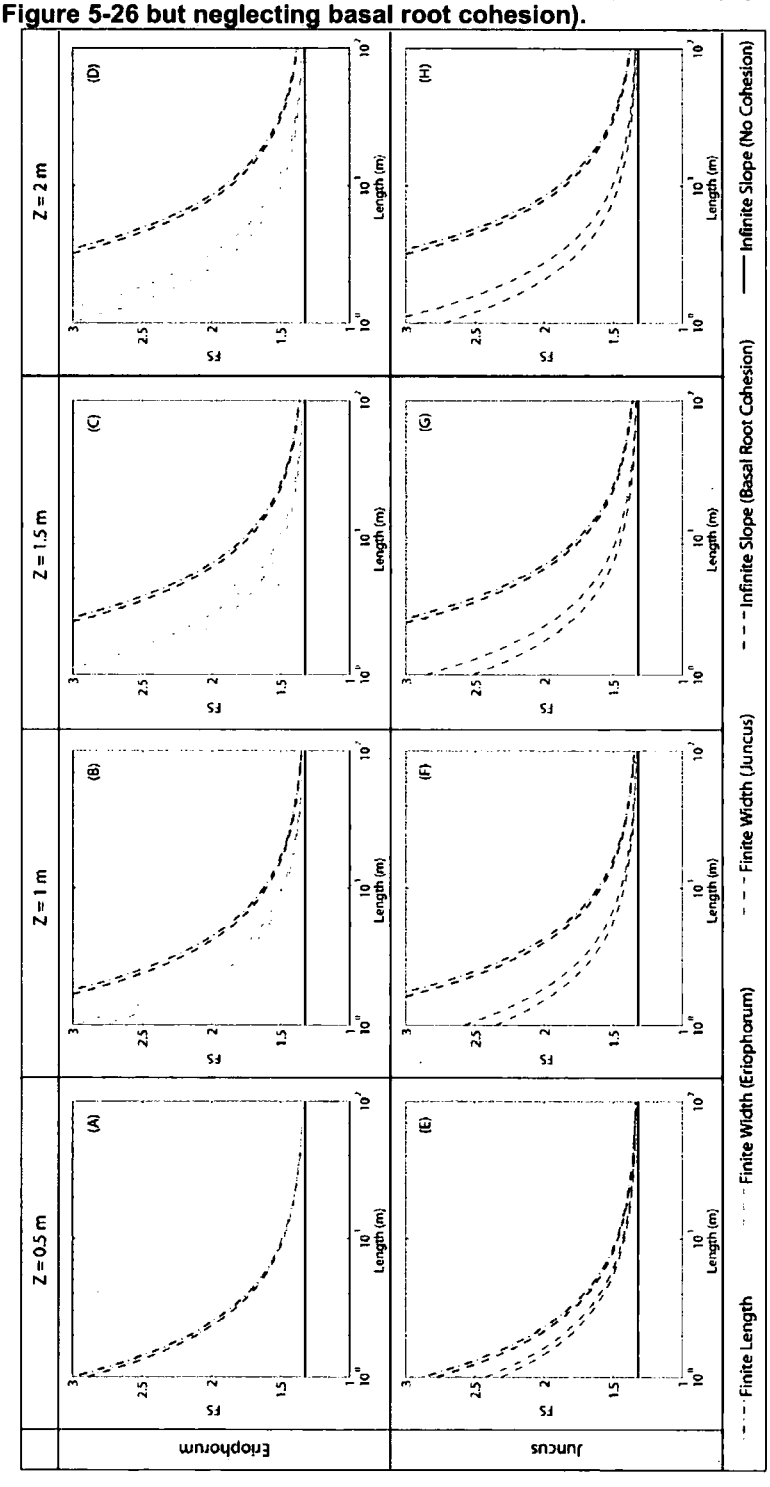

Figure 5-28 shows a contour plot of predicted FoS from a complete three-dimensional formulation of the Finite Slope model (accounting for both root cohesion and friction). The contours show a composite surface from the exponential two-dimensional width and length relationships with FoS (e.g.

Figure 5-27). At widths >20 m the width effect becomes negligible and the contours are pulled parallel to the x-axis; the same trend is visible for lengths >20 m. FoS decrease with width and length, they are lowest for the longest and widest blocks. The exponential relationships on both length scales are reflected in the inflexion in the FoS surface at low widths or lengths, with stability increasing rapidly with further decreases in length or width. Comparison of two-dimensional block geometry effects (length v width) on stability using the Finite Slope model suggest that length exerts a slightly stronger influence on the block's stability than width (Figure 5-23 - Figure 5-27). The full three-dimensional formulation (Figure 5-28) supports this suggestion. The contours in Figure 5-28 show slight asymmetry along the 1:1 axis; contours are pulled more strongly towards the y than x-axis indicating slightly higher FoS for a block that is 20 m long and 40 m wide than a block 40 m long and 20 wide. This asymmetry is more marked for the weaker vegetation and deeper soils (Figure 5-28B) where the earth pressure length control dominates. However, in both cases (Figure 5-28 A and B) the importance of aspect ratio in defining stability is small relative to the influence of the block's size.

Figure 5-28: FoS contours in landslide length-width space for an unsaturated slope inclined at 20°. The soils are (A) 0.5 m and (B) 1.5 m deep, both are cohesionless with a friction angle of 25.6°. Basal root reinforcement is ignored and lateral reinforcement modelled with the power law depth decay for: (A) *Eriophorum* and (B) *Juncus* covered slopes.

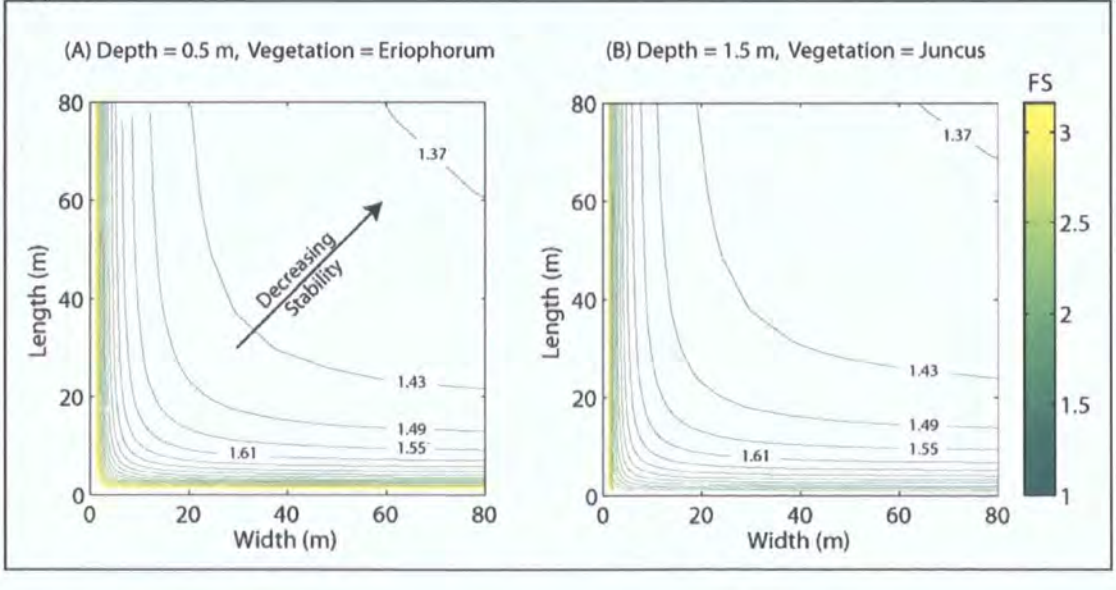

5.8. Discussion

5.8.1. Scope of the Section

In this section I draw together the key aspects of the results detailed above to address the aims of the chapter, in particular: establishing the effectiveness of the finite slope model and the control that a block's geometry exerts on its stability. In Section 5.8.2 I will address the first of these aims reviewing the results from benchmark tests to assess the effectiveness of the finite slope model and compare its predictive power with that of existing stability models. In Section 5.8.3 and 5.8.4 I draw together the factor of safety and back calculation results respectively to summarise the effects of block length on stability. In Sections 5.8.5 and 5.8.6 I do the same for Width, in each case drawing on examples or statistics from within the results and highlighting their relevance with respect to existing research. In Section 5.8.7 I investigate the implications of the relationship between failure plane depth and stability for our conceptualisation of the factors controlling shallow landslide depth. In Section 5.8.8 I draw on comparisons between the width and depth only formulations as well as the full three-dimensional finite slope model to summarise the implications of my sensitivity analysis for the controlling effect that the size and shape of a block exerts on its stability.

5.8.2. Finite Slope Model Performance

A key aim of this chapter was to establish the effectiveness of the Finite Slope model in representing profile geometry effects by benchmarking it against existing geotechnical models. Effective parameterisation, at minimum computational expense, will allow toe effects to be incorporated and compared within a complete three-dimensional FoS. The FSTC model predicts FoS most similar to those from the benchmark tests for weaker soils and the FSF model performs best for stronger soils (Figure 5-8). Both Finite Slope models predict an exponential decline in FoS with increasing block length. Error in the representation of slope stability can be assessed in absolute terms for dry slopes by comparing the mean absolute error of each Finite Slope representation (Coulomb and Rankine). The mean absolute error for limiting friction angles predicted by Finite Slope models ranged from 0.23°–1.43° for

Coulomb and 0.24°–3.82° for Rankine methods (Table 5-4). These errors are small relative to both the variability in limiting friction angle with landslide size and the measurement error / variability in soil strength input parameters. For the optimum parameterisation (using Coulomb passive earth pressure) this variability is always less than half the standard error in the friction angle input parameter.

Infinite Slope and Ordinary methods under-predict by up to 1 FoS. New methods provide an improved fit to the benchmark results (Figure 5-11). As expected, Infinite Slope stability estimates are consistently the least stable in all scenarios. However, the Ordinary method of slices is very similar to the Infinite Slope method in every case, indicating that edge effects in this model are negligible (Figure 5-9 and Figure 5-10). These models perform well for lengths >50 m but poorly for short blocks: under-predicting FoS by 5-15% at 10 m (Figure 5-9). This has important implications for existing three-dimensional catchment scale slope stability models, which often apply Hovland's (1977) three-dimensional extension of the Ordinary method. These results suggest that such models are likely to considerably under-represent the additional strength supplied by the down slope margin of the block and that additional parameterisation may be required to properly characterise these effects.

5.8.3. The Effects of Block Length on Stability

Method of slices results show a decline in FoS with block length, which is largest for short blocks (Figure 5-9). The same patterns are visible in the results from the FSF and FSTC models, where, for blocks ≤10 m, the variability with length is large relative to model uncertainty (Figure 5-9 and Figure 5-10). For blocks >10 m, the FoS from the Finite Slope models converges on that from the Infinite Slope method. For blocks ≥50 m, the variability with length is very small relative to model uncertainty. The predicted exponential decline in FoS with increasing block length is important for landslide length since, for blocks of 2 m length, the FoS can increase by >50% relative to those that are 10 m long. These results provide a mechanical explanation for observations, which suggest that landslides are rarely <2 m long. However, the calculations suggest that at lengths >12 m, the length effect is limited. Many of the observed landslides

have lengths >12 m and are unlikely to be heavily influenced by toe effects. However, it is likely that these effects are important in defining the minimum landslide length and the length-depth relationships for landslides close to this minimum length.

5.8.4. Length Effects Relative to Parameter Uncertainty

Back calculation allows us to quantify geometric stability effects and model errors in the units of one of the models input parameters. Comparing this with uncertainty in that parameter provides perspective on the importance of geometry in defining stability. By back calculating soil strengths, we can quantify the importance of landslide length and the magnitude of the error resulting from a Finite Slope model with reference to variability in the soil strength parameters. Measured friction angles in the study area are 37.3° for the full sample and 41.4° for landslide failure planes; their standard errors are 5.2° and 6.6° respectively (Section 3.2). The difference in limiting friction angles (those required to maintain stability) between slopes of 10–100 m ranged from 1–10° depending on slope angle, saturation, and soil cohesion (Figure 5-14). This range covers the full spectrum from insignificant to very significant length control relative to parameter variability. Changes in friction angle of 10° correspond to a change of around two standard errors in the measured soil strength parameters. Differences between blocks of 10 and 50 m can be equivalent to changes in friction angle of 1–9° (Figure 5-14). The upper end of these differences is larger than the standard error in friction angle measurements. At a length of 10 m and depth of 1 m, landslide length is an important control on stability relative to uncertainty in the soil's friction angle. Edge effects increase with depth (Figure 5-16), but for soils with a cohesion component this is complicated by the decreasing slope of the φ c_s relationship with depth (Figure 5-17). The effect of landslide profile geometry is only one aspect of the influence of edge effects on slope stability. Its influence and importance need to be considered relative to, and in combination with, that of the lateral edges discussed in the next section.

5.8.5. The Effects of Block Width on Stability

Landslide width influences stability, as friction and root cohesion effects combine to add strength at the block margins. The FoS decreases exponentially with block width from very high values up to twice that of the Infinite Slope estimates at widths ~1 m, they converge on the Infinite Slope predictions between 10 and 30 m depending on the vegetation type and parameterisation (Figure 5-17).

Lateral effects are split into friction and root cohesion effects. Root cohesion varies with depth but this is poorly constrained. It is commonly represented as either: 1) Uniform root cohesion over the full depth of the block; or 2) uniform root cohesion over partial depth (i.e. a root zone). I suggest a 3rd method assuming a linear relationship between root area ratio and root cohesion and a power law decline in root area ratio with depth. Uniform partial depth and power law decay root representations are very similar for all vegetation types. Uniform full depth representations are consistently more stable (Figure 5-17).

Friction effects can be represented using either 'at rest' or active earth pressure conditions. The difference in stability predictions resulting from the earth pressure assumptions is small in comparison with the magnitude of the friction and cohesion effects. However, its addition provides useful information by creating a band of possible values instead of a single line (Figure 5-17).

Root cohesion effects are almost always stronger than friction effects. The two are only equal for the weakest roots and root reinforcement representations. These results suggest that, in some cases, neglecting the friction effect, the approach taken by the majority of geomorphological studies (Reneau and Dietrich, 1987; Casadei *et al.*, 2003; Gabet and Dunne, 2002) may be reasonable but that this is extremely dependent on the choice of root representation as well as the estimated strength of the roots. In particular, assuming uniform root cohesion to full depth (a widely applied approach within the literature - e.g. Casadei *et al.*, 2003; Gabet and Dunne, 2002) is likely to overestimate the root effect in my study area significantly, where field measurement indicates a clear decline in root density with depth. It is included here as an estimate of maximum root reinforcement rather than as an equal

competing hypothesis with the other two scenarios. This has important implications for other studies, where lateral root reinforcement is included, the behaviour of root cohesion with depth needs to be carefully characterised in the model.

5.8.6. Width Effects Relative to Parameter Uncertainty

For back calculated friction angles the inflexion point at which the estimates from Finite Slope and Infinite Slope methods converge increases to 20–40 m width (Figure 5-18). These results indicate that while FoS becomes insensitive to width after 30 m, the stabilising effect often remains strong. This is particularly important since landslides commonly have widths <30 m, suggesting that lateral root reinforcement could provide significant additional strength at real landslide sites. The reinforcing effect of the edges on a block 10 m wide (Figure 5-18) is equivalent to 3–5° friction angle change (equivalent to ~0.5-1 standard error in the friction angle estimate). The strength of the roots and the method of representation alter the width over which the effect is important. For a given vegetation type, the increase is usually larger for shallower and partially saturated slopes (Figure 5-19).

5.8.7. Intrinsic Controls on Shallow Landslide Depth

Considering only the lateral margins (i.e. an infinite length formulation) and assuming no basal cohesion: the reinforcing effects of root cohesion and friction react in opposite ways to changes in block depth (Figure 5-21). Shallow blocks are stable and are controlled by root cohesion; whereas for deep blocks root cohesion effects are limited but the lateral earth pressures are high and therefore there is considerable friction on the edges. As a result, the lowest FoS values, are for blocks with failure planes at intermediate depths (~1–3 m). In the absence of other drivers, these least stable depths should represent the most likely potential failure planes for vegetated slopes. This represents an alternative hypothesis to the conventional assumption that landslides fail at a hydraulic or soil strength interface within the profile; instead suggesting that even assuming a homogeneous slope, shallow failures at depths similar to

those observed can be reproduced by considering only intrinsic controls on stability.

When basal cohesion is included in an infinite length formulation of the finite slope model, the depth of the zone with minimum FoS is increased so that failure planes should be deeper than many of those observed at Lake District landslide scars (Figure 5-22). This may be due to the infinite length formulation, since if a more complete treatment is analysed (accounting for the inverse relationship between FoS and depth for profile stability) the depth of the least stable zone is forced back towards the surface. Field observations at my sites and others indicate that soil profiles are not homogeneous and that landslides often (but not always) fail at interfaces within the soil or between soil and bedrock. Given these observations, it is unlikely that failure plane depths are entirely controlled by intrinsic factors related to lateral reinforcement. However, it may interact with other basal strength or hydraulic conductivity controls to define failure plane depth at a site.

5.8.8. Intrinsic Controls on Landslide Geometries from the Complete Three-Dimensional Model Formulation

Sensitivity analysis of the full three-dimensional formulation of the finite slope model clearly demonstrates that larger blocks are less stable (Figure 5-28). This is intuitive, but its contribution in defining the exponential form of this relationship and its inflexion point is important. It suggests that unstable areas must expand beyond a certain footprint size before they can overcome their lateral constraints. In this respect my analysis supports the findings of others (Reneau and Dietrich, 1987; Casadie *et al.*, 2003) who have already suggested such relationships based on analysis of lateral root reinforcement alone. The addition of friction effects (which differ depending on the strain conditions on each margin) is an important development both because: it more closely represents the forces on an unstable block; and it allows me to compare the relative influence of length and width on block stability (Figure 5-24). These may represent an important control on landslide geometry, and in particular on their length to width aspect ratios. By comparing length stability controls with those related to block width we can start to see whether landslides tend towards a

least stable geometry. The FoS increases more rapidly as length is reduced than width, suggesting that landslides should tend towards length width ratios >1 (Figure 5-28). This effect is accentuated with reduced root reinforcement, since roots play a larger role in supplying additional strength on the lateral edges than those at the upslope and downslope margins (Figure 5-23). Lateral strength is relatively insensitive to variation in failure plane depth (Figure 5-26 and Figure 5-27) due to the interaction between root cohesion and earth pressure driven friction (discussed in Section 5.8.7 above). The additional strength supplied by the downslope margin increases rapidly with failure plane depth since it is dominated by the passive earth pressure term. As a result stability becomes increasingly sensitive to landslide length relative to width as depth increases (Figure 5-26 and Figure 5-27). These results from initial sensitivity analyses suggest that the interaction between the lateral strength supplied at the margins of a block may have important implications for both the size and shape of unstable areas.

Applying these governing equations to spatially variable data represents a difficult operational and computational problem but is likely to yield extremely valuable results both in terms of spatial patterns of instability and the spatial configuration of parameters required to produce failures like those observed in the field.

5.9. Chapter Summary

Benchmark tests indicate that the parameterisation of profile effects in the Finite Slope model provides an improved representation of the effects of profile geometry on stability relative to the conventionally applied infinite slope and Ordinary methods. The agreement between Finite Slope and benchmark stability predictions quantified in terms of soil strength is within the uncertainty associated with the soil strength input parameters.

Both width and length exert a control on block stability, which decreases exponentially as width or length increase. As a result, influence is limited for landslides longer or wider than 30 m but can be extremely important for landslides <10 m long or wide. At these dimensions the additional strength

supplied by the margins is often larger than the uncertainty associated with the soil strength input parameters.

The form of the friction and root cohesion effects with block depth interact, so that blocks of ~1–3 m depth are least stable, this may constitute part of the explanation for the depth of shallow landslides in this study area and on other vegetated slopes. Length effects are slightly stronger than width effects, suggesting that if a blocks area is held constant, longer thinner blocks will be less stable. This corresponds well with observed landslide aspect ratios, since scars are commonly longer than they are wide. However, it needs to be emphasised that the interaction between length and width is very small relative to the size control (i.e. decreasing stability with increasing block surface area). It is likely that landslide scar geometry is a function of not only the geometric controls on stability but the spatial pattern of other important parameters such as: soil strength, root cohesion and pore water pressure.

6. Testing the hypothesis of topographic wetness

6.1. Scope of the Chapter

Landslides in the UK are triggered by high pore water pressures resulting from heavy rainfall (Section 2.4). Models designed to represent these processes at the catchment scale contain a geotechnical component that calculates the stability of a block based on its geometry, material properties and pore pressure condition; and a hydrological model that calculates the pore pressure required for the geotechnical model (Section 2.6). Pore water pressure is related to the spatial distribution of water in the landscape. As a result hydrological models designed to predict runoff are often used in slope stability analyses (Section 2.6.5). However, they must have the capability to spatially distribute their results to estimate either moisture content or phreatic surface height or both. As a result, hydrological models for slope stability must be either distributed or semi-distributed. Four types of hydrological model are commonly used in slope stability modelling: 1) fully distributed models (Simoni *et al.*, 2008); 2) dynamic models (Wu and Sidle, 1995); 3) steady state models (Montgomery and Dietrich, 1994); and vertical infiltration models (Godt *et al.*, 2008). While more detailed approaches represent significant advantages, they demand more information on rainstorm and soil properties than is typically available. However, common to all these models is an inherent assumption that water flow is Darcian: flowing from higher to lower pressures. On the steep slopes susceptible to landslides these hydraulic gradients are often assumed to be strongly related to surface topography (Tetzlaff *et al.*, 2008). Testing the extent to which or scale at which this 'topographic wetness hypothesis' holds within my Lake District study area is the key theme of this chapter.

In Section 6.2 I discuss the relevant background for this investigation focusing on the topographic wetness hypothesis: its origins, agreement with observations and the factors that can disrupt it. In Section 6.3 I detail the experimental design for this study, which will operate at two different scales, the hillslope (10^{-1} km^2) and catchment (10^0-10^2 km^2) scale. I deal with the methods that I applied at each of these scales in Sections 6.4 and 6.5 respectively. I apply the same structure to the results dealing first with the results at the hillslope scale

(Section 6.6) then at the catchment scale (Section 6.7). I finish the chapter by bringing the results at these two scales together and identifying their implications for slope stability modelling (Section 6.8).

6.2. Background

6.2.1. Scope of the Section

In this Section I aim to both justify my approach for the following Chapter and to provide enough background on landslide hydrology and the topographic wetness hypothesis to put the investigation into context. In Section 6.2.2 I identify the origins of the topographic wetness hypothesis and Section 6.2.3 I detail some of the field research that has assessed its applicability, these studies are inherently spatially and temporally specific and need to be viewed in the context of the methods that have been used to measure wetness (Section 6.2.4) but they do provide some indication of the extent to which this hypothesis holds in a range of environments. Finally, in Section 6.2.5 I address the complicating factors, often manifest at the hillslope scale, which disrupt the topographic control on wetness patterns.

6.2.2. Origins of the Topographic Wetness Hypothesis

Shallow landslides frequently occur on steep convergent slopes (Reneau and Dietrich, 1987; Ellen *et al.*, 1988; Montgomery and Dietrich, 1988). Hydrological models provide a framework for interpreting this important field observation, suggesting that topographically driven flow convergence and the resulting elevated pore pressures reduce soil strength in these zones (Dietrich and Dunne, 1978; Dietrich *et al.*, 1986).

The dynamic source area concept (Hewlett and Hibbert, 1967; Ragan, 1968) and a realisation of the importance of shallow subsurface flow (Hursh, 1936; Barnes, 1939; Whipkey, 1965; Hewlett and Hibbert, 1967) led to numerous studies on the relations between topography, subsurface flow convergence and runoff generation (Dunne, 1970; Dunne *et al.*, 1975; Anderson and Burt, 1978; Bonell and Gilmour, 1978; Anderson and Kneale, 1980, 1982; Pierson, 1983; Tanaka, 1982; Burt and Butcher, 1985, 1986).

Other research in a range of environments has supported and developed these theories. Harr (1977), Pierson (1983) and Montgomery *et al.* (1997) all report rapid increases in pore pressure in topographic hollows during storms in the Oregon Coast range, where the soils are highly conductive, bedrock is shallow and slopes are steep. Woods and Rowe (1996) found that for large rainstorms, the spatial variability of storm flow was reduced by accounting for common surface topography features (characterised by upslope contributing area). For a hillslope site in British Columbia, Hutchinson and Moore (2000) found that subsurface flow lines were control by the surface topography at high flows. In a glacial till environment, Hinton *et al.* (1993) determined that a combination of topography, sediment thickness and hydraulic conductivity were required to understand the dynamics of groundwater flow and stream discharge.

With a model that makes spatial predictions, the obvious check is against spatially distributed data. A considerable body of work exists that compares model predictions (or patterns of topographic index) with distributed measurements. These measurements range in technique and rigour but can be broadly grouped into those that measure soil moisture in the upper profile, depth to the water table in wells and piezometers, the spatial pattern of saturation during a rainfall event, or the spatial pattern of related soil or vegetation type.

6.2.3. Role of the Topographic Index in Defining Saturation

Saturation Patterns

Similarities in predicted and observed saturated areas and patterns of topographic index have been demonstrated by Dunne (1978) for the Sleepers River, Vermont; Beven and Kirkby (1979) for Crimple Beck, UK; Merot and Bruneau (1993) and Franks *et al.* (1998) for Brittany, France; Ambroise *et al.* (1996) in the Vosges, France; Guntner *et al.* (1999) in the Brugga catchment in Germany; and Blazkova *et al.* (2002) in the Uhlirska catchment, Czech Republic. In the Ringelbach catchment in France, predictions of the pattern of saturated areas based on the topographic index revealed broad agreement between the measurements and predictions, but also some points of departure

(Ambroise *et al.*, 1996; Freer *et al.*, 1996). Guntner *et al.* (1997) obtained similar results for a steep catchment in Germany, where although general patterns agreed, only one third of the observed saturated areas could be mapped by the index values. At Vallcebre, Spain, Gallart *et al.*, (2008) found that the topographic index was a fair predictor of local saturation patterns, but with a much more disperse topographic index distribution for saturated pixels than predicted. In this case, local conditions (sub-grid topographic features, local soil characteristics, non-topographic flow pathways and dynamic water flow) appear to be equally important in controlling local saturation (Gallart *et al.*, 1994; 1997; Latron and Gallart, 2007).

Groundwater Levels

Thompson and Moore (1996) found that the topographic index provided more reliable predictions of local groundwater levels than other topographic indices. Jordan (1994) found a strong correlation between topographic index and water table depth on some days but not on others in a small Swiss catchment. Seibert *et al.* (1997) showed that calibrating TOPMODEL using discharge data for a small Swedish catchment gave poor predictions of water table depth, but these could be greatly improved by using a single local observation of water table level as a local topographic index calibration. Lamb *et al.* (1997, 1998) found similar results in a small Norwegian catchment using observations from 105 piezometers and four recording boreholes.

6.2.4. Means of Measuring Saturation

Many studies restrict their examination to **shallow soil moisture** to the upper 0.3 m (e.g. Burt and Butcher, 1986; Moore *et al.*, 1988; Ladson and Moore, 1992; Nyberg, 1996; Western *et al.*, 1999; Sulebak *et al.*, 2000; Anctil, 2002; Meyles *et al.*, 2003). However, comparisons of patterns of topographic index with distributed near surface measurements are not really fair in that near surface conditions are not necessarily directly related to predictions of saturation resulting from downslope flow. Few studies have examined how well these shallow moisture patterns represent the soil moisture in the entire profile (for an exception see Tromp-van Meerveld and McDonnell, 2006).

Measuring the spatial distribution of **saturated areas** can provide a more complete indication of the topographic control on soil moisture than water table measurements from wells, in that they cover a larger area. However, these measurements are generally less precise both in mapping and classification.

Comparing topographic indices with **spatially distributed water table heights** (Jordan, 1994; Lamb *et al.*, 1997; Siebert *et al.*, 1997) provides an extremely rigorous test but has associated difficulties: 1) an additional parameter is required to convert soil moisture deficit to water table depth (Beven *et al.*, 1995); and 2) water table depth is a local measurement that may reflect the response only over a small area around the piezometer due to local variation in bedrock depth or effective contributing area associated with bedrock fractures, preferential flow or local variation of the relationship between transmissivity and depth (Beven, 1997).

Other catchment properties that have a strong process link to soil moisture have also been correlated with the topographic index. Soil and vegetation are the obvious variables.

Certain ecological conditions (climate, soil moisture regime, soil nutrient regime) are required for plant communities to survive or thrive. The ecological amplitude for each species is the range of these conditions (Wang *et al.*, 2000). Site conditions can be assessed from the performance of an **indicator plant species** and its ecological amplitude. By responding to changes in ecological factors and integrating the effects of many individual growth-related factors, plants can provide a quick and effective measure of site quality including soil moisture and nutrients (Wang, 2000). Such site properties are difficult to measure individually, so using vegetation as a surrogate measure is a tempting prospect. However, the effect of individual properties, such as soil moisture, on overall 'site quality' may be difficult to untangle.

The success of indicator plant approach depends on: 1) the existing knowledge of ecological amplitude of plant species and 2) the stability of the plant community in reflecting site quality given its dynamic nature (e.g. changes due to disturbance and succession). Climax or potential climax vegetation are

thought to reflect inherent site quality better than other succession stages (Daubenmire, 1976). However, Wang *et al.* (2000) suggest that the indicator plant approach can be applied to a wide range of plant communities at different stages of succession and with many different species compositions. Understory vegetation is particularly effective since it is more sensitive to changes in local site conditions under the same regional climate (Major, 1951; Daubenmire, 1976).

Several approaches to indicator plant analysis have been developed to interpret the ecological quality of a site such as soil moisture and nutrient regimes (Rowe, 1956; Bakuzis and Kurmis, 1978; Klinka *et al.*, 1989). These approaches have proved successful when tested against soil moisture measurements (Rowe, 1956; Wang, 2000). Several hydrological indices (based partially on topographic variables) have been produced to predict the distribution of vegetation types (Moore *et al.*, 1991; Ostendorf and Reynolds, 1998; Dorner *et al.*, 2002).

Species diversity can also be used as an effective indicator for site conditions in some environments (Zinko *et al.*, 2005). This method has similar advantages and problems to the indicator species approach but with the additional requirement that intensive fieldwork is a necessity. The connection between species diversity and topographic index is mediated in several steps. The topographic index predicts groundwater level, which affects soil factors (Giesler *et al.*, 1998), which in turn affects species diversity.

Plants are not only influenced by soil moisture but they exert an influence themselves through transpiration, which has been identified as important in some cases (Western *et al.*, 1999; Tromp-van Meerveld and McDonnell, 2006). This feedback between plant species, transpiration and soil moisture does not invalidate the species indicator approach, but it does highlight the non-linear nature of these systems which, needs to be remembered when one aspect of the system is used as a surrogate for another.

6.2.5. Complicating factors and additional drivers

Since the discovery of lateral subsurface flow and topographic control on soil moisture, further hillslope studies have revealed significant complexity and heterogeneity in hillslope responses to rainfall (McDonnell, 1990; Woods and Rowe, 1996; Hutchinson and Moore, 2000). These complexities are often explicitly linked to slope instability via their effect on pore water pressures and cited as reasons for the variability in locations of landslides or the mismatch between predictions and observations (Montgomery and Dietrich, 1994; Borga *et al.*, 2002).

Bedrock Topography

Studies that have measured bedrock topography often find that it is extremely non uniform, violating the assumptions of many of the commonly applied hydrological components to slope stability models. Concentration of groundwater flow into a limited area can induce slope instability and is influenced by the hydraulic conductivity and bedrock geometry (Reneau *et al.*, 1984; Okimura and Ichikawa, 1985). Freer *et al.* (2002) found that for uniform soils over relatively impervious granitic bedrock at the Panola research hillslope, the topographic index was a poor predictor of spatial saturation patterns using the surface topography but was extremely effective using bedrock topography. Tromp-van Meerveld and McDonnell (2006) found a threshold response in subsurface runoff at the Panola hillslope relating to a filling of microtopographic bedrock depressions before water was able to connect, at which point runoff increased more than fivefold.

Pipes

Preferential flow through pipes or macropores has been identified as an important aspect of runoff generation (Bouma *et al.*, 1977; Gilman and Newson, 1980; Bouma, 1981; Luxmoore, 1981; Beven and Germann, 1982; McDonnell, 1990; Wilson *et al.*, 1989; Muscutt *et al.*, 1993; Soulsby, 1992). Their presence poses serious limitations to the representativeness of the hydrological model. In some cases pipes may improve slope stability by increasing the rate of soil drainage and limiting the development of pore pressure. However, when these normally hydraulically efficient pipes become blocked they can affect water pressure distribution within a slope segment and contribute to landslide initiation

(Pierson, 1983; McDonnell, 1990). Our understanding of their ubiquity and distribution is limited at present although they have been related to the bedrock topographic index in some cases (Freer *et al.*, 2002). What is clear is that they are important and, especially at smaller spatial scales, could be more important than topographic controls (Tsuboyama *et al.,* 1994; Hutchinson and Moore, 2000).

Shallow Bedrock Flow / Fracture Flow

The location of shallow landsliding in steep terrain appears to be influenced by both topographically controlled flow convergence and spatial variabitily in the conductivity of near surface fractured bedrock (Montgomery *et al.*, 2002). The role of groundwater in upland areas is a poorly understood aspect of water transfer through catchments, largely because many such catchments have traditionally been considered to be impermeable at the base of the soils (Shand *et al.*, 2005). However, it is becoming increasingly apparent that many upland catchments, previously considered to be underlain by impermeable bedrock, contain groundwater which may play an important role in streamflow generation (Wilson and Dietrich, 1987; Mathewson, 1990; Genereux *et al.*, 1993; Herwitz, 1993; Montgomery *et al.*, 1997; Shand *et al.*, 1997; Onda *et al.*, 2001; Noguchi *et al.*, 2001; McGlynn *et al.*, 2002; McDonnell, 2003; Shand, 2005).

Several workers have suggested a significant role of shallow fracture flow in landslide initiation (Wilson and Dietrich, 1987; Mathewson *et al.*, 1990; Montgomery *et al.*, 1997; Montgomery *et al.*, 2002). In particular its influence on pore water pressures might help to explain landslides that occur on planar and convex hillslopes (Reneau and Dietrich, 1987; Ellen *et al.*, 1988). The differences in fracture network resulting from bedrock properties may then have important implications for slope stability at the catchment or landscape scale. For example, in Japan, areas underlain by granite generate many landslides while areas underlain by Cretaceous sedimentary rock have few landslides (Hayashi, 1985; Onda, 1994, Onda *et al.*, 2004).

If these apparently contingent entities control pore pressures in the overlying soil, given that knowledge of their distribution and characteristics is practically impossible to obtain, then dynamic hydrological models may prove no more

insightful for predicting the specific locations of shallow landslides than interpretation of simple topographically driven models to predict zones of high landslide potential (Montgomery *et al.*, 2002).

6.2.6. Section Summary

Existing literature suggests that it is unreasonable to expect local site conditions to be exclusively driven by topographic form. The heterogeneity of the material through which water flows makes this almost inevitable. However, it is clear that topography controls spatial soil moisture patterns at some level. The predictive power of topography based models varies considerably between studies. To some extent this is likely to be a result of the model or the methods used to test it. However, it makes sense that the predictive power is also related to the landscape scale characteristics of the catchment: its geology, contingent history, climatic zone and vegetation regime. The aim of this chapter is to establish the extent to which the Lake District study area conforms to the ideal topographically driven wetness, to suggest some plausible reasons for the exceptions and to briefly consider these results in the context of landscape scale controls on topographic wetness. The extent to which this is the case will define the effectiveness of catchment scale hydrological models (this is discussed in Chapter 7).

6.3. Designing an Experiment to Test the Topographic Wetness Hypothesis Across a Range of Scales

To obtain field data to accomplish this aim (to test the topographic wetness hypothesis), I have taken two different approaches at two different scales. Information on the depth to the phreatic surface for a point in space can be reliably obtained by sinking a well at that point. However, these are expensive, time consuming and provide information only at that point. Other studies suggest that phreatic surfaces can be extremely spatially and temporally variable over both the hillslope and the catchment scales. Hillslope patterns enable detailed understanding of the relevant processes at that scale but often highlight the heterogeneity and unpredictability of the slope. Emergent patterns at the catchment scale are difficult to capture from traditional hydrogeological field measurement where the cost and time required to install a suitably dense

network of monitoring equipment is prohibitive. Remote sensing offers the potential to obtain relevant information at a fine spatial resolution for large areas and as such may represent an important tool for understanding the larger scale emergent properties of the relationships between topography and soil moisture.

In this study I apply an intensive study using traditional hydrogeological methods at the hillslope scale (~10^{-1} km^2), nested within an extensive study (~10^2 km^2) taking advantage of high resolution remotely sensed data and making some key assumptions about the relationships between vegetation and soil moisture. Figure 6-1 shows the location of the study area in the northern Lake District and locates the nested study sites: the Newlands Valley study area (Figure 6-1B) and the study hillslope (Figure 6-1C). The setting for these experiments is the Newlands Valley is a ~30 km^2 catchment that drains into Bassenthwaite Lake. This area of the northern Lake District was particularly badly hit by landslides in the January 2005 event.

The solid geology of the area is entirely made up of Skiddaw group rocks, whose properties and configuration are strongly related to their origin as turbidity current deposits. The Kirk Stile Formation is made up of thinly laminated siltstones and mudstones, with local lenticular units of ithic wacke. The Buttermere Formation is an olistostrome of disrupted, sheared and folded mudstone, siltstone and sandstone turbidite olistoliths; within this the Robinson Member comprises a series of large sandstone-rich olistoliths of quartz-rich lithic wackes and granule conglomerates interbedded with siltstone and mudstone. Finally, the Loweswater Formation is composed of mainly sandstone with minor mudstone and quartz-rich greywacke. Basal beds are mainly thin, fine-grained sandstones interbedded with siltstones and mudstone (BGS rock lexicon). The study area is split into two dominant geologies: the Buttermere and Kirk Stile Formations. However, these differ very little in terms of their properties since both are composed largely of siltstone and mudstone.

The valley bottoms are covered with seasonally waterlogged loamy soils (Brickfield unit) whilst the slopes have a mix of well drained loamy or silty soils (Manod unit) and peaty upland soils (Skiddaw unit). All three soil types are underlain by similar solid geology (see above) but the valley bottom position of

the Brickfield series means that this unit often overlies glacial till. The Skiddaw unit contains very shallow acid peaty upland soils over rock often on steep slopes; it may also include some deeper peaty-topped soils with iron pan or thick peat on gentler slopes. Manod soils are classed as well drained fine loamy or fine silty soils over rock; they can be shallow in places and are common on steep slopes. The Brickfield unit contains deep slowly permeable seasonally waterlogged fine loamy soils. In places the unit may include fine loamy soils with only slight waterlogging and some deep well drained fine loamy soils. HOST classes refer to the Hydrology of Soil Type classification scheme applied across the UK (Boorman, *et al.*, 1995). They allow standardised description of British soils in terms of their hydrological characteristics. The HOST classification for the Skiddaw unit (27) indicates that these soils are: "permanently wet, peaty topped upland soils over hard impermeable rocks with no storage capacity" The Manod unit (17) soils are: "relatively free draining soils with a large storage capacity over hard impermeable rocks with no storage capacity". The Brickfield unit (24) soils are: "slowly permeable, seasonally waterlogged soils over slowly permeable substrates with negligible storage capacity".

Figure 6-2 provides some visual context on the character of the area, focussing in particular on Coledale. In common with much of the Lake District, the Newlands valley is largely unforested (vegetated with *Pteridium*, *Eriophorum*, *Calluna* and *Juncus* sp.); and has a strong glacial legacy both in terms of valley form (u shaped valleys with planar valley sides) and material properties (many of the slopes are drift mantled).

Figure 6-1: Location maps for the catchment and hillslope study areas: A) shows the study area (black box) in the context of the Northern Lake District and the 2005 landslides (Note the Portinscale raingauge, labelled P on A); B) is a larger scale map of the Newlands Valley catchment scale study area with the Coledale marked on; and C) shows the hillslope study area including the locations of the instrumentation, and of the transects from Figure 6-3. Contours are at 10 m intervals.

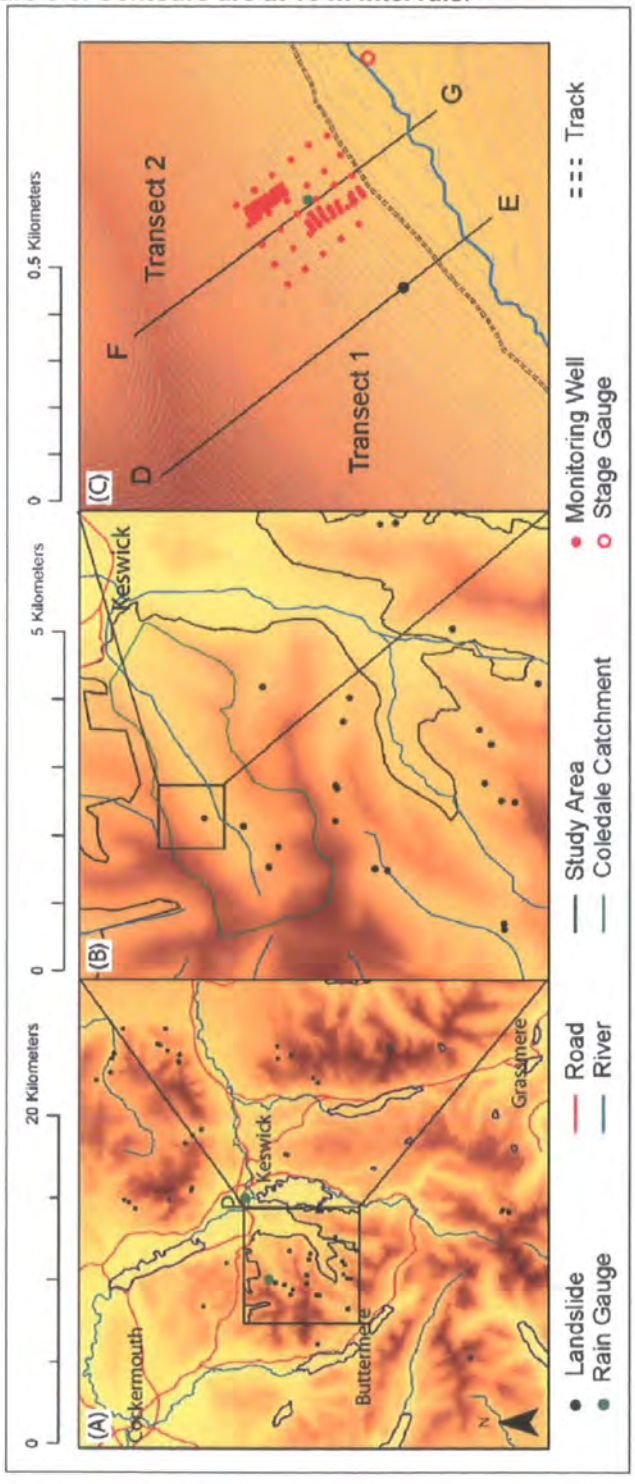

The Newlands valley study area was chosen because: 1) it is an area that suffered particularly dense landslide coverage in the January 2005 storm (Figure 6-1); and 2) high resolution aerial photographs were freely available for the area. The study was limited to upland areas, valley bottoms were excluded

because the strong human influence on vegetation in these areas would render them unsuitable for wetness classification from vegetation. Forest areas were also excluded because they mask the understory vegetation making classification from aerial photographs difficult. The study area's spatial extent was limited by photo coverage and logistic feasibility, it is 38 km^2, includes several valleys, and has a typical hypsometry for the northern Lake District.

6.4. Hillslope Scale (10^{-1} km^2) Method

6.4.1. Scope of the Section

To provide insight into the hydrological behaviour of the steep (Lake District) hillslopes on which landslides occur I designed a hillslope monitoring site on a slope susceptible to landslides. The site is located in Coledale, a typical glacial valley in the northern Lake District, with good access but limited recreational traffic. I applied conventional hydrogeological techniques (manual measurement of water table in monitoring wells) with strategically positioned automatic water level measurements to assess dynamic water table behaviour. I developed a nested monitoring strategy to allow measurement at a sufficient resolution in complex or interesting areas whilst maintaining their context at a coarser resolution. In the following sections I explain the rationale for the location of the study site (Section 6.4.2); then detail the monitoring strategy (Section 6.4.3); before describing the specific monitoring methods in more detail in Sections 6.4.4–6.4.9.

6.4.2. Study Hillslope

The Newlands Valley is a ~30 km^2 catchment that drains into Bassenthwaite Lake. This area of the northern Lake District was particularly badly hit by landslides in the January 2005 event. The area is underlain by solid geology of Skiddaw slates (Llanvirn and Arenig), dominated by Buttermere and Kirk Stile Formations. The valley bottoms are covered with slowly permeable seasonally waterlogged fine loamy soils (Brickfield unit) whilst the slopes have a mix of well drained fine loamy or fine silty soils (Manod unit) and very shallow very acid peaty upland soils (Skiddaw unit). Figure 6-2 provides some visual context on the character of the area, focussing in particular on Coledale. In common with

much of the Lake District, the Newlands valley is largely unforested (vegetated with *Pteridium*, *Eriophorum*, *Calluna* and *Juncus* sp.); and has a strong glacial legacy both in terms of valley form (u shaped valleys with planar valley sides) and material properties (many of the slopes are drift mantled).

Figure 6-2: Photographs illustrating the landscape character of the study area and hillslope study site. Ringed areas in D are the Topographic Hollow (TH), Hillslope Gully (HG) and Spring Seepage Zone (SSZ), these are described in detail in Section 6.4.3. White houses in the valley bottom provide scale in A, B and C; the SSZ in D is ~100 m long. A and B are oblique aerial images. Camera locations for photographs C and D are indicated where visible with green (C) and red (D) dots.

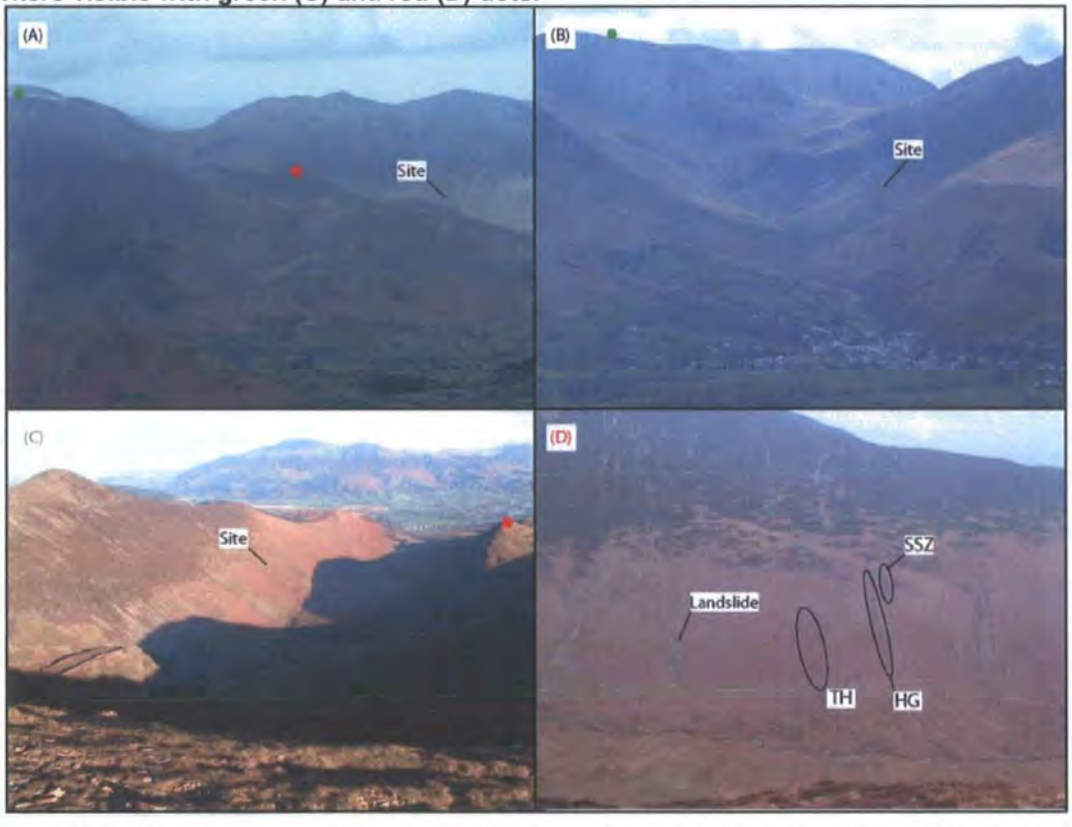

The Coledale sub-catchment is a long u-shaped glacial valley (Figure 6-2) containing a 3rd order stream in the northern Lake District (Figure 6-1). In many respects its topographic form and material composition are typical of the northern Lake District and the Newlands valley in particular. The catchment is underlain by Kirk Stile Formation laminated mudstones and siltstones and has long planar hillslopes (~500 m in profile, Figure 6-3), which are steep and largely unsaturated. Towards the ridge crests, these are mantled in talus and lower downslope towards the channel they are covered with a thick mantle of glacial drift. The soils throughout Coledale are from the Manod and Skiddaw units. The valley side slopes are largely covered with *Pteridium*, *Eriophorum* and *Calluna*, with *Calluna* dominating in the higher and steeper talus mantled

zones (Figure 6-2). *Juncus* on the valley side slopes is limited to small linear (downslope) patches associated with isolated seepage zones. The valley floors have a shallower gradient and are largely saturated for long periods. These areas are characterised by extensive *Juncus* cover. An access road runs up the north side of the valley at the break of slope that signifies the boundary between the hillslope and valley bottom conditions. In this valley the road location is a symptom of the valley form and hydrology rather than a cause, the influence of the road is limited to a maximum of 10 m upslope.

Figure 6-3: Transects from ridge to river down the line of steepest descent to intersect 1) a recent shallow landslide and 2) the study hillslope.

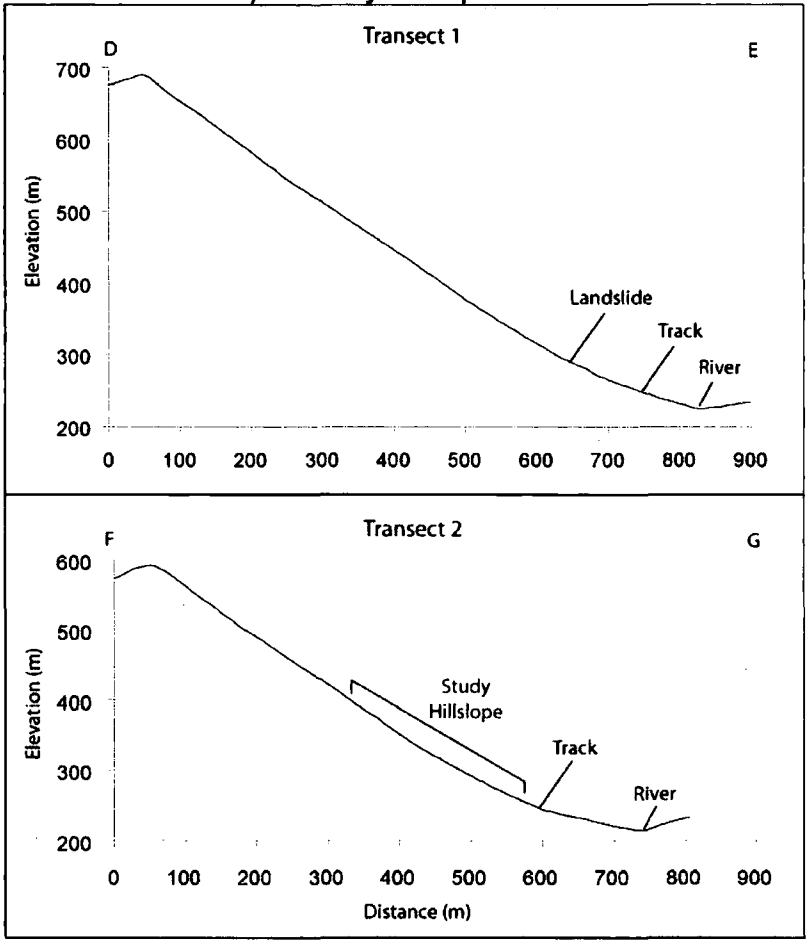

My interest is in hillslope hydrology in areas susceptible to shallow landslides in this respect I am interested in the upper hillslope. Two valley side transects show their steep planar profile and the break of slope at the track in transect 2. The study hillslope is located in the middle third of the hillslope, above the valley bottom influence but low enough to avoid the boundary conditions from summit plateau hydrology. The study hillslope's position along valley was chosen adjacent to a similar slope with a known failure from the January 2005 storm

(Figure 6-3), to include one of the most clearly defined topographic hollows on the side slopes of the valley and a spring seepage zone with clear evidence of overland flow on a section of steep planar hillslope.

6.4.3. Experimental Design

The study hillslope is a plot 200 m wide and 250 m long extending from the break of slope at the road to around half way up to the ridge crest (Figure 6-3). A coarse grid of wells at 50 m spacing provides the framework for the plot monitoring. The coarse grid includes three features of interest labelled on Figure 6-2D, Figure 6-4 and Figure 6-5. First, there is a Hillslope Gully (HG), a tight gully with strong topographic expression, which is narrow but deep with discontinuous ephemeral surface flow and evidence of wash erosion. Second, there is a Spring Seepage Zone (SSZ) an area with disconnected and discontinuous ephemeral flow emitting from distinct seepage points on a planar hillslope and partially re-infiltrating downslope. Third, there is a broad, deep Topographic Hollow (TH) which is steep at the top, with a lower slope at the toe and clear flow convergence according to the upslope contributing area predictions.

The location of monitoring wells within the coarse grid was modified so that their downslope position remained the same but their cross slope location was altered to the centre of the HG (Figure 6-4A). This produced a transect 250 m long at 50 m spacing from above the gully head to the fan at its base. Two additional wells were placed 10 m above and 10 m below the gully head.

Figure 6-4: A map of the study hillslope showing the locations of the raingauge, monitoring wells and Automatic level recorders for: A) the full slope; B) the topographic hollow (TH); and C) the spring seepage zone (SSZ). Contours are at 10 m intervals.

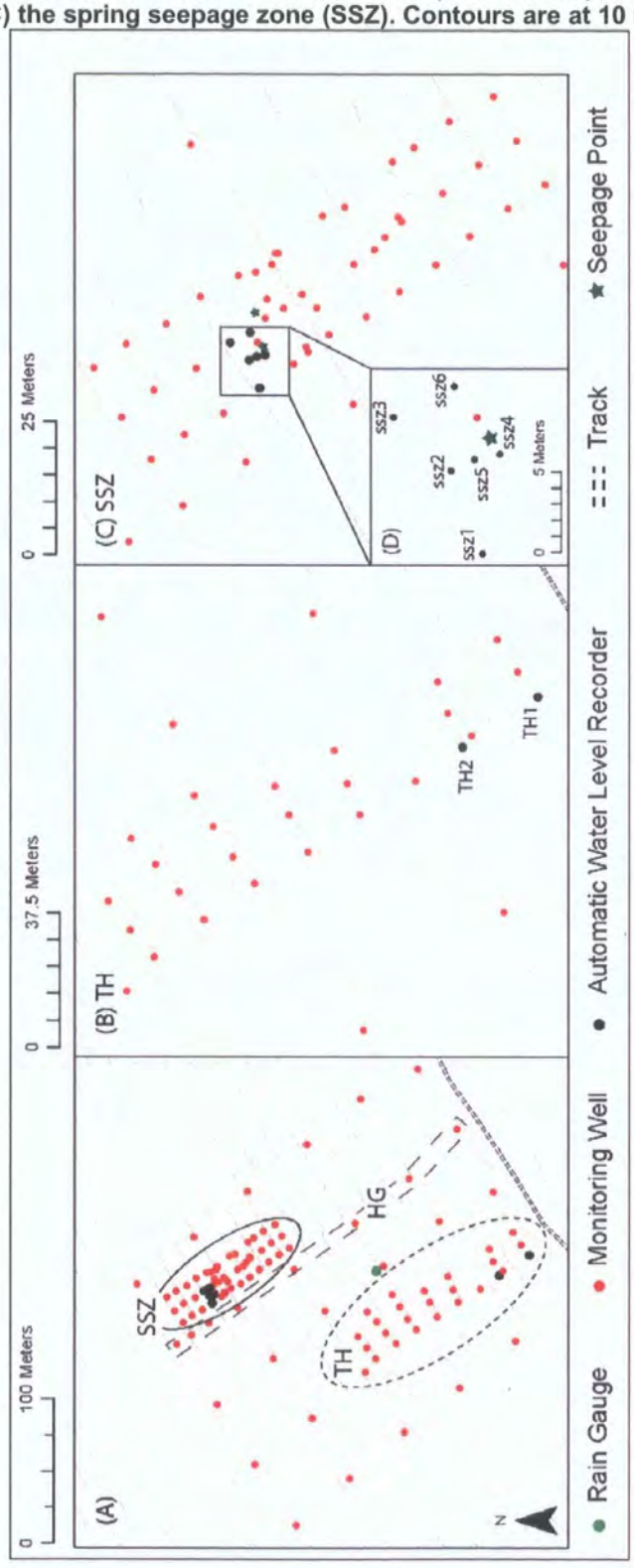

A nested grid was installed in the TH. Wells ran from the steep planar slope above the hollow to the break of slope at the access track (Figure 6-4B). They were installed as transects at 20 m intervals up the central axis of the hollow.

Each transect ran orthogonal to the central axis of the hollow from a well in the centre of the hollow and two or three further wells extending east at 10 m spacing out of the hollow. These transects were designed to sample the phreatic surface depth moving out from the centre to the margins of the hollow. Since the effects on either side of the hollows central axis were expected to be the same, an asymmetric sample strategy was considered the most efficient approach. A second nested grid was installed to cover the area of disconnected overland flow at the SSZ. Wells were installed with a grid spacing of 10 m with a central line running down the most frequently wet zone and a line of wells on either side which extend just outside the area covered by *Juncus* (Figure 6-4C). The grid extends 30 m upslope of the wet area up a steep heather covered slope. At the bottom it extends beyond the *Juncus* into an area where water infiltrates during the largest storms. The fully instrumented hillslope included a total of 105 observation wells.

Figure 6-5: Context photographs for the study site: A) looking downslope from the centre of the hillslope at the elevation of the head of the SSZ (the white van on the track provides scale); B) looking east from the same position towards the SSZ, viewed in profile; C) looking up slope from the base of the SSZ; and D) looking downslope from the head of the SSZ. Field equipment: raingauge (RG), automatic wells (SSZ 2-6) and logger boxes (L1 & L2) are labelled in red. Annotations are in black.

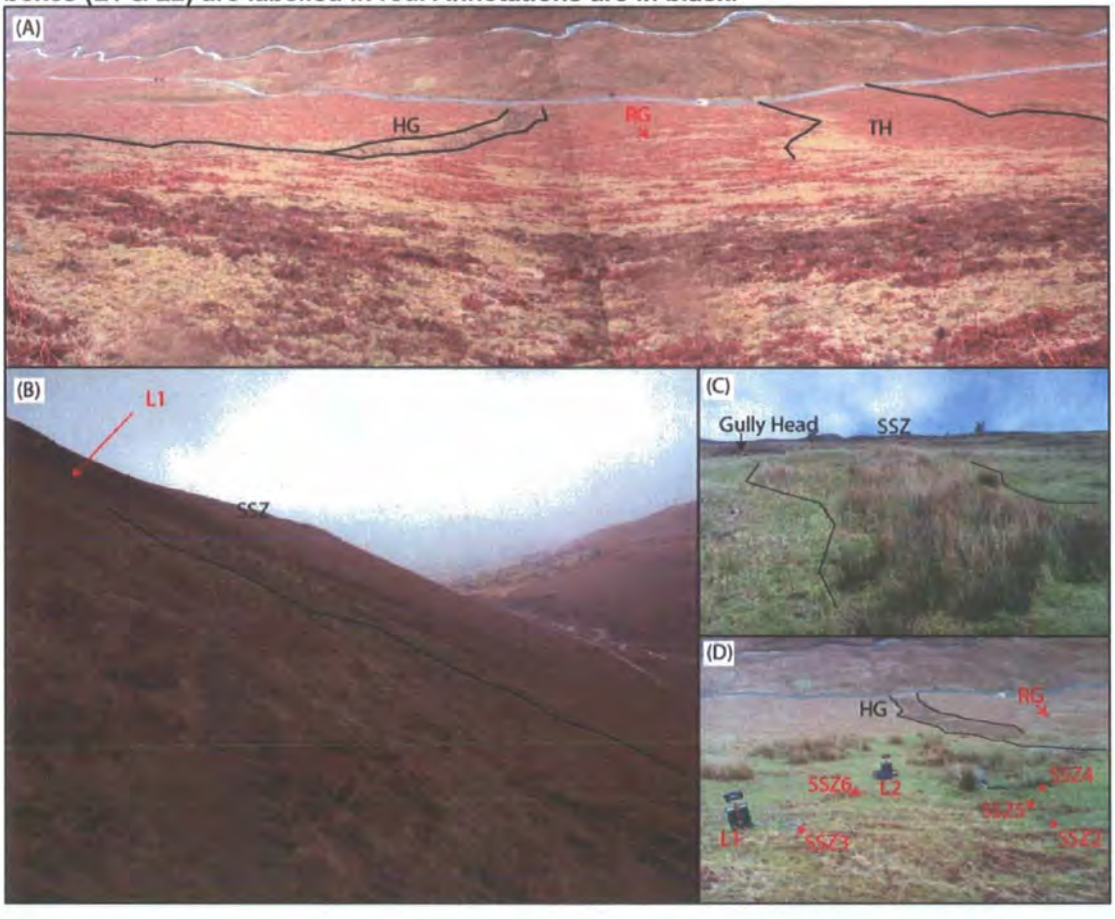

6.4.4. Soil depth measurement and well installation

Soil depth was measured using a knocking pole. Bedrock was identified through pole grounding and was measured to a maximum depth of 4 m. PVC tubes of 25 mm diameter were installed into the holes produced by the depth tests where they produced a snug fit with the edges of the hole. Tubes were sunk to bedrock or to a maximum depth of 3 m. The base of each tube was open and its sides were drilled with two 5 mm diameter holes every 25 mm up the full length of the tube. These wells were used to monitor the depth of the phreatic surface below the ground surface. Wells were used rather than piezometers because the network required broad coverage and wells appeared the most effective way of achieving this. The study aimed to characterise the water table behaviour on the slope and assess the extent to which this conformed to that

expected under the hypothesis of topographically driven flow. Water table measurements in wells provided the most effective way of collecting extensive data and a direct link to the hydrological models applied in most catchment scale slope stability models, which tend to assume slope parallel seepage and calculate pore water pressure from water table height.

6.4.5. Full Slope: Event-based Monitoring

Water depth in the network of wells was measured over a period of two years with an electronic water level meter to a precision of ±10 mm. The results from six of these event-based monitoring sets will be analysed in detail in this study. The event monitoring captured two of the wettest days on record according to the water height measured continuously in SSZ1 and SSZ3 at the head of the flush (Figure 6-4D). More detail on the hydrological conditions on the slope at the time of each monitoring set will be provided as context with the spatial wetness pattern results in Section 6.6.

6.4.6. Full Slope: Maximum Rise Monitoring

For slope stability, the wettest conditions that a slope experiences are often the most important. To capture the spatial pattern of water table height under the wettest conditions I developed a number of maximum rise crest stage tubes designed to identify the maximum water table height between installation and measurement. Sections of plastic coated tape measure were coated in washable ink on both sides then stretched along the inside of a PVC tube of 20 mm diameter (Figure 6-6). These tubes had a single small hole at the top of the tube to allow air circulation and were left open at the bottom to allow water to enter; they were placed inside each of the wells then capped leaving a hole to allowing air to circulate in the tubes. As the water level rose in the tubes ink was washed off to leave clean tape up to the height of the maximum water table (Figure 6-6C). On some tapes problems arose where condensation in the tubes washed some of the ink off, however these uncertainties were limited during data collection by two individuals reading both sides of the tape and comparing their maximum stage estimate. In cases where the results were unclear or the estimates differed by more than 2 mm the measurement was discarded. These

maximum rise crest stage tubes were installed into the wells over two measurement periods: 10/11/06 – 19/02/07 and 19/02/07 – 26/05/08.

Figure 6-6: Diagram showing the equipment design for the maximum rise crest stage tubes (A) with photographs of an example installed at the field site (B) and of a tape with the ink washed off to the maximum water level (C).

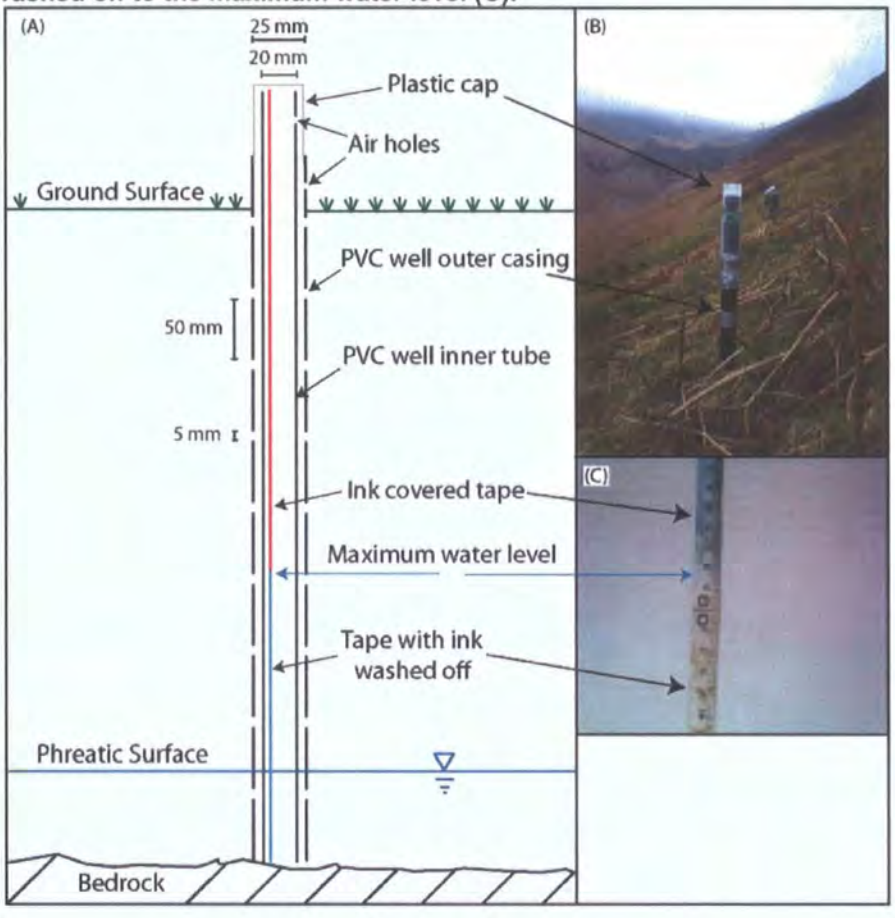

6.4.7. Continuous Water Table Monitoring

Water level was measured continuously using 350 mBar Druck pressure transducers and stored as 15 minute average values. Campbell (CR10 and CR10x) data loggers recorded the water table height at six locations at the head of the SSZ, Valeport loggers recorded the same information at the base of the TH (Figure 6-4). The continuous monitoring wells SSZ1-3 were located to provide a 10 m cross slope transect in a hillslope zone that had previously been identified as wet. SSZ3 at the centre of this transect was 5 m directly upslope of the head of a seepage point. SSZ5 was located equidistant between SSZ3 and the seepage point to establish downslope changes in phreatic surface close to a seepage point at high temporal resolution. SSZ4 was located 2 m away from

the seepage zone along contour in an attempt to capture the timing of any expansion in the saturated zone around the seepage point. SSZ6 was located 5 m downslope of SSZ3 and 5 m along contour from the seepage point, to combine downslope behaviour from SSZ3 with expansion in the saturated area from the seepage point (SSZ4 and 5). The two continuous monitoring wells in the topographic hollow (TH1 and 2) were located at the hollow apex at the theoretical point of maximum flow convergence and highest upslope contributing area. TH1 was located 20 m upslope of the track where the inclination of the hollow had dropped to a gentle (20°) slope. TH2 was located 20 m upslope of TH1 in the apex of the hollow but on a steeper (30°) slope. These wells were located to establish downslope behaviour of the phreatic surface and to capture the dynamics of any upslope expansion in the saturated zone. Data loggers were downloaded every 6 to 8 weeks and the pressure transducers examined and cleaned when necessary.

6.4.8. Continuous Rainfall Monitoring

The magnitude and timing of rainfall at the site is useful to provide context for the spatial and temporal water table behaviour recorded in the wells. Equipment failure at the Coledale hillslope raingauge lead to gaps in the rainfall record from 01/01/06 to 01/03/06 and after 04/07/06. As a result, data from the nearby (~5 km) Portinscale gauge is used in its place (labelled P on Figure 6-1A). Figure 6-7 shows a comparison of the two rainfall time series in terms of hourly rainfall intensities for two time periods: the 14th December 2005 to the 1st February 2006 (A) and the 2nd March to the 7th July 2006 (B). These plots indicate that the magnitude and timing of the rainfall was comparable between gauges.

Figure 6-7: Hourly rainfall Intensity data from the Coledale hillslope gauge and the nearby Portinscale gauge demonstrating the comparability of the records.

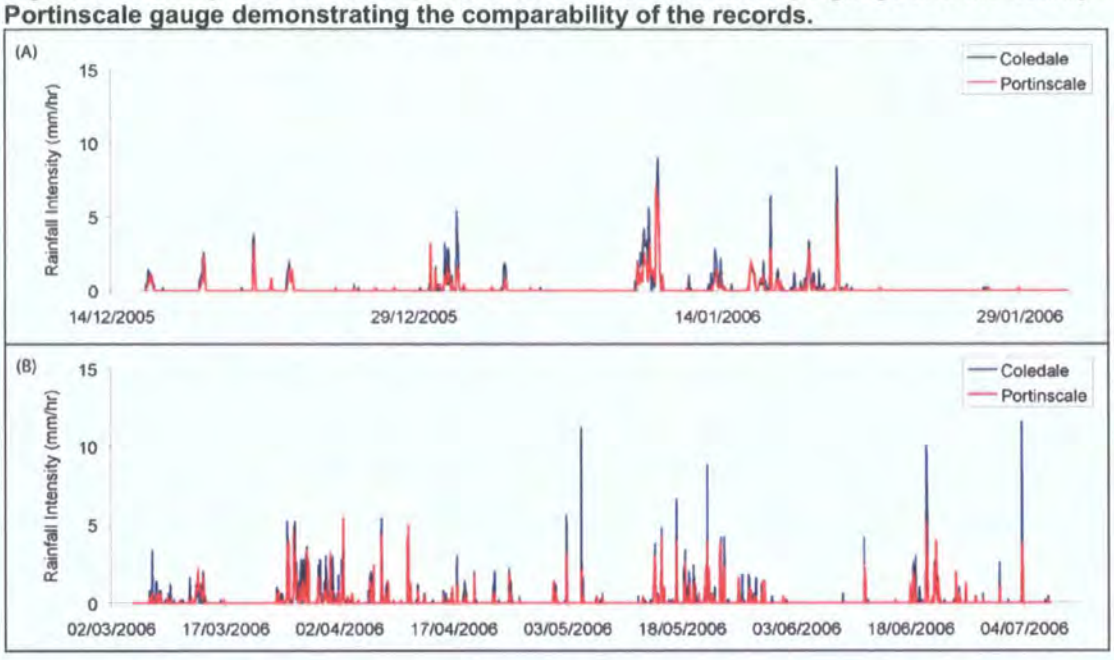

The level of direct agreement between the gauges can be assessed visually from Figure 6-8 and has been quantified using concordance correlation (Lin, 1989, 2000). The results (Table 6-1) suggest a significant (p=0.01) relationship between the two gauges. The reduced major axis intercept close to zero is expected from the large number of rain free timesteps in both series. The slope (1.472) suggests that the volume of rainfall is larger at the Coledale hillslope than the Portinscale gauge, again this is to be expected from the differences in location between the two gauges and in particular the increased altitude of the Coledale gauge (300 m O.D. compared to 90 m O.D. at Portinscale). A direct replacement in records (without any treatment for systematic bias) is appropriate here because the rainfall record supplies useful additional information on the hillslope's hydrological conditions during the measurement campaign but is not used as a basis for more detailed calculations. Instead this aspect of the study focuses on relative patterns of wetness across the hillslope assuming locally spatially uniform precipitation.

Table 6-1: Concordance correlation coefficient (r_c) results indicating the level of direct agreement between the Coledale hillslope gauge and the Portinscale gauge used to complete the record.

Reduced Major Axis		Lin's r_c	Pearson's r
Slope	Intercept		
1.472	0.004	0.753	0.815

Figure 6-8: Comparison of hourly rainfall intensity data from the Coledale hillslope gauge and the nearby Portinscale gauge used to extend the rainfall record.

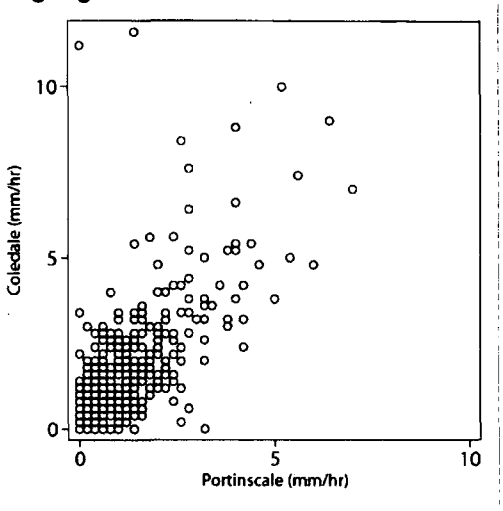

6.4.9. Continuous River Stage Monitoring

River stage was recorded in a stilling well on the right bank of Coledale Beck 100 m down valley from the study hillslope. This reach was chosen for its uniform geometry in cross section and profile, the channel was capable of high discharge flows without going over bank and the flow was relatively undisturbed (Figure 6-9). Water level was measured and recorded using a 500 mBar Eijelkamp Diver pressure transducer and corrected for changes in atmospheric pressure using corresponding data from a nearby (<5 km) barometric pressure transducer.

Figure 6-9: Photographs showing the site of the river stilling well, this photograph was taken during high flow conditions.

6.5. Catchment Scale (10^0 - 10^2 km^2) Method

6.5.1. Scope of the Section

In Section 6.2.4 I highlighted the strong link between vegetation type and soil moisture. Vegetation has been used as an indicator of soil moisture in Canada and Scandinavia (Rodhe and Siebert, 1999; Wang *et al.*, 2000; Zinko *et al.*, 2005), but to my knowledge no such studies have been undertaken in the UK. A further advantage of UK uplands in general and the Lake District in particular is the lack of forest cover across much of the landscape. This allows understory vegetation, likely to be the best indicator of soil moisture, to be clearly visible at long distances and from the air. High resolution colour imagery is now widely available for the UK. This represents a potential tool for identifying vegetation remotely. This study demonstrates the potential for such a technique, using the Newlands valley as a pilot study and manually digitising wet vegetation types from high resolution orthrecitified aerial photographs. In Section 6.5.2 I examine the available information on the ecological amplitude (tolerance to wet conditions) of the dominant vegetation types in the study area. In Section 6.5.3 I detail the method that I have used to map these vegetation types. In Section 6.5.4 I identify the relevant topographic variables to test the topographic

wetness hypothesis and explain how they are derived. In Section 6.5.5 I provide the necessary background on the sources of additional data from which I have inferred the material properties of my study area.

6.5.2. Lake District vegetation as an indicator of wetness

The Newlands valley study area is dominated by *Calluna vulgaris*, *Pteridium aquilinum*, *Eriophorum vaginatum*, *Juncus effusus* with *Sphagnum* and other mosses in some areas. This is in keeping with the description of Lake District vegetation outlined in Section 2.3.7. For each species there are two important properties to establish: 1) effectiveness as an indicator of moisture conditions (related to its ecological amplitude, Table 6-2); and 2) typical form and colour, providing information to distinguish between vegetation types in aerial imagery.

Table 6-2: Ecological amplitudes for soil moisture for common Lake District vegetation types based on literature review.

Vegetation Type	Ecological Amplitude for Soil Moisture
Calluna vulgaris	An indicator of relatively dry conditions (Gimingham, 1972; Equihua, 1990). **(Dry)**
Pteridium aquilinum	Occupies wetter zones than *Calluna* (Munoz-Reinoso, 2001), but still requires well drained soil (Poel, 1961) since it is intolerant of anaerobic conditions (USDA). **(Well Drained)**
Juncus effusus	A common and dominant emergent macrophyte in freshwater wetlands (Richards and Clapham, 1941; Thompson and Grime 1979; Ervin and Wetzel, 2002). Frequently abundant or dominant in zones of fluctuating water table (Richards and Clapham, 1941), probably as a result of its ability to maintain root growth under very low soil oxygen concentrations (as low as 0.5%) allowing it to survive extended periods of anaerobic soil conditions (US Army Corps of Engineers Wetlands Delineation Manual). **(Wet)**
Sphagnum mosses	Widely considered an indicator species for wetlands (USACE) and intrinsic in definition of 'bogs'. **(Very Wet)**

Juncus stems are bright or yellowish green, tall and stiffly erect, growing in dense tufts. It is particularly visible on aerial imagery due to not only a change in colour but also in texture, growing in tufts, which remain distinct, not forming continuous stands (Richards and Clapham, 1941). *Calluna* and *Pteridium* are good indicators of dry and probably dry conditions respectively, and are clearly distinguishable on the aerial imagery, minimising the risk of miss-classification in these areas. Because of its sensitivity to wet conditions (Richards and Clapham, 1941), its dominance under those conditions (Ervin and Wetzel, 2002) and the relative ease with which it can be identified in aerial imagery, *Juncus* is applied as a key indicator of wetness. It is unlikely to occur in dry conditions and as a result allows areas with *Juncus* to be confidently considered wetter than their surroundings. However, wet areas are not limited to those with *Juncus* cover, in some cases other vegetation types (such as *Sphagnum* mosses) occur in close proximity to, or surrounded by *Juncus*, in such situations these areas are also mapped as wet. These other 'wet' vegetation types are more difficult to distinguish in the imagery and as a result are mapped only where they are particularly clear, or where they occur in combination with *Juncus*.

6.5.3. Identifying Wet Zones from Aerial Imagery

True vertical aerial photographs were collected in July 2005 with a Zeiss LMK metric camera at an altitude of 1500 m with a photo scale of 1:10000 and pixel resolution of ~0.1 m. Thirty of these images covering an area of ~100 km^2 were orthorectified by direct linear transformation (El-Aziz and Karara, 1978) in ERDAS IMAGINE. Ground control points were collected from features identifiable on Ordnance Survey 1:25000 scale maps that were clearly visible in the images. Camera orientation was established with a Root Mean Square Error (RMSE) of ~2 m and always less than 5 m. This was important since the IfSAR DSM from which topographic attributes would be calculated has a 5 m resolution. This IfSAR DSM with a vertical precision of ~0.5 m was used to obtain the z values for the orthorectification. Orthorectifed images were generated by resampling the original images into the new coordinate space at 0.1 m resolution using bilinear interpolation. The resultant images have planimetric errors <3 m and pixel sizes ~0.1 m, they overlapped by ~60% in an

east / west direction and ~30% in a north / south direction. Because the photographs were to be used for manual vegetation identification there was no need for radiometric correction (which would inevitably result in some information loss). The large overlap enabled me to work with coverage of the same surface area on several images. The subtle changes in image radiometry, lighting conditions or camera 'look angle' enabled me to assimilate the data required for accurate classification and mapping.

Figure 6-10: a mosaic of some of the orthorectified aerial photographs for the Newlands valley study area (outlined in red).

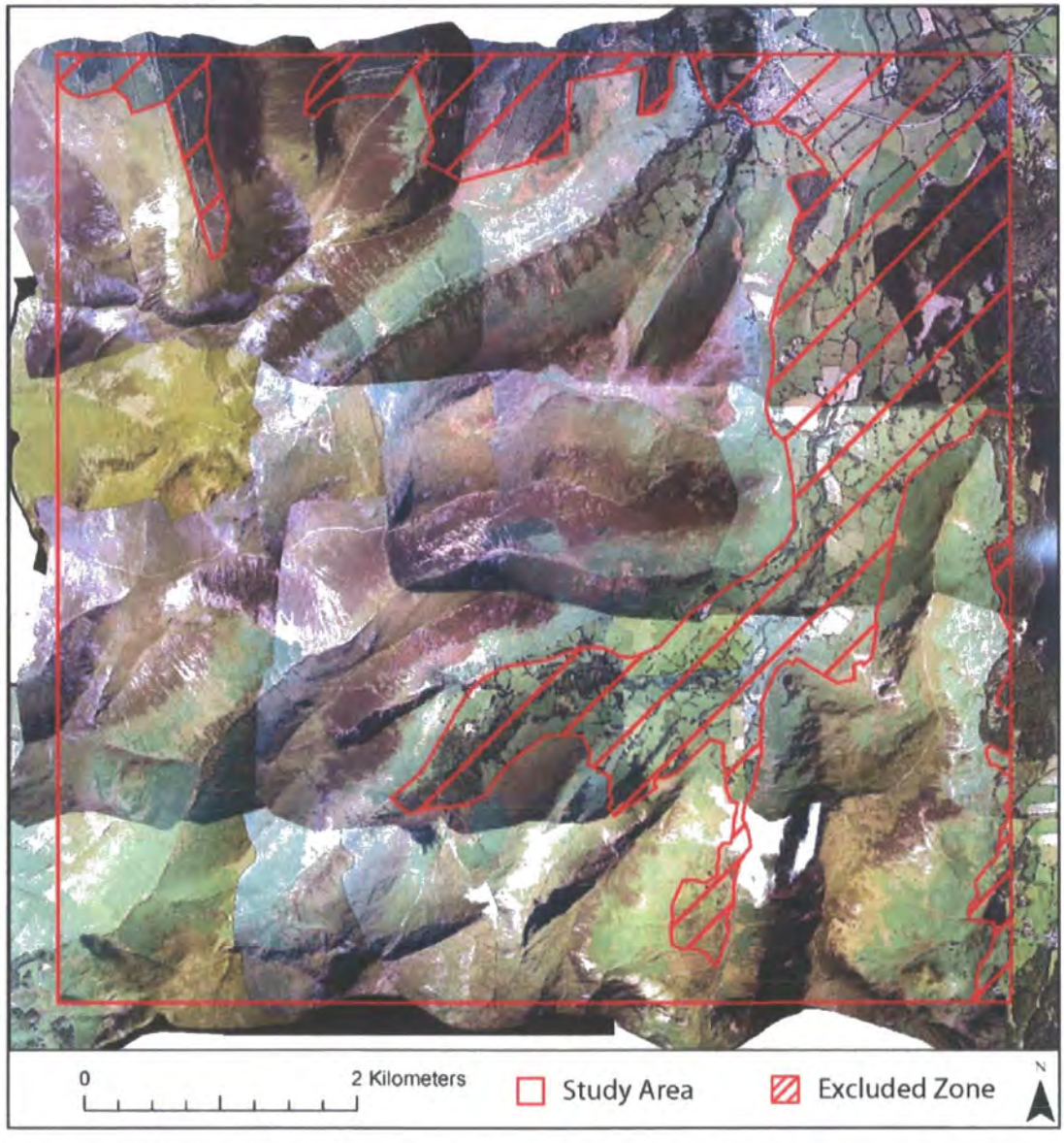

Wet zones were identified on the images based on indicative vegetation types, in particular *Juncus* Effusus and *Sphagnum* spp. The correct identification of wet vegetation types from aerial imagery is central to this technique. Images

were classified using a 'training' image set for Coledale valley where the vegetation types are known from field experience. Wet zones were digitised manually to generate vector polygons of wet areas. The correspondence between mapped vegetation and ground truth was qualitatively validated for two other valleys, the upper Newlands valley and Sail Beck. Topographic information for each cell tagged as wet is extracted using variables derived from the IfSAR DSM: slope, Upslope Contributing Area (UCA) and topographic index.

Figure 6-11: Mapping vegetation from orthorectified aerial photographs: A) the ortho-photo, B) the ortho-photo overlain onto a 1:25000 cartographic map, C) wet vegetation types (highlighted in red) identified from the ortho-photo, D) the mapped wet zones overlain on the cartographic map.

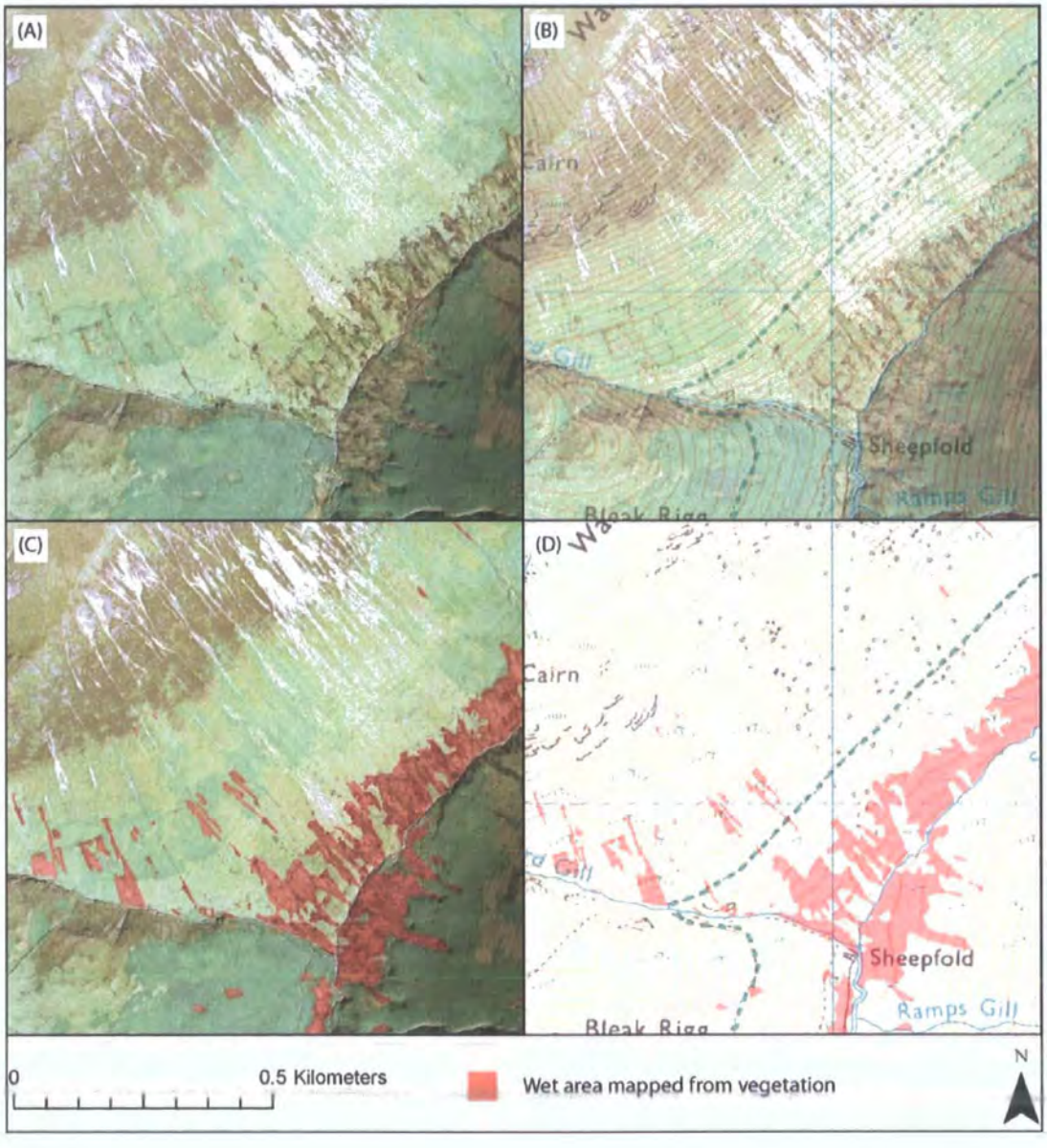

6.5.4. Deriving Relevant Topographic Variables

Topographic variables were derived from the IfSAR DSM because the filtering algorithm applied by Intermap (the elevation data providers) to filter non-ground points from the DSM has been found to smooth the surface causing loss of topographic representation in the DTM (Section 3.6.6). I calculated slope, upslope contributing area (UCA) and topographic index. Slope and UCA are both individually considered important in defining a cells wetness, slope because it controls the rate of downslope water transfer through the cell and contributing area because it controls the volume of water passing through that cell. Slope was calculated using the Zevenbergen and Thorne (1987) algorithm. Upslope contributing area was calculated using the deterministic infinity (D∞) algorithm (Tarboton, 1997) after sinks had been filled using the Planchon and Darboux (2002) algorithm. The topographic index (I) for defining hydrologically similar zones (Beven and Kirkby, 1979) was calculated using the equation:

Equation 6-1

$$I = \ln\left(\frac{a}{\tan\beta}\right)$$

where: a is the upslope contributing area per unit contour length and β is local slope.

6.5.5. Material Properties Data Sources for the Study Area

The entire study area and the wet areas were classed by solid geology, surficial geology and soil type to establish the effect of these material properties on soil moisture conditions. Geology maps at 1:25000 scale from the British Geological Survey provided in digital form through EDINA provided the spatial data on solid and surficial geology for the study area. The National Soil Resources Institute holds corresponding digital data (1: 250000) on the spatial patterns of soil types over the UK. These data were used to provide soil type information over the study area.

6.6. Results - Hillslope scale

6.6.1. Scope of the Section

Hillslope scale results provide reliable water table depth measurements: 1) at a high density over a small area and with limited temporal coverage (Section 6.6.2); 2) at high temporal resolution for a small number of strategically positioned wells (Section 6.6.3); and 3) from a dense network estimating minimum water table depth over a long time period but with uncertainty in the timing of these minima (Section 6.6.5). Each measure provides useful information to characterise the hydrological behaviour of this hillslope and to assess the extent to which this behaviour is driven by topography. I will deal with each in turn below.

First I detail the results from six event based measurement campaigns, providing context for these from continuous monitoring (Section 6.6.2). These results highlight two areas of particular interest, the topographic hollow (TH) and the spring seepage zone (SSZ). In Section 6.6.3 I expand on the data from continuous monitoring in these two zones to illustrate the range of hydrological behaviour over a year. In Section 6.6.4 I introduce the spatial patterns of derived topographic variables that are often used in predicting wetness patterns. In Section 6.6.5 I present spatial minimum water table depth estimates from two periods both >3 months, both highlight the SSZ as a particularly wet part of the hillslope. I then focus on the SSZ, analysing the water table dynamics at its head (Section 6.6.6) and developing a conceptual model for its behaviour (Section 6.6.7). Finally, in Section 6.6.8 I compare predicted wetness from the topographic variables from Section 6.6.4 with observed minimum water table depths from Section 6.6.5, to test the topographic wetness hypothesis at the hillslope scale.

6.6.2. Event Based Monitoring

The monitoring period on the study hillslope can be split into two subsets (Figure 6-12). The first, between 12/2005 and 04/2006 was a period of manual well measurements taken at the same time as the well network was installed. The second, from 08/2006 to 07/2007 was a period with maximum rise crest

stage tube measurements of water table depth and detailed continuous monitoring in 15 minute resolution time series from eight wells across the slope. Figure 6-12 shows the context for these two measurement periods in terms of rainfall and water table depth from the two longest records positioned at the head of the SSZ (labelled on Figure 6-4). These records and the context rainfall record indicate that the hydrological year of 2006-7 was particularly wet, with frequent storms preventing groundwater levels in the wells from receding to their base level.

Figure 6-12: Rainfall intensity, cumulative rainfall and water table depth for the full study period

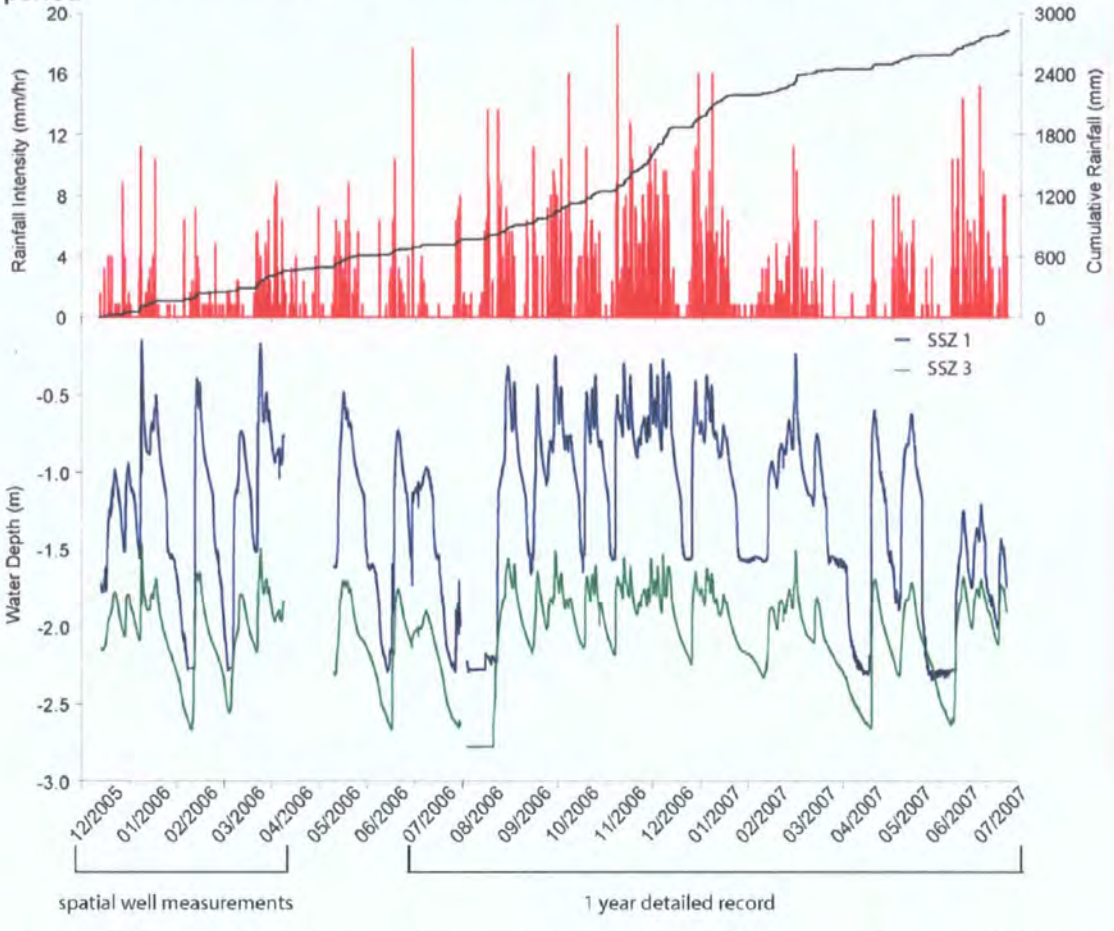

Figure 6-13 expands the first part of the record from Figure 6-12 (12/2005–04/2006) to give more detail on the hydrological conditions during the event based well measurement campaign. Boxes A, B and C highlight the periods when measurements were taken. These are expanded in Figure 6-14. In each case, rainfall intensity is plotted in red in mm hr^{-1} from 15 minute tipping-bucket raingauge data with water depth in SSZ1 (blue) and SSZ3 (green). Vertical black lines indicate the date and time of manual measurement. The six-event

based measurement campaigns capture the range of hydrological conditions on the slope (according to the time series data from SSZ 1 and 3) preferentially sampling wet conditions.

Figure 6-13: Rainfall Intensity, cumulative rainfall and water table depth for the period (Dec 05 – March 06) when manual water table depth measurements were recorded. Boxes A, B and C enclose periods of manual measurement, they are expanded in Figure 6-14.

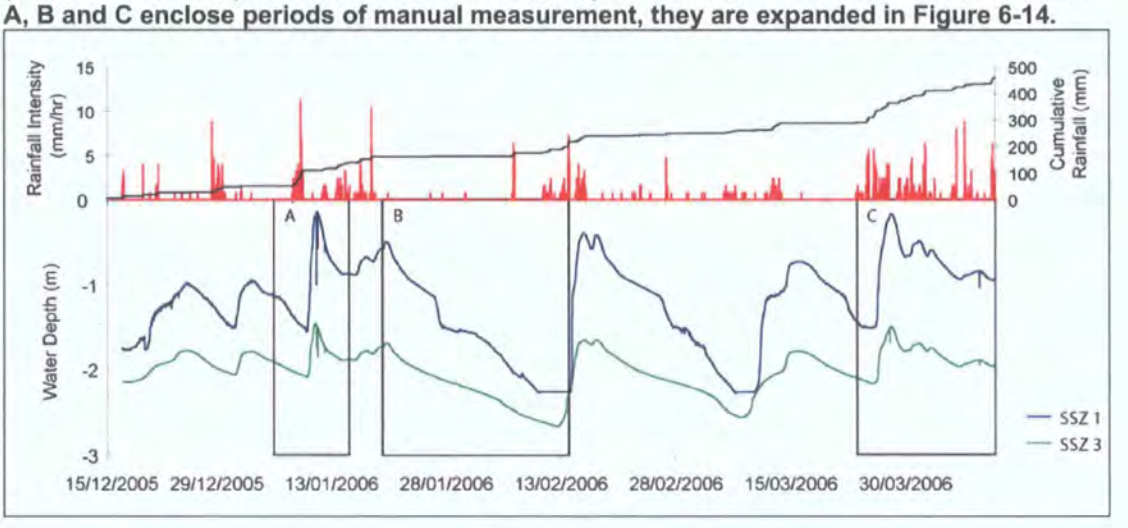

Three sets of measurements were taken at the peak of two storms; two sets in a single day in January (A1 and 2) and another during a storm in March (C1). The other three measurements capture varying stages of the falling limb: early on the falling limb (A3); several days after the peak, but with high water levels maintained by sustained low intensity rainfall (C2); and more than 15 days after a peak, during a period of very little rainfall (B) when water depths are close to their baseflow level. The high flow events (A1, A2 and C1) represent the wettest conditions in the record for these two wells. Both wells have very similar peak values for the two events, which have peaks within centimetres of each other. The water table in SSZ1 rises to within 0.15 m of the surface and that at SSZ3 rises above 1.5 m for the only times in the record.

Figure 6-14: Rainfall intensity and water table depth for the three periods during which manual water table height measurements were taken across the hillslope. Black lines indicate the precise dates and times of measurement.

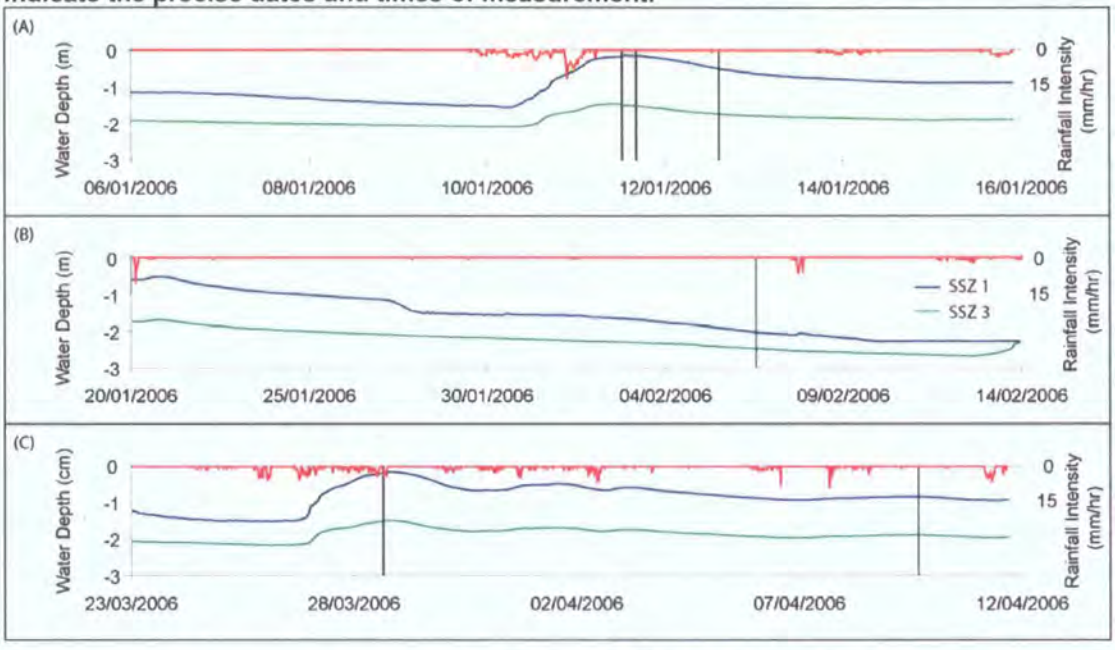

Results from these measurements (Figure 6-15) identify two areas where the water table is measureable on the hillslope. The SSZ, where water appears to flow down a central thread, corresponding to the areas of *Juncus* grass; and the base of the topographic hollow (TH), where we might expect high UCA's and low local slopes to generate elevated water tables. The surprising result from all these measurements is the extent of the dry conditions over the majority of the hillslope even in very wet periods (Figure 6-15). Although the phreatic surface is <1 m below ground level at the foot of the hollow (TH) it dissipates altogether only 20 m upslope and remains dry to 3 m in the mid and upper hollow in all conditions. Observations at this hillslope suggest step change behaviour in spatial wetness patterns. In both locations where the phreatic surface is intersected by measurement wells it is accompanied by steep hydraulic gradients with nearby wells completely dry to bedrock or to 3 m. This is important from a landslide perspective since wetness patterns will exert an important influence on pore water pressure distributions in storm events and in particular on not only the magnitude of these pressures but importantly on their spatial scale and pattern. These considerations are less important if landslides are considered as infinite slope stability problems. However, such a treatment is unreasonable unless the spatial scale of the wetness and therefore elevated pore water pressures is larger than the scale necessary to satisfy the infinite slope assumptions (i.e. width and length greater than 10 times depth; Brunsden,

1979, Chapter 2). Further, if a three-dimensional approach is taken (as considered in Chapter 4) then the size of the wet area and therefore of the higher pore water pressure defines the size of the potentially unstable area and the dimensions of this area in combination with soil properties define its stability at a given pore water pressure.

Figure 6-15: Manual measured water table depths (m) on the study hillslope for the six measurement periods identified in Figure 6-14.

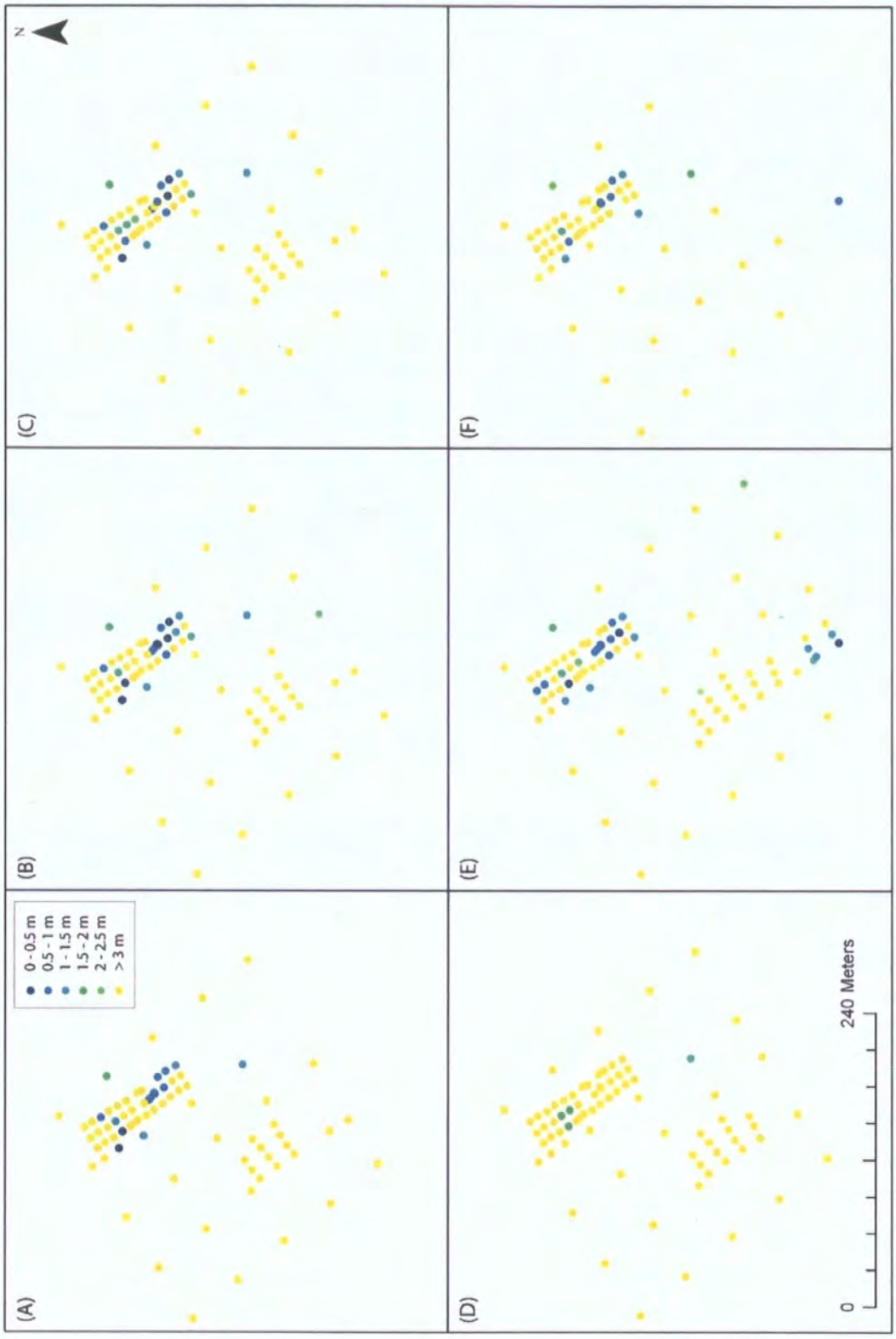

6.6.3. Continuous Monitoring

The second half of the record includes time series from automatically logging (15 minute intervals) water level recorders in a denser network of wells (Figure

6-16). This year long record (08/2006 – 07/2007) covers a period of sustained rainfall through the winter during which maximum rise crest stage tubes were installed (11/2006). Maximum water table heights in each tube were measured in January 2007 and again in May 2008 (Figure 6-20). The locations of wells with automatic water level recorders are detailed in Section 6.4.3 and Figure 6-4.

The SSZ wells have similar peak flow patterns but fall into three groups related to the offsets in their peak water table height (Figure 6-16). SSZ 1 and 2 have very high peak water tables, frequently rising to <0.2 m from the surface (Figure 6-16C). SSZ 3 and 5 have water table depths almost 1.5 m deeper than 1 and 2 but with a form similar to that of SSZ2 (Figure 6-16C). The water table rarely or never drops below the maximum depth of these wells over the course of the year. At this scale, the timings of the SSZ responses are synchronous. SSZ 4 and 6 are dry to their full depth for all but the largest storms, when they respond to capture the peak of the water table response, these peaks are synchronous with those from the other wells and to a similar (or slightly deeper) depth but their form is somewhat attenuated (Figure 6-16C). SSZ1 has three other interesting properties: 1) it is one of the flashiest wells, with a water table that varies by more than 2 m; 2) it appears to have an intermediate base level at ~1 m depth which is frequently attained during winter between storm sequences while in spring and summer the level drops to >2.2 m depth, below the maximum extent of the well; and 3) there are inflexions in its falling limbs, which occur as the water table drops below a certain depth and may be related to upslope connectivity.

Water table behaviour at TH1 and SSZ2 (Figure 6-16 B and C respectively) appears to be strongly similar in terms of absolute depths, synchronicity and the form of the curves. This is surprising since they are far apart and in very different settings, which might be expected to stimulate differing water table responses. TH2, which is 20 m upslope of TH1, behaves very differently to the rest of the wells (Figure 6-16B). It has steep rising and very slow falling limbs (e.g. 03/2007) and as a result the sequencing of rainstorms has an increased effect on water table height (e.g. 11-12/2006). When each event occurs on a falling limb, the peaks increase with the number of storms that have passed in

succession. However, considerable antecedent rainfall is required before the water table will be influenced by an individual storm. Storms after prolonged dry periods or with only limited antecedent rainfall do not influence the water table depth. TH2 appears to be a threshold system, moving into a responsive phase after a given amount of antecedent rainfall. It represents a more integrated response to longer term rainfall trends compared to the flashy behaviour of TH1 and the SSZ wells.

Figure 6-16: Rainfall intensity, cumulative rainfall (A) and water table depth in wells at TH (B) and SSZ (C) for the second part of the study period. The locations of these well are detailed in Section 6.4.3 and Figure 6-4. The gap in the measurement record for TH1 is a result of instrument failure.

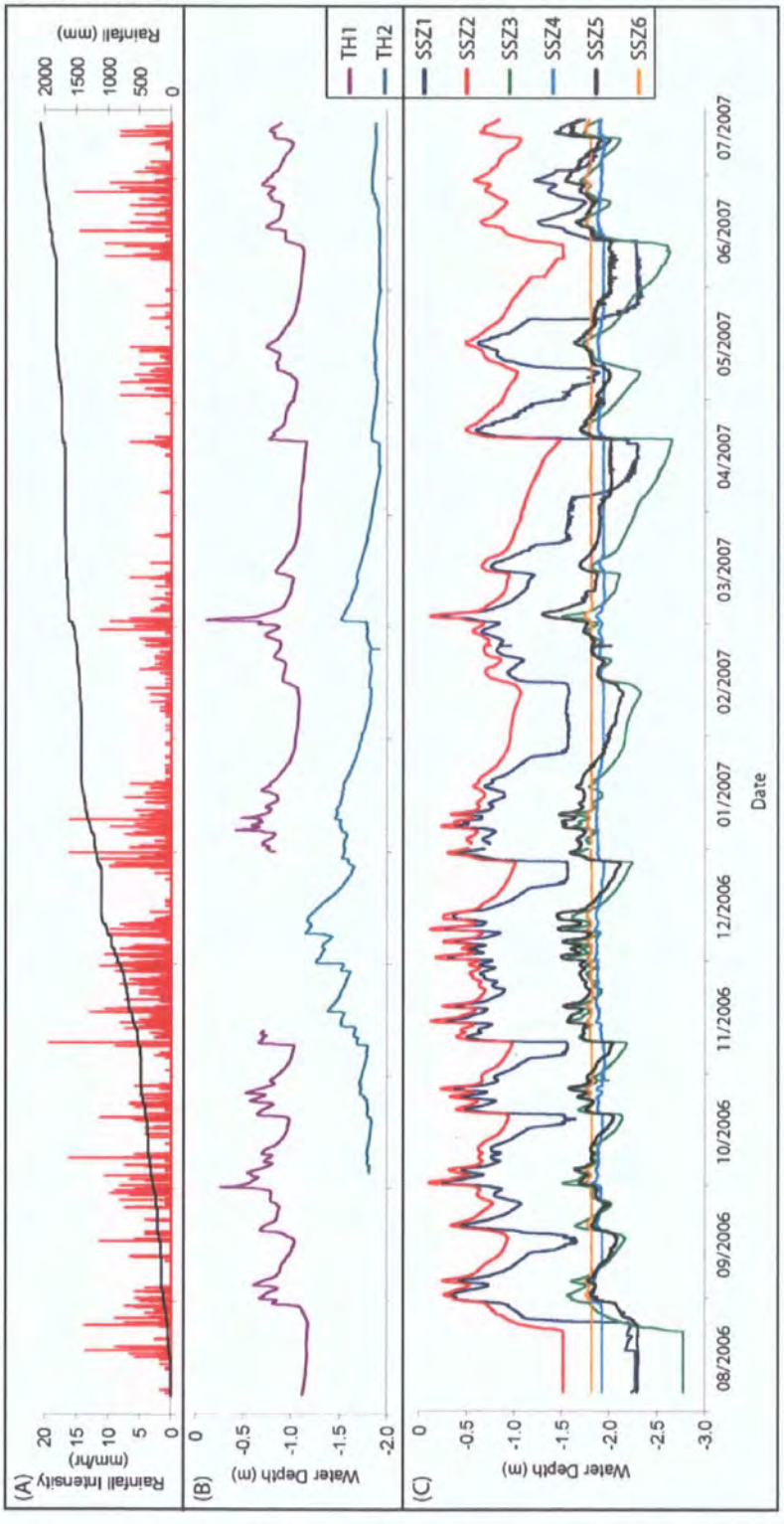

Several further properties of the water table response over time can be ascertained by looking in more detail at the time series from automatic well measurements. Figure 6-17 focuses on the period from 10/2006–02/2007 from the full record in Figure 6-16. This time series includes: rainfall intensity; water

depth from the six recorders at SSZ and two at TH; and the stage record from Coledale beck. The stage data are included for comparison and to give context for the 'peakiness' and lag of the water table response. As might be expected from a hillslope water table, the wells are less peaky than the stage data, with more gentle rising and falling limbs. As a result, there is a longer lag between rainfall and peak water level in the wells compared with the stream.

At this scale (months), peaks appear synchronous between water table response at TH and SSZ (Figure 6-17). However, once we consider the record at a higher resolution for a shorter period (1 month) some differences are visible (Figure 6-18). The peaks in TH1 appear to have steeper rising limbs and shorter lags than those at the SSZ (Figure 6-18). Figure 6-18 also highlights the extent of the lag between river stage and well level, which can peak almost a day after the river peak. The river responds almost immediately while the hillslope response is considerably slower in some cases. Both Figure 6-17 and Figure 6-18 show an inflexion in the decline in water height on the falling limb of SSZ1. This inflexion represents an increase in the rate of water depth decline which occurs consistently when water table in the well falls below 1.2 m from the surface.

Conserving mass, such a change in storage must represent a change in flux into or out of the soil column at this point. Since this inflexion is on the falling limb and often occurs in a prolonged dry period, inputs from infiltration can be neglected. Vertical losses from the soil column can also be considered constant so that the change must be the result of some change in lateral flux. Depth dependent output flux is related to the hydraulic conductivity – depth relationship. This is usually considered to decline with depth, a relationship that would produce the opposite depth output to that required if all else is held constant. In fact, the conductivity profile required to generate such an increase in flux out is difficult to imagine. It would have to be very unconductive to 1.2 m then very conductive and even then the pressure dependence of water velocity would tend to mitigate against such an inflexion, resulting from changes in conductivity with depth. However, a change in the input flux is reasonable and might represent a threshold response upslope which significant reduces or completely turns off the input flux from upslope. This might be a drop in water

level into a low conductivity material upslope or a lowering of the water table below a bedrock lip, breaking the connectivity between the well and its source area upslope.

Figure 6-17: An expanded section of the full year record of rainfall intensity, river stage (A) and water table depth in automatically logging wells at TH (B) and SSZ (C). The locations of these well are detailed in Section 6.4.3 and Figure 6-4. The gap in the measurement record for TH1 is a result of instrument failure.

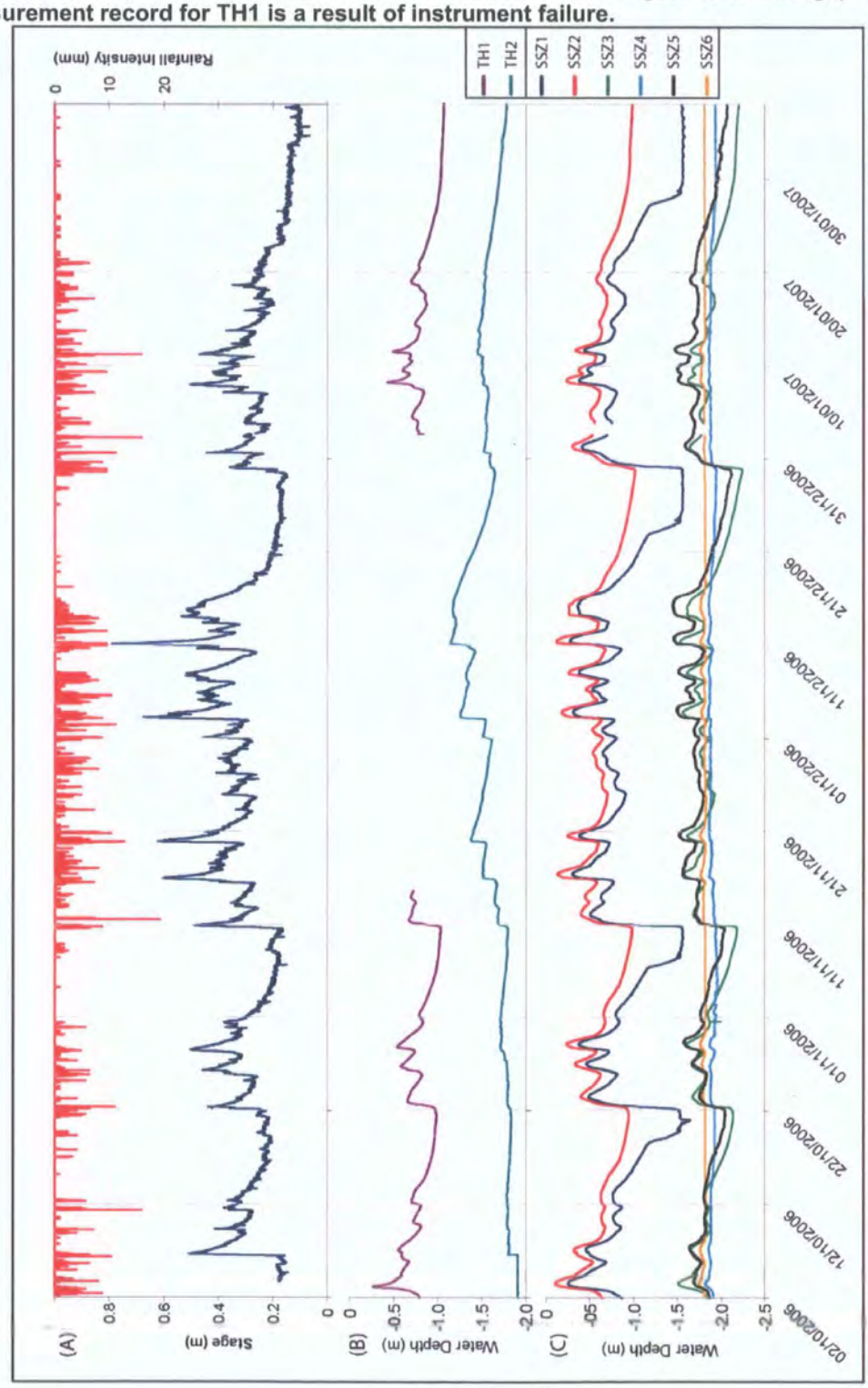

Figure 6-18: A further expansion of Figure 6-17 showing the fine detail in the records of rainfall intensity, stage (A) and water table depth at TH (B) and SSZ (C) for a small part of the year long record.

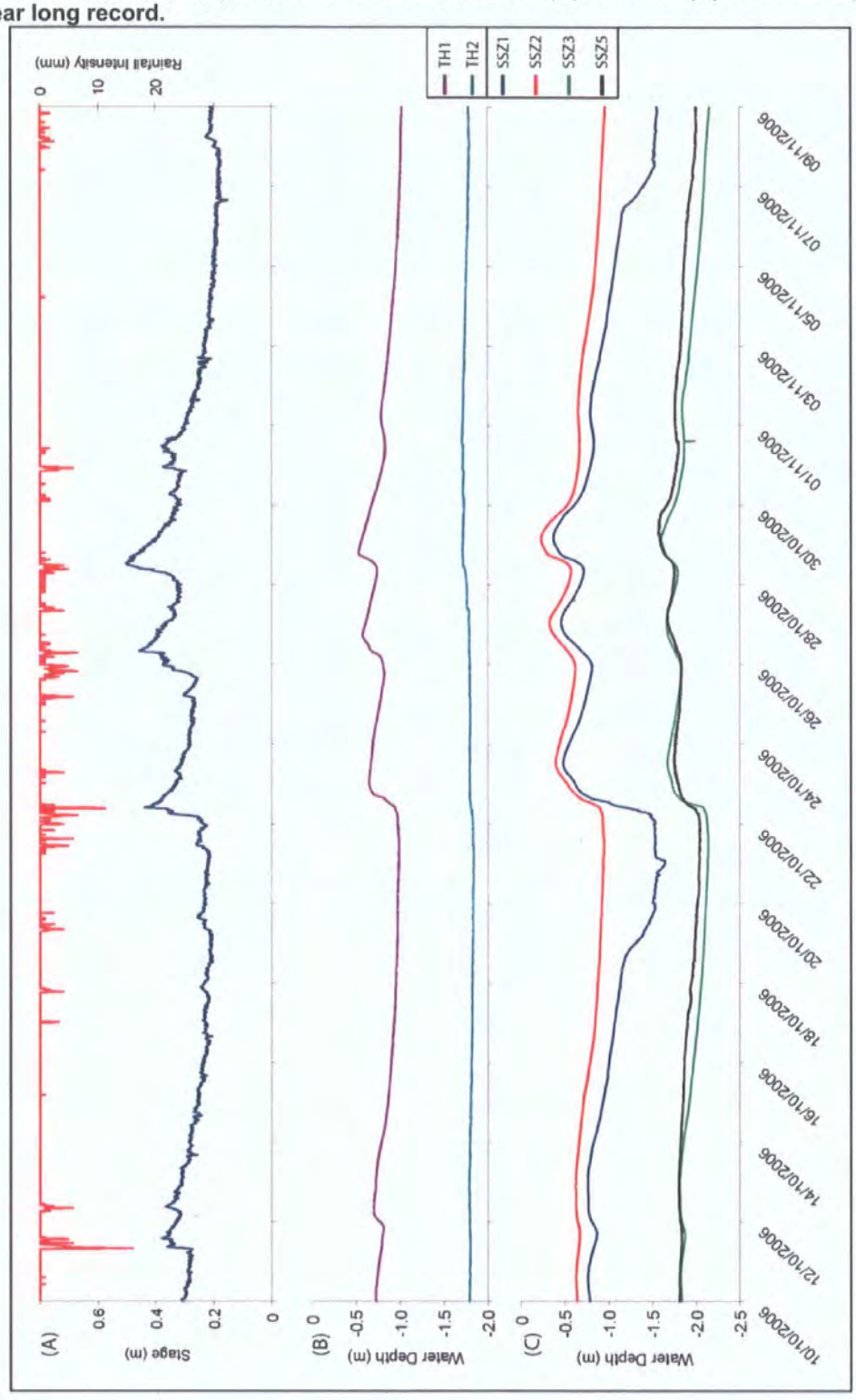

6.6.4. Topographically Derived Wetness Predictions

Figure 6-19 shows local slope (A), UCA (B) and topographic index (C) for the study hillslope, all derived from the 5 m IfSAR DSM. Local slope and UCA are

included both because they are relevant in calculating the topographic index and because they themselves can be effective predictors of moisture patterns on a slope. Red dots mark the location of monitoring wells and rings indicate the locations of the three zones of particular interest. The TH zone is predicted as particularly wet both in terms of UCA and TWI. The HG zone has clear flow convergence (high UCA) but is steep in many places and as a result is predicted as less wet by the TWI. The SSZ has no clear flow convergence and has TWI values ranging from quite to very low (dry).

Figure 6-19: The well network on the study hillslope (red dots) superimposed on topographic variables: A) local slope, B) upslope contributing area and C) topographic index calculated from the 5 m resolution IfSAR DSM.

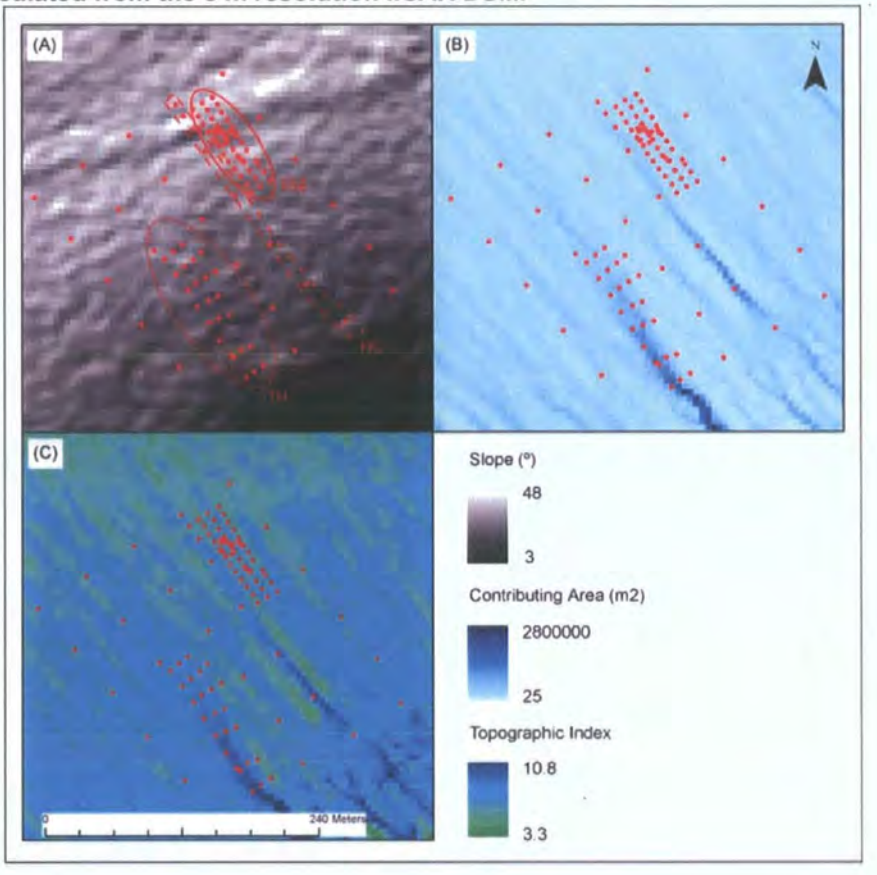

6.6.5. Minimum Water Table Depth Measurements

The minimum water table depth data (Figure 6-20) collected using the method detailed in Section 6.4.6 follow similar patterns to the results from event based monitoring. The dataset from 11/2006–03/2007 (Figure 6-20 A and C) is most complete and will be discussed in detail here. In the dataset from 02/2007–05/2008 (Figure 6-20 B and D) some of the maximum rise measurements were

unclear and therefore have been excluded, reducing the coverage of the wells. However, where data are available this dataset supports the observations from the first measurement period. The measured minimum water table depths in each well (i.e. the wettest conditions) indicate that a phreatic surface was present in many of the wells at some point over the measurement period. The gully (HG), hollow (TH) and seepage zone (SSZ) all have wells with water tables that have risen to <2.5 m from the surface during the measurement period. All of the gully wells recorded minimum water tables <2.5 m from the surface. The TH has a cluster of wells at its base identifying minimum water table depths <1.5 m from the surface and discontinuous patches of wells with water table depths <2.5 m extending the length of the hollow.

Figure 6-20: Minimum water table depths for the two measurement periods (22/2006–02/2007 and 02/2007–05/2008) collected using maximum rise crest stage tubes and expressed as an absolute water table depth and a percentage of the soil column saturated.

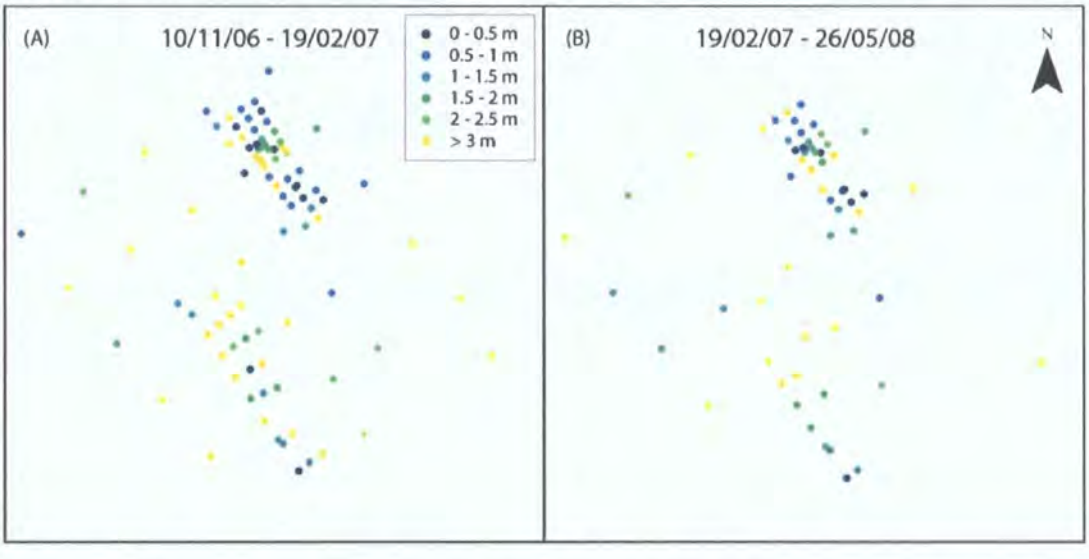

In the SSZ, many wells recorded a water table at some point over the measurement period (Figure 6-20). This is perhaps unsurprising since the zone contains two seepage points (localised zones of total saturation emitting water) and often experiences overland flow. However, the water table extends upslope of the seepage points even into the steep heather covered slope above. At these heather covered sites, the recorded water table, although close to the surface, extends only ~0.1 m above the soil-bedrock interface due to the shallow (~1 m) soil depth (Figure 6-21 and Figure 6-22). Immediately above the seepage points, the soil is deeper and the water table drops relative to that in the upslope wells. Once in the SSZ, wells tend to record either a water table <1

m from the surface or are completely dry. In some places this reflects shallow soils <1 m deep but in others it is an indication of the large variability in water table depth over fine spatial scales.

Field observations at the SSZ suggest that the zone reacts rapidly to rainfall events. This is supported by the time series data from automatically logging wells (Figure 6-17). During these conditions, the seepage points, which sustain very low flow throughout the year, quickly supply large discharges of water to the zone in the form of overland flow. Observations suggest that this overland flow is laterally discontinuous, forming threads. These generally (but not exclusively) expand from areas that sustain year-round flow and often flow over unsaturated soil. In this situation, flow emerges from discreet seepage points, flows overland re-infiltrating as it goes, until the discharge is exhausted towards the base of the zone, where all surface water has re-infiltrated. The situation is complicated by further seepage points and pipe outlets at other locations in the zone, which restart the process. These features will be split in two: firstly, the mechanism for surface water seepage from subsurface processes must be considered (Section 6.6.6); then the dynamics of the SSZ, as water flows downslope from the seepage point gravity (Section 6.6.7).

6.6.6. Water Table Dynamics at the Head of the SSZ

Water flowing overland at the SSZ emits from two seepage points discrete areas (~1 m width) of localised saturation. Bedrock depth measurements and maximum rise water table measurements on a dense (5 m) grid at the head of the SSZ allow me to identify interactions between the: bedrock, phreatic and ground surfaces. Through this I can hypothesise possible causes for the seepage points in this zone.

Ground and Bedrock Surfaces

In all three profiles (P1-3) the soil is shallow between the first and second cross sections (X1 and X2) and the bedrock surface runs parallel to the ground surface (Figure 6-21). In P1, a bedrock concavity between X2 and X5 is covered by a soil mantle to leave a planar ground surface (Figure 6-22). This results in deep soils between X3 and X4, becoming thinner again towards X5 as

the ground and bedrock surfaces converge. Similar bedrock concavities are visible in P2 and P3 but these start lower (at X3) and are less severe, finishing with soils >1 m deep (Figure 6-22). Ground, bedrock and phreatic surface elevations vary laterally, but these variations are small relative to the topographic and hydraulic gradients in the downslope direction (Figure 6-21). The ground surface tends to follow the bedrock surface reasonably closely in cross section. An exception is X6, where a bedrock hollow is masked by the ground surface.

Ground and Phreatic Surfaces

The phreatic surfaces in Figure 6-21 and Figure 6-22 are generated from the maximum rise crest stage tube water depth measurements for the measurement periods 11/2006–02/2007 (dark blue) and 02/2007–05/2008 (light blue). The results from the two periods are strikingly similar. For P3, the phreatic surface closely follows the bedrock surface even where this diverges from the ground surface in the bedrock concavity (Figure 6-22). Field observations suggest that P3 extends downslope across a dry area unaffected by the SSZ; these observations are supported by well measurements which find most of these tubes dry. P2 extends down the centre of the SSZ from ~25 m above the seepage points to ~10 m below them. However, surprisingly the phreatic surface never intersects the ground surface. Instead, they run almost parallel (or diverge slightly) with the phreatic surface following the ground surface rather than that of the bedrock surface (Figure 6-22). The water table in P1 between X3 and X5 is extremely elevated almost reaching the ground surface at X4. This may provide a link to seepage point 1 between X4 and X5 (Figure 6-21 and Figure 6-22). However, the form of the phreatic surface here is difficult to explain since it rises closest to the surface where the soil is deepest. The phreatic surface upslope of X3 on P1 remains below or close to the bedrock surface suggesting that water must be rapidly transferred into the zone between X3 and X5. No water is recorded in the tube directly downslope (P3X5), highlighting the importance of flowpaths oblique to the line of steepest descent on the surface and the fine scale of variations in the phreatic surface. Cross sections X5 and X6 suggest that the bedrock topography may channel this water towards the centre of the SSZ and field observations suggest that a considerable part of the flux is lost to overland flow at seepage point 1.

Site observations coupled with bedrock and water table depth measurements, suggest that seepage points result from very local saturation, but with very high hydraulic conductivities in the saturated flow pathways. These may be the result of bedrock exfiltration, bedrock topography and surface topography interactions or preferential flowpaths which end, constrict or come to the surface.

Figure 6-21: A three-dimensional representation of the relationship between the ground, bedrock and phreatic surfaces (from maximum rise crest stage tube data) at the head of the SSZ. The cross sections (X) and profiles (P) from Figure 6-22 are labelled.

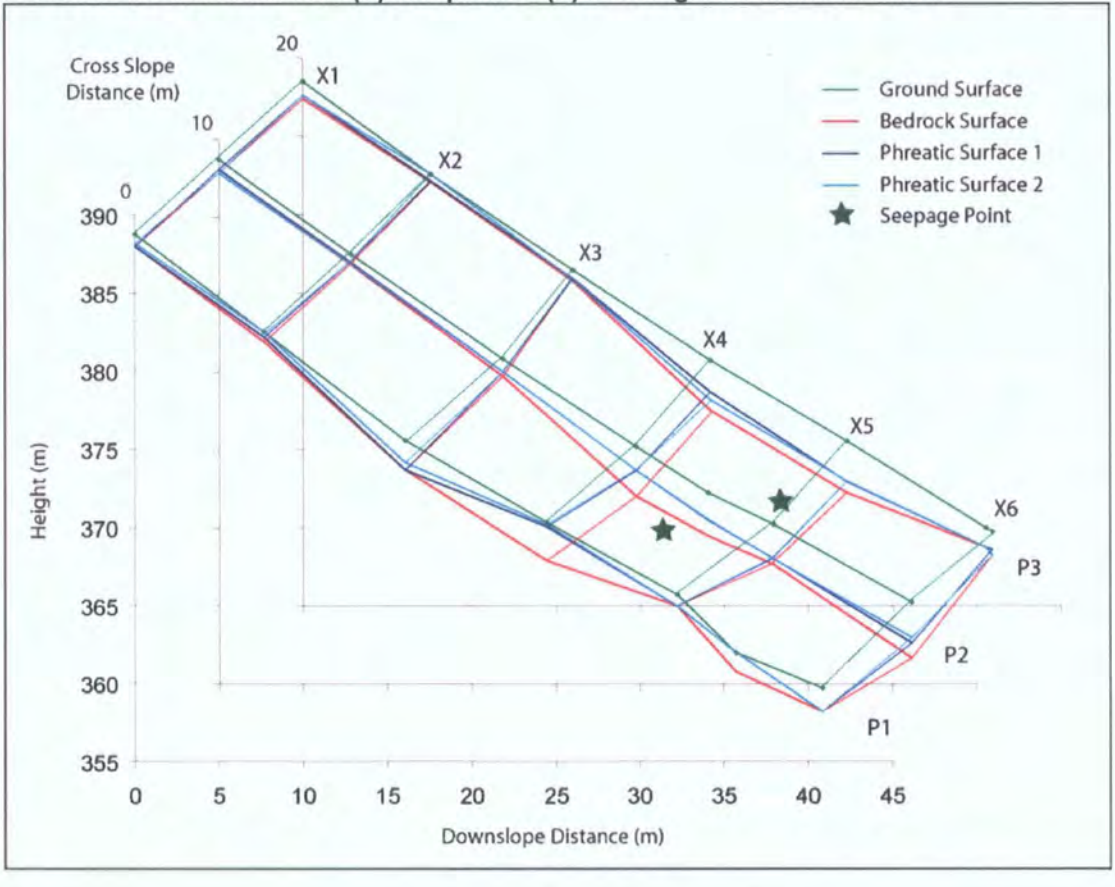

Figure 6-22: Profiles (P) and Cross Sections (X) showing the relation ship between ground bedrock and phreatic surfaces (from maximum rise crest stage tube data). Profiles are labelled 1 – 3 from left to right looking downslope. Cross sections labelled from 1 – 6 from upslope to downslope. Figure 6-21 shows the locations in 3D.

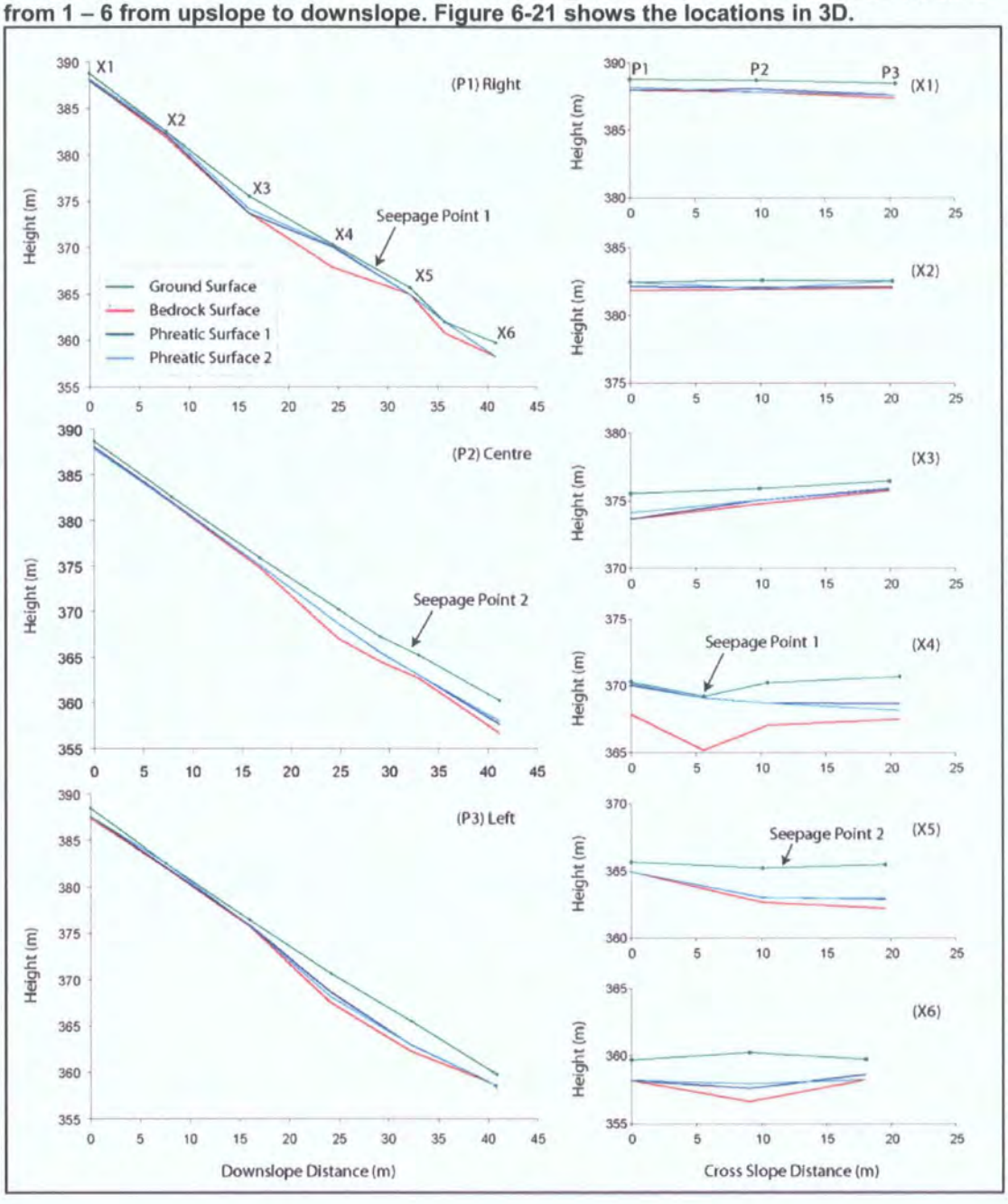

6.6.7. Conceptual Model for SSZ Hydrology

Figure 6-23 illustrates the second key feature of this conceptual model: the effect of surface water dissipation. The *Juncus* patch begins at the seepage point, where surface water is first visible. As the water flows downslope from this point it dissipates to some extent, covering and re-infiltrating over a larger area. The extent of this dissipation will be controlled by the downslope gradient

and local roughness but most flow will be concentrated in the central thread. As a result, the wet patch extends laterally with distance from the seepage point and so does the *Juncus*. If the seepage point is the sole water source and the water is flowing over an unsaturated surface thereafter, the discharge decreases with distance from the seepage point. If this situation is maintained, at some distance downslope all the discharge will be re-infiltrated into the soil and the overland flow will cease. The soil downslope of this point will be dryer without this water supply and *Juncus* will be out competed by other plants. The distance over which overland flow is sustained and therefore the length of the patch will be defined by the discharge at that point. Since discharge is concentrated in the centre of the flow immediately downslope of the seepage point this zone will sustain overland flow for the longest distance while the margins of the dissipated flow will only be sustained a short distance having only a small discharge (Figure 6-23).

Figure 6-23: A schematic illustrating the conceptual model for SSZ development on a planar slope; blue lines indicate flow with line weight proportional to discharge.

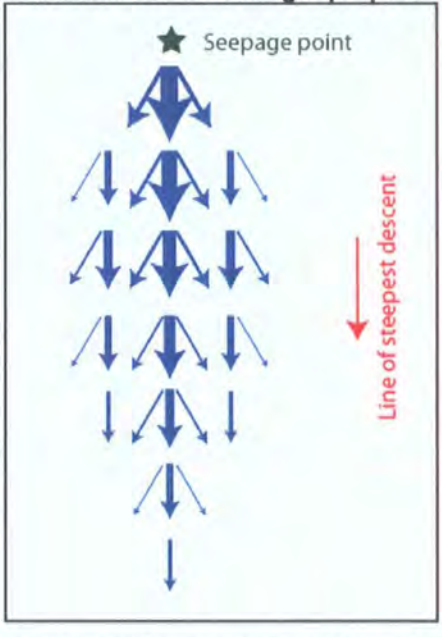

In this simple conceptual model the resulting form of the saturated zone and therefore the *Juncus* would be a diamond, with its length defined by seepage discharge / infiltration relationship and its length / width ratio defined by the amount of dissipation in the flow which in turn is defined by the relationship between local roughness and topographic gradient. This model broadly approximates the features of the SSZ, which has a long diamond shaped, *Juncus* covered wet patch at its centre (1 in Figure 6-24).

Figure 6-24: Examples of valley side seepage zones in the Newlands Valley study area, identified from high resolution aerial imagery, black arrows indicate line of steepest descent.

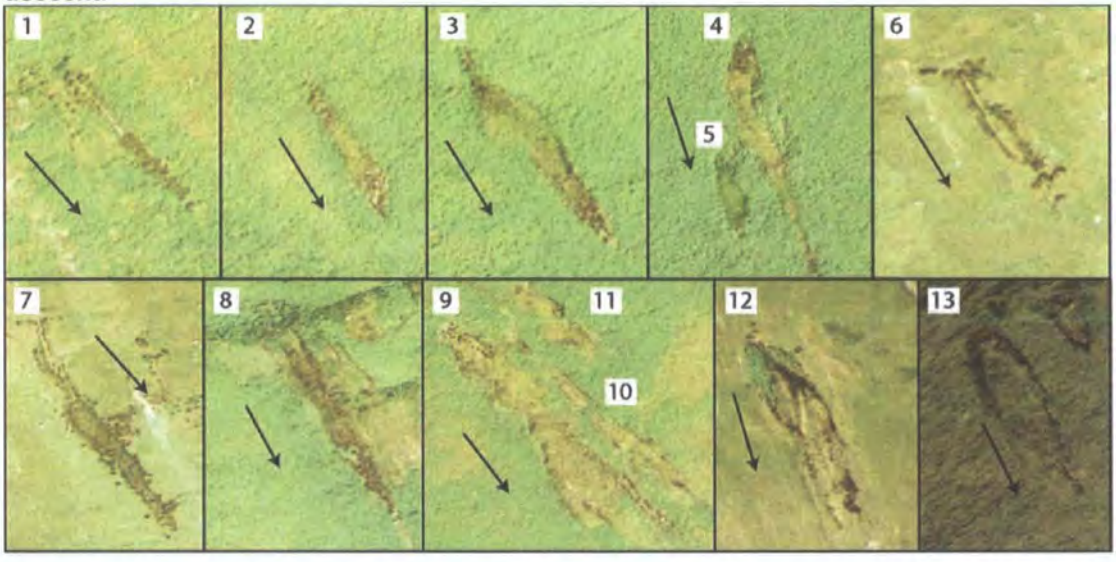

The model considers only a single seepage point, unsaturated soil downslope and no re-surfacing water, all factors that would complicate the scenario. However, it does capture the observed form of a subset of valley side wet zones similar to the SSZ on the study hillslope (Figure 6-24, Table 6-3).

Table 6-3: Widths, lengths and slope angles for the seepage zones pictured in Figure 6-24

	1	2	3	4	5	6	7	8	9	10	11	12	13
Length (m)	41	32	53	90	23	29	67	64	107	82	37	48	32
Width (m)	4	6	10	8	8	4	8	7	20	9	10	14	13
Aspect Ratio	10	5	5	11	3	7	8	9	5	9	4	3	2
Slope (°)	34	31	29	25	28	30	33	27	27	26	26	27	25

These are chiefly valley side phenomena, with the examples in Figure 6-24 occurring on generally planar slopes inclined between 25–34° (Table 6-3). They range in length from 23–107 m (suggesting variability in their discharge or infiltration rate) but have a broadly consistent form, with aspect ratios between 2 and 11. Deviation from the diamond form indicated by the model is probably the result of small scale topographic steering of the overland flow as it moves downslope (e.g. 9 in Figure 6-24).

6.6.8. Predicted Versus Observed Wetness at the Hillslope Scale

Plotting the minimum water table depth measurements (for 11/2006–02/2007 and 02/2007–05/2008) against topographic variables gives an indication of the extent to which wetness can be predicted from surface topographic properties (Figure 6-25). The relationship between topographic index and water table depth (Figure 6-25C) confirms the relationship suggested by comparing Figure 6-15 and Figure 6-20 with the topographic properties in Figure 6-19. We would expect a negative correlation between topographic index and water table depth (i.e. depth decreases with increased index value). However, there is no correlation between topographic index and water table depth in Figure 6-25C for the full sample. Ignoring dry wells and focussing on topographic index values >7, there does appear to be a positive correlation. However, index values as low as 5.2 record water tables <0.5 m from the surface.

Figure 6-25: Scatter plots of minimum water table depth against topographic variables: slope, contributing area and topographic index for 11/2006–02/2007 and 02/2007–05/2008 measurement periods.

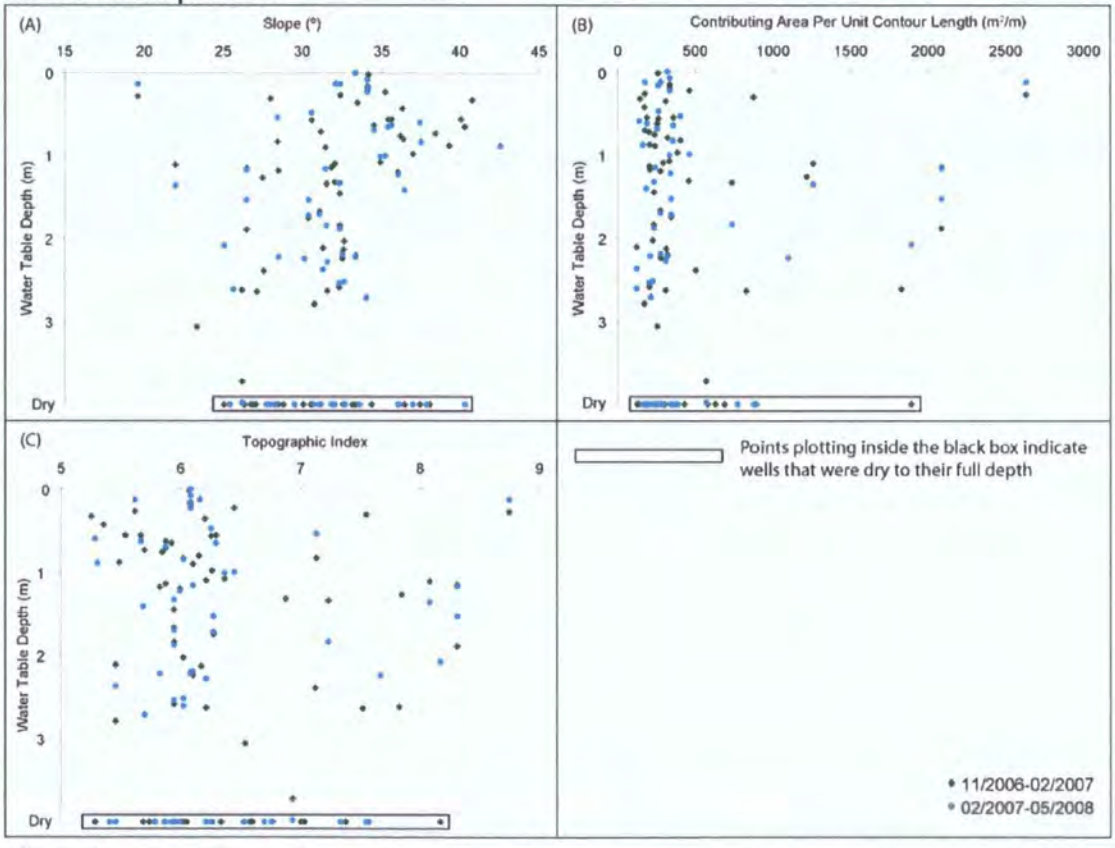

Decomposing the topographic index into its components (local slope and UCA), we would expect a positive correlation between water table depth and slope

(Figure 6-25A); and a negative correlation between water table depth and UCA (Figure 6-25B). In fact we see neither of these patterns. Instead water tables close to the surface (<1 m) are found across the full range of slopes (20°–40°) and contributing areas (100 $m^2 m^{-1}$). Dry wells were also recorded across almost the same range. Exceptions to this are the two tubes with lowest slopes and highest contributing areas that were wet. It is worth noting that all local slope values for the wells in the study are relatively steep (>20°) reflecting the types of slopes susceptible to landslides.

6.6.9. Section Summary

Many of the wet points in Figure 6-25 that are poorly predicted by topographic variables are in the SSZ, where measurements and field observations indicate wet conditions but the topography is steep and planar. These wet areas are related to discontinuous overland flow emitting from discrete seepage points; their extent is effectively indicated by patches of *Juncus* visible on an orthorectified air photo of the study area (Figure 6-26). Whilst this does not help to explain the causality behind the location of these wet zones (the *Juncus* is an indicator of the wet conditions rather than their cause), it does present a useful indicator. Given a seepage point the conceptual model outlined in Section 6.6.7 represents a reasonable explanation for the form of the SSZ. However, the cause of the seepage points remain unclear even with dense information on the location of phreatic and bedrock surfaces. They are probably related to zones of local saturation with high hydraulic conductivities possibly due to bedrock exfiltration, bedrock topography and surface topography interactions or preferential flowpaths which end, constrict or come to the surface.

The visibility of this vegetation type in high resolution aerial imagery and the capability to differentiate them from other vegetation types presents an opportunity to extend the spatial scale of the study. This is particularly important since the results from the hillslope site suggest that topography exerts a limited control on water table behaviour, but that this might be expected here. The uniqueness or ubiquity of this situation is important and can be quantified to some extent by using vegetation as a proxy for wetness and mapping spatial

vegetation and therefore wetness patterns to compare these with topographic attributes.

Figure 6-26: An orthorectified aerial image of the study hillslope at two scales showing the well network (red dots) for reference and the variations in vegetation over A) the entire slope and B) the SSZ. Note the patch of darker *Juncus* running down the centre of the SSZ.

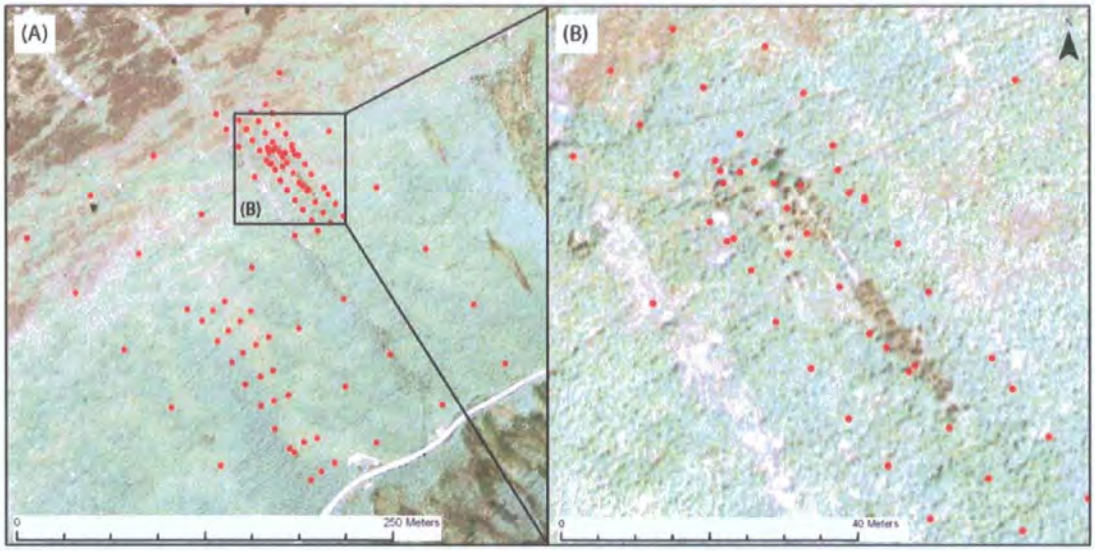

6.7. Results - Catchment scale

6.7.1. Scope of the Section

Expanding the study to the catchment scale allows assessment of the broader controls on where is wet in the landscape. We might hypothesise that the subsurface material from which an area is composed will influence the pattern and density of wet areas. This might include solid and surficial geology and soil type. An alternative hypothesis might be that the surface topographic form of the landscape drives the location of the wet patches. Finally these two hypotheses are not necessarily independent, the extent to which topographic form drives the area's hydrological behaviour may be related to its material properties (solid and surficial geology and soil); other catchment scale studies have found this to be the case (Hayashi, 1985; Onda, 1994, Onda *et al.*, 2004).

To test these hypotheses I first provide a brief synoptic view of the spatial configuration of these characteristics and their correlation with mapped wet areas before tackling each hypothesis in turn (Section 6.7.2). In Section 6.7.3 I focus on the area's material properties as represented by: solid geology,

surficial geology and soil type. In Section 6.7.4 I identify the topographic control using slope contributing area and topographic indices as metrics. Finally in Section 6.7.5 I consider the interaction between topography and material properties, to establish whether one is mitigating the controlling effect of the other.

6.7.2. Synoptic Analysis

Figure 6-27 shows the distribution of mapped wet zones projected onto maps of the study area showing solid geology, surficial geology, topographic index and soil type. The study area is split into two dominant geologies: the Buttermere and Kirk Stile Formations. However, these differ very little in terms of their properties since both are composed largely of siltstone and mudstone. Also, many of the slopes are mantled in a thick layer of Glacial till, talus or other surficial deposit (Section 2.3.3), which are likely to damp any solid geological control. As a result we might expect the solid geology differences within the study area to exert very little control on its hydrology. This is reflected in Figure 6-27A, which qualitatively suggests that wet patch location is not strongly related to solid geology. This will be revisited quantitatively in Section 6.7.3.

Wet areas do occur predominantly in certain types of surficial geology, Figure 6-27B, particularly glacial till. However, since areas covered with till occur predominantly towards the valley bottoms this relationship may be the result of the dependence of both variables on topographic form. Evidence in support of this is provided by wet patches in valley bottoms that are not till mantled, evidence against is in the form of valleys without a till mantle that do not contain wet zones. Alluvium is a similar but more extreme example since by definition it occurs under areas that are river dominated and so are frequently wet. Alluvial fan deposits, Alluvium and Till all appear to have a larger than average area covered by wet patches (I will return to this in Section 6.7.3 and Figure 6-28).

Figure 6-27C shows a broad correlation between mapped wet areas and areas of higher topographic index, indicating either: lower slope, higher UCA or both. This relationship is particularly clear at the large scale with wet valley bottoms and dryer valley sides. These results will be examined in more detail in Section

6.7.4. There also appears to be an aspect control on the location of wet areas with the north facing slopes of some valleys displaying a much higher density of wet patches than the south facing slopes opposite (e.g. Coledale). However, these north facing slopes often also have shallower gradients so the aspect and slope controls are difficult to untangle.

Table 6-4: Hydrologically relevant soil characteristics for the three units within the study area.

	Skiddaw	Manod	Brickfield
Depth to bedrock (m)	0.2	0.7	N/A
Depth to a low permeability layer (m)	0.2	N/A	0.34
Baseflow Index	0.26	0.61	0.31
Standard Percentage Runoff	60	29	40
HOST class	27	17	24

Table 6-4 indicates some of the hydrologically relevant characteristics of the study area's three dominant soil types. The depth to bedrock or to a low permeability layer (Robson and Thomasson 1977) will impact the soils storage capacity and its likely responsiveness. These are reflected in the baseflow index (fractional average flow volume represented by the contribution from groundwater storage) and the standard percentage runoff (percentage of rainfall that causes the short peak flow at the catchment outlet). These characteristics combined with the HOST classifications detailed in Section 6.3 suggest that: 1) Skiddaw soils (HOST 27) are shallow permanently wet and responsive with a low storage capacity; 2) Manod soils (HOST 17) are deeper and relatively free draining with a large storage capacity producing a less 'flashy' runoff response; and 3) Brickfield soils (HOST 24) are deep slowly permeable and seasonally waterlogged with an impermeable layer high up the profile, their storage capacity and responsiveness falls between that of Skiddaw and Manod soils.
Such differences suggest that soil type should exert a strong control on hydrological response that we might expect to be clearly visible in Figure 6-27D. However, care needs to be exercised because the relationships between soil type and hydrological response are based on the results from a limited number of studies and the resolution of the soil map is very coarse, splitting the study area into three units with Brickfield soils in the valley bottoms, Manod soils on the side slopes and Skiddaw soils on the hilltops, both of these factors mask the fine scale variability in soil types across the study area which is likely to be

strongly related to its catena and therefore to topography. An initial assessment from Figure 6-27D suggests that hilltop Skiddaw soils have the fewest wet patches Manod soils more and Brickfield soils in the valley bottoms the most, the strong relationship between soil type and topography means that this needs careful analysis to isolate topographic and soil type effects (Section 6.7.5).

Figure 6-27: The spatial pattern of wet cells (red) projected onto maps of the study area showing: A) solid geology, B) surficial geology, C) topographic index and D) soil type. The dark red line indicates the limits of the study area.

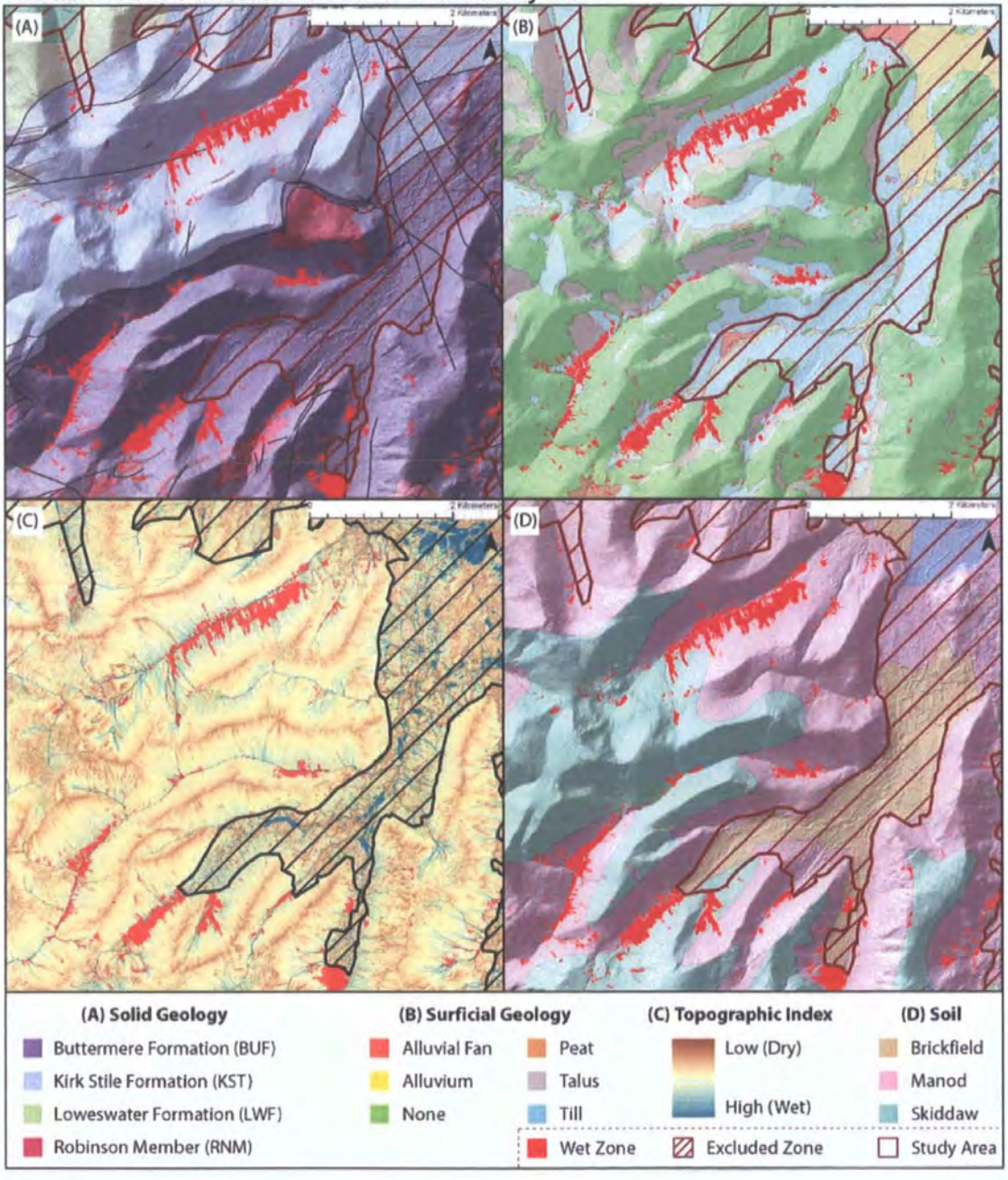

6.7.3. Material properties and wetness

Peat areas would be expected to contain a very high proportion of wet areas and have been used in other studies (Rodhe and Seibert, 1999) as an indicator of wetness itself. In this study area, peat does not differ from the average in its proportion of wet to dry areas (Figure 6-28). This is likely to be a result of poor classification performance in peat landscapes. The vegetation classification was developed in valley landscapes and may not effectively identify wet zones in peat moorland environments like the one here. This may be a result in particular of the differing vegetation types on peat and their different reactions to water stress. In this study the limitation is small since peat makes up less than 1% of the study area (Table 6-5). However, it is a key methodological limitation that would need to be overcome to transfer the technique to other study areas. Such a limit could be overcome by comparing training data air photos of peat areas with ground vegetation types and comparing these vegetation types with water table levels in a manner similar to that performed here for valley side conditions. The picture is completed by comparing the proportion of the study area that each class represents with the proportion of the wet areas of the catchment that the same classes represent (Table 6-5). Over 90% of the study area is made up of either Buttermere or Kirk Stile Formations. From Figure 6-28 we see that these differ very little from the full catchment in terms of their wetness likelihood. This is consistent with Table 6-5 which shows little difference between the solid geology make up of the full catchment and that of only the wet cells. One exception is the Loweswater Formation, which covers 4.4% of the study area but only 0.4% of the wet area. This is more likely to be a result of the small sample size than a broader trend.

Figure 6-28: The wet-dry percentage for study area zones classed by: A) solid geology, B) surficial geology or C) soil type. Note these have been standardised to account for differential areal coverage within study area (Table 6-5).

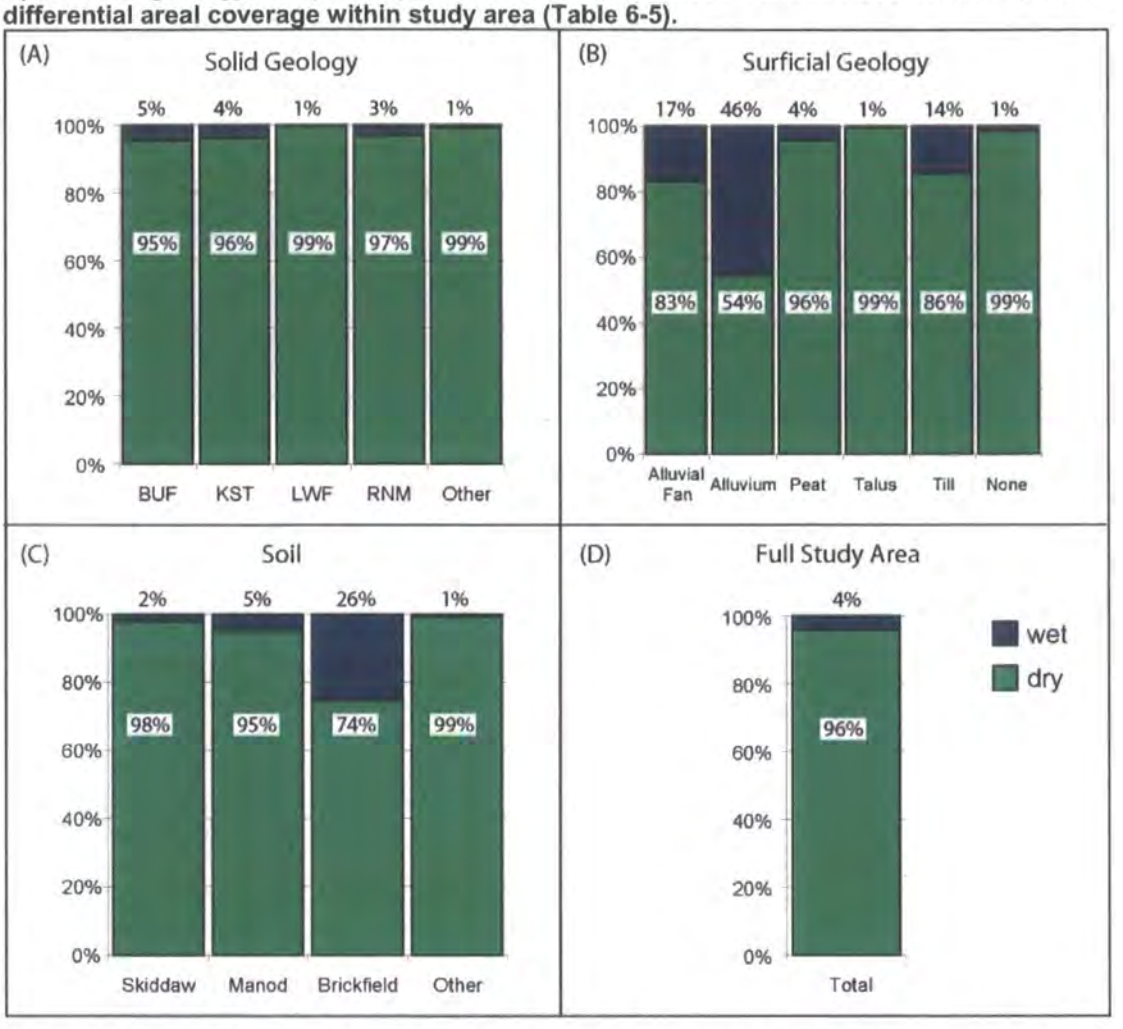

Around 64% of the study area does not have a mapped surficial geology ('none' in Figure 6-28B and Table 6-5), these areas are significantly underrepresented in the wet areas (only 21%), while Till, which covers 19% of the study area is significantly overrepresented in wet zones (66%). Talus is the third largest surficial geology covering (15%) but accounts for less than 2% of the wet areas, suggesting that talus areas are generally dryer than average. This is supported by Figure 6-28, which shows that a very low proportion of talus slopes are wet, significantly lower than would be expected at random. Alluvium and alluvial fans both make up a very small proportion of the total study area but are over represented in the wet zones (7% of the wet cells are in alluvium) as expected from their water worked nature and typical setting.

Table 6-5: The relationships between wet areas and solid geology, surficial geology and soil expressed in two different ways: as a wet or dry likelihood per class (expressed graphically in Figure 6-28); and as a proportion of the full study area and of wet areas made up by each class.

	Dry likelihood	Wetness likelihood	Percent of dry cells in class	Percent of wet cells in class
Solid Geology				
Buttermere Formation	95.4	4.6	49.7	56.5
Kirk Stile Formation	96.1	3.9	41.1	39.9
Loweswater Formation	99.6	0.4	4.4	0.4
Robinson Member	96.9	3.1	3.9	3.0
Other	99.0	1.0	0.8	0.2
Surficial Geology				
Alluvial Fan	83.3	16.7	0.5	2.2
Alluvium	54.6	45.4	0.7	7.5
Peat	95.8	4.2	0.8	0.8
Talus	99.5	0.5	15.4	1.8
Till	85.7	14.3	18.9	66.3
None	98.6	1.4	63.7	21.3
Soil				
Skiddaw	97.8	2.2	36.9	20.2
Manod	95.1	4.9	61.8	74.4
Brickfield	74.7	25.3	0.9	5.3
Other	99.2	0.8	0.5	0.1

Brickfield soils are particularly wet, with a wetness likelihood of >25%, considerably higher than average. However, care must be exercised here since these soils cover only a small portion of the study area (5.3%,Table 6-5) and they are preferentially located in valley bottoms so that they are likely to be strongly related to topography. The majority of the study area is made up of Skiddaw and Manod soils, of these, Manod soils are generally wetter, this is contrary to what we might expect from the properties of these soils since the HOST classification suggests that Skiddaw soil are wetter. The mismatch is probably related more to their location in the landscape, hilltops for Skiddaw soils and side slopes for Manod soils that to their material properties.

6.7.4. Topography and wetness

We might expect a cell's wetness to be related to two topographic attributes in particular: its slope, defining its hydraulic gradient which drives the speed at

which water moves through a cell; and its UCA, driving the volume of water that must move through that cell (Section 2.6.5). By plotting slope against UCA (Figure 6-29) we can visualise the relationship between these two properties for every cell in the landscape (green) and for all wet cells (blue). These plots are familiar to geomorphologists and landscape evolution researchers (Montgomery and Foufoula Georgio, 1993; Ijjasz Vasquez and Bras, 1995; Montgomery and Dietrich, 1994). However, they are also useful to hydrologists since they show the topographic index in two-dimensional ('slope area') space; and establish not only wetness index values but the key driving factors behind them. Mapped wet areas are plotted in blue (Figure 6-29) on top of the green landscape elements to give an indication of both the slope area space locations of wet zones and how those plot in comparison with the rest of the landscape.

If wet zones in the catchment are controlled by topography in the manner predicted by the topographic index we would expect them to plot preferentially at the lowest slopes and highest UCAs. In reality very few cells plot in this zone (Figure 6-29). The majority plot in the mid range slopes and UCAs. However, we would expect that low UCAs and high slopes would have a very sparse coverage of wet cells, and that higher UCAs would be required to maintain wet cells on steeper slopes.

For the full study area (Figure 6-29), wet cells cluster at UCAs between 500 and 5000 m^2 and slopes between 0.1 and 0.6 m/m (6–31°). In part this represents limits to the topographic settings in which wet zones develop. There is a clear upper limit to the slopes at which this occurs, with very few wet zones on slopes steeper than 1 m/m (45°). The lower UCA limits are less clear, with wet cells extending down to single cell areas (25 m^2). Whilst this is likely to be the result of fine scale topographic roughness features, it makes identifying a lower UCA limit for wet cells difficult. The upper UCA and lower slope limits to the cluster of wet cells are defined more by a reduction in the number of cells with these properties than by a reduction in the proportion of these that are wet. This is important, because if our test is to be unbiased in defining the topographic conditions that favour wet zones, we do not want to preference common areas of the landscape over rare ones. A further important point is that the landslide hydrology focus of this thesis lead me to censor valley bottom areas (excluded

zones in Figure 6-27). This is for two reasons: 1) the valley bottoms are the most heavily subjected to human interference so that the link between vegetation and wetness may be less strong; 2) the focus of this project is on the hydrology of steeper slopes likely to be susceptible to landslides. The slope area relationship formed by wet cells appears to be a cluster rather than a trend, with the cluster situated towards the higher contributing areas and lower slopes of hillslope elements in the plot (UCAs >10000 are commonly related to >1st order streams). Importantly, however, there is considerable scatter in this relationship, with many wet cells outside the cluster, particularly those within the same slope envelope, but with much lower contributing areas.

Figure 6-29: A plot of upslope contributing area against local slope (calculated from the 5 m IfSAR DSM) for all the cells in the study area (green) and wet cells only (blue).

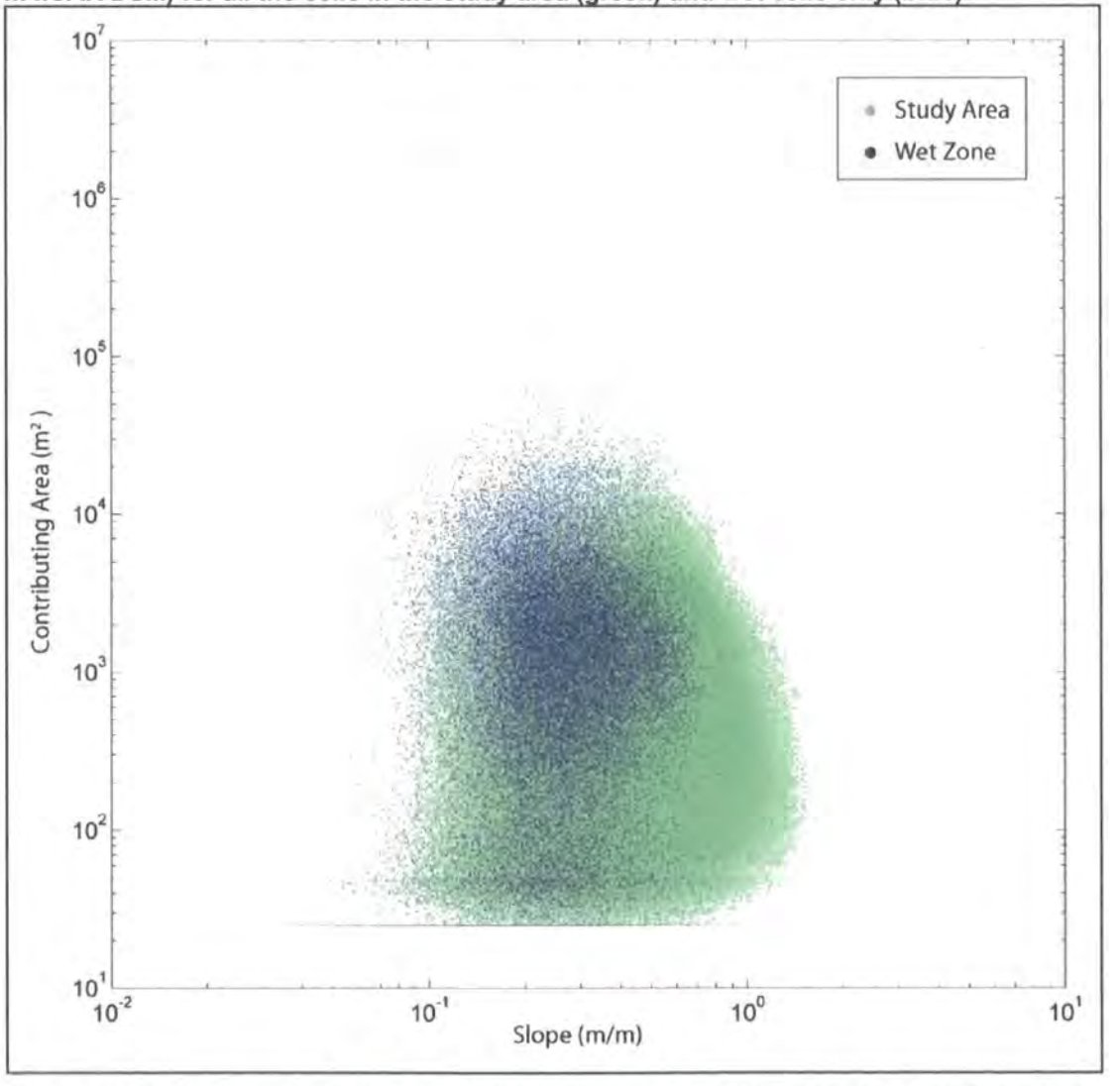

These plots give a useful picture of the slope area relationship for wet zones but they are difficult to interpret in terms of 'wetness likelihood', the frequency of wet

cells at a given slope area position compared to frequency of all cells. This is the most useful form of information in assessing the hypothesis that wetness is topographically driven. However, calculating these frequencies as conditional probability plots is difficult because of the distribution of the data, and because a relationship between slope and area needs to be defined to decide the shape of the kernel used to calculate the frequency distribution. Instead, I generate one-dimensional relative frequency distributions by compressing all the data onto one axis (slope or area) or by calculating the topographic index then plotting these as frequency distributions. The top plots A-C in Figure 6-30 show the relative frequency distributions of topographic variables for all cells and wet cells only. Peaks indicate variable values that make up the largest proportion of either the study area or all the wet cells. Although these only give the data in one dimension they do give a clear indication of the frequency distribution of each variable for all cells and wet cells and as a result allow calculation of a proportion of all the cells with those properties that are wet. This can be interpreted as the likelihood expressed as a percentage that a cell with a given variable value (TWI, local slope or UCA) will be wet: its 'wetness likelihood' (Figure 6-30 D-F).

Figure 6-30: Frequency distributions of wet and dry cells and the wetness likelihood for derived topographic variables: topographic index (A and D); slope (B and E); and upslope contributing area (C and F).

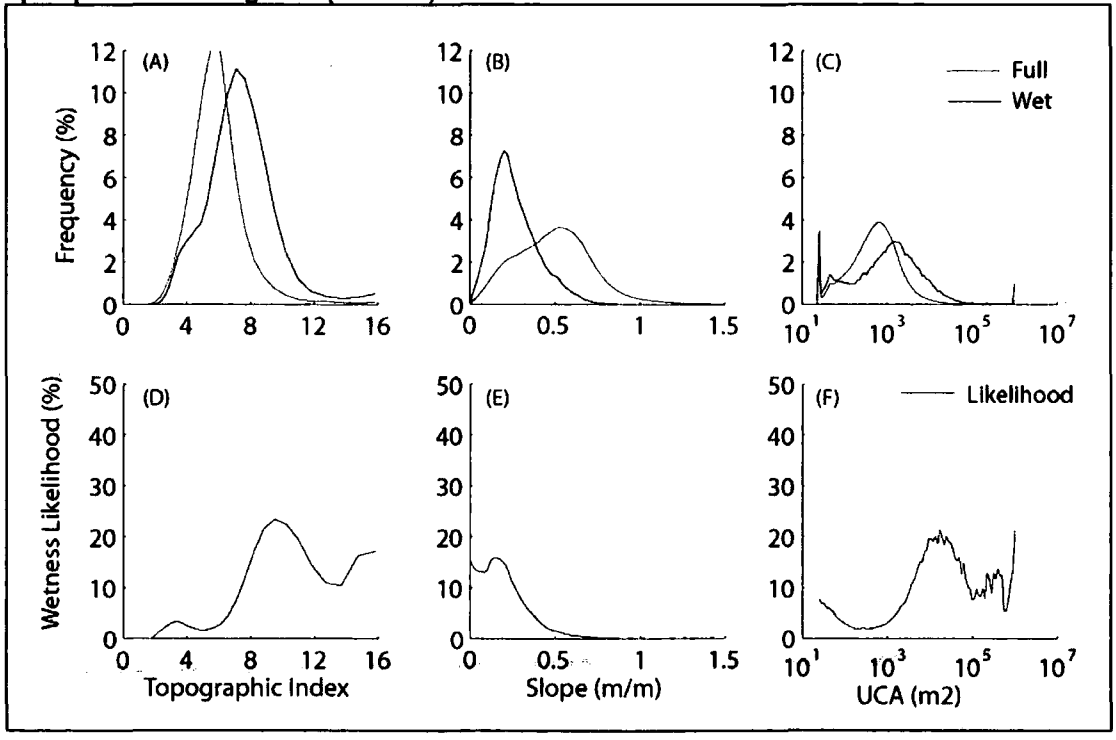

The distribution of TWI values for wet zones is very similar to that for the full study area up to ~3.5 (Figure 6-30A). At this point, there is an offset in the curves which is maintained over the rest of the range. The result in terms of wetness likelihood for each TWI value is an early peak (still <5% wet) reflecting the close agreement between the wet and full curves up to TWI=3.5 (Figure 6-30D). This is followed by a second much larger peak (~25% at TWI ~9.5), which is likely to reflect both a topographic control on wetness on the rising limb and a movement from wet hillslopes to channels on the falling limb.

The distributions of wet slope angles is skewed towards lower slopes, and is a tighter distribution than for the full study area, with much lower mean mode and median slope for wet cells (Figure 6-30B). The wetness likelihood at a given slope reflects this, with relatively high (~15%) wetness likelihood for slopes shallower than 0.5 m/m (27°), but a very low likelihood for slopes steeper than 0.5 m/m (Figure 6-30E). The peak wetness likelihood for cells with a given set of slope or UCA values is lower than for topographic index, reflecting the importance of the two variables in combination, since in isolation their effects may offset each other in some cases.

The UCA frequency distributions have several peaks (Figure 6-30C). The first at 25 m^2 (a single cell) reflects the influence of noise in the surface (due in part to cultural features such as walls and barns). This is present in both the wet and full samples but is more accentuated in the wet sample. A second peak occurs shortly after in both wet and full samples, again it is more accentuated in the wet cells than the full sample and again it is probably related to noise in the elevation data (it corresponds with ~50 m^2 or two cells). The third and largest peak for both datasets is offset, the most frequent UCA for wet zones is double that for the full study area (2000 m^2 compared to 1000 m^2 for all cells). The wet zones distribution also has a much longer tail than the full sample (Figure 6-30C).

The relationship between wetness likelihood and contributing area takes the form of a high initial value that is likely to be an artefact of the surface noise, a low proportion of wet cells for contributing areas between 10^2 and 10^3 m^2, rising thereafter to a peak at ~10^4 m^2 (Figure 6-30F). At this point ~20% of cells with

UCAs of 10^4 m^2 are wet. The likelihood of wet cells at higher UCAs declines slightly probably reflecting both the shift from hillslope to channel cells and the sparse data for cells with UCAs >10^4 m^2. Once UCA exceeds 10^5 m^2 the very limited data causes the signal to become sensitive to individual wet cells and therefore unreliable and noisy. The same effect is visible in topographic index values >12. These results are unreliable and should be ignored or considered in combination with the frequency distributions above them (Figure 6-30 A, B and C), which give additional information on the size of the sample from which the calculations are being made.

6.7.5. Topographic Effects Modified by Geology and Soil Type

In this section I deal with each control on the catchment's material properties (solid geology, surficial geology and soil type) in turn. I assess the effect that differences in these properties have on the topographic control on wetness using the methods introduced in Section 6.7.4.

Solid Geology

The Buttermere (BUF) and Kirk Stile (KSF) formations have an almost equal share of the study area and the wet cells. The KSF has a slightly lower proportion of wet cells (Figure 6-28) and makes up a smaller proportion of the wet geologies. The slope area plots (Figure 6-31) suggest that the wet areas in the KSF are more highly clustered and therefore more strongly topographically driven. In particular, the density of wet cells at high slopes and low UCAs is low for the KSF compared to the BUF and there are fewer wet cells with UCAs <10^2 m^2. This is also clear for the frequency plots of topographic index and UCA (Figure 6-32); where BUF wet cells have an initial peak not present in the wet KSF cells. The topographic index value with the highest wetness likelihood (peak in Figure 6-32D) is fairly consistent between geology types, occurring at a TWI of ~9. Despite a limited sample size the peak wetness likelihoods for LWF and RNM do appear to be influenced by topography. The RNM has a peak wetness likelihood at a topographic index similar to that of the KST. The wetness likelihood for LWF is much smaller and the peak is much broader but it also reaches its maximum wetness likelihood at and index value between 9 and 10.

Figure 6-31: Slope area plots for the study area (green) and wet zones (blue) for different solid geologies

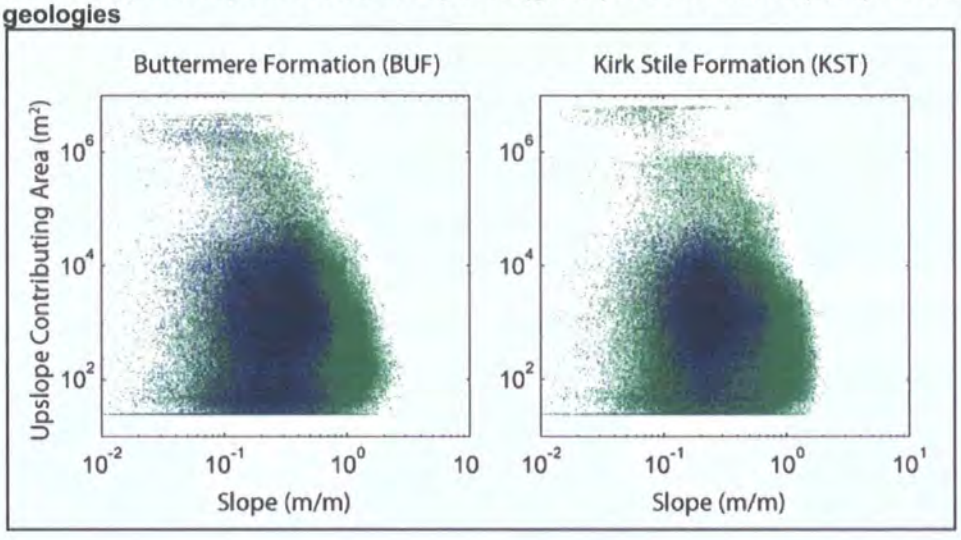

Figure 6-32: Frequency distributions for wet and dry cells and the percentage of cells that are wet with different solid geologies for: topographic index, slope and UCA

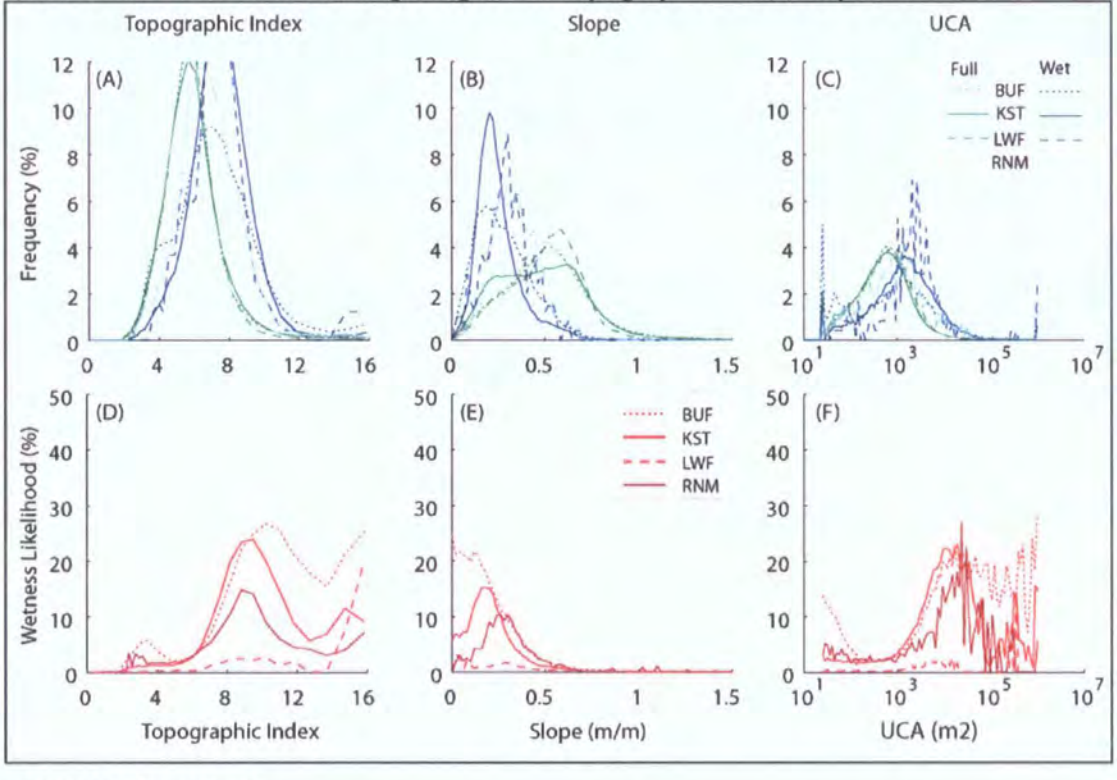

Surficial Geology

Alluvial fan cells have little variability in wetness likelihood over the full range of TWI values (Figure 6-34F), with peaks at the minimum and ~10. The high proportion of wet cells in these units appears to be more strongly related to their landscape setting (river dominated) than their topographic properties (which seem to differ little between wet areas and the full sample, Figure 6-34A), or

their material properties (which we might expect to be well drained). In slope-area space, wet cells appear to cluster as a band at higher slopes in the full study area cluster (Figure 6-33A). However, a physical explanation for this is difficult to conceive and the pattern may be an artefact of the relative point densities of wet and full study area cells across the slope area space. Alluvium covered areas have a high wetness likelihood (Figure 6-28B) but with little dependence on the topographic variables other than slope. In these fluvial environments; the river is likely to be a dominant control on the hydrological conditions and hillslope controls (e.g. UCA) less important. Slope still exerts some control evidenced by the sharp reduction in wet cells at slopes >0.5 m/m in Figure 6-33B. This may reflect both a local slope control on drainage and co-variance between higher local slopes and local elevation maxima, which are related to small scale roughness on the floodplain, creating less frequently inundated, dryer zones.

Talus covered slopes have very few wet cells (Figure 6-28B); they cluster at the centre of the full sample cluster on the slope area plot (Figure 6-33D). TWI values for all talus cells form a tight Gaussian distribution between 4 and 8 (Figure 6-34D), the distribution for wet cells is broader and less well defined. As a result the wetness likelihood plot for talus (Figure 6-34I) has two frequency peaks first at TWI <4 and second at TWI 9–13. Both these peaks are relatively small (<10% peak wetness likelihood), confirming that talus slopes are dryer than average (Figure 6-28). This may be partly a reflection of their material properties, which tend to be free draining, and partly of their topographic setting, on very steep slopes (10% of the talus cells with the wettest slope value are wet). This suggests that on talus local slope rather than UCA or topographic index drives wetness. The wetness likelihood for glacial till has two peaks, the minor peak at TWI of ~4 and a major peak (34%) at a TWI of ~10 (Figure 6-34J). The wet cell distribution is similar to the full study area (Figure 6-34E), but offset slightly towards higher TWI values. A large proportion of the till mantled area is wet (14% in Figure 6-28), much of this concentrated between TWI values of 8 and 12, with more than 30% of cells with a TWI of 10 being wet; suggesting that on till there is a strong topographic control on wetness.

Figure 6-33: Slope area plots for the study area (green) and wet zones (blue) for different surficial geologies

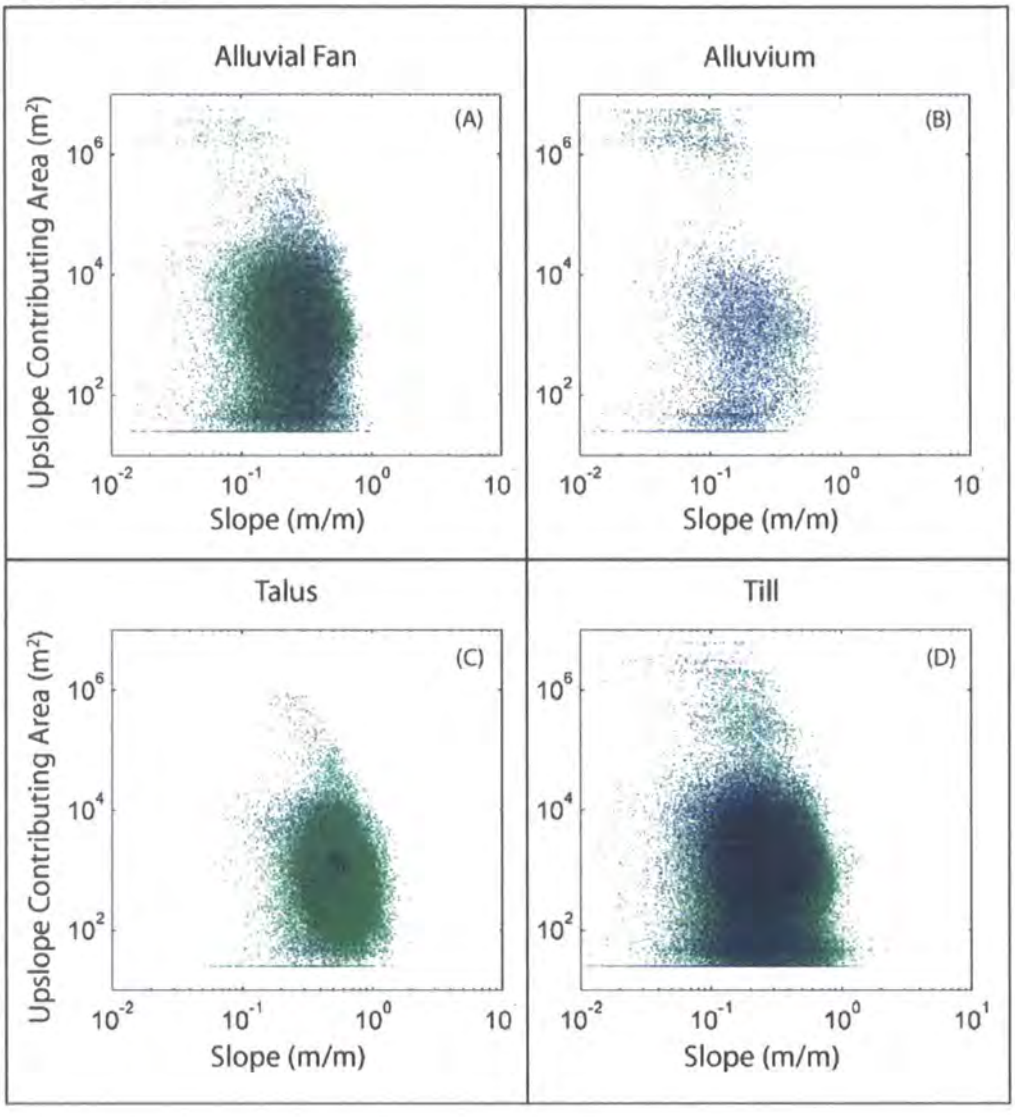

Figure 6-34: Frequency and cumulative frequency distributions of wet and dry cells and the percentage of cells that are wet for cells classed by topographic index, with different surficial geologies.

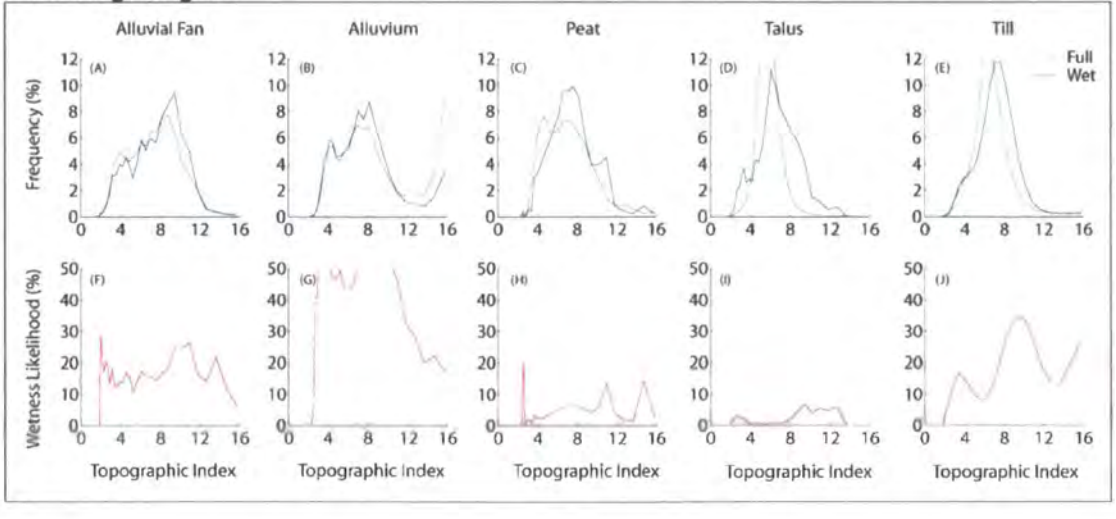

Soil Type

The slope area plots for the Skiddaw and Manod units are similar except that Manod units include the cells with largest UCAs, where Skiddaw units have very few cells with UCAs greater than 10^6 m^2 (Figure 6-35). Manod units make up a larger proportion of the wet cells in the study area and have a higher wetness likelihood (Figure 6-28C). The wet cells on Skiddaw soils are more tightly clustered. Although their limits in terms of maximum and minimum slope and UCA are the same, parts of the slope area space occupied by wet Manod cells contain no wet Skiddaw cells, in particular, the area with high slopes and low UCAs (Figure 6-35). We would expect this area to support few wet cells if topography were controlling wetness. This suggests that there is a stronger topographic control on wetness for Skiddaw than Manod soils. This result meshes well with what we might expect given the physical properties of these soils outlined in Section 6.7.2. The hydrology of Skiddaw soils that are shallow and have a low storage capacity might be expected to be more strongly connected to topography. Especially since the surface and bedrock topography should be more closely connected bringing the soil conditions into line with a key assumption within the topographic index. In Manod soils, which are deeper and less responsive this connection may be broken allowing other perturbations to have a stronger influence on the subsurface hydrology. These associations are extremely tentative, given the coarse resolution of the soil map but they do suggest that there may be a relationship between hydrology, topography and material properties, in terms of soil type (the characteristic that we might expect to exert the strongest influence of the three considered here).

Brickfield soils make up a small proportion of the study area, are found exclusively in the valley bottoms (Figure 6-27) and have a very high proportion of wet cells (Figure 6-28C). From the slope area plot there appears to be no single cluster of wet cells, instead, there are two poorly defined clusters centred around UCAs of 50 m^2 and 8000 m^2. The first is almost certainly related to noise in the elevation data, resulting from cultural features such as walls and barns. The full study area has the same clusters but they are more severe in the wet dataset, resulting in higher wetness likelihoods at very low UCA's. In the study area, Brickfield soils are limited to heads of valleys (Figure 6-27), other areas

having been excluded as unsuitable given the assumptions associated with applying vegetation as a surrogate for wetness. As a result, they generally have low UCAs despite their valley bottom location. Few cells have UCA $>10^4$ m^2. The slope control on wetness is somewhat clearer: few wet cells have a local slope greater than 0.5 m/m. The wet cells in the Brickfield unit have a similar slope distribution to the other units, but because Brickfield soils generally have low slope angles characteristic of valley bottoms, wet and dry cells have less distinct local slopes than normal (Figure 6-36). However, the high proportion of wet cells in the unit means that the wetness likelihood remains high (peak = 50%). The low slope values in the unit result in sub peaks at slopes between 0.5 and 0.7 m/m resulting from noise in the small sample.

The topographic index is particularly susceptible to noise in the elevation data, returning double peak frequency distributions for wet cells and the full study area (Figure 6-36). For the full area this peak at low values is small relative to the peak at higher values. For the wet cells the first peak is larger than the second and is synchronous with that of the full study site, while the second is offset towards higher TWI values. The resultant wetness likelihood is double peaked with the peaks almost equal (~40%), the first (~3) is almost certainly an artefact from noise in the data, the second ~10 is likely to represent the preference in wet cells towards higher TWI values.

Figure 6-35: Slope area plots for the study area (green) and wet zones (blue) for different soil types

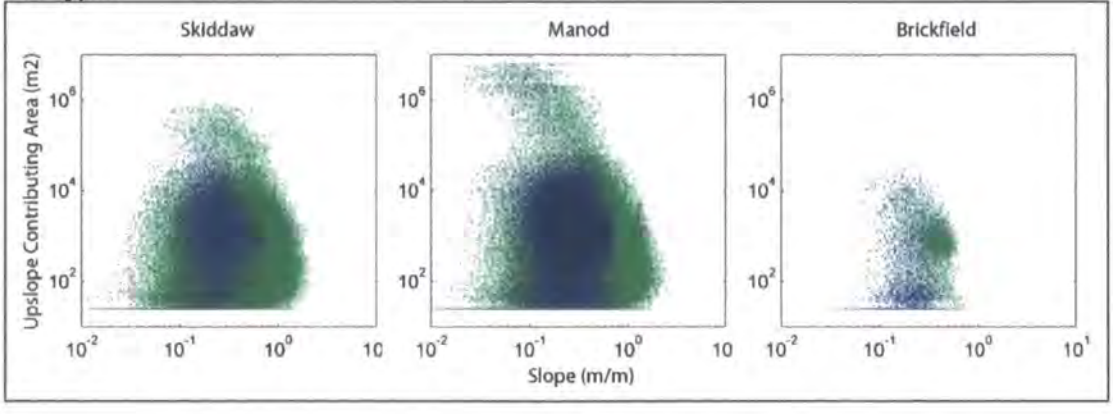

Figure 6-36: Frequency distributions for wet and dry cells and the percentage of cells that are wet with different soil types for: topographic index, slope and UCA

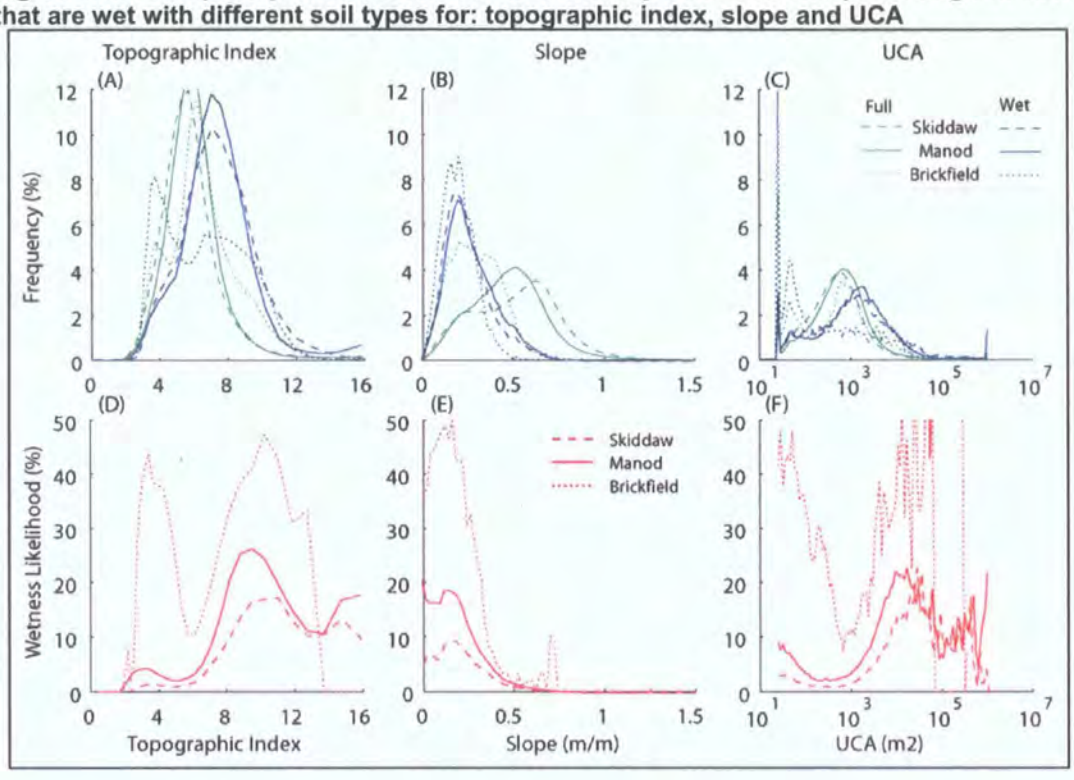

6.7.6. Section Summary

Solid geology is largely split between two formations whose physical properties are broadly similar and as a result any differences in their wetness likelihood are likely to be subtle. The results from catchment scale wet patch identification support this. Surficial geology and soil types appear to exert a stronger influence on wetness likelihood. However, this signal is complex since the formation processes for these geologies and soils are often strongly related to either their landscape position or their soil moisture conditions.

Analysing the topographic index values, slopes and UCAs of wet zones in comparison with the full study area indicates that there is some topographic control on the location of wet zones. However, there is also considerable scatter in this relationship. Some of this scatter is likely to be the result of noise in the topographic data; others though are real, reflecting wet zones like the SSZ in my hillslope study area. The wetness likelihood is a good measure of the topographic control on wetness since it normalises the differential sampling densities across the parameter space. Wetness likelihoods have two peaks for different topographic index values, the first, related to noise is small, the

second, much larger peak reflects the topographic control on wetness (at TWI~9.5).

Despite very similar material properties there appears to be stronger topographic control on the location of wet zones in the Kirk Stile Formation than the Buttermere Formation (this result should be treated cautiously since the driver in this relationship is unclear). All four solid geology types report peak wetness likelihoods at similar topographic index values (~9.5). Wet zones are common in alluvium but topographic control is limited, the relationships are more likely to be associated with the geomorphic setting of these deposits. Talus has few wet zones; those that are wet strongly cluster towards lower slopes, suggesting that slope is a stronger driver than topographic index or UCA for such zones. A large proportion of till mantled slopes are wet, much of this is concentrated at TWI 8-12, suggesting strong topographic control on wetness in till mantled areas. There is a stronger topographic control on wetness for Skiddaw than Manod soils. This corresponds well with the material properties for these soils, which suggest that Skiddaw soils are shallow and responsive while Manod soils are deeper with more opportunity for storage and development of hydrological perturbations. Brickfield soils cover a small percentage of the study area but have high wetness likelihood. Their valley bottom setting means that there is little topographic distinction between wet and dry cells (weak signal) and there are many cultural features (noise), which have a significant disruptive influence on the results and (due to the small sample size). In all the topographic analyses noise related to cultural features such as buildings and barns disrupts the derived variables, creating artefact peaks at low TWIs and UCAs and at high slopes.

6.8. Discussion

My aim in this chapter was to test the topographic wetness hypothesis: that water flows downslope under gravity collecting in topographic hollows and areas of low slope and as a result wetness (or water table depth) is topographically driven. I have consistently used the topographic index (Kirkby, 1975) to represent this hypothesis and have decomposed this into its components: slope, defining the hydraulic gradient at a point; and upslope

contributing area defining the volume of water to flow through that point. I have tested the hypothesis at two different scales: at the hillslope scale using traditional hydrogeological techniques; and at the catchment scale where I sought to pilot a new approach to characterise wetness, using remote sensing and vegetation indicator species. In the following section I look at the implications of my results for this hypothesis, first at the hillslope, then the catchment scale. Finally I summarise these findings and relate them to their application in catchment scale slope stability modelling.

Testing the topographic wetness hypothesis at the hillslope scale my results from event-based (Figure 6-15) and maximum rise (Figure 6-20) water table measurements agree on the spatial water table behaviour over the hillslope. They suggest that topographic variables (slope, UCA and topographic index) are poor predictors of wetness (Figure 6-25) in this upland environment. Instead I uncovered a complex hillslope hydrology where: soil depth was high and spatially variable; the phreatic surface was >3 m below ground over much of the hillslope (even in the wettest conditions), but there was frequent overland flow on planar slopes in the SSZ.

The areas that did experience overland flow did not fit the classic model of saturation excess overland flow, where variable source areas expand upslope from the channel (Hewlett and Hibbert, 1967). Instead the wettest area on the slope was the spring seepage zone (SSZ) where high discharges of water emit onto the hillslope from discrete seepage points or pipe outlets. These points were accompanied by extremely localised saturation and although water tables upslope of the seepage point were elevated (Figure 6-21) they never rose to closer than 0.2 m from the ground surface (Figure 6-16). The location of seepage points does not appear to be related to surface topographic form, but it is not immediately clear what they are related to. Their discharge was very high for their upslope contributing area, suggesting subsurface flow convergence of some form, but whether this is the result of bedrock topography, preferential flowpaths or bedrock flow is unclear. Once on the ground surface water flowed over unsaturated soil re-infiltrating as it moved downslope from the seepage point. This process, which I have observed at the SSZ on the study hillslope,

can be described in a conceptual model that provides an explanation for the form of many of the 'flush' zones throughout the broader study area.

The dynamics of water table behaviour can vary greatly over small distances. For example, the differences in rates of water table rise and fall at SSZ1 and SSZ2, or the differences between TH1 and 2 (Figure 6-17). At the topographic hollow in particular, TH1 displays behaviour similar to that at the SSZ, while TH2 responds more slowly and is more strongly influenced by long term rainfall trends (Figure 6-16). My results also suggest that lateral connectivity is important in defining water table height; for example at SSZ1, where water level drops rapidly when upslope inputs are reduced or switched off (Figure 6-18). However, there remains considerable uncertainty over the origin and form of the flowpaths responsible for such connectivity.

This complexity at the hillslope scale and the importance of apparently contingent perturbations (e.g. seepage points), suggests that deterministic prediction of hillslope scale wetness patterns may be unattainable (at least at present). Given the dependence of slope stability on pore water pressure and therefore wetness and given the scale on which this information is required (<25 m^2) can we hope to deterministically predict landslide locations or timings? This is not a new suggestion; working in the Oregon Coast Range Montgomery *et al.* (2002) state that: *"substantial uncertainty appears inevitable in basin-wide, spatially explicit predictions of the specific timing and location of debris-flow initiation due to the influence of bedrock heterogeneity on the locations of exfiltration gradients."*

The predictive ability of distributed catchment scale stability models then hinges on their ability to predict the areas of the landscape that are broadly susceptible to wetter conditions. In this respect, the Lake District is a particularly strict test. Tezlaff *et al.* (2008) suggest a distinction between simple landscapes dominated by fluvial erosion and mass wasting where topography is important in governing hydrological function; and terrain with a more complex history such as areas with a strong glacial legacy where soil hydrology and variation in drift permeability is important. The Lake District falls more closely into the second

category and so might not be expected to experience strongly topographically driven hydrology.

Measurements at scales that are wider than the hillslope scale are vital in establishing emergent patterns in hydrological behaviour. Vegetation as a surrogate for wetness identified remotely over large areas represents a potentially powerful tool in this. Developments for this technique might involve further validation and application in other settings to cement the Image – vegetation – wetness relationship and treat its associated uncertainty. The source of the topographic data and its level of post processing also require consideration. Noise in the elevation data related to measurement error or cultural features causes overrepresentation of high slopes and low contributing areas in the study area. These result in false clusters of wet patches in the slope area space and sub-peaks in the wetness likelihood plots at low topographic index values. However, the filters that remove these points often also remove important fine scale topographic features so that their outputs can be equally misleading (Section 3.6.6).

The differences in material properties between different solid geologies in the study area are subtle and do not exert a strong control on wetness, nor on the influence of topography on wetness. Future research might profitably use the approach piloted here to test these influences for two more different geological settings. Surficial geology exerts some control on wetness but this must be treated with care since the locations of these deposits are often strongly related to the local topographic or geomorphic setting. The trends in topographic control on wetness for different soil types and in particular the difference between Skiddaw and Manod soils is encouraging. The stronger topographic control in the shallower more responsive Skiddaw soils conforms to my expectations since these soils should mesh more closely with the assumptions of the topographic index. These suggest the possibility of applying empirical data such as those collected in Section 6.7 within a wetness likelihood framework to parameterise the influence of soil on the relationship between topography and wetness. However, these results are tentative and the Lake District soil information on which they are based needs to be treated with care. It is based on a limited number of observations and applies a very coarse resolution

classification to a landscape characteristic that is varies at very fine spatial scales and itself is strongly related to topography.

Results from this chapter, which span a range of scales, present a mixed picture for the relationship between hydrology and topography in the Lake District. At the largest scale, (valley scale) topography is an effective hydrological driver. Valley bottoms are wet, flat and have high upslope contributing areas. However, valley side seepage points exist not only at the study hillslope but across the broader Newlands study area (Figure 6-24). These appear effectively described by the simple conceptual model from Figure 6-23, which explains their existence and form given a seepage point but not the root cause for the seepage point itself. Between these end members, topographic control becomes stronger with increased scale but the form of this relationship is presently unknown.

In the context of catchment scale stability modelling these results suggest that spatial wetness patterns are likely to exert a strong control on the predictive ability of such models (in spatial terms). The broad topographic control on wetness means that simple GIS based slope stability models such as SHALSTAB continue to provide useful information on areas likely to be more susceptible to slope instability. However, these are most effective when they are framed probabilistically to account for the uncertainty within the system. Applying a deterministic stability model to predict locations and sizes of landslides in response to a rainfall time series is unlikely to yield fruitful results for catchments in areas such as the Lake District, where unmeasured and presently un-measureable perturbations disrupt the topographically driven flow. Future advances in measuring and modelling hillslope hydrological processes may alter this situation. However, the utility of these models is not limited to this spatially deterministic approach; in Chapter 7, I will return to this topic to provide one example of an alternative approach.

6.9. Chapter Summary

Landslides in the UK are triggered by high pore water pressures so an effective hydrological representation is an essential part of any stability model. Existing

literature suggests that topography controls spatial soil moisture patterns at some level, and that this relationship is controlled to some extent by the landscape scale characteristics of the catchment: its geology, contingent history, climatic zone, vegetation regime.

Results from my study hillslope suggest that topographic variables are poor predictors of wetness in this upland environment. I found surface seepage on a planar slope and overland flow over unsaturated ground at the spring seepage zone (SSZ) but dry conditions over the rest of the slope even in an area of topographic convergence. Overland flow generation does not fit the classic variable source area model but takes the form of localised flow over unsaturated ground that re-infiltrating as it moves downslope.

Spatial soil moisture data can be collected at large scales using vegetation as a surrogate for wetness, and identifying vegetation patterns from high resolution orthorectified imagery. This represents a powerful tool with exciting potential for future application. Its results suggest that topography controls wetness patterns at the largest scale but that this relationship has considerable scatter related to valley side wet zones similar to that at the study hillslope. These are effectively described by a simple conceptual model relating discharge, slope and infiltration to the geometry of the wet patch. However the model does not explain the origin of the seepage points from; which is likely to vary between sites and could be related to (soil pipes, bedrock topography or fractures). Between these end members (full valley - hillslope seepage), topographic control becomes stronger with increased scale but the form of this relationship is presently unknown. The relationship between topography and wetness is likely to vary between landscape scale settings and might be expected to be weaker in the Lake District which has a strong glacial legacy. The control of material properties on wetness is generally weak compared with that of topography (or strongly related to geomorphic setting). The mitigating effect of material properties on topographic wetness control is also limited in most cases. However, soil type does exert some control and this might be effectively parameterised using my empirical data in a likelihood scheme.

Wetness patterns are likely to exert a strong control on the predictive power of stability models. The broad topographic control on wetness suggests that a probabilistic approach to stability modelling maintains some utility. However, deterministic predictions of timings and volumes are likely to be unrealistic at present. In Chapter 7 I will introduce an alternative approach that focuses on landslide magnitude and frequency distributions.

7.Synthesis

7.1. Scope of the Chapter

To quantify their geomorphic importance landslides can be represented as either spatial distributions or magnitude frequency distributions. Both provide useful and important information on the geomorphic effect or effectiveness of landsliding (Benda and Dunne, 1997). Recently, some researchers (Hovius *et al.*, 1997, 2000; Guzzetti *et al.*, 2002; Malamud *et al.*, 2004) have argued that landslide magnitude frequency distributions have a particular form, suggesting that the frequency of medium and large landslides declines as a power function of magnitude but that this relationship breaks down at small magnitudes (~10^3 m^2). The reason that the form of and limits to this distribution are so widely debated relates to a long standing debate in geomorphological research over the extent to which landscape features are scale invariant and self organising (Hergarten and Neugebauer, 1998; Evans, 2003; Malamud *et al.*, 2004). Traditionally, geomorphologists have been interested in the location of events in Cartesian space as well as their size and timing. These spatial distributions are particularly useful since an event's importance often relates not only to its magnitude and frequency but also to its connectivity (to humans for risk, or to river networks for sediment delivery). Catchment scale slope stability models are usually assessed with reference to their ability to reproduce such spatial landslide distributions (Borga *et al.*, 1998; Reid *et al.*, 2007). Such models combine a geotechnical model, which uses limit equilibrium theory to predict stability at a point given a set of local parameters; and a hydrological model, which provides information on discrete or time integrated pore water pressures. This thesis has tackled each aspect of these models individually to show: 1) in Chapter 4, that improvements can be made to the widely applied infinite slope stability method by considering the additional strength supplied by the margins of an unstable block; 2) in Chapter 6, that the basic assumption that soil moisture conditions are topographically driven is reasonable at the landscape scale but is obscured by considerable scatter at the local scale resulting from contingent processes (e.g. bedrock exfiltration and preferential flow). This chapter will deal with each of these in turn, comparing theoretical controls on landslide distributions (spatial and non-spatial), derived from analytical models

or hydrological observations, with empirical data from the Lake District 2005 landslide inventory detailed in Chapter 2. First I examine the geotechnical and geometric controls on hillslope stability (Section 7.2); then the hydrological controls on stability (Section 7.3); before considering the implications for catchment scale stability modelling (Section 7.4). I finish the chapter by applying my findings using Lake District data to provide a physical explanation for the commonly debated form of landslide magnitude / frequency relationships.

7.2. Geotechnical and geometric controls on stability

The one-dimensional infinite slope method is widely applied as the geotechnical model in catchment slope stability models (Montgomery and Dietrich, 1994; Burton and Bathurst, 1998; Dhakal and Sidle, 2004; Baum *et al.*, 2008). This assumes that the failure plane is infinitely wide and long, so that stability can be estimated from the balance of stresses on the failure plane without considering edge effects (Section 2.6.3). However, research in this thesis (Section 3.3) and elsewhere (Schmidt *et al.*, 2001) suggests that lateral roots provide important additional strength to the soil block through its margins. More complete geotechnical models often require detailed high resolution data and involve computationally-expensive iterative calculations making them unfeasible at the catchment scale (Section 2.6). Following Dietrich *et al.* (2006) and Burroughs (1985), I have developed an alternative analytical approach, labelled the Finite Slope model. In Section 7.2.1 I summarise my findings from model development (Chapter 4), benchmark testing and sensitivity analysis (Chapter 5), highlighting their implications for current and future slope stability modelling. In Section 7.2.2 I compare the scaling relationships predicted by the model with those observed at landslide scars in my study area.

7.2.1. Model Development, Reliability and Sensitivity

The Finite Slope model predicts the stability of a block of soil treating it as a single body and accounting for additional strength at the block margins (Chapter 4). This additional strength has two components: friction strength and root reinforcement.

Friction strength on the lateral sides of the block is proportional to the normal force acting on this margin, which can be defined using either 'at rest' (upper stability bound) or active (lower stability bound) earth pressure theory (Section 4.4.4). The driving forces on the upslope plane of the block and resisting forces on its downslope plane can be approximated using active and passive earth pressure theory respectively (Section 4.4.5). By applying two classic soil mechanics methods (Rankine, 1857 and Coulomb, 1776), predictions can be framed as upper and lower bounds. Aside from block geometry (width and length), these calculations require no additional parameters relative to the commonly used infinite slope method.

I quantified **lateral root reinforcement** in a series of direct *in situ* field shear tests (Section 3.3). The results suggest that even grass roots can provide appreciable lateral reinforcement (3–6 kPa within the top 0.15 m of the soil) and that there is considerable variability both within and between vegetation types (Section 3.3.7). Root reinforcement is often proportional to the density of the root network (O'Loughlin, 1972; Ziemer, 1981; Ekanayake and Phillips, 1999), which varies with depth (Section 3.3.3). I have represented this relationship using three scenarios: 1) uniform root density over the full depth; 2) uniform root density in a root zone with no roots extending below this zone and 3) a power law decline in root density with depth (Section 4.4.4). Applying these within the analytical stability model: root zone treatment and power law decline produce similar results but the predicted reinforcement increases considerably when roots are assumed to extend to the full depth of the block (Section 5.6.2). This effect is similar in magnitude to the between-species variability in root strength. The important implication for landslide modelling is that root reinforcement parameterisation needs to be carefully applied in slope stability modelling. This can be separated into two key requirements. First, each method of measuring root cohesion (e.g. direct shear, thread strength and density or back calculation) differs in the physical property that it represents (e.g. point, depth integrated or aerially integrated reinforcement) (Section 3.3.4). Root reinforcement estimates from each method can be applied in my model but the measured and modelled processes need to be carefully matched to avoid misrepresentation. Second, existing models based on the infinite slope method assume that root strength acts along the entire failure surface (Section 2.6). Lake District observations

indicate that reinforcement acts chiefly along the scar perimeter (Section 2.4.3). Applying unadjusted basal root reinforcement values will result in overestimation of a block's stability, neglecting them will result in underestimation. This problem can be avoided by assuming failure size and applying apparent reinforcement values that have been adjusted with reference to results from models accounting for lateral root reinforcement (Hammond *et al.*, 1992; Montgomery *et al.*, 2000). However, model results will then be influenced by the assumption about landslide size used to calculate the apparent reinforcement. Applying my stability model at a catchment scale would remove the need for this assumption.

Benchmark tests (Sections 5.4 and 5.5) against standard geotechnical methods (Spencer, 1967; Sarma, 1973) indicate that my parameterisation of profile effects improves predictions relative to the conventionally applied Infinite Slope and Ordinary methods (Section 5.4.6). The agreement between Finite Slope and benchmark stability predictions quantified in terms of soil strength is within the uncertainty associated with the soil strength input parameters (Section 5.5).

Sensitivity analyses indicate that both length (Sections 5.4 and 5.5) and width (Section 5.6) exert a control on block stability, which decreases exponentially as width or length increase. As a result, influence is limited for landslides longer or wider than 30 m but can be extremely important for landslides <10 m long or wide. At these dimensions the additional strength supplied by the margins is often larger than the uncertainty associated with the soil strength input parameters (Sections 5.5 and 5.7). Friction effects on the lateral sides are small relative to other effects (Section 5.6.) suggesting that previous researchers (Reneau and Dietrich, 1987; Gabet and Dunne, 2002; Casadie *et al.*, 2003) may have been justified in neglecting them. However, representing these effects requires no additional parameters and uses assumptions that are consistent with those applied to calculate the forces on the block's upslope and downslope margins (Chapter 4). The effect of failure plane depth on stability is more complex, since root reinforcement effects decline with depth while friction strength increases (Section 5.6.4). These two relationships offset one another for shallow and deep failure planes leaving a zone of minimum stability at intermediate depths, which implies an intrinsic control on failure plane depth.

In its present form, the model provides useful insights into the scaling (length, width and depth) relationships intrinsic to the mechanics of an unstable block. These are clearly approximations of true failure conditions. However the model represents factors identified as the key controls on stability in these environments (Section 2.4.3) that have not previously been combined (i.e. the additional strength supplied by both friction and root reinforcement in three-dimensions). This is important because whilst other models (particularly continuum mechanics geotechnical models) might provide more complete representation of one aspect of the block's stability, they cannot provide the whole picture. This model allows us to see the differences in stabilising effects of the sides versus the toe and the roots versus the granular interactions. The simple model structure and small number of parameters make it possible to identify the influence of changes in root cohesion or the assumptions about root cohesion with depth. Accounting for three-dimensional geometric effects on stability is useful because: field evidence (Section 2.4 and 3.3) and literature review (Section 4.2) suggest that it is important; and because landslides appear to have characteristic length scales (length, width and depth), which may be related to stability at given geometries.

7.2.2. Comparing the Model with Data

Data on the geometry of Lake District landslides from the January 2005 event (Section 2.4.3) can be used to compare the theoretical relationships between landslide length width and depth with direct observations. By plotting landslide length against width for observed slides classed by their depth we can start to identify these scaling properties. Landslide width rarely exceeds landslide length (i.e. aspect ratio is greater than or equal to one). Landslides shallower than 0.5 m appear to follow a linear length-width trend, with a gradient of 1–2 and an intercept of ~0 m (Figure 7-1). The gradient of the line connecting any point to the origin reflects the aspect ratio (length / width) of that scar. For landslides shallower than 0.5 m, scar aspect ratios are low and independent of size. The size of these slides is well constrained with minimum lengths and widths of 2.6 m and 2.9 m respectively and maximum lengths and widths of 21 m and 17 m respectively (Table 7-1).

Table 7-1: Width and length statistics for landslides grouped by scar depth

Depth (m)	N	Length (m)			Width (m)		
		mean	min	max	mean	min	max
< 0.5	19	11.42	2.58	20.74	8.36	2.91	16.81
0.5 - 1	32	26.10	7.58	74.13	9.94	5.06	24.52
> 1.0	5	42.99	16.62	61.21	12.96	7.87	21.37

Landslides between 0.5 m and 1.0 m depth follow a steeper trend between width and length, with more scatter (Figure 7-1). Their minima are higher than the shallower scars, 7.6 m and 5.1 m for length and width respectively (Table 7-1); this may reflect some length and width control on stability. Landslides deeper than 1.0 m plot within the same space as the 0.5–1.0 m deep landslides; they have no clear length / width relationship and have minimum widths and lengths larger than the smaller depth classes (Figure 7-1). However, the small number (n=5) of landslides deeper than 1 m and their considerable scatter in width / depth space makes it difficult to draw many conclusions.

Figure 7-1: The geometry (width and length) of observed landslides in the January 2005 Lake District inventory. Depths are classed into three groups indicated by symbol type and colour, depth variability within each group is indicated by the size of the symbol (scaled to scar depth). The green distributions on x and y axes are kernel density functions for width and depth respectively. This figure is reproduced from Section 2.4.3.

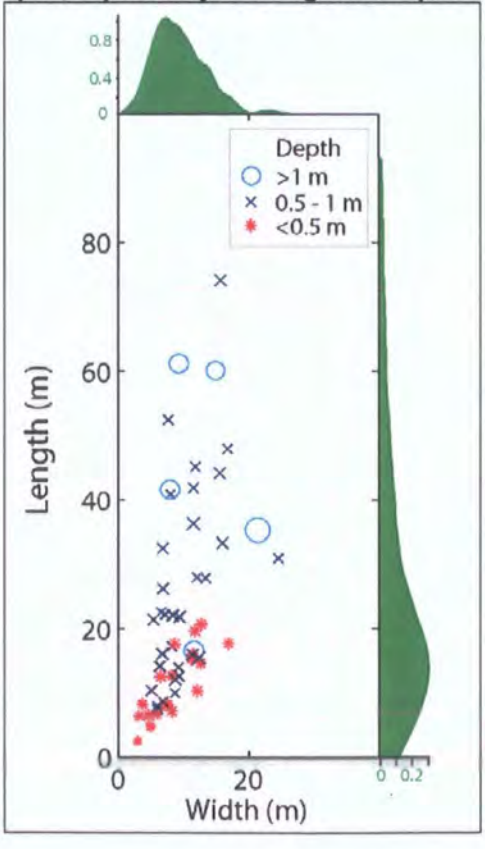

Plotting this data on top of predicted safety factors from a complete finite slope model (representing root cohesion and friction over a block of finite width and length; Section 5.3.5) connects model predictions with observed properties. Figure 5-28 shows the relationship between length, width and stability for an example scenario from my sensitivity analysis in Section 5.7 with the observed data from Figure 7-1 superimposed for comparison. Clearly the parameters used in this example will not represent those at each of these landslides, although I have shown in Chapter 5 that the exponential form of the factor of safety relationship with block geometry is maintained across the parameter space. Instead the plot is intended to allow comparison between the broad geometric trends in predicted stability and those of the observed landslides.

In the absence of any other control (i.e. if all other parameters were spatially invariant) we might expect landslides to cluster in the area of lowest predicted factor of safety (Figure 5-28). This zone will always be for the largest width / depth combinations (Section 1.8.8; Figure 5-28). However, observed landslides do not cluster here but towards the lower width and length scales (Figure 5-28). This divergence results from the interaction between the geometric stability controls and the spatial patterns of key parameters such as slope inclination, soil saturation, root cohesion and friction angle.

Nonetheless, several key scar characteristics do suggest that the effects of geometry on stability are reflected in the observations. First, there appears to be a strong control on minimum landslide size which is related to the depth of the unstable area. Landslides do not occur at lengths of less than 2.6 m or widths of less than 2.9 m for depths less than 0.5 m. Landslides do not occur if the unstable element is shorter than 7.6 m or narrower than 5.1 m for elements deeper than 0.5 m. These limits correspond well with the inflexion in the factor of safety surface (Figure 5-28). At lower widths or lengths than these, factor of safety increases very rapidly with further decreases in length or width. The shallowest slides have a different length / width relationship than deeper slides with much lower aspect ratios suggesting that for these slides the width and length effects are more equal. This agrees well with observations from model sensitivity analysis (Section 5.7).

Figure 7-2: Factor of safety contours in landslide length-width space for an unsaturated slope inclined at 20°, illustrating the 2D exponential trend for factor of safety with length and width, which is maintained across the parameter space. The soils are: A) 0.5 m and B) 1.5 m deep, both are cohesionless with a friction angle of 25.6°. Basal root reinforcement is ignored and lateral reinforcement modelled with the power law depth decay for blocks under: A) *Eriophorum* (stronger roots) and B) *Juncus* (weaker roots). The modelled factor of safety is compared with observed landslide lengths, widths and depths (indicated by symbol type, colour and size).

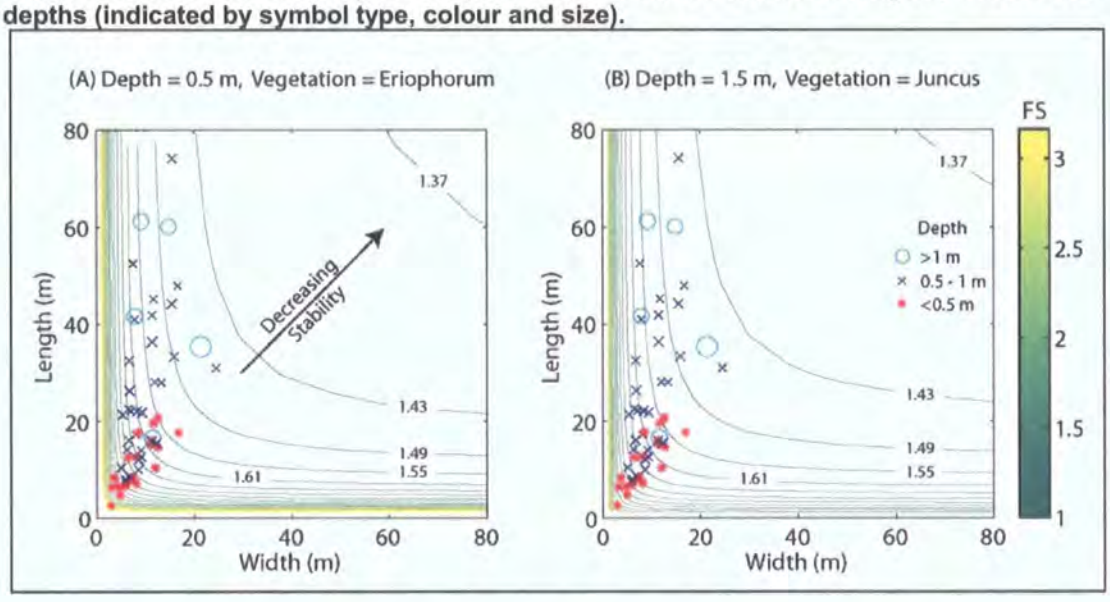

Landslides are rarely wider than they are long, but are often much longer than they are wide (Figure 5-28). This would appear to agree well with my analysis of geometry effects using the finite slope model. However, the importance of the aspect ratio in defining stability is small relative to the influence of block size. The contours in Figure 5-28 show a small asymmetry along the 1:1 axis, contours are pulled more strongly towards the y- than the x-axis indicating a slightly higher factor of safety at (for example) 20 m long and 40 m wide than at 40 m long and 20 m wide. This asymmetry is more marked for the weaker vegetation (*Juncus* in Figure 5-28B) and deeper soils (1.5 m in Figure 5-28) because under these conditions the additional strength supplied by the downslope margin of the block dominates (Section 5.8.8). The stability differences between length and width are weak relative to the much stronger size control on stability (exponential decrease in stability with increased landslide size; Figure 5-28 and Section 5.8.8). Therefore, the stabilising effects of block margins and the differences in relative importance of different margins do not seem to provide independently sufficient explanations to account for the observed landslide geometries. I have already suggested in this section that the spatial pattern of other important parameters (e.g. slope, soil strength or pore water pressure) strongly influences the size of an unstable area. It is likely that

the patterns of these parameters are also responsible to some extent for the landslides' geometric properties. The simplest example of such a control might be saturation patterns. The processes that drive these patterns (gravity driven flow) lead to patches that are strongly elongated in the down slope direction. As a result, landslide geometry will be defined by some combination of the spatial distribution of potentially unstable parameters and the geometric limits on stability.

The relationship between friction resistance and lateral root reinforcement with depth has interesting implications for the influence a block's thickness exerts on its stability (Section 5.6.4). The root reinforcement effects, which decline with depth and the friction strength effects, which increase with depth offset one another for shallow and deep failure planes but between these there is a zone of minimum stability (Figure 7-3). The form and location of this zone is extremely sensitive to assumptions about the form of the root reinforcement - depth relationship but tends to be ~1–3 m. In the absence of other drivers, these least stable depths should represent the most likely potential failure planes for vegetated slopes. This represents an alternative hypothesis to the conventional assumption that landslides fail at a hydraulic or soil strength interface within the profile (Brooks et al., 1995), instead suggesting that even assuming a homogeneous slope, shallow failures at depths similar to those observed can be reproduced by considering only intrinsic controls on stability. Observed failure plane depths for Lake District landslides have been estimated in Section 3.5, the probability distribution for these depths from ~70 landslides is plotted on Figure 7-3 to illustrate their agreement with the factor of safety minima for two example scenarios. The agreement is persuasive, and while field observations at my sites (Section 2.4.3) and others (Gifford, 1953) indicate that failure planes are often at soil interfaces, intrinsic block geometry effects may interact with other basal strength or hydraulic conductivity controls to define failure plane depth at a site.

Figure 7-3: Factor of safety with depth for a partially saturated (m = 0.5) soil element infinitely long and 10 m wide with a friction angle of 25.6°, lateral earth pressure is calculated using 'at rest' earth pressure and changes in lateral root cohesion with depth are represented by a power law decay function for: A) *Eriophorum* and B) *Juncus* vegetation types. The graphs show negative trends for factor of safety with depth when only lateral root cohesion is considered and positive trends when only lateral friction is considered. The complete treatment has a minimum value at ~1 m. The figure has been modified from Section 5.6.4 to include the probability distributions for mean and maximum depth to the failure plane from Section 3.4.

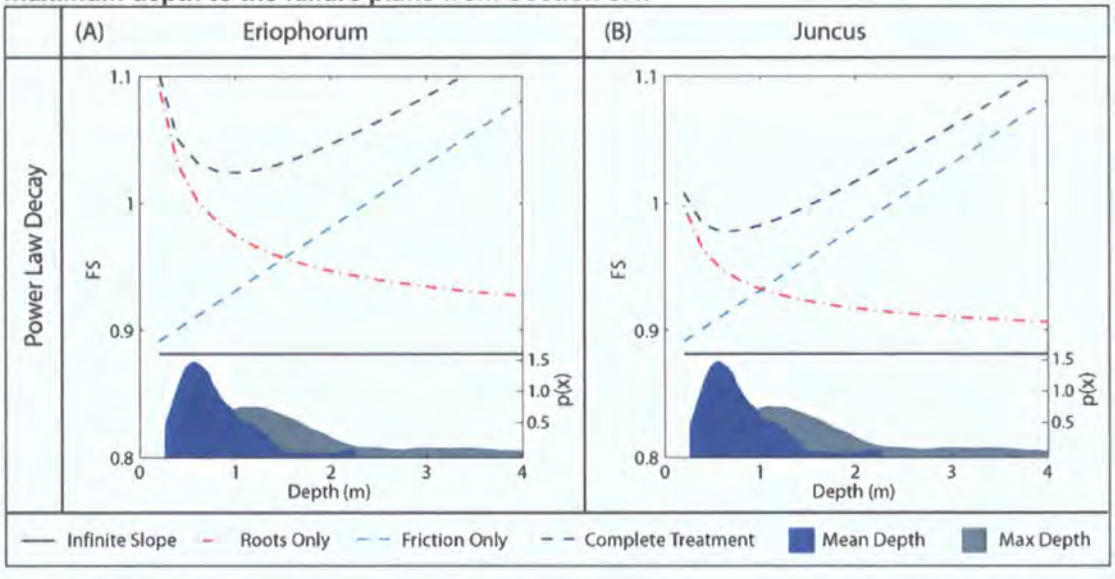

7.3. Hydrological Controls on Stability

Literature review and sensitivity analysis (Section 2.6) suggest that pore water pressure representation is key to stability predictions. In existing catchment scale stability models, a hydrological model provides the spatially- (and sometimes temporally-) distributed estimates of pore water pressure required by the geotechnical model. There is a range of models available to perform this task. Most assume that surface topography plays some role in concentrating flow and elevating water tables, either as a result of pressure gradients solved in a full Richards scheme (Simoni *et al.*, 2008) or from a simplified model using a topographic index with steady state assumptions (Montgomery and Dietrich, 1994).

Fine scale soil moisture patterns are difficult to predict, almost every hillslope study in the literature uncovers local drivers that confound the predictions from (even sophisticated) models (Freer *et al.*, 2002; Montgomery *et al.*, 2002). Field evidence from the Lake District at the plot-scale confirms this view (although note its inherent spatial (10^{-1} km^2) and temporal (2 yr) specificity; Section 6.6). At this scale the predicted wet areas differed considerably from those observed

(Section 6.6.4). I found surface seepage on a planar slope and overland flow over unsaturated ground at the spring seepage zone (SSZ) but dry conditions over the rest of the slope even in an area of topographic convergence. These results (Section 6.6) highlight a well known problem with existing hydrological models: they do not account for some soil water processes, such as preferential flow in soil macropores or fractures. However, it does not immediately provide a solution: there is currently no adequate descriptive equation to represent these features and information on subsurface properties remains difficult to obtain (Beven, 2001). Given these limitations, we are still interested in whether or not the scale at which these perturbations to the topographic control on hydrology occur dominates the system, or whether their impacts are small at the catchment scale, constituting noise on a trend rather than a chaotic or contingent signal.

Opinions differ over the extent to which this is the case (Thompson and Moore, 1996; Freer *et al.* 2002; Montgomery *et al.*, 2002; Gallart *et al.*, 2008) and much of this difference might be attributed to the differing settings in which research has been performed. The most reasonable approach is to note that probably some landscapes are "well behaved" with perturbations quickly eradicated or dwarfed by stronger deterministically tractable drivers such as topographically driven flow. Others may be dominated by apparently chaotic influences resulting from unmeasured and presently unmeasureable catchment characteristics such as strong preferential flow, vertically or laterally in soil or bedrock (Tetzlaff *et al.*, 2008). The relationship between the two is likely to be decided by the strength of the gravity driven flow control against the impact and frequency of perturbations to this control. Both will be related to landscape character, its material and topographic properties, its geomorphology and ecology. Steep topographically-variable landscapes with well developed hollows and colluvial soils such as the Oregon Coast Range (USA) might be expected to be dominated by gravity driven flow and surface topography. "Younger" landscapes with a strong glacial legacy, large valleys, planar valley sides and spatially variable glacially derived deposits might be expected to be more strongly influenced by contingency, since the topographic drivers are weaker and therefore less able to rapidly recover from perturbations (Tetzlaff *et al.*, 2008).

My catchment scale analysis (Section 6.7) has suggested that the Lake District soil moisture patterns are driven by topography at the largest scale (valley scale). Valley bottoms are wet, flat and have high contributing areas. However, valley side seepage points exist not only at the study hillslope but across the broader Newlands study area. These appear effectively described by the simple conceptual model developed at the hillslope site (Section 6.6.7), which explains their existence and form given a seepage point but not the origin of the seepage point itself. Within the Lake District study area topographic control becomes stronger with increased scale between these end members (from hillslope to valley scale), but the form of this relationship is presently unknown. The results for the Lake District (Section 6.7 and Figure 7-4) suggest that the assumption that soil moisture conditions are topographically driven is reasonable at the largest scale.

Figure 7-4 shows wet (blue), dry (green) and landslide (red) landscape elements (DEM cells) plotted in logarithmic space in terms of their local slope (x axis) and contributing area (y axis). They are partitioned into SHALSTAB relative stability predictions with three zones: 1) unconditionally stable, where the slope is too low to fail under any conditions; 2) unconditionally unstable, where the slope should fail even in dry conditions; and 3) conditionally stable, where the slope's stability depends on its saturation and slope. Conditional stability (solid lines) and saturation thresholds (dashed lines, based on a modified topographic index) are defined in slope area space for a given transmissivity to rainfall ratio (T/q). The exponential decline in contributing area required for failure in the conditional stability zone reflects the decreasing degree of saturation required to trigger failure as local slope increases towards the threshold of unconditional instability.

There is a clear cluster of wet (blue) cells in Figure 7-4, indicating that wet cells are found preferentially at locations with certain slopes and contributing areas. However there is also considerable scatter resulting from contingent features that cannot be predicted; in particular, wet cells cluster around contributing areas of 500–10000 m^2 but extend across the full range. The upper limit on slopes that sustain wet patches is better constrained (~0.7 m/m). When landslide cells are plotted in the same slope area space (Figure 7-4) they

overlay the wet cells occurring preferentially towards the steeper slopes but rarely extending to slopes steeper than the limit for wet cells (~0.7 m/m). Their lower contributing area limit is stricter than for wet patches, with very few landslide cells having contributing areas less than ~200 m^2.

These results suggest that both landslides and wet patches are topographically driven to some extent, but that there is considerable scatter around this relationship. Observations at a range of scales from the study hillslope (Section 6.6) to catchment scale (Section 6.7) suggest that these are the result of contingent perturbations (soil pipes, seepage zones etc). Figure 7-4 suggests a link between wet zones and landslides. Wet zones cluster largely between T/q ratios of 325–3250; landslides also cluster in this zone. The upper limit on the slopes at which landslides occur appears defined by the availability of wet cells at that inclination. The lower slope limit is defined not by availability of wet cells, (there are many wet cells at low slopes) but by a geotechnical control (relationship between friction angle and slope).

These results are unsurprising given the strong theoretical link between wetness and stability (Section 2.4.2) and the prevalence of wet vegetation types at Lake District landslide scars (Section 2.4.3). Slope instability is closely associated with soil moisture which is closely associated with vegetation type; the link between these variables and topography is present but weaker. In this situation, the ability of hydrological models to predict spatial soil moisture patterns appears to be the limiting control on the predictive power of catchment scale slope stability models.

Figure 7-4: A plot of upslope contributing area against local slope (calculated from the 5 m IfSAR DSM for: all cells in the Newlands valley study area (green); cells in wet zones mapped from *Juncus* (blue); and cells containing affected by landslides in January 2005 (red). Threshold lines are from SHALSTAB (explained in detail in Chapter 2) using parameters from Chapter 3.

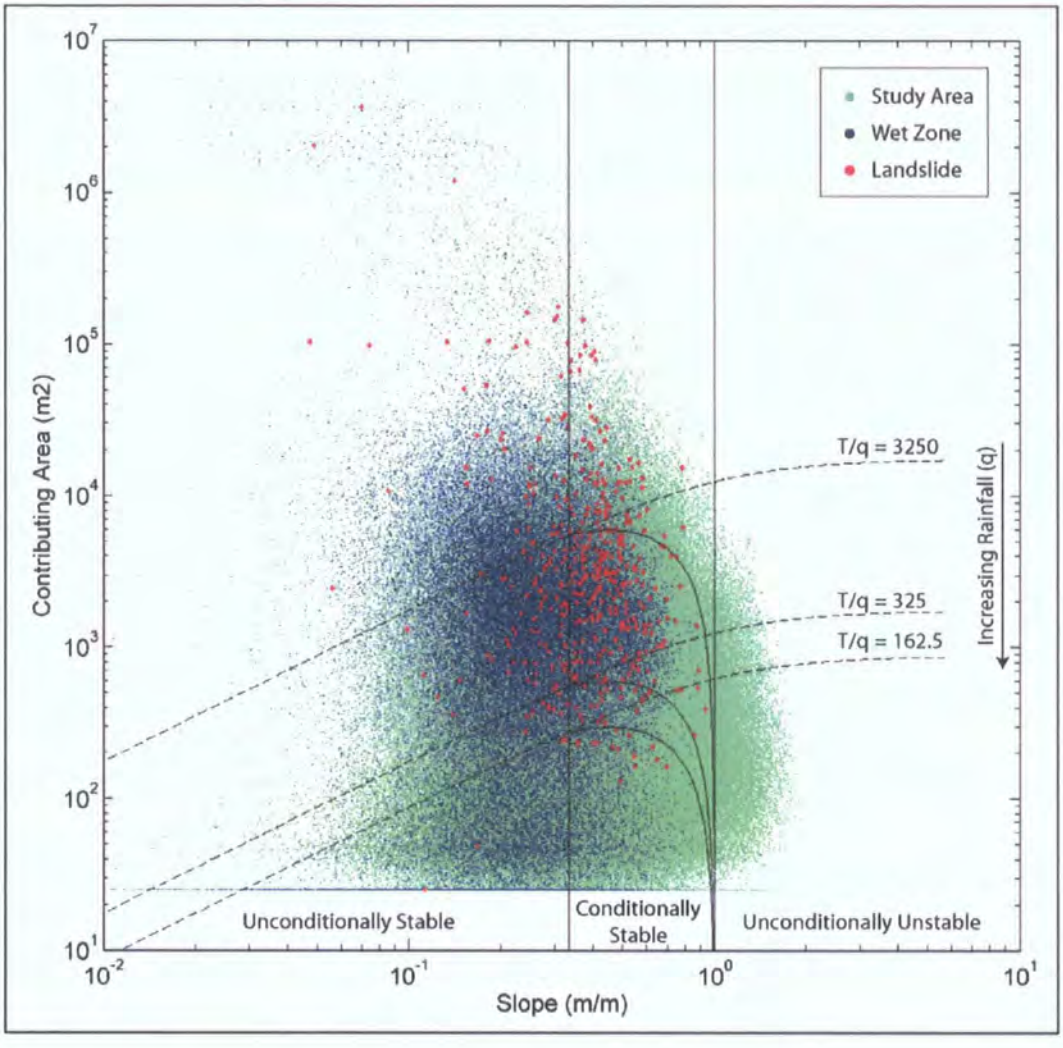

7.4. Implications for Catchment Scale Slope Stability Modelling

The broad topographic control on wetness means that simple GIS based slope stability models such as SHALSTAB continue to provide useful information on areas likely to be more susceptible to slope instability. However, pursuing this approach to predict deterministic locations and sizes of landslides in response to a rainfall time series is unlikely to yield fruitful results for catchments in areas such as the Lake District, where unmeasured and presently un-measureable perturbations disrupt the topographically driven flow. Future advances in measuring and modelling hillslope hydrological processes and in collecting the data necessary to ascertain boundary conditions for these processes may alter this situation. It is certainly an area with rich potential for future research.

However, the utility of these models is not limited to this spatially deterministic approach. Given the results from my study what can we say about catchment scale slope stability modelling?

The strong vegetation – wetness – stability link might lend itself to inclusion of vegetation as a surrogate for wetness within slope stability models, bypassing the problematic link between topography and wetness and the problematic step of modelling spatial soil moisture patterns. However, the location of the wet patches is then no longer explicable in terms of process so that scenario modelling becomes difficult. It is difficult to predict how wet patch behaviour might change over time without understanding the reason for their original location and extent. The vegetation surrogate approach does have potential as a semi-process based approach to current hazard predictions. Three-dimensional stability estimates using the analytical equations outlined in Chapter 4 could be readily calculated for wet patches identified from vegetation. These could be populated with topographic information from a DEM and probability distributions for the important material property parameters. The results could be given an instability rating related to their factor of safety or by rearranging the 3D stability equations to solve for critical saturation ratio (M_{crit}).

An alternative approach applied elsewhere in the literature (Benda and Dunne, 1997) is to move away from spatial determinism and treat the process in terms of its magnitude and frequency over a given area. This approach is still useful in terms of its implications for sediment delivery and hazard and brings the research into contact with a large and growing body of empirical research on landslide magnitude and frequency from landslide inventories. Some statistical properties of these inventories (power law decline in frequency with magnitude of medium and large landslides with under-sampling termed rollover at smaller magnitudes) have become a subject of considerable debate with the form of the distributions explained in a variety of ways (Noever, 1993; Pelletier *et al.*, 1997; Hergarten and Neugebauer, 1998, 2000).

Some of these explanations invoke the theory of self organised criticality originating from the sand pile model of Bak *et al.* (1987). In this case, self organization of the sand pile into a critical state results from the continuous

input of energy into the system and the action of large and small sand slides. An alternative hypothesis by Pelletier *et al.* (1997) links the magnitude frequency relationship for landslides to that of wet patches. They suggest that since soil moisture is known to be an important factor in slope instability and the magnitude frequency distributions of large landslides often obey power-law statistics, it is likely that patches of soil moisture above a threshold value, which also obey power law statistics, can be associated with landslides. They model instability with a threshold shear stress criterion proportional to the product of soil moisture and slope; and assume that soil moisture dynamics are independent of topography but obey power law scaling. Researchers studying spatial soil moisture patterns from passive microwave remote sensing have found that the magnitude and frequency of soil moisture patches follows a power law. These relationships have been explained by the spatial organisation of soil properties such as porosity, which control infiltration (Rodriguez-Iturbe *et al.*, 1995) or by spatial and temporal variations in evapotranspiration resulting from variable atmospheric conditions and heterogeneity in soil, topography and vegetation characteristics (Pelletier *et al.*, 1997).

Figure 7-5: Magnitude frequency relationships for wet zones steeper than 20° (for the Newlands valley study area) and landslides from the January 2005 inventory.

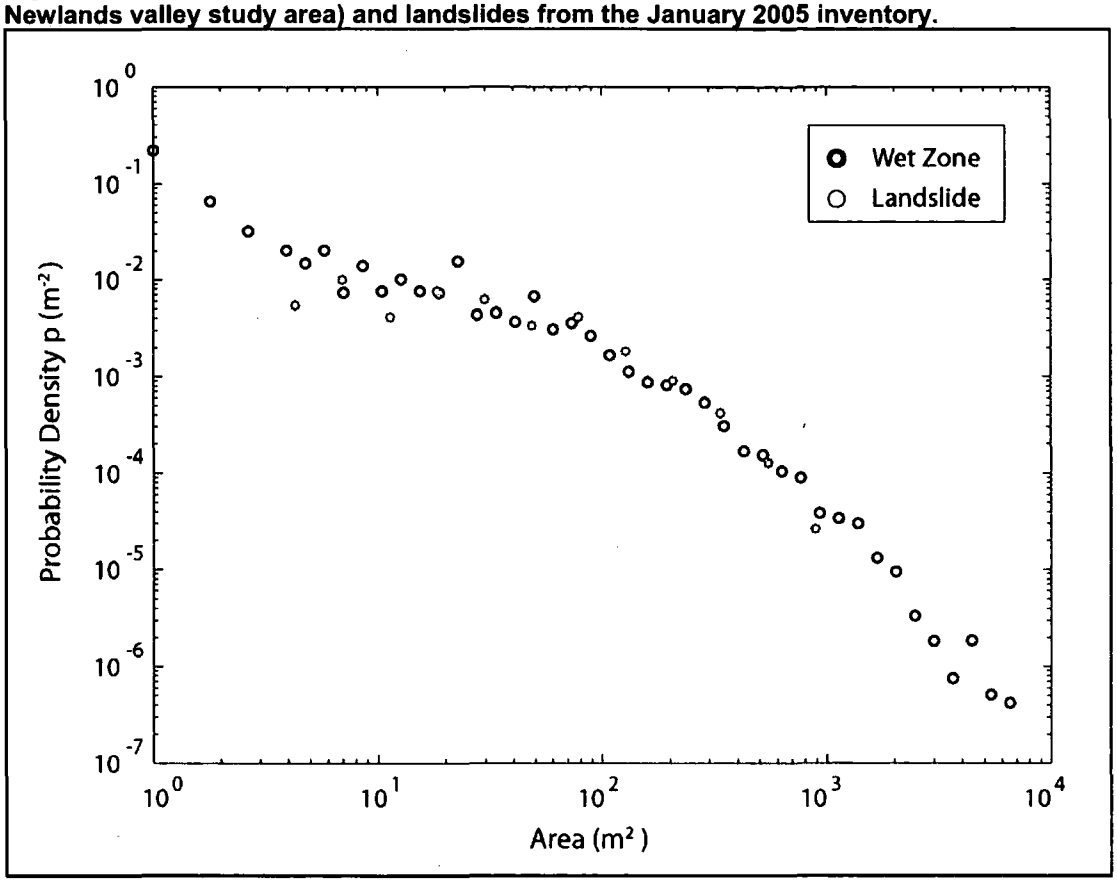

Whilst the magnitude frequency relationship for wet patches in the Lake District appears linear across certain ranges in logarithmic space (e.g. 10^0–10^2 and 10^2–10^4; Figure 7-5), I do not contend that it represents a power law, or make any suggestions as to the driving factors behind such a relationship. Instead, I compare the magnitude frequency relationships for wet patches and landslides in the Lake District and find that they are in close agreement over patch sizes ranging from 20–1000 m^2. The relationship appears to break down at small patch sizes. There is a weak inflexion in the magnitude frequency relationships for both landslides and wet patches at ~80 m^2. For wet patches this inflexion is weak and their frequency continues to increase at only a slightly reduced rate but the inflexion in the plot for landslides is sharper, so that the frequency of landslides increases more slowly once landslide area is <80 m^2. I interpret the strong similarity in magnitude frequency relationships (Figure 7-5) and length / width relationships (Figure 7-6) for landslides and wet patches as reflecting a strong soil moisture control on slope stability.

Figure 7-6: The relationship between width and length of wet zones steeper than 20° (mapped from *Juncus*) and landslides from the January 2005 inventory.

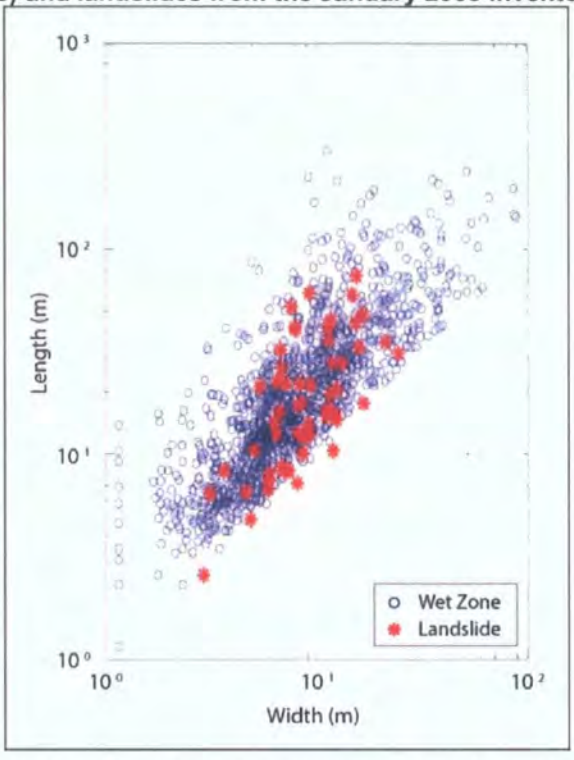

Medium and large (>80 m^2) landslides are sampled from within the distribution of available wet patches (supported by observations of *Juncus* grass at the margins of 85% of landslide scars). Smaller wet patches are more frequent than large ones following a quasi power increase in frequency with decreasing area. However, although these smaller patches are more frequent, geometric controls on stability related to the additional strength supplied by the margins of the potentially unstable block makes the probability of a landslide occurring in one of these patches increasingly small as patch size decreases. This relates directly to the exponential increase in factor of safety with decreasing landslide length or width (Figure 7-7). The result is a power law increase in frequency of potential landslide sites (wet patches) with decreasing size, but an exponential decrease in the conditional probability of failure at these sites, and hence a progressively increasing departure of landslide and wet patch frequency with decreasing size.

Figure 7-7: Example plots showing the dependence of factor of safety (FS) on block width (A) and length (B), these geometric stability controls are related to the magnitude frequency relationship for width (C) and length (D) of wet zones steeper than 20° and of landslides.

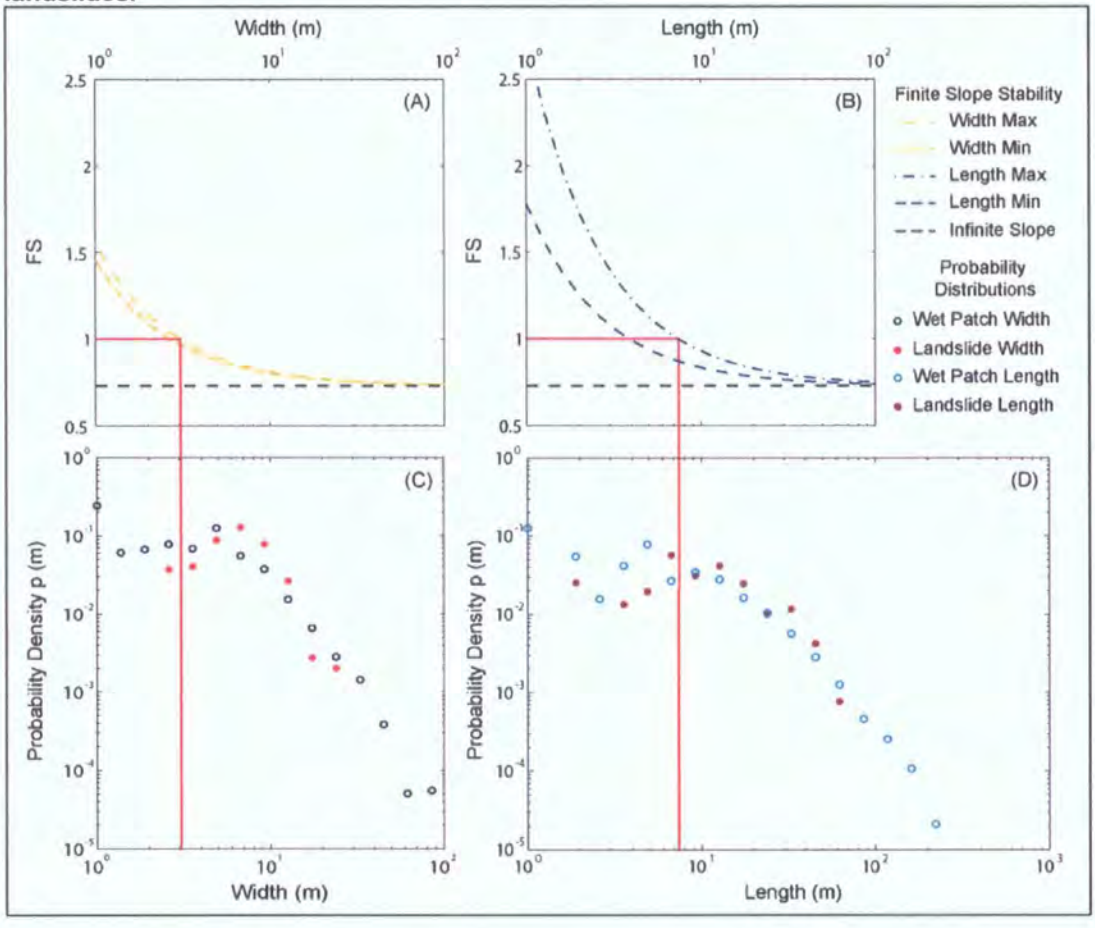

These assertions are tentative and represent an extremely simplified view of the driving forces behind slope stability. However, the theory fits with my conceptual view of Lake District slope stability and my observations of landslide characteristics (Section 2.4.3). The spatial locations and extents of landslides are driven largely by the locations and extents of wet patches on suitably steep slopes but this relationship is not scale independent. The upper limit on both wet patch and landslide size is set by the length of suitably steep ground. The lower limit on landslide size is set by geometric stability effects related to additional strength supplied at block margins by lateral roots and grain on grain interactions. The non-spatial analysis requires considerable refinement and in particular there is potential to combine the stability analyses performed on vegetation identified wet patches discussed above. This would allow a more complete picture of the interplay between patch geometry, other parameters and stability. However, based on my current understanding and existing data

from my Lake District study area, I tentatively suggest that the magnitude frequency relationship for landslide length and width follows the same relationship as for wet patches. The relationship breaks down at small lengths and widths, where the additional strength supplied by the margins of the block becomes important. Landslide dimensions are controlled by a combination of: 1) geometric stability effects, setting the minimum widths and lengths; and 2) the dimensions of available wet zones, defining maximum width and length. In some cases, the characteristic magnitude frequency relationships (power law and roll over) may be a function of this association.

7.5. Chapter Summary

The widely applied infinite slope model does not take lateral resistance on the block margins into account. However, research from Chapter 3 suggests that lateral roots can provide significant additional lateral resistance; and Finite Slope model results (Chapter 5) suggest that additional resistance on the margins are important for the stability of blocks shorter or narrower than 30 m.

In the absence of any other control landslides should cluster at the largest width depth combinations where factor of safety is lowest because edge strength is minimised. Observed landslides do not cluster here but towards lower lengths and widths as a result of the interaction between geometric stability controls and spatial patterns of key variables (e.g. slope, soil strength or pore water pressure). Geometry effects on stability are reflected in the minimum lengths and widths of observed landslides. These are likely to be related to the rapid increase in factor of safety for small blocks due to the two-dimensional exponential form of the factor of safety / block size relationship.

Friction effects on lateral sides are small relative to other effects (e.g. root cohesion) but have important implications from the depth of the failure plane. Root effects dominate shallow blocks and decline with failure plane depth, while friction effects increase to dominate deep blocks. The factor of safety minimum between the two agrees closely with observed landslide failure plane depths (Chapter 2), implying an intrinsic geometric control on failure plane depth.

Both landslides and wet patches are driven by topography to some extent but there is considerable scatter about this relationship in both cases (related to contingent perturbations). The ability of hydrological models to predict spatial soil moisture patterns appears to be a limiting control on the predictive power of catchment slope stability models in the Lake District.

Simple GIS based models (e.g. SHALSTAB) that take a probabilistic approach to stability prediction are still applicable within their predictive limits but deterministic models are unlikely to be successful in predicting failure volumes and timings for a given storm. Alternative approaches to predict slope stability in the Lake District might include applying a stability model using vegetation as a surrogate for wetness; however, this disconnects the model from the hydrological process. Another alternative is to move away from spatial determinism and treat the landslides in terms of their magnitude and frequency.

The magnitude frequency distribution for landslides and that for wet patches with local slopes >20° are strongly similar for slides larger than 1000 m2. The relationship breaks down at small widths and lengths. Based on these results and my observations, I tentatively suggest that landslide dimensions are controlled by a combination of: 1) geometric stability effects, setting the minimum widths and lengths; and 2) the dimensions of available wet zones, defining maximum width and length. In some cases, the characteristic magnitude frequency relationships (power law and roll over) may be a function of this association.

8. Conclusion

8.1. Scope of the Chapter

In this Chapter I will systematically revisit my objectives indicating the implications of my results for each one (Section 8.2). I will then draw these individual conclusions together to summarise the thesis contribution to our current understanding on modelling shallow landslides (Section 8.3) and finally indicate its implications for future research (Section 8.4).

8.2. Thesis Objectives Concluded

8.2.1. Collect High Quality Input Parameter Data for Slope Stability Analysis; Quantify Natural Variability and Error

The first data on root cohesion for three of the UK's most common upland vegetation types (*Pteridium*, *Eriophorum* and *Juncus*) suggests that even grass roots can provide appreciable lateral reinforcement and that there is considerable variability both within and between vegetation types (Table 8-1). Variation in root cohesion with depth is poorly constrained and predicted lateral reinforcement is highly sensitive to assumptions about the form of this relationship. In particular, reinforcement increases considerably when roots are assumed to extend to the full depth of the block. These results highlight the importance of lateral root reinforcement and of careful parameterisation in slope stability modelling; particularly, matching methods of measuring and modelling root cohesion.

Direct *in situ* soil shear strength measurements from landslide failure planes suggest that Lake District soils may be considered cohesionless, that the failure envelope is linear over the range of normal stresses under consideration and that peak and critical strengths can be used as upper and lower bounds to a material strength estimate for the soil (Table 8-1). For peak strength data there is considerable variability both within and between sites, which is reduced in both cases for critical strength data.

Soil density at the time of failure can be effectively approximated using field bulk density (an approach commonly applied in existing stability models). However, the density of organic and mineral horizons differ significantly; slope stability models could better represent the depth integrated density of the soil column by using relative depth of the organic horizon as a weighting factor to generate a composite from mineral and organic densities (Table 8-1).

Effective depth (to the failure plane) differs from depth to bedrock in many cases. Soil depth probes indicate that the soil mantle is often >3 m thick, surveys at landslide scars indicate that failure plane depths are rarely >2 m. Different methods of analysing survey data can lead to variability in depth estimates at a site but this variability is absorbed by spatially-lumped depth distributions. The effective soil depth is most reliably estimated by planform mean depth (scar volume / scar area; Table 8-1) and is best represented as a spatially-lumped depth distribution, which can then be applied in probabilistic frameworks for slope stability modelling.

Table 8-1: A summary table of the parameter values and their variability (represented using standard deviations) based on the results from Chapter 3. Note that: root cohesions are for lateral cohesion in the top 0.15 m of the soil; * = from failure plane samples only; # = true value -0.22 kPa is unphysical and is replaced with zero; ^ = depth calculated using planform mean scar depth from landslide sites.

Parameter	Central Value	Variability / Error
Peak Friction Angle	38.7°	±13.7°
Peak Soil Cohesion	2.64 kPa	±1.6 kPa
Critical Friction Angle	41.3°	±6.6°
Critical Soil Cohesion	0.0 kPa #	±0.8 kPa
Eriophorum Root Cohesion	6.2 kPa	±3.1 kPa
Pteridium Root Cohesion	5.7 kPa	±2.2 kPa
Juncus Root Cohesion	3.4 kPa	±2.1 kPa
Mineral Soil Density	1603 kg m^{-3}	±356 kg m^{-3}
Organic Soil Density	1158 kg m^{-3}	±246 kg m^{-3}
Organic Soil Weighting Factor	0.41	±0.25
Soil Depth ^	0.71 m	±0.33 m
IfSAR Elevation Data	N/A	0.53 m

Elevation error propagates through derived surface variables non-linearly; high frequency random error disrupts all variables while gross errors strongly influence their spatial patterns. Improvements in precision from digital photogrammetry were small and the processing cost required to generate photogrammetric DEMs was prohibitive relative to the free full coverage available from IfSAR. The IfSAR DSM (Table 8-1) was chosen in preference to the DTM because filtering degraded the quality of the elevation data but this caused problems in Chapter 6 where elevation errors related to non-ground points in the DSM disrupted the wetness likelihood analysis used to assess the topographic wetness hypothesis. Filtering elevation data significantly impacts derived variables and should be performed with the processes of interest in mind.

8.2.2. Establish the Importance of Lateral Reinforcement for Slope Stability in a Catchment Scale Modelling Context

To achieve this objective I needed to first develop a three-dimensional model for slope stability that accounted for lateral reinforcement due to both friction and root cohesion. This new 'Finite Slope model' follows Chen (1981), Burroughs (1985) and Dietrich *et al.* (2006) by considering the forces on each plane of a block and applying limit equilibrium analysis and earth pressure theory to calculate stability. Shear strength due to friction and root reinforcement is represented on each plane. Resisting forces (on the base and all the lateral margins) are summed and divided by the driving forces (from the block itself and the soil upslope) to obtain a factor of safety. Friction resistance is dependent on normal stress, represented using vertical geostatic stress on the base and 'at rest' and active earth pressures on the lateral sides (providing a predictive uncertainty envelope). For the upslope and downslope boundaries, driving or resisting force (normal to the plane) is calculated using active and passive earth pressure theory (uncertainty bounds are provided by applying Coulomb and Rankine theory). Root reinforcement on each plane is represented as a depth varying apparent cohesion and has a flexible treatment of the relationship between root reinforcement and depth. This model differs from previous formulations by: 1) using earth pressure coefficients suitable for sloping ground; 2) applying Rankine and Coulomb theory in combination to

quantify predictive uncertainty; 3) accounting for root cohesion variation with depth on basal and lateral planes; and 4) using active and 'at rest' earth pressure to quantify uncertainty in normal stresses on the lateral margins.

Benchmark tests indicate that the parameterisation of profile effects in the Finite Slope model improve their representation relative to the conventionally applied Infinite Slope (Taylor, 1948) and Ordinary (Fellenius, 1936) methods. The agreement between Finite Slope and benchmark stability predictions quantified in terms of soil strength is within the uncertainty associated with the soil strength input parameters.

Both width and length exert a control on block stability, which decreases exponentially as width or length increase. As a result, influence is limited for landslides longer or wider than 30 m but can be extremely important for landslides <10 m long or wide. At these dimensions the additional strength supplied by the margins is often larger than the uncertainty associated with the soil strength input parameters. The interaction between friction and root cohesion effects minimises stability at a failure plane depth ~1–3 m. Length effects are slightly stronger than width effects, suggesting that if a block's area is held constant, longer thinner blocks will be less stable but this effect is very small relative to the size control (decreasing stability with increasing block surface area).

8.2.3. Assess the Topographic Control on Temperate Upland Hydrology and the Influence of Scale and Material properties

At the hillslope scale topographic variables are poor predictors of wetness in this environment. I found surface seepage and overland flow on a planar slope but dry conditions over the rest of the slope even in an area of topographic convergence. Overland flow generation does not fit the classic variable source area model but takes the form of localised flow over unsaturated ground re-infiltrating as it moves downslope.

Using vegetation as a surrogate for wetness, and identifying vegetation patterns from high resolution orthorectified imagery spatial patterns of soil moisture can

be collected at large scales. This data indicates that topography controls wetness patterns at the largest scale but this relationship has considerable scatter related to valley side wet zones similar to that at the study hillslope. Between these end members, topographic control becomes stronger with increased scale but the form of this relationship (i.e. the strength of topographic control at intermediate scales) is presently unknown. The relationship between topography and wetness is likely to vary between landscape scale settings and might be expected to be weaker in the Lake District which has a strong glacial legacy. Material properties exert little control on wetness patterns compared with topography. The mitigating effect of material properties on topographic wetness control is also limited in most cases. Soil type does exert some control which merits further investigation and might be effectively parameterised using my empirical data in a likelihood scheme.

8.3. Conclusion

I began this thesis with the stated aim: *"to improve our understanding of why the predictions from shallow landslide models differ from observations"*. My results suggest that all three hypotheses on factors contributing to this mismatch are correct to some extent.

8.3.1. Variability in input parameters

The variability in input parameters, characterised in Chapter 3 indicates that parameters vary both due to measurement error and spatial variability. The sensitivity analysis in Chapter 2 indicates that for certain parameters, such as soil strength and local slope, this variability will have a profound effect upon stability predictions. The hypothesis here is that large potentially unstable zones under a spatially uniform set of parameters (like that of the original SHALSTAB) will contain more and less stable zones due to fine scale spatial variation in other parameters. In this scenario failure will occur in the zones where both: the probability of failure due to slope and contributing area is high and the material properties combine in a weaker than normal configuration. Such scenarios might be effectively represented in a probabilistic scheme, the distributions for the relevant parameters are now available for the Lake District study area and

this would be a clear next step for further research. However, this is not straightforward since the parameter covariance is poorly constrained.

8.3.2. Lateral reinforcement

The differences in stability predictions using Finite relative to Infinite Slope models declines exponentially with both width and length. As a result, the impact of a Finite Slope representation is large for slides <10 m but small for slides >30 m. This is important because most of the observed slides are smaller than 30 m (width and length) and many are smaller than 10 m, suggesting that for real landslides the reinforcement at the margins will have a significant stabilising effect. This offers the potential to reduce the candidate instability zones by discarding isolated patches too small to fail. However, the patterns of instability predicted by GIS stability models rarely include a large number of unstable isolated patches. Instead, the unstable cells tend to cluster in large groups. In such a situation (i.e. where patch length is >30 m) the Finite Slope model will predict stabilities similar to those from the Infinite Slope model. This represents a clear mismatch between predictions and observations not only in terms of the number of cells that fail but also in the size of the unstable zones. This is unlikely to be a function of the geotechnical representation since, if everything else were held constant, we might expect increasing stability with decreasing patch size. It is likely instead to be related to uncharacterised spatial variability in the geotechnical model's input parameters (including pore water pressure from the hydrological model).

If this is the case then a finite slope formulation added to the stability model will be effective only if it can be applied in combination with another alteration to the model that introduces some fine scale variability in these parameters. This might involve characterising the variability in the input parameters (discussed above and in Chapter 3); although in this case the problem is further complicated since there will be not only covariance between parameters but also spatial covariance. An interesting experiment here might be to 'reverse engineer' the kind of spatial covariance in the input parameters (e.g. soil strength) that would be required to produce the characteristic landslide scar geometries. This is possible given the available data describing the variability in

each parameter but difficult because: 1) the spatial and inter-parameter covariances are very poorly constrained and outcomes are likely to experience equifinality; and 2) there are computational difficulties associated with running the Finite Slope stability model in a GIS based framework (even at the hillslope scale). The second problem is tractable and a clear and urgent avenue for future research since it will unlock many other interesting applications as discussed below.

8.3.3. Hydrological Controls

A second, simpler explanation, for the mismatch in the size of predicted and observed unstable zones, related to the spatial variability in pore water pressures, has been outlined in Chapter 7. It suggests that in landscapes such as the Lake District the model's characterisation of hillslope hydrology, spatial wetness patterns and pore water pressures is the limiting factor in predicting failure locations and geometries.

This theory is persuasive because of the match between predicted and observed landslide geometries. The geometric and geotechnical controls on stability suggest that landslides should cluster at the largest widths and lengths but instead they cluster towards the lower widths and lengths. They should be slightly longer than they are wide, in fact they are much longer than they are wide, suggesting that their shape is influenced not only by the intrinsic geometric stability control but also by the spatial configuration of their parameters. Their consistent elongate downslope form (aspect ratios >1) suggests that at least one of their parameters has a least stable configuration that is anisotropic. Pore water pressure linked to wetness patterns is a good candidate, since these patterns are defined by gravity driven flow and wet patches are usually elongated in the downslope direction, similar to landslides (Chapter 7). Further, the magnitude frequency distribution for landslides and that for wet patches with local slopes >20° are strongly similar for slides larger than 1000 m^2. The relationship breaks down at small widths and lengths, suggesting that landslide dimensions are controlled by a combination of: 1) geometric stability effects, setting the minimum widths and lengths; and 2) the dimensions of available wet zones, defining maximum width and length. Not all

steep wet patches fail, reflecting either: the variability in other parameters (e.g. soil strength) at each patch; or the incomplete hydrological characterisation, which is likely since wet patches are likely to result from a range of processes.

These suggestions are tentative and at present represent only a new set of hypotheses for further testing. However, some important conclusions from this thesis are: 1) the importance of hillslope hydrology in defining the locations of potential failures; 2) the spatial variability in the hydrology that reflects a topographic signal and contingent perturbations; 3) the identification of a new technique to characterise these relationships, which opens the door for both pragmatic landslide prediction and more rigorous testing of the driving forces behind hillslope hydrology; 4) the suggestion that by combining a more complete geotechnical treatment with a more accurate hydrological representation we can offer a process explanation for the scaling relationships, magnitudes and frequencies of observed landslides.

8.4. Future Research

This study provides either full probability distributions or central values and standard deviations for each of the parameters commonly used in catchment slope stability models. These lend themselves to a **probabilistic treatment** of failure likelihoods that take into account the distribution of soil material properties. This can be performed either analytically (Haneberg, 2004) or using Monte-Carlo simulation (Hammond *et al.*, 1991) and would produce a rich set of results in terms of the spatial pattern of the distributions of stability estimates.

Three-dimensional catchment stability modelling using the Finite Slope model has powerful potential and has been shown to be a robust approach. It is analytically tractable and could be applied in the framework provided by Hovland's (1977) three-dimensional method of columns without additional computational or data requirements. However, implementing these analytical equations in a GIS framework is not straightforward since stability becomes dependent not only on the values of parameters at a point but also on those of surrounding cells. Stability of a neighbourhood of cells becomes dependent on the neighbourhood's size and shape and the stability of each of its component

cells. Full exploration of this parameter space, which would involve testing all possible combinations of cells, is unfeasible. Developing computationally efficient methods to identify the least stable neighbourhoods of cells is a clear avenue for future research.

Hydrological characterisation using remotely sensed imagery to identify vegetation types indicative of soil moisture properties has been piloted in this study and has considerable future potential. High resolution, three band, aerial imagery is widely available in the UK and other data from multi- or hyper-spectral sensors are available for parts of the UK and could be used to validate / calibrate the classification technique. These techniques can then be used to approach a range of hypotheses including: the power law scaling in magnitude frequency distributions for wet patches (Pelletier, 1997; Rodriguez-Iturbe, 1995); and the topographic wetness hypothesis discussed in detail here. In each case the answers are unlikely to be simply a global pass or fail for that hypothesis but instead to be strongly related to landscape character. A key contribution would be to move towards landscape classification in terms of its likely hydrological drivers. These might be: topographically driven; infiltration driven, dominated by contingency or scale invariant. Catchments are likely to plot not in one class but on a continuum between classes. These classes are simply suggestions but they illustrate the potential of using remote sensing of high resolution orthorectified aerial imagery to quickly obtain spatial wetness data over a wide area which can then be applied to test some of our traditional hypotheses about wetness patterns and their behaviour at different scales.

Finally, the findings in this thesis might be applied within a **pragmatic approach** to stability prediction attractive to land managers and stakeholders who are interested in contemporary landslide likelihoods within a catchment and do not require a model that is entirely physically based.

The Finite Slope stability model needs further research before it can be applied at the catchment scale. The connection between topography, wet zones and stability is present but with considerable scatter. The connection between vegetation and wet zones is stronger. Observations at the hillslope scale suggest that wet patches during rainfall events expand from areas where soil

moisture is initially high. Given these findings, a pragmatic alternative might be to use this information in a hybrid model that applies a physically based geotechnical treatment to areas identified as initially wet from vegetation patterns. These predictions could be framed in terms of a saturation ratio required to cause failure (a critical M value), conceptually similar to the *q/T* of SHALSTAB in that it incorporates a probabilistic approach to stability. In this case each wet patch might be initially treated equally as an object that has the potential to fail. This significantly reduces the problem of iteratively searching the landscape for least stable geometric configurations of the Finite Slope model since the patch geometry is either predefined by or constrained within the wet zone from the vegetation – wetness prediction.

Such a model would allow rapid assessment of stability in a quasi-physical manner that would account for key properties identified as important in this thesis, particularly the interplay between wet patch geometry and geometric stability controls. It disconnects the process basis for hydrology and so cannot be applied in scenario testing, but may be useful to managers as a quick method of establishing current probabilistic spatial landslide likelihoods. The approach could be applied using an Infinite or Finite Slope formulation, with single valued soil parameters or using distributions to simulate the spatial variability.

9. References

Abe K, Iwamoto M. 1986. Preliminary experiment on shear in soil layers with a large direct shear apparatus. *Journal Japan Forestry Society* **68**: 61-65.

Abe K, Iwamoto M, Sammori T. 1986. Strength of binding soil by tree roots. In, *38th Annual Meeting Kanto Japan Forestry Society*. Kanto, Japan.

Abe K, Ziemer RR. 1991. Effect of Tree Roots on a Shear Zone - Modeling Reinforced Shear-Stress. *Canadian Journal of Forest Research-Revue Canadienne De Recherche Forestiere* **21**: 1012-1019.

Abe K, Ziemer RR. 1991. Effect of Tree Roots on Shallow-Seated Landslides. *Proceedings of the Iufro Technical Session on Geomorphic Hazards in Managed Forests* **130**: 11-20.

Abernethy B, Rutherfurd ID. 2001. The distribution and strength of riparian tree roots in relation to riverbank reinforcement. *Hydrological Processes* **15**: 63-79.

Abramson LW, Lee TS, Sharma S, Boyce. 1996. *Slope Stability and Stabilisation Methods*. John Wiley and Sons: New York.

Addison K. 1987. Debris flow during intense rainfall in Snowdonia, North Wales - A preliminary survey. *Earth Surface Processes and Landforms* **12**: 561-566.

Albatineh N. 2006. Slope stability analysis using 2D and 3D methods (p. 143): University of Akron.

Alexander D. 2007. Making research on geological hazards relevant to stakeholders' needs. *Quaternary International* **171-72**: 186-192.

Alexander DE. 2005. Vulnerability to landslides in landslide hazard and risk. Glade T, Anderson MG, Crozier M (eds). Wiley: Chichester; 175-198.

Alexander EB. 1989. Bulk density equations for southern Alaska soils. *Canadian Journal of Soil Science* **69**.

Ambroise B, Freer J, Beven K. 1996. Application of a generalized TOPMODEL to the small Ringelbach catchment, Vosges, France. *Water Resources Research* **32**: 2147-2159.

Anagnosti P. 1969. Three-dimensional stability of fill dams. In *7th International Conference on Soil Mechanics and Foundation Engineering*. Mexico; 275-280.

Anctil F, Mathieu R, Parent LE, Viau AA, Sbih M, Hessami M. 2002. Geostatistics of near-surface moisture in bare cultivated organic soils. *Journal of Hydrology* **260**: 30-37.

Anderson CJ, Coutts MP, Ritchie RM, Campbell DJ. 1989. Root Extraction Force Measurements for Sitka Spruce. *Forestry* **62**: 127-137.

Anderson MG, Burt TP. 1978. Role of topography in controlling throughflow generation. *Earth Surface Processes and Landforms* **3**: 331-344.

Anderson MG, Kneale PE. 1980. Pore water-pressure and stability conditions on a motorway embankment. *Earth Surface Processes and Landforms* **5**: 37-46.

Anderson MG, Kneale PE. 1982. The influence of low-angled topography on hillslope soil-water convergence and stream discharge. *Journal of Hydrology* **57**: 65-80.

Anderson SP, Dietrich WE, Montgomery DR, Torres R, Conrad ME, Loague K. 1997. Subsurface flow paths in a steep, unchanneled catchment. *Water Resources Research* **33**: 2637-2653.

Arellano D, Stark TD. 2000. Importance of three-dimensional slope stability analysis in practice. In *Slope Stability*, Griffiths DV (ed). ASCE: Reston, VA; 18-32.

Azzouz AS, Baligh MM. 1978. Three-dimensional stability of slopes. In: Massachusetts Institute of Technology.

Bak P, Tang C, Wiesenfeld K. 1987. Self-organized criticality: an explanation of 1/f noise. *Physical Review Letters* **59**.

Bakuzis EV, Kurmis V. 1978. Provisional list of synecological coordinates and selected ecographs of forest and other plant species in Minnesota. In, *Staff Paper Series 5* (p. 31): University of Minnesota, Department of Forest Resources.

Baladi GY, Wu TTH. 1986. Interpretation of triaxial test results of cohesionless soils: a new model. In, *Advanced Triaxial Testing of Soil and Rock* (pp. 567-581). Louisville, Kentucky: American Society for Testing and Materials.

Baligh MM, Azzouz AS. 1975. End effects on the stability of cohesive slopes. *Journal of Geotechnical Engineering Division ASCE* **101**: 1105-1117.

Ballantyne CK. 1981. Periglacial Landforms and Environments on Mountains in the Northern Highands of Scotland (p. 593): University of Edinburgh.

Ballantyne CK. 1991. Scottish Landform examples.2. The landslides of Trotternish, Isle-of-Skye. *Scottish Geographical Magazine* **107**: 130-135.

Ballantyne CK. 2002. Geomorphological changes and trends in Scotland: debris flows. In (p. 27): Scottish Natural Heritage.

Band LE, Moore ID. 1995. Scale - Landscape attributes and geographical information systems. *Hydrological Processes* **9**: 401-422.

Barnes BS. 1939. The structure of discharge-recession curves. *American Geophysical Union Transactions* **Part 4**: 721-725.

Bates PD, Dawson RJ, Hall JW, Horritt MS, Nicholls RJ, Wicks J, Mohamed Ahmed Ali Mohamed H. 2005. Simplified two-dimensional numerical modelling of coastal flooding and example applications. *Coastal Engineering* **52**: 793-810.

Bathurst JC, Moretti G, El-Hames A, Moaven-Hashemi A, Burton A. 2005. Scenario modelling of basin-scale, shallow landslide sediment yield, Valsassina, Italian Southern Alps. *Natural Hazards and Earth System Sciences* **5**: 189-202.

Baum RL, Savage WZ, Godt JW. 2008. TRIGRS - a fortran program for transient rainfall infiltration and grid-based regional slope stability analysis, version 2.0. In, *Open File Report* (p. 81): U.S. Geological Survey.

Benda L, Dunne T. 1997. Stochastic forcing of sediment supply to channel networks from landsliding and debris flow. *Water Resources Research* **33**: 2849-2863.

Benda LE, Cundy TW. 1990. Predicting deposition of debris flows in mountain channels *Canadian Geotechnical Journal* **27**: 409-417.

Bendelow VC. 1984. Soils, geology and climate in the Lake District National Park. In *Proceedings of the North of England Soils Discussion Group*. Keswick; 82.

Beven K. 1981. Kinematic subsurface stormflow. *Water Resources Research* **17**: 1419-1424.

Beven K. 1995. Linking Parameters across Scales - Subgrid Parameterizations and Scale-Dependent Hydrological Models. *Hydrological Processes* **9**: 507-525.

Beven K. 1997. TOPMODEL: A critique. *Hydrological Processes* **11**: 1069-1085.

Beven K. 2001. *Rainfall-Runoff Modelling: The Primer*. John Wiley: London.

Beven K, Germann P. 1982. Macropores and Water-Flow in Soils. *Water Resources Research* **18**: 1311-1325.

Beven K, Lawson A, McDonald A. 1978. Landslip-Debris Flow in Bilsdale, North-York-Moors, September 1976. *Earth Surface Processes and Landforms* **3**: 407-419.

Beven KJ, Kirkby MJ. 1979. A physically based variable contributing area model of basin hydrology. *Hydrological Sciences Bulletin* **24**: 43-69.

Beven KJ, Warren R, Zaoui J. 1980. SHE: towards a methodology for physically-based distributed forecasting in hydrology. *International Association of Hydrological Sciences* **Publication No. 129**: 133-137.

Bischetti GB, Chiaradia EA, Simonato T, Speziali B, Vitali B, Vullo P, Zocco A. 2005. Root strength and root area ratio of forest species in Lombardy (Northern Italy). *Plant and Soil* **278**: 11-22.

Bishop AW. 1954. The use of pore pressure coefficients in practice. *Geotechnique* **4**: 148-152.

Bishop AW. 1955. The use of the slip circle in the stability analysis of slopes. *Geotechnique* **5**: 7-17.

Bishop AW. 1967. Progressive failure with special reference to the mechanism causing it. In *Geotechnical Conference*. Oslo; 142-150.

Bishop AW, Al-Dhahir Z. 1969. Some comparisons between laboratory tests, in-situ tests, and fullscale performance, with special reference to permeability and coefficient of consolidation. In *Conference on in-situ investigations in soils and rocks*, Society BG (ed). London.

Bishop AW, Bjerrum L. 1960. The relevance of the triaxial test to the solution of stability problems. In *ASCE research conference on shear strength of cohesive soils*. Boulder, Colorado; 437-501.

Bishop DM, Stevens M. 1964. Landslides on logged areas in southeast Alaska. In, *Research Paper* (p. 18): U.S. Department of Agriculture, Forest Service, Northern Forest Experiment Station.

Bjerrum L. 1972. Embankments on soft ground. In *ASCE Speciality Conference on Performance of Earth and Earth-Supported Structures*. Purdue University, West Lafayette, IN; 1-54.

Blazkova S, Beven K, Tacheci P, Kulasova A. 2002. Testing the distributed water table predictions of TOPMODEL (allowing for uncertainty in model calibration): The death of TOPMODEL? *Water Resources Research* **38**.

Boardman J. 1992. Periglaical Geomorphology. *Progress in Physical Geography* **16**: 339-345.

Boardman J. 1996. *Classic Landforms of the Lake District*. British Geomorphological Research Group.

Bolstad PV, Stowe T. 1994. An Evaluation of Dem Accuracy - Elevation, Slope, and Aspect. *Photogrammetric Engineering and Remote Sensing* **60**: 1327-1332.

Bonell M, Gilmour DA. 1978. Development of Overland Flow in a Tropical Rainforest Catchment. *Journal of Hydrology* **39**: 365-382.

Boorman DB, Hollis JM, Lilly A. 1995. Hydrology of soil types (HOST): a hdrologically-based classification of the soils of the United Kingdom. In: Institute of Hydrology.

Borga M, Dalla Fontana G, Da Ros D, Marchi L. 1998. Shallow landslide hazard assessment using a physically based model and digital elevation data. *Environmental Geology* **35**: 81-88.

Borga M, Dalla Fontana G, Gregoretti C, Marchi L. 2002. Assessment of shallow landsliding by using a physically based model of hillslope stability. *Hydrological Processes* **16**: 2833-2851.

Borga M, Fontana GD, Cazorzi F. 2002. Analysis of topographic and climatic control on rainfall-triggered shallow landsliding using a quasi-dynamic wetness index. *Journal of Hydrology* **268**: 56-71.

Bouma J. 1981. Soil Morphology and Preferential Flow Along Macropores. *Agricultural Water Management* **3**: 235-250.

Bouma J, Jongerius A, Boersma O, Jager A, Schoonderbeek D. 1977. Function of Different Types of Macropores During Saturated Flow through 4 Swelling Soil Horizons. *Soil Science Society of America Journal* **41**: 945-950.

Brabb EE. 1993. Priorities for Landslide Mapping During the International-Decade-of-Hazard-Reduction. In *Landslides - Seventh International Conference & Field Workshop*, Novosad S, Wagner P (eds). A.a.Balkema: Rotterdam; 7-14.

Bradbrook K, Waller S, Morris D. 2005. National floodplain mapping: Datasets and methods - 160,000 km in 12 months. *Natural Hazards* **36**: 103-123.

Brand EW. 1981. Some thoughts on rainfall induced slope failures. In *10th International Conference of Soil Mechanics and Foundation Engineering*; 373-376.

Brand EW, Dale MJ, Nash JM. 1986. Soil pipes and slope stability in Hong-Kong. *Quarterly Journal of Engineering Geology* **19**: 301-303.

Brardinoni F, Church M. 2004. Representing the landslide magnitude-frequency relation: Capilano River Basin, British Columbia. *Earth Surface Processes and Landforms* **29**: 115-124.

Braun J, Heimsath AM, Chappell J. 2001. Sediment transport mechanisms on soil-mantled hillslopes. *Geology* **29**: 683-686.

Breusch TS, Pagan AR. 1979. Simple Test for Heteroscedasticity and Random Coefficient Variation. *Econometrica* **47**: 1287-1294.

Brinkgreve RBJ, Vermeer PA. 2001. *Plaxis 3D tunnel.* Balkema Publishers: Tokyo.

Bromhead EN. 1998. *The Stability of Slopes.* Taylor and Francis.

Brooks SM, Anderson MG. 1995. The Determination of Suction-Controlled Slope Stability in Humid Temperate Environments. *Geografiska Annaler Series a-Physical Geography* **77A**: 11-22.

Brooks SM, Collison A. 1996. The significance of soil profile differentiation to hydrological response and slope instability: a modelling approach. In *Advances in Hillslope Processes*, Anderson MG, Brooks SM (eds). Wiley: Chichester.

Brooks SM, Collison A, Anderson MG. 1995. Modelling the role of climate, vegetation and pedogenesis in shallow translational hillslope failure. *Earth Surface Processes and Landforms* **20**: 231-242.

Brooks SM, Richards KS. 1993. Establishing the role of pedogenesis in changing soil hydraulic properties. *Earth Surface Processes and Landforms* **18**: 573-578.

Brooks SM, Richards KS, Anderson MG. 1993. Approaches to the study of hillslope development due to mass movement. *Progress in Physical Geography* **17**: 32-49.

Brunsden D. 1979. Mass movements. In *Process in Geomorphology*, Embleton C, Thornes JB (eds). Edward Arnold: London; 130-186.

Buchanan P, Savigny KW, Devries J. 1990. A method for modeling water tables at debris avalanche headscarps. *Journal of Hydrology* **113**: 61-88.

Bucknam RC, Coe JA, Chavarria MM, Godt JW, Tarr AC, Bradley L, S.A. R, Hancock D, Dart RL, Johnson ML. 2001. Landslides triggered by Hurricane Mitch in Guatemala - inventory and discusson. In, *U.S. Geological Survey Open File Report* (p. 39).

Burroughs ER, Thomas BR. 1977. Declining Root Strength in Douglas-fir after Felling as a Factor in Slope-Stability. In (p. 27). Ogden, Utah: Intermountain Forest and Range Experiment Station, US Forest Service.

Burroughs ER, Thomas BR. 1977. Identification of Landslide Hazard Areas in Western Oregon. *Transactions-American Geophysical Union* **58**: 166-166.

Burroughs ERJ. 1985. Landslide hazard rating for portions of the Oregan Coast range In *Symposium on effects of forest land use on erosion and slope stability*, O'Loughlin CL, Pearce AJ (eds). Honolulu, HI: University of Hawaii; 265-274.

Burt T, Butcher D. 1986. Stimulation from Simulation - a Teaching Model of Hillslope Hydrology for Use on Microcomputers. *Journal of Geography in Higher Education* **10**: 23-39.

Burt TP, Butcher DP. 1985. Topographic Controls of Soil-Moisture Distributions. *Journal of Soil Science* **36**: 469-486.

Burton A, Bathurst JC. 1998. Physically based modelling of shallow landslide sediment yield at a catchment scale. *Environmental Geology* **35**: 89-99.

Cadling L, Odenstad S. 1950. The vane borer. *Proceedings of the Swedish Geotechnical Institute* **2**: 7-56.

Caine N. 1980. The rainfall intensity - Duration control of shallow landslides and debris flows. *Geografiska Annaler Series a-Physical Geography* **62**: 23-27.

Cameron AC, Trivedi PK. 1990. Regression-Based Tests for Overdispersion in the Poisson Model. *Journal of Econometrics* **46**: 347-364.

Campbell D, Church M. 2003. Reconnaissance sediment budgets for Lynn Valley, British Columbia: Holocene and contemporary time scales. *Canadian Journal of Earth Sciences* **40**: 701-713.

Campbell IB. 1975. Pattern of variation in steepland soils - soil differences in complex topography. *New Zealand Journal of Science* **18**: 53-66.

Cannon SH, Ellen SD. 1985. Rainfall conditions for abundant debris avalanches. *California Geology* **38**.

Caquot A, Kerisel J. 1948. *Tables de poussee et de butee*. Gauthier-Villars: Paris.

Carrara A, Cardinali M, Detti R, Guzzetti F, Pasqui V, Reichenbach P. 1991. GIS techniques and statistical-models in evaluation landslide hazard. *Earth Surface Processes and Landforms* **16**: 427-445.

Carson MA. 1977. Angles of repose, angles of shearing resistance and angles of talus slopes. *Earth surface Processes* **2**: 363-380.

Casadei M, Dietrich WE. 2003. Controls on shallow landslide size. In *Debris-Flow Hazards Mitigation: Mechanics, Prediction, and Assessment, Vols 1 and 2*, Rickenmann D, Chen C (eds); 91-101.

Casadei M, Dietrich WE, Miller NL. 2003. Testing a model for predicting the timing and location of shallow landslide initiation in soil-mantled landscapes. *Earth Surface Processes and Landforms* **28**: 925-950.

Cazzuffi D, Corneo A, Crippa E. 2006. Slope Stabilisation by Perennial "Gramineae" in Southern Italy: Plant Growth and Temporal Performance. *Geotechnical and Geological Engineering* **24**.

Centre BAD. 2008. *Met Office - Nimrod Data*. http://badc.nerc.ac.uk/data/nimrod/, accessed: 29/08/08.

Chandler J. 1999. Effective application of automated digital photogrammetry for geomorphological research. *Earth Surface Processes and Landforms* **24**: 51-63.

Chandler JH, Brunsden D. 1995. Steady-State Behavior of the Black-Ven Mudslide - the Application of Archival Analytical Photogrammetry to Studies of Landform Change. *Earth Surface Processes and Landforms* **20**: 255-275.

Chandler M, Parker DC, Selby MJ. 1981. An Open-sided Field Direct Shear Box with Applications in Geomorphology. In, *Technical Bulletin No. 27* (p. 45): British Geomorphological Research Group.

Chandler RJ. 1973. The inclination of talus, arctic talus terraces, and other slopes composed of granular materials. *Journal of Geology* **81**.

Chen RH. 1981. Three-dimensional slope stability analysis. In, *JHRP Reports* (pp. 81-17): Purdue University.

Chen RH, Chameau JL. 1983. 3-Dimensional Limit Equilibrium-Analysis of Slopes. *Geotechnique* **33**: 31-40.

Chen ZY, Wang J, Wang YJ, Yin JH, Haberfield C. 2001. A three-dimensional slope stability analysis method using the upper bound theorem - Part II: numerical approaches, applications and extensions. *International Journal of Rock Mechanics and Mining Sciences* **38**: 379-397.

Chok YH, Kaggwa WS, Jaksa MB, Griffiths DV. 2004. Modelling the effects of vegetation on stability of slopes. In *9th Australia New Zealand Conference on Geomechanics*. Auckland.

Chugh AK. 2003. On the boundary conditions in slope stability analysis. *International Journal for Numerical and Analytical Methods in Geomechanics* **27**: 905-926.

Claessens L, Heuvelink GBM, Schoorl JM, Veldkamp A. 2005. DEM resolution effects on shallow landslide hazard and soil redistribution modelling. *Earth Surface Processes and Landforms* **30**: 461-477.

Claessens L, Schoorl JM, Veldkamp A. 2007. Modelling the location of shallow landslides and their effects on landscape dynamics in large watersheds: An application for Northern New Zealand. *Geomorphology* **87**: 16-27.

Collins AJ. 2001. The role of willow root architecture and character in root reinforcement potential. Nottingham: University of Nottingham.

Collison A, Wade S, Griffiths J, Dehn M. 2000. Modelling the impact of predicted climate change on landslide frequency and magnitude in SE England. *Engineering Geology* **55**: 205-218.

Collison AJC, Anderson MG. 1996. Using a combined slope hydrology stability model to identify suitable conditions for landslide prevention by vegetation in the humid tropics. *Earth Surface Processes and Landforms* **21**: 737-747.

Common R. 1954. A report on the Lochaber, Appin and Benderlock floods, May, 1953. *Scottish Geographical Magazine* **70**: 6-20.

Cook RD, Weisberg S. 1983. Diagnostics for Heteroscedasticity in Regression. *Biometrika* **70**: 1-10.

Cornforth DH. 2004. *Landslides in practice*. John Wiley and Sons: New Jersey.

Coulomb CA. 1776. Essai sur une application des regles des maximis et minimis a quelques problemes de statique relatifs a l'architecture. *Memoires de l'Achademie Royale pres Divers Savants* **7**.

Cox NJ. 2006. Assessing agreement of measurements and predictions in geomorphology. *Geomorphology* **76**: 332-346.

Cox NJ. 2007. Kernel estimation as a basic tool for geomorphological data analysis. *Earth Surface Processes and Landforms* **32**: 1902-1912.

Craig RF. 2004. *Craig's Soil Mechanics*. Routledge.

Crudden DM, Varnes DJ. 1996. Landslide Types and Processes In Turner AK, Schuster RL (eds), *Landslides: investigations and mitigation* (pp. 36-75): Transportation Research Board.

Dai FC, Lee CF. 2001. Terrain-based mapping of landslide susceptibility using a geographical information system: a case study. *Canadian Geotechnical Journal* **38**: 911-923.

Danjon F, Fourcaud T, Bert D. 2005. Root architecture and wind-firmness of mature Pinus pinaster. *New Phytologist* **168**: 387-400.

Daubenmire R. 1976. Use of Vegetation in Assessing Productivity of Forest Lands. *Botanical Review* **42**: 115-143.

Davis JL, Annan AP. 1989. Ground-Penetrating Radar for High-Resolution Mapping of Soil and Rock Stratigraphy. *Geophysical Prospecting* **37**: 531-551.

Deans JD, Ford ED. 1983. Modeling Root Structure and Stability. *Plant and Soil* **71**: 189-195.

Densmore AL, Anderson RS, McAdoo BG, Ellis MA. 1997. Hillslope evolution by bedrock landslides. *Science* **275**: 369-372.

DeRose RC, Blaschke PM. 1991. Geomorphic Change Implied by Regolith - Slope Relationships on Steepland Hillslopes, Taranaki, New-Zealand. *Catena* **18**: 489-514.

DeRose RC, Trustrum NA, Blaschke PM. 1993. Post-Deforestation Soil Loss from Steepland Hillslopes in Taranaki, New-Zealand. *Earth Surface Processes and Landforms* **18**: 131-144.

Deschamps R, Yankey G. 2006. Limitations in the back-analysis of strength from failures. *Journal of Geotechnical and Geoenvironmental Engineering* **132**: 532-536.

Dhakal AS, Sidle RC. 2004. Distributed simulations of landslides for different rainfall conditions. *Hydrological Processes* **18**: 757-776.

Dietrich WE, Bellugi D, Real de Asua R. 2001. Validation of the shallow landslide model, SHALSTAB, for forest management. In *Land Use and Watersheds: Human influence on hydrology and geomorphology in urban and forest areas*, Wigmosta MS (ed); 195-227.

Dietrich WE, Dunne T. 1978. Sediment budget for a small catchment in mountainous terrain. *Zeitschrift fur Geomorphology Supplement Band* **29**.

Dietrich WE, McKean J, Bellugi D. 2006. The prediction of landslides size using a multi-dimensional stability analysis. In, *American Geophysical Union*. San Francisco.

Dietrich WE, Montgomery DR. 1998. SHALSTAB: a digital terrain model for mapping shallow landslide potential. In, *Technical Report* (p. 29): NCASI.

Dietrich WE, Reiss R, Hsu ML, Montgomery DR. 1995. A Process-Based Model for Colluvial Soil Depth and Shallow Landsliding Using Digital Elevation Data. *Hydrological Processes* **9**: 383-400.

Dietrich WE, Wilson CJ, Reneau SL. 1986. Hollows, colluvium and landslides in soil-mantled landscapes. In *Hillslope Processes, Sixteenth Annual Geomorphology Symposium*, Abrahams A (ed): Allen and Unwin ltd; 361-388.

Docker BB. 2003. Biotechnical engineering on alluvial riverbanks of southeastern Australia: A quantified model of the earth-reinforcing prperties of some native riparian trees. *School of Geosciences* (p. 255). Sydney: University of Sydney.

Doornik JA, Hansen H. 1994. An omnibus test for univariate and multivariate normality. In, *Working Paper* (pp. 1-16). Oxford: Nuffield College.

Dorner B, Lertzman K, Fall J. 2002. Landscape pattern in topographically complex landscapes: issues and techniques for analysis. *Landscape Ecology* **17**: 729-743.

Duncan JM. 1996. State of the art: Limit equilibrium and finite-element analysis of slopes. *Journal of Geotechnical Engineering-Asce* **122**: 577-596.

Dunne T. 1991. Stochastic aspects of the relations between climate, hydrology and landform evolution. *Transactions of the Japanese Geomorphological Union* **12**: 1-12.

Dunne T. 1998. Critical data requirements for prediction of erosion and sedimentation in mountain drainage basins. *Journal of the American Water Resources Association* **34**: 795-808.

Dunne T, Black RD. 1970. An Experimental Investigation of Runoff Production in Permeable Soils. *Water Resources Research* **6**: 478-&.

Dunne T, Moore TR, Taylor CH. 1975. Recognition and prediction of runoff-producing zones in humid regions. *Hydrological Science Bulletin* **20**: 305-327.

Dupuy L, Fourcaud T, Stokes A, Danjon F. 2005. A density-based approach for the modelling of root architecture: application to Maritime pine (Pinus pinaster Ait.) root systems. *Journal of Theoretical Biology* **236**: 323-334.

Dussauge C, Grasso JR, Helmstetter AS. 2003. Statistical analysis of rockfall volume distributions: Implications for rockfall dynamics. *Journal of Geophysical Research-Solid Earth* **108**: 11.

Dussauge-Peisser C, Helmstetter AS, Grasso JR, Hantz D, Desvarreux P, Jeannin M, Giraud A. 2002. Probabilistic approach to rock fall hazard assessment: potential of historical data analysis. *Natural Hazards and Earth System Sciences* **2**: 15-26.

Dykes AP. 2008. Properties of peat relating to instability of blanket bogs. In *10th International Symposium on Landslides and Engineered Slopes*. Rotterdam: AA Balkema.

Dykes AP, Kirk KJ. 2006. Slope instability and mass movements in peat deposits. In *Peatlands: evolution and records of environmental and climate changes*, Martini IP, Martinez Cortizas A, Chesworth W (eds). Elsevier: Amsterdam; 377-406.

Dykes AP, Warburton J. 2007. Mass movements in peat: A formal classification scheme. *Geomorphology* **86**: 73-93.

Dykes AP, Warburton J. 2007. Significance of geomorphological and subsurface drainage controls on failures of peat-covered hillslopes triggered by extreme rainfall. *Earth Surface Processes and Landforms* **32**: 1841-1862.

Dykes AP, Warburton J. 2008. Characteristics of the Shetland Islands (UK) peat slides of 19 September 2003. *Landslides* **5**: 213-226.

Ekanayake JC, Phillips CJ. 1999. A method for stability analysis of vegetated hillslopes: an energy approach. *Canadian Geotechnical Journal* **36**: 1172-1184.

El-Aziz YA, Karara HM. 1978. Direct linear transformation from comparator coordinates into object space coordinates in close-range photogrammetry. *Proceedings of the ASP/UI Symposium on Close Range Photogrammetry*: 420-475.

El-Khouly MA. 1995. Analysis of soil-reinforcement interaction: Ohio State University.

Ellen SD, Algus MA, Cannon SH, Flemming RW, Lahr PC, Peterson DM, Reneau SL. 1988. Description and mechanics of soil slip / debris flows in the storm. In Ellen SD, Wieczorek GF (eds), *Landslides, Floods and Marine Effects of the Storm of January 3-5, 1982, in the San Francisco Bay Region, California* (pp. 63-112).

Endo T, Tsuruta T. 1969. The effect of tree roots upon the shearing strength of soil. In, *Annual Report of the Hokkaido Branch* (pp. 168-179): Tokyo Forest Experiment Station.

Ennos AR. 1990. The Anchorage of Leek Seedlings - the Effect of Root Length and Soil Strength. *Annals of Botany* **65**: 409-416.

Ervin GN, Wetzel RG. 2002. Influence of a dominant macrophyte, Juncus effusus, on wetland plant species richness, diversity, and community composition. *Oecologia* **130**: 626-636.

Evans IS. 1997. Cirques and moraines of the Helevellyn Range, Cumbria: Grisedale and Ullswater In *Geomorphology of the Lake District: a field guide*, Boardman J (ed). British Geomorphological Research Group; 63-87.

Evans IS. 2003. Scale-specific landforms and aspects of the land surface. In *Concepts and Modelling in Geomorphology: Interantional Perspectives*, Evans IS, Dikau R, Tokunaga E, Ohmori H, Hirano M (eds). Terrapub: Tokyo; 61-84.

Fannin RJ, Wise MP. 2001. An empirical-statistical model for debris flow travel distance. *Canadian Geotechnical Journal* **38**: 982-994.

Felicisimo AM. 1994. Parametric statistical method for error-detection in digital elevation models. *ISPRS Journal of Photogrammetry and Remote Sensing* **49**: 29-33.

Fellenius W. 1936. Calculation of the stability of earth dams. In *Second Congress on Large Dams*. Washington D.C.

Fernandes NF, Guimaraes RF, Gomes RAT, Vieira BC, Montgomery DR, Greenberg H. 2004. Topographic controls of landslides in Rio de Janeiro: field evidence and modeling. *Catena* **55**: 163-181.

Fielding A, Hayworth PF. 1999. *Upland Habitats*. Routledge.

Fisher PE, Tate NJ. 2006. Causes and consequences of error in digital elevation models. *Progress in Physical Geography* **30**: 467-489.

Fisher PF. 1991. 1st Experiments in Viewshed Uncertainty - the Accuracy of the Viewshed Area. *Photogrammetric Engineering and Remote Sensing* **57**: 1321-1327.

Fitter AH. 1987. An Architectural Approach to the Comparative Ecology of Plant-Root Systems. *New Phytologist* **106**: 61-77.

Franks SW, Gineste P, Beven KJ, Merot P. 1998. On constraining the predictions of a distributed moder: The incorporation of fuzzy estimates of saturated areas into the calibration process. *Water Resources Research* **34**: 787-797.

Freer J, Beven K, Ambroise B. 1996. Bayesian estimation of uncertainty in runoff prediction and the value of data: An application of the GLUE approach. *Water Resources Research* **32**: 2161-2173.

Freer J, McDonnell JJ, Beven K. 1997. Topographic controls on subsurface storm flow at the hillslope scale for two hydrologically distinct small catchments. *Hydrological Processes* **11**: 1347-1352.

Freer J, McDonnell JJ, Beven KJ, Peters NE, Burns DA, Hooper RP, Aulenbach B, Kendall C. 2002. The role of bedrock topography on subsurface storm flow. *Water Resources Research* **38**.

Freeze RA. 1972. Role of subsurface flow in generating surface runoff. 2: Upstream source areas. *Water Resources Research* **8**.

Freeze RA, Harlan RL. 1969. Blueprint for a physically-based, digitally-simulated hydrologic response model. *Journal of Hydrology* **9**: 237-258.

Fujii Y. 1969. Frequency distribution of the magnitude of the landslides caused by heavy rainfall. *Journal of Seimological Society of Japan* **22**: 244-247.

Gabet EJ, Dunne T. 2002. Landslides on coastal sage-scrub and grassland hillslopes in a severe El Nino winter: The effects of vegetation conversion on sediment delivery. *Geological Society of America Bulletin* **114**: 983-990.

Gallart F, Amaxidis Y, Botti P, Cane G, Castillo V, Chapman P, Froebrich J, Garcia-Pintado J, Latron J, Llorens P, Lo Porto A, Morais M, Neves R, Ninov P, Perrin JL, Ribarova I, Skoulikidis N, Tournoud MG. 2008. Investigating hydrological regimes and processes in a set of catchments with temporary waters in Mediterranean Europe. *Hydrological Sciences Journal-Journal Des Sciences Hydrologiques* **53**: 618-628.

Gallart F, Clotetperarnau N, Bianciotto O, Puigdefabregas J. 1994. Peat Soil Flows in Bahia-Del-Buen-Suceso, Tierra-Del-Fuego (Argentina). *Geomorphology* **9**: 235-241.

Gallart F, Latron J, Llorens P, Rabada D. 1997. Hydrological functioning of Mediterranean mountain basins in Vallcebre, Catalonia: Some challenges for hydrological modelling. *Hydrological Processes* **11**: 1263-1272.

Gallart F, Llorens P, Latron J. 1994. Studying the Role of Old Agricultural Terraces on Runoff Generation in a Small Mediterranean Mountainous Basin. *Journal of Hydrology* **159**: 291-303.

Gardiner V, Dackombe R. 1983. *Geomorphological field manual.* Allen and Unwin: London.

Genereux DP, Hemond HF, Mulholland PJ. 1993. Spatial and temporal variability in streamflow generation on the west fork of Walker Branch watershed. *Journal of Hydrology* **142**: 30.

Genet M, Stokes A, Salin F, Mickovski S, Fourcaud T, Dumail JF, van Beek R. 2005. The influence of cellulose content on tensile strength in tree roots. *Plant and Soil* **278**: 1-9.

Gens A, Hutchinson JN, Cavounidis S. 1988. 3-Dimensional Analysis of Slides in Cohesive Soils. *Geotechnique* **38**: 1-23.

Gerrard AJ. 1990. *Mountain environments: an examination of the physical geography of mountains.* Belhaven Press: London.

Gessler PE, Chadwick OA, Chamran F, Althouse L, Holmes K. 2000. Modeling soil-landscape and ecosystem properties using terrain attributes. *Soil Science Society of America Journal* **64**: 2046-2056.

Gessler PE, Moore ID, McKenzie NJ, Ryan PJ. 1995. Soil-landscape modelling and spatial prediction of soil attributes. *International Journal of Geographical Information Systems* **9**: 421-432.

Gifford J. 1953. Landslides on Exmoor caused by the storm of 15th August 1952. *Geography* **38**: 9-17.

Giger MW, Krizek RJ. 1975. Stability analysis of vertical cut with variable corner angle. *Soils and Foundations* **15**: 63-71.

Gilbert RB, Wright SG, Liedtke E. 1998. Uncertainty in back analysis of slopes: Kettleman Hills case study. *Journal of Geotechnical and Geoenvironmental Engineering* **124**: 10.

Gilman K, Newson MD. 1980. *Soil pipes and pipeflow - a hydrological study in upland wales*. GeoBooks: Norwich.

Gish TJ, Dulaney WP, Kung KJS, Daughtry CST, Doolittle JA, Miller PT. 2002. Evaluating use of ground-penetrating radar for identifying subsurface flow pathways. *Soil Science Society of America Journal* **66**: 1620-1629.

Glade T. 2003. Landslide occurrence as a response to land use change: a review of evidence from New Zealand. *Catena* **51**: 18.

Glade T, Crozier M, Smith P. 2000. Applying probability determination to refine landslide triggering rainfall thresholds using an empirical 'Antecedent daily rainfall model'. *Pure and Applied Geophysics* **157**: 1059-1079.

Godt JW, Baum RL, Savage WZ, Salciarini D, Schulz WH, Harp EL. 2008. Transient deterministic shallow landslide modelling: requirements for susceptibility and hazard assessments in a GIS framework. *Engineering Geology* **in press**.

Goldsmith W. 2006. Soil strength reinforcement by plants. In *Proceedings of the 37th International Erosion Control Association Conference*. Long Beach, California.

Gooch MJ, Chandler JH. 2001. Failure prediction in automatically generated digital elevation models. *Computers & Geosciences* **27**: 913-920.

Gray DH. 1974. Reinforcement and stabilization of soil by vegetation. *Journal of Geotechnical Engineering -ASCE* **100**: 695-699.

Gray DH. 1978. Role of woody vegetation in reinforcing soils and stabilising slopes. In *Soil Reinforcing and Stabilising Techniques*. Sydney, Australia; 253-306.

Gray DH, Leiser AJ. 1982. *Biotechnical Slope Protection and Erosion Control*. Van Nostrand Reinhold: New York.

Gray DH, Ohashi H. 1983. Mechanics of Fiber Reinforcement in Sand. *Journal of Geotechnical Engineering-Asce* **109**: 335-353.

Grayson RB, Bloschl G, Moore ID. 1995. Distributed parameter hydrologic modelling using vector elevation data: THALES and TAPES-C. In *Computer Models and Watershed Hydrology*, Singh VP (ed). Water Resource Publications; 669-696.

Grayson RB, Moore ID, McMahon TA. 1992. Physically based hydrologic modelling .1. a terrain based model for investigative purposes. *Water Resources Research* **28**: 2639-2658.

Grayson RB, Moore ID, McMahon TA. 1992. Physically based hydrologic modelling .2. is the concept realistic. *Water Resources Research* **28**: 2659-2666.

Greenway DR. 1987. Vegetation and slope stability. In *Slope Stability*, Anderson MF, Richards KS (eds). Wiley: New York.

Greenway DR, Anderson MG, Brian-Boys KC. 1984. Influence of vegetation on slope stability in hong Kong. In *4th International Symposium on landslides*. Toronto, Canada; 399--404.

Griffiths DV, Lane PA. 1999. Slope stability analysis by finite elements. *Geotechnique* **49**: 387-403.

Guntner A, Uhlenbrook S, Seibert J, Leibundgut C. 1999. Multi-criterial validation of TOPMODEL in a mountainous catchment. *Hydrological Processes* **13**: 1603-1620.

Guntner A, Uhlenbrook S, Siebert J, Leibundgut C. 1997. Estimation of saturation excess overland flow areas - comparison of topographic index calculations with field mapping. In *Regionalization in Hydrology*, Diekkruger B, Richter O (eds). TU Braunschweig; 93-96.

Guthrie RH, Evans SG. 2004. Ananlysis of landslide frequencies and characteristics in a natural system, Coastal British Columbia. *Earth Surface Processes and Landforms* **29**: 19.

Guzzetti F, Cardinali M, Reichenbach P, Carrara A. 2000. Comparing landslide maps: A case study in the Upper Tiber River basin, central Italy. *Environmental Management* **25**: 247-263.

Guzzetti F, Malamud BD, Turcotte DL, Reichenbach P. 2002. Power-law correlations of landslide areas in central Italy. *Earth and Planetary Science Letters* **195**: 169-183.

Hammond C, Hall D, Miller S, Swetik P. 1992. Level 1 Stability Analysis (LISA) Documentation for Version 2.0. In (p. 190). Ogden: Department of Agriculture, Forest Service, Intermountain Research Station.

Hammond CJ, Hardcastle JH. 1987. Shear strengths and densities of micaceous sands. In *8th Pan American Conference of Soil Mechanics and Foundation Engineering*. Cartagena, Colombia: National University of Columbia; 45-56.

Haneberg WC. 1991. Observation and analysis of pore pressure-fluctuations in a thin colluvium landslide complex near Cincinnati, Ohio. *Engineering Geology* **31**: 159-184.

Haneberg WC. 2000. Deterministic and probabilistic approaches to geologic hazard assessment. *Environmental & Engineering Geoscience* **6**: 209-226.

Haneberg WC. 2004. A rational probabilistic method for spatially distributed landslide hazard assessment. *Environmental & Engineering Geoscience* **10**: 27-43.

Haneberg WC. 2006. Effects of digital elevation model errors on spatially distributed seismic slope stability calculations: An example from Seattle, Washington. *Environmental & Engineering Geoscience* **12**: 247-260.

Haria AH, Shand P. 2004. Evidence for deep sub-surface flow routing in forested upland Wales: implications for contaminant transport and stream flow generation. *Hydrology and Earth System Sciences* **8**: 11.

Harp EL, Jibson RW. 1995. Seismic instrumentation of landslides - Building a better model of dynamic landslide behavior. *Bulletin of the Seismological Society of America* **85**: 93-99.

Harp EL, Jibson RW. 1996. Landslides triggered by the 1994 Northridge, California, earthquake. *Bulletin of the Seismological Society of America* **86**: S319-S332.

Harr RD. 1977. Water Flux in Soil and Subsoil on a Steep Forested Slope. *Journal of Hydrology* **33**: 37-58.

Harris A, Bryant RG, Baird AJ. 2005. Detecting near-surface moisture stress in Sphagnum spp. *Remote Sensing of Environment* **97**: 371-381.

Harvey AM. 1986. Geomorphic effects of a 100 year storm in the Howgill Fells, Northwest England. *Zeitschrift fur Geomorphologie* **30**: 71-91.

Harvey AM. 2001. Coupling between hillslopes and channels in upland fluvial systems: implications for landscape sensitivity, illustrated from the Howgill Fells, Northwest England. *Catena* **42**: 225-250.

Hastings A, Byers JE, Crooks JA, Cuddington K, Jones CG, Lambrinos JG, Talley TS, Wilson WG. 2007. Ecosystem engineering in space and time. *Ecology Letters* **10**: 153-164.

Hathaway RL, Penny D. 1975. Root strength in some *Populus* and *Salix* clones. *New Zealand Journal of Botany* **13**: 333-344.

Hayashi S. 1985. Some relationships between the landslide-area ratio and hydrologic data. *Journal of Japanese Forestry Society* **67**: 209-217.

Heimsath AM, Chappell J, Dietrich WE, Nishiizumi K, Finkel RC. 2000. Soil production on a retreating escarpment in southeastern Australia. *Geology* **28**: 787-790.

Heimsath AM, Dietrich WE, Nishiizumi K, Finkel RC. 1997. The soil production function and landscape equilibrium. *Nature* **388**: 358-361.

Hergarten S, Neugebauer HK. 1998. Self-organised criticality in a landslide model. *Geophysical Research Letters* **25**: 4.

Hergarten S, Neugebauer HK. 2000. Self-organised criticality in two-variable models. *Physical Review*: 4.

Heritage G, Hetherington D. 2007. Towards a protocol for laser scanning in fluvial geomorphology. *Earth Surface Processes and Landforms* **32**: 66-74.

Herwitz SR. 1993. Stemflow influences on the formation of solution pipes in Bermuda Eolianite. *Geomorphology* **6**: 19.

Hewlett JD, Hibbert AR. 1967. Factors affecting the response of small watersheds to precipitation in humid areas. In *Forest Hydrology*, Sopper WE, Lull HW (eds). Pergamon Press; 275-290.

Hinton MJ, Schiff SL, English MC. 1993. Physical-Properties Governing Groundwater-Flow in a Glacial Till Catchment. *Journal of Hydrology* **142**: 229-249.

Holden J. 2005. Controls of soil pipe frequency in upland blanket peat. *Journal of Geophysical Research-Earth Surface* **110**.

Holmes KW, Chadwick OA, Kyriakidis PC. 2000. Error in a USGS 30-meter digital elevation model and its impact on terrain modeling. *Journal of Hydrology* **233**: 154-173.

Holtz WG, Ellis W. 1961. Triaxial shear characteristics of clayey gravel soils. In *5th International Congress on Soil Mechanics and Foundation Engineering*. Paris.

Holtz WG, Gibbs JJ. 1956. Engineering properties of expansive clays. *Transactions of the American Society of Civil Engineers* **121**: 641-663.

Horn HM, Deere DU. 1962. Frictional characteristics of minerals. *Geotechnique* **12**: 319-335.

Hough BK. 1957. *Basic soils engineering*. Ronald Press Company: New York.

Hovius N, Stark CP, Allen PA. 1997. Sediment flux from a mountain belt derived by landslide mapping. *Geology* **25**: 231-234.

Hovius N, Stark CP, Chu HT, Lin JC. 2000. Supply and removal of sediment in a landslide-dominated mountain belt: Central Range, Taiwan. *Journal of Geology* **108**: 73-89.

Hovius N, Stark CP, Tutton MA, Abbott LD. 1998. Landslide-driven drainage network evolution in a pre-steady-state mountain belt: Finisterre Mountains, Papua New Guinea. *Geology* **26**: 4.

Hovland HJ. 1977. 3-Dimensional Slope Stability Analysis Method. *Journal of the Geotechnical Engineering Division-Asce* **103**: 971-986.

Hungr O. 1987. An Extension of Bishops Simplified Method of Slope Stability Analysis to 3 Dimensions. *Geotechnique* **37**: 113-117.

Hungr O. 1994. A General Limit Equilibrium-Model for 3-Dimensional Slope Stability Analysis - Discussion. *Canadian Geotechnical Journal* **31**: 793-795.

Hungr O, Salgado FM, Byrne PM. 1989. Evaluation of a 3-Dimensional Method of Slope Stability Analysis. *Canadian Geotechnical Journal* **26**: 679-686.

Hunter GJ, Goodchild MF. 1997. Modeling the uncertainty of slope and aspect estimates derived from spatial databases. *Geographical Analysis* **29**: 35-49.

Huntington WC. 1957. *Earth Pressures and Retaining Walls*. John Wiley and Sons.

Hursh CR. 1936. Storm-water and absorption. *Transactions of the American Geophysical Union* **17**: 301-302.

Hutchinson DG, Moore RD. 2000. Throughflow variability on a forested hillslope underlain by compacted glacial till. *Hydrological Processes* **14**: 1751-1766.

Hutchinson JN, Sarma SK, Chen RH, Chameau JL. 1985. 3-Dimensional Limit Equilibrium-Analysis of Slopes - Discussion. *Geotechnique* **35**: 215-216.

IFRC. 2004. *Information Bulletin: The Philippines: Tropical Storms, Floods and Landslides*. http://www.ifrc.org/cgi/pdf_appeals.pl?rpts04/philiptyphoonIB3, accessed: 5 April.

Ijjasz-Vasquez EJ, Bras RL. 1995. Scaling regimes of local slope versus contributing area in digital elevation models. *Geomorphology* **12**: 299-311.

Innes JL. 1982. Debris flow activity in the Scottish Highlands (p. 638). Cambridge: University of Cambridge.

Innes JL. 1983. Lichenometric sating of debris flow deposits in the Scottish Highlands. *Earth Surface Processes and Landforms* **8**: 579-588.

Intermap. 2004. *Intermap product handbook and quick start guide*. Intermap Technologies: Englewood, Colorado.

Intermap. 2007. *Nextmap 3D mapping program*. http://intermap.com/right.php/pid/1/sid/318, accessed: 22 August 2007.

Iverson RM. 2000. Lanslide triggering by rain infiltration. *Water Resources Research* **36**: 14.

Iverson RM, Lahusen RG. 1989. Dynamic Pore-Pressure Fluctuations in Rapidly Shearing Granular-Materials. *Science* **246**: 796-799.

Iverson RM, Reid ME, LaHusen RG. 1997. Debris-flow mobilization from landslides. *Annual Review of Earth and Planetary Sciences* **25**: 85-138.

Jaky J. 1944. The coefficient of earth pressure at rest. *Journal of the Union of Hungarian Engineers and Architects*: 355-358.

Janbu N, Bjerrum L, Kjaernsli B. 1956. Soil mechanics applied to some engineering problems. *Norwegian Geotechnical Institute* **Publication 16**.

Jenkins A, Ashworth PJ, Ferguson RI, Grieve IC, Rowling P, Stott TA. 1988. Slope failures in the Ochil Hills, Scotland, November 1984. *Earth Surface Processes and Landforms* **13**: 69-76.

Johnson KA, Sitar N. 1990. Hydrologic conditions leading to debris-flow initiation. *Canadian Geotechnical Journal* **27**: 789-801.

Johnson RM. 2001. Torrent erosion in Lake District Mountain catchments. *Department of Geography*. Durham: Durham University.

Johnson RM. 2003. Regional assessment of contemporary debris flow activity in Lake District mountain catchments, northern England: occurrence, scale and process. In *Debris-flow Hazards Mitigation: Mechanics, Prediction and Assessment*, Rickenmann D, Chen GL (eds). Millpress: Rotterdam; 965-976.

Johnson RM, Warburton J, Mills AJ. 2008. Hillslope-channel sediment transfer in a slope failure event: Wet Swine Gill, Lake District, northern England. *Earth Surface Processes and Landforms* **33**: 394-413.

Jonckheere I, Muys B, Copplin P. 2005. Allometry and evaluation of *in situ* aptical LAI determination in Scots pine: a case study in Belgium. *Tree Physiology* **25**: 723-732.

Jones CG, Lawton JH, Shachak M. 1997. Positive and negative effects of organisms as physical ecosystem engineers. *Ecology* **78**: 1946-1957.

Jordan JP. 1994. Spatial and temporal variability of stormflow generation processes on a Swiss catchment. *Journal of Hydrology* **153**: 357-382.

Karakouzian M, Avar BB, Hudyma N, Moss JA. 2003. Field measurements of shear strength of an underconsolidated marine clay. *Engineering Geology* **67**: 233-242.

Kerisel J, Absi E. 1990. *Active and Passive Earth Pressure Tables*. Swets and Zeitlinger: Rotterdam.

Khuder H, Danjon F, Stokes A, Fourcaud F. 2006. Growth response and root architecture of black locust seedlings growing on slopes and subjected to mechanical peturbation. In *5th Plant Biometrics Conference*, Salmen L (ed). Stockholm; 299-303.

King CAM. 1976. *The Geomorphology of the British Isles: Northern England*. Methuen: London.

Kirk KJ. 2001. Instability of blanket bog slope in Cuilcagh Mountain, North West Ireland. Huddersfield: University of Huddersfield.

Kirkby MJ. 1975. Hydrograph modelling strategies. In *Process in Physical and Human Geography*, Reel R, Chisholm M, Haggett P (eds). Heinemann; 69-90.

Kirkby MJ. 1978. Implications for Sediment Transport. In *Hillslope Hydrology*, Kirkby MJ (ed). John Wiley: Chichester.

Kirkby MJ. 1997. TOPMODEL: A personal view. *Hydrological Processes* **11**: 1087-1097.

Klinka K, Krajina VJ, Ceska A, Scagel AM. 1989. *Indicator plants of coastal British Columbia*. University of British Columbia Press: Vancouver, British Columbia.

Koler TE. 1998. Evaluating slope stability in forest uplands with deterministic and probabilistic models. *Environmental & Engineering Geoscience* **4**: 185-194.

Kopacsy J. 1957. Three-dimensional stress distribution and slip surfaces in earth works at rupture. In *4th International Conference on Soil Mechanics and Foundation Engineering*. London; 339-342.

Kosugi K, Uchida T, Mizuyama T. 2004. Numerical calculation of soil pipe flow and its effect on water dynamics in a slope. *Hydrological Processes* **18**: 777-789.

Kotarba A. 1992. High-Energy Geomorphic Events in the Polish Tatra Mountains. *Geografiska Annaler Series a-Physical Geography* **74**: 123-131.

Kotarba A. 1992. Natural-Environment and Landform Dynamics of the Tatra Mountains. *Mountain Research and Development* **12**: 105-129.

Kraus K, Pfeifer N. 1998. Determination of terrain models in wooded areas with airborne laser scanner data. *ISPRS Journal of Photogrammetry and Remote Sensing* **53**.

Ladson AR, Moore ID. 1992. Soil-Water Prediction on the Konza Prairie by Microwave Remote-Sensing and Topographic Attributes. *Journal of Hydrology* **138**: 385-407.

Lam L, Fredlund DG. 1993. A General Limit Equilibrium-Model for 3-Dimensional Slope Stability Analysis. *Canadian Geotechnical Journal* **30**: 905-919.

Lamb R. 1997. Discharge and water table predictions using a generalized TOPMODEL formulation. *Hydrological Processes* **11**: 23.

Lamb R, Beven K, Myrabo S. 1998. Use of spatially distributed water table observations to constrain uncertainty in a rainfall-runoff model. *Advances in Water Resources* **22**: 305-317.

Lambe TW, Whitman RV. 1969. *Soil Mechanics*. John Wiley: New York.

Lan HX, Zhou CH, Wang LJ, Zhang HY, Li RH. 2004. Landslide hazard spatial analysis and prediction using GIS in the Xiaojiang watershed, Yunnan, China. *Engineering Geology* **76**: 109-128.

Lane SN. 2000. The measurement of river channel morphology using digital photogrammetry. *Photogrammetric Record* **16**: 937-957.

Lane SN, Brookes CJ, Heathwaite AL, Reaney S. 2006. Surveillant Science: Challenges for the Management of Rural Environments Emerging from the New Generation Diffuse Pollution Models. *Journal of Agricultural Economics* **57**: 239-257.

Lane SN, Brookes CJ, Kirkby AJ, Holden J. 2004. A network-indexbased version of TOPMODEL for use with high-resolution digital topographic data. *Hydrological Processes* **18**: 191-201.

Lane SN, Chandler JH, Porfiri K. 2001. Monitoring river channel and flume surfaces with digital photogrammetry. *Journal of Hydraulic Engineering-Asce* **127**: 871-877.

Lane SN, Chandler JH, Richards KS. 1994. Developments in Monitoring and Modeling Small-Scale River Bed Topography. *Earth Surface Processes and Landforms* **19**: 349-368.

Lane SN, James TD, Crowell MD. 2000. Application of digital photogrammetry to complex topography for geomorphological research. *Photogrammetric Record* **16**: 793-821.

Lane SN, Reid SC, Tayefi V, Yu D, Hardy RJ. 2008. Reconceptualising coarse sediment delivery problems in rivers as catchment-scale and diffuse. *Geomorphology* **98**: 227-249.

Lane SN, Reid SC, Westaway RM, Hicks DM. 2004. Remotely sensed topographic data for river channel research: the identification, explanation and management of error. In *Spatial Modelling of the Terrestrial Environment*, Kelly R, Drake N, Barr S (eds). Wiley: Chichester; 157-174.

Lane SN, Westaway RM, Hicks DM. 2003. Estimation of erosion and deposition volumes in a large, gravel-bed, braided river using synoptic remote sensing. *Earth Surface Processes and Landforms* **28**: 249-271.

Latron J, Gallart F. 2007. Seasonal dynamics of runoff-contributing areas in a small Mediterranean research catchment (Vallcebre, Eastern Pyrenees). *Journal of Hydrology* **335**: 194-206.

Lawrance CJ, Rickson RJ, Clark JE. 1996. The Effect of Grass Roots on the Shear Strength of Colluvial Soils in Nepal. In *Advances in Hillslope Processes*, Anderson MG, Brooks SM (eds). John Wiley and Sons Ltd; 857-868.

LDNPA. 1999. *Lake District National Park Management Plan*. Lake District National Park Authority: Kendal.

Leach B, Herbert R. 1982. The genesis of a numerical-model for the study of the hydrogeology of a steep hillside in Hong-Kong. *Quarterly Journal of Engineering Geology* **15**: 243-259.

Lee IWY. 1985. A review of vegetative slope stabilisation. *Journal of the Hong Kong Institution of Engineers*: 9-21.

Lee KL, Seed HB. 1967. Dynamic strength of anisotropically consolidated sand. *Journal of Soil Mechanics Foundations Division ASCE* **93**: 169-190.

Lefebvre G, Duncan JM. 1973. Finite Element Analyses of Traverse Cracking in Low Embankment Dams. In, *Geotechnical Engineering Report*. Berkeley, CA: University of California, Berkeley, CA.

Lehre AK. 1982. Sediment budget of a small coast range drainage in north-central California. In, *Sediment budgets and routing in forested drainage basins*: Pacific Forest and Range Experimental Station General Technical Report.

Leshchinsky D, Baker R, Silver ML. 1985. 3 Dimensional Analysis of Slope Stability. *International Journal for Numerical and Analytical Methods in Geomechanics* **9**: 199-223.

Leslie DD. 1963. Large scale triaxial tests on gravelly soils. In *2nd Pan-American Conference on Soil Mechanics and Foundation Engineering*. Sao Paulo, Mexico; 181-202.

Li X, Tennant K, Lawrence G. 2004. Three-dimensional mapping with airborne IfSAR based STAR technology - Intermap's experiences. In *Proceedings of ISPRS Commission III symposium*. Istanbul, Turkey.

Lin LI. 1989. A concordance correlation coefficient to evaluate reproducibility. *Biometrics* **45**: 255-268.

Lin LI. 2000. A note on the concordance correlation coefficient. *Biometrics* **56**: 324-325.

Lopez C. 1997. Locating some types of random errors in Digital Terrain Models. *International Journal of Geographical Information Science* **11**: 677-698.

Luckman BH. 1992. Debris Flows and Snow Avalanche Landforms in the Lairig Ghru, Cairngorm Mountains, Scotland. *Geografiska Annaler Series a-Physical Geography* **74**: 109-121.

Luxmoore RJ. 1981. Microporosity, Mesoporosity, and Macroporosity of Soil. *Soil Science Society of America Journal* **45**: 671-672.

Major J. 1951. A functional factorial approach to plant ecology. *Ecology* **32**: 392-412.

Malamud BD, Turcotte DL, Guzzetti F, Reichenbach P. 2004. Landslide inventories and their statistical properties. *Earth Surface Processes and Landforms* **29**: 687-711.

Manley G. 1973. Climate. In *The Lake District*, Pearsall WH, Pennington W (eds). London: Collins; 106-120.

Marachi ND, Chan CK, Seed HB, Duncan JM. 1969. Strength and Deformation Characteristics of Rockfill Materials. In. Berkeley, CA: University of California, Berkeley, CA.

Mathewson CC, Keaton JR, Santi PM. 1990. Role of bedrock ground water in the initiation of debris flow and sustained post-flow stream discharge. *Bulletin of the Association of Engineering Geologists* **27**: 73-83.

Mayniel K. 1808. *Traite experimental, analytiqueet preatique de la poussee des terres et des murs de revetement*: Paris.

McDonnell JJ. 1990. The influence of macropores on debris flow initiation. *Quarterly Journal of Engineering Geology* **23**: 325-332.

McDonnell JJ. 2003. Where does water go when it rains? Moving beyond the variable source area concept of rainfall-runoff response. *Hydrological Processes* **17**.

McGlynn BL, McDonnell JJ, Brammer DD. 2002. A review of the evolving perceptual model of hillslope flowpaths at the Maimai catchements, New Zealand. *Journal of Hydrology* **257**: 1-26.

Mercer B. 2004. DEMs created from airborne IFSAR - an update. In *Proceedings of ISPRS Commission II symposium.* Istanbul, Turkey.

Merot P, Bruneau P. 1993. Sensitivity of bocage landscapes to surfaces run-off - Application of the Kirkby Index. *Hydrological Processes* **7**: 167-176.

Meyles E, Williams A, Ternan L, Dowd J. 2003. Runoff generation in relation to soil moisture patterns in a small Dartmoor catchment, Southwest England. *Hydrological Processes* **17**: 251-264.

Micheli ER, Kirchner JW. 2002. Effects of wet meadow riparian vegetation on streambank erosion. 2. Measurements of vegetated bank strength and consequences for failure mechanics. *Earth Surface Processes and Landforms* **27**: 687-697.

Milledge DG. 2009a. Digital filtering of generic topographic data in geomorphological research. *Earth Surface Processes and Landforms* **34**: 63-74.

Milledge DG. 2009b. Optimisation of stereo-matching algorithms using extant DEM data. *Photogrammetric Engineering and Remote Sensing* **In Press**.

Miller SM, Borgman LE. 1984. Probabilistic Characterization of Shear-Strength Using Results of Direct Shear Tests. *Geotechnique* **34**: 273-276.

Mills AJ. 2002. Peat Slides: Morphology, Mechanisms and Recovery. *Department of Geography*. Durham: Durham University.

Millward D. 1978. Ordovician Lake District volcanoes: a review. *Amateur Geologist* **8**: 4-14.

Montgomery DR, Dietrich WE. 1988. Where Do Channels Begin. *Nature* **336**: 232-234.

Montgomery DR, Dietrich WE. 1994. A Physically-Based Model for the Topographic Control on Shallow Landsliding. *Water Resources Research* **30**: 1153-1171.

Montgomery DR, Dietrich WE. 1995. Hydrologic processes in a low-gradient source area. *Water Resources Research* **31**: 1-10.

Montgomery DR, Dietrich WE, Heffner JT. 2002. Piezometric response in shallow bedrock at CB1: Implications for runoff generation and landsliding. *Water Resources Research* **38**: 18.

Montgomery DR, Dietrich WE, Torres R, Anderson SP, Heffner JT, Loague K. 1997. Hydrologic response of a steep, unchanneled valley to natural and applied rainfall. *Water Resources Research* **33**: 91-109.

Montgomery DR, Foufoula-Georgiou E. 1993. Channel network source representation for digital elevation models. *Water Resources Research* **29**: 3925-3934.

Montgomery DR, Pess G, Beamer EM, Quinn TP. 1999. Channel type and salmonid spawning distributions and abundance. *Canadian Journal of Fisheries and Aquatic Sciences* **56**: 377-387.

Montgomery DR, Schmidt KM, Greenberg HM, Dietrich WE. 2000. Forest clearing and regional landsliding. *Geology* **28**: 311-314.

Montgomery DR, Sullivan K, Greenberg HM. 1998. Regional test of a model for shallow landsliding. *Hydrological Processes* **12**: 943-955.

Moore ID, Gessler PE, Nielsen GA, Peterson GA. 1993. Soil Attribute Prediction Using Terrain Analysis (Vol 57, Pg 443, 1993). *Soil Science Society of America Journal* **57**: 1548-1548.

Moore ID, Grayson RB, Ladson AR. 1991. Digital terrain modelling: a review of hydrological, geomorphological and biological applications. *Hydrological Processes* **5**: 3-30.

Moore ID, O'Loughlin EM, Burch GL. 1988. A contour-based topographic model for hydrological and ecological applications. *Earth Surface Processes and Landforms* **13**: 305-320.

Moseley F. 1978. *The Geology of the Lake District*. Yorkshire Geological Society.

Moseley F. 1990. *The Lake District: Geologists' Association Guide*. The Geologists' Association.

Muller-Breslau H. 1906. *Erddruck auf Stutzmauern*. Alfred Kroner: Stuttgart.

Mulligan M, Wainwright J. 2004. Modelling and Model Building. In *Environmental Modelling: Finding Simplicity in Complexity*, Wainwright J, Mulligan M (eds). Wiley: Chichester; 430.

Murray AB. 2007. Reducing model complexity for explanation and prediction. *Geomorphology* **90**: 178-191.

Muscutt AD, Reynolds B, Wheater HS. 1993. Sources and Controls of Aluminum in Storm Runoff from a Headwater Catchment in Mid-Wales. *Journal of Hydrology* **142**: 409-425.

Nakane K, Nakagawa K, Takahashi F. 1983. Change in tensile strength of Japanses red pine roots after death by fire. *Journal Japan Forestry Society* **65**: 155-165.

Neal A. 2004. Ground-penetrating radar and its use in sedimentology: principles, problems and progress. *Earth-Science Reviews* **66**: 261.

Negussey D, Wijewickreme WKD, Vaid YP. 1988. Constant-Volume Friction Angle of Granular-Materials. *Canadian Geotechnical Journal* **25**: 50-55.

Ni LQ, Markenscoff X. 2003. The logarithmic singularity of an accelerating edge dislocation. *Philosophical Magazine* **83**: 3723-3734.

Nicoll BC, Berthier S, Achim A, Gouskou K, Danjon F, van Beek LPH. 2006. The architecture of Picea sitchensis structural root systems on horizontal and sloping terrain. *Trees-Structure and Function* **20**: 701-712.

Nicoll BC, Duncan R. 1996. Adaptive growth of tree root systems in response to wind action and site conditions. *Tree Physiology* **16**: 891-898.

Noever DA. 1993. Himalayan Sandpiles. *Physical Review* **47**: 724-725.

Noguchi S. 2001. Subsurface runoff characteristics from a forest hillslope soil profile including macropores, Hitachi Ohta, Japan. *Hydrological Processes* **15**: 2131-2149.

Norris JE. 2006b. Root mechanics applied to slope stability. Nottingham: Nottingham Trent University.

Norris JE, Greenwood JR. 2006. Assessing the role of vegetation on soil slopes in urban areas. In, *International Association of Engineering Geologists 2006*. Nottingham, UK: The Geological Society of London.

Nyberg L. 1996. Spatial variability of soil water content in the covered catchment at Gardsjon, Sweden. *Hydrological Processes* **10**: 89-103.

Ohmori H, Hirano M. 1988. Magnitude, frequency and geomorphological significance of rocky mud flows, landcreep and the collapse of steep slopes. *Zeitschrift fur Geomorphologie* **67**: 55-65.

Okimura T. 1983. A slope stability method for predicting rapid mass movements on granite. *Journal of Natural Disaster Science* **5**: 13-30.

Okimura T. 1989. Prediction of slope failure using the estimated depth of the potential failure layer. *Journal of Natural Disasater Science* **11**: 67-89.

Okimura T. 1994. Prediction of the Shape of a Shallow Failure on a Mountain Slope - the 3-Dimensional Multi-Planar Sliding Surface Method. *Geomorphology* **9**: 223-233.

Okimura T, Ichikawa R. 1985. A prediction method for surface failures by movements of infiltrated water in a surface soil layer. *Journal of Natural Disaster Science* **7**: 41-85.

Okuda S, Okunishi K, Suwa H. 1980. Observation of debris flow at Kamikamihori valley of Mt. Yakedake. In *Third Meeting of IGU Commission on Field Experiments in Geomorphology*, Okuda S, Suzuki T, Hirano K, Okunishi M, Suwa H (eds): Japan; 116-139.

O'Loughlin C, Watson A. 1979. Root-Wood Strength Deterioration in Radiata Pine after Clearfelling. *New Zealand Journal of Forestry Science* **9**: 284-293.

O'Loughlin CL. 1974a. The effects of timber removal on the stability of forest soils. *Journal of Hydrology (New Zealand)* **13**: 121-134.

O'Loughlin CL. 1972. An investigation of the stability of the steepland forest soils in the Coast Mountains, southwest British Columbia. Vancouver, Canada: University of British Columbia.

O'Loughlin CL. 1974b. A study of tree root strength deterioration following clear felling. *Canadian Journal of Forest Research* **4**: 107-113.

O'Loughlin CL. 1981. Tree roots and slope stability. . In, *What's new in forest research*: Forest Research Institute.

O'Loughlin CL, Ziemer RR. 1982. The importance of root strength and deterioration rates upon edaphic stability in steepland forests. In *Carbon uptake and allocation in subalpine ecosystems as a key to management. Proceedings of an I.U.F.R.O. workshop P.I. 107-00 Ecology of subalpine zones*

Warring RH (ed): Corvallis, Oregon, USA; 70-78.

O'Loughlin EM. 1981. Saturation regions in catchments and their relations to soil and topographic properties. *Journal of Hydrology* **53**: 229-246.

O'Loughlin EM. 1986. Prediction of surface saturation zones in natural catchments by topographic analysis. *Water Resources Research* **22**: 794-804.

Olson CG, Doolittle JA. 1985. Geophysical Techniques for Reconnaissance Investigations of Soils and Surficial Deposits in Mountainous Terrain. *Soil Sci Soc Am J* **49**: 1490-1498.

Onda Y. 1994. Seepage Erosion and Its Implication to the Formation of Amphitheater Valley Heads - a Case-Study at Obara, Japan. *Earth Surface Processes and Landforms* **19**: 627-640.

Onda Y. 2001. The role of subsurface runoff through bedrock on storm flow generation. *Hydrological Processes* **15**: 1693-1706.

Onda Y, Tsujimura M, Tabuchi H. 2004. The role of subsurface water flow paths on hillslope hydrological processes, landslides and landform development in steep mountains of Japan. *Hydrological Processes* **18**: 637-650.

Operstein V, Frydman S. 2000. The influence of vegetation on soil strength. *Ground Improvement* **4**: 81-89.

Ostendorf B, Reynolds JF. 1998. A model of arctic tundra vegetation derived from topographic gradients. *Landscape Ecology* **13**: 187-201.

Oven KJ. 2005. The analysis of spatial patterns and controls governing the global occurrence of fatal landslides. *Department of Geography*. Durham: Durham University.

Pack RT, Tarboton DG, Goodwin CN. 1998. The SINMAP approach to terrain stability mapping In, *8th International Congress of the International Association for Engineering Geology and the Environment*. Vancouver, Canada.

Paylor ii ED, Evans DL, Tralli DM. 2005. Theme issue: Remote sensing and geospatial information for natural hazards characterization. *ISPRS Journal of Photogrammetry and Remote Sensing* **59**: 181-184.

Pearsall WH, Pennington W. 1973. *The Lake District, A Landscape History*. Collins: London.

Pelletier JD, Malamud BD, Blodgett T, Turcotte DL. 1997. Scale-invariance of soil moisture variability and its implications for the frequency-size distribution of landslides. *Engineering Geology* **48**: 255-268.

Pennington W. 1997. History of the vegetation. In *Flora of Cumbria*, Halliday G (ed). University of Lancaster: Lancaster; 42-50.

Petley DN, Mantovani F, Bulmer MH, Zannoni A. 2005. The use of surface monitoring data for the interpretation of landslide movement patterns. *Geomorphology* **66**: 133-147.

Pierson TC. 1983. Soil Pipes and Slope Stability. *Quarterly Journal of Engineering Geology* **16**: 1-11.

Pitman E, Nichita C, Patra A, Bauer A, Bursik M, Weber A. 2003. A model of granular flows over an erodible surface. *Discrete and Continuous Dynamical Systems-Series B* **3**: 589-599.

Planchon O, Darboux F. 2002. A fast, simple and versatile algorithm to fill the depressions of digital elevation models. *Catena* **46**: 159-176.

Pollen N. 2004. The effects of riparian vegetation on streambank stability: mechanical and hydrological interactions. *Kings College* (p. 320). London: University of London.

Pollen N. 2007. Temporal and spatial variability in root reinforcement of streambanks: Accounting for soil shear strength and moisture. *Catena* **69**: 197-205.

Pollen N, Simon A. 2005. Estimating the mechanical effects of riparian vegetation on stream bank stability using a fiber bundle model. *Water Resources Research* **41**.

Pollen N, Simon A, Collison AC. 2004. Advances in assessing the mechanical and hydrologic effects of riparian vegetation on streambank stability. In *Riparian Vegetation and Fluvial Geomorphology, Water Science and Applications*, Bennett S, Simon A (eds); 125-139.

Powrie W. 2002. *Soil Mechanics: Concepts and Applications*. Spon Press: Abingdon.

Preston NJ, Crozier MJ. 1999. Resistance to shallow landslide failure through root-derived cohesion in east coast hill country soils, North Island, New Zealand. *Earth Surface Processes and Landforms* **24**: 665-675.

Qiu C, Esaki T, Xie M, Mitani Y, Wang C. 2007. Spatio-temporal estimation of shallow landslide hazard triggered by rainfall using a three-dimensional model. *Environmental Geology* **52**: 1569-1579.

Qui C, Esaki T, Xie M, Mitani Y, Wang C. 2006. A GIS system development for evaluating 3D slope stability.

Quinn P, Beven K, Chevallier P, Planchon O. 1991. The prediction of hillslope flow paths for distributed hydrological modeling using digital terrain models. *Hydrological Processes* **5**: 59-79.

Quinn PF, Beven KJ, Lamb R. 1995. The ln(a/tan-beta) index - how to calculate it and how to use it within the TOPMODEL framework. *Hydrological Processes* **9**: 161-182.

Rabus B, Eineder M, Roth A, Bamler R. 2003. The shuttle radar topography mission--a new class of digital elevation models acquired by spaceborne radar. *ISPRS Journal of Photogrammetry and Remote Sensing* **57**: 241-262.

Ragan RM. 1968. Integration of Digital Models and Experimental Data for Hydrograph Separation. *Transactions-American Geophysical Union* **49**: 164-&.

Rankine W. 1857. On the stability of loose earth. *Philosophical Transactions of the Royal Society of London* **147**.

Rapp A. 1960. Recent developments of mountain slopes in Karkvagge and surroundings, Northern Scandinavia. *Geografiska Annaler* **42**: 71-200.

Ratcliffe DA. 1997. Climate. In *A flora of Cumbria*, Halliday G (ed). Centre for North west regional studies: Lancaster; 611.

Ratcliffe DA. 1997. Vegetation. In *A flora of Cumbria*, Halliday G (ed). Centre for North west regional studies: Lancaster; 611.

Reddi LN, Wu TH. 1991. Probabilistic analysis of groundwater levels in hilside slopes. *Journal of Geotechnical Engineering-Asce* **117**: 872-890.

Reid LM. 1998. Calculation of average landslide frequency using climatic records. *Water Resources Research* **34**: 869-877.

Reid ME. 1994. A pore-pressure diffusion model for estimating landslide-inducing rainfall. *Journal of Geology* **102**: 709-717.

Reid ME, Iverson RM. 1992. Gravity-driven groundwater-flow and slope failure potential .2. effects of slope morphology, material properties, and hydraulic heterongeneity. *Water Resources Research* **28**: 939-950.

Reid ME, LaHusen RG, Iverson RM. 1997. Debris-flow initiation experiments using diverse hydrologic triggers. *Debris-Flow Hazards Mitigation: Mechanics, Prediction & Assessment*: 1-11.

Reid ME, Nielsen HP, Dreiss SJ. 1988. Hydrologic factors triggering a shallow hillslope failure. *Bulletin of the Association of Engineering Geologists* **25**: 349-361.

Reid SC. 2004. Coarse sediment delivery and transfer within an upland gravel-bed river. *School of Geography*. Leeds: University of Leeds.

Reid SC, Lane SN, Montgomery DR, Brookes CJ. 2007. Does hydrological connectivity improve modelling of coarse sediment delivery in upland environments? *Geomorphology* **90**: 263-282.

Reistenberg MM. 1994. Anchoring of thin colluvium by roots of sugar maple and white ash on hillslopes in Cincinnati. In. Washington DC.: U.S. Geological Survey

Reistenberg MM, Sovonick-Dunford S. 1983. The role of woody vegetation on stabilising slopes in the Cincinnati area. *Geological Society of America Bulletin* **94**: 506-518.

Reneau SL, Dietrich WE. 1987. Size and location of colluvial landslides in a steep forested landscape. In *Proceedings of the International Symposium on Erosion and Sedimentation in the Pacific Rim*; 39-48.

Reneau SL, Dietrich WE, Wilson CJ, Rogers JD. 1984. Colluvial deposits and associated landslides in the northern San Francisco Bay Area, California, USA. In *4th International Symposium on Landslides*. Toronto; 425-430.

Reubens B, Poesen J, Danjon F, Geudens G, Muys B. 2007. The role of fine and coarse roots in shallow slope stability and soil erosion control with a focus on root system architecture: a review. *Trees - Structure and Function* **21**: 385-402.

Richards LA. 1931. Capillary conduction of liquids in porus mediums. *Physics* **1**: 318-333.

Richards PW, Clapham AR. 1941. Juncus effusus. *Journal of Ecology* **29**: 375-380.

Robson JD, Thomasson AJ. 1977. Soil water regimes, a study of seasonal waterlogging in English lowland soils. In (p. 57). Harpenden: Rothamsted Experimental Station.

Rodhe A, Seibert J. 1999. Wetland occurrence in relation to topography: a test of topographic indices as moisture indicators. *Agricultural and Forest Meteorology* **98-9**: 325-340.

Rodrigueziturbe I, Vogel GK, Rigon R, Entekhabi D, Castelli F, Rinaldo A. 1995. On the spatial-organisation of soil-moisture fields. *Geophysical Research Letters* **22**: 2757-2760.

Roering JJ, Kirchner JW, Sklar LS, Dietrich WE. 2001. Hillslope evolution by nonlinear creep and landsliding: An experimental study. *Geology* **29**: 143-146.

Rogers NW, Selby MJ. 1980. Mechanisms of shallow transitional landsliding buring summer rainstorms - North Island, New-Zealand. *Geografiska Annaler Series a-Physical Geography* **62**: 11-21.

Rosser NJ, Petley DN, Lim M, Dunning SA, Allison RJ. 2005. Terrestrial laser scanning for monitoring the process of hard rock coastal cliff erosion. *Quarterly Journal of Engineering Geology and Hydrogeology* **38**: 363-375.

Rowe JS. 1956. Uses of understory plant species in forestry. *Ecology* **37**.

Rowe PW. 1962. The stress-dilatancy relation for static equilibrium of an assembly of particles in contact. *Proceedings of the Royal Society London* **A269**: 500-527.

Rowe RK. 2001. *Geotechnical and geoenvironmental engineering handbook*. Springer.

Sarma SK. 1973. Stability analysis of embankments and slopes. *Geotechnique* **23**: 423-433.

Sasaki Y. 1991. Fractals of slope failure number-size distribution. *Journal of the Japanese Society of Engineering Geology* **32**: 1-11.

Saulnier GM, Beven K, Obled C. 1997. Digital elevation analysis for distributed hydrological modeling: Reducing scale dependence in effective hydraulic conductivity values. *Water Resources Research* **33**: 2097-2101.

Saulnier GM, Beven K, Obled C. 1997. Including spatially variable effective soil depths in TOPMODEL. *Journal of Hydrology* **202**: 158-172.

Savage WZ, Godt JW, Baum RL. 2003. A model for spatially and temporally distributed shallow landslide initiation by rainfall infiltration. *Debris-Flow Hazards Mitigation: Mechanics, Prediction & Assessment* **1-2**: 179-187.

Schenk HJ, Jackson RB. 2005. Mapping the global distribution of deep roots in relation to climate and soil characteristics. *Geoderma* **126**: 129-140.

Schietchtl HM. 1980. *Bioengineering for Land Reclamation and Conservation*. University of Alberta Press: Edmonton, Alberta, Canada.

Schlosser F, Long N. 1972. Comportement de la terre armee dans les ouvrages de soutenement. In *European Conference on Soil Mechanics and Foundation Engineering*. Madrid; 299-306.

Schmidt KM, Roering JJ, Stock JD, Dietrich WE, Montgomery DR, Schaub T. 2001. The variability of root cohesion as an influence on shallow landslide susceptibility in the Oregon Coast Range. *Canadian Geotechnical Journal* **38**: 995-1024.

Schroeder WL, Alto JV. 1983. Soil properties for slope stability analysis - Oregan and Washington coastal mountains. *Forest Science* **29**: 823-833.

Schroeder WL, Swanston DN. 1987. Application of geotechnical data to resource planning in sourtheast Alaska. In, *General Technical Report* (p. 22). Portland, Oregon: Department of Agriculture, Forest Service, Pacific Northwest Research Station.

Seed RB, Mitchell JK, Seed HB. 1990. Kettleman-Hills Waste Landfill Slope Failure .2. Stability Analyses. *Journal of Geotechnical Engineering-Asce* **116**: 669-690.

Seibert J, Bishop KH, Nyberg L. 1997. A test of TOPMODEL's ability to predict spatially distributed groundwater levels. *Hydrological Processes* **11**: 1131-1144.

Selby MJ. 1993. *Hillslope materials and processes* Oxford University Press: New York.

Shand P, Haria AH, Neal C, Griffiths KJ, Gooddy DC, Dixon AJ, Hill T, Buckley DK, Cunningham JE. 2005. Hydrochemical heterogeneity in an upland catchment: further characterisation of the spatial, temporal and depth variations in soils, streams and groundwaters of the Plynlimon forested catchment, Wales. *Hydrology and Earth System Sciences* **9**: 621-644.

Shapiro SS, Wilk MB. 1965. An analysis of variance test for normality (complete samples). *Biometrika* **52**: 591-611.

Shewbridge S. 1985. The influence of reinforcement properties on the strength and deformation characteristics of reinforced sand. Berkeley, California: University of California.

Shields FD, Gray DH. 1992. Effects of Woody Vegetation on Sandy Levee Integrity. *Water Resources Bulletin* **28**: 917-931.

Siddiqi FH. 1984. Strength evaluation of cohesionless soils with oversize particles (p. 170). Davis: University of California.

Sidle RC. 1984. Relative importance of factors influencing landsliding in coastal Alaska. In *21st Annual Engineering Geology and Soils Engineering Symposium*. Moscow, Idaho: University of Idaho.

Sidle RC, Swanston DN. 1982. Analysis of a small debris-slide in coastal Alaska. *Canadian Geotechnical Journal* **19**: 167-174.

Simoni S, Zanotti G, Bertoldi G, Rigon R. 2008. Modelling the probability of occurence of shallow landslides and channelized debris flows using GEOtop-FS. *Hydrological Processes* **22**: 2248-2263.

Singh VP. 1996. *Kinematic Wave Modelling in Water Resources: Surface Water Hydrology*. Wiley: New York.

Sithole G. 2001. Filtering of laser altimetry data using a slope adaptive filter. In *Proceedings of the ISPRS workshop: land surface mapping and characterization using laser altimetry*. Annapolis, MD, USA; 203-210.

Sithole G, Vosselman G. 2005. Filtering of airborne laser scanneer data based on segmented point clouds. In *Proceedings of the ISPRS workshop: laser scanning 2005.* Enschede, Netherlands.

Skempton AW. 1985. Residual Strength of Clays in Landslides, Folded Strata and the Laboratory. *Geotechnique* **35**: 3-18.

Skempton AW, Hutchinson JN. 1969. Stability of natural slopes and embankment foundations. In *7th International Conferenced on Soil Mechanics and Foundation Engineering*. Mexico City.

Smith MJ, Rose J, Booth S. 2006. Geomorphological mapping of glacial landforms from remotely sensed data: An evaluation of the principal data sources and an assessment of their quality. *Geomorphology* **76**: 148-165.

Soethe N, Lehmann J, Engels C. 2006. Root morphology and anchorage of six native tree species from a tropical montane forest and an elfin forest in Ecuador. *Plant and Soil* **279**: 173-185.

Soethe N, Lehmann J, Engels C. 2006. The vertical pattern of rooting and nutrient uptake at different altitudes of a south ecuadorian montane forest. *Plant and Soil* **286**: 287-299.

Soulsby C. 1992. Hydrological Controls on Acid Runoff Generation in an Afforested Headwater Catchment at Llyn Brianne, Mid-Wales. *Journal of Hydrology* **138**: 431-448.

Spencer E. 1967. A method of analysis of the stability of embankments assuming parallel interslice forces. *Geotechnique* **17**: 11-26.

Stark CP, Hovius N. 2001. The characterization of landslide size distributions. *Geophysical Research Letters* **28**: 1091-1094.

Stark TD, Eid HT. 1998. Performance of three-dimensional slope stability methods in practice. *Journal of Geotechnical and Geoenvironmental Engineering* **124**: 1049-1060.

Statham I. 1976. Debris flows on vegetated screes in the Black Mountains, Carmarthenshire. *Earth surface Processes* **1**: 173-180.

Stokes A, Fitter AH, Coutts MP. 1995. Responses of Young Trees to Wind and Shading - Effects on Root Architecture. *Journal of Experimental Botany* **46**: 1139-1146.

Styczen ME, Morgan RPC. 1995. Engineering properties of vegetation. In *Slope stabilisation and erosion control: a bioengineering approach*, Morgan RPC, Rickson RJ (eds). E&FN Spon: London.

Sugai T. 1994. Rock control on the magnitude–frequency distribution of landslides. *Transactions of the Japanese Geomorphological Union* **15**: 233-251.

Sugawara M. 1995. Tank Model. In *Computer Models of Watershed Hydrology*, Singh VP (ed). Water Resources Publications: Colorado.

Sulebak JR, Tallaksen LM, Erichsen B. 2000. Estimation of areal soil moisture by use of terrain data. *Geografiska Annaler Series a-Physical Geography* **82A**: 89-105.

Sutherland DG, Ball MH, Hilton SJ, Lisle TE. 2002. Evolution of a landslide-induced sediment wave in the Navarro River, California. *Geological Society of America Bulletin* **114**: 1036-1048.

Tanaka T. 1982. The role of subsurface water exfiltration in soil erosion processes. *International Association of Hydrological Sciences* **Pub. No. 137**: 73-80.

Tarboton DG. 1997. A new method for the determination of flow directions and upslope areas in grid digital elevation models. *Water Resources Research* **33**: 309-319.

Tarn A, Wilson L. 1994. *Lake District National Park - Facts and Figures.* Lake District National Park Authority.

Tarolli P, Tarboton DG. 2006. A new method for determination of most likely landslide initiation points and the evaluation of digital terrain model scale in terrain stability mapping. *Hydrology and Earth System Sciences* **10**: 663-677.

Taylor DW. 1948. *Fundamentals of Soil Mechanics.* Wiley: New York.

Taylor J. 1997. *Introduction to error analysis, the study of uncertainties in physical measurements.* University Science Books: New York.

Terwilliger VJ, Waldron LJ. 1991. Effects of Root Reinforcement on Soil-Slip Patterns in the Transverse Ranges of Southern California. *Geological Society of America Bulletin* **103**: 775-785.

Tetzlaff D, McDonnell JJ, Uhlenbrook S, McGuire KJ, Bogaart PW, Naef F, Baird AJ, Dunn SM, Soulsby C. 2008. Conceptualizing catchment processes: simply too complex? *Hydrological Processes* **22**: 1727-1730.

Thompson JC, Moore RD. 1996. Relations between topography and water table depth in a shallow forest soil. *Hydrological Processes* **10**: 1513-1525.

Thompson K, Grime JP. 1979. Seasonal variation in the seed banks of herbaceous species in ten contrasting habitats. *Journal of Ecology* **67**: 893-921.

Tobias S. 1994. Shear strength of the soil-root system: *in situ* shear tests. In *Conserving Soil Resources: European Perspectives*, Rickson RJ (ed). CAB International; 405-412.

Tobias S. 1995. Shear strength of the soil root bond system. In *Vegetation and Slopes - Stabilisation, Protection and Ecology*, Barker DH (ed); 280-286.

Tochiki S. 1985. The investigation of decomposed granite slopes. In *International Symposium on Erosion, Debris Flow and Disaster Prevention*, Takei A (ed). Tsukuba, Japan: The Erosion Control Engineering Society, Tokyo; 329-333.

Tóvári D, Pfeifer N. 2005. Segmentation based robust interpolation - a new approach to laser data filtering. In *Proceedings of the ISPRS workshop: laser scanning 2005.* Enschede, Netherlands; 79-84.

Tromp-van Meerveld HJ, McDonnell JJ. 2006. On the interrelations between topography, soil depth, soil moisture, transpiration rates and species distribution at the hillslope scale. *Advances in Water Resources* **29**: 293-310.

Tromp-van Meerveld HJ, McDonnell JJ. 2006. Threshold relations in subsurface stormflow: 2. The fill and spill hypothesis. *Water Resources Research* **42**.

Tsuboyama Y, Sidle RC, Noguchi S, Hosoda I. 1994. Flow and Solute Transport through the Soil Matrix and Macropores of a Hillslope Segment. *Water Resources Research* **30**: 879-890.

Tsukamoto Y, Kusakabe O. 1984. Vegetative influenceson debris slide occurrences on steep slopes in Japan. In *Symposium on the Effect of Forest Land Use on Erosion and Slope Stability*, O'Loughlin CL, Pearce AJ (eds). Honolulu: Environment and Policy Institute, University of Hawaii.

Tucker GE, Bras RL. 1998. Hillslope processes, drainage density, and landscape morphology. *Water Resources Research* **34**: 2751-2764.

Tufnell L. 1997. Northwest England and the Isle of Man. In *Regional Climates of the British Isles*, Wheeler D, Mays J (eds). Routledge: London.

Turmanina VI. 1965. On the strength of tree roots. *Bulletin Moscow Society of Naturalists* **70**: 36-45.

Uchida T, Kosugi K, Mizuyama T. 2001. Effects of pipeflow on hydrological process and its relation to landslide: a review of pipeflow studies in forested headwater catchments. *Hydrological Processes* **15**: 2151-2174.

Uchida T, McDonnell JJ, Asano Y. 2006. Functional intercomparison of hillslopes and small catchments by examining water source, flowpath and mean residence time. *Journal of Hydrology* **327**: 627-642.

UNEP/OCHA. 2004. *Hurricanes Ivan and Jeanne in Haiti, Granada and the Dominican Republic - A rapid environmental impact assessment.* http://ochaonline.un.org/GetBin, accessed: 26 January.

USGS. 2008. *Landslide Hazards Program Page.* http://landslides.usgs.gov/, accessed: 29/08/08.

van Beek LPH, Wint J, Cammeraat LH, Edwards JP. 2005. Observation and simulation of root reinforcement on abandoned Mediterranean slopes. *Plant and Soil* **278**: 55-74.

van Genuchen M. 1980. A closed-form equation for predicting the hydraulic conductivity of unsaturated soils. *Soil Science Society of America Journal* **44**: 892-898.

van Overmeeren RA. 1998. Radar facies of unconsolidated sediments in The Netherlands: A radar stratigraphy interpretation method for hydrogeology. *Journal of Applied Geophysics* **40**: 1-18.

Vanacker V, Vanderschaeghe M, Govers G, Willems E, Poesen J, Deckers J, De Bievre B. 2003. Linking hydrological, infinite slope stability and land-use change models through GIS for assessing the impact of deforestation on slope stability in high Andean watersheds *Geomorphology* **52**: 299-315.

Varnes DJ. 1978. Slope movement types and processes. In L. SR, J. KR (eds), *Landslides, analysis and control. Transportation Research Board Special Report* (pp. 11-33): National Academy of Sciences.

Veneman PLM, Edil TB. 1988. Micromorphological aspects of the vane shear test. In *Vane Shear Strength Testing in Soils: Field and Laboratory Studies ASTM STP 1014*, Richards AF (ed). American Society for Testing and Materials: Philadelphia; 182-190.

Vertessy RA, Elsenbeer H. 1999. Distributed modeling of storm flow generation in an Amazonian rain forest catchment: Effects of model parameterization. *Water Resources Research* **35**: 2173-2187.

Vertessy RA, Hatton TJ, O'Shaughnessy PJ, Jayasuriya MDA. 1993. Predicting water yield from a Mountain Ash forest catchment using a terrain analysis based catchment model. *Journal of Hydrology* **150**: 665-700.

Vidal H. 1969. The Principle of Reinforced Earth. *Highway Research Record*: 1-16.

Vosselman G. 2000. Slope based filtering of laser altimetry data. *IAPRS* **XXXIII**: 935-942.

Wagner W, Ullrich A, Melzer T, Briese C, Kraus K. 2004. From single-pulse to full-waveform airborne laser scanners: potential and practical challenges. In, *Proceedings of ISPRS Commission III symposium.* Istanbul, Turkey.

Waldron LJ. 1977. Shear Resistance of Root-Permeated Homogeneous and Stratified Soil. *Soil Science Society of America Journal* **41**: 843-849.

Waldron LJ, Dakessian S. 1981. Soil Reinforcement by Roots - Calculation of Increased Soil Shear Resistance from Root Properties. *Soil Science* **132**: 427-435.

Waldron LJ, Dakessian S, Nemson JA. 1983. Shear Resistance Enhancement of 1.22-Meter Diameter Soil Cross-Sections by Pine and Alfalfa Roots. *Soil Science Society of America Journal* **47**: 9-14.

Walker JP, Willgoose GR. 1999. On the effect of digital elevation model accuracy on hydrology and geomorphology. *Water Resources Research* **35**: 2259-2268.

Walker JP, Willgoose GR. 2006. A comparative study of Australian cartometric and photogrammetric digital elevation model accuracy. *Photogrammetric Engineering and Remote Sensing* **72**: 771-779.

Wang G. 2000. Use of understory vegetation in classifying soil moisture and nutrient regimes. *Forest Ecology and Management* **129**: 93-100.

Wang Y, Mercer B, Tao VC, Sharma J, Crawford S. 2001. Automatic generation of bald earth digital elevation models from digital surface models created using airborne IfSAR. In *Proceedings of ASPRS 2001*. Washington DC, USA.

Warburton J, Milledge DG, Johnson RM. 2008. Assessment of shallow landslide activity following the January 2005 storm, Northern Cumbria. *Proceedings of the Cumberland Geological Society* **In Press**.

Ward TJ. 1981. Use of a mathematical model for estimating potential landslide sites in steep forested drainage basins. *International Association of Hydrological Sciences* **Publication 132**: 21-41.

Wehr A, Lohr U. 1999. Airborne laser scanning - an introduction and overview. *Isprs Journal of Photogrammetry and Remote Sensing* **54**: 68-82.

Weiler M, Naef F. 2003. Simulating surface and subsurface initiation of macropore flow. *Journal of Hydrology* **273**: 139-154.

Wells SG, Harvey AM. 1987. Sedimentologic and geomorphic variations in storm-generated alluvial fans, Howgill Fells, Northwest England. *Geological Society of America Bulletin* **98**: 182-198.

Westaway RM, Lane SN, Hicks DM. 2003. Remote survey of large-scale braided, gravel-bed rivers using digital photogrammetry and image analysis. *International Journal of Remote Sensing* **24**: 795-815.

Western AW, Grayson RB, Bloschl G, Willgoose GR, McMahon TA. 1999. Observed spatial organization of soil moisture and its relation to terrain indices. *Water Resources Research* **35**: 797-810.

Whipkey RZ. 1965. Subsurface stormflow from forested slopes. *International Association of Hydrological Sciences* **Bulletin 10**: 74-85.

Whitehouse IE, Griffiths GA. 1983. Frequency and hazard of large rock avalanches in the central southern Alps, New-Zealand. *Geology* **11**: 331-334.

Wilson CJ, Dietrich WE. 1987. The contribution of bedrock groundwater flow to storm runoff and high pore pressure development in hollows. In *International Symposium on Erosion and Sedimentation in the Pacific Rim.* Corvallis, Oregon: International Association of Hydrological Sciences Bulletin; 49-59.

Wilson CJ, Reneau SL, Dietrich WE. 1989. Hydrologic and erosional processes in hollows, Lone Tree Creek, Marin County, California. In *Landslides in Central California, Field Trip Guidebook T381*, Brown WM (ed). American Geophysical Union; 75-90.

Wilson RC, Wieczorek GF. 1995. Rainfall thresholds for the initiation of debris flow at La Honda, California. *Environmental & Engineering Geoscience* **1**: 11-27.

Winchester V, Chaujar RK. 2002. Lichenometric dating of slope movements, Nant Ffrancon, North Wales. *Geomorphology* **47**: 61-74.

Wise S. 2000. Assessing the quality for hydrological applications of digital elevation models derived from contours. *Hydrological Processes* **14**: 1909-1929.

Wolock DM, Price CV. 1994. Effects of digital evenation model map scale and data resolution on a topography-based watershed model. *Water Resources Research* **30**: 3041-3052.

Woods RA, Rowe LK. 1996. The changing spatial variability of subsurface flow across a hillside. *Journal of Hydrology (NZ)* **35**: 51-86.

Wu S, Li J, Huang GH. 2007. Modeling the effects of elevation data resolution on the performance of topography-based watershed runoff simulation. *Environmental Modelling & Software* **22**: 1250-1260.

Wu TH. 1976. Investigation of Landslides on Prince of Wales Island. In (p. 94). Columbus, Ohio: Civil Engineering Department, Ohio State University.

Wu TH. 1984. Effect of vegetation on slope stability. In, *Transportation Research Record* (pp. 37-46): Transportation Research Board.

Wu TH. 1984. Soil movements on permafrost slopes near Fairbanks, Alaska. *Canadian Geotechnical Journal* **21**: 699-709.

Wu TH, Beal PE, Lan CC. 1988. Insitu Shear Test of Soil-Root Systems. *Journal of Geotechnical Engineering-Asce* **114**: 1376-1394.

Wu TH, Bettadapura DP, Beal PE. 1988. A Statistical-Model of Root Geometry. *Forest Science* **34**: 980-997.

Wu TH, McKinnnell III WP, Swanston DN. 1979. Strength of tree roots and landslides on Prince of Wales Island, Alaska. *Canadian Geotechnical Journal* **16**: 19-33.

Wu TH, McOmber RM, Erb RT, Beal PE. 1988. Study of Soil-Root Interaction. *Journal of Geotechnical Engineering-Asce* **114**: 1351-1375.

Wu TH, Watson A. 1998. In situ shear tests of soil blocks with roots. *Canadian Geotechnical Journal* **35**: 579-590.

Wu WM, Sidle RC. 1995. A Diatributed Slope Stability Model for Steep Forested Basins. *Water Resources Research* **31**: 2097-2110.

Xie M, Esaki T, Zhou G, Mitani Y. 2003. Three dimensional stability evaluation of landslides and a sliding process simulation using a new geographic information systems component. *Environmental Geology* **43**: 503-512.

Xie MW, Esaki T, Cai MF. 2004. A GIS-based method for locating the critical 3D slip surface in a slope. *Computers and Geotechnics* **31**: 267-277.

Xie MW, Esaki T, Cai MF. 2006. GIS-based implementation of three-dimensional limit equilibrium approach of slope stability. *Journal of Geotechnical and Geoenvironmental Engineering* **132**: 656-660.

Xie MW, Esaki T, Qiu C, Wang CX. 2006. Geographical information system-based computational implementation and application of spatial three-dimensional slope stability analysis. *Computers and Geotechnics* **33**: 260-274.

Xie MW, Esaki T, Zhou GY. 2004. GIS-based probabilistic mapping of landslide hazard using a three-dimensional deterministic model. *Natural Hazards* **33**: 265-282.

Xing Z. 1988. Three-dimensional stability analysis of concave slopes in plan view. *Journal of Geotechnical Engineering* **114**: 658-671.

Yokoi Y, Carr JR, Watters RJ. 1995. Fractal character of landslides. *Environmental & Engineering Geoscience* **1**: 75-81.

Zaitchik BF, van Es HM, Sullivan PJ. 2003. Modeling Slope Stability in Honduras: Parameter Sensitivity and Scale of Aggregation. *Soil Sci Soc Am J* **67**: 268-278.

Zanutta A, Baldi P, Bitelli G, Cardinali M, Carrara A. 2006. Qualitative and quantitative photogrammetric techniques for multi-temporal landslide analysis. *Annals of Geophysics* **49**: 1067-1080.

Zevenbergen LW, Thorne CR. 1987. Quantitative-Analysis of Land Surface-Topography. *Earth Surface Processes and Landforms* **12**: 47-56.

Zhang WH, Montgomery DR. 1994. Digital elevation model grid size, landscape representaion , and hydrologic simulations. *Water Resources Research* **30**: 1019-1028.

Zhang Y, Tao VC, Mercer B. 2004. An initial study on automatic reconstruction of ground DEMs from airborne IfSAR DSMs. *Photogrammetric Engineering and Remote Sensing* **70**: 427-438.

Zhou Y, Watts D, Li Y, Cheng X. 1998. A case study of effect of lateral roots of Pinus yunnanensis on shallow soil reinforcement. *Forest Ecology and Management* **103**: 107-120.

Zhu JJ, Ding XL, Chen YQ. 2001. Dynamic model for landsliding monitoring under rigid body assumption. *Transactions of Nonferrous Metals Society of China* **11**: 301-306.

Zhu TX. 1997. Deep-seated, complex tunnel systems - a hydrological study in a semi-arid catchment, Loess Plateau, China. *Geomorphology* **20**: 255-267.

Ziadat FM. 2005. Analyzing digital terrain attributes to predict soil attributes for a relatively large area. *Soil Science Society of America Journal* **69**: 1590-1599.

Ziemer RR. 1981. Roots and the stability of forested slopes. In, *Erosion and Sediment Transport in Pacific Rim Steeplands* (pp. 343-361). London: International Association of Hydrological Sciences.

Ziemer RR, Swanston DN. 1977. Root Strength Changes oafter Logging in Southeast Alaska. In, *Pacific Northwest Forest and Range Experiment Station - USFS* (p. 9). Portland, Oregon.

Zinko U, Seibert J, Dynesius M, Nilsson C. 2005. Plant species numbers predicted by a topography-based groundwater flow index. *Ecosystems* **8**: 430-441.

10. Appendix 1: Earth Pressure Theory

10.1. Scope of This Appendix

In this appendix I briefly introduce earth pressure theory in general (Section 10.2) before going on to describe the empirical or mathematical basis behind each of the coefficients. I start with 'at rest' earth pressure (Section 10.3) then deal with active and passive pressure together (Section 10.4) explaining first the available theories then deriving those that are most suitable for my application, and that are used in my Finite Slope stability model.

10.2. Background

Theories to quantify lateral earth pressure originate from the need to assess the stability of retaining walls and are commonly applied to the design of ground engineering structures such as walls, basements, tunnels and foundations. Lateral earth pressure is assumed to be proportional to the vertical stress at any point in the soil profile. It is represented by the lateral earth pressure coefficient (K), which defines the ratio of lateral to vertical stresses ($K=\sigma_x/\sigma_z$). Lateral earth pressures can depend on the soil properties and the stress history of the soil and are highly strain dependent. They are treated in three categories depending on the degree and direction of strain that they have experienced. 'At rest' earth pressure represents the lateral pressure exerted by the soil on a plane where there is either no strain, or the strain is limited and is orientated parallel to the plane. 'Active' pressure results from the force that earth exerts on a retaining structure or soil block as it moves away from the soil. Triaxial tests suggest that a strain of only 0.5% is required to develop active stresses and to move from 'at rest' to active conditions (Lambe and Whitman, 1969). 'Passive' pressure results from the force that a structure or soil block exerts on the soil when the

structure moves towards the soil. The normal stress on the landslide sides can be represented using either 'at rest' (Stark and Eid, 1998) or active (Albataineh, 2006) earth pressure conditions to calculate the frictional resistance on these planes. Active pressure conditions can be assumed at the head to estimate the force applied by the soil upslope of the block and the passive pressure required for failure of the material downslope of the block can be used to establish the additional strength supplied by the toe.

The theories use the concept of plastic collapse to establish the failure condition of the 'retained' soil mass. A soil mass is said to be in a state of plastic equilibrium if the shear stress at every point within the mass reaches the value represented by point Y' in Figure 10-1. Plastic collapse occurs after the state of plastic equilibrium has been reached in part of a soil mass so that it slips relative to the rest of the mass.

Figure 10-1: An idealised plastic stress strain relationship (from Craig, 2004)

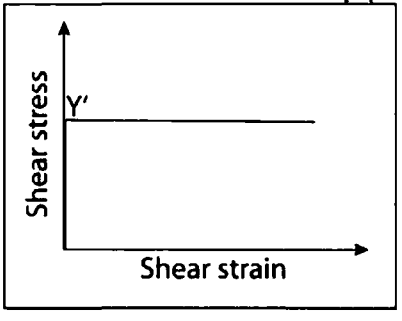

The limit theorems of plasticity can be used to calculate lower and upper bounds to the true collapse load. The upper bound theorem, which uses a rigid perfectly plastic soil model, states that the internal energy dissipated by any kinematically admissible velocity field can be equated to the work done by external loads, and so enables a strict upper bound on the actual solution to be deduced. The lowest possible upper bound solution is sought by trying various possible failure surfaces. A kinematically admissible velocity field is the one that satisfies compatibility, a plastic flow rule and the velocity boundary conditions. The lower bound theorem, which also uses a rigid perfectly plastic soil model, assumes that stress fields are in equilibrium with surface tractions and body forces and do not violate the yield criterion anywhere in the soil mass. The application of the lower bound theorem will provide a lower bound estimation of the true solution. By using the two theorems, the range in which true solution

falls can be found. As with 'at rest' conditions, active and passive lateral stresses are proportional to vertical stress. They can be calculated using active (K_a) or passive (K_p) earth pressure coefficients.

10.3. 'At Rest' Earth Pressure Theory

The coefficient of 'at rest' earth pressure (K_o) depends on the amount of frictional resistance mobilised at contact points between particles. For some soils K_o can be predicted by a theoretical equation based upon the study of an idealized packing of elastic spheres. However, it depends intimately on the stress history of the soil and observations are generally better matched by empirical formulae. If we assume that the soils are normally consolidated, granular (cohesionless) and have an Over-Consolidation Ratio (*OCR*) of unity, (i.e. where the former maximum effective overburden stress is equal to the present effective overburden stress), then we can use Jaky's empirical relation for the 'at rest' or no lateral yield condition (Jacky, 1944; in Lambe and Whitman, 1969):

Equation 10-1

$$K_0 = 1 - \sin\varphi$$

10.4. Active and Passive Earth Pressure Theories

Three theories are commonly used to represent active and passive earth pressure in geotechnical engineering: 1) Coulomb Theory (Coulomb, 1776), an upper bound theorem, which treats the problem in terms of forces; 2) Rankine Theory (Rankine, 1857), a lower bound theorem, which treats the problem in terms of stresses; and 3) Logarithmic Spiral Theory (Caquot and Kerisel, 1948; Kerisel and Absi, 1990). The latter provides more accurate estimates of passive pressures where the wall has a high friction angle relative to the soil, but is less widely used because of its complexity. These reasons also make it unsuitable for characterising the forces acting on a soil block in my simplified stability analysis. All earth pressure theories make several common assumptions: 1) strains in the longitudinal direction of the structure are assumed to be zero (plane strain); 2) the stress-strain behaviour of the soil can be represented by the rigid-perfectly plastic idealisation in which both yielding and shear failure occur at the same state of stress, unrestricted plastic flow takes place at this stress level; and 3) the soil is homogeneous and isotropic. In the

following sections I will describe and derive Rankine's (Section 10.4.1) and Coulomb's (10.4.2) earth pressure theories.

10.4.1. Rankine's Theory

Rankine's theory considers the state of stress in a soil mass when the condition of plastic equilibrium has been reached, i.e. when shear failure is on the point of occurring throughout the mass. The theory satisfies the conditions of a lower bound plasticity solution. The Mohr circle representing the state of stress at failure in a horizontal 2D element is shown in Figure 10-2. Shear failure occurs along a plane at an angle of $45°+\varphi/2$ to the major principal plane (σ_1). If the soil mass as a whole is stressed such that the principal stresses at every point are in the same directions then, theoretically, there will be a network of failure planes (known as a slip line field) equally inclined to the principal planes (σ_1 σ_3), as shown in Figure 10-2.

Figure 10-2: The Mohr circle for a state of plastic equilibrium (from Craig, 2004).

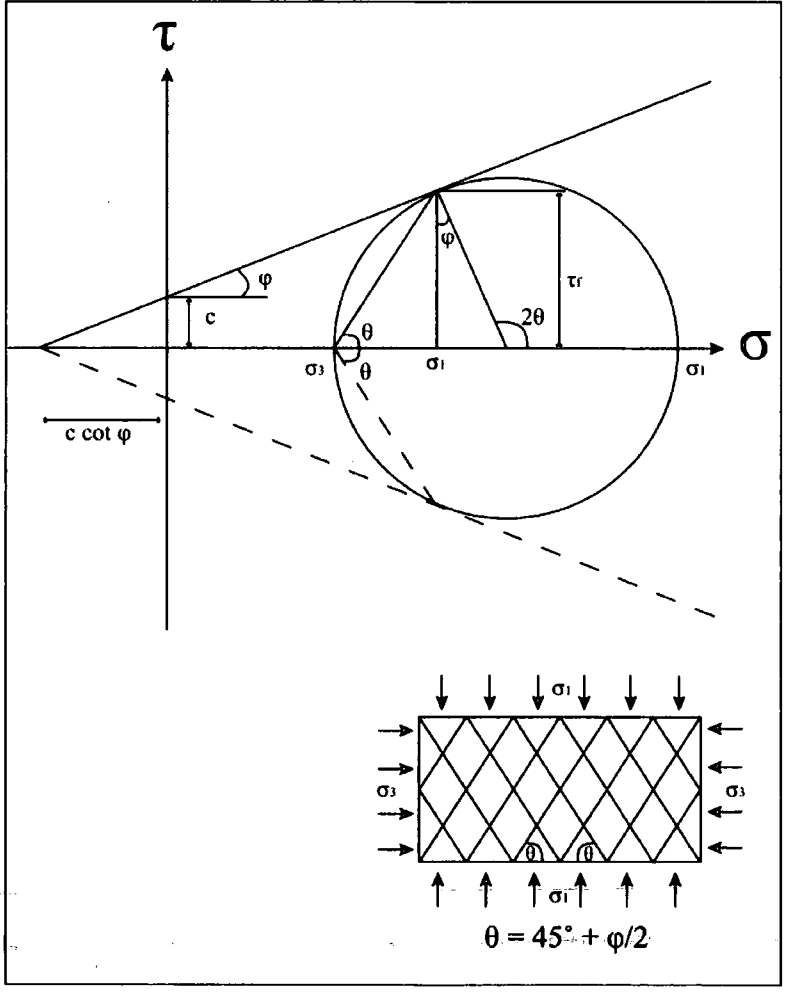

If a soil element at depth z is subjected to a vertical stress σ_z and a horizontal stress σ_x then these are principal stresses for a horizontal surface because no shear stresses exist on the horizontal or vertical planes. If there is a movement of the wall away from the soil then σ_x decreases as a function of the lateral strain in the soil as it dilates and expands outwards. If the expansion is large enough, σ_x decreases to a minimum value when plastic equilibrium is reached. In this case, σ_x is the minor principal stress (σ_3) and σ_z the major principal stress (σ_1). The stress σ_1 ($=\sigma_z$) is the overburden pressure at depth z and is a fixed value for any depth. The value of σ_3 ($=\sigma_x$) is determined when a Mohr circle through the point representing σ_1 touches the failure envelope for the soil. The relationship between σ_1 and σ_3 when the soil reaches a state of plastic equilibrium can be derived from the Mohr circle. So that the active earth pressure coefficient is:

Equation 10-2

$$K_a = \tan^2\left(45 - \frac{\varphi}{2}\right)$$

and passive earth pressure can be represented as:

Equation 10-3

$$K_p = \tan^2\left(45 + \frac{\varphi}{2}\right)$$

Rankine's theory can also be applied to cases in which the soil surface slopes at a constant angle (β). In this case we assume that active and passive pressures act in a direction parallel to the sloping surface (Figure 10-3). These stresses are not principal stresses since they are not normal to their respective planes (i.e. there are shear components).

For the Active case the vertical stress σ_z at depth z on a plane inclined at angle β to the horizontal is represented by the distance OA in Figure 10-3. If lateral expansion of the soil is sufficient to induce plastic equilibrium the Mohr circle representing the sate of stress in the element must pass through point A and touch the failure envelope for the soil. The active pressure is represented by OB (numerically equal to OB') on the diagram. The relationship between p_a and σ_z giving the active pressure coefficient can be derived from the diagram geometry:

Equation 10-4

$$Ka = \frac{p_a}{\sigma_z} = \frac{OB}{OA} = \frac{OB'}{OA} = \frac{OD - AD}{OD + AD}$$

Equation 10-5

$$OD = OC\cos\beta$$

Equation 10-6

$$AD = \sqrt{(OC^2 \sin^2\phi - OC^2 \sin^2\beta}$$

Therefore, substituting Equation 10-5 and Equation 10-6 into Equation 10-4 Rankine's active earth pressure coefficient for sloping cohesionless soils is:

Equation 10-7

$$K_a = \frac{\cos\beta - \sqrt{(\cos^2\beta - \cos^2\phi)}}{\cos\beta + \sqrt{(\cos^2\beta - \cos^2\phi)}}$$

Figure 10-3: The Mohr circle for active and passive states with a sloping surface (from Craig, 2004).

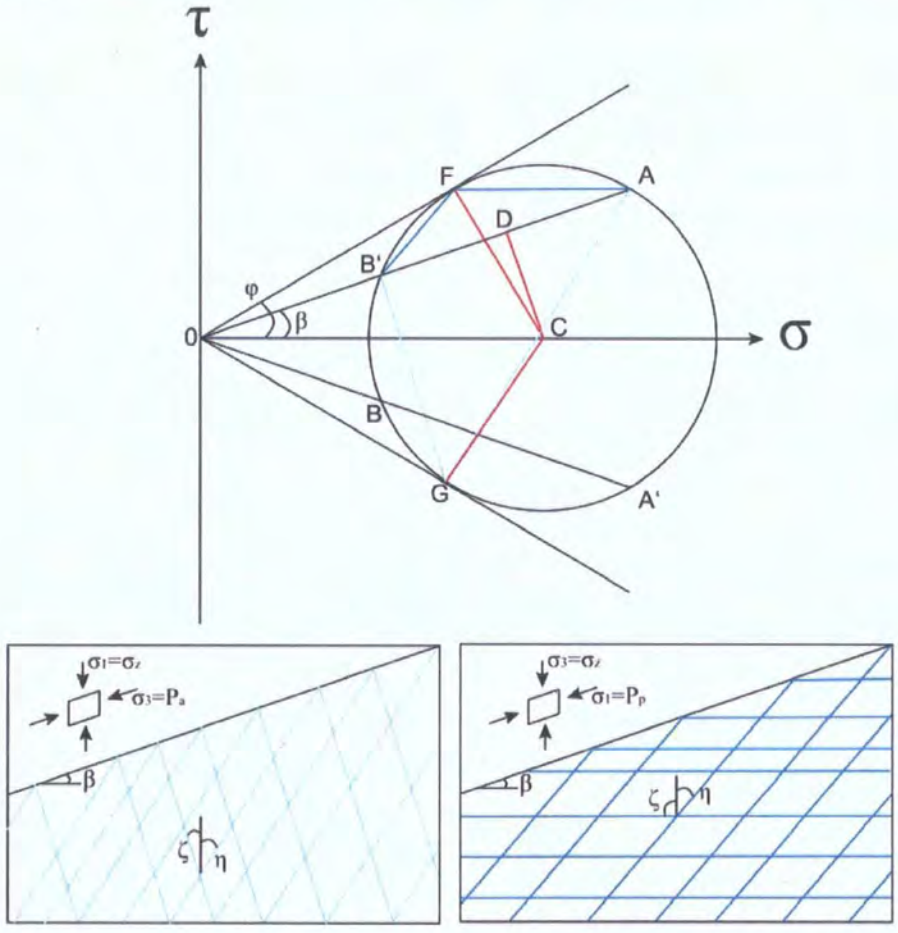

In the passive case the vertical stress (σ_z) is represented by the distance OB' in Figure 10-3. The Mohr circle representing the state of stress in the element, after a state of plastic equilibrium has been induced by lateral compression of the soil, must pass through B' and touch the failure envelope. Passive pressure

(p_p) is then represented by OA' (numerically equal to OA) and the passive pressure coefficient is:

Equation 10-8

$$K_p = \frac{p_p}{\sigma_z} = \frac{OA'}{OB'} = \frac{OA}{OB'} = \frac{OD + AD}{OD - AD}$$

Using the same diagram geometry as above:

Equation 10-9

$$K_p = \frac{\cos\beta + \sqrt{(\cos^2\beta - \cos^2\phi}}{\cos\beta - \sqrt{(\cos^2\beta - \cos^2\phi}}$$

The directions of the two sets of failure planes can be obtained from Figure 10-3. In the active case the coordinates of point A represent the state of stress on a plane inclined at angle β to the horizontal, therefore point B' is the origin of planes. A line drawn from the origin of planes intersects the circumference of the circle at a point whose coordinates represent the state of stress on a plane parallel to that line. The coordinates of point B represent the state of stress on a vertical plane. The failure planes in Figure 10-3 are parallel to B'F and B'G (F and G lying on the failure envelope). In the passive case, the coordinates of point B' represent the state of stress on a plane inclined at angle β to the horizontal, therefore point A is the origin of planes: the state of stress on a vertical plane is represented by the coordinates of point A' and the failure planes are parallel to AF and AG.

In the active case the angle between the sets of shear planes is equal to $90° - \varphi$ (see Figure 10-3). According to Huntington (1957) the angle (η) between the vertical and the shear planes inclined upward to the right is:

Equation 10-10

$$\eta = \frac{1}{2}(90° - \phi) + \frac{1}{2}(\varepsilon - \beta)$$

where:

Equation 10-11

$$\sin\varepsilon = \frac{\sin\beta}{\sin\phi}$$

The angle (ζ) between the vertical and the shear planes inclined upwards to the left is:

Equation 10-12

$$\zeta = \frac{1}{2}(90° - \phi) - \frac{1}{2}(\varepsilon - \beta)$$

For the passive case the angle between the sets of shear planes is $90^o + \varphi$. The angle (η') between the vertical and the shear planes inclined upward to the right is:

Equation 10-13

$$\eta' = \frac{1}{2}(90° + \phi) - \frac{1}{2}(\varepsilon + \beta)$$

The angle (ζ') between the vertical and the shear planes inclined upwards to the left is:

Equation 10-14

$$\zeta' = \frac{1}{2}(90° + \phi) + \frac{1}{2}(\varepsilon + \beta)$$

When the ground is horizontal (β=0) the formulas above simplify to:

Equation 10-15

$\eta = \zeta = 45° - \frac{1}{2}\phi$ in the active case, and

Equation 10-16

$\eta' = \zeta' = 45° + \frac{1}{2}\phi$ in the passive case

From the equations above when $\beta=\varphi$: the passive failure plane orientations are η'=0 (vertical) and $\zeta'=90+\varphi$ (parallel with the ground surface); the active failure plane orientations are $\eta=\varphi$ (perpendicular to the ground surface) and ζ=0 (vertical). In this situation both K_a and K_p are equal to unity, this is incompatible with real soil behaviour. Hence use of the theory is inappropriate in such circumstances (Craig, 2004).

10.4.2. Coulomb's Theory

Coulomb's theory (1776) is generally interpreted as an upper bound plasticity solution (although analysis is based on force equilibrium and not on the work-energy balance). Failure of the soil mass above the chosen failure plane occurs as the wall moves away from (active) or into (passive) the soil. In general the theory underestimates the total active thrust and overestimates the total passive resistance giving the upper bounds of the true force required for failure. The theory is based on limit equilibrium methods, considering the failing block as a free body to determine the limiting horizontal earth pressure. Limiting horizontal pressures in extension or compression are used to determine the K_a and K_p respectively. The friction between the wall and the adjacent soil is taken into account (Mayniel, 1808) using a wall friction angle (δ). At any point on the wall

surface a shearing resistance per unit area of $\sigma \tan \delta$ will develop, where σ is the normal pressure on the wall at that point. Due to wall friction the shape of the failure surface is curved near the bottom of the wall in both the active and the passive cases. However, in Coulomb theory the failure surfaces are always assumed to be planar. In the active case the curvature is slight and the error involved in assuming a plane surface is relatively small. This is also true in the passive case for values of $\delta > \varphi/3$, but for the higher values of δ normally appropriate in practice the error becomes relatively large. For a frictionless (δ=0) vertical (α=90) wall and horizontal soil surface (β=0) Coulomb theory gives results identical to Rankine theory (see Equation 10-3 and Equation 10-4). In this case the solution is exact as the upper and lower bound results coincide. The equations have been extended to account for non-horizontal backfill and non-vertical soil-wall interface (Muller-Breslau, 1906).

For a cohesionless soil (C=0) in the active state, Figure 10-4 shows the forces acting on the soil wedge between a wall surface AB, inclined at angle α to the horizontal, and a trial failure plane BC, at angle χ to the horizontal. The soil surface AC is inclined at angle β to the horizontal.

Figure 10-4: The forces acting on a wedge of cohesionless soil in the active case (from Craig, 2004).

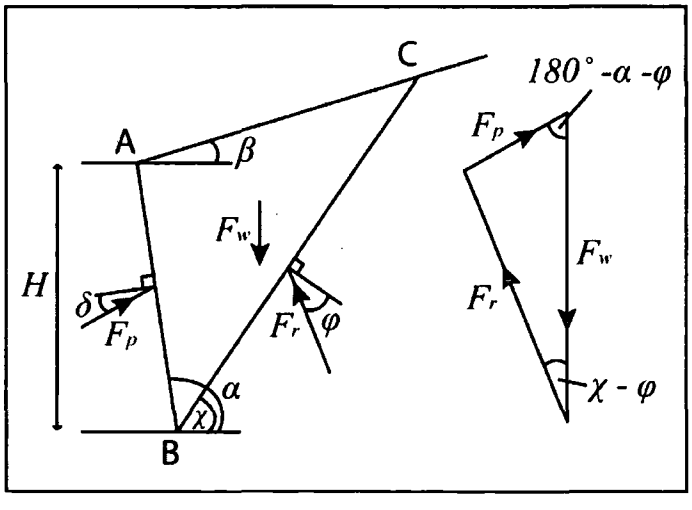

For the failure condition the soil wedge is in equilibrium under: its own weight (F_w), the reaction to the force (F_p) between the soil and the wall, and the reaction (F_r) on the failure plane. Because the soil wedge tends to move down the plane BC at failure, the reaction F_p acts at angle δ below the normal to the

wall. At failure, when the shear strength of the soil has been fully mobilized, the direction of F_r is at angle φ below the normal to the failure plane (since F_r is the resultant of the normal and shear forces on the failure plane). The directions of all three forces, and the magnitude of F_w, are known, and therefore the triangle of forces can be drawn and the magnitude of F_p determined for each trial wedge. A number of trial failure planes would have to be selected to obtain the maximum value of F_p, which would be the total active thrust on the wall. However, using the sine rule, F_p can be expressed in terms of: F_w and the angles in the triangle of forces. Then the maximum value of F_p, corresponding to a particular value of χ is given by:

Equation 10-17

$$\frac{\partial P}{\partial \chi} = 0$$

Leading to the following solution for P_a:

Equation 10-18

$$P_a = \frac{1}{2} K_a \rho g H^2$$

where:

Equation 10-19

$$K_a = \left(\frac{\frac{\sin(\alpha - \phi)}{\sin \alpha}}{\sqrt{(\sin(\alpha + \delta))} + \sqrt{\left(\frac{\sin(\phi + \delta)\sin(\phi - \beta)}{\sin(\alpha - \beta)} \right)}} \right)^2$$

In the passive case the reaction F_p acts at angle δ above the normal to the wall surface and the reaction F_r at angle φ above the normal to the failure plane. In the triangle of forces the angle between F_w and F_p is $180°-(\alpha+\delta)$ and the angle between F_w and F_r is $\chi+\varphi$. The total passive resistance, equal to the maximum value of F_p is given by:

Equation 10-20

$$P_p = \frac{1}{2} K_p \rho g H^2$$

where:

Equation 10-21

$$K_p = \left(\frac{\frac{\sin(\alpha + \phi)}{\sin \alpha}}{\sqrt{(\sin(\alpha - \delta))} + \sqrt{\left(\frac{\sin(\phi + \delta)\sin(\phi + \beta)}{\sin(\alpha - \beta)} \right)}} \right)^2$$

11. Appendix 2: Modelling Root Reinforcement

Wu (1976) developed a simple theoretical model for predicting a shear strength increase due to the presence of roots. Similar methods were developed independently by several other researchers (Waldron, 1977; Gray and Leiser, 1982). Following Gray (1974) these models represent root reinforcement as an additional effective cohesion. Waldron extended the Coulomb equation (Section 2.5) for root permeated soils from:

Equation 11.1

$$S = c + \sigma_n \tan\phi;$$

to

Equation 11.2

$$S = c + \Delta S + \sigma_n \tan\phi$$

where: S is the soil shearing resistance (kPa), σ_n is the normal stress on the failure plane, φ is soil friction angle (°) and ΔS represents the increased shear strength due to roots (kPa). To do this he assumed that all roots extend vertically across a horizontal shearing zone, and that the roots behave like laterally loaded piles, so tension is transferred to them as the soil is sheared. The tension developed in the root as the soil is sheared is resolved with a tangential component resisting shear and a normal component increasing the confining pressure on the shear plane. ΔS can be represented as:

Equation 11.3

$$\Delta S = T_r(\sin\theta + \cos\theta \tan\varphi)\left(A_r/A\right)$$

where: T_r is average tensile strength of roots per unit area of soil (kPa), calculated from root tensile strength tests; A_r/A is the root area ratio (RAR); and θ is the angle of root shear displacement. Sensitivity analysis by Wu *et al.* (1979) showed that the value of the bracketed term ($\sin\theta + \cos\theta \tan\varphi$) is insensitive to normal variations in θ and φ, ranging from 1.0 to 1.3. They chose an average value of 1.2 to replace the bracketed term so that:

Equation 11.4

$$\Delta S = 1.2T_r\left(A_r/A\right)$$

According to this model, the magnitude of root reinforcement depends only on the root density (RAR) and strength of roots in the soil.

The model assumes that: 1) a flexible elastic root extends across the shear zone (see Figure 11-1); 2) the root is anchored in the soil on either side of the shear zone by friction or adhesion and will not pull out of the soil; 3) all roots are oriented perpendicular to the slip plane; 4) the tensile strength of all roots is fully mobilised; and 5) the roots do not alter the friction angle of the soil itself.

Figure 11-1: Model of a flexible, elastic root extending vertically across a horizontal shear zone (from Docker, 2003).

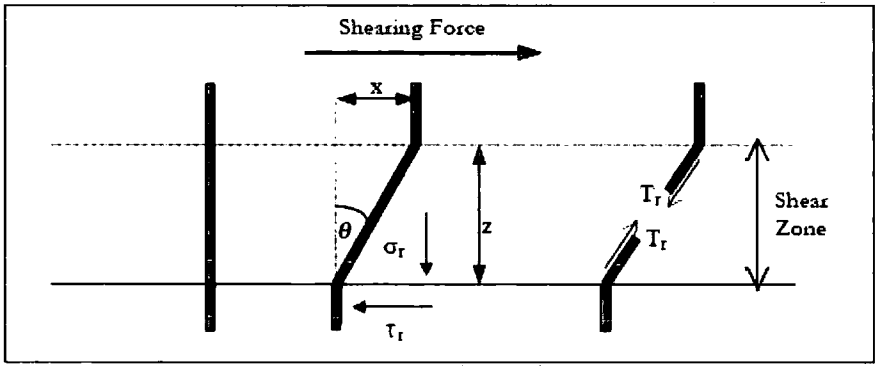

Gray and Leiser (1982) modified the model to relax the assumption of perpendicular root orientation and adjust for roots inclined with respect to the slip plane. Their results suggest that perpendicular orientation is not optimum, but is reasonably representative. Gray and Ohashi (1983) found from laboratory tests that reinforcement from perpendicular and randomly orientated fibres was comparable. This suggests that the assumption of perpendicular root orientation is reasonable if a random root orientation within the slope is assumed.

Waldron and Dakessian (1981) suggested that these models tended to overestimate root reinforcement due to the assumption that full tensile strength of the root is mobilised during soil shearing and that the roots all break simultaneously. Greenway (1987) suggested adopting a conservative 'mean' root

tensile strength value to account for this effect. Field measurements of root extraction (Riestenberg, 1994; Docker, 2003; Pollen, 2004; Pollen *et al.*, 2004) suggest that branches of a root break sequentially as roots are displaced within the soil and confirm this overestimation. Pollen and Simon (2005) identified this assumption as the limiting factor in modelling root cohesion from root density and strength information. They applied a fibre bundle model to account for the different strains at which individual roots mobilise their tensile strength. Fibre bundle models offer a mechanically reasonable approach to relaxing this assumption and appear to effectively reduce the over-prediction of root reinforcement that resulted from the previous perpendicular root models. However, these models have yet to be applied in hillslope stability modelling.

The energy approach (Ekanayake and Phillips, 1999) represents the effect of roots in maintaining shear strength at high strain. It considers the energy consumed during the shearing process by calculating the area under shear stress - displacement curves so that both increased peak resistance and shear displacement contribute to improved stability. However, it requires a large number of labour-intensive direct shear tests to characterise the stress strain curves for a given vegetation type and study area.